



**Calhoun: The NPS Institutional Archive**  
**DSpace Repository**

---

Theses and Dissertations

1. Thesis and Dissertation Collection, all items

---

1998-09

# An experimental investigation of vortex breakdown in tubes at high reynolds numbers

Novak, Francis G.

Monterey, California. Naval Postgraduate School

---

<http://hdl.handle.net/10945/8370>

---

*Downloaded from NPS Archive: Calhoun*



Calhoun is the Naval Postgraduate School's public access digital repository for research materials and institutional publications created by the NPS community. Calhoun is named for Professor of Mathematics Guy K. Calhoun, NPS's first appointed -- and published -- scholarly author.

**Dudley Knox Library / Naval Postgraduate School**  
**411 Dyer Road / 1 University Circle**  
**Monterey, California USA 93943**

<http://www.nps.edu/library>

**NPS ARCHIVE**  
**1998.09**  
**NOVAK, F.**

DUDLEY KNOX LIBRARY  
NAVAL POSTGRADUATE SCHOOL  
MONTEREY CA 93943-5101







# NAVAL POSTGRADUATE SCHOOL

## Monterey, California



## DISSERTATION

AN EXPERIMENTAL INVESTIGATION  
OF VORTEX BREAKDOWN IN TUBES  
AT HIGH REYNOLDS NUMBERS

by

Francis G. Novak

September 1998

Thesis Advisor:

T. Sarpkaya

Approved for public release; distribution is unlimited.



# REPORT DOCUMENTATION PAGE

Form Approved  
OMB No. 0704-0188

Public reporting burden for this collection of information is estimated to average 1 hour per response, including the time for reviewing instruction, searching existing data sources, gathering and maintaining the data needed, and completing and reviewing the collection of information. Send comments regarding this burden estimate or any other aspect of this collection of information, including suggestions for reducing this burden, to Washington headquarters Services, Directorate for Information Operations and Reports, 1215 Jefferson Davis Highway, Suite 1204, Arlington, VA 22202-4302, and to the Office of Management and Budget, Paperwork Reduction Project (0704-0188) Washington DC 20503.

1. AGENCY USE ONLY (Leave blank)		2. REPORT DATE September 1998		3. REPORT TYPE AND DATES COVERED Doctoral Dissertation	
4. TITLE AND SUBTITLE AN EXPERIMENTAL INVESTIGATION OF VORTEX BREAKDOWN IN TUBES AT HIGH REYNOLDS NUMBERS				5. FUNDING NUMBERS	
6. AUTHOR(S) Novak, Francis G.					
7. PERFORMING ORGANIZATION NAME(S) AND ADDRESS(ES) Naval Postgraduate School Monterey, CA 93943-5000				8. PERFORMING ORGANIZATION REPORT NUMBER	
9. SPONSORING / MONITORING AGENCY NAME(S) AND ADDRESS(ES)				10. SPONSORING / MONITORING AGENCY REPORT NUMBER	
11. SUPPLEMENTARY NOTES The views expressed in this thesis are those of the author and do not reflect the official policy or position of the Department of Defense or the U.S. Government.					
12a. DISTRIBUTION / AVAILABILITY STATEMENT Approved for public release; distribution is unlimited.				12b. DISTRIBUTION CODE	
13. ABSTRACT (maximum 200 words) This thesis deals with non-cavitating swirling flows with vortex breakdown in various tubes. Phenomenological and quantitative investigations were carried out at Reynolds numbers ( $Re_D = U_0 D_0 / \nu$ ) as high as 300,000. It was shown that a high $Re_D$ vortex transitions to its new state (breaks down) via a rapidly spinning spiral form, as demonstrated with 4,000 frame per second video, short exposure time (6 ns) imaging, and Digital Particle Image Velocimetry. Of the known types, the spiral emerges as the fundamental breakdown form and the axisymmetric bubble may now be regarded as a relatively low $Re_D$ occurrence that is bypassed at sufficiently high $Re_D$ . Some new phenomena were observed at high $Re_D$ : Extremely rapid spiral rotation (over 1,000 revolutions per second), core bifurcation, and changes in the sense of the spiral windings. Familiar features of breakdowns, such as the transition from a jet-like to wake-like axial velocity profile and the rapidly expanding vortex core, were observed in extensive time averaged velocity and turbulence results ascertained with Laser Doppler Velocimetry. However, a mean stagnation point and recirculation were absent in the highest $Re_D$ flow. The core meandering and stagnation point darting in the turbulent flow field were quantified and discussed in detail.					
14. SUBJECT TERMS Vortex Breakdown, Turbulence, Laser Doppler Velocimetry, Particle Image Velocimetry, Swirling Flow, Spectra				15. NUMBER OF PAGES 336	
				16. PRICE CODE	
17. SECURITY CLASSIFICATION OF REPORT Unclassified	18. SECURITY CLASSIFICATION OF THIS PAGE Unclassified		19. SECURITY CLASSIFICATION OF ABSTRACT Unclassified		20. LIMITATION OF ABSTRACT UL

NSN 7540-01-280-5500

Standard Form 298 (Rev. 2-89)  
Prescribed by ANSI Std. Z39-18  
298-102





Approved for public release; distribution is unlimited

**AN EXPERIMENTAL INVESTIGATION OF VORTEX BREAKDOWN  
IN TUBES AT HIGH REYNOLDS NUMBERS**

Francis G. Novak  
Lieutenant Commander, United States Navy  
B.S.M.E., United States Naval Academy, 1985  
M.S.M.E., Naval Postgraduate School, 1992  
M.E., Naval Postgraduate School, 1992

Submitted in partial fulfillment of the  
requirements for the degree of

**DOCTOR OF PHILOSOPHY IN MECHANICAL ENGINEERING**

from the

**NAVAL POSTGRADUATE SCHOOL  
September, 1998**



## ABSTRACT

This thesis deals with non-cavitating swirling flows with vortex breakdown in various tubes. Phenomenological and quantitative investigations were carried out at Reynolds numbers ( $Re_D = U_0 D_0 / \nu$ ) as high as 300,000. It was shown that a high  $Re_D$  vortex transitions to its new state (breaks down) via a rapidly spinning spiral form, as demonstrated with 4,000 frame per second video, short exposure time (6 ns) imaging, and Digital Particle Image Velocimetry. Of the known types, the spiral emerges as the fundamental breakdown form, and the axisymmetric bubble may now be regarded as a relatively low  $Re_D$  occurrence that is bypassed at sufficiently high  $Re_D$ . Some new phenomena were observed at high  $Re_D$ : Extremely rapid spiral rotation (over 1,000 revolutions per second), core bifurcation, and reversals in the sense of the spiral windings. Familiar features of breakdowns, such as the transition from jet-like to wake-like axial velocity profiles and the rapidly expanding vortex core, were observed in extensive time averaged velocity and turbulence profiles ascertained with Laser Doppler Velocimetry. However, a mean stagnation point and recirculation were absent in the highest  $Re_D$  flow. The core meandering and stagnation point darting in the turbulent flow field were quantified and discussed in detail.





## TABLE OF CONTENTS

I.	INTRODUCTION .....	1
A.	BACKGROUND .....	1
B.	SURVEY OF PREVIOUS RESEARCH ON THE SUBJECT OF VORTEX BREAKDOWN IN TUBES .....	8
1.	Introductory Remarks .....	8
2.	Phenomenological Observations .....	9
3.	Quantitative Measurements and Numerical Simulations .....	11
C.	SCOPE OF THE PRESENT WORK .....	14
II.	EXPERIMENTAL EQUIPMENT AND PROCEDURES .....	17
A.	FLOW APPARATUS .....	17
B.	LASER DOPPLER VELOCIMETRY (LDV) .....	19
C.	DIGITAL PARTICLE IMAGE VELOCIMETRY (DPIV) .....	22
D.	FLOW VISUALIZATION TECHNIQUES .....	24
E.	MOTION ANALYSIS OF THE VORTEX CORE AND BREAKDOWN POSITION .....	25
III.	HIGH REYNOLDS NUMBER VORTEX BREAKDOWN AND RELATED PHENOMENA .....	29
A.	EVOLUTION OF PHYSICAL EVENTS .....	29
B.	VORTEX CORE MEANDERING .....	33
1.	Introduction .....	33
2.	Experimental Characterization of a Meandering Core .....	35
3.	Assessment of the Effect of Meandering on the Measurements ...	37
4.	Corrections to Velocity Profiles .....	39

5.	Corrections to Turbulence Moments.....	43
6.	Concluding Remarks.....	45
C.	STAGNATION POINT DARTING.....	46
IV.	LASER DOPPLER VELOCIMETRY MEASUREMENTS OF HIGH REYNOLDS NUMBER VORTEX BREAKDOWNS .....	53
A.	GENERAL REMARKS .....	53
B.	RESULTS FROM A REPRESENTATIVE HIGH REYNOLDS NUMBER FLOW.....	54
C.	VARIATIONS INDUCED BY A CHANGE IN TUBE PROFILE..	61
D.	EFFECTS OF REYNOLDS NUMBER VARIATION .....	64
E.	SPECTRA OF TURBULENCE.....	69
F.	ESTIMATION OF THE TURBULENCE DISSIPATION RATE.....	72
1.	Introduction.....	72
2.	Methods for Estimating Dissipation.....	74
3.	Discussion of Results.....	81
4.	Concluding Remarks.....	84
V.	DISCUSSION OF RESULTS.....	85
A.	TECHNOLOGICAL RELEVANCE OF PHENOMENOLOGICAL OBSERVATIONS .....	85
B.	RELEVANCE TO THEORETICAL MODELS.....	92
C.	APPLICABILITY OF PRESENT RESULTS TO NUMERICAL SIMULATION .....	95
VI.	CONCLUSIONS AND RECOMMENDATIONS.....	99

APPENDIX A. FIGURES.....	103
APPENDIX B. MEASUREMENT DETAILS AND EXPERIMENTAL UNCERTAINTY .....	291
LIST OF REFERENCES .....	299
INITIAL DISTRIBUTION LIST.....	307





## LIST OF FIGURES

1-1.	The vortex breakdown forms that are observed in laminar flow (images from the experiments of Sarpkaya (1971)) .....	103
1-2.	The conical vortex breakdown form, which is observed in turbulent flows (images from the experiments of Sarpkaya (1995)) .....	104
1-3.	Instances where more than one axisymmetric bubble appeared in the flow field.....	105
1-4.	The internal structure of a laminar, axisymmetric bubble with two recirculation cells, $Re_D = 2,560$ (experiments of Faler and Leibovich (1978)).....	106
1-5.	The internal structure of a laminar, axisymmetric bubble with two recirculation cells (numerical work of Spall, et al (1990), and Spall and Gatski (1991)).....	107
1-6.	Velocity profiles of a laminar flow field with vortex breakdown and an axisymmetric bubble, $Re_D = 2,300$ (experiments of Uchida, et al (1985)).....	108
1-7.	Internal structure of a laminar, axisymmetric bubble with a single recirculation cell, $Re_D = 840$ (experiments of Brücker and Althaus (1992)).....	109
1-8.	Internal structure of a laminar spiral vortex breakdown, $Re_D = 840$ (experiments of Brücker (1993)).....	110
1-9.	Internal structure of a laminar spiral vortex breakdown (numerical work of Spall and Gatski (1991)) .....	111
1-10.	Internal structure of a turbulent vortex breakdown (numerical work of Spall and Gatski (1995)) .....	112
2-1.	Flow apparatus employed in the present work.....	113
2-2.	Profiles of the tubes used in the present work.....	114
2-3.	Experimental flow apparatus and LDV arrangement .....	115
2-4.	Forward detection receiver optics and manual 3-D traverse.....	116
2-5.	Experimental coordinate system .....	117
2-6.	Physical arrangement of the tube, camera, and light used to record the vortex core motion.....	118

3-1.	Spiral vortex breakdowns in low and high $Re_D$ flows .....	119
3-2.	Low $Re_D$ vortex breakdowns with axisymmetric bubbles.....	120
3-3.	Vortex breakdowns at $Re_D = 44,000$ .....	121
3-4.	Vortex breakdowns at $Re_D = 87,000$ .....	122
3-5.	Vortex breakdowns at $Re_D = 130,000$ .....	123
3-6.	Vortex breakdowns at $Re_D = 175,000$ .....	124
3-7.	Vortex breakdowns at $Re_D = 300,000$ .....	125
3-8.	Low Reynolds number ( $Re_D = 8,700$ ) vortex breakdown with axisymmetric bubble and spiral.....	126
3-9.	Interesting vortex breakdown form observed at $Re_D = 17,500$ .....	127
3-10.	Bubble dimensions and core recovery length variation with $Re_D$ .....	128
3-11.	Images of the spiral breakdown form in the $Re_D = 230,000/h6$ flow state (6 ns exposure) .....	129
3-12.	Images of the spiral form in the $Re_D = 230,000/h6$ flow state (high speed video sequence) .....	130
3-13.	Images of “bifurcated” spirals in the $Re_D = 230,000/h6$ flow state (6 ns exposure).....	131
3-14.	Images of the collapsed spiral in the $Re_D = 230,000/h6$ flow state (6 ns exposure).....	132
3-15.	Images of the conical-like form in the $Re_D = 230,000/h6$ flow state (6 ns exposure).....	133
3-16.	Typical vortex breakdown appearances in the $Re_D = 230,000/h6$ flow state (6 ns exposure).....	134
3-17.	Sequence of images showing compression and expansion of the helix in the $Re_D = 230,000/h6$ flow.....	135
3-18.	Instantaneous velocity vectors and stream traces (DPIV results) in the $Re_D$ $= 230,000/h6$ flow.....	136
3-19.	Instantaneous vorticity and axial velocity contours (DPIV results) in the $Re_D = 230,000/h6$ flow.....	137
3-20.	Time history of vortex core position based on 60 frames per second video.....	138

3-21. Time history of vortex core position based on 1,000 frames per second video.....	139
3-22. Short segment of 1,000 frames per second core position time history.....	140
3-23. Fourier analysis of the vortex core position based on the 60 frames per second video.....	141
3-24. Fourier analysis of the vortex core position based on the 1,000 frames per second video.....	142
3-25. Histograms of the Y and Z coordinates of the vortex core position in the $Re_D = 230,000/h6$ flow state.....	143
3-26. Histograms of tangential velocity at positive Y positions at $X = 70$ mm in the $Re_D = 230,000/h6$ flow state.....	144
3-27. Histograms of tangential velocity at negative Y positions at $X = 70$ mm in the $Re_D = 230,000/h6$ flow state.....	145
3-28. Histograms of tangential velocity near the mean flow centerline at $X = 70$ mm in the $Re_D = 230,000/h6$ flow state.....	146
3-29. Measured and apparent turbulence at $X = 70$ mm in the $Re_D = 230,000/h6$ flow state.....	147
3-30. Measured and apparent Reynolds stress profiles at $X = 70$ mm in the $Re_D = 230,000/h6$ flow state.....	148
3-31. Measured and “corrected” velocity profiles at $X = 70$ mm in the $Re_D = 230,000/h6$ flow state.....	149
3-32. Variation of the time length and estimated true turbulence with window size.....	150
3-33. Histograms of vortex breakdown positions in various $Re_D$ /tube flow states.....	151
3-34. Fourier analysis of the vortex breakdown position history for the $Re_D = 230,000$ flow states.....	152
3-35. Vortex breakdowns in the $Re_D = 120,000/h0$ flow state.....	153
3-36. Vortex breakdown in the $Re_D = 300,000/h3$ flow state.....	154
4-1. Map of LDV data stations in the $Re_D = 230,000/h6$ flow state.....	155
4-2. $U/U_0$ profiles at the inlet of the $Re_D = 230,000/h6$ flow state.....	156



4-3.	W/ $U_o$ profiles at the inlet of the $Re_D = 230,000/h6$ flow state .....	157
4-4.	U and W profiles at $X = 80$ mm in the $Re_D = 230,000/h6$ flow state .....	158
4-5.	U/ $U_o$ profiles at $X = 100$ mm to $X = 140$ mm in the $Re_D = 230,000/h6$ flow state .....	159
4-6.	U/ $U_o$ profiles at $X = 140$ mm to $X = 250$ mm in the $Re_D = 230,000/h6$ flow state .....	160
4-7.	Birds' eye view of the transition from a jet-like to wake-like axial velocity profile in the $Re_D = 230,000/h6$ flow state .....	161
4-8.	Birds' eye view of the evolution of the wake-like profile in the $Re_D = 230,000/h6$ flow state .....	162
4-9.	Reversed flow region and core radii in the $Re_D = 230,000/h6$ flow state .....	163
4-10.	W/ $U_o$ profiles at $X = 110$ mm to $X = 140$ mm in the $Re_D = 230,000/h6$ flow state .....	164
4-11.	W/ $U_o$ profiles at $X = 80$ mm to $X = 190$ mm in the $Re_D = 230,000/h6$ flow state .....	165
4-12.	W/ $W_m$ vs. $Y/R_c$ at various sections in the $Re_D = 230,000/h6$ flow state .....	166
4-13.	Variation of the $U_c$ , $W_m$ , and $R_c$ with X .....	167
4-14.	$u_{rms}/U_o$ profiles in the inlet region of the $Re_D = 230,000/h6$ flow state .....	168
4-15.	$w_{rms}/U_o$ profiles in the inlet region of the $Re_D = 230,000/h6$ flow state .....	169
4-16.	$u_{rms}/U_o$ and $w_{rms}/U_o$ vs. $Y/R_0$ at $X = 110$ mm in the $Re_D = 230,000/h6$ flow state .....	170
4-17.	$u_{rms}/U_o$ and $w_{rms}/U_o$ vs. $Y/R_0$ at $X = 120$ mm in the $Re_D = 230,000/h6$ flow state .....	171
4-18.	$u_{rms}/U_o$ and $w_{rms}/U_o$ vs. $Y/R_0$ at $X = 130$ mm in the $Re_D = 230,000/h6$ flow state .....	172
4-19.	$u_{rms}/U_o$ and $w_{rms}/U_o$ vs. $Y/R_0$ at $X = 135$ mm in the $Re_D = 230,000/h6$ flow state .....	173
4-20.	$u_{rms}/U_o$ and $w_{rms}/U_o$ vs. $Y/R_0$ at $X = 140$ mm in the $Re_D = 230,000/h6$ flow state .....	174
4-21.	$u_{rms}/U_o$ and $w_{rms}/U_o$ vs. $Y/R_0$ at $X = 145$ mm in the $Re_D = 230,000/h6$ flow state .....	175

4-22.	$u_{rms} / U_o$ and $w_{rms} / U_o$ vs. $Y/R_0$ at $X = 150$ mm in the $Re_D = 230,000/h6$ flow state.....	176
4-23.	$u_{rms} / U_o$ and $w_{rms} / U_o$ vs. $Y/R_0$ at $X = 170$ mm in the $Re_D = 230,000/h6$ flow state.....	177
4-24.	$u_{rms} / U_o$ and $w_{rms} / U_o$ vs. $Y/R_0$ at $X = 190$ mm in the $Re_D = 230,000/h6$ flow state.....	178
4-25.	$u_{rms} / U_o$ and $w_{rms} / U_o$ vs. $Y/R_0$ at $X = 250$ mm in the $Re_D = 230,000/h6$ flow state.....	179
4-26.	$\overline{u'w'} / U_o^2$ vs. $Y/R_0$ in the inlet region of the $Re_D = 230,000/h6$ flow state.....	180
4-27.	$\overline{u'w'} / U_o^2$ vs. $Y/R_0$ at $X = 110$ mm to $X = 122.5$ mm in the $Re_D = 230,000/h6$ flow state.....	181
4-28.	$\overline{u'w'} / U_o^2$ vs. $Y/R_0$ at $X = 125$ mm to $X = 140$ mm in the $Re_D = 230,000/h6$ flow state.....	182
4-29.	$\overline{u'w'} / U_o^2$ vs. $Y/R_0$ at $X = 150$ mm to $X = 250$ mm in the $Re_D = 230,000/h6$ flow state.....	183
4-30.	$\overline{u'w'} / U_o^2$ vs. $Y/R_0$ at $X = 80$ mm to $X = 190$ mm in the $Re_D = 230,000/h6$ flow state.....	184
4-31.	$u_{rms} / U_o$ and $w_{rms} / U_o$ vs. $Y/R_c$ at $X = 80$ mm in the $Re_D = 230,000/h6$ flow state.....	185
4-32.	$u_{rms} / U_o$ and $w_{rms} / U_o$ vs. $Y/R_c$ at $X = 130$ mm in the $Re_D = 230,000/h6$ flow state.....	186
4-33.	$u_{rms} / U_o$ and $w_{rms} / U_o$ vs. $Y/R_c$ at $X = 150$ mm in the $Re_D = 230,000/h6$ flow state.....	187
4-34.	$u_{rms} / U_o$ and $w_{rms} / U_o$ vs. $Y/R_c$ at $X = 170$ mm in the $Re_D = 230,000/h6$ flow state.....	188
4-35.	$u_{rms} / U_o$ and $w_{rms} / U_o$ vs. $Y/R_c$ at $X = 190$ mm in the $Re_D = 230,000/h6$ flow state.....	189
4-36.	Circulation ( $\Gamma$ ) profiles at $X = 80$ mm to $X = 190$ mm in the $Re_D = 230,000/h6$ flow state.....	190
4-37.	Normalized circulation ( $\Gamma/\Gamma_c$ ) at $X = 80$ mm to $X = 250$ mm in the $Re_D = 230,000/h6$ flow state.....	191

4-38.	$U/U_0$ profiles at the inlet of the $Re_D = 230,000$ flow state. ....	192
4-39.	$U/U_0$ profiles at the inlet in the core region of the $Re_D = 230,000$ flow state. ....	193
4-40.	$W/U_0$ profiles at the inlet of the $Re_D = 230,000$ flow state. ....	194
4-41.	$W/U_0$ profiles at the inlet of the $Re_D = 230,000$ flow state (core region). ....	195
4-42.	$U/U_0$ profiles in the breakdown region of the $Re_D = 230,000/h3$ flow state.....	196
4-43.	$R_c$ vs. $X$ in the $Re_D = 230,000$ flow states.....	197
4-44.	$W_m$ vs. $X$ in the $Re_D = 230,000$ flow states.....	198
4-45.	$U_c$ vs. $X$ in the $Re_D = 230,000$ flow states.....	199
4-46.	$U/U_m$ vs. $Y/R_t$ at $X = 170$ in the $Re_D = 230,000$ flow states.....	200
4-47.	$W/U_0$ vs. $Y/R_t$ at $X = 170$ mm in the $Re_D = 230,000$ flow states.....	201
4-48.	$u_{rms}/U_0$ vs. $Y/R_0$ at $X = 80$ mm in the $Re_D = 230,000$ flow states.....	202
4-49.	$w_{rms}/U_0$ vs. $Y/R_0$ at $X = 80$ mm in the $Re_D = 230,000$ flow states.....	203
4-50.	$u_{rms}$ vs. $Y$ at $X = 170$ mm in the $Re_D = 230,000$ flow states.....	204
4-51.	$w_{rms}$ vs. $Y$ at $X = 170$ mm in the $Re_D = 230,000$ flow states.....	205
4-52.	Axial variation of $(u_{rms}/U_m)_{r=0}$ in the $Re_D = 230,000$ flow states.....	206
4-53.	Axial variation of $(w_{rms}/U_m)_{r=0}$ in the $Re_D = 230,000$ flow states.....	207
4-54.	$U/U_0$ profiles in the inlet region of various $Re_D$ /tube flow states (core region).....	208
4-55.	$U/U_0$ profiles in the inlet region of various $Re_D$ /tube flow states (full tube).....	209
4-56.	$U$ profiles in the inlet region of various $Re_D$ /tube flow states.....	210
4-57.	Variation of $U_c/U_0$ with $Re_D$ .....	211
4-58.	Variation of $(U_c/U_0)/(\Gamma/\nu)$ with $Re_D$ .....	212
4-59.	$W/U_0$ profiles in the inlet region of various $Re_D$ /tube flow states (core region).....	213
4-60.	$W/U_0$ profiles in the inlet region of various $Re_D$ /tube flow states (full tube).....	214
4-61.	Variation of $W_m/U_0$ with $Re_D$ .....	215

4-62.	Variation of $(W_m/U_0)/(\Gamma/v)$ with $Re_D$ .....	216
4-63.	Variation of $R_c/R_0$ with $Re_D$ .....	217
4-64.	Axial Variation of $R_c$ in various $Re_D$ /tube flow states .....	218
4-65.	$U/U_0$ vs. $Y/R_0$ at $X = 150$ mm in various $Re_D$ /tube flow states .....	219
4-66.	$U/U_0$ vs. $Y/R_0$ at $X = 170$ mm in various $Re_D$ /tube flow states .....	220
4-67.	$U/U_0$ vs. $Y/R_0$ at $X = 190$ mm in various $Re_D$ /tube flow states .....	221
4-68.	$W/U_0$ vs. $Y/R_0$ at $X = 150$ mm in various $Re_D$ /tube flow states .....	222
4-69.	$W/U_0$ vs. $Y/R_0$ at $X = 170$ mm in various $Re_D$ /tube flow states .....	223
4-70.	$W/U_0$ vs. $Y/R_0$ at $X = 190$ mm in various $Re_D$ /tube flow states .....	224
4-71.	$U/U_m$ vs. $Y/R_t$ at $X = 150$ mm in various $Re_D$ /tube flow states .....	225
4-72.	$U/U_m$ vs. $Y/R_t$ at $X = 170$ mm in various $Re_D$ /tube flow states .....	226
4-73.	$U/U_m$ vs. $Y/R_t$ at $X = 190$ mm in various $Re_D$ /tube flow states .....	227
4-74.	$W/U_m$ vs. $Y/R_t$ at $X = 150$ mm in various $Re_D$ /tube flow states .....	228
4-75.	$W/U_m$ vs. $Y/R_t$ at $X = 170$ mm in various $Re_D$ /tube flow states .....	229
4-76.	$W/U_m$ vs. $Y/R_t$ at $X = 190$ mm in various $Re_D$ /tube flow states .....	230
4-77.	$W/W_m$ vs. $Y/R_c$ at $X = 170$ mm in various $Re_D$ /tube flow states .....	231
4-78.	Axial variation of $U_c/U_0$ in various $Re_D$ /tube flow states .....	232
4-79.	Axial variation of $W_m/U_0$ in various $Re_D$ /tube flow states .....	233
4-80.	$u_{rms}/U_0$ profiles in the inlet region of various $Re_D$ /tube flow states .....	234
4-81.	$u_{rms}$ profiles in the inlet region of various $Re_D$ /tube flow states .....	235
4-82.	$w_{rms}/U_0$ profiles in the inlet region of various $Re_D$ /tube flow states .....	236
4-83.	$w_{rms}$ profiles in the inlet region of various $Re_D$ /tube flow states .....	237
4-84.	$u_{rms}/U_0$ profiles in the wake region of various $Re_D$ /tube flow states .....	238
4-85.	$u_{rms}$ profiles in the wake region of various $Re_D$ /tube flow states .....	239
4-86.	$w_{rms}/U_0$ profiles in the wake region of various $Re_D$ /tube flow states .....	240
4-87.	$w_{rms}$ profiles in the wake region of various $Re_D$ /tube flow states .....	241



4-88.	$u_{rms}/U_0$ (vs. $R_t$ ) profiles in the wake region of two high $Re_D$ flow states .....	242
4-89.	$u_{rms}/U_0$ (vs. $R_c$ ) profiles in the wake region of two high $Re_D$ flow states .....	243
4-90.	$\Gamma_c/\Gamma$ profiles in various flow states.....	244
4-91.	Variation of $\Gamma/v$ and $\Gamma_c/v$ with $Re_D$ .....	245
4-92.	Variation of $\Gamma_c/\Gamma$ with $Re_D$ .....	246
4-93.	$W_m/U_0$ vs. $R_c$ for all flow configurations and sections.....	247
4-94.	Measured and q-vortex inlet tangential velocity profiles of the $Re_D = 120,000/h6$ flow state.....	248
4-95.	Measured and q-vortex inlet tangential velocity profiles of the $Re_D = 230,000/h6$ flow state.....	249
4-96.	Measured and q-vortex inlet tangential velocity profiles of the $Re_D = 300,000/h3$ flow state.....	250
4-97.	Spectra of U at X = 250 mm in the $Re_D = 230,000/h6$ flow state .....	251
4-98.	Spectra of W at X = 250 mm in the $Re_D = 230,000/h6$ flow state.....	252
4-99.	Spectra of U at X = 190 mm in the $Re_D = 230,000/h6$ flow state .....	253
4-100.	Spectra of W at X = 190 mm in the $Re_D = 230,000/h6$ flow state.....	254
4-101.	Spectra of U at X = 170 mm in the $Re_D = 230,000/h6$ flow state .....	255
4-102.	Spectra of W at X = 170 mm in the $Re_D = 230,000/h6$ flow state.....	256
4-103.	Spectra of U at X = 150 mm in the $Re_D = 230,000/h6$ flow state .....	257
4-104.	Spectra of W at X = 150 mm in the $Re_D = 230,000/h6$ flow state.....	258
4-105.	Spectra of U at X = 145 mm in the $Re_D = 230,000/h6$ flow state .....	259
4-106.	Spectra of W at X = 145 mm in the $Re_D = 230,000/h6$ flow state.....	260
4-107.	Spectra of U at X = 140 mm in the $Re_D = 230,000/h6$ flow state .....	261
4-108.	Spectra of W at X = 140 mm in the $Re_D = 230,000/h6$ flow state.....	262
4-109.	Spectra of U at X = 135 mm in the $Re_D = 230,000/h6$ flow state .....	263
4-110.	Spectra of W at X = 135 mm in the $Re_D = 230,000/h6$ flow state.....	264
4-111.	Spectra of U at X = 130 mm in the $Re_D = 230,000/h6$ flow state .....	265

4-112. Spectra of W at X = 130 mm in the $Re_D = 230,000/h6$ flow state.....	266
4-113. Spectra of U at X = 80 mm in the $Re_D = 230,000/h6$ flow state .....	267
4-114. Spectra of W at X = 80 mm in the $Re_D = 230,000/h6$ flow state.....	268
4-115. Spectra of U at X = 250 mm in the $Re_D = 120,000/h6$ flow state .....	269
4-116. Spectra of W at X = 250 mm in the $Re_D = 120,000/h6$ flow state.....	270
4-117. Spectra of U at X = 170 mm in the $Re_D = 120,000/h6$ flow state .....	271
4-118. Spectra of W at X = 170 mm in the $Re_D = 120,000/h6$ flow state.....	272
4-119. Spectra of U at X = 170 mm in the $Re_D = 300,000/h3$ flow state .....	273
4-120. Spectra of W at X = 170 mm in the $Re_D = 300,000/h3$ flow state.....	274
4-121. Spectra of U at X = 150 mm in the $Re_D = 120,000/h6$ flow state .....	275
4-122. Spectra of W at X = 150 mm in the $Re_D = 120,000/h6$ flow state.....	276
4-123. Spectra of U at X = 150 mm in the $Re_D = 300,000/h3$ flow state .....	277
4-124. Spectra of W at X = 150 mm in the $Re_D = 300,000/h3$ flow state.....	278
4-125. Spectra of U at X = 135 mm in the $Re_D = 120,000/h6$ flow state .....	279
4-126. Spectra of W at X = 135 mm in the $Re_D = 120,000/h6$ flow state.....	280
4-127. Spectra of U at X = 135 mm in the $Re_D = 300,000/h3$ flow state .....	281
4-128. Spectra of W at X = 135 mm in the $Re_D = 300,000/h3$ flow state.....	282
4-129. Axial variation of frequency of spectral peaks and core rotation rate in the $Re_D = 230,000/h6$ flow state .....	283
4-130. Axial variation of frequency of spectral peaks and core rotation rate in the $Re_D = 120,000/h6$ flow state .....	284
4-131. Axial variation of frequency of spectral peaks and core rotation rate in the $Re_D = 230,000/h3$ flow state .....	285
4-132. Axial variation of frequency of spectral peaks and core rotation rate in the $Re_D = 300,000/h3$ flow state .....	286
4-133. Isotropy parameter in the upstream sections of a swirling flow with vortex breakdown.....	287



4-134. Isotropy parameter in the downstream sections of a swirling flow with vortex breakdown.....	288
4-135. Turbulence kinetic energy dissipation rates in the wake of a vortex breakdown.....	289

## LIST OF TABLES

2-1.	Characteristic parameters of the flows studied in the present work.....	18
3-1.	Pressure gradient parameters in the tubes used in the present work .....	48
3-2.	Standard deviation of the axial position of the vortex breakdown .....	49
4-1.	Equations and numerical constants used to estimate dissipation.....	73
5-1.	Parameters for q-vortex approximations.....	94
B-1.	Uncertainty of various experimental quantities .....	294
B-2.	Estimated experimental uncertainty of velocity measurements in the upstream sections, inside the vortex core.....	295
B-3.	Estimated experimental uncertainty of velocity measurements in the upstream sections, outside the vortex core. ....	296
B-4.	Estimated experimental uncertainty of velocity measurements in the downstream sections.....	297
B-5.	Estimated experimental uncertainty of turbulence measurements. ....	298



## LIST OF SYMBOLS

$A$	Tube cross sectional area
$A_0$	Tube cross sectional area at inlet
$d$	Length scale of the axial velocity jet (or wake) profile
$C$	Numerical constant
$C_\mu$	Empirical constant used to estimate turbulence dissipation
$D$	Tube diameter
$E(\kappa)$	Wave number energy spectra
$E(\psi)$	Flow force
$f$	Frequency (cycles per second)
fps	Frames per second (video recording frame speed)
$H$	Total head function
$I$	Extended circulation
Iso	Isotropy parameter ( $= u_{rms}/w_{rms}$ )
$k$	Turbulence kinetic energy (TKE)
$L$	Characteristic length
$M$	Window size
$N$	Number of instances (Doppler bursts, etc.)
$p$	pressure
$P$	Probability density function of the vortex position
$q$	Nondimensional swirl quantity (Batchelor, 1964)
$Q$	Volumetric flow rate
$r$	radial distance from mean vortex axis (i.e., $ Y $ )
$R$	Tube radius
$R_c$	Core radius
$R_0$	Tube radius at inlet

$R_t$	Tube radius (local)
$Re$	Reynolds number
$Re_c$	Core Reynolds number $\left( = \frac{U_0(2R_c)}{\nu} \right)$
$Re_D$	Tube Reynolds number $\left( = \frac{U_0 D_0}{\nu} \right)$
$Re_\Gamma$	Circulation Reynolds number $\left( = \frac{\Gamma}{\nu} \right)$
$S(f)$	Spectral density function
$u, v, w$	Axial, radial, and tangential velocities (e.g., $u = U + u'$ )
$u', v', w'$	Axial, radial, and tangential turbulent velocity fluctuations
$\tilde{u}, \tilde{v}, \tilde{w}$	Axial, radial, and tangential velocity fluctuation due to unsteadiness
$u_{rms}, v_{rms}, w_{rms}$	Root mean square of velocity fluctuations
$U, V, W$	Ensemble averaged axial, radial, tangential velocity
$\overline{u' v'}$	Cross moment of axial and radial
$\overline{u' w'}$	Cross moment of axial and tangential velocity
$\overline{v' w'}$	Cross moment of radial and tangential velocity
$U_c$	Centerline axial velocity
$U_e$	Axial velocity excess or deficit at the centerline ( $= U_c - U_m$ )
$U_m$	Local mean velocity ( $= Q/A$ )
$U_0$	Mean velocity at tube inlet ( $= Q/A_0$ )
$X$	Axial position from tube inlet
$y$	transformed distance from the centerline ( $= r^2/2$ )
$Y, Z$	Lateral and vertical position from vortex axis
$Y_v, Z_v$	Lateral and vertical position in moving frame (relative to vortex axis)

$Y_p, Z_p$	Lateral and vertical position in measurement probe frame
$\alpha$	Constant used in q vortex equation by Devenport, et al (1996)
$\delta$	Velocity excess normalized by the mean velocity ( $= U_e/U_m$ )
$\varepsilon$	Dissipation of turbulence
$\gamma$	Swirl strength ( $= \Gamma/U_0 D_0$ )
$\Gamma$	Circulation ( $m^2/s$ )
$\kappa$	wave number
$\mu$	molecular viscosity
$\mu_e$	effective viscosity ( $= \mu + \mu_t$ )
$\mu_t$	turbulent viscosity
$\nu$	Kinematic viscosity
$\theta$	Azimuthal position
$\rho$	Density
$\sigma$	Standard deviation
$\sigma_k$	Empirical constant
$\Omega$	Vortex solid body rotation rate
$\omega$	rotation rate (revolutions per second)
$\omega_0$	Minimum swirl level for vortex breakdown (necessary condition)
$\omega_1$	Critical swirl level for vortex breakdown (sufficient condition)
$\psi$	Stream function



CONTENTS

CHAPTER I. THE HISTORY OF THE ART OF PRINTING IN ENGLAND, FROM THE FIRST INTRODUCTION OF THE ART, TO THE PRESENT TIME. 1

CHAPTER II. OF THE ART OF PRINTING IN FRANCE, FROM THE FIRST INTRODUCTION OF THE ART, TO THE PRESENT TIME. 15

CHAPTER III. OF THE ART OF PRINTING IN ITALY, FROM THE FIRST INTRODUCTION OF THE ART, TO THE PRESENT TIME. 25

CHAPTER IV. OF THE ART OF PRINTING IN SPAIN, FROM THE FIRST INTRODUCTION OF THE ART, TO THE PRESENT TIME. 35

CHAPTER V. OF THE ART OF PRINTING IN PORTUGAL, FROM THE FIRST INTRODUCTION OF THE ART, TO THE PRESENT TIME. 45

CHAPTER VI. OF THE ART OF PRINTING IN GERMANY, FROM THE FIRST INTRODUCTION OF THE ART, TO THE PRESENT TIME. 55

CHAPTER VII. OF THE ART OF PRINTING IN SWITZERLAND, FROM THE FIRST INTRODUCTION OF THE ART, TO THE PRESENT TIME. 65

CHAPTER VIII. OF THE ART OF PRINTING IN THE NETHERLANDS, FROM THE FIRST INTRODUCTION OF THE ART, TO THE PRESENT TIME. 75

CHAPTER IX. OF THE ART OF PRINTING IN DENMARK, FROM THE FIRST INTRODUCTION OF THE ART, TO THE PRESENT TIME. 85

CHAPTER X. OF THE ART OF PRINTING IN SWEDEN, FROM THE FIRST INTRODUCTION OF THE ART, TO THE PRESENT TIME. 95

CHAPTER XI. OF THE ART OF PRINTING IN RUSSIA, FROM THE FIRST INTRODUCTION OF THE ART, TO THE PRESENT TIME. 105

CHAPTER XII. OF THE ART OF PRINTING IN POLAND, FROM THE FIRST INTRODUCTION OF THE ART, TO THE PRESENT TIME. 115

CHAPTER XIII. OF THE ART OF PRINTING IN GREECE, FROM THE FIRST INTRODUCTION OF THE ART, TO THE PRESENT TIME. 125

CHAPTER XIV. OF THE ART OF PRINTING IN TURKEY, FROM THE FIRST INTRODUCTION OF THE ART, TO THE PRESENT TIME. 135

CHAPTER XV. OF THE ART OF PRINTING IN INDIA, FROM THE FIRST INTRODUCTION OF THE ART, TO THE PRESENT TIME. 145

CHAPTER XVI. OF THE ART OF PRINTING IN CHINA, FROM THE FIRST INTRODUCTION OF THE ART, TO THE PRESENT TIME. 155

CHAPTER XVII. OF THE ART OF PRINTING IN JAPAN, FROM THE FIRST INTRODUCTION OF THE ART, TO THE PRESENT TIME. 165

CHAPTER XVIII. OF THE ART OF PRINTING IN SINGAPORE, FROM THE FIRST INTRODUCTION OF THE ART, TO THE PRESENT TIME. 175

CHAPTER XIX. OF THE ART OF PRINTING IN MALACCA, FROM THE FIRST INTRODUCTION OF THE ART, TO THE PRESENT TIME. 185

CHAPTER XX. OF THE ART OF PRINTING IN BATAVIA, FROM THE FIRST INTRODUCTION OF THE ART, TO THE PRESENT TIME. 195

CHAPTER XXI. OF THE ART OF PRINTING IN SUMATRA, FROM THE FIRST INTRODUCTION OF THE ART, TO THE PRESENT TIME. 205

CHAPTER XXII. OF THE ART OF PRINTING IN CEYLON, FROM THE FIRST INTRODUCTION OF THE ART, TO THE PRESENT TIME. 215

CHAPTER XXIII. OF THE ART OF PRINTING IN MALAYA, FROM THE FIRST INTRODUCTION OF THE ART, TO THE PRESENT TIME. 225

CHAPTER XXIV. OF THE ART OF PRINTING IN SINGAPORE, FROM THE FIRST INTRODUCTION OF THE ART, TO THE PRESENT TIME. 235

CHAPTER XXV. OF THE ART OF PRINTING IN MALACCA, FROM THE FIRST INTRODUCTION OF THE ART, TO THE PRESENT TIME. 245

CHAPTER XXVI. OF THE ART OF PRINTING IN BATAVIA, FROM THE FIRST INTRODUCTION OF THE ART, TO THE PRESENT TIME. 255

CHAPTER XXVII. OF THE ART OF PRINTING IN SUMATRA, FROM THE FIRST INTRODUCTION OF THE ART, TO THE PRESENT TIME. 265

CHAPTER XXVIII. OF THE ART OF PRINTING IN CEYLON, FROM THE FIRST INTRODUCTION OF THE ART, TO THE PRESENT TIME. 275

CHAPTER XXIX. OF THE ART OF PRINTING IN MALAYA, FROM THE FIRST INTRODUCTION OF THE ART, TO THE PRESENT TIME. 285

CHAPTER XXX. OF THE ART OF PRINTING IN SINGAPORE, FROM THE FIRST INTRODUCTION OF THE ART, TO THE PRESENT TIME. 295

## ACKNOWLEDGMENTS

There are innumerable people I would like to thank personally, but since it would be impossible to include them all, I will mention only those who stand out.

First of all, I feel a deep sense of gratitude to my advisor, Distinguished Professor Sarpkaya. Working for him on the subject of vortex breakdown was a particular honor because of his important previous contributions in the area. It was a fascinating topic that provided seemingly boundless challenges. During the course of this research, he shared countless hours with me. His guidance and discussions instilled in me an appreciation for the art of scientific research as well as the awesome complexity of nature. He has been an inspiration, and a tireless role model. In short, he provided a priceless education.

I also feel indebted to LCDR Craig Merrill, who was the ideal friend and companion during every step of this journey. I wish him and Susan all the best.

I am thankful for being blessed with four wonderfully loving and lovable children. They helped immensely to keep a smile on my face.

From the bottom of my heart, I thank my wife Allison for the love and support she gave me during the past three years. The burdens she bore during this project surely exceeded my own. She was always generous with her time and energy, and gracious and patient with me.

Finally, I thank God for this enriching experience.



# I. INTRODUCTION

## A. BACKGROUND

Vortices found in nature or technology may experience breakdown: a sudden and dramatic change in the structure of the vortex. The occurrence of a vortex breakdown can have profound implications in technological applications such as aerodynamics (most notably in connection with high performance, swept back wing aircraft); and combustion physics (in cases where swirl is imparted on the air and fuel, as in the case of swirl burners). Motivated largely by its importance in these two applications, vortex breakdown has commanded a great deal of attention as a research topic during the past four decades. At the heart of the problem is the desire to develop an understanding of the phenomenon, as well as the ability to predict and control it.

Current practical knowledge remains largely in the qualitative realm, despite voluminous efforts to solve the vortex breakdown problem. Review articles by Hall (1972), Leibovich (1978), Escudier (1988), Delery (1994), and Althaus, et al (1995) summarize previous research, which concentrated on breakdowns in laminar flows. Before discussing reasons for the lack of qualitative knowledge, especially in the more important high Reynolds number regime turbulent flows, it is fitting to describe the phenomenon itself.

When a breakdown occurs, a highly axisymmetric, slender vortex transforms into a turbulent 3-D structure. A jet-like axial velocity profile, and concentrated vorticity in a relatively narrow core characterize the upstream flow. After the breakdown, the axial velocity profile becomes wake-like, and the vorticity spreads out over a larger core that has a much smaller maximum tangential velocity. Also, the flow becomes turbulent in the wake.

One of four apparently distinct forms (or “modes” or “types”, depending on the author) may appear in the immediate vicinity of breakdown. Figure 1-1 shows a

representative photograph of the three that appear in laminar flow. Figure 1-2 gives a picture of the conical breakdown form, which is found in high Reynolds turbulent flows. Nature's selection of the form and location of a breakdown depends upon the parameters of the flow and the environmental conditions. The characteristic parameters include the Reynolds number and swirl number. The ambient factors include, but are not limited to, the type of swirl generator, the symmetry of the boundaries, the magnitude of the adverse pressure gradient, and turbulence.

The first form is the double helix (Fig. 1-1a). This has been observed (Sarpkaya, 1971b) in confined vortices that are characterized by rather low Reynolds number  $Re_D = U_0 D_0 / \nu$  (where  $U_0$  is the mean axial velocity,  $D_0$  is the tube diameter, and  $\nu$  is the kinematic viscosity) and in a narrow range of swirl number  $\gamma = \Gamma / U_0 D_0$  (where  $\Gamma$  is the circulation). Apparently due to an instability, a dye filament introduced at the vortex centerline flattens, and begins to rotate. As it continues to thin, it bifurcates into two distinct filaments. The dye streaks remain coherent for a while, as their span of rotation eventually expands to nearly the radius of the tube. Also, the bifurcated filaments are likely to subdivide again before eventually giving way to turbulence. The double helix is very captivating, but receives less attention than the other forms because it occurs in restrictive circumstances, and is not known to occur in technologically important flows.

A few words about the present selection of Reynolds number are in order. In many cases, the parameter is computed using a constant multiple of  $Re_r = WR_c / \nu$  (where  $W$  is the tangential velocity, and  $R_c$  is the core radius). Although this different Reynolds number gives important clues as to the nature of the flow, there are cases in which it is very large even though viscous effects dominate the flow. For example, in a rotating pipe or cylinder,  $W$  and  $R_c$  may be large because of the solid body-like rotation of the viscous core, but the high Reynolds number is not indicative of the true character of the flow. Thus, we have chosen to use the Reynolds number based on the axial velocity and the tube diameter, as described above.



The second form is the spiral breakdown (Fig. 1-1b). This form also has been regarded as a low  $Re_D$  swirling phenomenon, but one that occurs over a larger range of  $\gamma$  than the double helix. Numerous observations of spiral breakdowns indicate that there is a rapid axial deceleration towards what appears to be a stagnation point. Then, after an abrupt kink, the dye filament expands outward into a helix. After one or two windings of the spiral, the filament breaks up in large scale unsteadiness and turbulence. Among the many interesting features of spiral breakdowns, one that has yet to be explained is that the sense of *windings* is opposite to the main swirling flow when the vortex is confined to a tube, but in agreement with it in the case of free vortices, such as that over a delta wing.

The third form is the axisymmetric “bubble” (Fig. 1-1c). A slight increase in  $Re_D$  or  $\gamma$  precipitates a transformation from the spiral to this ostensibly different form. Sometimes, the breakdown appearance makes periodic changeovers between the two types, and in other instances, a stable bubble appears. In either case, the upstream axial flow in the core decelerates to a stagnation point rapidly, like the spiral, but then expands axisymmetrically into an egg shaped “bubble.” A gyrating torroid that exists in the bubble induces a continuous exchange of fluid with the outer flow by filling and emptying through the downstream end. What appears in the wake of a bubble varies considerably with  $Re_D$ . In the lower range, the vortex core often appears to undergo an impressive reconstruction to nearly its original dimensions, before ultimately breaking down into a spiral structure. In rare cases, this spiral may be preceded by another bubble (or bubbles). Figure 1-3 gives some photographs of this remarkable occurrence. At higher  $Re_D$ , the reconstruction does not appear but rather, the dye emanates uniformly in the shape of a truncated conical tail, extending from the rear end of the bubble. As the  $Re_D$  is raised further, this conical expansion moves upstream until it begins to reside within the bubble itself, as shown in Fig. 1-3a. Another change that occurs when  $Re_D$  is raised is the vortex core and breakdown unsteadiness increases. While low  $Re_D$  breakdowns may hold their



position precisely, higher  $Re_D$  breakdowns undergo irregular radial meandering and axial darting motions.

Until recently, investigators believed these three breakdown forms that appear in laminar flows provided a complete description of the phenomenon. They assumed that an increase in Reynolds number, to the range that it is likely to appear in technology, would not alter the fundamental nature of the breakdown.

However, Sarpkaya (1995a,b) showed that in high  $Re_D$  turbulent swirling flows, the breakdown assumes a conical form, which differs from the three that were just described. The features of the bubble fade as the cone shaped tail moves forward and becomes the defining feature of the breakdown. As shown in Fig. 1-2 (b and c), the dye filament expands gradually into a sharp conical shape. From naked eye flow visualization, it is unclear whether a stagnation point or recirculation zone reside within the cone. Also, the conical breakdown is highly unsteady, because the point at which the dye begins to expand darts to and fro along the axis. Currently, there is no evidence that if  $Re_D$  were raised significantly, a new form would appear.

The conical breakdown appears in real life settings because  $Re_D$  and  $\gamma$  are invariably high in these flows. Since almost all of the research centered on low  $Re_D$  laminar flows, a great deal needs to be learned about the conical form. This will become more clear in the next section. Now, we give a brief discussion of the role vortex breakdown plays in technological applications, and the reasons the problem remains unsolved.

The vortex that results from separation roll-up at the leading edge of a sweptback ( $\delta$ ) wing is liable to break down when the angle of attack is sufficiently high. If the breakdown should occur over the wing, it limits the lift and can cause aircraft stability problems. Another undesirable consequence of the breakdown is the large scale turbulence found in the wake of the breakdown which can induce cyclic stresses, leading

to premature fatigue failure of downstream protuberances on the aircraft. In his review, Delery (1994) discusses vortex breakdown over delta wings in detail.

Combustion is another major application where vortex breakdowns may occur. Many combustion chambers employ swirl for flame stabilization and mixing enhancement, and additionally, if the imparted swirl is sufficiently strong, the vortex is likely to breakdown. Unlike the delta wing, the breakdown is often a desirable feature because the recirculation zone can act as a fluid dynamic flame holder. It enables longer fuel and air mixing times, and when designed properly, the result is more efficient, cleaner combustion. Making optimum use of the breakdown is of great practical consequence, and engineers strive for design parameters that serve this purpose. See for example, Syred and Beer (1974) and Lilley (1977).

A final application in which it is hoped vortex breakdown could play a role is in the demise of trailing vortices generated by large commercial aircraft. For the safety of following aircraft, the time between take-offs and landings must be sufficient for these destructive vortices to dissipate. If a practicable means to precipitate a breakdown can be developed, the delay between runway events may be reduced considerably. The positive consequences would be far reaching in terms of airline scheduling, fuel savings, as well as noise and pollution reduction.

In the applications just described, it is not yet possible to fully exploit the potential benefits of vortex breakdown, or to prevent the deleterious effects to the maximum extent possible. This is because the phenomenon is still not well understood. Four of the reasons the problem defies solution will be discussed here.

The first reason is the various theories that were put forth did not gain wide acceptance. Among the various methods of categorizing the theoretical work, we follow Spall and Gatski (1991) and group them in the following manner:

- Theories based on the critical state concept, Squire (1960), Benjamin (1962, 1964), Bossel (1969). Vortex breakdown is taken to be a transition from a supercritical to a subcritical vortex, analogous to hydraulic jumps and shock waves in compressible flow. A related approach utilizes the mathematical description of wave motion in vortex flows (e.g., Leibovich, 1970).
- Methods analogous to boundary layer approximation (Hall, 1967). The breakdown flow field is treated as being analogous to boundary layer separation. This approach employs a forward marching scheme, under the assumptions that the flow is steady, axisymmetric, laminar, and inviscid. The location in the domain where the computations diverge indicates the predicted position of the breakdown.
- Theories based on hydrodynamic instability, Ludwig (1962), Howard and Gupta (1962), and Lessen, et al (1974). Ludwig treated the flow field as that of a fluid between concentric rotating cylinders. Others sought solutions for infinitesimal disturbances that amplified.
- Recent idealizations, Rusak and his coworkers (e.g., Wang and Rusak, 1997b). Starting with the axisymmetric, inviscid equations of motion, a solution leading to an axisymmetric vortex breakdown in high-Reynolds number swirling flows in a pipe was found from stability and steady state analyses.

The aim of this brief discussion was to introduce the concepts and terms because the theories will be mentioned later. Hall (1972) and Stuart (1987) gave excellent critical reviews of the earlier theories. In essence, none of the theories became regarded as a possible answer to the vortex breakdown problem because they do not possess predictive or explanatory power, or are difficult to test.

Second, parametric investigations for a predictive criteria have met with some success, but only within a confined range of geometric and flow conditions (e.g., Spall, et



al (1987), and Gursul (1995)). For example, in the case of delta wings, modifications to wing geometry, wing dynamics, or free stream turbulence precipitate profound changes to the behavior of the breakdown, making the development of a universal criterion unlikely. Even if a criterion was to be found, the desire to unveil the physics of the phenomenon probably would motivate further studies.

Along the same lines, fluid mechanical means such as suction and blowing (e.g., Myose and Blackwelder (1995), Parmenter and Rockwell (1996), and Yang and Gursul (1997)) and mechanical means such as wing design and wing adaptation (Lowson and Riley (1995), and Deng and Gursul (1997)) can be used to control the occurrence of breakdown, at least at very low Reynolds number. However, a practical means of controlling breakdown in realistic (turbulent) conditions remains elusive.

Another reason the problem has not been solved stems from the difficulties in measuring a swirling flow with vortex breakdown. Physical probes, such as hot wire and pitot tubes, alter the flow field to the extent that it is difficult or impossible to rely upon the results. The advent of non-intrusive means, such as Laser Doppler Velocimetry (LDV) and Digital Particle Image Velocimetry (DPIV), was fortuitous, but not without shortcomings. The LDV measurement volume size can approach the size of the vortex core, and in some cases flow unsteadiness affects the results. DPIV holds promise as a tool to fill the gap in these areas, but only after sizable improvements in frame capture rate, and to a lesser extent resolution, can be made.

The final reason is that numerical prediction schemes have not realized their potential yet, primarily because of the complex nature of the phenomenon, and the lack of experimental data. Any flow field that is highly nonlinear, unsteady, and contains a recirculation zone will challenge any current prediction scheme, and to a high degree, defy success. Vortex breakdown not only possesses these features, but also turbulence. Modeling of turbulence to alleviate the well known closure problem, especially in complex flows, is the topic of intense research. Reviews by Launder (1989), Hanjalic

(1994), and Bradshaw (1996) give details. The predictive capabilities have advanced considerably in the last decade, but nevertheless, conspicuous weaknesses remain. For the present purposes, we note that streamline curvature and adverse pressure gradients, both characteristics of flows with vortex breakdown, compound the difficulties of turbulence modeling. As for empirical data, a set of inlet boundary conditions represents the minimum requirement to support progress in predictive capability of numerical models. Quantitative information regarding the flow field in the breakdown region and in its wake for assessment of the model results also would be of great value. Some data that fits this description, albeit for laminar breakdowns, exist and will be described in the next section. Computer studies hold promise to deliver predictive and explanatory power, but only after advances in turbulence modeling are made, and a comprehensive set of data becomes available.

In summary, despite a great deal of research into this fascinating and important topic the current understanding of the phenomenon is mostly descriptive. Two of the reasons given were the lack of experimental data and the difficulties for numerical work. In the next section, a survey of the progress in these areas will be given.

## **B. SURVEY OF PREVIOUS RESEARCH ON THE SUBJECT OF VORTEX BREAKDOWN IN TUBES**

### **1. Introductory Remarks**

Most investigators studying vortex breakdown employ one of four different types of apparatus: a delta wing mounted in a wind or water tunnel, a swirling flow through a mock combustor, a rotating cylinder or a cylinder with a rotating end (or ends), and swirling flow in a tube. Other devices have been used, but since they are found in a small fraction of the investigations, they will not be discussed here. The delta wing and mock combustor directly model an application where vortex breakdowns are known to occur and to play an important role. The cylinder with a rotating end, on the other hand, does

not match any application. It is ideally suited for comparison with numerical investigations in laminar flows because all of the boundary conditions are known. However, its applicability is questionable because some of the important features of the breakdowns that appear in technology are not preserved (e.g.,  $Re_D = 0$ , no axial deceleration).

Although a swirling flow through a tube is not modeled directly after a real life application, the important features of the breakdown are preserved. Moreover, the tube radius to vortex core radius is very large so that the core is effectively imbedded in an “infinite” environment. While similar to the mock combustor in that the vortex is confined, the angle of tube wall divergence is usually relatively small. An important consequence of this is that the vortex is afforded the opportunity to develop before experiencing breakdown, provided  $\gamma$  is not too strong. This makes the results similar to those of a delta wing. Tubes are ideal for laboratory studies, as evidenced by the numerous important and enlightening flow visualization studies that were done in this type of apparatus.

In the present study, a tube will be employed. As such, a review of previous experimental and numerical research on the subject will be given in this section.

## **2. Phenomenological Observations**

Harvey (1962) conducted a series of flow visualization experiments on vortex breakdown in a tube. Apparently, he was the first to argue that breakdowns could be studied in this setting without compromising the important features of breakdowns that appeared over delta wings. In his experiments, he used a set of guide vanes to introduce swirl to air as it entered a tube. It was clear from observations of smoke that was injected at the centerline, that under appropriate conditions, a nearly axisymmetric bubble appeared. Also, with a suitable flow restriction device placed downstream of the bubble, he found that vortex reconstruction took place and, a short distance downstream, a second



bubble appeared. A photograph is shown in Fig. 1-3. He concluded that the breakdown was a transition between two fundamentally different types of vortex flows, though without much convincing evidence. Also, the formation of a second bubble indicated that this transition was reversible to some degree, leading to his suggestion that a theory based on a “critical” state, such as the one that was later proposed by Benjamin (1962), would be more credible than one based on an instability.

Sarpkaya (1971a, 1971b, 1974) conducted a comprehensive set of experiments designed to examine the behavior and nature of breakdowns under a wide range of flow conditions, and compare the findings to theoretical predictions. He used a guide vane apparatus to impart swirl on water as it entered a tube, and visualized the breakdowns using dye introduced through both centerline and off axis ports. In addition to the bubble, his experiments included extensive observations of the spiral and double helix forms. He observed the phenomenon under a wide range of  $Re_D$  and  $\gamma$ , as well as in transient conditions and various adverse pressure gradients. Hall (1972) had shown mathematically that external pressure gradients are magnified at the centerline of a vortex. Sarpkaya (1974) examined the effect on vortex breakdown by utilizing tubes with various wall profiles.

His experiments lead to the conclusion that it seemed unlikely that a single theory could predict or explain the widely varied characteristics and behavior of vortex breakdowns. Like Harvey, he came to the conclusion that there was good accord between the finite transition theory and observations of the nearly axisymmetric bubble. However, the spiral and double helix forms of breakdown were highly sensitive to small disturbances and gradually expanded before breaking up into turbulence, indicating that these types were a consequence of a hydrodynamic instability. It seemed that no theory could explain both forms.

Beyond demonstrating that the theories seemed insufficient, he also uncovered some complexities of breakdowns. For example, the response to transient flow settings

and in the varied adverse pressure gradient was rather enigmatic. An increase in  $\gamma$  caused the equilibrium position of the breakdown to move toward the swirl generator, an expected result. However, a rapid change in  $\gamma$  caused an initial movement away from the swirl generator before a migration to the final steady location. At the final stages of the excursion, the bubble overshot its equilibrium position. The external pressure gradient also affected vortex breakdown profoundly. Generally, a larger adverse pressure gradient (more rapid tube wall divergence) caused the breakdown to move upstream. However, if the flow separated at the wall, the equilibrium position moved downstream because the effective adverse pressure gradient was reduced. Thus, not only did it appear that more than one physical mechanism was involved, there also was complicated interplay between the breakdown and its surroundings.

Many of the observations made by Sarpkaya have been corroborated by Bellamy-Knights (1976), Faler and Leibovich (1978), Garg and Leibovich (1979), and Suematsu (1982).

The discovery of the conical form of breakdown by Sarpkaya (1995) will alter the emphasis of vortex breakdown research. It had been the prevailing view that breakdowns would be similar whether the flow was laminar or turbulent. Since this new form exhibits striking differences in appearance from the laminar forms, it is assumed that there is a concomitant change to the internal structure.

### **3. Quantitative Measurements and Numerical Simulations**

Faler and Leibovich (1978) gave results of 2-D LDV measurements of the velocity profiles within an axisymmetric “bubble” for  $Re_D = 2,560$ . An important result they reported was the presence of two torroidal recirculation zones within the bubble, as shown by the streamlines in Fig. 1-4. This finding was corroborated numerically by Spall, et al (1990), and Spall and Gatski (1991). Fig. 1-5 shows these simulation results that are qualitatively similar to the experimental findings. Also, Uchida et al (1985)

presented similar experimental results for a bubble in a flow with  $Re_D$  equal to 2,300. In addition to taking measurements in the bubble, they also measured the velocity profiles in the wake, where the vortex had recovered, and all the way to the spiral structure. Figure 1-6 provides these axial velocity profiles. Downstream of the bubble, the axial velocity at the centerline became jet-like in the region the vortex recovery was observed. However, in the vicinity of the spiral structure further downstream, the centerline velocity decelerated to another stagnation point and became negative. Both the flow visualization and the velocity profiles suggest that the structure of the second reverse flow region differs from those inside the bubble. In the bubble, the regions where the flow is against the mean is off the axis, but in the second reverse flow region, the centerline velocity is negative.

Another study of vortex breakdown in a tube was conducted by the group in Aachen, Germany. In this experiment,  $Re_D$  was 840, and  $\gamma$  was such that the breakdown form made periodic transitions between the axisymmetric bubble and spiral. Brücker and Althaus (1992) reported DPIV and flow visualization results for a bubble with an internal structure as shown in Fig. 1-7. The results clearly demonstrated the presence of a single torroidal structure (confirming Sarpkaya's (1971) original observations), with the centerline velocity becoming negative inside the bubble. This important difference from the results of Faler and Leibovich (1978) has not been explained. Brücker (1993) gave similar results for the spiral form. Clearly, this flow field also contained a negative velocity region at the centerline, as shown in Fig. 1-8. The reversed flow region is enveloped by, and intuition suggests that it is induced by, the interspersed regions of positive and negative azimuthal vorticity moving downstream with the flow. This was corroborated in a numerical simulation by Spall and Gatski (1991). Their computed vector field for a spiral breakdown appears in Fig. 1-9. In other numerical work, Spall (1996) produced a vortex breakdown which changed from the spiral to bubble. Under the circumstances of his model, a modest increase in the free stream axial velocity



deceleration, a prescribed boundary condition, would provoke this changeover. The bubble subsequently reverted back to the spiral form.

Brücker (1993) noted the similarities between the spiral and bubble in the experiments where this transition occurred, and made the suggestion that the spiral is the “basic” form of vortex breakdown. He went on to propose that the axisymmetric bubble is actually a spiral, but takes on the different appearance only due to the flow visualization technique. His suggestion was in good accord with his own experimental observations, but he did not make any statements regarding the existing experimental evidence to the contrary, such as Faler and Leibovich (1978) or Uchida et al (1985), or the numerical results of Spall et al (1990) and Spall and Gatski (1991). Moreover, it was not known at the time that the high Reynolds number conical vortex breakdown is distinctively different than those that appear at low Reynolds numbers. Spall and Gatski (1995) investigated a higher Reynolds number flow ( $Re_c = U_o(2R_c)/\nu$  was 10,000, where  $R_c$  is the vortex core radius) in a numerical study. Their scheme predicted a stagnation point followed by a highly axisymmetric bubble with a single recirculation cell, as shown in Fig. 1-10. However, their boundary conditions were based on somewhat arbitrary assumptions because no experimental data existed. Furthermore, there were no flow visualization studies to support or refute their findings.

With the exception of the numerical study of Spall and Gatski (1995), all of the experimental and computational results just described were for rather low  $Re_D$ , laminar flows. No turbulence data were presented in any of the experimental investigations. Measurements of the turbulence moments, such as the root mean square of the velocity fluctuations and the Reynolds stresses, have been measured for high Reynolds number flows in other studies, but not for a swirling flow in a tube. For example, Nejad, et al (1989), and Kihm, et al (1990) presented LDV data that included turbulence moments for vortex breakdown in a mock combustor. In these results, the first streamwise profile

exhibits a wake-like profile. Thus, quantitative measurements of a well developed vortex that is yet to break down do not exist.

Measurements of the spectrum of turbulence in swirling flows with vortex breakdown are also surprisingly limited. Garg and Leibovich (1979) gave results for both spiral and bubble breakdowns in a tube, with  $Re_D$  ranging from 1,480 to 20,660. Although this Reynolds number regime is well below what is likely to be found in nature or technology, some important trends were noticed. Upstream of the breakdown, the curves were rather featureless. Downstream, peaks indicative of coherent structures could be found at about 3 to 18 Hz (3.1 to 17.8, as reported) in the case of the bubble. The characteristic frequencies in the spiral breakdown were slightly higher for a given Reynolds number and position relative to the breakdown (although the highest frequency reported was for a bubble). The sampling frequency was 100 Hz. Conclusions that could be drawn from the data, and agree with expected results, are that the frequency of the energy containing eddies goes up with Reynolds number and down with streamwise distance from the breakdown. A less expected result, the presence of two peaks near the bubble, was likely due to harmonics, as the two frequencies were nearly integral multiples of each other and there was not an appreciable frequency range separating the peaks (as is required if two statistically independent features of the mean flow are producing turbulence).

To our knowledge, there have been no other spectral measurements for vortex breakdown in tubes. Others (Gursul (1996) and Chao, et al (1991)) have done so in a combustor-like apparatus. Since they were done with intrusive measurement techniques, however, the results are of questionable validity and will not be discussed here.

### **C. SCOPE OF THE PRESENT WORK**

The present work was concerned primarily with vortex breakdown in high  $Re_D$ , high  $\gamma$ , swirling turbulent flows in tubes. The objectives of the research were two fold.

One was to raise the overall understanding of the vortex breakdown phenomenon. The other was to use Laser Doppler Velocimetry (LDV) to measure velocities and turbulence quantities of a swirling flow with vortex breakdown in a tube, particularly those of conical breakdown. Hopefully, this data bank will enable numerical investigations to be carried out against the backdrop of archival quality experimental data.

To convey the spirit of the phenomenological results and to prepare the reader for the presentation, a very brief listing of some of the important findings will be given here. At both very high and very low  $Re_D$ , a vortex transitions to its new state, i.e., undergoes a breakdown, via a spiral form. Thus, the spiral emerges as the fundamental form of breakdown, and the captivating axisymmetric bubble is relegated to a secondary position. A number of heretofore unobserved phenomena accompany the high Reynolds number spiral breakdowns: The transition to turbulence and relatively high degree of unsteadiness in the immediate vicinity of the stagnation point, extremely rapid rotation rates, and a number of structural changes to the nascent spiral before an explosive burst into turbulence. The foregoing, as well as their effect on the time averaged LDV results, will be discussed in detail. It will be seen that answers to some of the older, important questions about vortex breakdown will be answered, but explanations for these new phenomena are not known, and perhaps cannot be ascertained using current investigative techniques.





## II. EXPERIMENTAL EQUIPMENT AND PROCEDURES

### A. FLOW APPARATUS

The flow apparatus consisted of a Plexiglastube in which the vortex breakdown occurred, and an adjustable swirl vane assembly housed in an outer chamber, as illustrated in Fig. 2-1. Additional ancillary components not shown included a centrifugal pump, air escape lines, a bank of in-line flow meters, a large (1 m x 1 m x 12 m) reservoir, and requisite valves and piping.

A total of 32 adjustable swirl vanes generated the azimuthal velocity. After entering the outer chamber, the water traveled to the other side, and then passed through the swirl vane assembly and into the test tube. A bellmouth transition piece and curved centerbody ensured a smooth conveyance of the fluid and provided a source of vorticity.

The shaded section of the pipe in Fig. 2-1 was interchangeable, and was the region of interest because this is where the vortex breakdown occurred. The flexibility to change out this section allowed for the breakdown to be observed and measured in tubes with different wall profiles. Three tubes, shown in Fig. 2-2, were used at various stages of the experiment. Each had a gentle  $1.4^\circ$  divergence for the first 100 mm, but varied after that. One continued to diverge at  $1.4^\circ$  until the final diameter was reached, but the other two converged to a throat located 140 mm from the entrance, and then diverged to the final diameter at about 225 mm from the inlet. The tubes were named based on the height of the nozzle wall relative to the straight (diverging)walled tube. Thus, the tube with no convergence is referred to as the “h = 0” tube, and the others are referred to as the “h = 3,” or “h = 6” tubes. The shorthand “h0”, “h3” and “h6” will be used throughout the thesis.

The tubes were machined from three inch solid Plexiglas rods. The factory finish on the outer wall was preserved. The inner wall was machined to the desired profile, ground such that there were no sharp corners, and then polished to a mirror finish.

The concave centerbody that was mounted to the inside end wall of the steel chamber not only ensured smooth flow into the test piece, but also served as inlet ports for flow visualization agents such as food coloring and fluorescein. One port was located at the flow axis, and the other was slightly off the centerline.

The outer chamber was constructed of steel to withstand the pressures necessary to drive the flow at a relatively high rate, and to maintain a sufficient static pressure to prevent cavitation. Valves at the chamber inlet and discharge provided a means to control the flow rate and the static pressure in the chamber independently. Four windows (457 mm by 140 mm by 12.7 mm thick) were installed on the top, bottom and either side of the chamber to provide optical access to the test piece.

In the piping configuration, four in-line flow meters were installed in parallel, downstream of the apparatus. The flow ranges of the meters were 2-20 gpm, 4-40 gpm, 10-100 gpm, and 20-170 gpm.

As shown in Table 2-1, data runs were made with the different test pieces and at various flow settings. In every case, the vane angle was adjusted until the circulation level was sufficient for the vortex breakdown to occur 130 mm to 140 mm from the pipe inlet, but weak enough to avoid the formation of cavitation at the flow axis.

$Re_D = \frac{U_o(2R_o)}{v}$	$Re_c = \frac{U_o(2R_c)}{v}$	$Re_\Gamma = \frac{\Gamma}{v}$	tube	LDV mode
72,000	6,720	50,000	h0	back
120,000	6,000	77,000	h0	back
120,000	7,400	80,000	h6	forward
230,000	10,000	140,000	h6	forward
230,000	10,800	140,000	h3	forward
300,000	10,600	175,000	h3	forward

Table 2-1. Characteristic parameters of the flows studied in the present work.

Throughout the experiments, care was taken to minimize system induced fluctuations. A foam baffle in the chamber damped large scale unsteadiness, and another prevented sloshing in the holding tank. A Helmholtz resonator damped pressure fluctuations in the chamber, and the piping to and from the chamber rested on wooden supports. Escapes for trapped air in the system were opened periodically.

System cleanliness also was carefully maintained. Before and after experiments, the water was filtered through a chamber bypass line with a 10 micron filter. Periodically, a window of the chamber was removed to enable cleaning of the interior surfaces and the outer wall of the test tube. Before a new run was commenced, the test tube was removed to facilitate cleaning of the inside wall as well. At this time, dirt accumulation also was wiped off the vanes and bellmouth.

The apparatus was very similar to that of Sarpkaya (1971a, 1971b, 1974, 1995). In fact, many of the components were used in his earlier investigations.

## **B. LASER DOPPLER VELOCIMETRY (LDV)**

The measurement system was comprised of a 10 Watt Innova Coherent Laser, a Dantec 3-D LDV, a 3-D motorized traversing system for the laser probes, and forward scatter receiving optics mounted on a manual 3-D traverse. Additionally, a personal computer loaded with the "Burstware" software devised and provided by Dantec was used to control the (motorized) traverse as well as the electronics configuration. The Bragg cell in the system was enabled, bringing about a frequency shift between the beams of a given color, allowing for directional ambiguity resolution.

The two traversing systems were stationed on opposite sides of the chamber, as shown in the photograph given in Fig. 2-3. The laser beams passed through a side window and then into the chamber. The scattered light could be detected either by the probes themselves (back scattered energy), or by a separate receiver positioned on the traverse at the opposite side of the chamber (forward scattered energy). Figure 2-4 gives



a reverse angle picture of the forward scatter receiving optics and traverse. The motorized traverse, on which the Laser probes were mounted, moved to designated data collection stations based on an input file in the "Burstware" program. The receiver optics, mounted on the manual traverse, required an adjustment before data collection began at each data station. Additional details of the LDV system, probes, diffraction effects, and the dimensions of the measurement volume are discussed in Appendix B together with the measurement uncertainties.

The LDV was used to measure velocity and turbulence moments profiles as well as the frequency spectrum of the turbulence at selected locations. By ensuring that the measurement volume was in a plane which contained the vortex axis, the velocities in cylindrical polar coordinates could be measured relatively directly. The vertical component was the tangential velocity, while the components in the horizontal plane were converted into the axial and radial components through the use of a transformation matrix. Figure 2-5 shows the coordinate system. Before any data collection run was commenced, some checks were completed to ensure that the coordinates of the traverse (and hence, the measurement volume) were aligned well with the vertical center of the vortex. Methods for checking this included visual observation of the angle at which the beams reflected from the tube (for gross adjustments), and completion of a preliminary data run comprised of 15 to 25 points across the tube. Symmetry and harmony of the velocity profiles, or lack thereof, indicated qualitatively whether the measurement volume was centered. At the final stages of adjustment, the measurement volume position was adjusted in vertical increments of 0.1 mm between these preliminary data runs. When it appeared as though the center had been passed since the last check, the measurement volume height was adjusted one half of an increment back in the other direction and earnest data collection was commenced. No such procedure was employed to center the origin of the measurement coordinates in the horizontal direction because any necessary correction could be done in the computer after the data were collected.



The dimensions of the measurement volumes for each pair of beams was dependent upon the wavelength, but was approximately 0.25 mm in diameter by 7 mm in length. Since all measurements were taken in coincidence mode (0.1 ms window), the effective measurement volume is the intersection of the beams, about 1.3 mm.

In a few of the earlier runs, the back scatter mode was used for velocity profile measurement. At this time, artificial seeding was necessary to achieve reasonable data rates. Some preliminary investigation was done with various reflective particles. The data rates were similar for the different particles tested, but silver hollowed spheres, manufactured by Potter Industries, were selected because they caused less optical fouling over time.

However, it was determined early in this investigation that even with reflective particles, data rates sufficient for measuring turbulence spectra could not be achieved in the coincidence mode with back scattered energy detection. Thus, for almost all of the LDV results that will be presented, the forward scatter detection mode (in coincidence) was used. There were several advantages to using this method. Most importantly, the data rate almost invariably could be made to be in excess of 1 kHz, even with rather low laser power and photomultiplier gain. Another advantage was that reflective particles were unnecessary. All of the runs completed in the forward scatter mode were done without any artificial seeding. A final advantage is that the receiving optics had a 100  $\mu\text{m}$  aperture, the benefit being a further reduction in the measurement volume size (estimated to be 0.1 mm in diameter by 1.2 mm in length).

The number of bursts collected at a particular data station and the spatial increment between adjacent points were decided on the basis of the character of the flow measured and the objective of the measurement (velocity or spectra). The experiments were conducted in such a way that the inlet conditions were determined with the greatest precision possible, and the downstream conditions were investigated sufficiently to elucidate the important and interesting features. As such, the number of bursts and the

linear density of data stations were highest in the core region, upstream of the vortex breakdown. Here, where the velocity gradients were steepest, 30,000 bursts were collected at each station and the spacing was about 0.2 mm. Upstream of breakdown but outside the core, the gradients are nearly zero (except near the pipe wall). In this region, 10,000 bursts were collected and the spacing was 1 mm. Further down the tube, in the wake of the breakdown, 20,000 bursts were collected and the spacing gradually became wider. For example, about 20 mm downstream of the stagnation region, the spacing was about 0.5 mm, but well downstream of breakdown, 1 mm generally was sufficient.

When the purpose of measurements was the determination of the turbulence spectra, the LDV settings such as the laser power and photomultiplier gain and voltage were adjusted to achieve a higher data rate. Typically, the data rate was 1.5 kHz or higher. Also, a much larger number of bursts, in most cases one million, was collected.

### **C. DIGITAL PARTICLE IMAGE VELOCIMETRY (DPIV)**

Some features of the flow were measured, albeit as a largely qualitative exploration, using a TSI Digital Particle Imaging Velocimetry (DPIV) system. This device was comprised of dual New Wave Ng: YAG lasers capable of pulsing at 14.7 Hz each, optical lenses to spread the laser beam into a sheet, a 1000 x 1000 pixel digital PIVCAM manufactured by Kodak Inc., a synchronizer, and a personal computer loaded with TSI Insight software.

The laser probe was mounted above the chamber, with the 2 mm thick pulsing light sheet aimed into the chamber via the top window, and through the axis of the tube. The PIVCAM was stationed on a tripod, viewing the illuminated plane through a side window.

DPIV systems are used to measure the velocity field in the plane of the laser sheet. In the configuration used in this investigation, the axial and radial velocities (and therefore the azimuthal vorticity) were measured. The region near the center of the tube

was captured, but due to laser light reflections, it was not possible to measure the full cross section extending to the tube wall. As such, the vector field in a region extending about 5 mm to 10 mm up and down from the vortex axis was obtained.

As expected, reflective particles were always necessary for successful operation of the DPIV. In the present experiments, hollow glass beads, manufactured by TSI were employed. The particles have a specific gravity of 1.05 to 1.15, and a particle diameter of 6-12  $\mu\text{m}$ . It is impossible to give an accurate quantitative description of the concentration of particles passing through the test piece. Particles were added near the pump suction until a sufficient image density was achieved. About 2 teaspoons of particles added to a clean water in the holding reservoir (1 m x 1 m x 12 m) was sufficient to proceed. Then, the particles resided in holding tank but with time, began to settle out (over a period of days). When the image density dropped due to this settling out, more reflective particles were added. The tank was drained and flushed out periodically because the particles tended to become discolored, and fouled the optical surfaces.

Of the various modes of operation which are available with the system, the “frame straddle” mode was used exclusively in the present work. In this mode, one laser is made to pulse at the end of a camera frame, and the other laser is made to pulse at the beginning of the next frame. Velocities are computed using cross-correlation between the adjacent frames. The advantage of this mode is that since the pulse separation can be reduced to 5  $\mu\text{s}$  or even less, rather large velocities can be resolved. However, the data rate for the pairs of frames is limited to 15 Hz. Low frame capture rate remains an inherent limitation of all DPIV systems.

TSI Insight Software was used to calculate the velocity vectors. Of the choices available, the Whitaker algorithm was used to locate the particle center. Either a 16 x 16 pixel, or a 32 x 32 pixel interrogation spot size was used, corresponding roughly to 0.8 mm x 0.8 mm, or 1.6 mm x 1.6 mm physical spots. Vectors were computed such that there was about one vector for every 8 pixels, yielding roughly 50% overlap of the 16 x



16 pixel spots, and 75% overlap of the 32 x 32 pixel spots. Smaller spots proved to yield a relatively large number of unreliable velocity vectors, about 20%. Larger spots made it impossible to resolve the fine scaled structures in the flow.

The local flow settings dictate a reasonable pulse separation. As a rule of thumb, the greatest distance a fluid particle is expected to travel in a pulse separation time ought to be less than 0.25 times the interrogation spot size. This reduces the likelihood that a large portion of the particles will be unavailable for correlation because they departed the interrogation spot. On the other hand, the pulse separation should be long enough that the particle moves a sufficient distance to discriminate the change in the image position. In the present experiments, the pulse separation was set to  $5\mu\text{s}$  to  $10\mu\text{s}$ , depending on the location of the flow under investigation.

As a closing statement regarding our DPIV results, it should be emphasized that they are intended to be qualitative in nature. A vortex breakdown flowfield is highly three dimensional, so that flow normal to the light sheet is expected to be significant. Also, the steep velocity gradients make it difficult to satisfy the pulse separation time requirements for the entire field of view. Although these features of the flow field create difficulties when using DPIV, the opportunity to obtain interesting qualitative information exists.

#### **D. FLOW VISUALIZATION TECHNIQUES**

Various combinations of cameras, lighting, and flow visualization agents were used to capture the features of vortex breakdown over a range of Reynolds numbers from 2,500 to over 300,000. Each of these combinations will be described here.

A Redlake Motionscope camera and monitor system, with frame rates up to 4,000 frames per second (fps) and shutter speeds up to 20 times (i.e.,  $1/80,000$  second exposure), was used to record high speed video sequences. Medium diffuse back lighting was used to illuminate the vortex core and/or breakdown, and food coloring was introduced either at the center of the vortex or just off the axis. After being recorded, the

Motionscope system footage can be previewed at various playback frame rates on the monitor. For archival purposes, the footage was played back at 30 fps and recorded on SVHS tape.

Either an NEC CCD camera or a Sony Shoulder mounted camera were used to record video sequences at the standard speed of 30 frames per second. The NEC camera images exhibited excellent clarity, even with rather low lighting. Although the Sony camera required more lighting, it possessed the advantage of a variable shutter speed up to 1/2000 sec. For both cameras, medium or low back and/or front lighting was employed, and food coloring was introduced through the center or off center ports.

The NEC camera also was used in a configuration in which a pulsing laser was used for illumination. The Ng:YAG laser, which is a component of the PIV system (see preceding section), was used as a "flash." Although the camera does not have a variable shutter, the duration of the laser pulse, only 6 ns, becomes the effective exposure time for each frame. Fluorescein sodium salt with 70% dye content was mixed with water and used as the visualization agent. It was introduced through the center or off-center ports.

## **E. MOTION ANALYSIS OF THE VORTEX CORE AND BREAKDOWN POSITION**

A flow visualization technique was designed with the specific objective of establishing the instantaneous 2-D position of the vortex core. A Spectra Physics Stabilite 2017 laser with an optical train was used to generate a light sheet. The laser probe was mounted above the chamber and oriented with the light aiming downward, and through the top window of the chamber. The position and orientation of the probe was selected such that the light was vertical, and sliced through the tube at about 70 mm from the entrance (which was about 65 mm upstream of the breakdown). The plane was not normal to the tube axis, however, but rather at a 45° angle. Figure 2-6 illustrates the configuration.



By introducing fluorescein dye through the centerbody injection port that is located at the flow axis, a bright spot appeared at the intersection of the dye filament and the light sheet. This spot indicated the position of the vortex core within the plane of the light. The Redlake Motionscope camera was mounted on a tripod adjacent to the chamber, such that it viewed the events through a side window, along an optical path which was perpendicular to the flow axis.

The camera was used to record the motion of the bright spot. Sequences of images were made at two rates, 60 fps, and 1,000 fps, to allow for both the long and short scale unsteadiness to be resolved. The images were stored on SVHS tape, and then digitized as they were downloaded to a PC using a frame grabber.

The vertical position of the spot was a direct representation of the vertical position ( $Z$ ) of the vortex core, and the lateral position of the spot was a projection of the position towards (or away) from the camera ( $Y$ ). Because of the orientation of the light, if the core moved away from the camera, the spot moved an equivalent distance to the left, as observed by the camera. On the other hand, if the vortex core moved toward the camera, the bright spot moved to the right.

A scale for spatial calibration was mounted on the tube wall, directly below the centerline of the tube.

Using OPTIMAS MA software, each spot image was viewed, and “targets” were assigned to the top, bottom, left, and right edges of the spot. The software uses the position of the targets to generate a file containing, among other things, the position and velocity of each target at each time (frame).

The time history of each target was exported to a spreadsheet. The horizontal position of the vortex at each time was taken to be the average of the left and right targets, and the vertical position was the average of the top and bottom targets. Since the origin assumed by the software is the lower left hand corner of the field of view, which was an arbitrary position, the mean position of all images was subtracted from the  $Y$ ,  $Z$

coordinates at each time. This made the coordinates relative to an approximate mean centerline.

This final, conditioned file was further manipulated to establish statistical quantities such as histograms, and standard deviation of the position of the vortex core.

In a similar manner, the axial position of the vortex breakdown was ascertained from recordings made with the Redlake Motionscope camera and monitor system. Food coloring was introduced through the centerline dye introduction port, and illuminated with medium diffuse backlighting. The footage was recorded on SVHS tape, and subsequently digitized to a PC using a frame grabber. Using OPTIMAS MA software, each frame was viewed and a “target” was assigned to the location where the dye filament began to expand. The software generated a time history of the target.

The time history was exported to a spreadsheet. After some conditioning to make the image coordinate system origin coincident with the physical origin, the file was used to analyze the motion of the vortex breakdown stagnation point.



### III. HIGH REYNOLDS NUMBER VORTEX BREAKDOWN AND RELATED PHENOMENA

#### A. EVOLUTION OF PHYSICAL EVENTS

The conical breakdown was described in the first chapter of this thesis as a form that emerged from the axisymmetric bubble over an ostensibly wide range of Reynolds numbers. Subsequent high speed video images of the “cone” revealed that a rapidly spinning spiral structure that bears a strong resemblance to the low  $Re_D$  spirals is present, as shown in Fig. 3-1. Although the structure is helical, it appears conical to the naked eye because of its very high rotation rate. Since the high  $Re_D$  vortex breakdown is the central topic of this thesis, it was decided to investigate thoroughly the emergence of this new form using the short exposure time and high frame rate video recording devices.

A flow visualization study was undertaken with the objective of depicting the evolution of the high  $Re_D$  vortex breakdown form. During this aspect of the present work,  $Re_D$  was varied from 2,600 to over 300,000, and the circulation was set such that the breakdown occurred between  $X \approx 60$  mm and  $X \approx 135$  mm (where  $X$  is the axial distance from the tube entrance).

In low  $Re_D$  regime flows (below about 35,000), a nearly axisymmetric bubble form appeared. Figure 3-2 gives representative images that were captured using the 6 ns laser pulse for illumination. In each of the flows, there was a well formed axisymmetric bubble with a “tail” extending from the downstream end, indicating that a reconstruction of the vortex core had taken place. This recovery region persisted for approximately one bubble length, where a structure that strongly resembles the spiral breakdown developed. Numerous investigators reported this sort of appearance before (e.g., Fig. 6 in Sarpkaya (1971a), Fig. 7 in Sarpkaya (1971b), Fig. 1 in Bellamy-Knights (1976), Fig. 1 in Faler and Leibovich (1978), Fig. 4 in Uchida, et al (1985), or Fig. 13 in Escudier (1988)).



In these relatively low  $Re_D$  flows, the size of the bubble and the length of the recovery region decreased with increasing  $Re_D$ , a fact that is readily apparent because the scale for each of the images in Fig. 3-2 is the same. The bubble observed in the  $Re_D = 2,600$  flow (Fig. 3-2a), for example, was about twice the size of the bubble found in the  $Re_D = 35,000$  flow (Fig. 3-2f).

As  $Re_D$  was increased through the intermediate range (roughly, 35,000 to 100,000), the bubble continued to decrease in size and the core recovery length became so short that the spiral encroached upon the bubble. Representative images of these breakdowns are shown in Figs. 3-3 and 3-4, which also were captured with the 6 ns illumination. When  $Re_D = 44,000$  (Fig. 3-3), there was still a well formed bubble and recovery in some of the images (Fig. 3-3a, b, c), even though the spiral was very near the bubble. In other images, however (Fig. 3-3 d,e), the spiral was disturbing the smooth bubble surface. When  $Re_D = 87,000$  (Fig. 3-4), this interaction and mutual interference between the spiral and bubble occurred almost constantly. However, the spiral imposed its influence on the bubble more assertively, agitating and distorting the bubble form to the extent that it was barely discernible.

In high  $Re_D$  flows (above 100,000 or so), the spiral bypassed the bubble form. Figures 3-5 through 3-7 show these breakdowns in another presentation of images taken with the 6 ns illumination. When  $Re_D = 130,000$  (Fig. 3-5), the breakdown form was a spiral, to the exclusion of the axisymmetric form that preceded it in the lower  $Re_D$  flows. In the  $Re_D = 175,000$  and  $Re_D = 300,000$  flows (Figs. 3-6 and 3-7, respectively), this became even more prominent. The dye filament apparently decelerated, developed a kink, and evolved into a helical structure, just as it would in a low  $Re_D$  spiral breakdown. A difference noted here is that frequently, there were fewer identifiable spirals before the dye filament experienced an explosive burst into turbulence.

Besides the visual images, the size of the bubble and recovery length at various  $Re_D$  also suggest that the spiral bypasses the low  $Re_D$  axisymmetric form. Some



quantitative results that were extracted from the flow visualization images support this. A low  $Re_D$  breakdown with an axisymmetric bubble form is shown in Fig. 3-8. The average bubble length (AB) and recovery length (BC), as shown in Fig. 3-8, as well as the bubble diameter, were determined from a number of images corresponding to each  $Re_D$  below 50,000. At higher  $Re_D$ , these dimensions became indiscernible because the spiral resided within the bubble, making it unclear where the bubble ended and spiral began. Furthermore, the estimated “bubble diameter” was ambiguous at such an intermediate  $Re_D$  because it could actually represent the diameter of the first spiral winding. Figure 3-9 gives an interesting example where, even at  $Re_D$  as low as 17,500, the bubble length and diameter were unidentifiable.

The average dimensions of the bubble and recovery are shown in Fig. 3-10. They exhibit a clear tendency to decrease with increasing  $Re_D$  and apparently, both quantities would vanish when  $Re_D \approx 100,000$ . This is in good agreement with the qualitative observations just described, i.e., the spiral bypasses the bubble at high  $Re_D$ .

Additional images of the high Reynolds number spiral breakdown, taken with 6 ns illumination, are shown in Fig. 3-11, and a sequence of high frame rate video is presented in Fig. 3-12. These are provided to emphasize that the appearance of the high Reynolds number breakdown is amazingly similar to what is observed at very low Reynolds number. Attempts were made to ascertain the rotation rate of the spiral, but the breakdown appearance made frequent, but non-periodic transitions to other degenerate forms that will be described next. Even with 4,000 fps video recordings, it was impossible to estimate the rotation rate with confidence, except that it is in the neighborhood of 1,000 Hz. Thus, to the naked eye or in standard speed video, this spiral structure appeared as a conical wedge (Fig. 1-2) because it is spinning so rapidly.

Had the breakdown been free from the darting motion and other disturbances in the flow, we believe that the spiral would have exhibited itself at all times. However, in reality, three transitional forms appeared occasionally. One appeared much like a plain

spiral, except that at some point between the germination of the spiral and its demise into turbulence, the helical winding bifurcated into two filaments. Figure 3-13 provides examples of bifurcated spirals. In some instances, the core was observed to give rise to multiple windings, or ‘trifurcate’. This phenomenon is not known to occur at low  $Re_D$ . After splitting, the filaments rotated about a common axis, and after a few windings, broke up into turbulence. In the second transient form, shown in Fig. 3-14, the individual windings became temporarily indistinguishable because of changes to the helix angle of the spiral. When the windings compress sufficiently, the spiral momentarily collapses into a single torroidal structure. The final transitional form, shown in Fig. 3-15, had a conical appearance. It seemed that this form arose when the transition to turbulence at the centerline moved upstream of the stagnation point. Even when frozen by a 6 ns exposure time, the filament expanded smoothly and axisymmetrically into a conical wedge. Further downstream, there were hints of a spiral-like structure within the well mixed wedge of dye.

It is pointed out that the typical appearance of the breakdown was a combination of the spiral and perhaps one or more of its transient forms. A few examples are given in Fig. 3-16. In Fig. 3-16a, the helix angle of the windings appears so steep that the spiral is about to collapse upon itself. In Fig. 3-16b, the form at the stagnation point seems to be a collapsed helical structure, but what followed was clearly spiral windings with bifurcations. Finally, to further illustrate the spiral collapsing into a single torroid, Fig. 3-17 gives a high speed video sequence of images that illustrate the spiral compressing and expanding.

The existence of a spiral structure in the high  $Re_D$  vortex breakdown was confirmed using DPIV. Representative results are shown in Fig. 3-18. The vector diagram and stream traces portray a flow field that is characterized by alternating vortices being shed from a stagnation point. Qualitatively, the appearance is nearly identical to the very low  $Re_D$  breakdown reported by Brücker (1993). The vorticity and axial

velocity contours, shown in Fig. 3-19, also conform with what one would expect of a spiral. There were interspersed regions of azimuthal vorticity, positive on one side of the centerline and negative on the other, slowly expanding away from the axis. Clearly, the regions of concentrated vorticity correspond to the vortical structures in Fig. 3-18. The axial velocity often becomes negative near the centerline, as seen in Fig. 3-19b, because the vorticity in the spiral windings is sufficient to induce a velocity that is against the prevailing flow direction.

The DPIV results were not strictly redundant with the flow visualization. When the fluorescein dye diffuses rapidly because of turbulence, the internal structure is indiscernible. The DPIV results, however, show the presence of a spiral, even 50 mm downstream of the breakdown. This is remarkable when one considers the dye filament becomes nearly conical within, at most, 20 or 30 mm of the stagnation point.

To summarize the main points of this section, we have seen that the high  $Re_D$  breakdown can take on a number of forms, but the most basic structure is the spiral. As  $Re_D$  is increased from relatively low values, the spiral breakdown that was found in the wake of the axisymmetric bubble bypasses the axisymmetric form.

It is pointed out that the foregoing should be kept in mind when considering the results of a time averaged measuring device such as LDV. Althaus, et al (1995) made the observation that the LDV measurements of a spiral vortex breakdown (Nakamura and Uchida, 1987) look similar, as expected, to those of a bubble-type breakdown.

## **B. VORTEX CORE MEANDERING**

### **1. Introduction**

It seems likely that all vortices are characterized by some amount of unsteadiness in the form of core meandering. In most previous experiments on vortical flows, when the Reynolds number and circulation were relatively low, the amplitude of the core motion was probably inconsequential. In the present work, however, it was noticed that when



$Re_D$  was increased above roughly 50,000, the core began to move visibly about a mean centerline.

When an unsteady flow is measured by an Eulerian measurement technique, e.g. LDV, the ensemble results represent an average over both time and space because the measuring location remains fixed but the flow gradient does not. This complicates the interpretation of the results, especially when the velocity gradients are steep, as they were in the present investigation.

The qualitative effect of this motion on the results can be determined intuitively. First, recall that LDV results are analogous to the terms that appear in the time averaged equations of motion, such as the Reynolds Averaged Navier Stokes (RANS) equations. An underlying assumption, in both the experimental and analytical cases, is that the instantaneous velocity used to estimate the ensemble averages is the simple sum of the mean and turbulent components. For example, we have for the axial velocity:

$$u = U + u' \quad (3-1)$$

Here,  $u$  is the instantaneous velocity,  $U$  is the mean velocity, and  $u'$  is the instantaneous fluctuation from the mean. In an unsteady flow, however, the instantaneous velocity is comprised of three components: the mean and turbulent components, plus the variation from the mean which is due to meandering. Incorporating this term, we have the following equation for the instantaneous velocity:

$$u = U + u' + \tilde{u} \quad (3-2)$$

Here,  $\tilde{u}$  is the deviation from the mean which arises because of unsteadiness, but not because of turbulence. It is referred to as “induced” or “apparent” turbulence because it is absorbed into the measurement of the fluctuations ( $u_{rms}$ ) as well as the Reynolds stress (e.g.,  $\overline{u' w'}$ ).

A nontrivial unsteady component in a swirling flow will contaminate the experimental results such that the maximum measured velocities will be less than what physically exists. Imagine we have a perfectly laminar vortex that is not meandering, with

a measurement volume positioned precisely at the point where the tangential velocity is maximum. If this fictitious vortex were caused to meander, the true maximum velocity will be “seen” only as it passes through the measuring volume. At all other times, lower velocities will be recorded and the resulting time averaged value will be reduced. Through similar reasoning, one can conclude that the centerline axial velocity excess (or deficit) will be underestimated, and the size of the vortex core will be overestimated. Also, the time averaged results will suggest that the flow is turbulent, at least to some degree.

The magnitude of this effect may be significant. Devenport, et al (1996) reported that if the standard deviation of the meandering amplitude is 50% of the core radius ( $R_c$ ), the measurements will overestimate  $R_c$  by 64% and underestimate  $W_m$  (the maximum tangential velocity) by the same amount. His estimates were made using a velocity correction scheme based on the work of Baker, et al (1974). This technique will be summarized and implemented using actual experimental results later in this section.

Meandering also may contaminate the turbulence measurements. As an example, Westphal and Mehta (1989) conducted an experiment in which a vortex was forced to oscillate (by moving the apparatus) at a low frequency and at an amplitude roughly equal to the core radius. When compared to the measurements of a vortex that was not oscillated, the Reynolds stress  $\overline{u'w'}$  was 50% larger. At present, instrumentation is unable to discriminate between velocity fluctuations which are due to unsteadiness and those which are due to turbulence. Therefore, quantities such as turbulent kinetic energy (TKE) and the Reynolds stresses will be overestimated by an amount that is dictated by the velocity gradients and meandering amplitudes.

## **2. Experimental Characterization of a Meandering Core**

It is important to assess the degree of influence of meandering on the measurement of velocities and accelerations. Under circumstances (relatively low Reynolds numbers) where the vortex core is sufficiently stationary, it will be safe to assume that the



measurements will be highly reliable, i.e., unaffected by meandering. However, in swirling flows with very high Reynolds numbers, meandering of the core in all diametrical directions becomes perceptible, as well as measurable. This fact, coupled with the large radial gradients, makes it necessary that the effect of meandering on all velocities and turbulence quantities be assessed in as much detail as possible. In cases where this assessment suggests the results have been contaminated, a correction to the profiles and decomposition of apparent and true turbulence seem mandatory. However, the procedures for doing so are not well established, but rather comprise a current subject of research. Even in cases where the unsteadiness is due to a relatively easily quantified aspect of the apparatus, as in the case of flow near a turbomachinery blade, this matter is unsettled (e.g., Eisele, et al, (1997), and Zhang, et al (1997)).

To this end, a quantitative investigation of the meandering motion was conducted. The results were used to assess the effect of meandering on the experimental results, and to facilitate corrections schemes. The  $X = 70$  mm section in the  $Re_D = 230,000/h6$  flow configuration was studied. Time histories of the vortex core position, based on the 60 fps (frame per second) and 1,000 fps video are given in Figs. 3-20 and 3-21, respectively. At times, the core wandered over 0.75 mm from the centerline, which is remarkable because it will be shown in the next section that the measured core radius is only about 1 mm.

Strictly speaking, meandering was neither periodic nor random. The core oscillated about its mean position but neither the frequency nor the amplitude was fixed. This is apparent from visual inspection of Figs. 3-20 and 3-21, and also of Fig. 3-22, which shows a shorter segment of the high speed data. The higher frame rate results demonstrate that rapid irregular oscillations occurred about a more slowly changing vortex position. Fourier analysis results did not reveal dominant, characteristic frequencies in either the slow or the fast video results. The results are shown in Fig. 3-23 for the 60 fps video, and Fig. 3-24 for the 1000 fps video. Since the motion does display cyclic behavior, an effective amplitude of sinusoidal motion was estimated, and found

from visual observations to be about  $A = 0.40$  mm. The histograms of both the Y and Z coordinates of the vortex core were approximated well by Gaussian probability density distributions, as shown in Fig. 3-25. The standard deviations ( $\sigma$ ) were 0.23 mm for both the lateral (Y) and vertical (Z) positions, and 0.32 mm for the distance from the centerline. As expected, the most probable distance from the mean axis was non zero, roughly 0.2 mm. This is in close agreement with the probability density function of the total radial distance from the mean centerline, which is the transformed variable  $r = \sqrt{X^2 + Z^2}$ . This, coupled with the lack of dominant frequencies suggests that the motion is perhaps more random than periodic.

### **3. Assessment of the Effect of Meandering on the Measurements**

Two methods were used to ascertain whether the LDV results in the present investigation were influenced by the vortex core meandering just described. One was an inspection of the velocity histograms, and the other was a rough calculation of the “induced” turbulence based on the measured velocity gradients and the experimentally determined meandering amplitude. It will be shown that both of these methods clearly indicate that the core motion affected the results.

The histograms of the measured tangential velocity at various radial stations (in the same flow state described in the last section) are shown in Figs. 3-26 and 3-27. Examining Fig. 3-26, it is apparent that as the measuring volume approached the vortex core from a positive Y position outside the core (Fig. 3-26), the histogram became wider as the mean velocity increased (Figs. 3-26a and 3-26b). Then, when positioned within the measured core radius, a large amount of relatively high velocity particles continued to pass through the measuring volume, but a second concentration of velocities with zero mean velocity also was observed (Fig. 3-26c). Near the centerline, there were a large number of instances centered about three different values: a large negative and positive velocity, along with the zero mean velocity (Fig. 3-26d). Proceeding away from the

centerline in the other direction, the same trends were observed in reverse (Fig. 3-27). The two histograms that correspond to positions very near the mean centerline, shown in Fig. 3-28, make it apparent that during the course of measurement, both edges of the vortex core reside in the measuring volume for an appreciable amount of time.

Estimating induced turbulence has been done before by others. For example, Chow, et al (1997) gave a reasonable and simple approach. They deduced a meandering amplitude based on visual observations, and assumed the motion was sinusoidal. Under these conditions, the root mean square of the velocity fluctuations that was due to meandering is roughly equal to:

$$\sqrt{\bar{u}^2} \leq \frac{A}{\sqrt{2}} \left| \frac{\partial U}{\partial r} \right| \quad (3-3)$$

If the quantity estimated with Eq. (3-3) is small relative to the measured fluctuations, then it is safe to assume that the vortex core motion is not influencing the results.

The effect of meandering on the present results was estimated in this manner, and also using a technique that is arguably more accurate. In the second approach, the velocity profiles were approximated by q-vortex equations (Batchelor, 1964), and the motion of the mean vortex axis was simulated by displacing the vortex centerline through a single cycle of a sinusoidal. The root mean square of the velocity fluctuations in a stationary reference frame was then computed. The two methods yielded nearly identical predictions of the induced turbulence, as shown in Fig. 3-29. Since the method given by Chow, et al (1997) is considerably simpler, it is recommended.

Figure 3-29 also shows that within about 3 core radii of the centerline, where the radial velocity gradients are large, the induced turbulence is on the same order as the measured. It would be dangerous to draw conclusions about specific values because the induced turbulence profile is strictly a rough estimate, but it is safe to assume that the induced turbulence is a significant component of the measurements in this region. Outside



this central region of the tube, the induced turbulence is small, raising the confidence that the measured data in this portion of the flow field is reliable.

The outcome is similar in the case of the Reynolds stresses, as shown in Fig. 3-30. Using the q-vortex equation subjected to simulated meandering as described before, an estimate of the apparent  $\overline{u'w'}$  profile was determined. Within about three core radii of the mean centerline, where the radial velocity gradients are steepest, the profile of the apparent Reynolds stress shares the same shape and the same order of magnitude as the measured values. This leaves little doubt that the measured stresses in the central part of the tube, where the vorticity is concentrated, are greatly affected by the core motion. It is interesting that just outside the core, the induced value exceeds the measured value. This would be physically possible if the “true” stress is actually a negative value. Again, it would be dangerous to extract any exact values from the apparent stress curve, but there is concern that beyond changes to the values of the measurements, the overall shape of the profile may have been altered.

#### **4. Corrections to Velocity Profiles**

It was stated earlier that vortex core meandering will influence the measured velocity profiles. Physical reasoning leads to the conclusion that the maximum tangential velocity and centerline axial velocity will be underestimated, and the core radius will be overestimated.

The most rigorous attempt to “correct” swirling flow data to compensate for meandering was done by Devenport, et al (1996), using a scheme that was first reported by Baker, et al (1974). After using a hot wire to collect velocity and turbulence data for a trailing vortex, Devenport, et al (1996) set out to resolve the profiles that would have been measured by an instrument that was positioned in a reference frame whose origin was on the meandering vortex axis. The procedure will be outlined briefly, followed by the a description of the findings upon application to the present results.

They started with the assumption that the probability density function of the vortex core position was known:

$$P = P(Y_v, Z_v) \quad (3-4)$$

Then, the time averaged measured velocity should be represented by:

$$U(Y_p, Z_p) = \int_{-\infty}^{\infty} \int_{-\infty}^{\infty} P(Y_v, Z_v) U(Y_v, Z_v) dY_v dZ_v \quad (3-5)$$

The subscripts  $p$  and  $v$  denote probe and vortex, respectively. Thus,  $U(Y_p, Z_p)$  is the measured mean axial velocity in the static physical coordinate system of the probe.  $U(Y_v, Z_v)$ , which is one component of the desired results, is the mean axial velocity in a coordinate system that is relative to the vortex center. They used two methods to arrive at an estimated  $U(Y_v, Z_v)$  and  $W(Y_v, Z_v)$  (the axial and tangential velocities). The first was called the “q-vortex method,” because equations similar to those given by Batchelor (1964) were employed for the purpose of approximating the profiles. The second, which they referred to as the “general method,” makes use of a series of exponential terms to approximate the measured profiles.

To implement the q-vortex method, the joint probability density function of the core position was assumed to be Gaussian:

$$P(Y_v, Z_v) = \frac{1}{2\pi\sigma^2} \exp\left(-\frac{Y_p^2 + Z_p^2}{2\sigma^2}\right) \quad (3-6)$$

As shown in earlier, this is a reasonable assumption. They substitute  $r_p^2 = Y_p^2 + Z_p^2$ , and assumed the “actual” velocity profiles, i.e. those in the moving frame, can be represented by the q-vortex equations:

$$U_v = U_{c,v} \exp\left(-\alpha \frac{r_v^2}{d_v^2}\right) \quad (3-7)$$

$$W_v = W_{m,v} (1 + 0.5/\alpha) \frac{R_{c,v}}{r_v} \left[ 1 - \exp\left(-\alpha \frac{r_v^2}{R_{c,v}^2}\right) \right] \quad (3-8)$$



There are a few slight departures from standard convention in these equations. First, a separate length scale,  $d$ , is established for the axial velocity jet (or wake) thickness. Usually,  $R_c$  serves this purpose. Also,  $\alpha$  appears in the exponential, and also as a constant outside the exponential in the Eq. (3-8), implying a one to one relationship between the maximum tangential velocity,  $W_m$ , and the core radius,  $R_c$ . Neither of these modifications have a significant bearing on the quality of the curve fit. In fact, the distinction between  $R_c$  and  $d$  allows for a better approximation of the axial velocity profile.

Continuing, the probability density function of the core position (Eq. (3-6)), and the equations for desired velocity (Eq. (3-7) and (3-8)) were substituted into Eq. (3-5). The resulting expression was integrated analytically, yielding a pair of equations that approximate the measured profiles:

$$U_p = U_{c,p} \exp\left(-\alpha \frac{r_p^2}{d_p^2}\right) \quad (3-9)$$

$$W_p = W_{m,p} (1 + 0.5/\alpha) \frac{R_{c,p}}{r_p} \left[ 1 - \exp\left(-\alpha \frac{r_p^2}{R_{c,p}^2 + 2\alpha\sigma^2}\right) \right] \quad (3-10)$$

By finding the best fit between the experimental data and Eqs. (3-9) and (3-10), all of the required quantities for the corrected profiles (Eqs. (3-7) and (3-8)) are known. They also presented the following relationships that describe the connection between the defining quantities of the measured and corrected profiles. As expected, the centerline axial velocity and maximum tangential velocities increase:

$$U_{c,v} = U_{c,p} (1 + 2\alpha\sigma^2 / d_v) \quad (3-11)$$

$$W_{m,v} = \frac{W_{m,p}}{\sqrt{1 - 2\alpha\sigma^2 / R_{c,p}^2}} \quad (3-12)$$

On the other hand, the core radius and jet thickness decrease:

$$\frac{R_{c,v}}{R_{c,p}} = \frac{d_v}{d_p} = \sqrt{1 - 2\alpha\sigma^2 / R_{c,p}^2} \quad (3-13)$$

Note that the circulation at the edge of the core remains unchanged.

Using the meandering data and a representative set of velocity profiles, this method was implemented. Discussion of the details of the velocity profiles will be deferred until Chapter IV. The best fit for Eqs. (3-9) and (3-10) was determined by the method of least squares, giving each data point within two core radii equal weight. A difficulty arose because the q-vortex equation does not adequately approximate profiles measured at high  $Re_D$ , a point which will be given further discussion later. Potentially, this shortcoming could be overcome by using the general method given by Devenport, et al (1996). Very briefly, this method uses a summation of exponential terms to fit the measured profile, and an approximation for the “corrected” profiles was found using Eq. (3-6). However, this method required knowledge of the correlation coefficient of the Y and Z meandering data, but the numerical value for this quantity exhibited a high degree of scatter. Since the “general method” proved to be rather sensitive to the choice of the correlation coefficient (for example), we were unable to obtain reliable results.

Returning to the results obtained using the q-vortex method, the measured and corrected profiles are presented in Fig. 3-31. There was a 7 % increase in the centerline axial velocity, and a 50 % increase in the maximum tangential velocity. However, the velocity histograms do not point to the presence of such a large tangential velocity (12 m/s) anywhere in the flow.

In the future, it may be possible to validate (or refute) this correction using DPIV, because the “corrected” profile would be determined directly from the instantaneous vector fields. Volkert (1996) explored this for a swirling flow in a closed cylinder with a rotating end. Such an apparatus gives rise to a vortex characterized by a zero cross sectional axial velocity and a very large core radius, features that make it highly suitable for DPIV measurements. In the present work, the vortex core radius was 1 mm or less, which could not be resolved using existing DPIV technology.

## 5. Corrections to Turbulence Moments

We will now make an attempt to ascertain the quantitative value of the fluctuations that represent only true turbulence. In other words, we seek to dissect the measured value of the velocity fluctuations into the true and apparent turbulence components. Theoretically, this should be possible to do using a suitable time history of the velocity, but in practice, there are difficulties. The time series of a velocity in an unsteady turbulent flow may be described as the superposition of a random signal (turbulence) and a nearly deterministic function (unsteadiness). Bendat and Piersol (1986) describe three methods for separating the two constituents. Here, we will discuss the methods and also the problems encountered in the process of implementation.

One approach involves approximating trends in the data (e.g., using regression analysis), and then determining the instantaneous fluctuations relative to the smooth curve. The “true” turbulence is taken to be the root mean square of this new set of velocity fluctuations. This method is appealing in situations where the unsteady nature of the flow is readily determined, such as that in the vicinity of a turbomachinery blade, or during a transient occurrence such as the starting or stopping of a pump. In the present work, the vortex core motion was not readily approximated, so the method would not yield reliable results.

The second method involves filtering the data. When the unsteadiness and turbulence occur at frequencies separated by a wide gap, one or the other can be filtered. It would seem that such an approach might be possible in this investigation because the meandering frequency should be lower than the characteristic turbulence. However, the analysis of meandering data in the present investigation did not yield a clear upper cut-off frequency to use in filter definition. Thus, even if the data were filtered, it would be impossible to interpret the results because the remaining value could not be guaranteed to be representative of the true turbulence.

The third and final method described involves estimating the nature of the fluctuations based on segments of the time history which are short relative to the characteristic time scale of the unsteadiness. The underlying assumption is that the fluctuations are computed relative to juxtaposed quasisteady mean values. Selection of an appropriate window size is imperative in this process because the window must be very short relative to the time scale of the meandering, or the mean velocity will have changed appreciably during the interval. However, if the window is so short that the sample size in the window becomes small, random errors become large. To satisfy both requirements, it is essential that the sampling rate be very high relative to the characteristic frequencies of the unsteadiness.

Since this final method seemed to be the most promising in the present work, it was decided to explore whether reasonable results could be obtained. A representative time history of LDV velocity measurements near the edge of the vortex core was selected. A data file from the spectral measurements was selected because the LDV configuration was such that the data rate was relatively high (800 Hz).

The fluctuating component of velocity was computed relative to the mean of its immediate neighbors. That is,

$$u'_j = \left( u_j - \frac{\sum_{k=j-m}^{j+m} u_k}{2m+1} \right) \quad (3-14)$$

The turbulence was then estimated by computing the root mean square of these fluctuations. The window size,  $M = 2m + 1$ , was left as a variable because guidance on its determination is scant. For example, Zhang, et al (1997), and Eisele, et al (1997) employed this method in the context of the flow about a turbomachinery blade, and concluded that the window should be “short”.

The results, shown in Fig. 3-32, lead to two important observations. First, the estimate of the “true” turbulence using this method depends on the window size,  $M$ . To



some degree this is expected because as  $M$  increases, the meandering will manifest itself in the results in the form of a velocity change during the “window”. Then, the estimate of the true turbulence will no longer be made to the exclusion of the unsteadiness we are trying to eliminate. The second observation is that even with a very short window ( $M = 5$ ), the turbulence is quite high:  $u_{rms}$  was 30 % of  $U_0$  and  $w_{rms}$  was 100 % of  $U_0$ .

Upon further consideration, it was concluded that the large LDV measuring volume is the most likely explanation for the lack of success in determining a reasonable estimate of the turbulence with this method. Since the measuring volume size is on the same order as the viscous core, a large range of velocities may be recorded at any given instant, even in the absence of meandering.

In order to achieve reliable turbulence data near the centerline of a strongly swirled flow with a meandering viscous core, the measurement volume must be very small relative to the size of the vortex. Currently this is not achievable.

## **6. Concluding Remarks**

In this section, the vortex core meandering phenomenon was examined in some detail. An assessment of the effect of meandering indicated that the core meandering profoundly affects the LDV results, especially the turbulence moments. Corrections to the velocity profiles with proposed methods yielded results that did not seem to be in harmony with the statistical data (histograms). The evidence suggests that the mean velocity data is more accurate than previously believed. Correction to the turbulence moments was not possible using existing methods. Thus, the turbulence measurements within 3 core radii are not reliable.



### C. STAGNATION POINT DARTING

In a high Reynolds number swirling flow, the vortex breakdown tends to dart back and forth along the axis, compounding matters beyond what was introduced by the vortex core meandering. Early in the investigation, it was observed that a breakdown in a gently diverging tube, i.e., the h0 tube, made rather long excursions (15 mm or more) in either direction from its mean position. Thus, even if the meandering could be eliminated completely, time averaged Eulerian measurements such as LDV results will represent an average over both time and space, at least in the sections near the stagnation point.

The anticipated affect of the darting on the quantitative LDV results can be explored through intuitive reasoning. First, let us assume the breakdown induces a discrete change to the velocity profiles. If the stagnation point, i.e., the location of the sudden change, is stationary, then the LDV results would represent the changes along the axis of such an idealized breakdown quite accurately. In reality, the stagnation point darts back and forth. Although the measurements at distant sections should not be affected, the LDV results near the mean position of the breakdown will reflect the fact that they are a weighted average of the velocity before and after the discrete change. The idealized discrete breakdown would appear as a more gradual change, spread out over an axial distance that is dictated by the amplitude of the darting. Another important consideration is the frequency of the darting motion relative to the frequency and record length of the measurements. Should the axial motion occur so slowly that a large number of cycles do not occur during the LDV record length, the partial cycles at the beginning and end would affect the mean values in an unpredictable manner. For these reasons, it was determined that in order to ascertain the flow field reliably, without excluding the stagnation point region, the darting motion needed to be accounted for or minimized.

Alternatives included attempting to work around the problem through selective measurement, or minimizing the motion to the maximum extent possible. Faler and Leibovich (1978) operated their LDV intermittently to diminish the effect of axial motion.

They interrupted the measurement process when the breakdown moved out of a prescribed zone, and resumed it when the breakdown returned to the desired location. Theoretically, this could be done in the present work, but the motion was more random and characterized by shorter time scales than what was found in the previous investigation. It seemed virtually impossible that such a technique would be practicable in high a  $Re_D$  flow.

The method that was deemed achievable was the suppression of the darting motion by manipulation of the axial pressure gradient. It is well known that in general, adverse pressure gradients promote the occurrences of breakdowns, and that favorable gradients inhibit them. It was conjectured that even at high  $Re_D$ , a tube with a converging-diverging section might trap the breakdown in the vicinity of the throat. Such a device was used by Althaus and Brücker (1992), and Brücker (1993), albeit at much lower  $Re_D$ . Thus, the motivation for utilizing various tubes during this investigation was to inhibit as much as possible the darting motion of the vortex breakdown without altering any other important features of the flow. The tube profiles designed and used during the present work were depicted in Fig. 2-2 and described in Section II-A

The purpose of this section is to describe the effects of the various converging-diverging sections on the breakdown motion, and demonstrate that the fundamental nature of the breakdown remained intact.

In order to quantify the pressure gradients in the converging and diverging sections of the tubes in a simple straightforward manner, a dimensionless parameter was developed. An approximation of the convective acceleration serves as the starting point:

$$U \frac{\partial U}{\partial X} \approx \frac{U_2 + U_1}{2} \frac{U_2 - U_1}{X_2 - X_1} \quad (3-15)$$

After some manipulation, normalization of the lengths by  $R_0$  and the velocities by  $U_0$ , and dropping the factor of 2, one has:

$$\left( U \frac{\partial U}{\partial X} \right) \frac{R_0}{U_0^2} \approx \frac{R_0^5}{X_2 - X_1} \left( \frac{1}{R_2^4} - \frac{1}{R_1^4} \right) \quad (3-16)$$

The magnitude of this term indicates the severity of the axial pressure gradient. A large positive (negative) number would indicate a strong favorable (adverse) pressure gradient. The values for this term in the h0 tube and between the transition regions of the h3 and h6 tubes (i.e.,  $X = 100$  mm and 140 mm, and then  $X = 140$  mm and the end of the diverging section) are given in Table 3-1.

	Convective Acceleration Parameter	
	converging	diverging
tube h0	-0.059	
tube h3	0.16	-0.15
tube h6	0.56	-0.34

Table 3-1. Pressure gradient parameters in the tubes used in the present work.

An investigation was conducted to quantify the darting motion of the vortex breakdown when subjected to these various pressure gradients. Time histories of the stagnation point position were recorded using the method described in Section II-E. From these, histograms of the breakdown location were constructed, and Fourier analysis was carried out.

Figure 3-33 gives the histograms of the vortex breakdown position in various  $Re_D$ /tube states. The velocity distribution corresponding to the straight wall (h0) tube exhibits considerably more scatter than those with the converging-diverging sections (h3, h6). Thus, it is readily apparent that the restrictive profiles suppressed the axial motion of the breakdown. In all cases, the measured histograms were well represented by Gaussian probability density functions.

The difference in the motion between the h3 and h6 tubes was relatively small when compared to the difference between the h0 and either the h3 or h6 tube. This is plainly evident in Fig. 3-33b, and from the standard deviations of the breakdown position, given in Table 3-2. The mild adverse pressure gradient in the straight (h0) tube is obviously sufficient to promote a vortex breakdown under suitable swirl conditions, but allows the stagnation point to roam about in response to the slightest disturbances in the flow. The presence of either converging-diverging section, on the other hand, furnishes the requisite resistance to long excursions of the stagnation point. Apparently, the diverging section imposes the requirement that if a breakdown occurs, it must take place towards its upstream end. The converging section, however, denies migration to the further upstream sections, except in very strongly swirled flows. Consequently, the breakdown darts back and forth in a relatively narrow range as it is subjected to these two competing forces. This change in the unsteadiness of the breakdown was regarded as favorable in that it enabled more reliable measurements to be conducted even in the vicinity of the breakdown.

	$Re_D = 120,000$	$Re_D = 230,000$	$Re_D = 300,000$
tube h0	7.8 mm	8.5 mm	
tube h3		3.2 mm	4.0 mm
tube h6	3.6 mm	2.8 mm	

Table 3-2. Standard deviation of the axial position of the vortex breakdown.

There were two other changes observed when the tubes were interchanged. First, the converging-diverging tube profile caused the axial darting motion to occur at higher frequencies. Figure 3-34 gives the results of the Fourier analysis of the breakdown position in all three tubes for  $Re_D = 230,000$ . Although a dominant frequency does not appear in any of the results, there was a relatively large amount of energy in the very low frequency ( $< 5$  Hz) range in the h0 tube. There was less energy in this frequency range in



the h3 tube, and lesser still in the h6 tube. These results are in agreement with visual inspections of the breakdown motion in the various tubes. The increase in the frequency of motion could have been anticipated if we again view the breakdown as being subjected to two competing forces induced by the converging and diverging sections. It is natural that the frequency response should be higher as these forces increase, provided neither is so strong that the position becomes unstable. A positive outcome of the more rapid motion (in the h3 and h6 tubes) is that the LDV measurement record length was on the order of hundreds of darting cycles, safely eliminating the possibility that the effect of the partial cycles at the beginning and end of the measurements was strong.

The second change that was noticed after changing from the h0 to either the h3 or h6 tube was that the circulation needed to be increased. If both the  $Re_D$  and the circulation were left unchanged after installing a converging-diverging tube, the vortex did not break down. When the swirl strength was increased gradually to initiate a breakdown, the stagnation point formed at a far downstream location and then traveled rapidly to the throat when a sufficient, slightly higher circulation was reached. Further increases in swirl strength would bring about a deliberate upstream migration of the breakdown (and eventually cavitation). Thus, the presence of a converging-diverging section inhibited the breakdown for a given  $Re_D$  and circulation.

Now that it has been shown rather conclusively that the presence of a throat alters the characteristic motion of the vortex breakdown in a high  $Re_D$  flow, it will be argued that the fundamental nature of the phenomenon was unchanged. After viewing countless images from extensive high speed video recordings of the breakdowns under wide ranges of  $Re_D$  and circulation in all three tubes, we came to the sound conclusion that except for the difference in motion, the breakdowns were identical in the various tubes. The spiral and its variants appeared, and the transition to turbulence occurred within a few windings. There were no distinguishing features based on a change in tube alone. It is impossible to

replace the process of laboriously watching film with a few pictures, but Figures 3-7, 3-11, 3-35, and 3-36 show some of the images of the breakdown in various  $Re_D$ /tube states.



## IV. LASER DOPPLER VELOCIMETRY MEASUREMENTS OF HIGH REYNOLDS NUMBER VORTEX BREAKDOWNS

### A. GENERAL REMARKS

Some preliminary comments are in order prior to the presentation of quantitative results.

First of all, an investigation of this nature yields an enormous number of plots. For the purposes of this discussion, selected figures will be provided to convey the physics. Many of the salient features were extracted from the whole data set and used to construct graphical summaries of the trends. These will be presented also. The tabulated, as well as electronic versions of the entire data set are available from the Naval Postgraduate School upon written request\*.

Throughout this thesis, the  $Re_D^* = 230,000/h_6$  flow is used as the default state for the presentation and discussion of a typical high  $Re_D$  swirling flow with vortex breakdown in a tube. The choice was somewhat arbitrary, as any of the high  $Re_D$  flows that were measured (i.e.,  $\geq 100,000$ ) are equally qualified to serve this purpose. For the sake of consistency, this flow is described as a default state or baseline, and the others are introduced in the context of comparisons and contrasts.

As a reminder, the wall profiles for all three tubes used in the present investigation are shown in Fig. 2-2. Additional details about the data runs are provided in Table 2-1.

The majority of the data presented herein are normalized by a suitable parameter. In most cases, the characteristic velocity is  $U_0$  (the cross-sectional mean axial velocity at the tube inlet), and the length is  $R_0$  (the tube radius at the inlet). However, since there are a variety of instances when different quantities are used or the data are presented without

---

\* Requests should be addressed to:  
Dist. Prof. T. Sarpkaya  
Mechanical Engineering, Naval Postgraduate School  
Monterey, CA 93943



normalization, no abbreviated notation is introduced. Rather, the quantity and the normalization variable, if utilized, are defined explicitly.

As stated in Section II-B, measurements were possible in the range from  $X = 60$  mm to  $X = 350$  mm. Outside these limits, LDV measurements could not be conducted due to optical path constraints. The farthest upstream stations are used to define the “inlet” conditions. It will be demonstrated at this section that the vortex was well developed, but not on the verge of breakdown. The swirl strength was set (by adjusting the vane angle) such that the vortex breakdown occurred at roughly  $X = 135$  mm to  $X = 140$  mm.

The LDV measurements were subjected to velocity-bias correction but they have not been subjected to any other post conditioning or correction.. As stated in Section II-B, a residence time weighting was used to alleviate, to the maximum extent possible, the potential consequences of velocity bias in the ensemble average. However no modifications to the profiles were made. Moreover, no data points were removed because they seemed to be out of harmony with the rest of the set. Although great care was taken to maintain archival quality, it is inevitable that some points will appear errant. Besides statistical randomness, this may be the result of an obstruction in the optical path of the laser beam, or the difference in the diffraction indices of Plexiglas and water, among other possible causes.

The estimated experimental uncertainty of the measurements on the basis of 95% confidence is given in Appendix B.

## **B. RESULTS FROM A REPRESENTATIVE HIGH REYNOLDS NUMBER FLOW**

The  $Re_D = 230,000/h_6$  flow will be described in some detail as a representative high Reynolds number swirling flow with vortex breakdown. The mean position of the breakdown was at  $X \approx 138$  mm, with a standard deviation of 2.8 mm. Using LDV, mean

velocity, turbulence and spectra were measured at the stations indicated in Fig. 4-1. The discussion will begin with the evolution of the velocity profiles, and then proceed to the fundamental elements of the turbulence. Then, the vorticity distributions in the flow field will be taken up.

It will become apparent that there are three global regions in the vortex breakdown topology. First, in the upstream sections, the flow is virtually invariant. It remains so until about 10 to 15 mm upstream of the nominal breakdown position. Then, a region of dramatic changes is entered as the stagnation point is approached. Every feature of the flow undergoes a rather abrupt change in this range of about 30 to 40 mm. Finally, there is a downstream wake region where the flow relaxes, and the velocity profiles and turbulence all tend toward uniformity. Let us now examine these regions in more detail.

The axial velocities in the inlet region are given in Fig. 4-2. The vortex was well developed, as evidenced by the characteristic jet profile, and by the small amount of change which was found between that section and the two succeeding sections. The centerline velocity was nearly three times the cross sectional mean, and the numerical values for all three profiles were within experimental error of each other. Outside the jet, the axial velocity extended to the boundary layer near the tube wall with a nearly zero radial gradient. This, as well as turbulence measurements, demonstrates that the ambient flow was turbulent.

Normalized tangential velocity profiles in the inlet and neighboring sections are shown in Fig. 4-3. As was true for the axial velocities, there was very little change over the span of 20 mm. Admittedly, Fig. 4-3b may suggest that some slight axial gradient exists, but this cannot be verified because the profiles are within the experimental error of each other. As expected, outside the viscous core, the profile was potential-like out to the region where wall effects became important. Deviations from the potential curve will be discussed at some length in the context of Reynolds number variations, given in Section IV-D.

The axial and tangential velocity profiles in the inlet region are very similar to what many others have reported, but at the same time different. Figure 4-4 shows a single tangential and axial velocity profile, with physical dimensions, to help illustrate this point. The shape of the profiles are familiar to those who dealt with vortical flows: The jet-like axial velocity profile, the nearly linear tangential velocity inside the viscous core, and a potential-like velocity distribution outside the core. However, the scale of the vortex is unlike what others have investigated. The maximum tangential velocity ( $W_m$ ) was over 8 m/s, and was found at only 1 mm from the centerline (where the  $W$  velocity was zero). A conservative estimate of the solid body rotation rate at the axis,  $\omega = W_m / 2\pi R_c$ , is over 1,200 revolutions per second. The axial velocity was maximum at the centerline, where the magnitude was about 14 m/s.

Also evident from Fig. 4-4 is that the viscous core is small when compared to the tube dimensions. A turbulent region of at least 15 core radii separates the edge of the jet from the wall boundary layer. This distinguishes this investigation from low  $Re_D$  experiments, in which the laminar boundary layer rapidly grows and interacts with the vortex. In the present work, we can claim that in the upstream sections, the tube wall does not influence the embedded vortex.

The inlet region may be the most important from the viewpoint of an investigator wishing to conduct numerical simulations. However, the downstream sections bring the subject to life. Minuscule changes along the axis characterized the inlet profiles, but violent changes were the trademarks of the breakdown and wake regions.

Figure 4-5 shows axial velocity profiles in the region where the vortex was breaking down. At  $X = 110$  mm, the jet still appeared robust, but by  $X = 120$  mm, it is evident that deceleration had begun to occur. The rate of change increased with larger  $X$ , and was swiftest between  $X = 120$  mm and  $X = 130$  mm. A notable property of these profiles was that the collapse of the jet profile seemed to be directed outward from the centerline. At the periphery of the jet, the velocity excess persisted even while dramatic



changes were occurring in the interior. This suggests that the structure of high  $Re_D$  breakdowns may be similar to the downstream recirculation zone in the laminar flow studied by Uchida et al (1985), but unlike the two celled structure in the upstream bubble of Uchida et al (1985), and in the axisymmetric bubble reported by Faler and Leibovich (1978).

Figure 4-6 continues where Fig. 4-5 ended, and shows that the axial velocity profiles continued to change with distance along the axis, but at a more gradual pace. At  $X = 140$  mm, there was still evidence of the jet-like profile, but overall, the plot was wake-like and the centerline velocity was slightly negative. At the next section ( $X = 150$  mm), there were no longer any remnants of the jet profile. The prominent changes observed were the increasing breadth of the wake and strength of the reversed flow region. Beyond this, the wake began to relax, so the width increased but the velocity deficit decreased.

Figures 4-7 and 4-8 give birds' eye views of the evolution of the axial velocity profile. The first shows the breakdown region where the profile transformed from jet-like to wake-like, and the second portrays the region where the wake relaxed in the downstream sections. In both figures, the mean  $U = 0$  contour is indicated.

Figure 4-9 provides another look at the boundaries of the reversed flow region. It has been overlaid on the tube profile to give physical perspective. The long, slender, closed shape extending from  $X = 138$  mm to  $X = 188$  mm represents the contour where the mean axial velocity is zero. The time averaged axial velocity is negative inside, and positive outside this curve.

Figure 4-9 also shows that the location of the maximum tangential velocity moves away from the centerline in the breakdown and wake regions. The position of the vortex core (distance from the vortex axis to the peak tangential velocity) are indicated by the dots. While intense changes in the axial velocity profiles were occurring, the vortex was expanding. Figure 4-10 shows the time averaged tangential velocity profiles in the same



region that the axial velocity transformed from a jet-like to a wake-like profile. The peak velocity decreased to roughly half the magnitude found at the inlet section and the vortex core increased by a factor of 3.

Figure 4-11 shows tangential velocity profiles selected from a wider range of axial sections, with the inlet as well as the wake regions being represented. The structure of the vortex continues to change steadily in the wake. In all, the peak tangential velocity decreased to less than one fourth its original value and the vortex core expanded by ~1000 %. Figure 4-11 also demonstrates that the tangential velocity outside the core remains virtually unchanged for all axial stations, indicating that the maximum circulation is invariant, as expected.

Figure 4-12 gives, for various sections, tangential profiles that are normalized by the local maximum tangential velocities and core radii. A point that emerges from these profiles is that the upstream and downstream profiles are different, but self similarity is found within each set. The profile at  $X = 130$  mm, which is very near the mean stagnation point, lies between the two sets of curves. In essence, outside the viscous core, the tangential velocity profile is more potential-like in the downstream sections.

Some of the foregoing can be summarized on a plot with the axial distance on the horizontal axis. Figure 4-13 gives the centerline axial velocity ( $U_c$ ), maximum tangential velocity ( $W_m$ ), and core radius ( $R_c$ ) variation along the axis. Units are included here again to convey a physical feel for the evolution of the flow. The three global regions are evident. Immediately following the inlet, there was a region where the changes to the vortex were too small to measure. This ostensibly began before the first upstream profile at  $X = 60$  mm, and lasted until roughly  $X = 100$  mm. Then, changes commenced, and were rapid from about  $X = 120$  mm to  $X = 140$  mm, a span of about 20 core radii. The axial velocity decelerated from about 14 m/s to zero (30 mph to zero within 0.78 inches), and the tangential velocity decreased by a factor of 2. The core radius also abruptly began changing. Thereafter, the evolution continued, but at a relatively gradual rate. The

centerline axial velocity became negative at  $X = 140$  mm, reached a minimum at  $X = 155$  mm, and did not become positive until a few mm before  $X = 190$  mm. The tangential velocity slowly evolved towards its final value of about 1.5 m/s. Throughout this region, the changes to velocity seemed to be relaxing toward equilibrium. At roughly  $X = 200$  mm, the core radius abruptly leveled off at about 11 mm.

Now, the topic of discussion is shifted from the velocities to turbulence moments. The attention will be given to the global transformations taking place in the three major regions that appeared in the velocity profiles. We will see that the turbulence profiles are nearly invariant in the inlet sections. As the nominal breakdown location is approached, the large data scatter clearly signals proximity to the darting stagnation point. In the wake, turbulence decays and tends toward isotropy.

It was pointed out in Section III-B that in regions where the vorticity is highly concentrated, the measurement of turbulence is complicated by the effects of meandering. As such, in the upstream sections (i.e., before breakdown), attention is directed away from the large turbulence values within 3 core radii of the centerline. It is believed that this outer portion of the upstream flow, as well as the downstream sections, were relatively free from the influence of meandering.

Figures 4-14 to 4-35 show a large sampling of the turbulence data for the  $Re_D = 230,000/h_6$  flow. Since it is useful to visualize the profiles in a manner that depicts the distance from the axis in terms of the core radius, some of the plots are shown with this normalization (Figs. 4-31 to 4-35).

Upstream, all turbulence values are nearly invariant until about 15 mm before the nominal vortex breakdown position (Figs. 4-14 to 4-17, and Fig. 4-26). Outside the vortex core, the turbulence of each component is on the order of 2 to 4 % of  $U_0$ . This is low relative to the value within the core, but the flow is not laminar, as shown by the very flat axial velocity profiles outside the core (e.g., Figs. 4-2 and 4-4).

At the “stagnation point” (time averaged), there are certain clear indications of changes (Figs 4-17 to 4-20, and Figs. 4-27 and 4-28). Even though one cannot extract a precise value, the large scatter is a reflection of the combined effects of the unsteady phenomena discussed in Sections III-B and III-C. In particular, the shape of the Reynolds stress profiles undergo a dramatic change because of the combined effects of the darting and meandering (Fig. 4-27).

Shortly after the breakdown, the measured turbulence levels near the centerline rapidly decay from the exceedingly high values where the unsteadiness was playing a central role. In the meantime, the turbulence levels away from the centerline begin to increase slowly, as expected. A little further past the stagnation region, at about  $X = 150$  mm, we enter into the new region where the transformations are relatively gradual (Figs. 4-22 to 4-25, and Figs. 4-33 to 4-35) and the entire flow field is relaxing toward uniformity. The large values near the centerline decay, but expand in breadth to fill a greater portion of the tube. Also, turbulence tends towards isotropy, as expected on physical grounds.

In the foregoing, we have seen the major features of the turbulence moments from way upstream, where the flow is unaffected by the vortex breakdown, to the downstream sections where the flow is relaxing and becoming increasingly isotropic.

The discussion will now turn to the circulation and vorticity distribution. Figure 4-11 presented the tangential velocity profiles from all the global regions of the flow, and lead to the observation that the circulation is invariant throughout the tube. Figure 4-36 shows the circulation at the same sections. At first glance, the plots may suggest that there is a quantitative variation of the maximum circulation with  $X$ . However, the value of the maximum circulation at a given section is, for understandable reasons, rather sensitive to the shifts in the origin of the  $Y$  coordinate. This is reflected in the uncertainty of this value (Appendix B). Considering this and the fact that no post-conditioning was



performed on the data, the agreement of the maximum circulation  $\Gamma$  between the various sections in Fig. 4-36 is quite good.

Although the maximum circulation remained nearly invariant, the vorticity distribution sustained an interesting change. As shown in Fig. 4-37, the expanding vortex contained a larger percent of the total circulation. In the inlet, the circulation at the core was only 40 % of the maximum value. It increased steadily through the breakdown region, and seemed to settle on a final value in the vicinity of about 80 %.

The small fraction of vorticity that was found in the core of the inlet vortex is another distinguishing characteristic between the high and low  $Re_D$  swirling flows. In previous investigations, the core contained 60 % to 70 % or more of the vorticity. Apparently, the turbulence outside the core is sufficient to allow for the diffusion of vorticity away from the centerline. As shown by Sarpkaya (1998), this is an important decay mechanism for the trailing vortices. This subject will be discussed again in Section IV-D, but in the context of varying Reynolds numbers.

The evolution of the flow kinematics have been described in this section for a single  $Re_D$ /tube arrangement. These results will also be discussed further in the context of variations to the flow configuration.

### **C. VARIATIONS INDUCED BY A CHANGE IN TUBE PROFILE**

In this section, we expand the topic of discussion to cover multiple tubes, but still at a single Reynolds number. Specifically, the subject is not confined to just the  $Re_D = 230,000/h6$  flow, but rather includes the  $Re_D = 230,000/h3$  configuration as well. In this context, the effect of tube wall variation can be shown almost entirely to the exclusion of changes in other variables. When the tube was replaced, the  $Re_D$  and static pressure in the chamber were left unchanged. The circulation needed only a slight increase (via the vane angle), as described in Section III-C. Also, the mean breakdown position in the h3 tube was about 3 to 5 mm further upstream of that in the h6 tube.



The results presented in Section III-C demonstrated that the presence of a first favorable then adverse pressure-gradient sequence induced a change in the nature of the darting motion of vortex breakdown. The stronger the said pressure gradients, the more stable was the breakdown position. It is inevitable that when the breakdown moves about more freely, the LDV results will be affected accordingly. Thus, the time averaged LDV results from the flow in the h3 tube reflect that they are also an average over a larger axial interval. The three global regions are still plainly evident, but in the breakdown and wake regions, the changes seem to be more mild. Also, the differences in the acceleration and deceleration in the converging-diverging section affects the development of the flow turbulence.

First the velocity profiles in the inlet are examined. These are given in Figs. 4-38 to 4-41. The normalization by  $U_0$  and  $R_0$  is appropriate because the tube profiles are identical until  $X = 100$  mm. There was virtually no change in the overall jet profile (Fig. 4-38), except that the centerline velocity was slightly lower in the h3 tube (Fig. 4-39). The tangential velocity profiles also were very similar (Fig. 4-40), but the maximum tangential velocity was about 10 percent lower in the h3 tube (Fig. 4-41). Both of these variations between the tubes could have been anticipated because of the higher circulation in the h6 tube.

Figure 4-42 gives axial velocity profiles in the vicinity of the stagnation point. As can be seen, the collapse of the mean jet profile begins at the axis and moves outward. This is qualitatively identical to what occurred in the h6 tube (Fig. 4-5). However, as expected, the span over which this occurs is extended by about 10 mm or so in the case of the h3 flow.

Before describing a few of the downstream velocity profiles at a selected section, a sequence of summary plots are provided in Figs. 4-43 through 4-45 to point out some trends. These plots will illustrate the differences and similarities in a more distilled fashion than laboriously poring over a large number of profiles.

In essence, when compared to the data corresponding to the h6 tube, the LDV results from the h3 tube give the impression that the breakdown occurred over a longer axial span. The variation of the core radius with  $X$ , shown in Fig. 4-43, probably shows this most clearly. In both flow configurations, the core radius abruptly began to increase in the neighborhood of  $X = 115$  mm. However, the results indicate a more rapid increase when the h6 tube was installed.

The identical trend is seen in Figs. 4-44 and 4-45, which show the axial variation of the maximum tangential velocity and centerline axial velocity, respectively. The larger values of  $W_m$  and  $U_c$  at the inlet of the h6 flow can be attributed to the larger circulation. The main point of the plots is that the features indicative of the breakdown, i.e., the axial gradients, are less pronounced in the h3 tube. It seems certain that when the breakdown is free to move about more, as it is in this tube, the LDV results at any section will be a reflection of the averages taken over a relatively large axial interval.

In the downstream sections, there are only minor differences. The axial and tangential velocity profiles are given in Figs. 4-46 and 4-47 at a representative wake section. The normalization was modified slightly from the usual convention to account for the difference in the tube radius. The smaller adverse pressure gradient in the h3 tube brings about a smaller velocity deficit, which in turn gives rise to a larger velocity in the outer region of the flow. There are a few obvious quantitative differences in the tangential velocity profiles, but qualitatively, they are very similar.

Turbulence profiles in the inlet and wake regions are shown in Figs. 4-48 to 4-51. There is a subtle difference in the inlet sections (Figs. 4-48 and 4-49). Because of the laminarizing effect of the larger convective acceleration in the h6 tube, the flow is slightly less turbulent near the wall. In the wake sections (Figs. 4-50 and 4-51), on the other hand, the turbulence is considerably larger because of the destabilization brought about by the axial deceleration. Figures 4-52 and 4-53 show the variation of the centerline value of  $u_{rms}$  and maximum  $w_{rms}$  with  $X$ , showing that the flow in the h6 tube is more turbulent

throughout the wake region. For these plots, the fluctuations were normalized by the local cross sectional mean velocity. It is pointed out that this mean velocity at a given section in the h6 tube is always equal or greater to the corresponding velocity in the h3 tube. Therefore, even by the most conservative measure, the flow is more turbulent in the h6 tube.

To summarize the main points of this section, the LDV results give the appearance that the breakdown is more mild in the less restrictive tube. It is surmised that this is due to the greater darting motion. Overall, the velocity profiles are similar, but there are a few differences, e.g., the velocity deficit is reduced in the tube with the gentler converging-diverging section. Also, the stronger acceleration and deceleration of the axial flow in the h6 tubes gives rise to slightly lower turbulence levels in the converging section, and significantly higher turbulence levels in the diverging sections. However, such an observation is also true for non-swirling flows subjected to similar accelerations and decelerations.

#### **D. EFFECTS OF REYNOLDS NUMBER VARIATION**

At this point, the data from all the  $Re_D$ /tube states will be brought into the discussion. The majority of the additional results are from the  $Re_D = 120,000/h6$  and  $Re_D = 300,000/h0$  flows, but some of the details of the  $Re_D = 120,000/h0$  and  $Re_D = 70,000/h0$  will be incorporated into the discussion as well. Also, the results of previous low  $Re_D$  flow experiments will be drawn upon to give the most panoramic view possible. Specifically, salient details from the  $Re_D = 2,300$  data (Uchida, et al, 1985) and  $Re_D = 2,360$  data (Faler and Leibovich, 1978) will appear in places.

It will be self evident that the gross features of the breakdown remain intact throughout the full range of  $Re_D$ : jet-like profiles upstream, wake-like profiles downstream, and vortex core growth. However, there also are some interesting changes that occur. The character of the inlet vortex is modified with increasing  $Re_D$ , a point that



will be given considerable attention. Of course, the viscous effects are confined to a smaller region, the effect being evident in the vortex core size throughout the flow field, the wake breadth, and the boundary layer thickness. A surprising aspect of the high  $Re_D$  breakdown is the absence of a negative mean axial velocity (flow reversal) at the centerline of any section. This had been regarded as a defining feature of breakdowns. Finally, the nature of the turbulence is a complicated function of the  $Re_D$ , circulation, and adverse pressure gradient.

As usual, the characteristics of the vortex in the inlet region will be taken up first. Figures 4-54 through 4-56 show the axial velocity profiles in the inlet region for various flows. In non-dimensional form (Figs. 4-54 and 4-55) the jet strength seems to be decreasing with  $Re_D$ . However, the physical jet is stronger and narrower in the higher  $Re_D$  flows, as expected (Fig. 4-56).

Figure 4-57 shows that the ratio  $U_c/U_0$  (at the inlet) was scattered about a nominal mean value of about 2.6. Some trends were noted that offer clues as to possible reasons why the variation was too large to be explained in terms of data scatter alone. First, for a given  $Re_D$ ,  $U_c/U_0$  is larger in the more restrictive tubes. This was expected since the vane angle of the swirl generator needed to be increased after installation of these tubes, even in the absence of other changes to the flow configuration. In Fig. 4-58,  $U_c/U_0$  is weighted by the inverse of circulation. The new ratio does not exhibit the scatter caused by the difference in tube, but still decreases sharply with  $Re_D$ . Apparently, azimuthal vorticity is transported into the main flow via turbulent diffusion.

Some inlet tangential profiles are shown in Figs. 4-59 and 4-60. Although the profiles share the same broad features, neither normalization schemes used in Fig. 4-59 gave rise to a single scalable shape. In the high  $Re_D$  flow, the core is narrower, as expected. However, the swirl velocity falls off more slowly in the “potential” portion of the flow. This indicates that less circulation, expressed as a fraction of the overall value, resides within the viscous core.



In the full range of  $Re_D$ , the ratio  $W_m/U_0$  exhibits only a weak dependence on  $Re_D$ , as shown in Fig. 4-61. The data is scattered about a mean value of roughly 1.6. The only trend that can be gathered from this plot is that for a given  $Re_D$ ,  $W_m/U_0$  is greater in the more restrictive converging-diverging tubes. This is a natural consequence of the slight increase that was made to circulation when these tubes were installed. Using the inverse of circulation as a weighting factor again, Fig. 4-62 shows that the ratio  $(W_m/U_0)/(\Gamma/v)$  falls dramatically in the observed  $Re_D$  range. It shares a similarity with Fig. 4-63 that neither value seems to be making an asymptotic approach to a terminal value, i.e., one that would occur at infinite  $Re_D$ .

Figure 4-63 shows that the viscous core at the inlet is smaller in high  $Re_D$  flows. This is an expected result, because the boundary layer on the centerbody which gives rise to the vortex is thinner at high  $Re_D$ . Figure 4-64 shows the expansion of the core along the vortex axis. Even as the vortex breaks down and transitions to its new state, it continues to be relatively smaller in the large  $Re_D$  flows.

Some representative velocity profiles from the wake regions are shown in Figs. 4-65 through 4-77. In some of the plots, the data are normalized with the usual variables,  $U_0$  and  $R_0$  (Figs. 4-65 through 4-70). Since this convention can make it difficult to compare profiles in different tube radii, the plots are also given after normalization with  $U_m$  and  $R_t$  (Figs. 4-71 through 4-76).

A few trends are noted. The wake breadth and boundary layer are narrower in the higher  $Re_D$  flows, giving rise to a larger velocity outside the wake. Also, the profile corresponding to the  $Re_D = 300,000/h3$  flow is noticeably flatter outside the wake, indicating a higher level of turbulence. This is strictly a Reynolds number effect, as evidenced by the difference between the two flows in the h3 tube.

The tangential velocity profiles in the inlet region showed some variation with  $Re_D$ , but the profiles in the wake region show a high degree of similarity. This feature becomes very clear in Fig. 4-77. Essentially, the swirl velocities in the wake region relax

to a single form. The departures from similarity at the periphery are expected because the boundary layer thickness and the core radius (used to scale the lateral distances) naturally vary with  $Re_D$ .

Figures 4-78 and 4-79 show the axial variation of the mean centerline velocity and maximum tangential velocity, respectively. It was pointed out in the last section that the breakdowns appear milder in the gentler tubes. The same is true of higher  $Re_D$  breakdowns. When normalized, the changes are less dramatic, to the extent that a mean reverse flow region does not exist in the  $Re_D = 300,000/h^3$  flow.

Some turbulence profiles are shown in Figs. 4-80 through 4-89 for both the inlet and wake regions. The data are presented with various normalizations and, in some cases, without normalization. The discussion of turbulence can become complicated beyond what is warranted by current understanding of the phenomenon. The larger  $Re_D$  flows are also characterized by larger circulation, so the impetus to become more turbulent is accompanied by a stabilizing force. To compound the matters further, it was shown in the last section that the tube wall profile also affects the measured turbulence results profoundly. A perusal of the figures can lead to counter-intuitive or confusing conclusions unless it is kept in mind that all three of these factors are critical in the shaping of the turbulence structure. To give a single example, the turbulence data would indicate that the  $Re_D = 300,000/h^3$  flow, the highest Reynolds number presented, is in many instances the least turbulent (e.g., Figs. 4-80, 4-84 through 4-86). This trend defies intuition, unless one considers the factors of higher circulation and the gentler tube divergence. Also, the flat axial velocity profile in the wake (Figs. 4-71 through 4-73) lead to the opposite conclusion: that the high  $Re_D$  flow is, in reality, more turbulent.

This discussion will end with a description of the vorticity distributions in the various  $Re_D$ /tube configurations. Profiles of  $\Gamma/\Gamma_c$  (circulation normalized by circulation at the edge of the core) are shown for various  $Re_D$  in Fig. 4-90. As  $Re_D$  is increased, the core becomes smaller, as noted before, and a lower fraction of the vorticity is contained in

the core. This is true in both the inlet and wake regions of the flow. Examining this in another manner, Figure 4-91 shows the variation of both  $\Gamma/v$  and  $\Gamma_c/v$  with  $Re_D$ . At higher  $Re_D$ , the maximum circulation is larger, as one would expect. However, the percent of vorticity within the viscous core rises at a more gradual rate. Figure 4-92 shows how the ratio of these two terms varies with  $Re_D$ . It is interesting to note that in the range of  $Re_D$  measured, the circulation does not appear to be leveling off asymptotically to any particular value (Fig. 4-91). Along the same lines, the  $\Gamma_c/\Gamma$  ratio is decreasing sharply through the entire high  $Re_D$  range (Fig. 4-92).

Figure 4-93 shows the relationship between the maximum tangential velocity and the vortex core radius. Without claiming that  $3.5/R_c$  is a physically significant representation of the data, one may regard it as a useful reference. If the data on this curve fell along any line that varied as  $C/R_c$  (with  $C$  being any constant) it would indicate that as the vortex was expanding (i.e., breaking down), the maximum tangential velocity would be found at a point that moved outward along a curve traced by a potential vortex profile. However, it is evident that when the core radius is small, the maximum tangential velocity is less than such a model would predict. The difference between the data and this line is a consequence of the vorticity found outside the core in the upstream sections.

Another consequence of the presence of vorticity outside the core is that the q-vortex equations (Batchelor, 1964) do not approximate the high  $Re_D$  swirling flow profiles well. Some examples are shown in Figs. 4-94 through 4-96. The parameters for the q-vortex were determined based on a least squares fit, giving each data point within 2 core radii equal weight, and the data points in the outer portion of the flow zero weight. A number of variations on the weighting scheme were tested, but the result was always the same: the fit becomes worse, both visually and in terms of the residuals, as the  $Re_D$  was increased.

In the foregoing, we saw that none of the broad features of the breakdowns changed when the  $Re_D$  was increased. However, some important differences in the nature



of the inlet profiles were described. As  $Re_D$  is increased, the viscous core accommodates less vorticity, when expressed as a fraction of the total. This brings about a change in the shape of the swirl velocity distribution. Nevertheless, the downstream tangential velocity profiles are highly similar. The presence of a mean recirculation zone, considered a defining characteristic of vortex breakdowns, is not found at sufficiently high Reynolds number. Finally, the turbulence levels in the flow depend on a number of parameters in a highly non-linear fashion.

## E. SPECTRA OF TURBULENCE

For the sake of completeness, some remarks from Section I-B regarding previous similar measurements will be repeated here. Garg and Leibovich (1979) reported results of spectral measurements in swirling flows with vortex breakdown at  $Re_D$  up to 20,660. They used LDV to ascertain the spectral characteristics of both the axial and tangential velocity upstream of, and in the wake of spiral and bubble breakdowns. There were no interesting features in the spectra of velocity in the upstream sections. Downstream, peaks were found in the 10 Hz to 20 Hz range. The frequencies decreased with axial distance from the breakdown. Other investigations have been carried out (Chao, et al (1991), and Gursul (1996)), but with intrusive probes. Since it is known that such devices alter the flow field, the results may not be reliable.

During the course of the present investigation, the spectra in all three of the global regions (upstream, breakdown, and wake) of the high  $Re_D$  flow fields were measured using LDV. The discussion will begin with the results from the  $Re_D = 230,000/h6$  flow state. The locations where the spectra was measured in this flow are presented graphically in Fig. 4-1. Some results from the other flows, measured at similar locations, will follow immediately. Figures 4-97 through 4-128 give the spectral measurements for the  $Re_D = 230,000/h6$ ,  $Re_D = 120,000/h6$ , and  $Re_D = 300,000/h3$  flows. As there were many



common features of the results in all the flow configurations, the salient points will be discussed rather than examining each plot.

Spectral peaks, suggestive of turbulent eddies in the flow, were observed only in the wake sections primarily because of the fact that the lower turbulence levels and axisymmetrization of the flow by the very nature of LDV measurements obscured the presence of significant energy bearing eddies. Thus, they were relatively muted upstream, but became more conspicuous with increasing distance from the breakdown. The flat nature of the peaks gave the impression that they are broad, but in reality, their bandwidth is approximately equal to the most energetic frequency, conforming with the descriptions of Tennekes and Lumley (1972).

The central frequency decreased with axial distance, and seemed to be related to the rotation rate of the vortex. For example, at the  $X = 250$  mm section in the  $Re_D = 230,000/h6$  flow (Figs. 4-97 and 4-98), there were relatively well defined peaks in the neighborhood of 50 Hz. A line corresponding to  $-5/3$  power rule is drawn for each data station. The significance of this will be discussed in Section IV-F, which deals with the turbulence dissipation. Further upstream, at the  $X = 150$  mm and  $X = 145$  mm sections (Figs. 4-103 through 4-106), some of the radial stations had peaks in the vicinity of 160 Hz and 200 Hz, respectively. Although there was clear indication of energy in these frequencies, the features of the plots were less distinct than the downstream sections. Moving to  $X = 140$  mm, there is some evidence of coherent energy at about 270 Hz, but the shape is smeared almost beyond recognition.

In the inlet region and all the remaining upstream sections near the stagnation point, the curves were almost entirely featureless. The single notable trait observed was a small "blip" in the curve at 38 Hz. It is possible that this may be due to the vortex core meandering. However, since it occurred in flows of various  $Re_D$  and tube profiles, a systemic cause cannot be ruled out.

The spectral curves from the other data runs exhibited very similar trends. The notable difference was that, as expected, the dominant frequencies in the spectra were lower in the lower  $Re_D$  flow and higher in the larger  $Re_D$  flow (Figs. 4-115 through 4-128).

Concerning the orderly decrease in frequency of the broad peaks in the spectra, it was observed that this closely parallels the rotation rate of the vortex. By this, we mean the solid body rotation rate of the viscous core as estimated by  $\omega = W_m / 2\pi R_c$ . Although the maximum rotation rate of the fluid is higher than this value within the core, this quantity suffices to demonstrate the relationship to the spectral peaks. Figures 4-129 through 4-132 show variation of the frequency of the spectral peaks at an axial section, as well as the solid body rotation rate of the vortex core,  $\omega$ , for the various flows. As can be seen, the center frequency of the coherent structure decreases with, but is almost invariably greater than the rotation rate.

It should be expected that the dominant frequencies in the spectra are greater than the characteristic frequencies of the mean flow, i.e., the rotation rate. In the cascading energy model of turbulence, the kinetic energy is produced at a frequency that is lower than the energy containing eddies themselves. The eddies in turn are characterized by a frequency that is lower than that of the molecular dissipation. Since the mean flow produces the turbulence, the spectral energy will be found at a frequency higher than the characteristic frequency of the flow. In this sense, the present results conformed with the canonical description (e.g., Hinze, 1975) of spectra.

However, this may be an oversimplification of the physics. It is known from the results of Chapter III-A that the vortex breakdown is a rotating spiral. Thus, the LDV spectral measurements are an average of the turbulent conditions that exist in an annular ring that may simultaneously contain multiple scale eddies. On top of this, the stagnation point is darting back and forth, making the effective measurement volume in this region a wide cylindrical sleeve, as opposed to a torroidal ring. This, perhaps, sheds some light on

the muted nature of the peaks as well. Since the spectra presented here reflect a spatial average, it is natural to assume that a number of more discrete frequencies may have existed but were masked by the averaging process. The fact that the peaks are especially smeared in the region where the breakdown darts back and forth lends credence to this idea.

Perhaps the most valuable information that could be gleaned from the spectral plots is the distribution of the turbulence dissipation. Data for this term is generally regarded as the weakest in the current numerical models. The methods for estimating the dissipation, as well as the difficulties they entail, will be taken up in the next section.

## **F. ESTIMATION OF THE TURBULENCE DISSIPATION RATE**

### **1. Introduction**

The dissipation rate of turbulent kinetic energy is an important component in the energy budget of turbulence, and also is a necessary input parameter for numerical prediction schemes that employ turbulence models. It is the rate at which the kinetic energy is converted to heat through viscous action.

Unfortunately, quantitative values of dissipation are not easily obtained, even for relatively simple flows. Data for the dissipation rate in a swirling flow, with or without vortex breakdown, do not exist. Consequently, when attempting to model turbulent swirling flows, investigators use ad hoc equations to obtain numerical values for the inlet boundary conditions. The equation for the dissipation  $\varepsilon$  usually takes the form given by Launder and Spalding (1974):

$$\varepsilon = C_{\mu}^{3/4} \frac{k^{3/2}}{L} \quad (4-1)$$

$C_{\mu}$  is an empirical constant and  $L$  is a characteristic length. When it is used,  $C_{\mu}$  usually is given a value of 0.09, but the length scale is selected rather arbitrarily. Table 4-1 gives a

few examples of the variations on Eq. (4-1) that appear in the literature, as well as the assumed values for the length scale. Clearly, a need for quantitative data exists.



Reference	Application	Equation for $\epsilon$	Value of L
Hoggand Leschziner (1989)	combustion chamber	$\epsilon = \frac{C_\mu^{3/4} k^{3/2}}{L}$	L was varied from 0.06 to 0.34 $R_0$
Jones and Pascau (1989)	combustion chamber	$\epsilon = \frac{k^{3/2}}{L}$	$L = R - R_0$
Rhode and Stowers (1989)	combustion chamber	$\epsilon = \frac{2k^{3/2}}{L}$	$L = 0.0025 R_0$
Armfield, et al (1990)	diffuser	$\epsilon = \frac{C_\mu k^{3/2}}{L}$	$L = 0.005 R_0$
Khodadadi and Vlachos (1990)	tube	$\epsilon = \frac{k^{3/2}}{L}$	$L = 0.01 R_0$
Spall and Gatski (1995)	wing tip	$\epsilon = \frac{k^{3/2}}{L}$	L is equated to the inlet core radius
Lai (1996)	combustion chamber	$\epsilon = \frac{k^{3/2}}{L}$	$L = 0.36 R_0$

Table 4-1. Equations and numerical constants used to estimate dissipation.

In this section, we discuss the procedures, and the difficulties, in obtaining the dissipation rate of turbulence. The methods will be described in the context of a swirling flow with vortex breakdown. We attempted to estimate the dissipation rate of turbulence using the present results, and achieved some limited success.

## 2. Methods for Estimating Dissipation

To measure dissipation experimentally in the most direct manner possible, one would acquire all the terms in the tensor:

$$\epsilon = \nu \overline{\left( \frac{\partial u_i}{\partial x_j} + \frac{\partial u_j}{\partial x_i} \right) \frac{\partial u_j}{\partial x_i}} \quad (4-2)$$

Fully expanded, Eq. 1-1 includes twelve terms. Hot wire is the measurement device of choice because of the need for two point measurements. However, as described in Section

I-A, intrusive devices are ill suited for measuring strongly swirling flows because they alter the flow field. Even when using hot wire in less complex flows, investigators who seek to measure these terms reliably face challenges because of instrumentation and error accumulation. Browne, et al (1987) discussed the significant difficulties in obtaining all the constituents of Eq. (4-2). Some of the terms in Eq. (4-2) simply cannot be measured reliably. Others, such as those with like indices (e.g.,  $(\partial u_i / \partial x_i)^2$ ), are best obtained indirectly by measuring the mean temporal derivative, and invoking Taylor's "frozen turbulence" hypothesis:

$$\frac{\partial}{\partial t} = -\bar{u}_i \frac{\partial}{\partial x_i} \quad (4-3)$$

The errors become significant because of the rather large number of velocity derivatives required to arrive at a single estimate. A small number of investigators (for example Browne, et al (1987), and Schenck, et al (1998)) attempted to obtain dissipation by measuring most of the terms in Eq. (4-2), and then invoking isotropic relations to arrive at the few remaining values.

Four more tractable methods for estimating the dissipation appear in the literature. Even though the approaches may be theoretically sound, obtaining reliable results remains difficult. The problem is more acute in the case of swirling flows, because of the limitations on measuring techniques.

The first method flows from the notion that if some of the terms in Eq. (4-2) can be measured, the rest can be derived under an assumption of isotropy. In the extreme case where the turbulence is taken to be fully isotropic, one has (e.g., Tennekes and Lumley, 1972):

$$\varepsilon = 15\nu \left( \overline{\frac{\partial u}{\partial x}} \right)^2 \quad (4-4)$$

Ostensibly, the distribution of dissipation rates can be estimated from the measured fluctuations of a single velocity (and even at a single point if Taylor's

hypothesis is invoked) using Eq. (4-4). The drawback of Eq. (4-4) is the relatively low reliability when isotropy is questionable. This was studied by Browne, et al (1987), who used hot wire to measure 9 of the 12 terms in Eq. (4-1) in the far wake of flow past a circular cylinder. He then made an estimate of the error introduced when using Eq. (4-4), and found that even 420 diameters downstream of the cylinder, the estimate based on Eq. (4-4) was 45 to 80 % smaller, than that made using 9 of the 12 terms in Eq. (4-2). Unfortunately, the actual uncertainty is even worse because he used Taylor's hypothesis. Taylor envisioned his hypothesis to be applied in the limit of low turbulent intensities, but, as stated by Dahm et al (1997), investigators invoke it "more liberally" than originally intended. Using a laser induced fluorescence (LIF) technique in the far field of an axisymmetric turbulent jet, Dahm, et al (1997) estimated a correlation of 0.74 between the streamwise derivative and those estimated using Taylor's hypothesis. The inevitable conclusion is that Eqs. (4-4) should be used with care, and the results treated with caution.

In the present work, this method would not yield reliable results. Most importantly, in a strongly swirled flow, the anisotropy is very likely to be more severe than what is found in the far wake of a circular cylinder. The ratio between the axial and tangential velocity fluctuations, shown in Figs. 4-133 and 4-134 for various axial sections for  $Re_D = 230,000/h6$  flow, suggests this conclusion. A value of  $Iso = u_{rms}/w_{rms}$  near 1.0 would suggest that the turbulence is isotropic. From a review of these plots, the conclusion which can be drawn is that the turbulence does not seem to be isotropic. Additionally, the values for the fluctuations may be contaminated by meandering, especially in the core region. This was described in Section III-B. This method for estimating dissipation was employed by Azad and Kassab (1989), Schenck, et al (1998), and others, but at locations where the turbulence was afforded the opportunity to relax towards isotropy. Near a vortex breakdown, the underlying assumption of isotropy would not hold.

The second method involves the determination of the dissipation from a turbulent kinetic energy budget (TKEB). Simply stated, when all the other terms in the TKE transport equation can be measured or assumed to be small, the dissipation rate may be estimated directly. The transport equation for TKE was given in cylindrical polar coordinates by Abujelala & Lilley (1984, 1985).

$$\rho U \frac{\partial k}{\partial X} + \rho V \frac{\partial k}{\partial r} = \frac{1}{r} \frac{\partial}{\partial r} \left( r \frac{\mu_e}{\sigma_k} \frac{\partial k}{\partial r} \right) + \frac{\partial}{\partial X} \left( \frac{\mu_e}{\sigma_k} \frac{\partial k}{\partial X} \right) + G - \rho \epsilon \quad (4-5)$$

Here, the effective viscosity  $\mu_e$  is the sum of the laminar and turbulent viscosities, i.e.,  $\mu_e = \mu + \mu_t$ . Also,  $\sigma_k$  is an empirical constant ( $\approx 1$ ). The left hand side of Eq. (4-5) represents the convection of the turbulent kinetic energy. The first two terms on the right hand side are diffusion terms. The third term on the right hand side,  $G$ , is the turbulence production, which may be calculated from:

$$G = \mu_e \left[ 2 \left[ \left( \frac{\partial U}{\partial X} \right)^2 + \left( \frac{\partial V}{\partial r} \right)^2 + \left( \frac{V}{r} \right)^2 \right] + \left( \frac{\partial U}{\partial r} + \frac{\partial V}{\partial X} \right)^2 + \left( r \frac{\partial}{\partial r} \left( \frac{W}{r} \right) \right)^2 + \left( \frac{\partial W}{\partial X} \right)^2 \right] \quad (4-6)$$

The last term in Eq. (4-5) is the dissipation, which we seek.

Some simplifying assumptions allow a considerable reduction in the complexity of these equations. At a station which is in the gently diverging section of the pipe, sufficiently upstream of the breakdown, all terms involving the  $V$  (radial) component of velocity will be small. Also, one may reason that the changes along the axis are small when compared to the changes with respect to the radial distance. Thus, the equation for the TKE transport reduces to:

$$\rho \epsilon = \frac{1}{r} \frac{\partial}{\partial r} \left( r \frac{\mu_e}{\sigma_k} \frac{\partial k}{\partial r} \right) + G \quad (4-7)$$

The equation for the production reduces to:



$$G = \mu_e \left[ \left( \frac{\partial U}{\partial r} \right)^2 + \left( r \frac{\partial}{\partial r} \left( \frac{W}{r} \right) \right)^2 \right] \quad (4-8)$$

The laminar viscosity is small compared to the turbulent viscosity (verified). Thus, we take  $\mu_e \approx \mu_t$ , which may be estimated from:

$$-\overline{\rho u_i u_j} = \mu_t \left( \frac{\partial u_i}{\partial x_j} + \frac{\partial u_j}{\partial x_i} \right) - \frac{2}{3} \rho k \delta_{ij} \quad (4-9)$$

Equation (4-9) yields six equations, two of which will be given here. The rest can be determined from rotating the indices. Notice that the axial derivatives cannot be assumed to be small here, or the effective viscosity would be undefined.

$$-\overline{\rho u'^2} = 2\mu_{xx} \frac{\partial U}{\partial X} - \frac{2}{3} \rho k \quad (4-10a)$$

$$-\overline{\rho u' w'} = \mu_{x\theta} \frac{\partial W}{\partial X} \quad (4-10b)$$

If the turbulence is isotropic and the measurements sufficiently accurate, one would arrive at an equivalent value for turbulent viscosity if either equation were used.

The dissipation is estimated by direct substitution of Eqs. (4-8) and (4-10) into Eq. (4-7). The entire profile of dissipation may be calculated from measured profiles of the velocities and turbulence moments.

The advantages and disadvantages are similar to those of the first method. While the measurement and determination of the terms on the right hand side of Eq. (4-3) are more involved than that of Eq. (4-4), they are not especially difficult. Unfortunately, difficulties arise due to error propagation. Some calculations were carried out, and it was found that the values of the production and diffusion are several orders of magnitude larger than the expected value of the dissipation. Moreover, the uncertainty in the estimates of the production and diffusion exceed the expected value of the dissipation. One can develop an intuitive feel for these troubles by perusing the equations. The discernment of effective viscosity relies upon accurate measurements of the axial derivatives of the velocities. Since these derivatives are small, yet appear in the

denominator of the final equation, large errors are likely to ensue. Continuing through the procedure, the troubles only worsen. The measured values for turbulent kinetic energy are susceptible to contamination by meandering, for example. Unfortunately, to rectify the foregoing would mandate a great deal of approximations that, in the end, would yield exactly what we are trying to avoid: a contrived value. It was concluded that the obstacle of error accumulation could not be overcome in the present case, even though this method apparently has been used successfully in other contexts (see, for example Lawn (1971), and Azad and Kassab (1989)).

The third method to be discussed here is perhaps the most commonly used. It makes use of the widely accepted theory that the energy spectrum in the inertial subrange is given by:

$$E(\kappa) = C\varepsilon^{2/3}\kappa^{-5/3} \quad (4-11)$$

The value for the dissipation falls out immediately by finding the best fit between Eq. (4-11) and the measured spectra in the inertial subrange (if it exists). Such an approach has been used in numerous flows, such as atmospheric boundary layers (Caughey, et al (1979), Kaimal, et al (1972), and Yadav, et al (1996)), laboratory boundary layers (Klebanoff (1954), and Ligrani and Moffat (1986)), the internal boundary layer of a pipe flow (Azad and Kassab, 1989)), turbulent pipe flows (Lawn (1971), and Azad and Kassab (1989)), in the wake of a circular cylinder (Virk and Azad, 1992), and diffuser flows (Okwuobi and Azad, 1973).

The allure of this method stems from its basis on physical reasoning, and its simple, straightforward nature. Moreover, the required experimental data is merely the spectra of velocity in the inertial subrange. This portion of wave numbers usually is relatively easy to measure when compared to the high and low wave number regions.

There are some drawbacks, however. One is the reliance on the empirical constant,  $C$ . This has become known as the “universal constant”, although there is not especially good agreement on what value it should take. In their review, Elsner and Elsner

(1996) report that empirical data indicate that it should be assigned a value between 0.45 and 0.57. Values in this range appear in all of the references just cited, as well as the text of Bradshaw (1971). (A word of caution: if a 3-D wave number magnitude spectra is used, the recommended value is in the neighborhood of 1.5 rather than 0.5. See, for example, Bradshaw (1971), Tennekes and Lumley (1972), and Doviak and Zrnic (1993).)

Another limitation is the requirement to use Taylor's hypothesis to transform an experimentally measured frequency spectra to a wave number spectra. The potential error introduced by this procedure was discussed earlier.

The final drawback, which at times will render this method unusable, is that the inertial subrange must exist in the flow at the station being measured. This portion of the spectra emerges with increasing turbulence Reynolds number. When the range of eddy sizes becomes sufficiently wide that there is an appreciable region in the spectra which is statistically independent of both the energy containing eddies (low wave number), and the molecular dissipation (high wave number), the intermediate wave number portion of the spectra is the inertial subrange. Some contend that it is difficult to create such a flow in a laboratory settings (Tennekes and Lumley, 1972) while others argue that the conditions often are close enough to warrant the use of Eq. (4-11) (e.g., Lawn 1971).

In the present study, some limited success was achieved by applying this method to the spectra measured with LDV. The results are given in the next section. To our knowledge, this is the first report of any measured dissipation distributions in a swirling flow.

The fourth and final approach also is grounded in the spectral density curve. It is found by integrating the equation:

$$\varepsilon = 2\nu \int_0^{\infty} \kappa^2 E(\kappa) d\kappa \quad (4-12)$$

Details on the physical reasoning can be found in Tennekes and Lumley (1972), or Hinze (1975). Like the method that utilizes a curve fitting approach in the inertial subrange, the attractive qualities of this process are that it is based on physical reasoning, is



straightforward, and only requires a spectra. Moreover, there is no stipulation that the turbulence Reynolds number be high enough for an inertial subrange to exist. However, a potential difficulty in using this method is that both the high and low wave number spectra must be known with acceptable precision. This obstacle may not present a problem when hot wire is the measurement device, or when the characteristic frequencies in the flow are low (atmospheric boundary layers). In the present work, the noise in the higher wave numbers prevented the spectral energy from falling off rapidly enough for the integration to converge. It seems that at a minimum, the region where the spectra falls off at -7 power should be present. This method has been used by Azad and Kassab (1989), and Virk and Azad (1992).

Further details concerning the four methods just described, albeit in the context of hot wire measurements, can be found in the informative review by Elsner and Elsner (1996). Also, Azad and Kassab (1989) and Virk and Azad (1992) apparently employed all of the methods successfully, and gave a brief discussion. The flows in their studies were boundary layer, fully developed pipe flow, diffuser flow, and the far wake of flow past a circular cylinder. They also proposed that any of these methods can be improved upon by estimating the dissipation using hot wires of various length. Since longer hot wires tend to introduce errors, the dissipation which would be measured by a zero length hot wire can be estimated by extrapolation. They show that by using this technique, their results were similar to those of Browne et al (1987).

### **3. Discussion of Results**

Credible distributions of the dissipation of turbulence were obtained using the method that employs the curve fitting technique in the inertial subrange of the spectral estimates. Data were used from  $Re_D = 230,000/h_6$  flow state. The constant  $C$  that appears in Eq. (4-11) was set to 0.5.



Figure 4-135 shows the radial distribution of dissipation in the wake of the breakdown. At  $X = 190$ , the values were determined from the turbulence spectra of the axial velocity. At  $X = 250$ , they were determined from both the axial and tangential velocities.

To explain why profiles were not given for other areas, the spectra of the tangential velocity at  $X = 190$ , and the spectra for both velocities at all stations upstream of this, exhibited no inertial subrange. To demonstrate, we present the spectra beginning at  $X = 250$  mm, and proceed upstream. Figs. 4-97 and 4-98 give the spectra of the axial and tangential velocities at  $X = 250$ , respectively. The curves from Eq. (4-11) are superposed for each curve that seems to have an inertial subrange. As can be seen, all of the axial velocity spectra curves contain an identifiable range where the slope is constant, and obeys the  $-5/3$  power rule. Near the vortex centerline, this is found between 70 and 100 Hz, and the frequency where the inertial subrange is found increases with distance from the centerline. At  $r = 11$  mm, for example, it is found between 100 and 200 Hz. Most of the tangential velocity spectra also suggest the presence of inertial subranges at similar frequencies (Fig. 4-98). Figures 4-99 and 4-100 show the spectral curves for measurements made at  $X = 190$ . A single line with a  $-5/3$  power slope is drawn on both plots. Most of the axial velocity spectral curves at  $X = 190$  show evidence of inertial subrange between 100 and 200 Hz. The spectra for the tangential velocity do not. Continuing upstream, the spectra at  $X = 170$ , shown in Figs. 4-101 and 4-102, contain no evidence of an inertial subrange. Two possible reasons may explain this. First, it is possible that the inertial subrange simply does not exist, because the turbulence Reynolds number may not be sufficiently high at this location. The second is that if one does exist, it may be at a frequency which pushes the limit of the instrumentation. Further upstream, there continues to be no indication of an inertial subrange. As a representative section, some spectra from  $X = 80$  mm are given in Figs. 4-113 and 4-114. A single line at  $-5/3$  power slope is superposed on each plot.

Now we return to the dissipation profiles shown in Fig. 4-135. At  $X = 190$  (Fig. 4-133a), a maximum value of about  $650 \text{ (m/s)}^2 / \text{s}$  is found near the centerline. The value drops off smoothly with distance from the axis, and approaches zero at about 12 mm from the centerline. Compared to the values at  $X = 190$  mm, the dissipation rates at  $X = 250$  mm (Fig. 4-133b) are quite small. From the axial velocity spectra, it appears that the dissipation is more or less flat in the core region, and then drops off outside the wake. From the tangential velocity spectra, the profile is more similar to what was found at  $X = 190$ , albeit at a much smaller magnitude. A noteworthy feature of the two curves at  $X = 250$  is that they appear to have the same value in the range from about 10 to 20 mm from the flow axis. This lends some credibility to the results. For the dissipation to be isotropic, which it should be in the inertial subrange, the values should be the same.

It is regrettable that only the downstream sections could be estimated. The inlet profiles would be more valuable to advance the prospects for success of a numerical code. However, it is hoped that this investigation will promote further exploration into the subject.

An important question that arose during this analysis was the selection of a “mean velocity.” A quantity was required for Taylor’s hypothesis, which was utilized to transform values from the frequency domain to the wave number domain. Others who have measured dissipation have done so for steady, highly unidirectional flows, making the selection obvious. In the present case, where unsteadiness and streamline curvature are significant, the choice becomes unclear. The mean (time averaged) value of the individual component of the spectra seems to be the most reasonable alternative, and is the velocity that was used to estimate the results presented in this section. However, arguments can be made against this choice. First, the turbulent conditions at a point in the flow are not convected along this component of the vector, but rather along the total instantaneous velocity. To illustrate, consider the velocities near the flow centerline at  $X=190$  mm. Both the axial and tangential time averaged velocities are close to zero.

Consequently, whether the axial, tangential, or total velocity is used, the estimated value of the dissipation becomes undefined. The cross sectional mean axial velocity is perhaps better behaved, but is an ill suited quantity to use in the transformation because of physical considerations. It simply does not represent what is occurring at the station under consideration. The time averaged mean velocity of the individual component seems to be the best choice among a set of quantities that all have flaws.

The uncertainty of the results are rather difficult to assess. The most important reason is the selection of velocity just described. Another reason is none of the other methods are feasible, denying the opportunity to develop a basis for comparison. Other authors (Azad and Kassab (1989), Virk and Azad (1992), for example) were able to obtain similar results using several of the methods described in the last section, lending credibility to the data. Unfortunately, this is not yet possible for strongly swirling flows.

#### **4. Concluding Remarks**

Methods for determining the dissipation rate of turbulence were discussed in the context of swirling flows. Acquiring the necessary quantities to estimate the dissipation in strongly swirling flows is particularly difficult because of the inherent problems with using intrusive measurement techniques. Of the several methods described, only one seems to be practicable in the present investigation.

The radial distribution of the dissipation rate in the wake of a vortex breakdown was estimated using the inertial subrange of the spectral curves. The results were in line with expected values, but it is difficult to place a value on the uncertainty of the measurements. Primarily, this is because of the questions surrounding the selection of a mean velocity for use in connection with Taylor's frozen turbulence hypothesis.



## V. DISCUSSION OF RESULTS

### A. TECHNOLOGICAL RELEVANCE OF PHENOMENOLOGICAL OBSERVATIONS

To an aerodynamicist wishing to predict or prevent a vortex breakdown over a delta wing, an engineer striving to extract the benefits of the phenomenon in a combustion chamber, or any scientist investigating vortex breakdown, an understanding of the underlying physics provides an ideal framework in which to conduct his study. In the preceding discussions, a great deal has been presented about different aspects of high Reynolds number vortex breakdowns.

In this section, various facets of the experimental results will be incorporated into a fairly coherent picture of vortex breakdowns at all  $Re_D$ . We will discuss the fundamental questions surrounding the proposed dominance of the spiral form, as well as the structure of the low  $Re_D$  axisymmetric bubble. In doing so, a taxonomy of vortex breakdown will emerge in which the spiral is the fundamental form. Then, related phenomena that occur only in high  $Re_D$  flows will be taken up. These include the core meandering, breakdown darting, and turbulence, as well as other interesting observations recorded only in high  $Re_D$  flows. Plausible explanations for some of these features of the flow will be given, but the fact remains that the phenomena are not fully understood. In addition to answering some of the old questions about vortex breakdown, the new ones that arose from this investigation will be highlighted.

Historically, investigators regarded the three laminar forms of vortex breakdown (i.e., the spiral, axisymmetric bubble, and the double helix) as a complete set that embodies the varied nature of the phenomenon. Since then, Sarpkaya (1995a,b) expanded the group when he reported a fourth mode: the conical breakdown. The accurate categorization of vortex breakdown is an important technological and scientific matter. Apparently, no single mechanism can explain all the features observed in the various



modes, as discussed in Section I-A. This suggests that, serendipity aside, an accurate prediction of a vortex breakdown on theoretical or numerical grounds requires an understanding of the physical distinctions between the modes.

The presence of a spiral at high  $Re_D$ , demonstrated in the present work (Figs. 3-1, 3-7, and 3-12, among others), lends support to Brückner's (1993) notion that the spiral truly is the basic form of breakdown. However, his assertion was based on experiments that were conducted at a single, rather low  $Re_D$  in search of comparisons between the bubble and spiral forms. He observed a breakdown that made periodic transitions between the spiral and bubble-like form, whereas many other investigators reported stable axisymmetric bubbles. Moreover, there was still controversy over whether one or two recirculation cells reside within the bubble.

Based on the results of this and previous investigations, a  $Re_D$  based taxonomy of vortex breakdown can be constructed that distinguishes the spiral as the fundamental form of breakdown, and also provides a consistent explanation of the structures of low  $Re_D$  bubbles. This requires the definition of new (approximate) boundaries to the Reynolds number ( $Re_D$ ) regimes for swirling flows with vortex breakdown in tubes. In most previous investigations,  $Re_D$  above 5,000 to 10,000 was considered relatively high. Now, we may adopt a new convention:

- $Re_D \leq 35,000$                       low  $Re_D$  regime
- $35,000 \leq Re_D \leq 100,000$       transitional  $Re_D$  regime
- $100,000 \leq Re_D$                       high  $Re_D$  regime

Some points should be made regarding these limits. First, they are approximate because discrete behavioral transitions do not occur at any of these values. Second, there is evidence that a “very low”  $Re_D$  range could be carved out of the low  $Re_D$  regime. For example, the double helix form is only known to occur when  $Re_D$  is below 2,000, and other features of the breakdown are different at the extreme ends of this range. However, this investigation focused on the high  $Re_D$  regime, and further investigation should precede

any subdivision. The final point is that even a modest change to the experimental apparatus or axial pressure gradients may cause shifts in the range limits. The importance is not found in the exact numerical values, but rather in the suggestion that the previous boundaries have shifted at least an order of magnitude to the right. With this backdrop, the proposed taxonomy will now be described.

In the low  $Re_D$  regime, the double helix, spiral, and bubble forms are observed. The double helix only occurs at the lower end of this regime, and in a narrow range of swirl numbers  $\gamma$ . Also in the lower end of the low  $Re_D$  regime, a spiral may exist to the exclusion of other forms. Under certain conditions, the spiral may periodically degenerate to a form which has a bubble-like appearance, and a single recirculation cell with reversed axial flow at the centerline, as observed by Brücker (1993). In the rest of the low  $Re_D$  regime, the spiral breakdown is likely to be preceded by an axisymmetric bubble that is distinct from the degenerate spiral form whose appearance is bubble-like. This second type of bubble has two recirculation cells, and the centerline axial velocity remains positive. The true vortex breakdown is a spiral, of course, and occurs in the wake of the bubble. When  $Re_D$  is increased within the low  $Re_D$  regime, the distance between the bubble form and the spiral breakdown decreases (Figs. 3-2 and 3-10), and the spiral rotates more rapidly.

In the intermediate range, the two-celled type of bubble continues to precede the spiral. This is referred to as the transition/intermediate regime because the separation between the bubble and the spiral decreases to the extent that there begins to be mutual interference between the two forms. The bubble and spiral interact, but the spiral retains its form more robustly than the bubble.

In the high  $Re_D$  regime, the spiral breakdown bypasses the two-celled bubble form. Thus, the conical vortex breakdown form is actually a few spirals that are rotating and bursting into turbulence so rapidly that it is nearly impossible to visualize the inception of the “cone” without ultra-high speed recordings. From the high-frame-rate

video, it is estimated that the spiral ( $Re_D = 230,000/h_6$  state) is rotating at over 1,000 revolutions per second. It should be pointed out that to the naked eye, any time the  $Re_D$  is greater than about 35,000, the spiral or spiral structure that forms in the wake of the bubble spins fast enough to appear as a conical wedge of the dye. This was shown in Fig. 1-2a for  $Re_D = 50,000$ .

In the absence of the bubble, the spiral is nearly identical to those observed at low  $Re_D$  (Fig. 3-1), except for the number of identifiable turns. There is a stagnation point, and after one or two windings, the spiral breaks up into turbulence, as noted above.

Despite physical similarities in the still images, it would not be meaningful to assume that a low  $Re_D$  "solution" to spiral vortex breakdown would be a satisfactory simulation of the high  $Re_D$  flows. First of all, the development of the high  $Re_D$  breakdown form is highly evolutionary in nature. Second, there are a number of phenomena which accompany the high  $Re_D$  breakdowns, but are not observed when the  $Re_D$  is low. These will be taken up next.

For one, the stagnation point of the high  $Re_D$  breakdown darts back and forth along the axis. Intuition suggests that when the spiral moves downstream, the windings will tend to compress. On the other hand, it seems they would expand when the stagnation point is moving toward the swirl generator. This, in combination with the compressive force induced by the windings upon themselves, is a plausible explanation for the tendency of the spiral to collapse temporarily into a structure resembling a single torroid. When sufficiently compressed, the dye that is slowly diffusing away from the center of the winding would be recirculated by the adjacent windings, causing the windings to become indistinguishable. Figure 3-17 shows a sequence of high speed video of the breakdown in the  $Re_D = 230,000/h_6$  flow state. In the first few frames (beginning at an arbitrary  $t = 0$ ), an unmistakable spiral structure is observed, but after  $t = 1$  ms, the dye filament in the helical structure ceases to remain coherent. From  $t = 1.25$  ms to  $t = 2.0$  ms, dye recirculates in the vicinity of the stagnation point, making the spiral windings



indistinguishable. Finally, from  $t = 2.25$  ms to the end of the sequence, the spiral reappears. It is not certain whether the darting motion causes this, or vice versa, but the two occurrences seem to be related.

Second, the vortex core in a high  $Re_D$  flow meanders about the mean axis, whereas at low  $Re_D$ , the vortex core remains steady (based on a visual inspection). The underlying mechanism responsible for the high  $Re_D$  meandering has been the subject of some speculation (e.g., Corsiglia, et al (1973), Baker, et al (1974), Green and Acosta (1991), Devenport, et al (1996), Chow, et al (1997)). The cause of meandering usually is attributed to free stream turbulence, or in other applications, wind tunnel unsteadiness. The combined action of an instability and interaction with the ambient turbulence, as implied by Chow, et al (1997), seems to be a likely explanation. They postulated that small disturbances originate near the swirl generator (in their case, a wing tip), and amplify because of the turbulent wind tunnel environment. In the present work, the source of the disturbance could be asymmetry in the flow about the centerbody, or perhaps asymmetry of the vanes. Since the ambient flow was turbulent, sufficient kinetic energy to sustain and amplify the disturbances is conceivable.

A third complicating factor is the non-stationary transition to turbulence in the close proximity to the stagnation point. In the low  $Re_D$  breakdowns, the spiral would persist for a few windings, and then break up into large scale turbulence. This was more or less true in the high  $Re_D$  flow states, except that the location of the transition to turbulence was less fixed relative to the helical structure. Sometimes, the transition even seems to move upstream of the breakdown, as was shown in Fig. 3-15. When this occurs, a conical wedge of fully mixed dye masks any structures that may exist within the breakdown region. However, the DPIV results indicated a persistent spiral structure, still evident well into the wake region. Thus, even after the dye filament has diffused into a conical wedge containing no visibly discernible structure, a well defined helical form or footprints of the spiral remain embedded within the cone.



The complications connected with turbulence are not limited to the transition region. Many of the controllable aspects of this investigation are known to contribute to the overall structure of the turbulence. The  $Re_D$ , the circulation, and the tube profile (convergence and divergence) are all important and highly nonlinear factors in the development of a turbulent flow. At present, however, the fundamental nature of turbulence remains largely unexplained. In such a complex environment, it appears hopeless to elucidate the physics behind some of the observations with regard to the flow turbulence. This is an aspect of the flow that numerical models may illuminate, when they become sufficiently mature to deal with the effects of streamline curvature and radial pressure gradients.

The present work advanced the current understanding of the aforementioned accompanying phenomena, but they had been discussed in the context of breakdowns before. In this regard, they are not new discoveries. During the course of this investigation, there were other findings about the nature of the high  $Re_D$  breakdowns that are interesting, important, and have not been previously observed. Moreover, they further differentiate the nature of the high and low  $Re_D$  flows.

The sense of the spiral windings of the high  $Re_D$  breakdowns exhibited freedom to reverse direction. Figure 3-7 gives images of the spiral breakdown that clearly show the sense of winding had changed. From previous studies of low  $Re_D$  (laminar) breakdowns, it was the consensus view that the sense of the windings of the spiral structure is always opposite to the main swirling flow in tubes, but with the main flow over delta wings. There seemed to be a built in bias associated with each apparatus. Now, it has been demonstrated that the bias in tubes exists only at low and intermediate  $Re_D$ . A possible explanation for this may be the difference in tube wall effects. The laminar boundary layer in low  $Re_D$  swirling flows quickly grows to engulf the vortex near the centerline (Fig. 1-6). One influence of the complicated swirling boundary layer structure may be the directional bias on the windings. In sharp contrast, the wall effects

were relatively distant from the vortex in the present work, at least in terms of the characteristic viscous lengths, i.e., core size (Fig. 4-4). With respect to delta wings, there is a fundamental difference in the physics of the flow that suggests the bias will always be present. Vorticity is being fed into the vortex from the leading edge of the entire length of the wing. Such a physical bias in the flow will not be overcome, even if the Reynolds number were increased significantly. Thus, it is believed that the sense of the spiral will invariably agree with the main swirling flow over delta wings.

Another observation was the tendency for the spiral windings to bifurcate. Figure 3-13 shows images which illustrate that the dye filaments would suddenly branch out into two coherent rotating windings. In other instances, the main filament would give rise to three or more windings (Fig. 3-36). It seems possible that the bifurcations and the intermittent collapse of the spiral into a bubble form may be related. The shear stresses induced on the windings by adjacent parts of the structure certainly play a role in the collapse of the spiral into a torroid, and may also be partially responsible for the filament bifurcations. Admittedly, physical understanding of the mechanism that gives rise to these occurrences is rather tentative.

An additional distinguishing feature between the high and low  $Re_D$  breakdowns was discerned from the LDV results. It was seen that the mean axial velocity at the centerline never became negative (reversed flow) in the  $Re_D = 300,000/h^3$  state. Although this velocity became essentially zero, and there were a number of recorded Doppler bursts indicating instantaneous negative velocity in the course of the fluctuations, its mean value remained positive at all axial sections. The presence of recirculation had often been regarded as a defining characteristic of breakdowns, but here we see that it is not an essential or defining characteristic.

Finally, a question that must be raised is whether a new breakdown form would appear if  $Re_D$  were increased significantly beyond that achieved in the present investigation. No observations were made during the flow visualization that would

suggest an alternate form. Also, within the quantitative results, the only trend indicative of a significant change with increasing  $Re_D$  was the greater diffusion of vorticity from the core to the outer flow. This occurrence is understandable on physical grounds because at higher  $Re_D$ , the diffusion mechanism is turbulence rather than molecular viscosity. It would be expected that the inlet velocity profiles would continue to change with increasing  $Re_D$ . The normalized jet profile will become weaker due to the transport of azimuthal vorticity, and the tangential velocity profiles will be less potential-like due to the transport of axial vorticity. This does not, however, suggest that an entirely new form exists at very high  $Re_D$ . However, there is no doubt that the onset of turbulent burst in the nascent spirals will begin ever sooner with increasing  $Re_D$  and the shape of the breakdown may resemble a more pointed cone than those observed at  $Re_D \approx 300,000$ . Also, it should be pointed out that experiments at  $Re_D$  well beyond those of the present work would be an expensive undertaking, because it becomes increasingly difficult to prevent cavitation.

We have attempted to gather the most important observations made during this investigation and to present a fairly complete picture of the vortex breakdown phenomenon. A Reynolds number based taxonomy was constructed, and a number of observations that place distance between the high and low  $Re_D$  vortex breakdowns in tubes have been discussed. In essence, the high  $Re_D$  form is a highly unsteady, asymmetric spiral vortex breakdown residing in, interacting with, and merging into swirling turbulent surroundings.

## **B. RELEVANCE TO THEORETICAL MODELS**

Our interpretation of the findings concerning high  $Re_D$  vortex breakdown will be discussed briefly in the context of past and present theoretical models.

Over the past 40 years, a number of theories were proposed that purported to explain or predict vortex breakdown. Some of these were described in Section I-A.



Invariably, the theories that have been in existence for more than a few years have been criticized for falling short of predicting or explaining vortex breakdown. Mostly, they are based on the assumptions of laminar, inviscid, axisymmetric, and steady flow. Since this is not in agreement with the nature of the high Reynolds number breakdowns presented herein, it seems impossible that any of these theories could capture the physics of the breakdown.

We will now dispense with the older models and take up only the most recent theoretical work which has appeared in a number of papers (Wang and Rusak (1996a,b, 1997b), Rusak, et al (1996), Rusak, et al (1997b), and Rusak, et al (1998)). The authors (Rusak, et al, 1997b) claim that “The theory provides, for the first time, a consistent explanation of the physical mechanism leading to the axisymmetric vortex breakdown phenomenon in high Reynolds number flow in a pipe, as well as the conditions for its occurrence.” Based on a comparison with the existing data (Garg and Leibovich, 1979), they noted “good agreement between the theoretical predictions and the experimental results is found in all cases.” Clearly, they too assume an axisymmetric breakdown. More importantly, however, Garg and Leibovich (1979) data, taken in an apparatus which is an exact copy of that first devised by Sarpkaya (1971), are not at “high Reynolds numbers.” In fact, by our current standards, they are at relatively low Reynolds numbers.

Rusak, et al (1997b) provided a methodology to compute swirl levels denoted  $\omega_0$  and  $\omega_1$ . “The swirl level  $\omega_0$  is a threshold level for breakdown and the condition  $\omega > \omega_0$  is a necessary condition for breakdown to appear. The condition  $\omega > \omega_1$  is a sufficient condition for breakdown.” In order to compute  $\omega_0$ , “it is necessary to find all the solutions of the (following) ODE for a given  $\omega$ , including solutions with a stagnation zone around the centerline.”

$$\begin{aligned} \psi_{yy} &= H(\psi) - I'(\psi)/2y \\ \psi(0) &= 0, \quad \psi(1/2) = \psi_0(1/2) \end{aligned} \tag{5-1}$$



Here,  $\psi$  is the stream function,  $y = r^2/2$ ,  $H$  is the total head function, and  $I$  is the extended circulation. “Then, for each solution the integral  $E(\psi)$  (given below) is computed and compared with that of the base inlet state with the same  $\omega$ ,  $E(\psi_0)$ .”

$$E(\psi) = \int_0^{1/2} \left( \frac{\psi_y^2}{2} + H(\psi) - \frac{I(\psi)}{2y} \right) dy \quad (5-2)$$

$E(\psi)$  is the “ ‘flow force’ that characterizes the flow.” The values of  $\omega_0$  and  $\omega_1$  become apparent from the nature of the bifurcation diagrams,  $\psi$ - $E(\psi)$ , for various  $\omega$ .

The authors carried out the calculations using the well known Burgers’ vortex approximations (Rusak, et al (1996, 1998), and q-vortex equations (Rusak, et al, 1997b). The q-vortex approximations for the present work were shown in Figs. 4-94 through 4-96, and the values are given in Table 5-1.

	q	$U_e$	$\delta = U_e/U_m$	$\omega = \frac{q\delta}{U_e}$
120,000/h6	1.34	5.5	2.4	0.58
230,000/h3	1.55	9.0	2.1	0.35
230,000/h6	1.68	7.3	1.8	0.40
300,000/h3	1.95	8.1	1.4	0.34

Table 5-1. Parameters for q-vortex approximations.

It is probable that if the calculations were carried out, they would demonstrate that the experimental swirl falls between  $\omega_0$  and  $\omega_1$ , indicating the presence of an “axisymmetric” breakdown where one does not exist in that form, but only as a spiral. On the other hand, we have deemed it to be more important to understand the basics rather than the consequences of the simplified equations. A perusal of the papers by Rusak and his coworkers (references listed earlier) shows that, although they began with the unsteady Euler equations, the critical swirl levels are based on a steady state. They wrote (Wang and Rusak, 1997b) “We study the stability characteristics as well as the time-asymptotic behaviour of the flow as it relates to the steady-state solutions.” The

other fundamental assumptions are inviscid, incompressible, axisymmetric flow through a constant-area pipe. Concerning two of these simplifications, they (Rusak, et al, 1997b) noted “when viscous effects or pipe divergence become significantly dominant, the instability mechanism disappears and vortex breakdown develops as a disturbance that gradually grows with the increase of the incoming swirl. Still, even for these cases,  $\omega_0$  provides a good estimate for the conditions that breakdown will first appear.” In subsequent papers, they investigated the effects of small tube wall divergence (Rusak, et al, 1997a), slight viscosity (Wang and Rusak, 1997a), and vorticity perturbations (Rusak, 1998). They found that each of these introduces a singular behavior around the critical swirl. “This singularity infers that large-amplitude disturbances may be induced by the (additionally considered effect) when the incoming flow to the pipe has a swirl level around the critical swirl.”

The emerging fact is that the high  $Re_D$  breakdown form is assumed to be an axisymmetric body, at least in the vicinity of the vortex breakdown. Without the assumption of axisymmetry, it would have been impossible to arrive at the equations and conclusions described by Rusak and Wang. The presentation of their analyses was partly to point out this fact, and partly to state, as demonstrated throughout this entire thesis, the “high Reynolds number” vortex breakdown is not axisymmetric in the vicinity of the stagnation point (see, e.g., Figs. 3-7, 3-11, 3-12, and 3-36). It is for this reason that the time consuming numerical calculations described above have been dispensed with.

### **C. APPLICABILITY OF PRESENT RESULTS TO NUMERICAL SIMULATION**

Devising a theory that predicts the occurrence, or explains the underlying mechanisms of vortex breakdown would be a crowning achievement. However, since such a theory has proven to be elusive, it seems inevitable that numerical computations will

receive ever increasing emphasis. In this section, we will discuss how the results presented herein can be used for the benefit of breakdown simulations.

It is appropriate to begin by looking at the various approaches behind the numerical methods themselves. Direct Numerical Simulation (DNS) makes use of the full, time dependent Navier Stokes equations. The method is attractive because of the reliability of the results, but is very expensive computationally. Owing to time and length scale considerations, current simulations are limited to Reynolds numbers on the order of 1,000. Large Eddy Simulation (LES) also employs the full Navier Stokes equations, but only for the large scale motion. Reynolds numbers on the order of 10,000 are achievable because of the coarser mesh and longer time intervals compared with those used in DNS. The theory behind LES is that the small scale, higher frequency turbulent motion is universal, and can be modeled rather than computed. However, such a model is yet to be found, despite the high level of research interest. A final method employs time averaged equations of motion, such as Reynolds Averaged Navier Stokes (RANS), and Favre Averaged Navier Stokes (FANS). The assumption is that the mean flow can be computed using the averaged equations of motion, and the remaining terms, i.e., turbulence, can be modeled. Although this approach allows for Reynolds numbers on the order of 100,000 or more, turbulence models have conspicuous weaknesses. For example, even among relatively simple applications, the models are not portable because the empirical constants require adjustment for each change to a geometric or flow parameter. Complex flows are even more problematic, especially when characterized by streamline curvature, adverse pressure gradients, the transition to turbulence, or anisotropic turbulence. Additional information about turbulence models and the three methods just described abounds in the literature (e.g., Launder (1989), Bradshaw (1994, 1996), Hanjalic (1994), Marvin (1995), Rodi, et al (1997)). For our purposes, it is sufficient to present this brief discussion, noting that the three broad categories of codes have relatively clear advantages and disadvantages relative to the others.



In the results of the present work, the phenomenological descriptions and LDV measurements show the same vortex breakdown under different lights. In essence, even though it is known that the breakdown form is asymmetric, the LDV velocity and turbulence profiles were axisymmetric. The presence of a rotating spiral, as opposed to an axisymmetric form, has profound implications on the connection between the data and the truth because time averaged results do not, and cannot, depict the essence of the instantaneous breakdown flow field, as evidenced by the DPIV results. In the mean, a spiral appears as a single celled axisymmetric bubble. Thus, the flow can be taken to be axisymmetric only in the inlet region. For this reason, we will depart from discussion of axisymmetric cases.

There has been some work in which the spiral breakdown was predicted (Spall and Gatski (1991), Spall (1996)). These simulations were made using the time-dependent, 3-D equations of motion, albeit at low Reynolds numbers.

Having described this, we can now state that the monumental challenge is to move to higher Reynolds number, higher circulation flow states characterized by small core radii (unlike flows in rotating pipes). Among the formidable tasks is the development of the appropriate means and/or turbulence models for such an undertaking. The use of DNS for such a flow simply will not be practicable in the foreseeable future. The remaining alternatives, LES or time averaged codes, will only perform to the level of the turbulence model. Currently, turbulence itself defies explanation, a fact that is even more acute in the case of strongly swirling flows because the damping of turbulence by centrifugal forces and the effect of pressure gradients pose special problems. Thus, whether it is feasible in the near future, the fact remains that everything the time averaged LDV provided, and more, will have to be predicted. The spiral character of the breakdown region and anything that is associated with unsteadiness should be simulated, using for validation the time averaged values in appropriate regions of the flow.





## VI. CONCLUSIONS AND RECOMMENDATIONS

It has been shown that the vortex breakdown is the transformation of a slender vortex into three-dimensional forms. Where, how, and under what circumstances does this transformation occur in viscous vortical flows constitute the essence of the breakdown problem. Neither a stagnation point, nor a region of reversed flow, nor the bridging of laminar-turbulent states is necessary.

The difficulties experienced in describing the nature, identifying the occurrence, and predicting the characteristics of laminar vortex breakdowns in tubes and over delta wings have been reviewed in detail. It suffices to note that after forty years of observations, measurements, and numerical experiments, the phenomenon remains largely in the qualitative, descriptive realm of knowledge. There are neither exact solutions nor universally accepted theoretical models which capture the essential physics, weave ‘understanding’ into large amounts of numerical, experimental, and observational records, and offer methods of prediction. Theories based on the inviscid (often axisymmetric) flow assumption have become a rival faith to physical and numerical experiments.

This dissertation described experiments on various types of vortex breakdown in non-cavitating swirling flows in a number of axisymmetric tubes at Reynolds numbers as large as 300,000. The results refute the conjectures that the circumstances of breakdown are insensitive to the Reynolds number and the local turbulence properties. These two factors have a strong influence on the evolution of the flow. Of all the known forms, the spiral emerges as the most fundamental breakdown form. All other forms may be regarded as transient states affected by various types of instabilities. The nearly axisymmetric form has served to excite imagination, to test some numerical schemes, and to produce numerous ‘explanations’ of the breakdown phenomenon. However, at very high Reynolds numbers, the breakdown acquires forms and characteristics never seen before: Extremely high rates of revolution, onset of core-bifurcation or core-trifurcation,

intense nonisotropic turbulence, and a conical shape, resembling a spiraling and swirling jet. It is clear that the vortex breakdown over a delta wing is not what it appears to be in the model tests but rather more like what is described herein.

If there is any hope of making realistic numerical simulations of the turbulent vortex breakdowns, all boundary conditions, in particular the velocity and turbulence profiles and the turbulence dissipation upstream of the breakdown, need to be known with great precision. In this effort, one cannot emphasize strongly enough the need for a robust turbulence model which can deal with nonisotropic turbulence in swirling flows subjected to streamline curvature and strong radial pressure gradients.

Using Laser Doppler Velocimetry (LDV), archival quality results of the mean velocities, turbulence moments, and spectra were obtained in various tubes for various  $Re_D$  (between 120,000 and 300,000). The presence of a mean negative axial velocity became weaker with increasing  $Re_D$  and there was no (mean) reverse flow region in the  $Re_D = 300,000$  flow state. Also, because of turbulent diffusion of vorticity, the fraction of overall circulation contained in the viscous core decreased with increasing Reynolds number, a phenomenon which is of extreme importance in the decay of trailing vortices.

The affects of the unsteadiness on the time averaged LDV results were discussed and assessed. Even though LDV cannot capture the essence of the instantaneous flow field, the time averaged results will hopefully serve as a benchmark for future computational predictions, partly because even the time-dependent 3-D calculations can be subjected to azimuthal averaging for comparison with LDV measurements.

Numerical simulation is the most natural extension of this research. Data are available for inflow conditions, and the wealth of phenomenological and quantitative results can be used for performance evaluation. The simulation of the results presented herein will be a major challenge because of a number of reasons, including the high degree of asymmetry, the short time and length scales, anisotropy of turbulence, transition to turbulence, streamline curvature, and the adverse pressure gradients.

As far as the experiments are concerned, one might wish to compare the behavior of high Reynolds number breakdowns in tubes with that of vortex breakdown over delta wings at high angles of attack and in combustion chambers. In so doing, it is imperative that realistic conditions be maintained. It is noted that it would be dangerous to assume that conclusions extracted from experiments in calm, low Reynolds number environments apply to the turbulent conditions that exist in real-life settings. This is not only because of the differences between the high and low Reynolds number breakdowns, but also the evolutionary development of the phenomena with increasing Reynolds number.

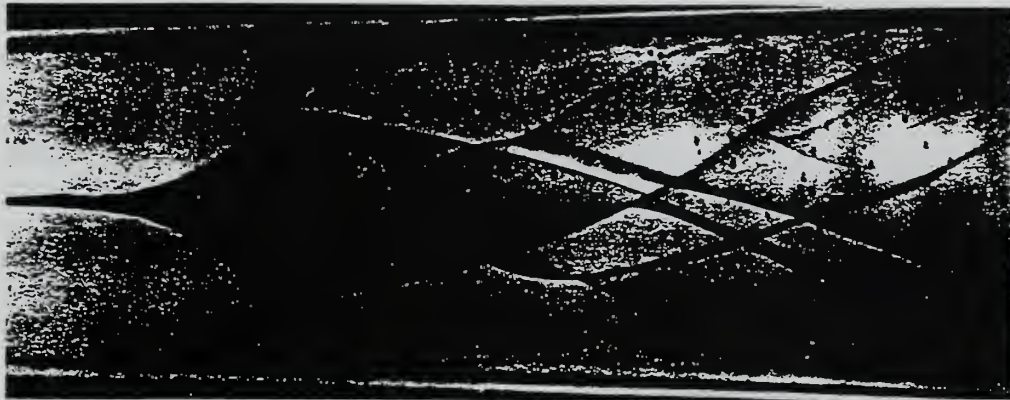
Finally, there are basic research issues that can be investigated. At high Reynolds number, the most prominent are the unsteadiness (meandering, darting) and of course, turbulence in swirling flows. At low  $Re_D$ , the nature and importance of the double helix form needs further examination.



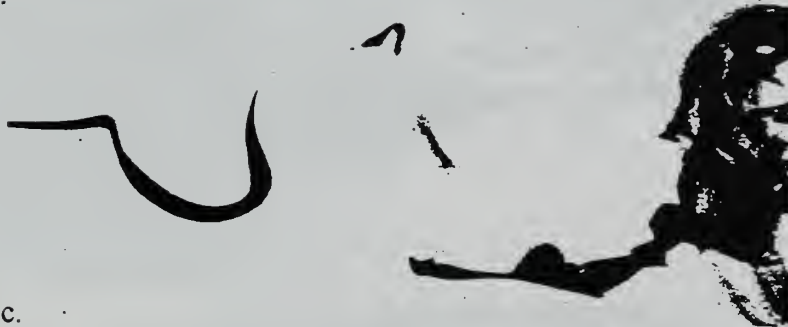


## APPENDIX A. FIGURES

a.



b.



c.

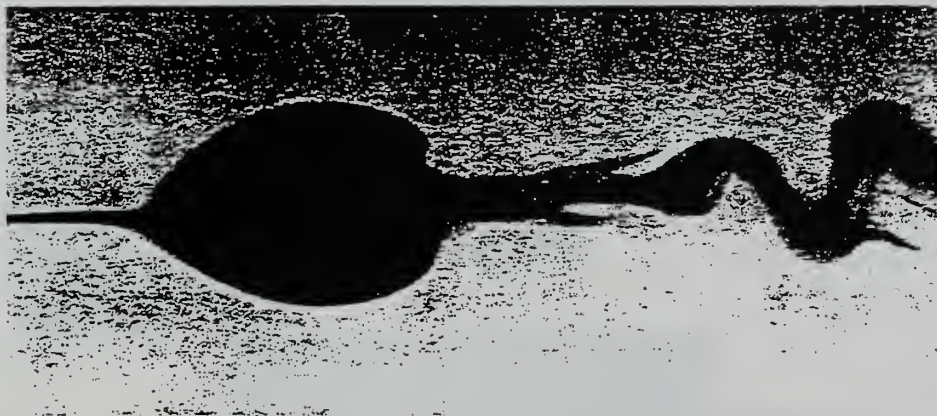


Figure 1-1. The vortex breakdown forms that are observed in laminar flow (images from the experiments of Sarpkaya (1971)). (a.) Double helix. (b.) Spiral. (c.) Axisymmetric bubble form.

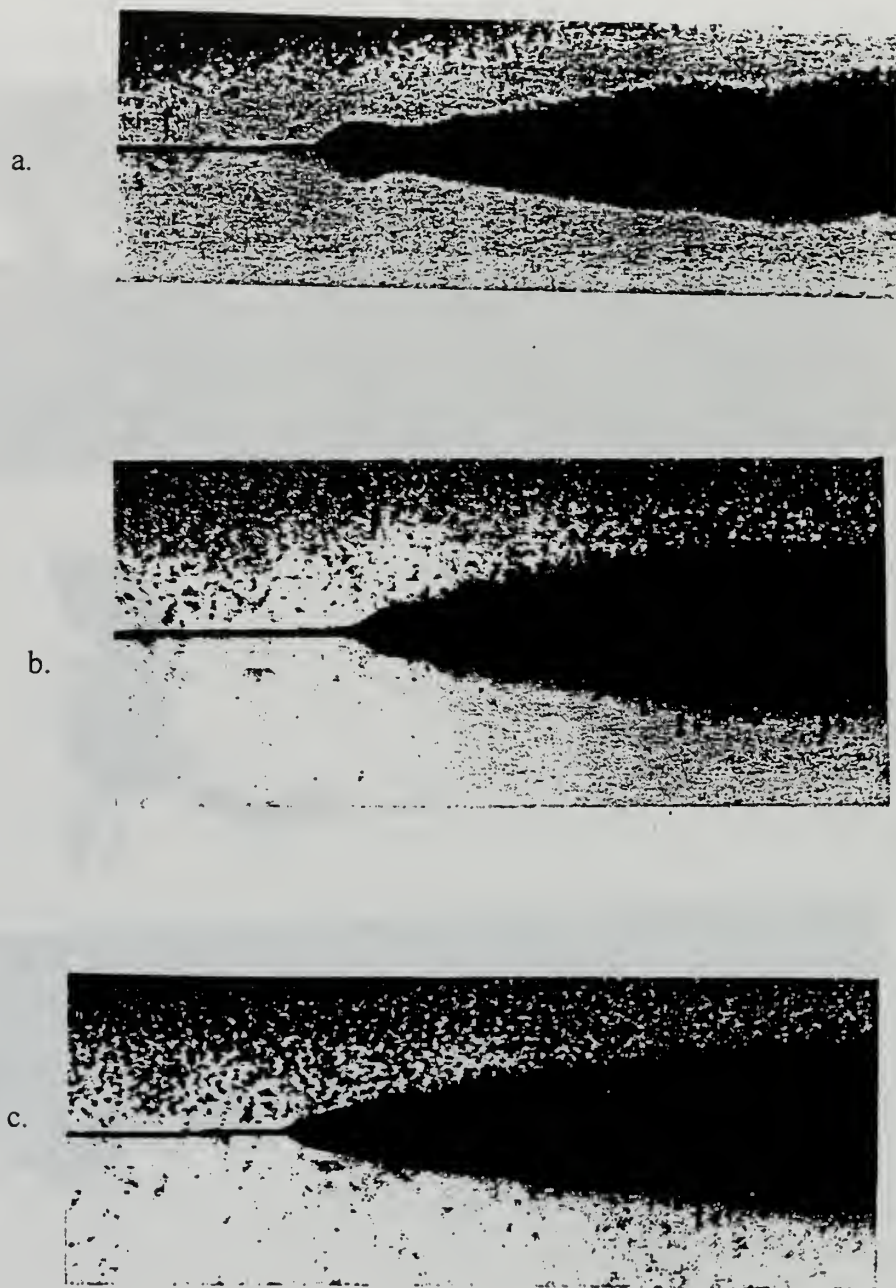


Figure 1-2. The conical vortex breakdown form, which is observed in turbulent flows (images from the experiments of Sarpkaya (1995)). (a.)  $Re_D = 50,000$ . (b.)  $Re_D = 100,000$ . (c.)  $Re_D = 200,000$ .

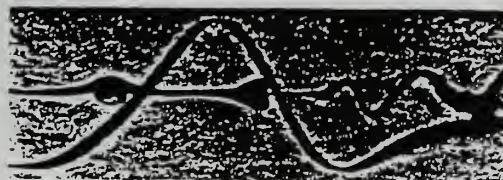
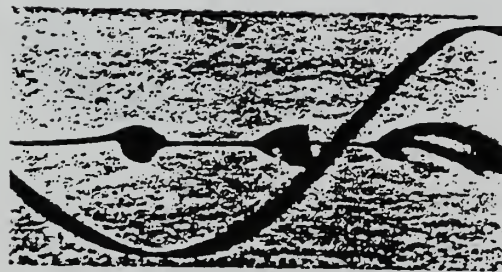
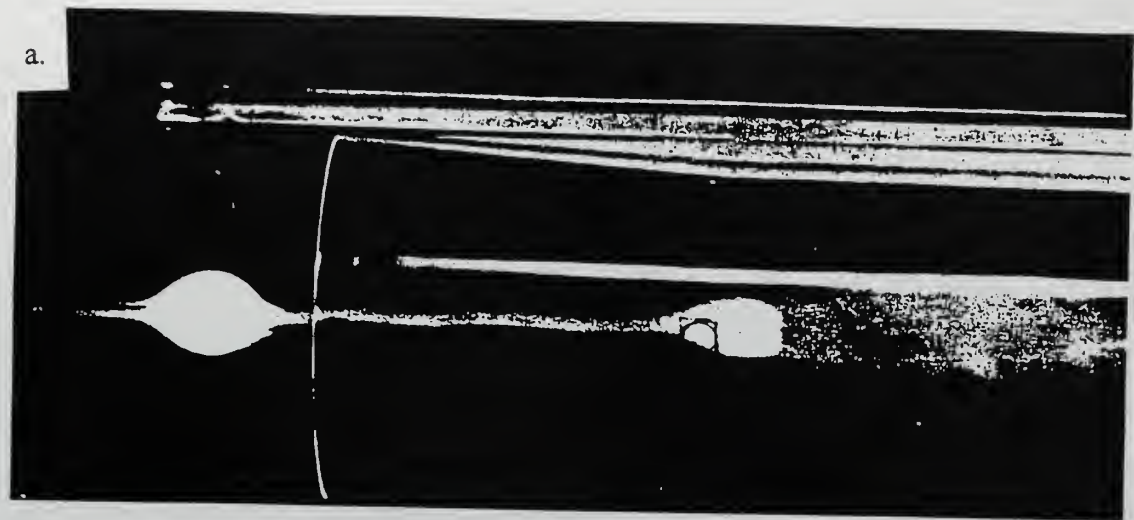


Figure 1-3. Instances where more than one axisymmetric bubble appeared in the flow field. (a.) Harvey, 1962 (b.) Sarpkaya, 1971



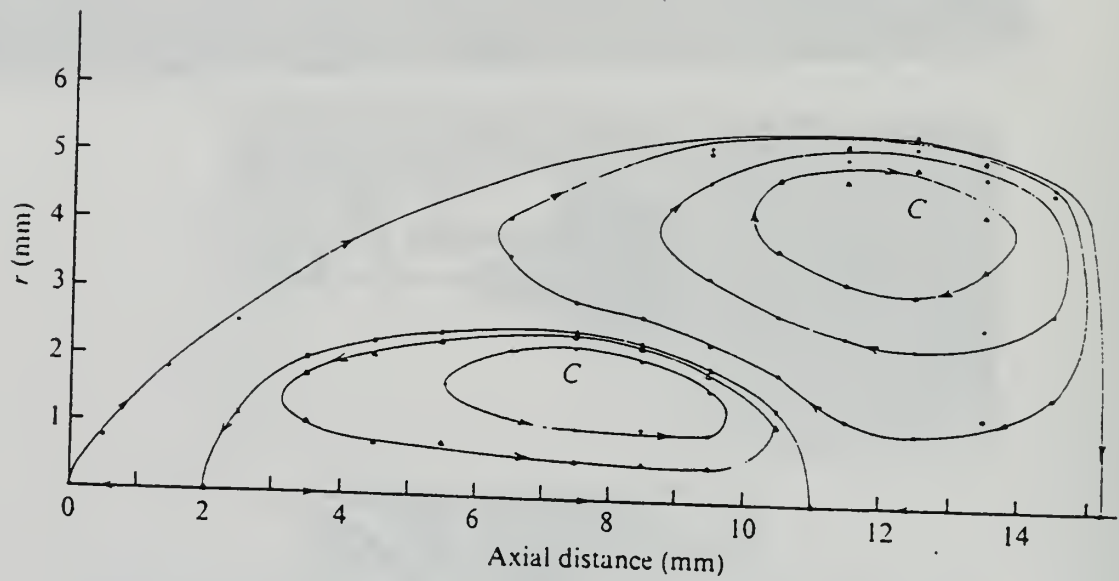
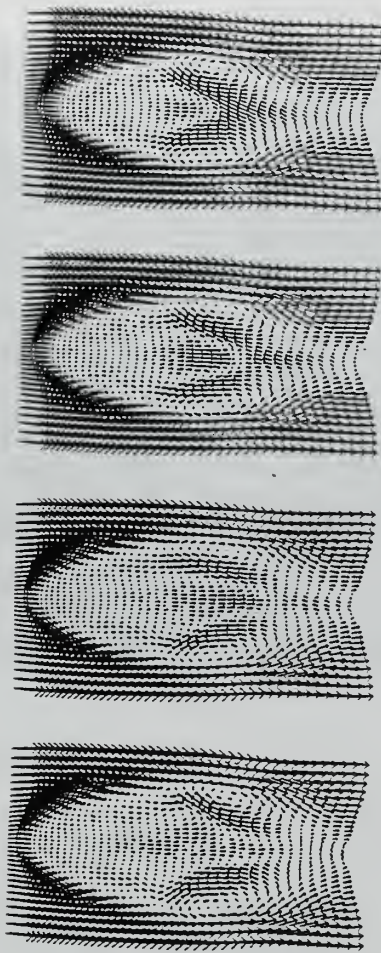


Figure 1-4. The internal structure of a laminar, axisymmetric bubble with two recirculation cells ,  $Re_D = 2,560$  (experiments of Faler and Leibovich (1978)).

a.



b.

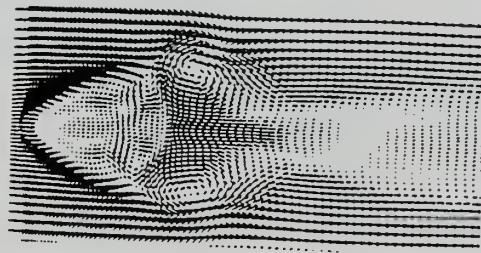


Figure 1-5. The internal structure of a laminar, axisymmetric bubble with two recirculation cells (numerical work of Spall, et al (1990), and Spall and Gatski (1991)).

(a.) Spall, et al, 1990. (b.) Spall and Gatski, 1991.

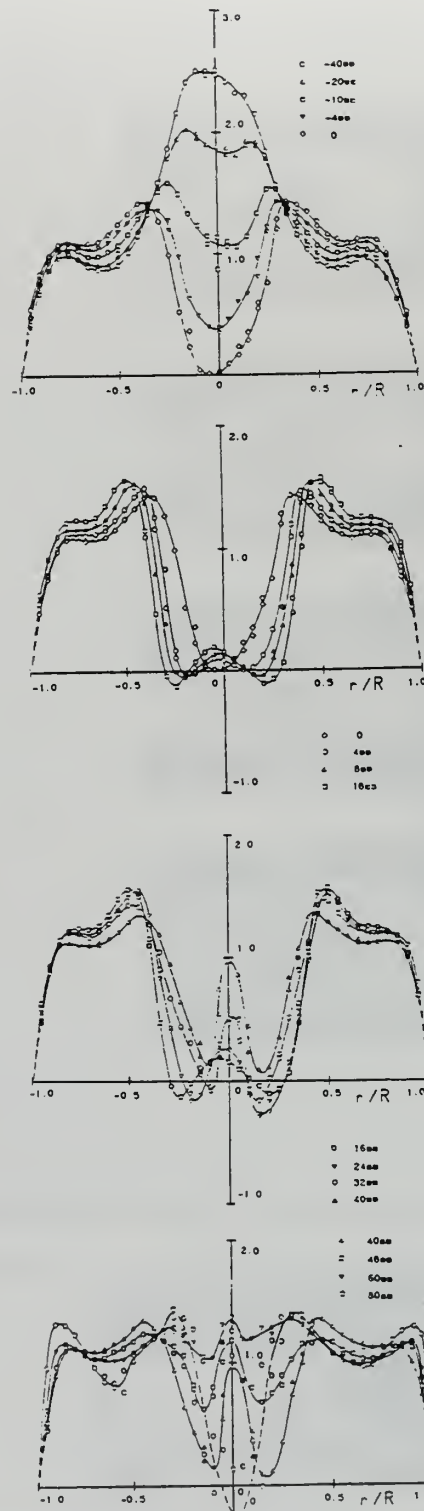


Figure 1-6. Velocity profiles of a laminar flow field with vortex breakdown and an axisymmetric bubble,  $Re_D = 2,300$  (experiments of Uchida, et al (1985)).

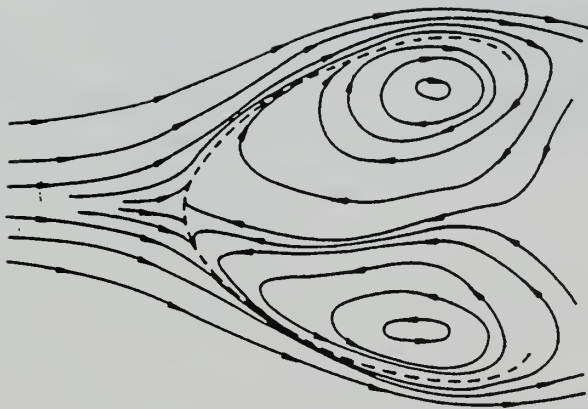
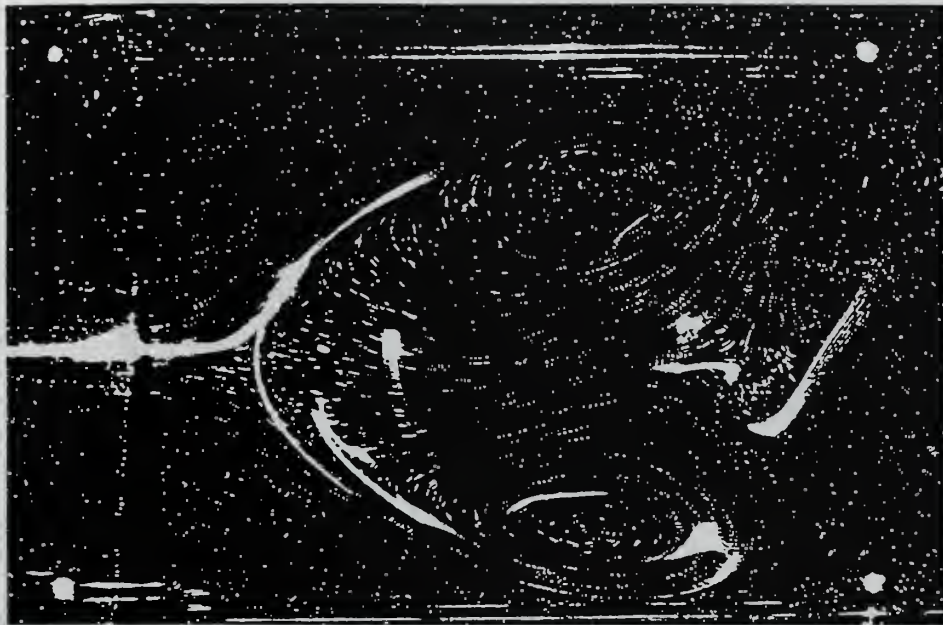


Figure 1-7. Internal structure of a laminar, axisymmetric bubble with a single recirculation cell,  $Re_D = 840$  (experiments of Brücker and Althaus (1992)).



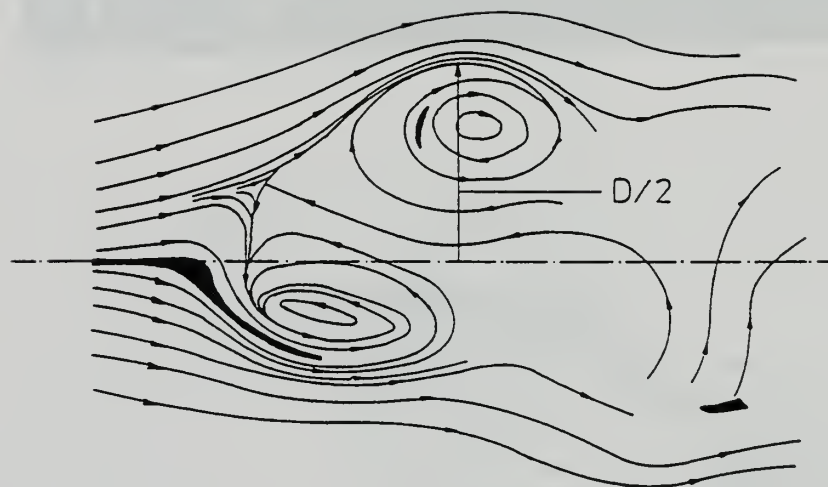
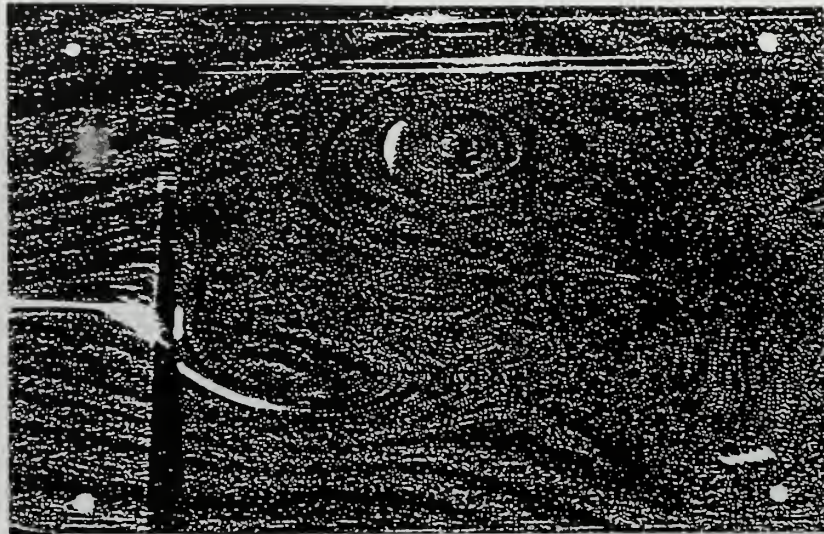


Figure 1-8. Internal structure of a laminar spiral vortex breakdown,  $Re_D = 840$  (experiments of Brücker (1993)).

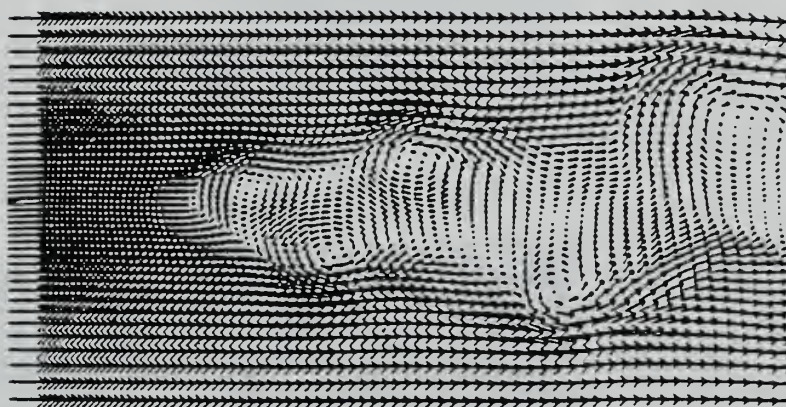


Figure 1-9. Internal structure of a laminar spiral vortex breakdown (numerical work of Spall and Gatski (1991)).

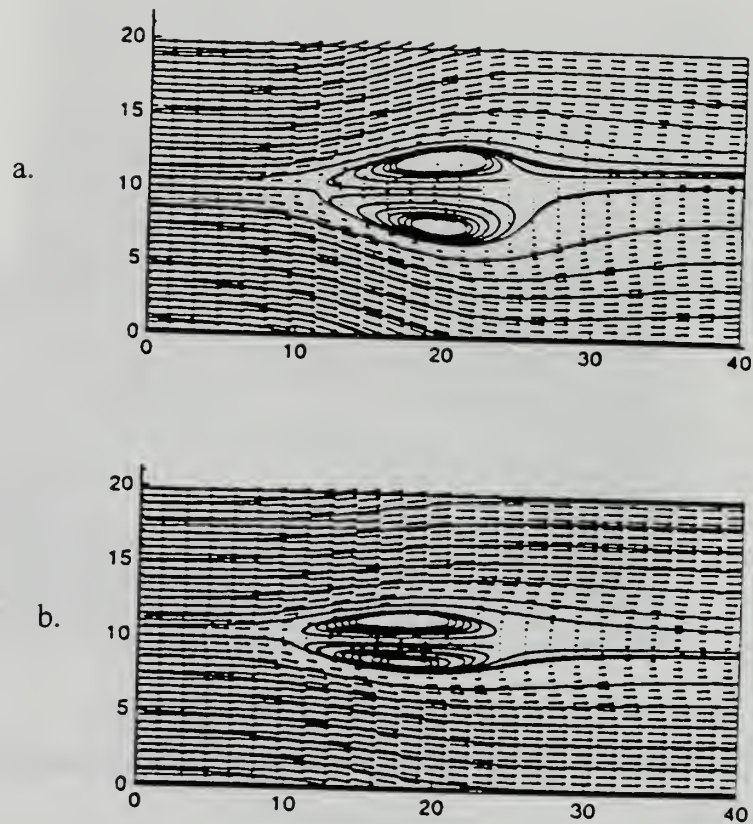


Figure 1-10. Internal structure of a turbulent vortex breakdown (numerical work of Spall and Gatski (1995)). (a.)  $k$ - $\epsilon$  turbulence model. (b.) Algebraic Reynolds stress model.

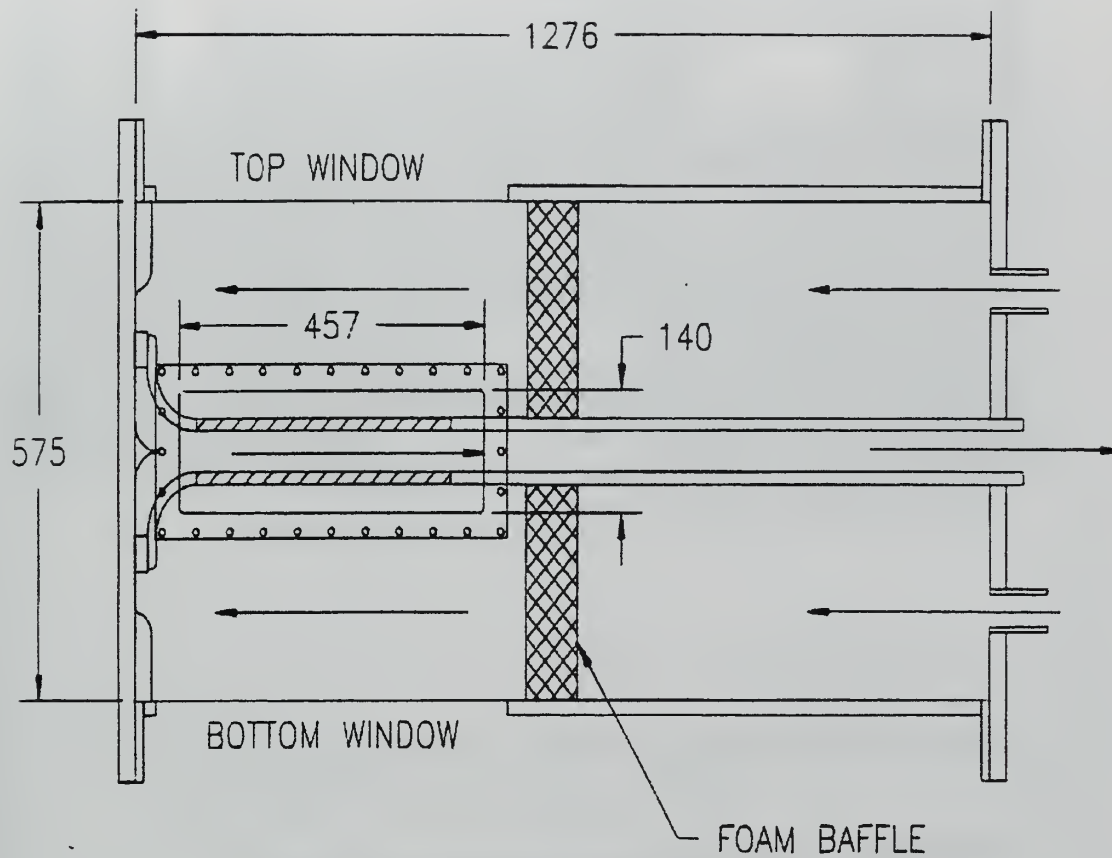


Figure 2-1. Flow apparatus employed in the present work. All dimensions are in mm. Arrows not denoting a length indicate direction of flow.



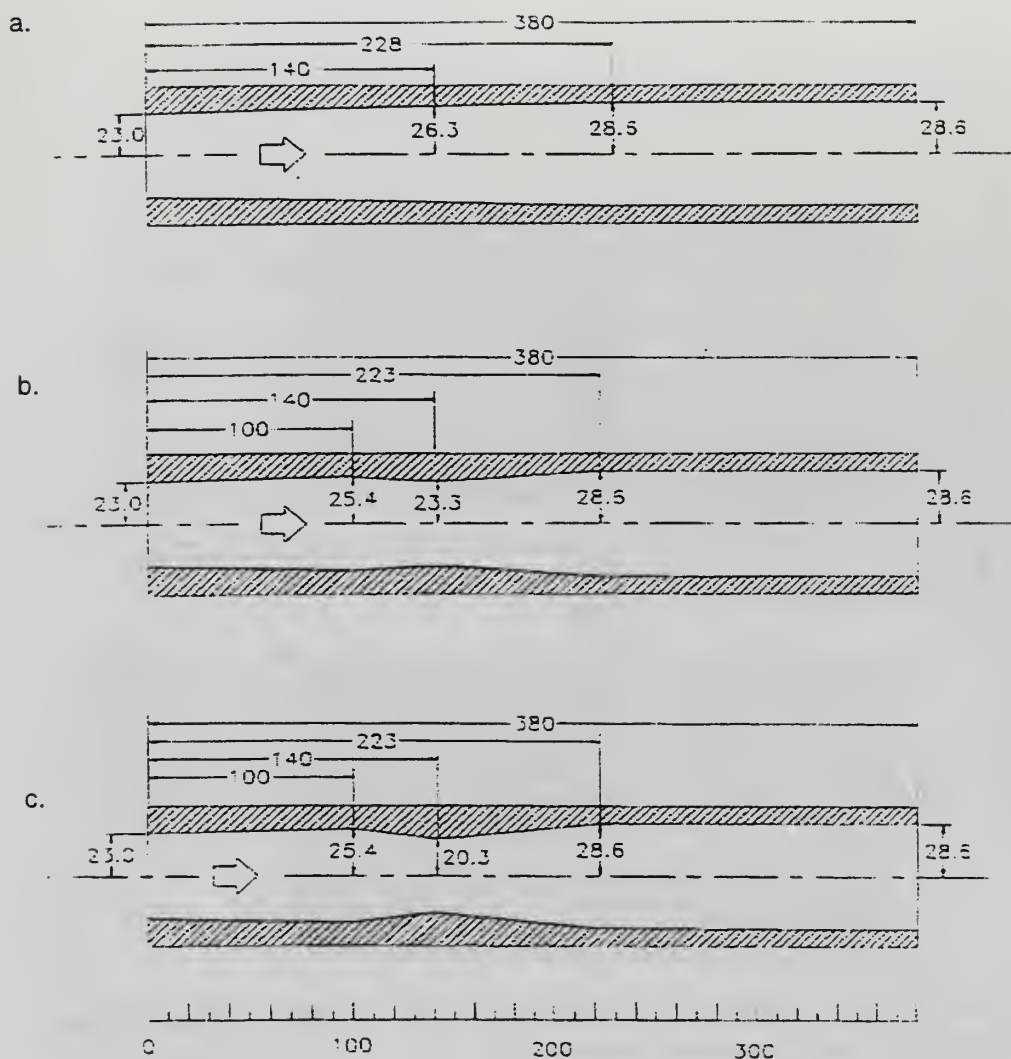
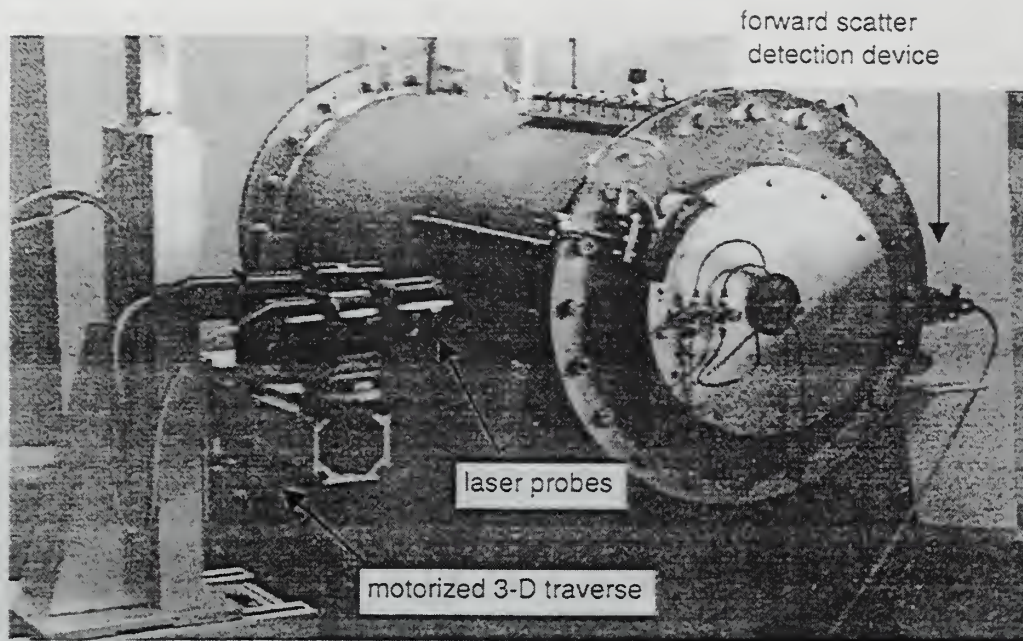
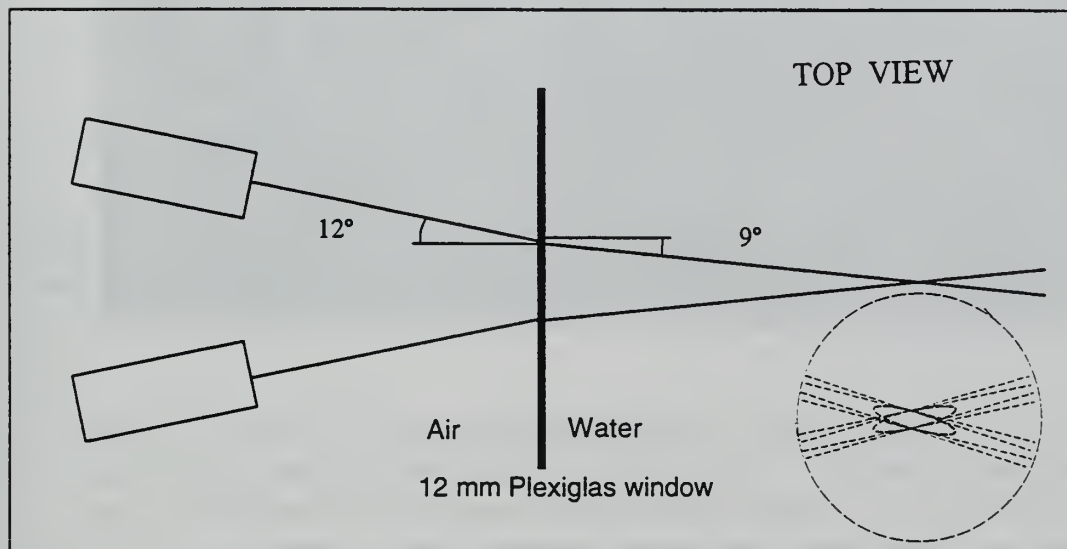


Figure 2-2. Profiles of the tubes used in the present work. All dimensions are in mm. The fat arrows indicate the direction of flow. The radius at the throat, compared to what is found in the straight wall tube, was used for the naming convention. The tube names are as follows. (a.) The "h0" tube. (b.) The "h3" tube. (c.) The "h6" tube.



a.



b.

Figure 2-3. Experimental flow apparatus and LDV arrangement. The laser beams entered the chamber through one of the side windows. When used, the forward scatter detection device was mounted on the opposite side of the chamber. (a.) Photograph of physical arrangement. (b.) Schematic of probe and beam arrangement. Inset picture (beam cross-section) taken from Dantec User's Guide, 60X Series FiberFlow, p. 26.

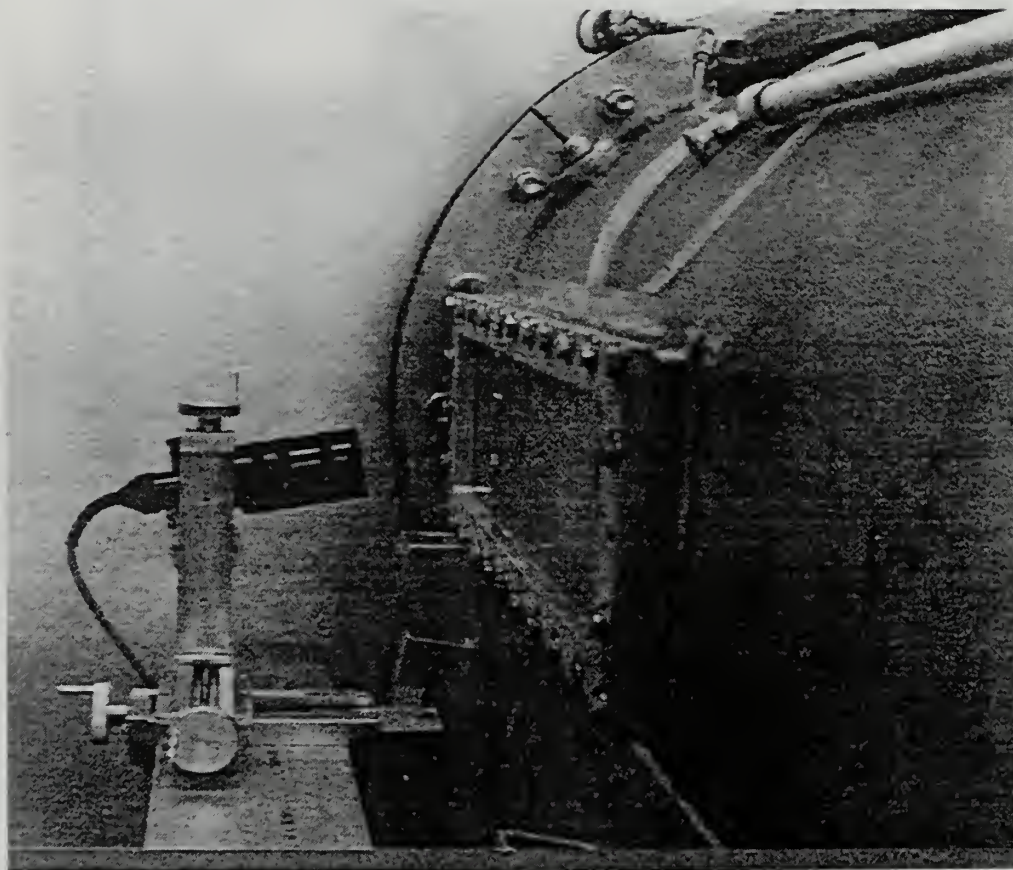


Figure 2-4. Forward detection receiver optics and manual 3-D traverse. This is a reverse angle from Fig. 2-3. The receiver optics detected scattered light through the side window on the opposite side of the chamber from the laser probes. The device was mounted at an angle of about 10 degrees from horizontal.

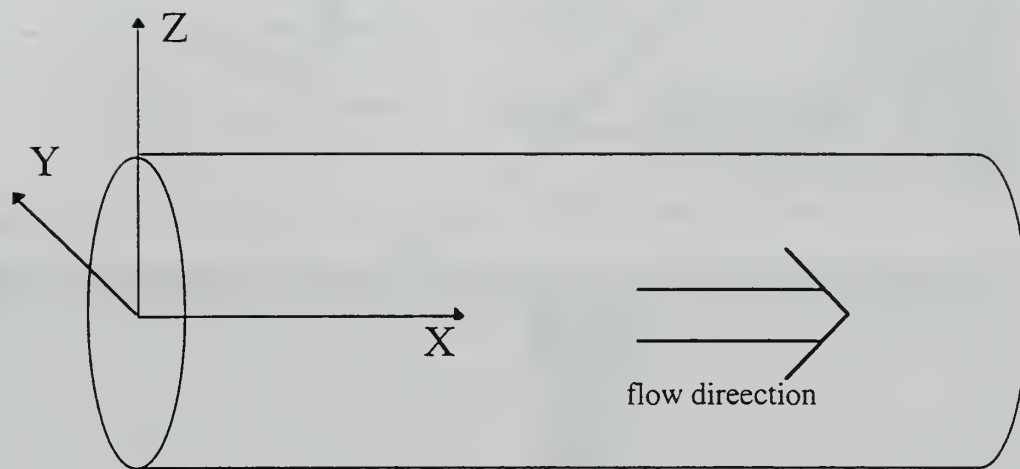


Figure 2-5. Experimental coordinate system. Care was taken to ensure that the Z coordinate of the measuring volume was close to zero.



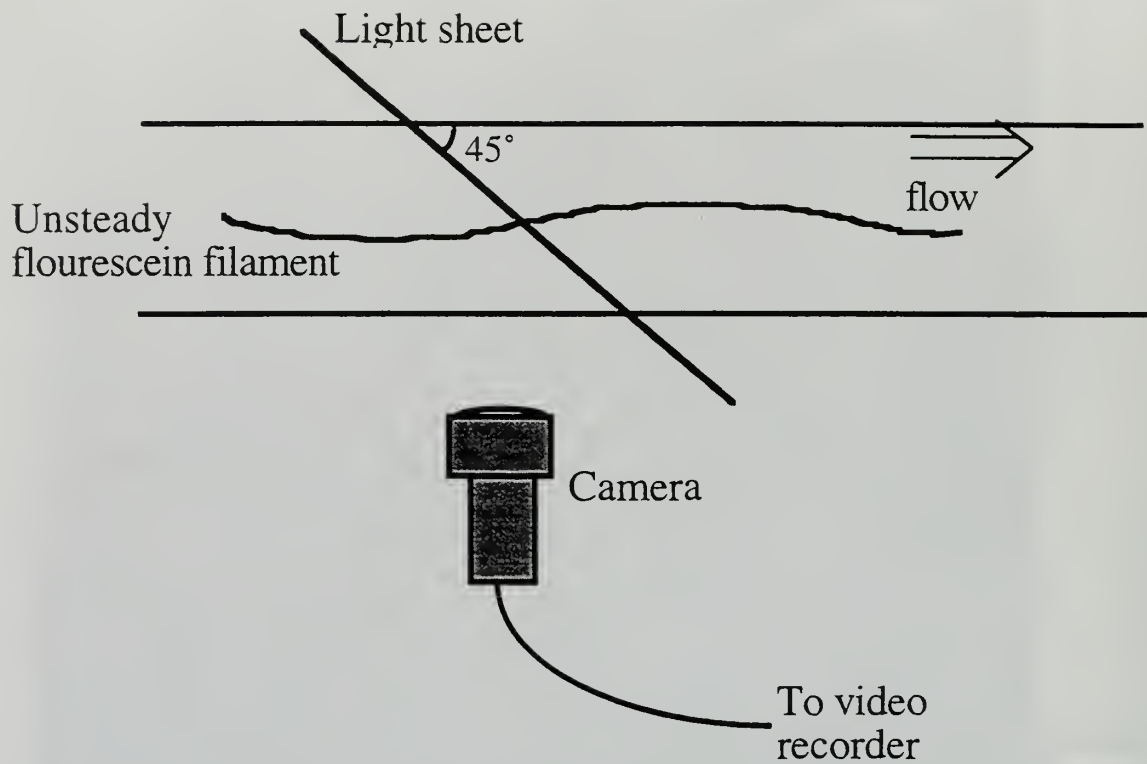
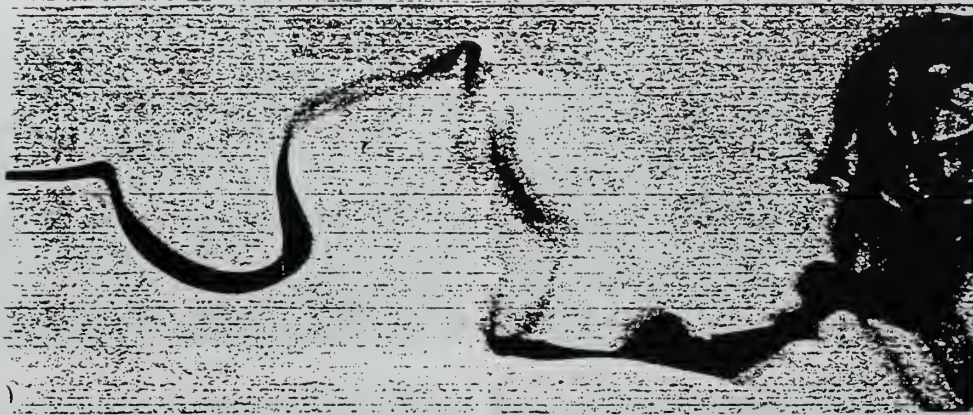
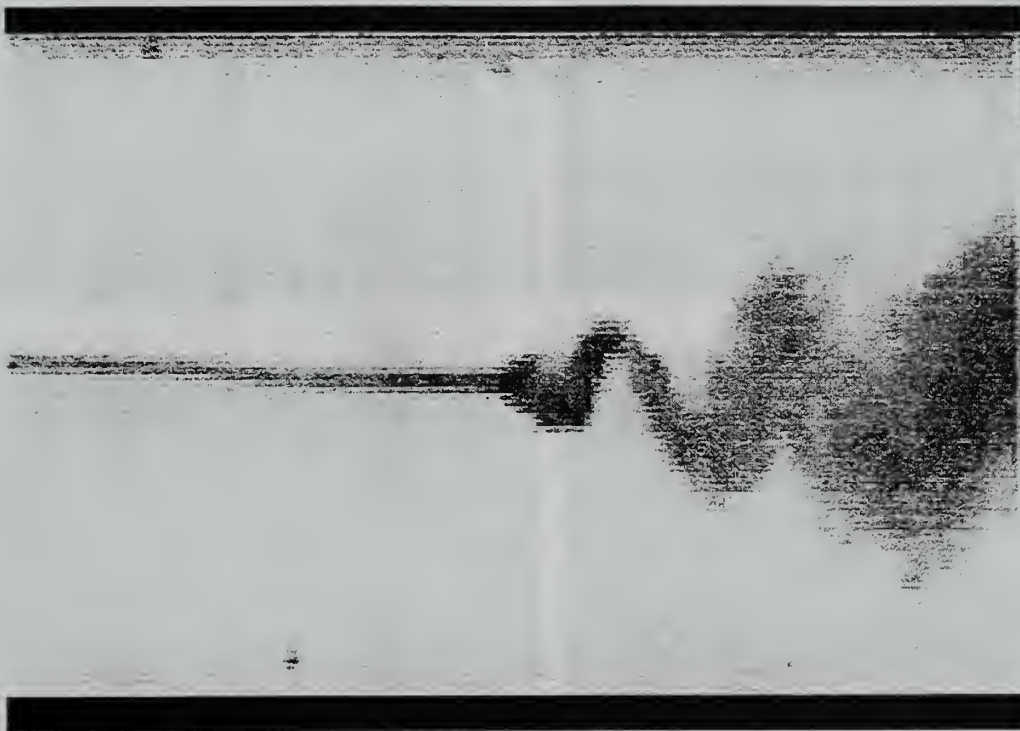


Figure 2-6. Physical arrangement of the tube, camera, and light that were used to record the vortex core motion. Top view. The camera recorded the bright spot that appeared at the intersection of the fluorescein filament and the light sheet.



a.



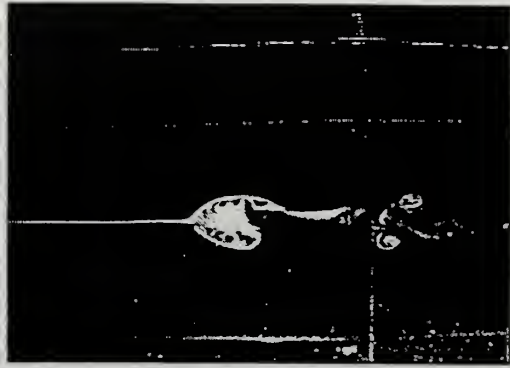
b.

Figure 3-1. Spiral vortex breakdowns in low and high  $Re_D$  flows. (a.) Low  $Re_D$  flow, from Sarpkaya (1971a). (b.) High  $Re_D$  flow, from present work ( $Re_D = 230,000$  flow state).

a.  $Re_D = 2,600$



b.  $Re_D = 5,200$



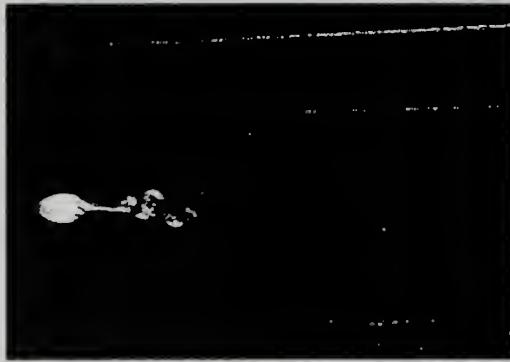
c.  $Re_D = 8,700$



d.  $Re_D = 17,500$



e.  $Re_D = 26,000$



f.  $Re_D = 35,000$



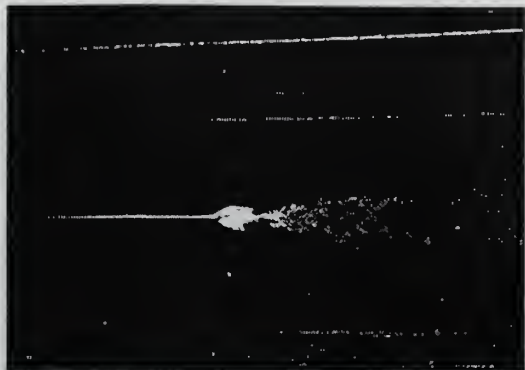
1 cm  
|-----|

Figure 3-2. Low  $Re_D$  vortex breakdowns with axisymmetric bubbles.

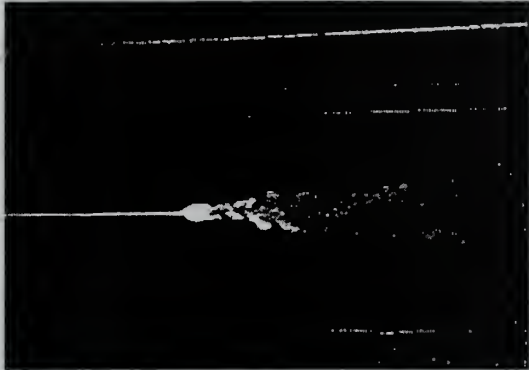
a.



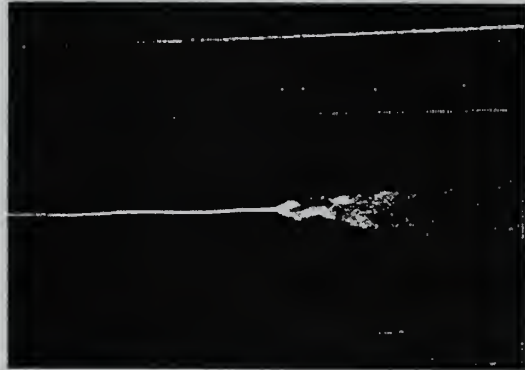
b.



c.



d.



e.



1 cm  
|-----|

Figure 3-3. Vortex breakdowns at  $Re_D = 44,000$ .



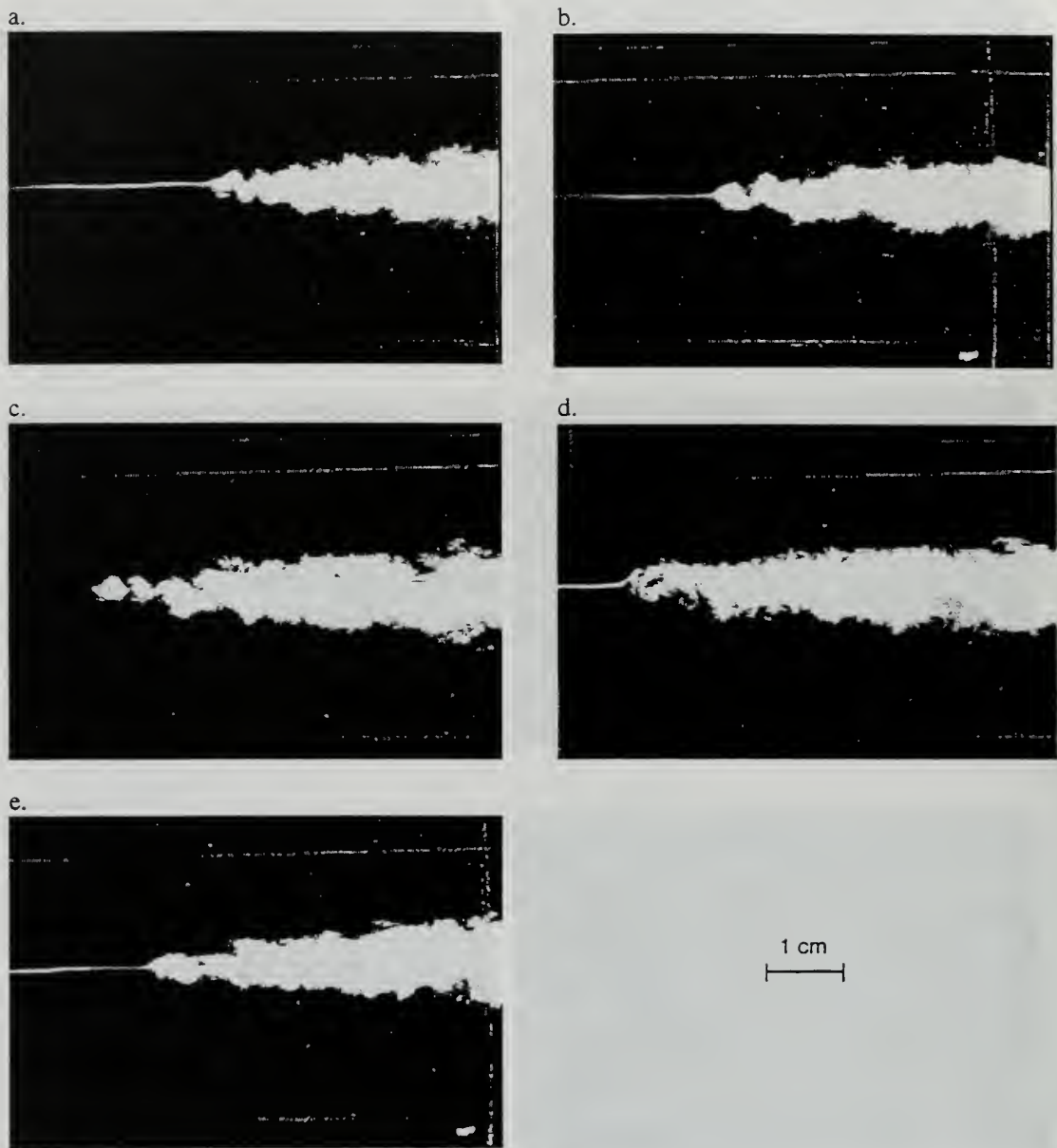
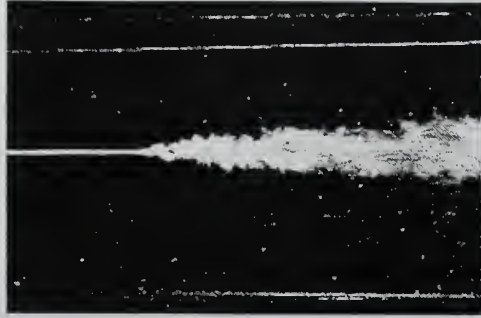


Figure 3-4. Vortex breakdowns at  $Re_D = 87,000$ .

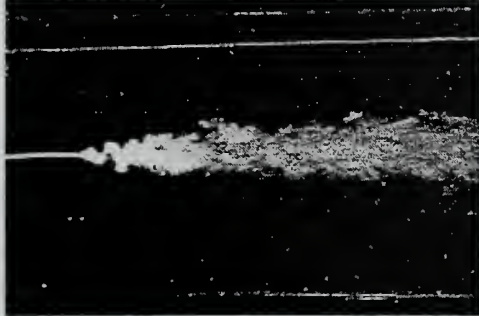
a.



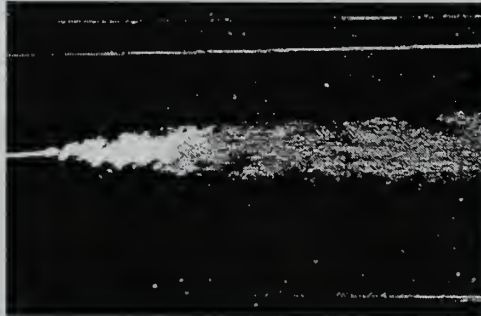
b.



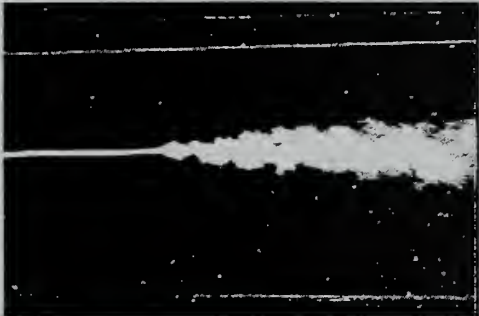
c.



d.



e.



1 cm

Figure 3-5. Vortex breakdowns at  $Re_D = 130,000$ .

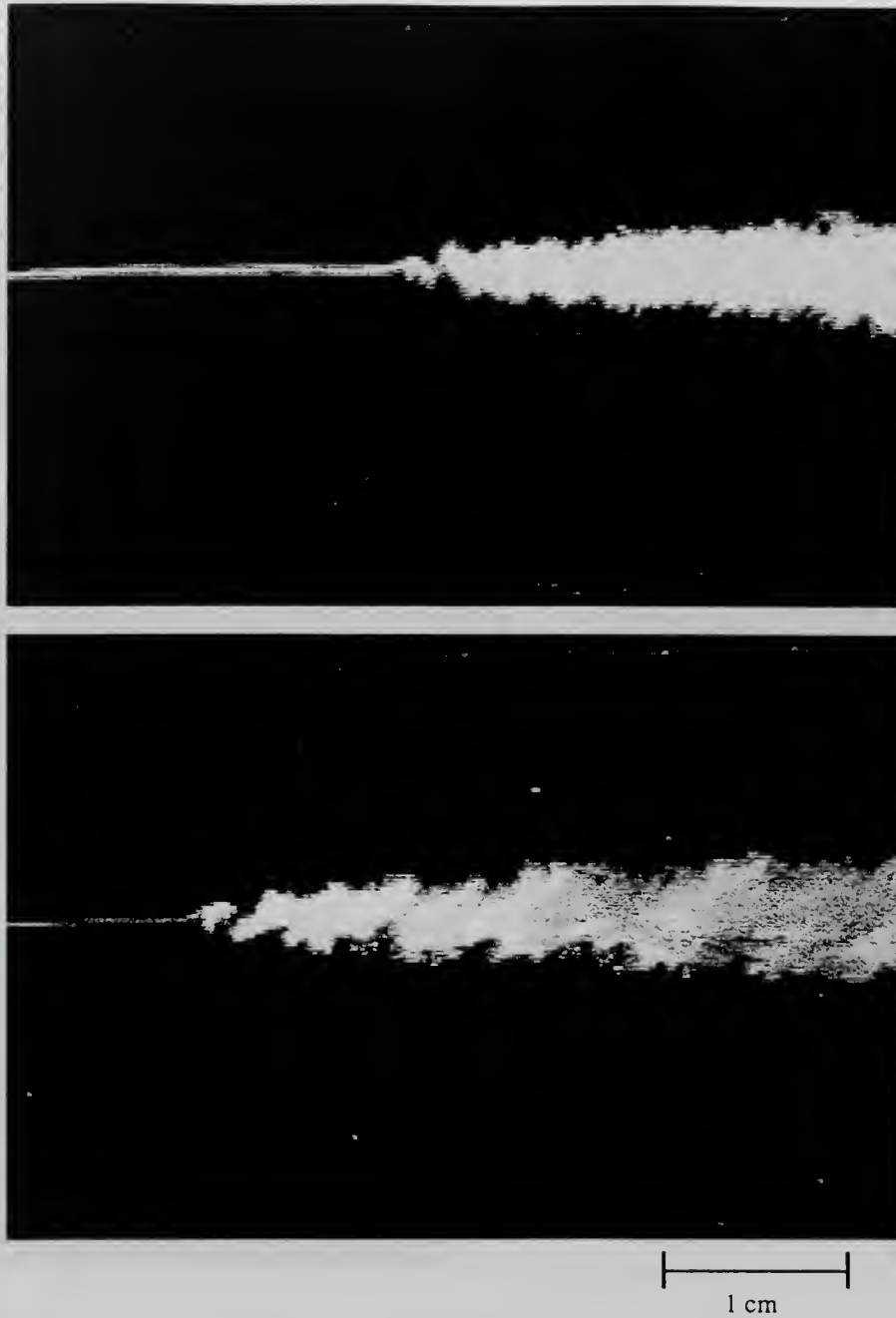


Figure 3-6. Vortex breakdowns at  $Re_D = 175,000$ .

a.



b.



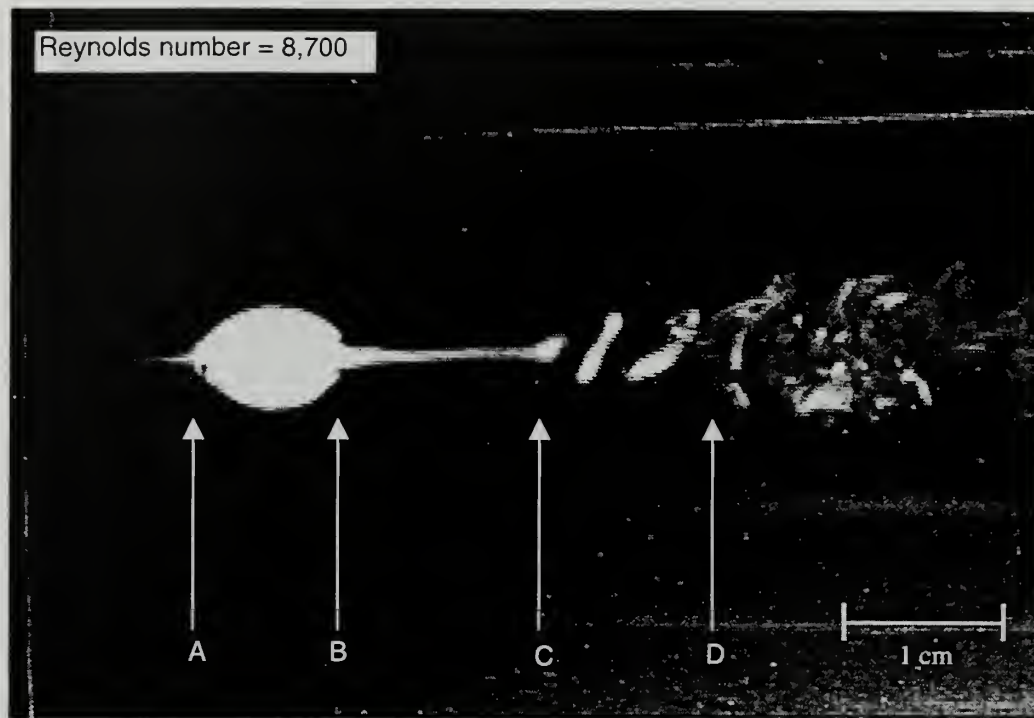
c.



1 cm

Figure 3-7. Vortex breakdowns at  $Re_D = 300,000$ .





- A. Stagnation point where the axisymmetric bubble forms.
- B. Downstream end of the bubble, and the beginning of the vortex core recovery region.
- C. Inception of the spiral, where the recovered vortex breaks down.
- D. Spiral windings break up into turbulence.

Figure 3-8. Low Reynolds number ( $Re_D = 8,700$ ) vortex breakdown with axisymmetric bubble and spiral.



Figure 3-9. Interesting vortex breakdown form observed at  $Re_D=17,500$ .

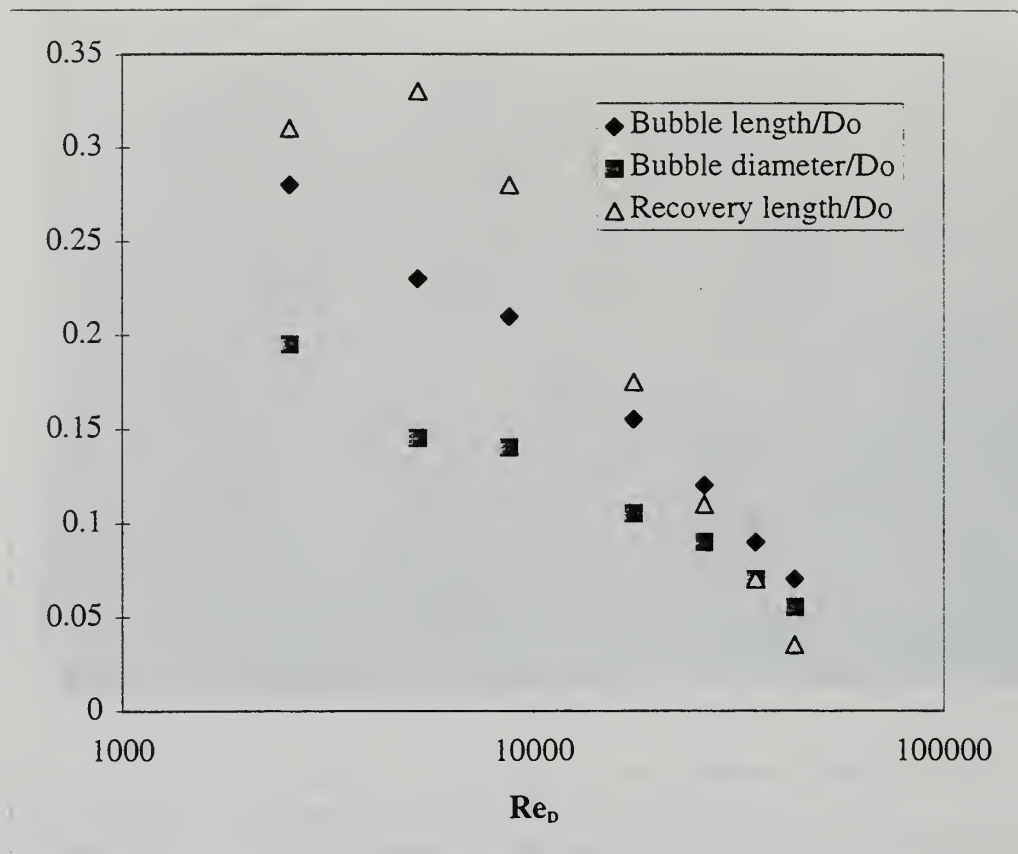


Figure 3-10. Bubble dimensions and core recovery length variation with  $Re_D$ .



Figure 3-11. Images of the spiral breakdown form in the  $Re_D = 230,000/h6$  flow state (6 ns exposure).



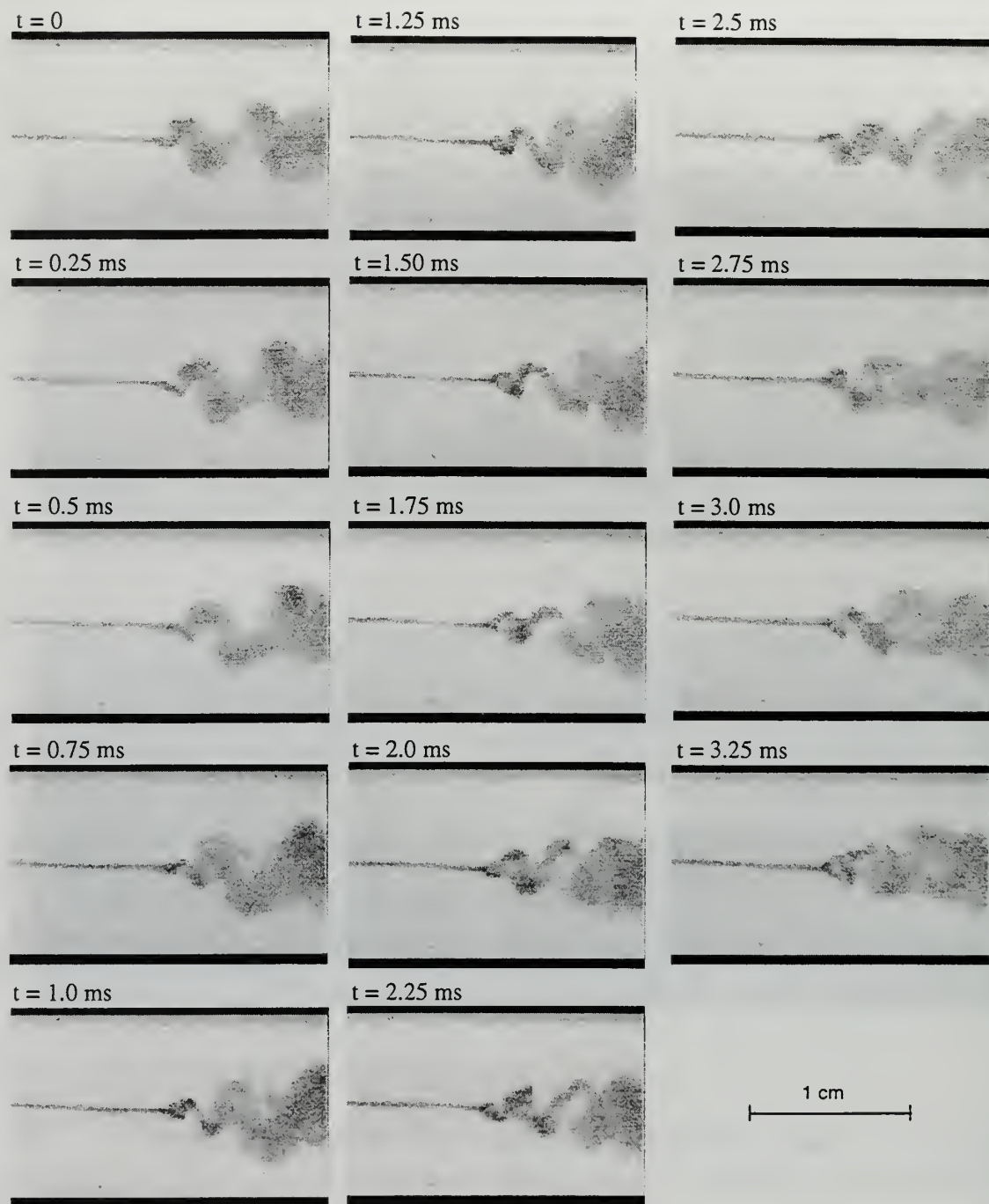


Figure 3-12. Images of the spiral form in the  $Re_D = 230,000/h6$  flow state (high speed video sequence).



Figure 3-13. Images of "bifurcated" spirals in the  $Re_D = 230,000/h6$  flow state (6 ns exposure).



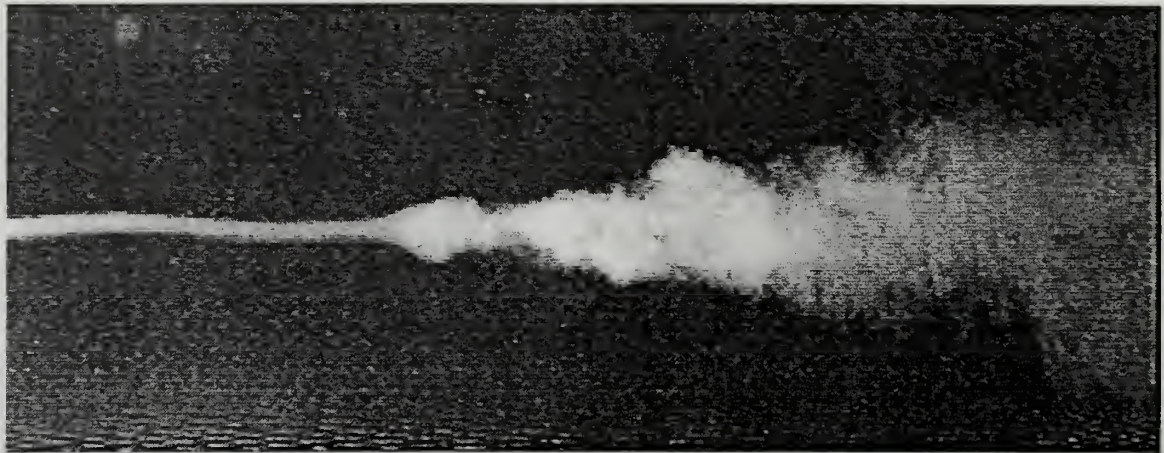


Figure 3-14. Images of the collapsed spiral in the  $Re_D = 230,000$  flow state (6 ns exposure).

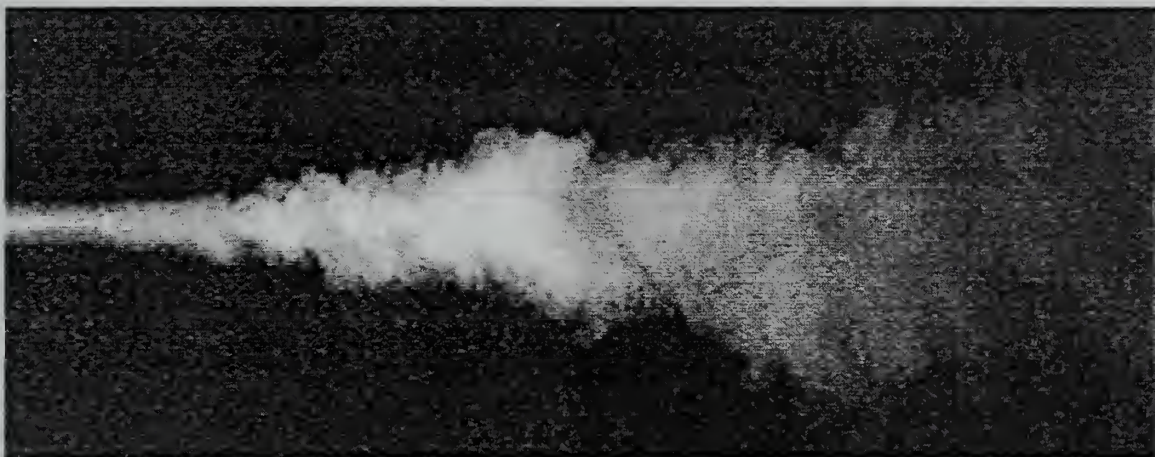


Figure 3-15. Images of the conical-like form in the  $Re_D = 230,000/h6$  flow state (6 ns exposure).



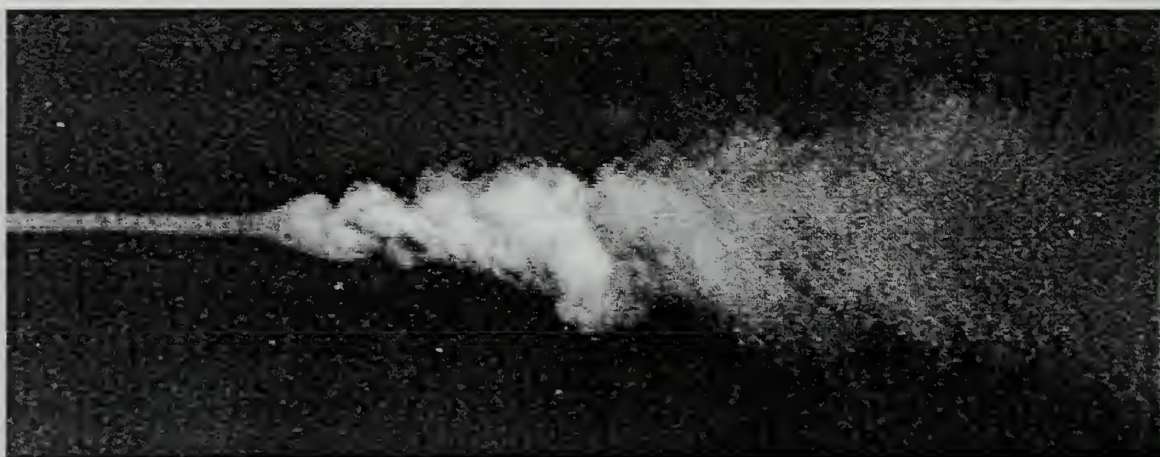


Figure 3-16. Typical vortex breakdown appearances in the  $Re_D = 230,000/h_6$  flow state (6 ns exposure).

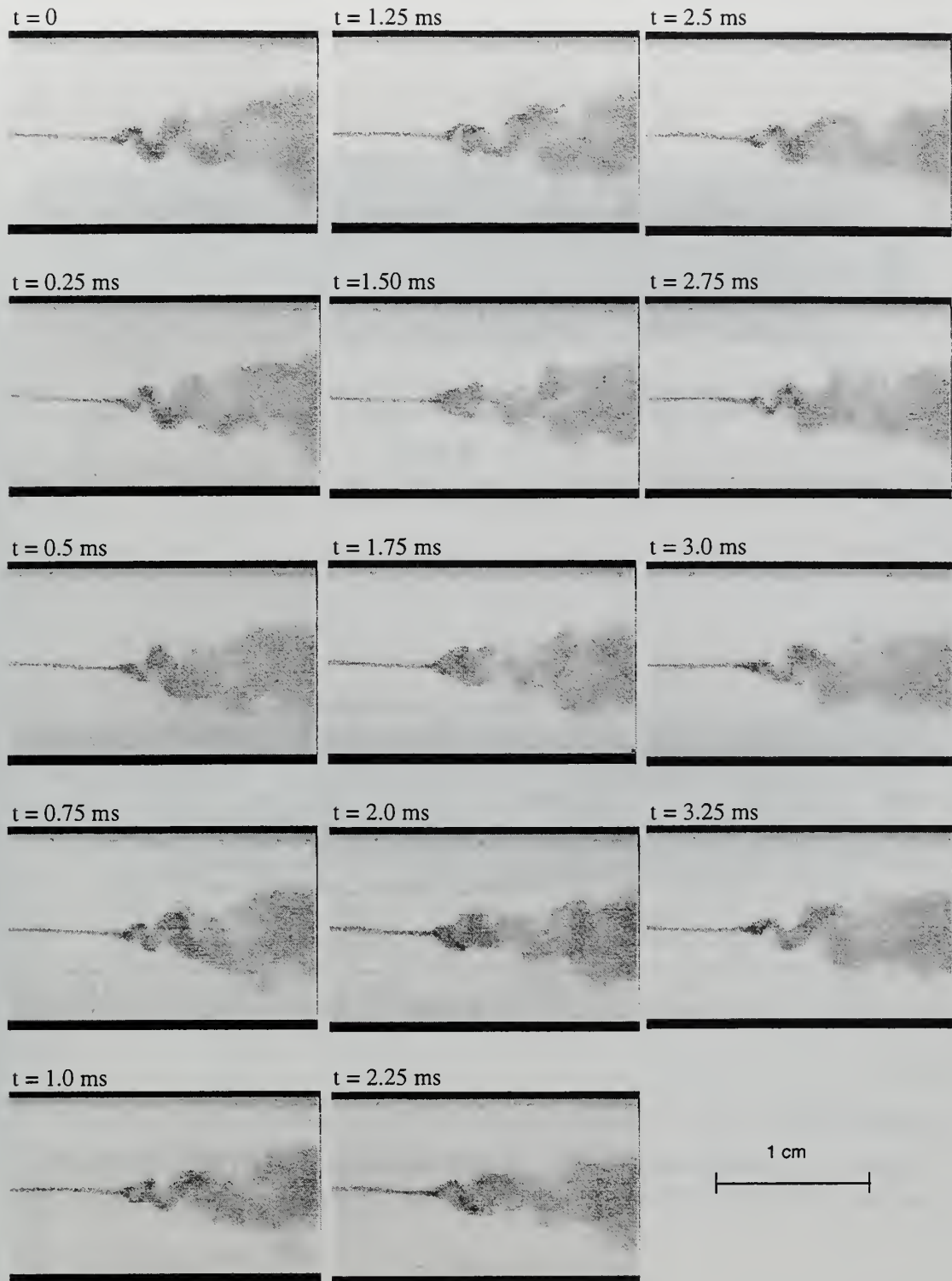
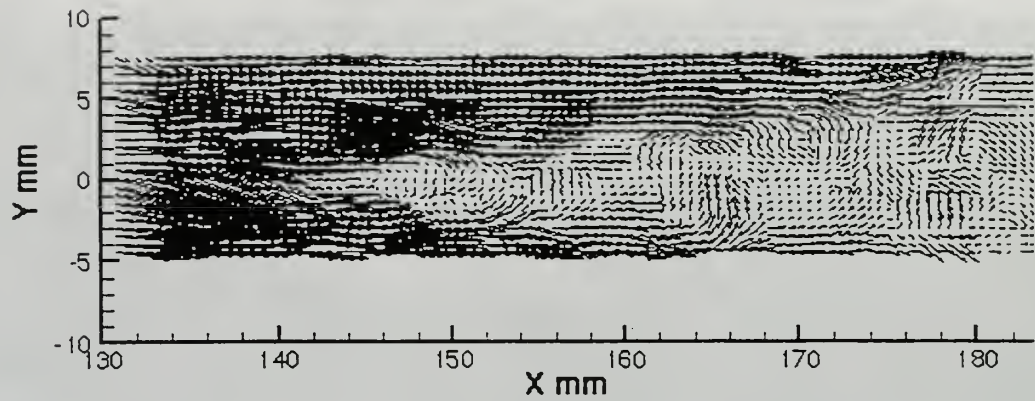
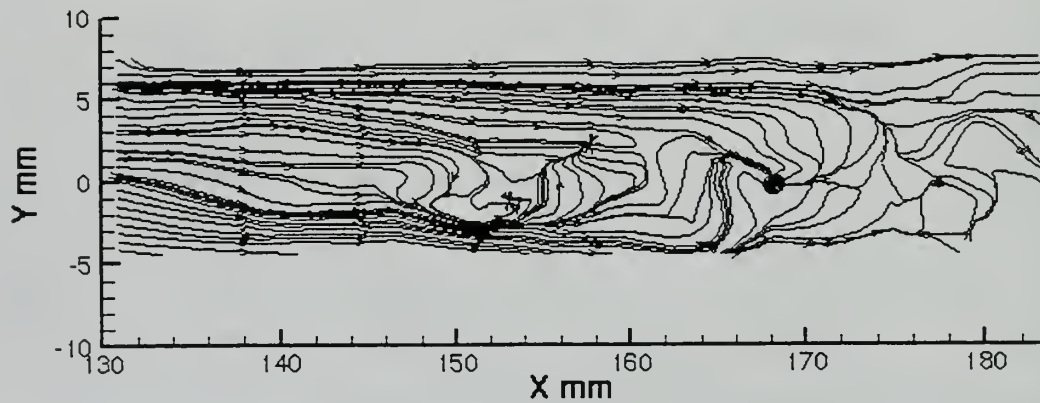


Figure 3-17. Sequence of images showing compression and expansion of the helix in the  $Re_D = 230,000/h_6$  flow state.



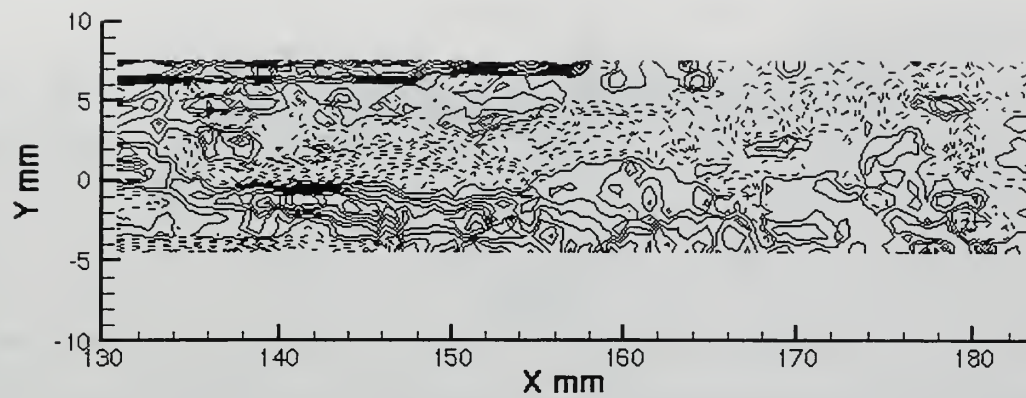
a.



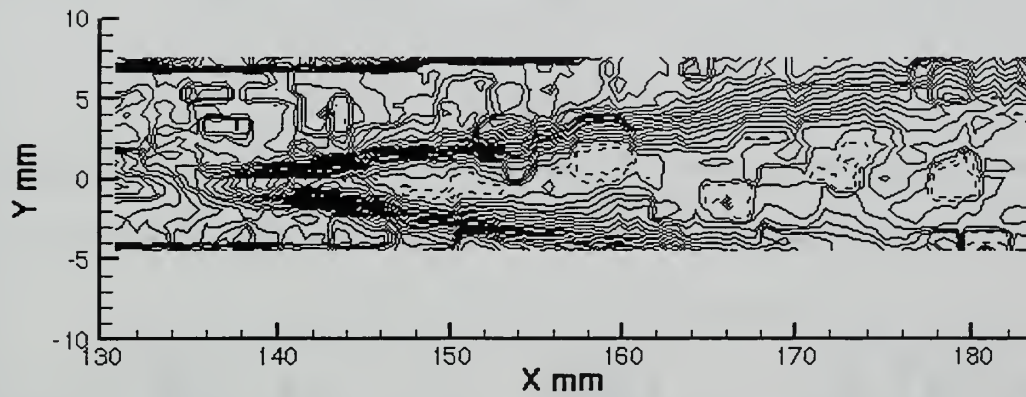
b.

Figure 3-18. Instantaneous velocity vectors and stream traces (DPIV Results) in the  $Re_D = 230,000/h6$  flow. (a.) Velocity vectors. (b.) Stream traces.





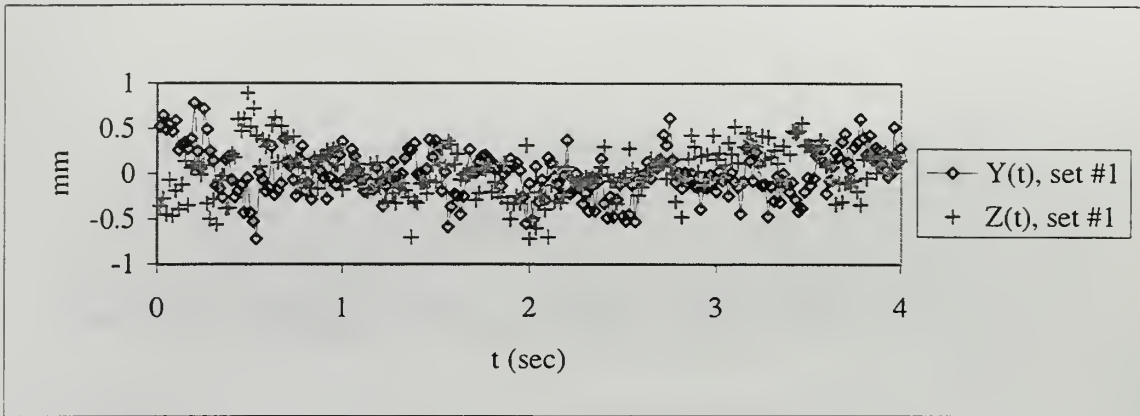
a.



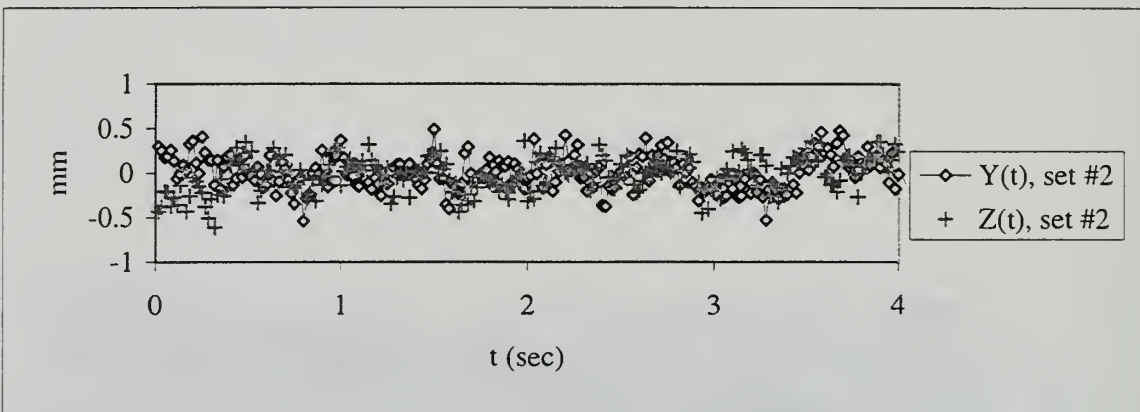
b.

Figure 3-19. Instantaneous vorticity and axial velocity contours (DPIV Results) in the  $Re_D = 230,000/h_6$  flow . (a.) Vorticity. (b.) Axial velocity.

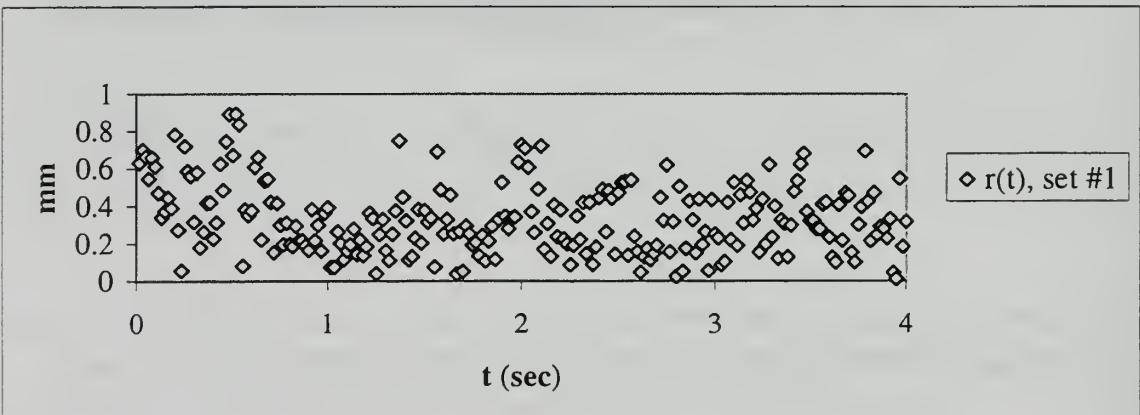




a.

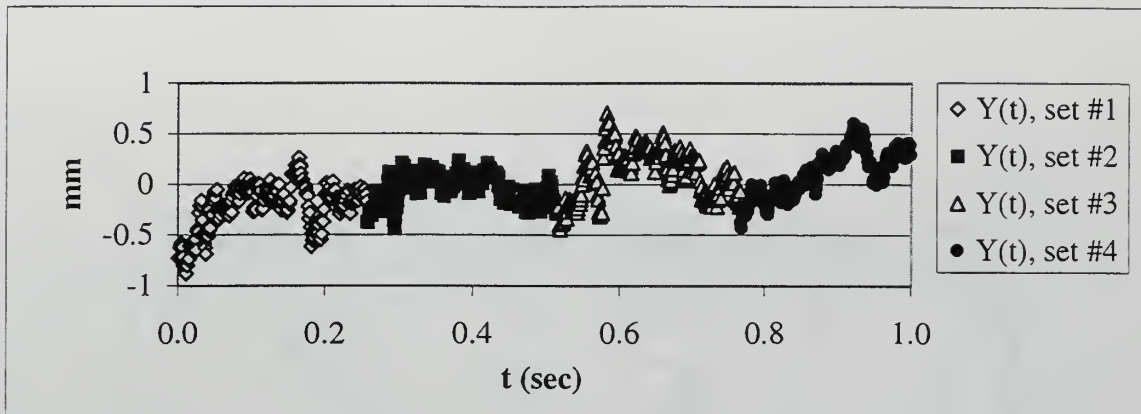


b.

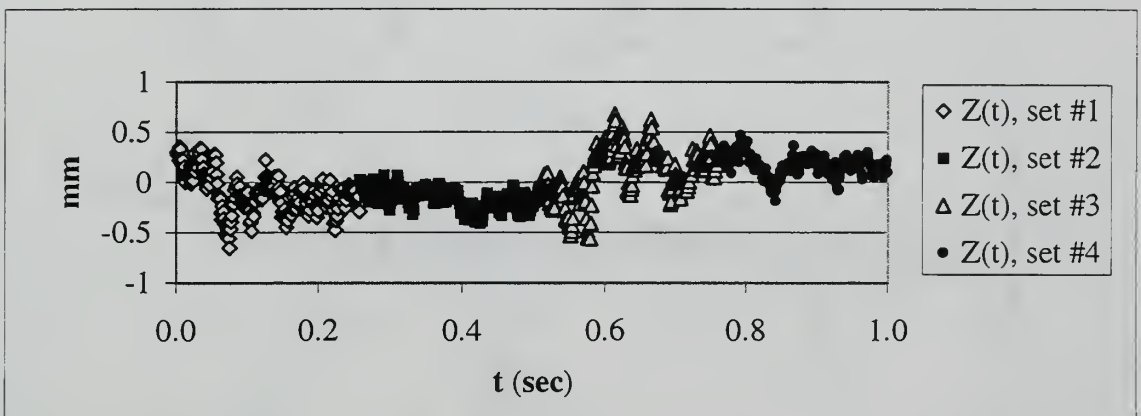


c.

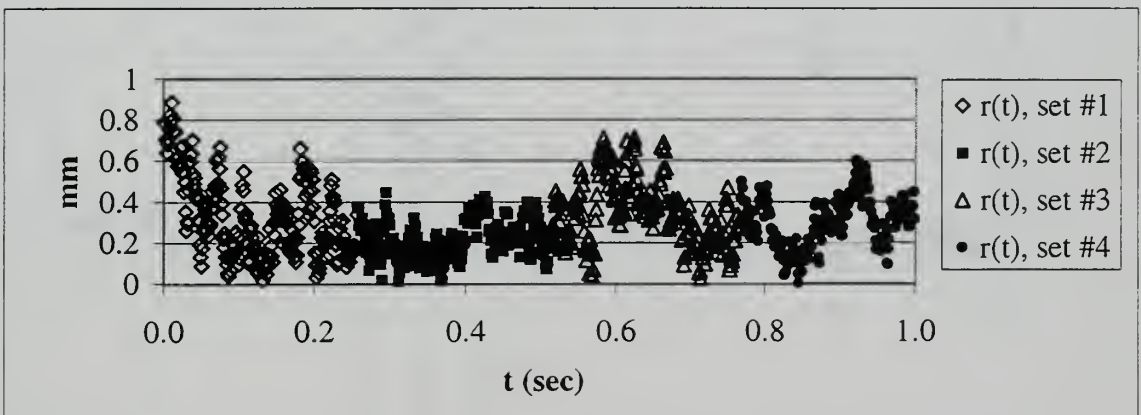
Figure 3-20. Time history of vortex core position based on 60 frames per second video. (a.) First set of 256 data points. (b.) Second set of 256 data points. (3) Time history of the total distance from the centerline for the first set of data.



a.



b.



c.

Figure 3-21. Time history of the vortex core position based on 1,000 frames per second video. (a.) Lateral position. (b.) Vertical position. (c.) Total distance from axis.

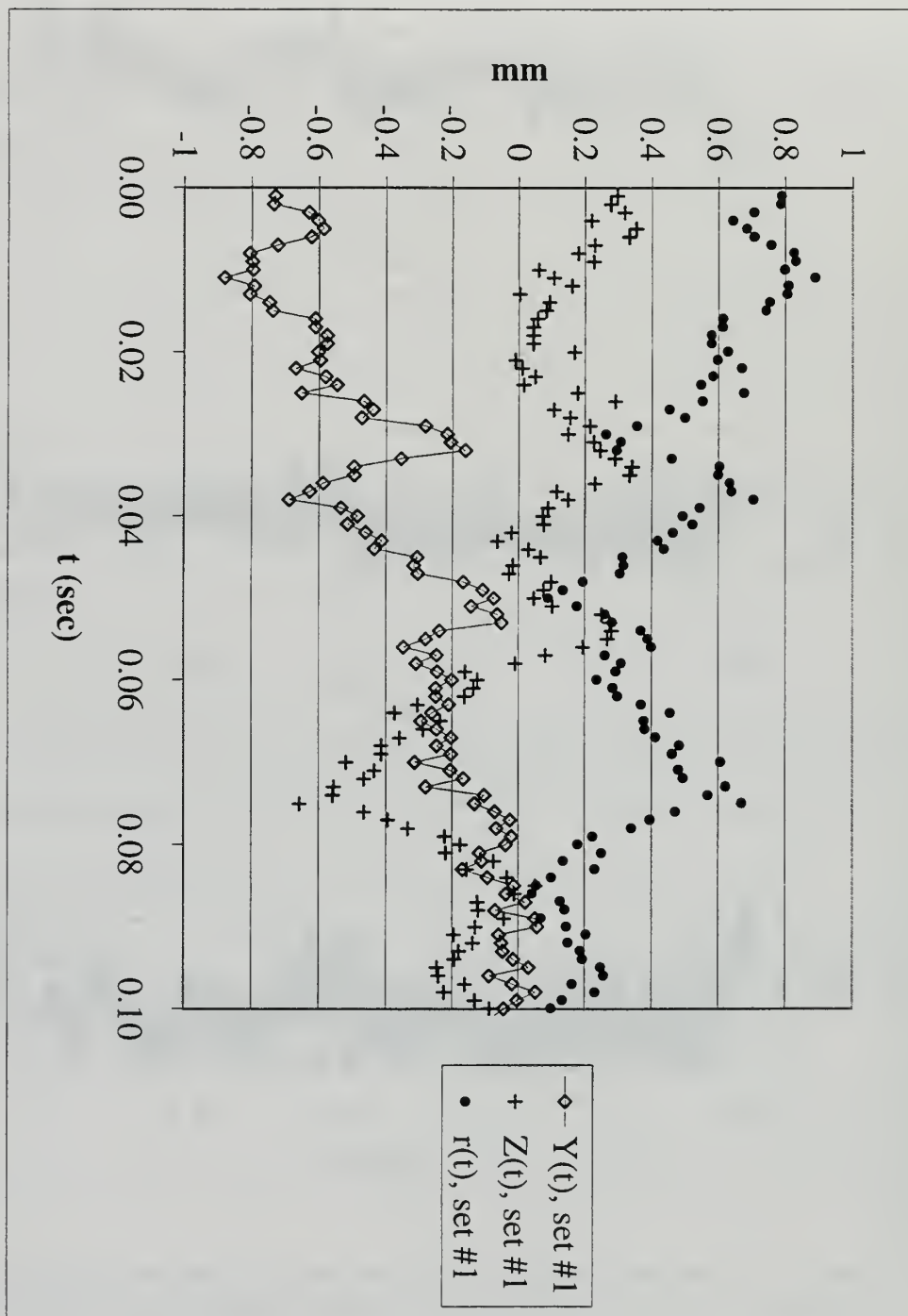
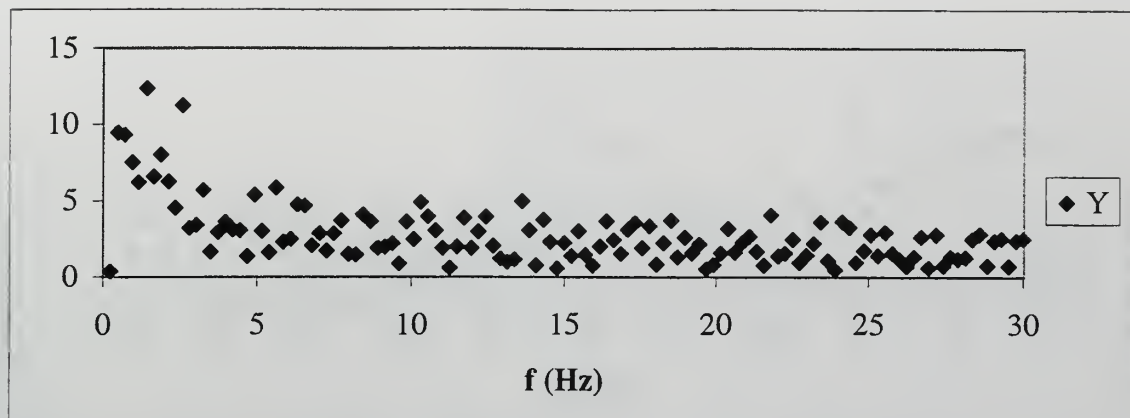
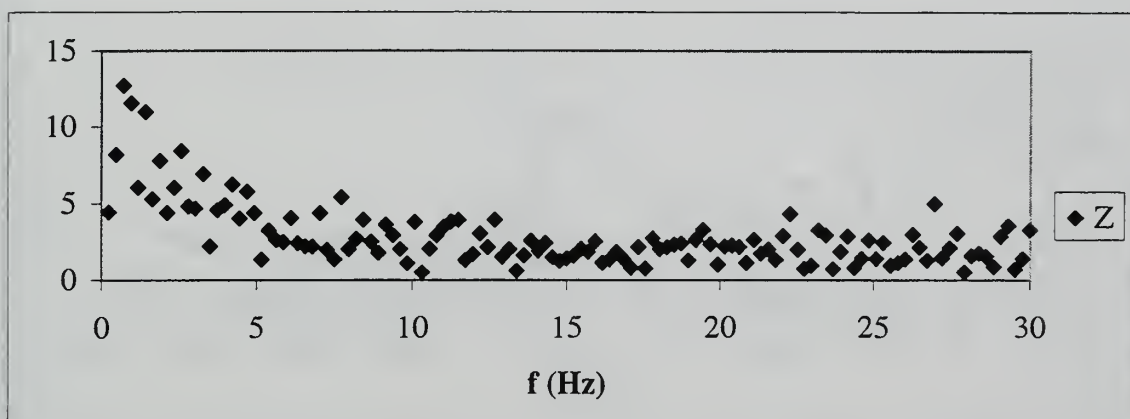


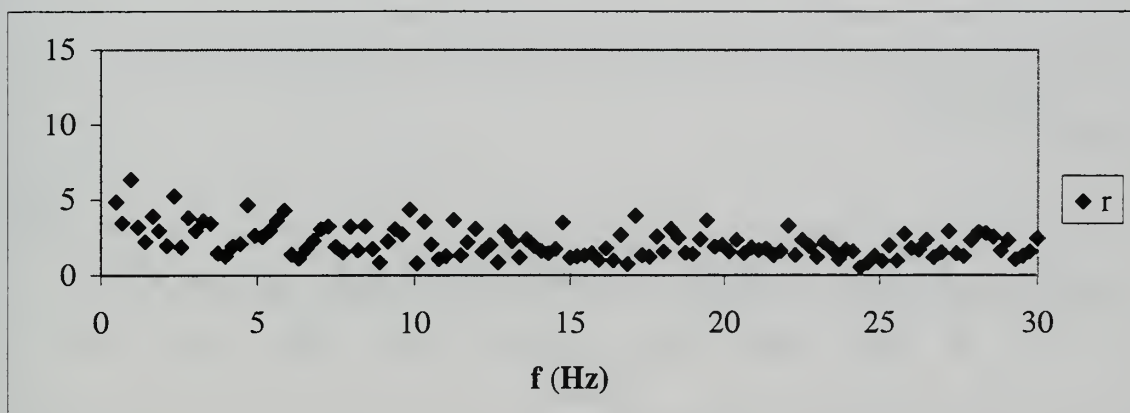
Figure 3-22. Short segment of 1,000 frames per second core position time history.



a.



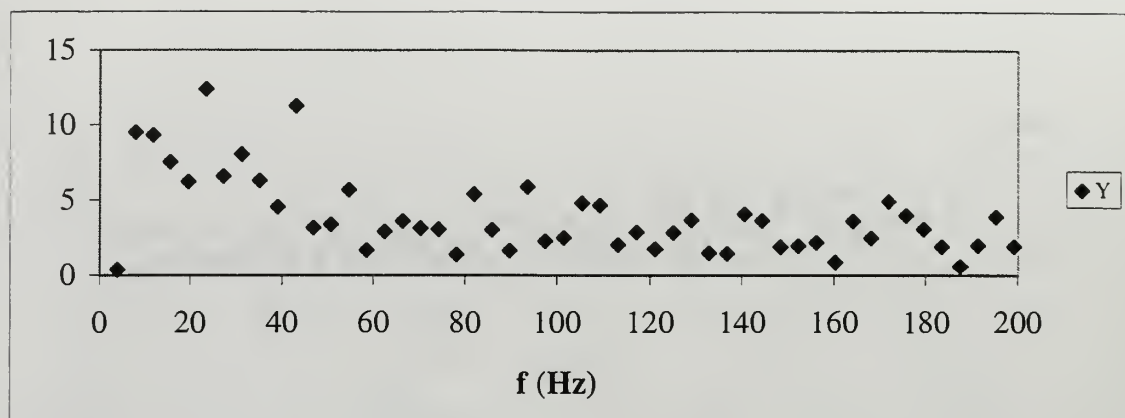
b.



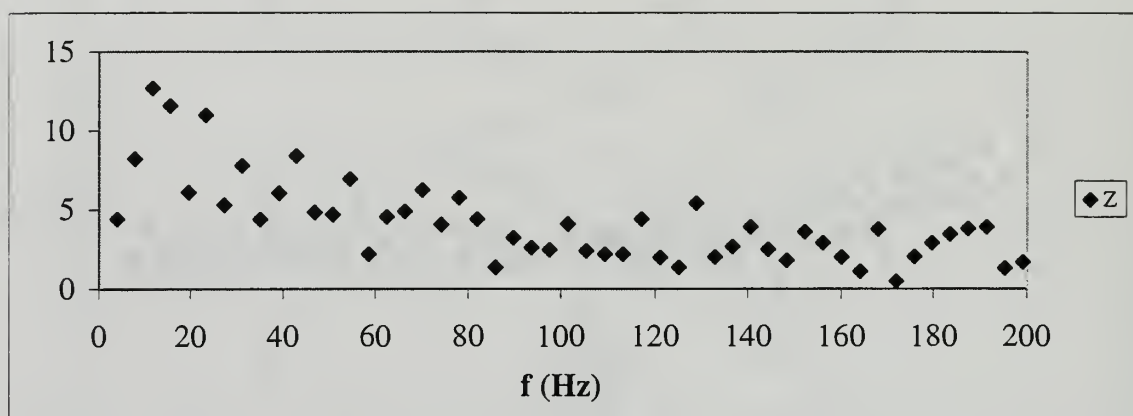
c.

Figure 3-23. Fourier analysis of the vortex core position based on the 60 frames per second video. (a.) Lateral position. (b.) Vertical position. (c.) Distance from the centerline.

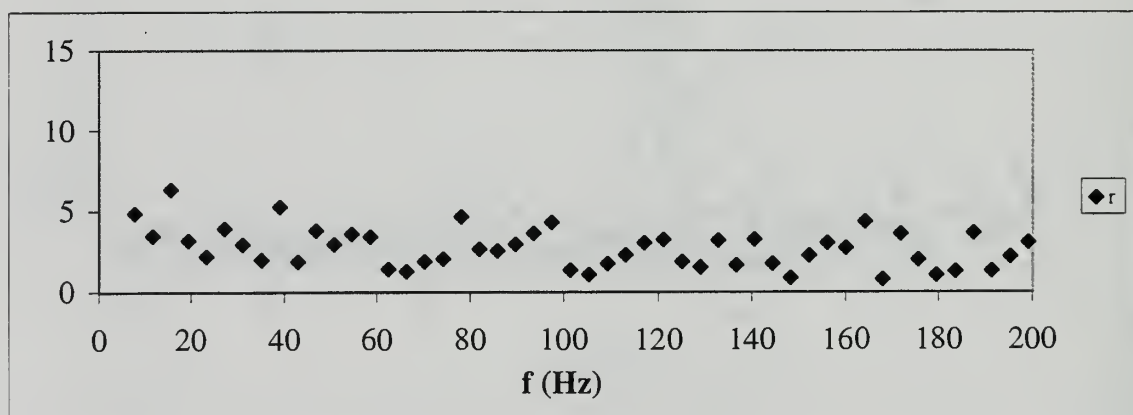




a.

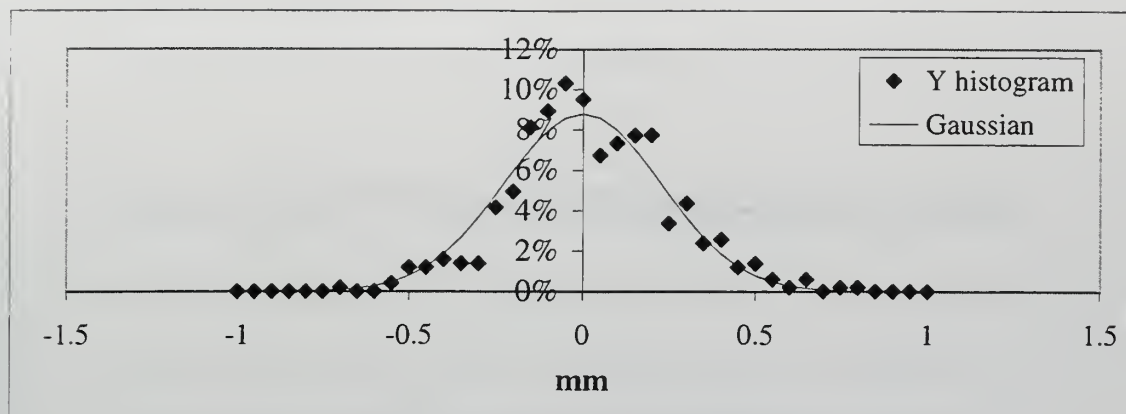


b.

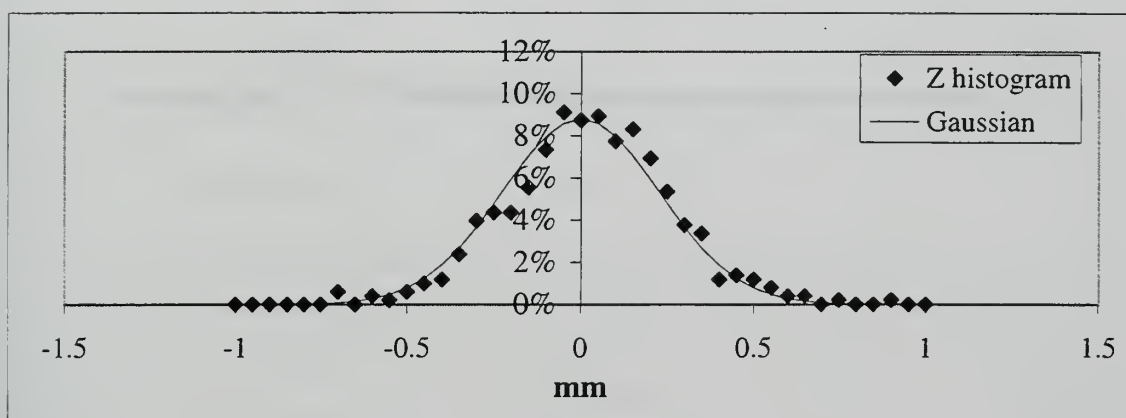


c.

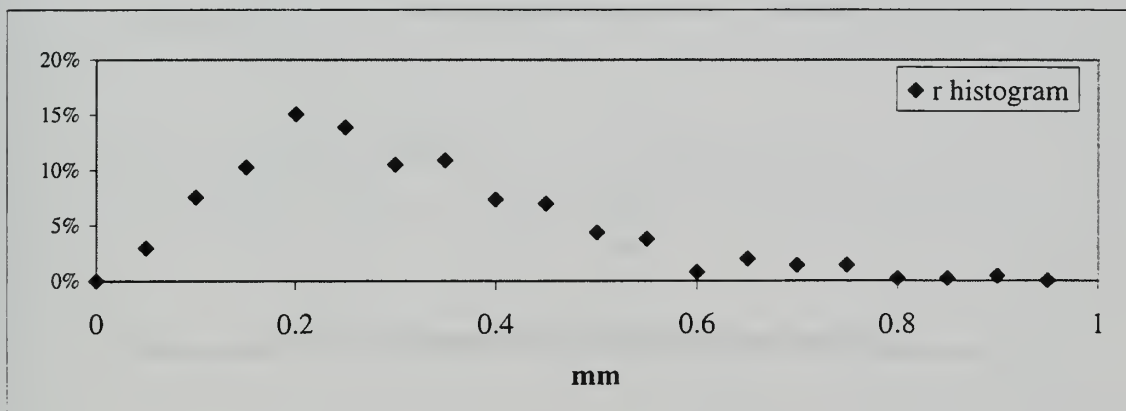
Figure 3-24. Fourier analysis of the vortex core position based on the 1,000 frames per second video. (a.) Lateral position. (b.) Vertical position. (c.) Distance from centerline.



a.

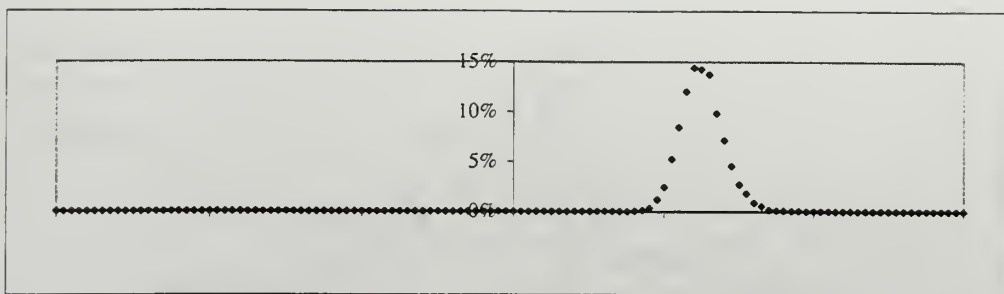


b.

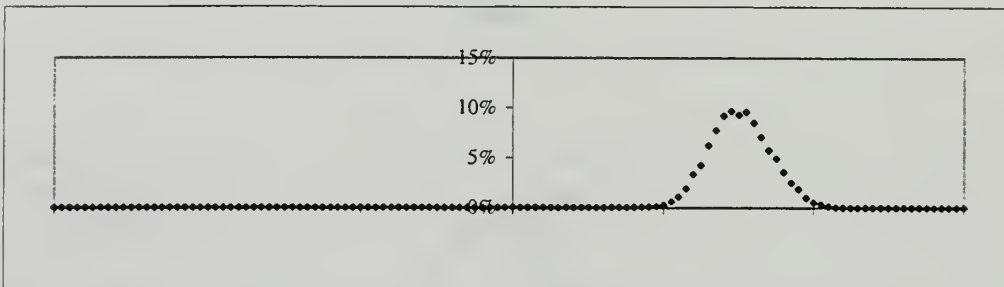


c.

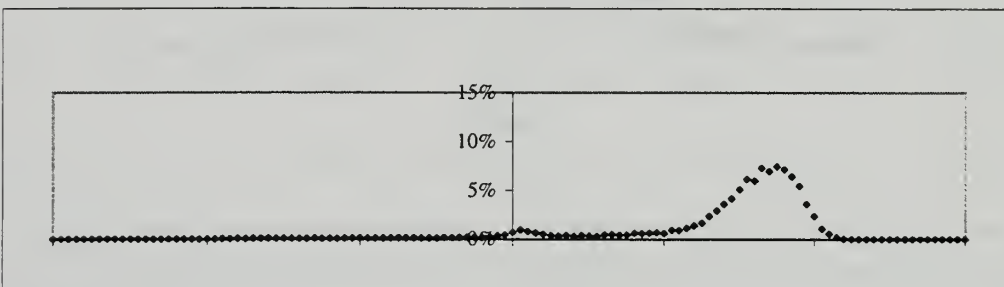
Figure 3-25. Histograms of the Y and Z coordinates of the vortex core position in the  $Re_D = 230,000/h_6$  flow state. (a.) Lateral position. (b.) Vertical position. (c.) Total distance from the mean axis.



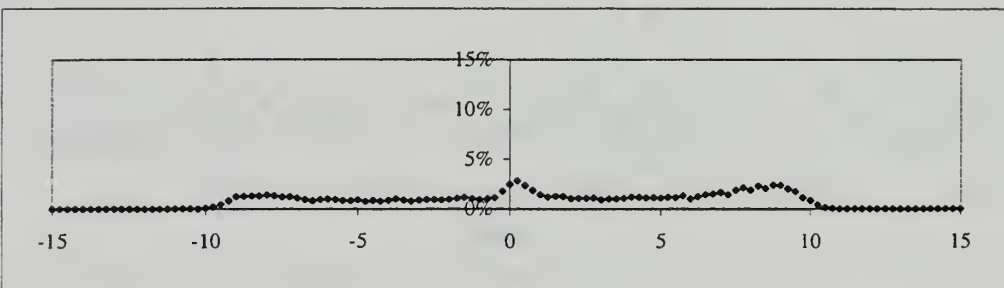
a.



b.



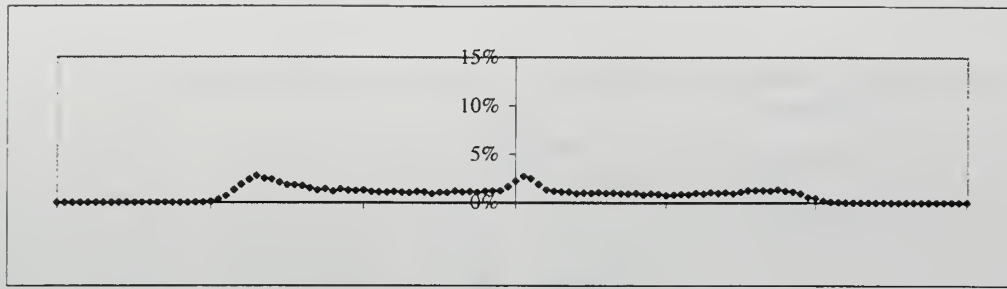
c.



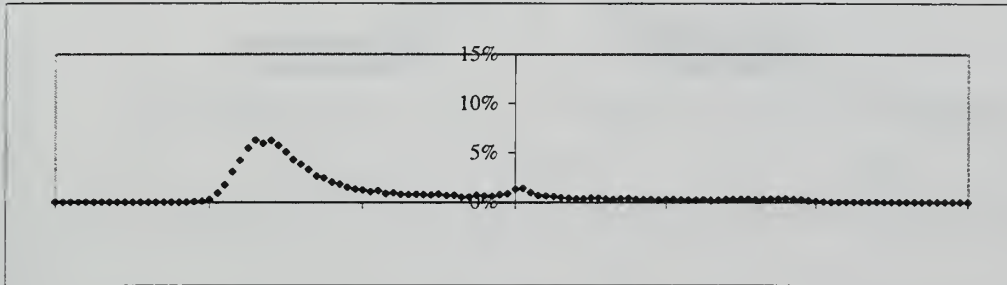
d.

Figure 3-26. Histograms of tangential velocity at positive Y positions at  $X = 70$  mm in the  $Re_D = 230,000/h_6$  flow state. Units of horizontal axis are m/s.

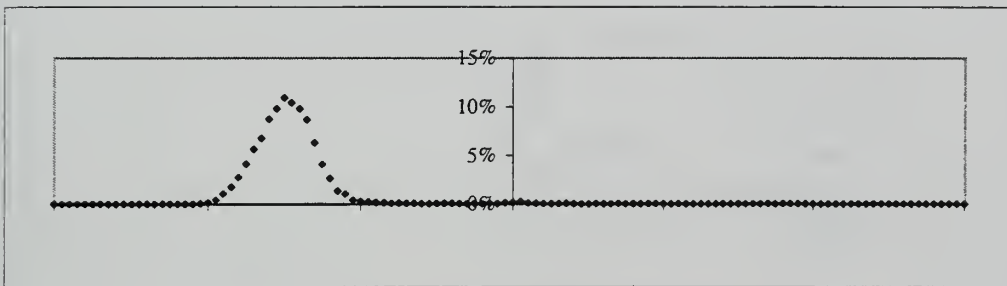
(a.)  $Y = 2.0$  mm. (b.)  $Y = 1.0$  mm. (c.)  $Y = 0.5$  mm. (d.)  $Y = 0^+$  mm



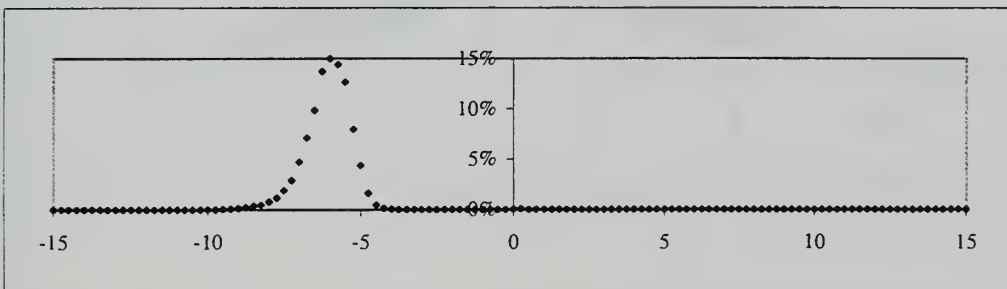
a.



b.



c.

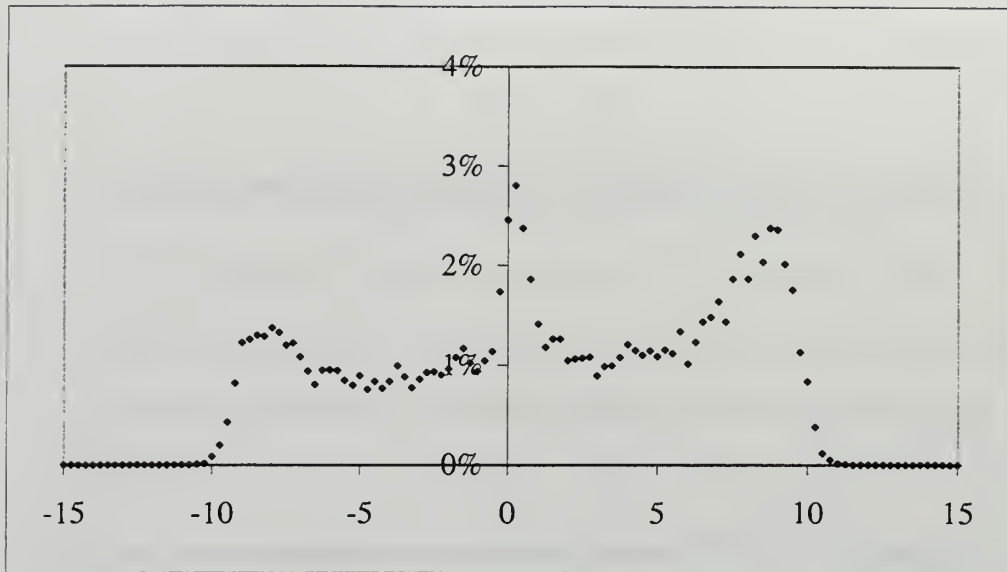


d.

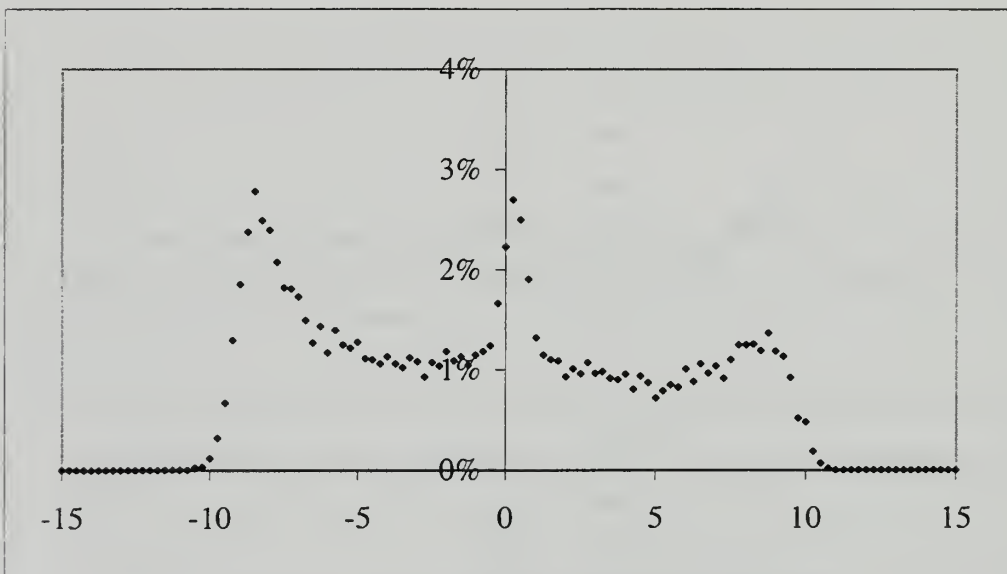
Figure 3-27. Histograms of tangential velocity at negative Y positions at  $X = 70$  mm in the  $Re_D = 230,000/h_6$  flow state. Units of horizontal axis are m/s.

(a.)  $Y = -2.0$  mm. (b.)  $Y = -1.0$  mm. (c.)  $Y = -0.5$  mm. (d.)  $Y = 0$  mm



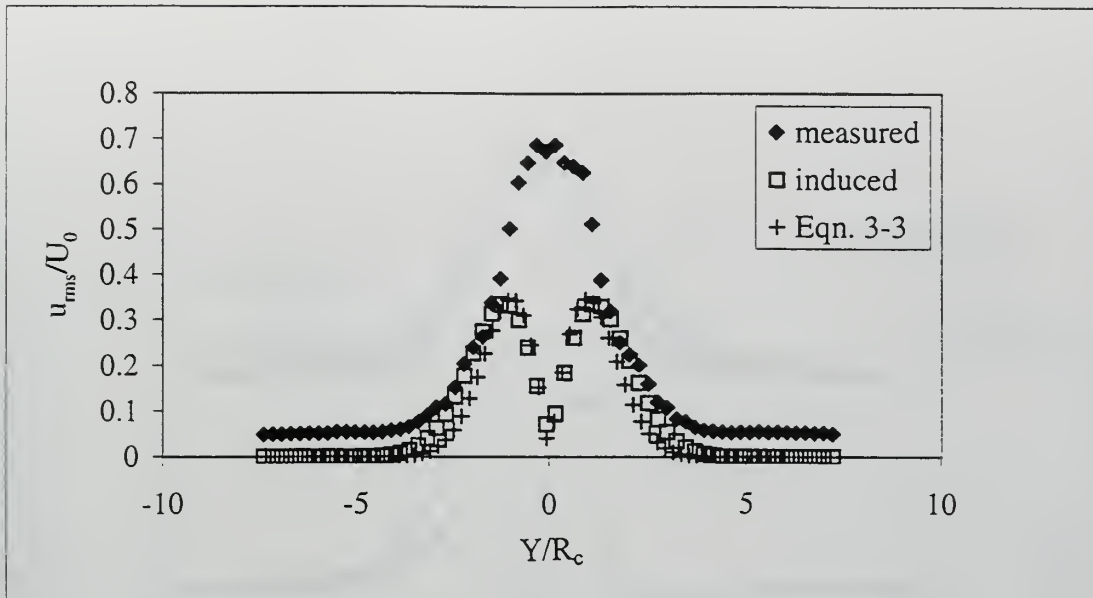


a.

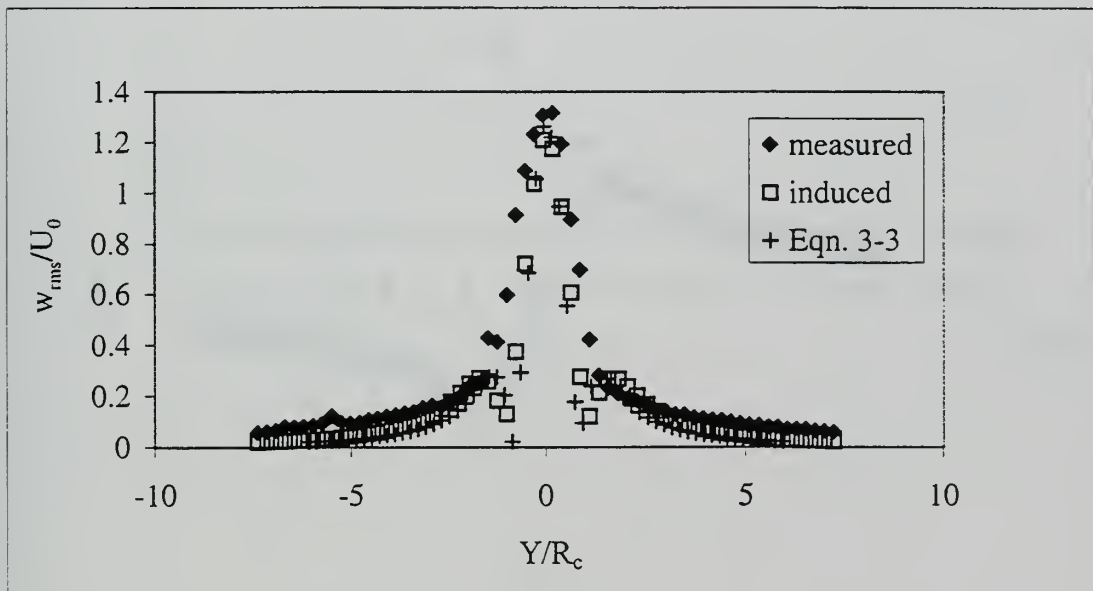


b.

Figure 3-28. Histograms of tangential velocity near the mean flow centerline at  $X = 70$  mm in the  $Re_D = 230,000/h_6$  flow state. Units of horizontal axis are m/s. (a.) Positive side of axis. (b.) Negative side of axis.



a.



b.

Figure 3-29. Measured and apparent turbulence at  $X = 70$  mm in the  $Re_D = 230,000/h_6$  flow state. (a.) Axial velocity. (b.) Tangential velocity.

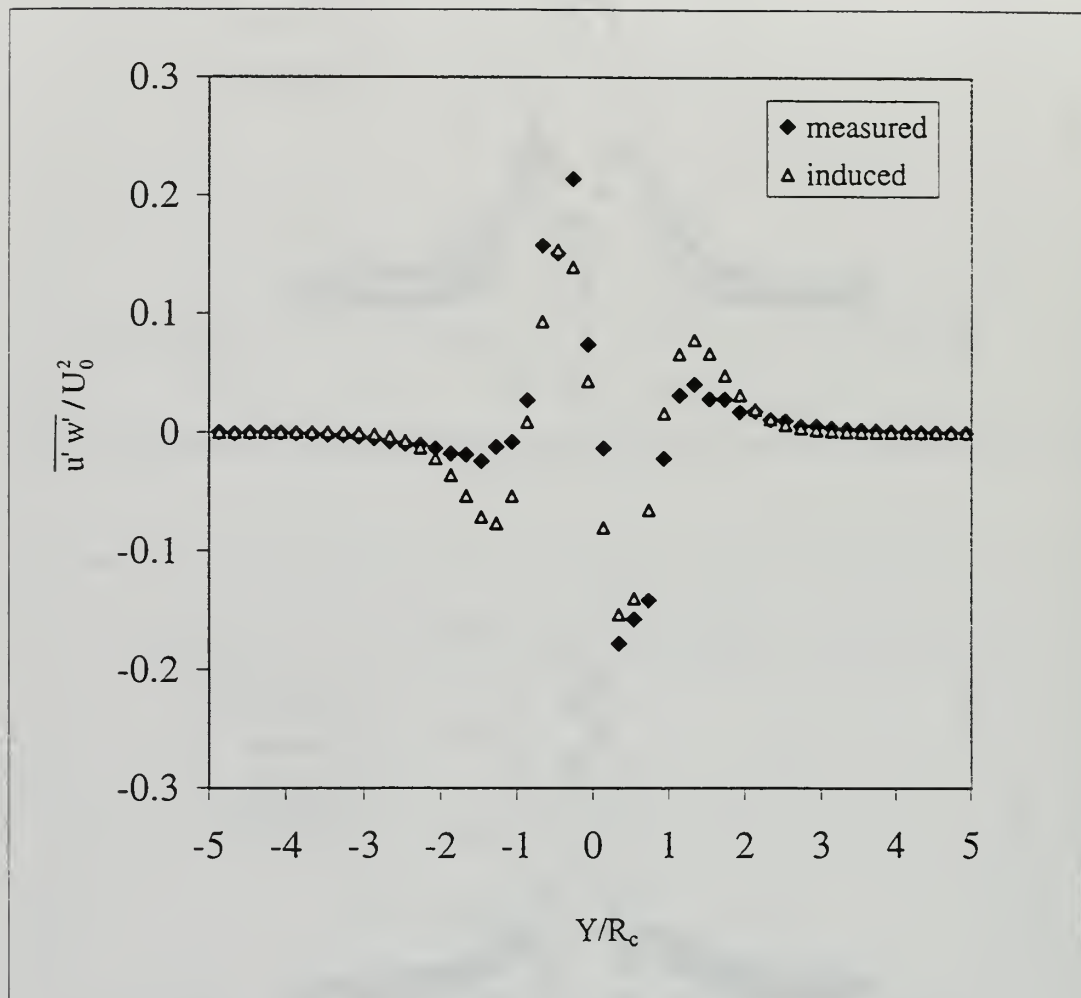
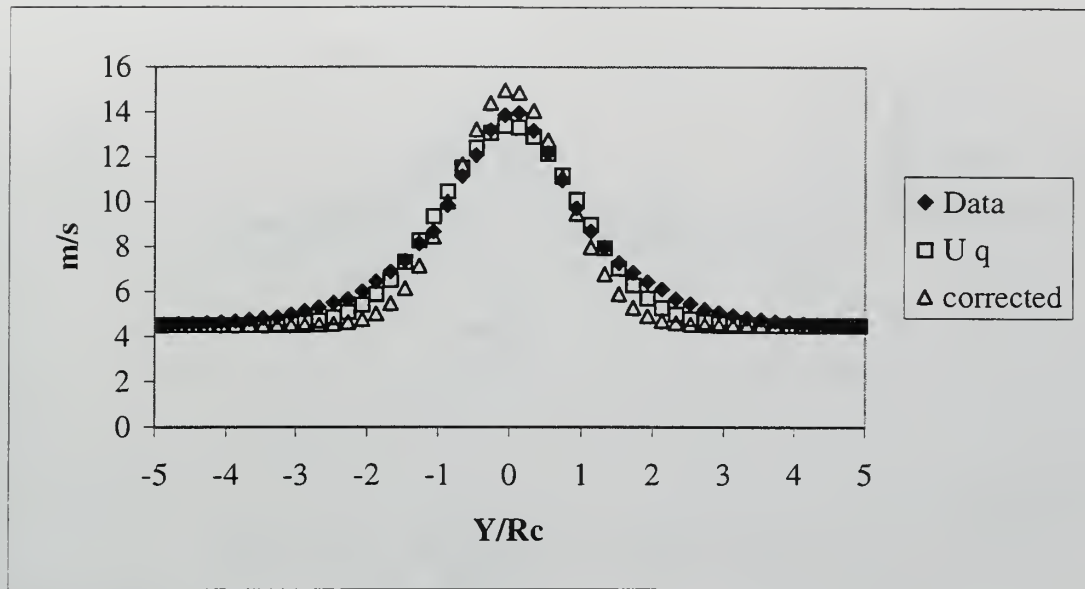
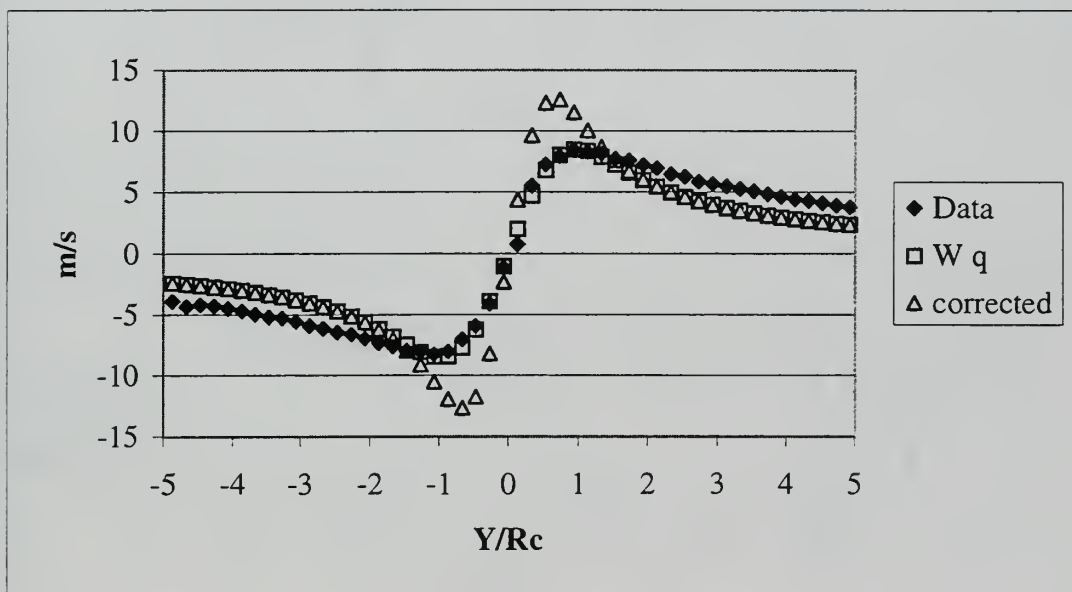


Figure 3-30. Measured and apparent Reynolds stress profiles at  $X = 70$  mm in the  $Re_D = 230,000/h_6$  flow state.



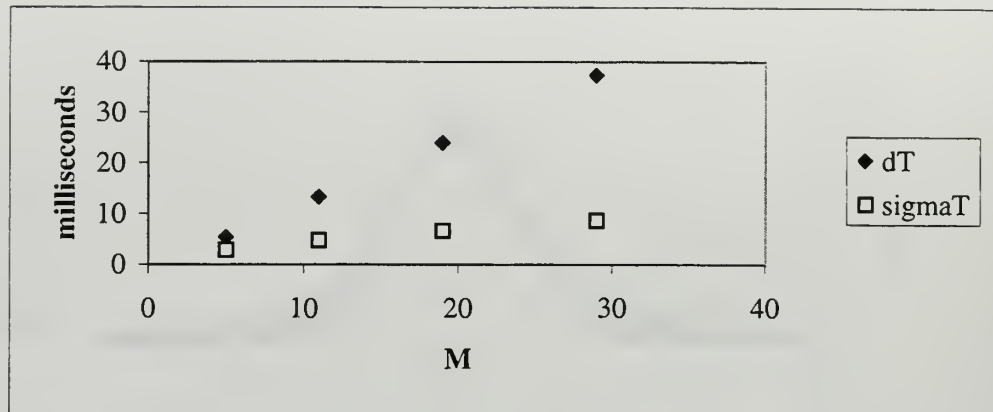
a.



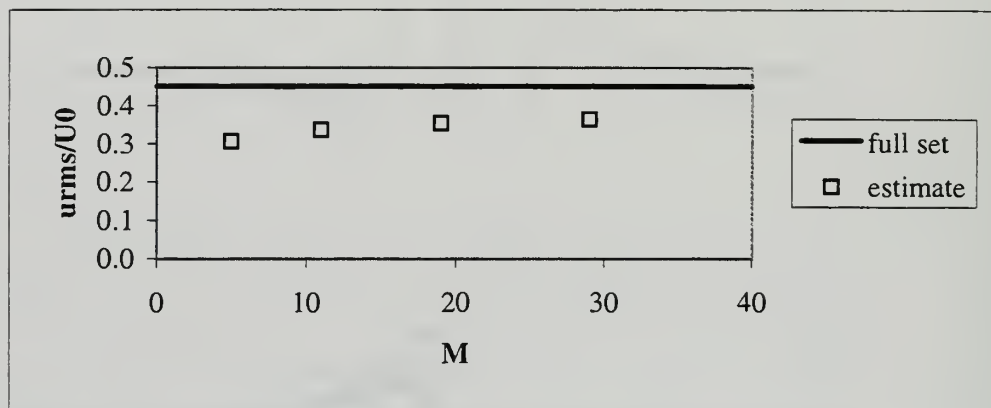
b.

Figure 3-31. Measured and "corrected" velocity profiles at  $X = 70$  mm in the  $Re_D = 230,000/h_6$  flow state.

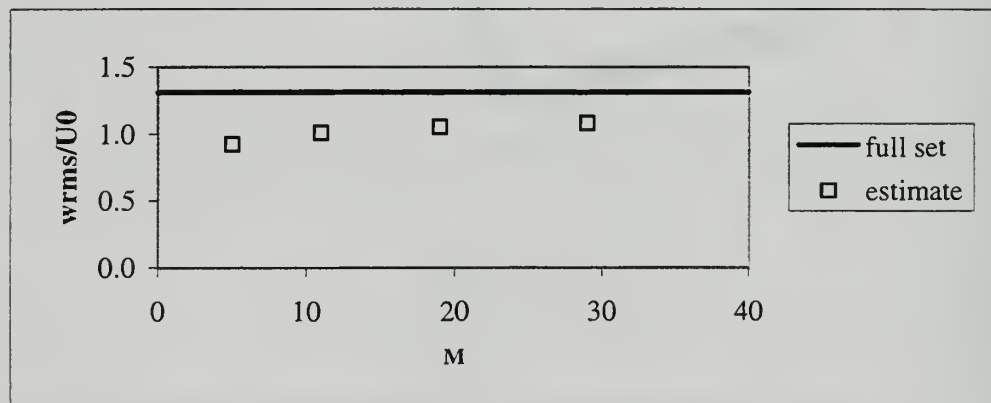




a.

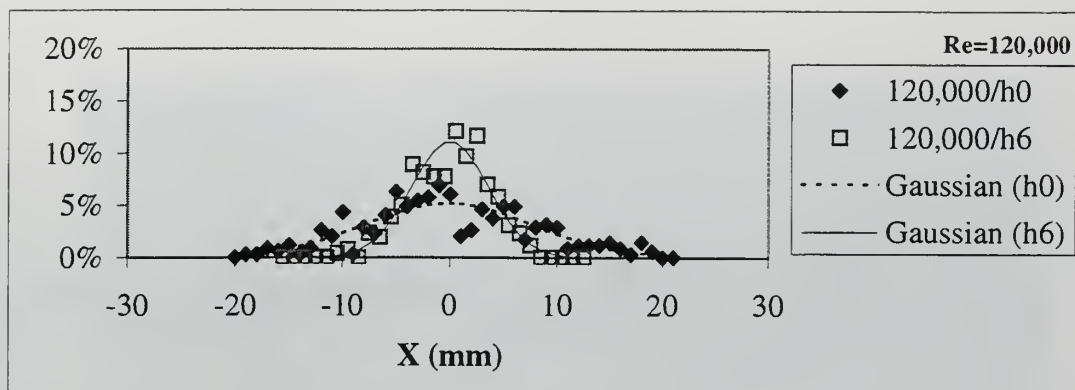


b.

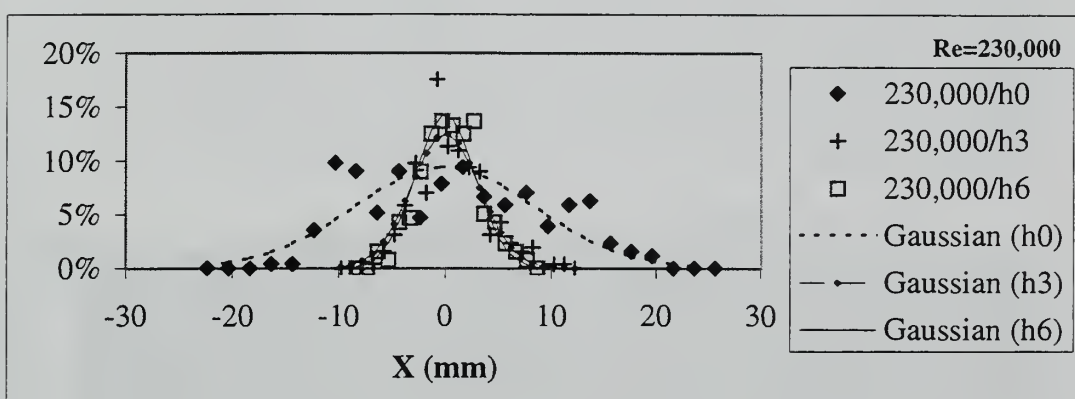


c.

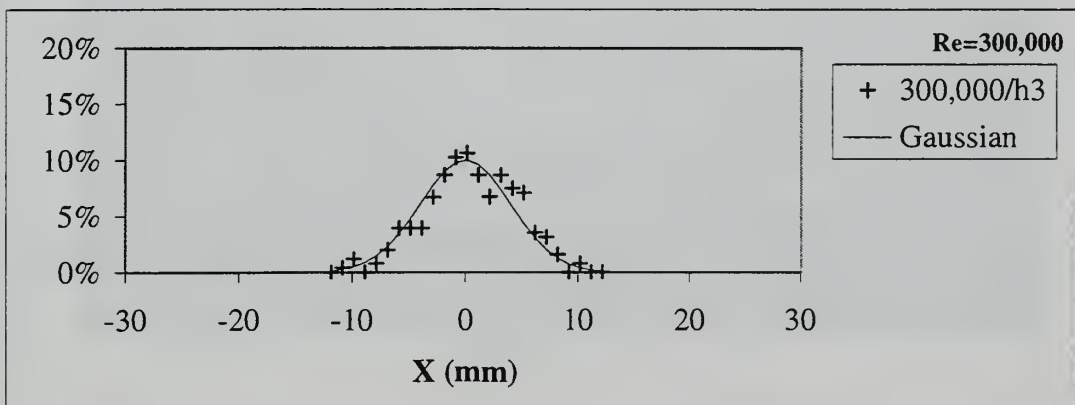
Figure 3-32. Variation of time length and estimated turbulence with window size.  $Re_D = 230,000/h\delta$ .  $X = 70$  mm and  $r = 0.0$  mm. (a.) The average and standard deviation of the window length. (b.) The normalized axial velocity fluctuations. (c.) The normalized tangential velocity fluctuations.



a.

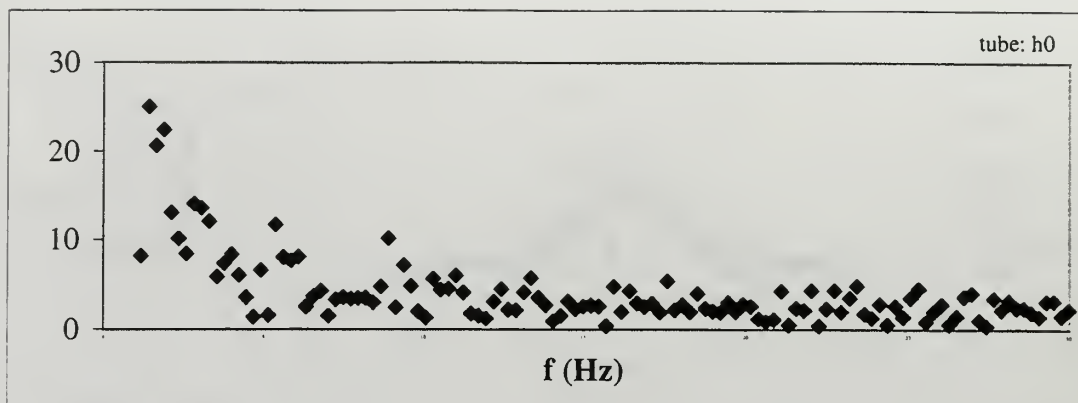


b.

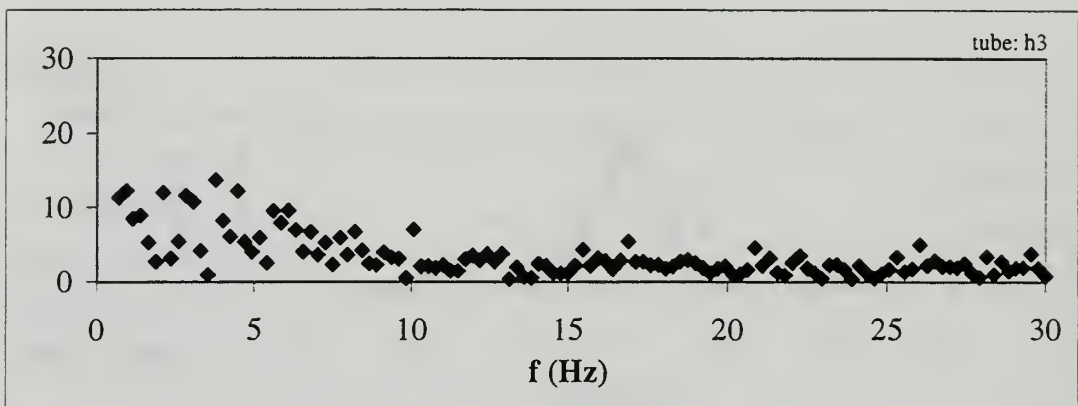


c.

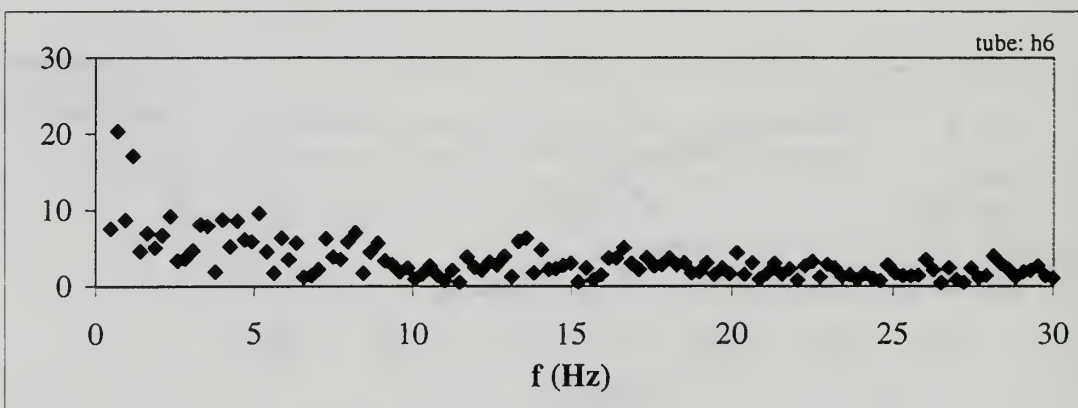
Figure 3-33. Histograms of the vortex breakdown position in various  $Re_D$ /tube flow states. (a.)  $Re_D = 120,000$ . (b.)  $Re_D = 230,000$ . (c.)  $Re_D = 300,000$ .



a.



b.



c.

Figure 3-34. Fourier analysis of the vortex breakdown position history for the  $Re_D = 230,000$  flow states. (a.) h0 tube. (b.) h3 tube. (c.) h6 tube.

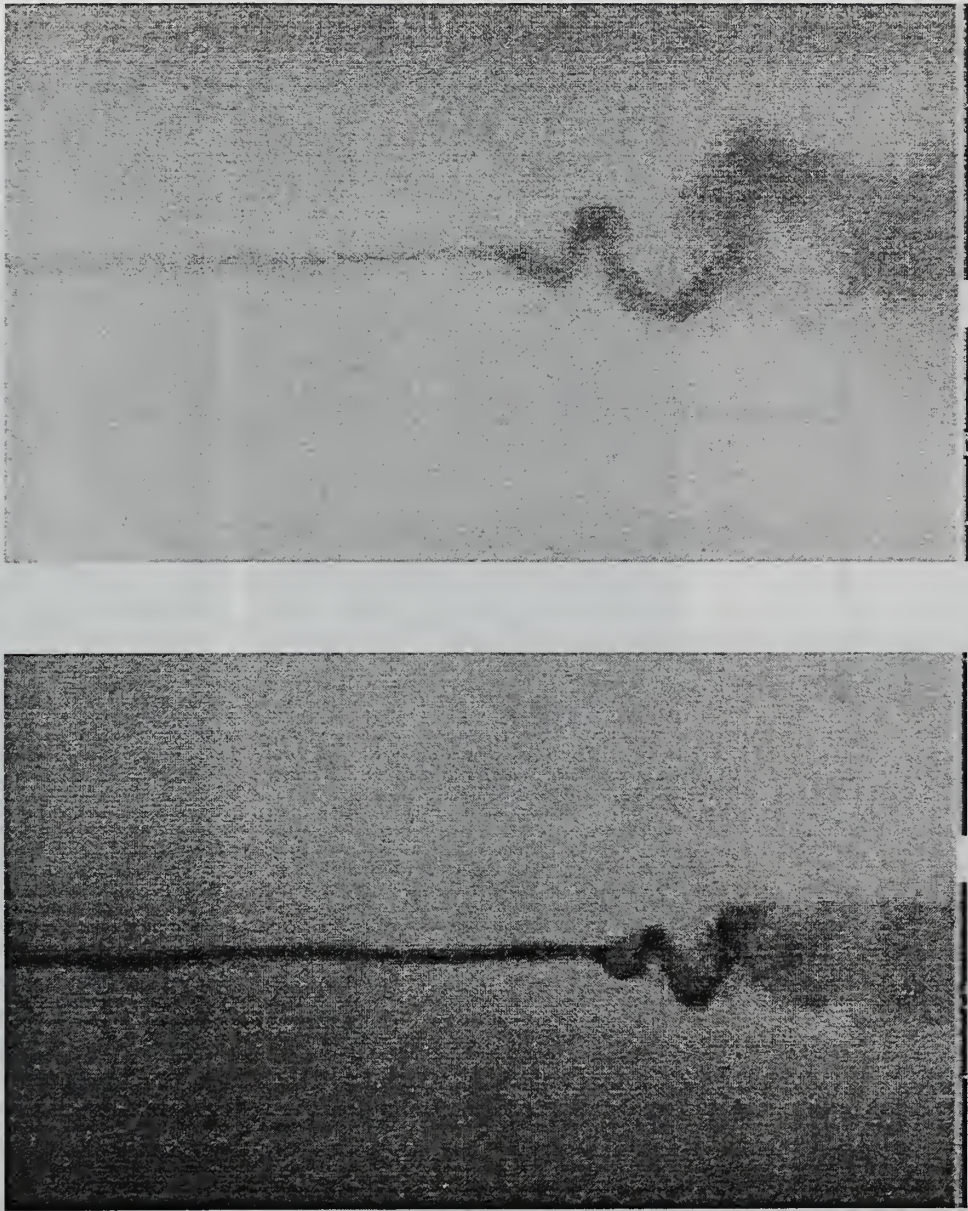


Figure 3-35. Vortex breakdowns in the  $Re_D = 120,000/h_0$  flow state.



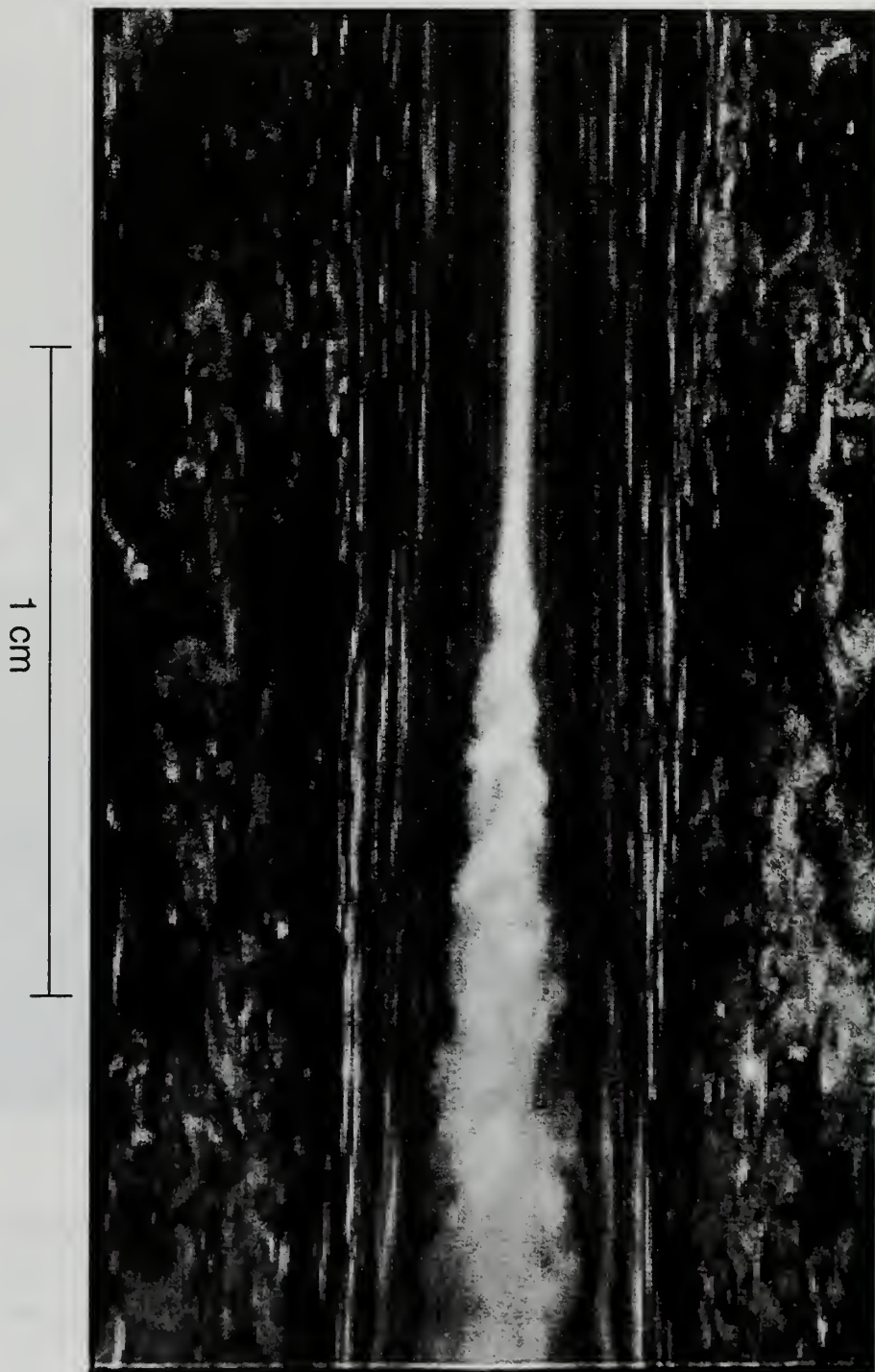
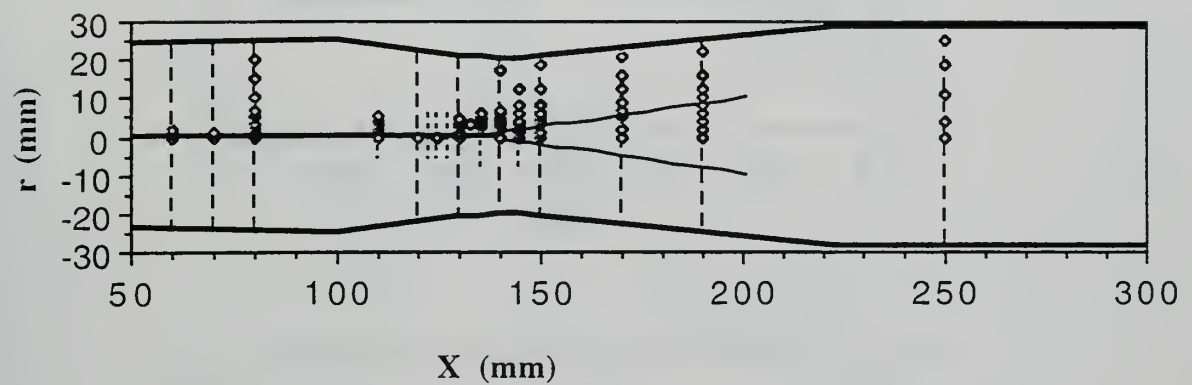


Figure 3-36. Vortex breakdown in the  $Re_D = 300,000/h^3$  flow state.



dashed lines: velocity and turbulence moments  
 diamonds: turbulence spectra  
 solid line dye contour

Figure 4-1. Map of LDV data stations in the  $Re_D = 230,000/h6$  flow state.

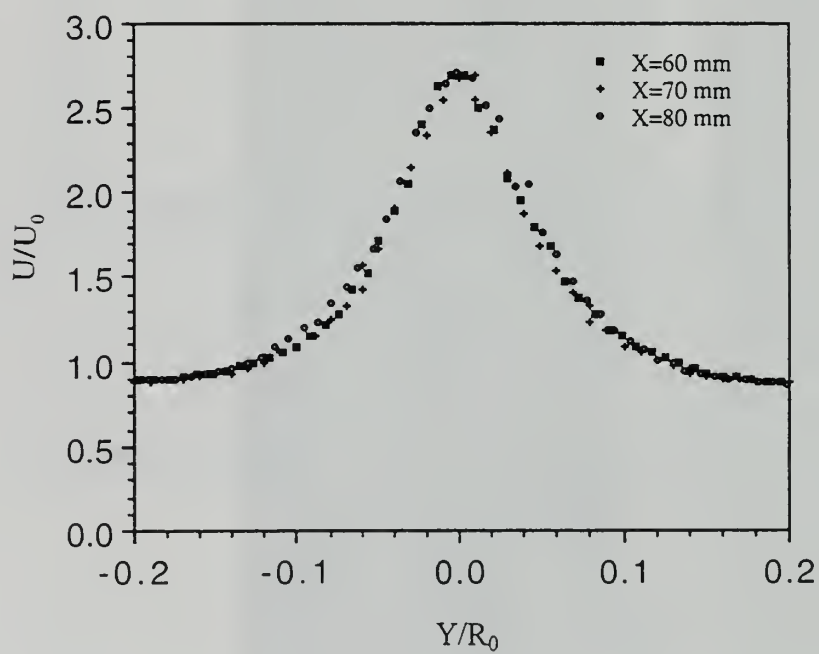
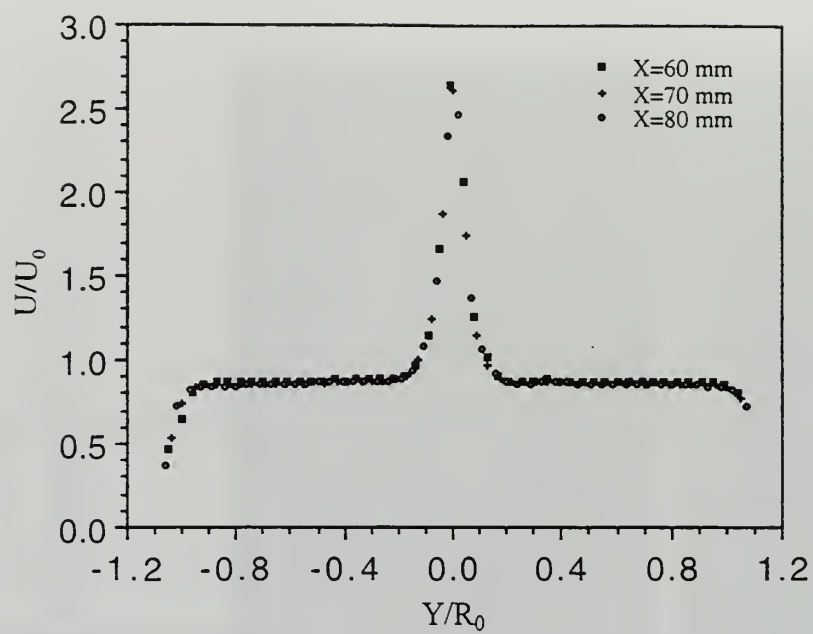


Figure 4-2.  $U/U_0$  profiles at the inlet of the  $Re_D = 230,000/h_6$  flow state.

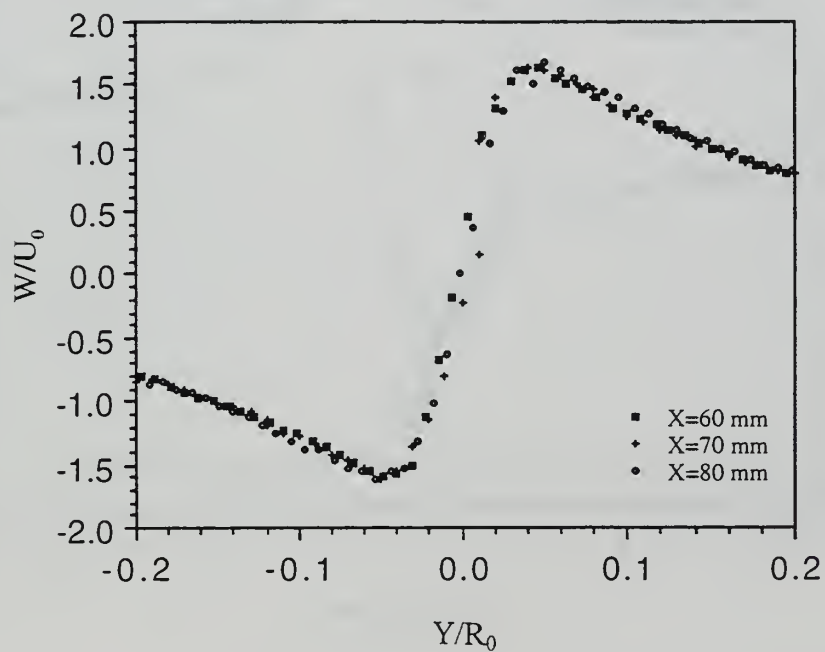
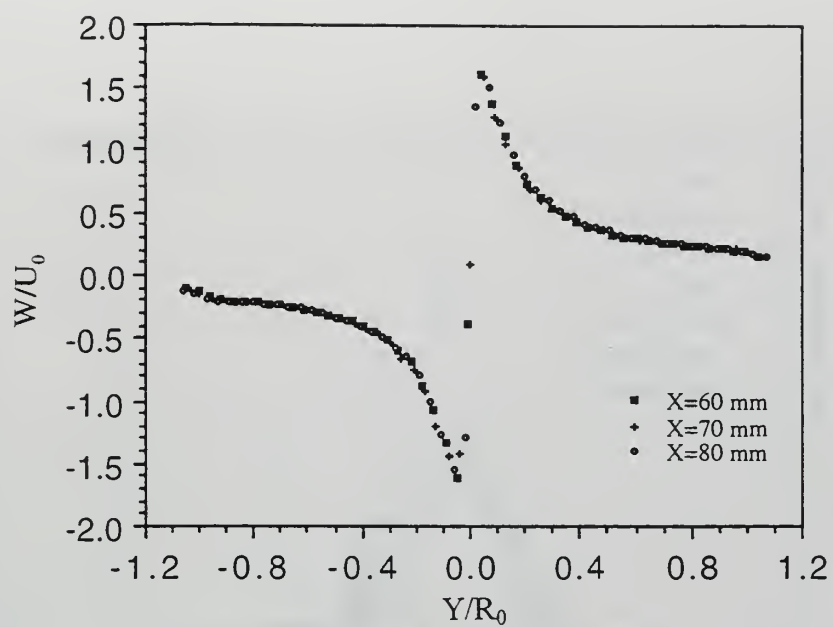


Figure 4-3.  $W/U_0$  profiles at the inlet of the  $Re_D = 230,000/h_6$  flow state.



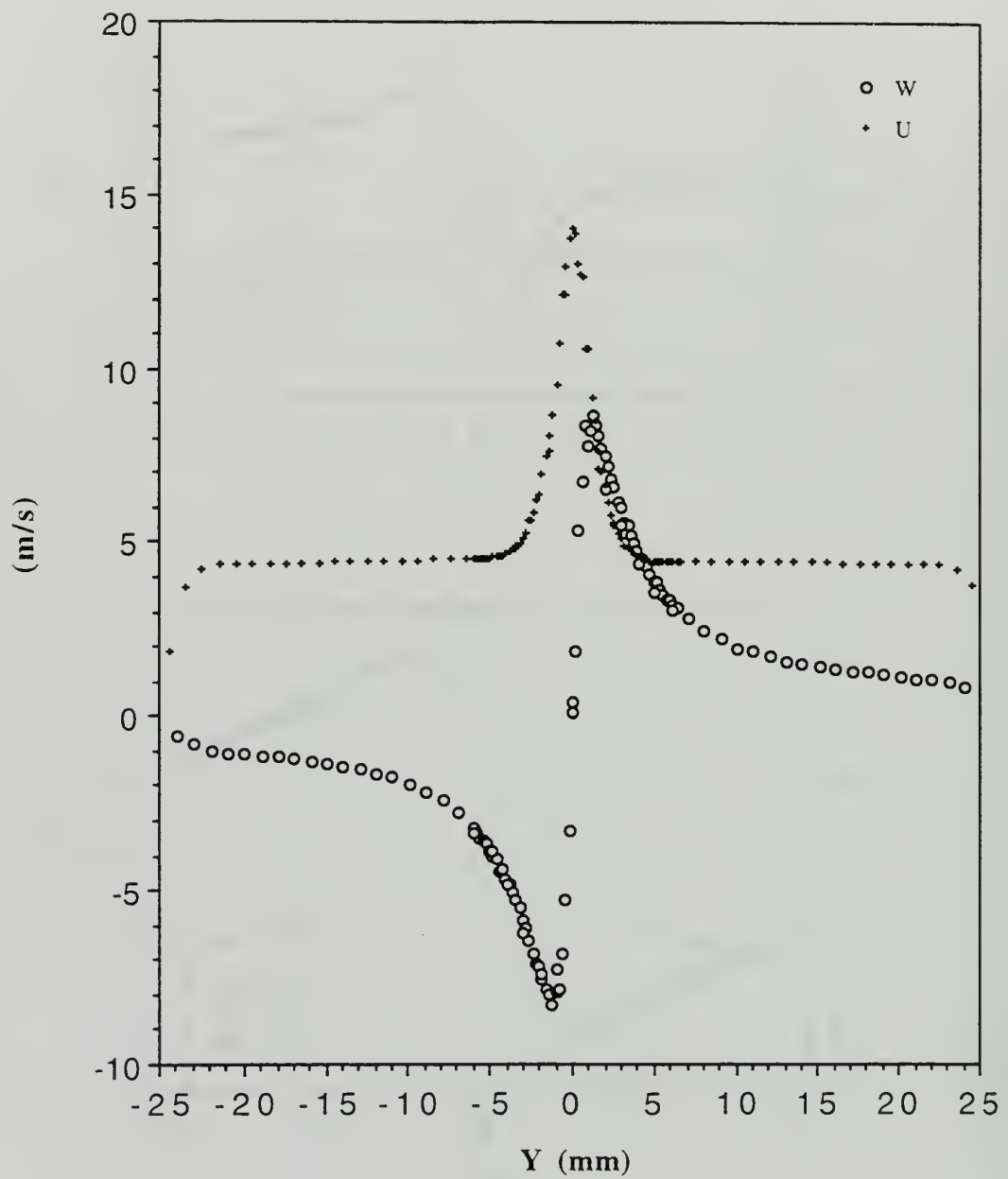


Figure 4-4.  $U$  and  $W$  profiles at  $X = 80$  mm in the  $Re_D = 230,000/h6$  flow state.

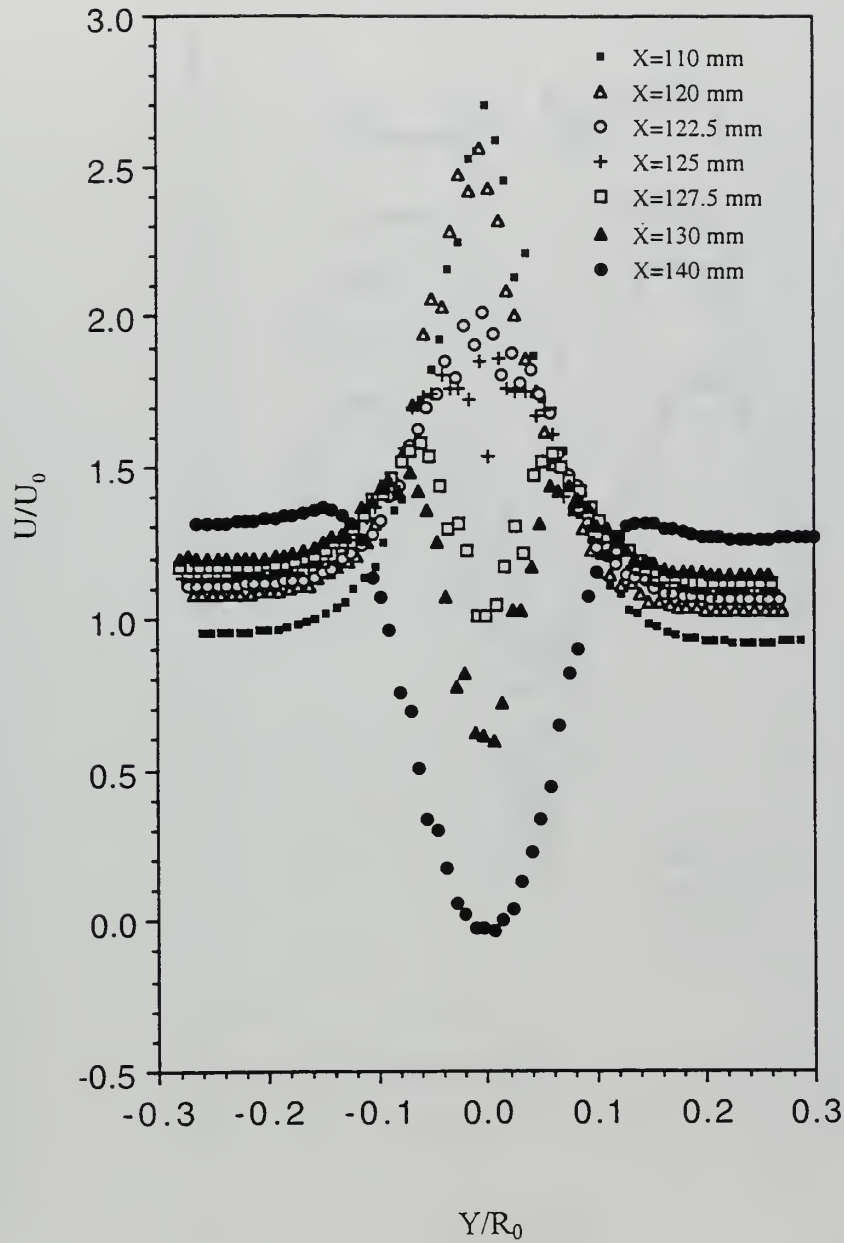


Figure 4-5.  $U/U_0$  profiles at  $X = 100$  mm to  $X = 140$  mm in the  $Re_D = 230,000/h6$  flow state.

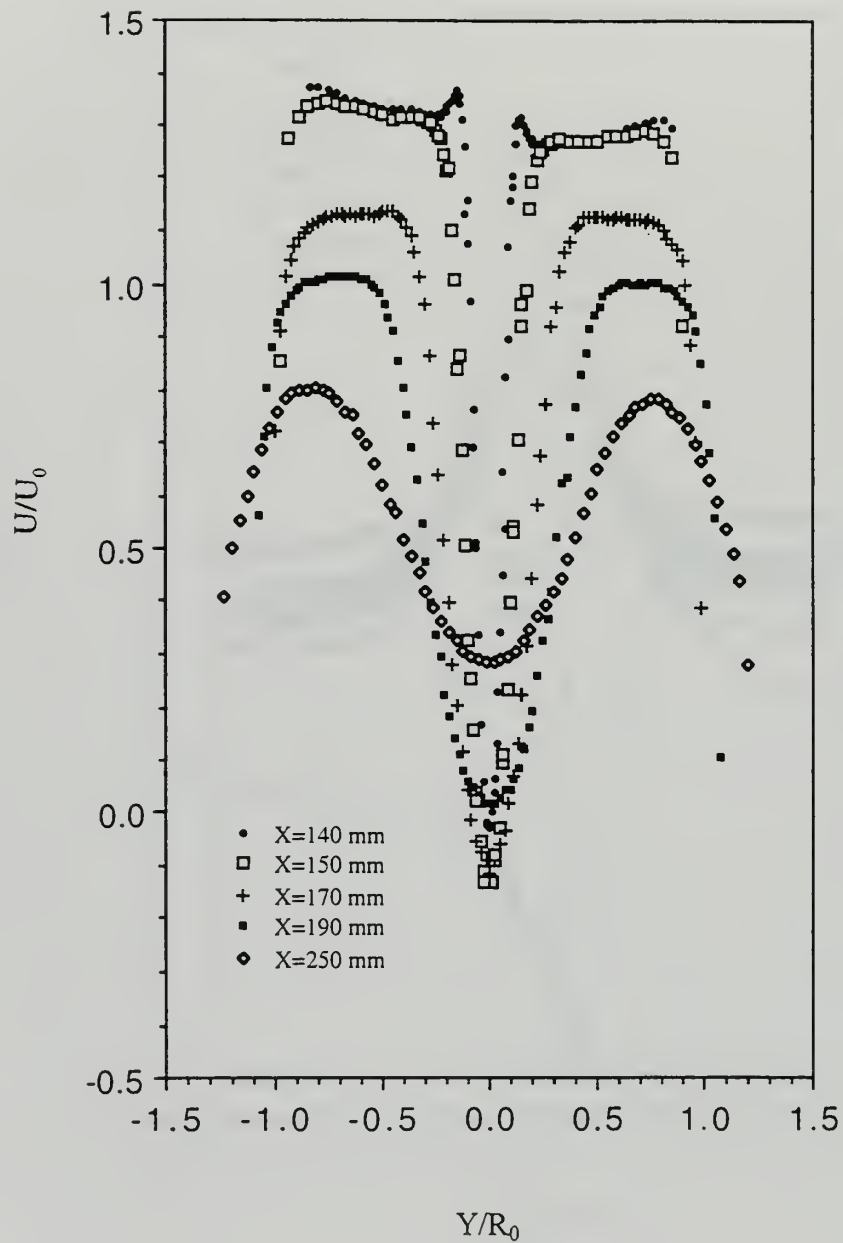


Figure 4-6.  $U/U_0$  profiles at  $X = 140$  mm to  $X = 250$  mm in the  $Re_D = 230,000/h6$  flow state.

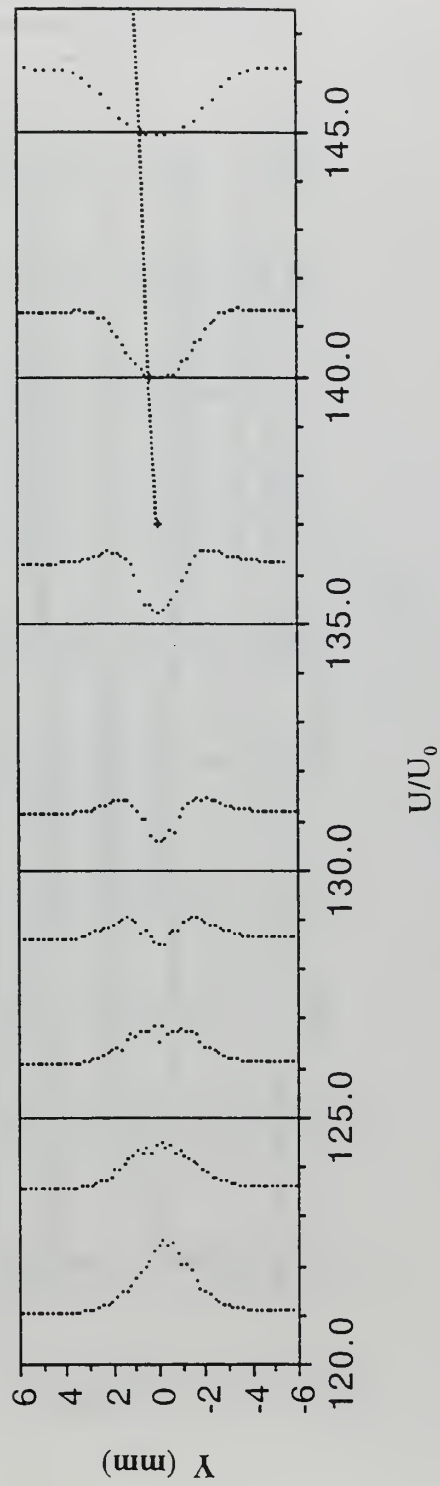


Figure 4-7. Birds' eye view of the transition from a jet-like to wake-like axial velocity profile in the  $Re_D = 230,000/h_6$  flow state.



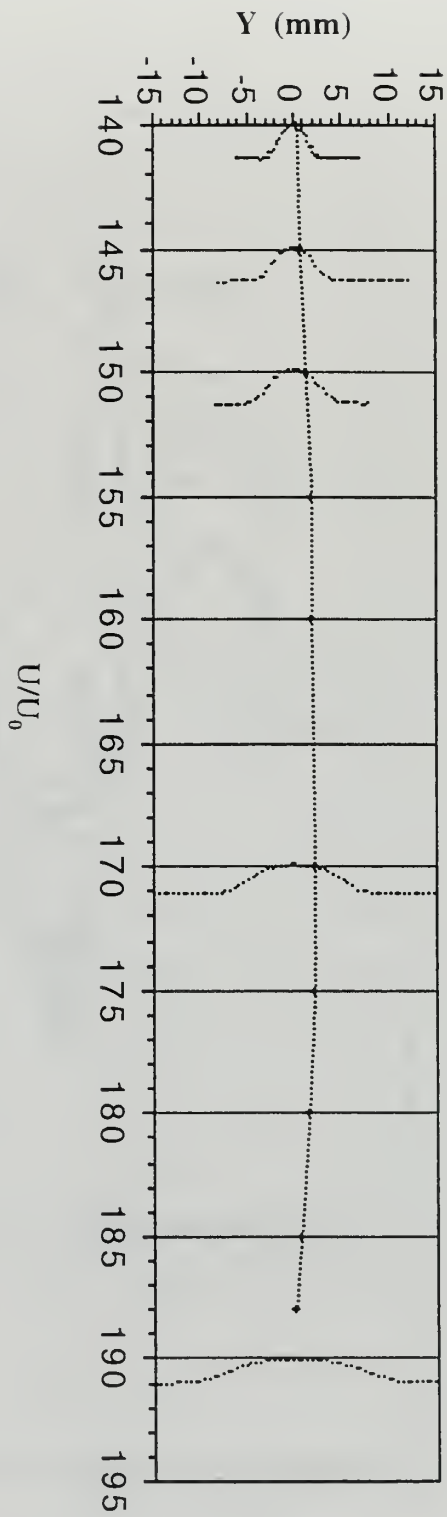


Figure 4-8. Birds' eye view of the evolution of the wake-like profile in the  $Re_D = 230,000/h6$  flow state.

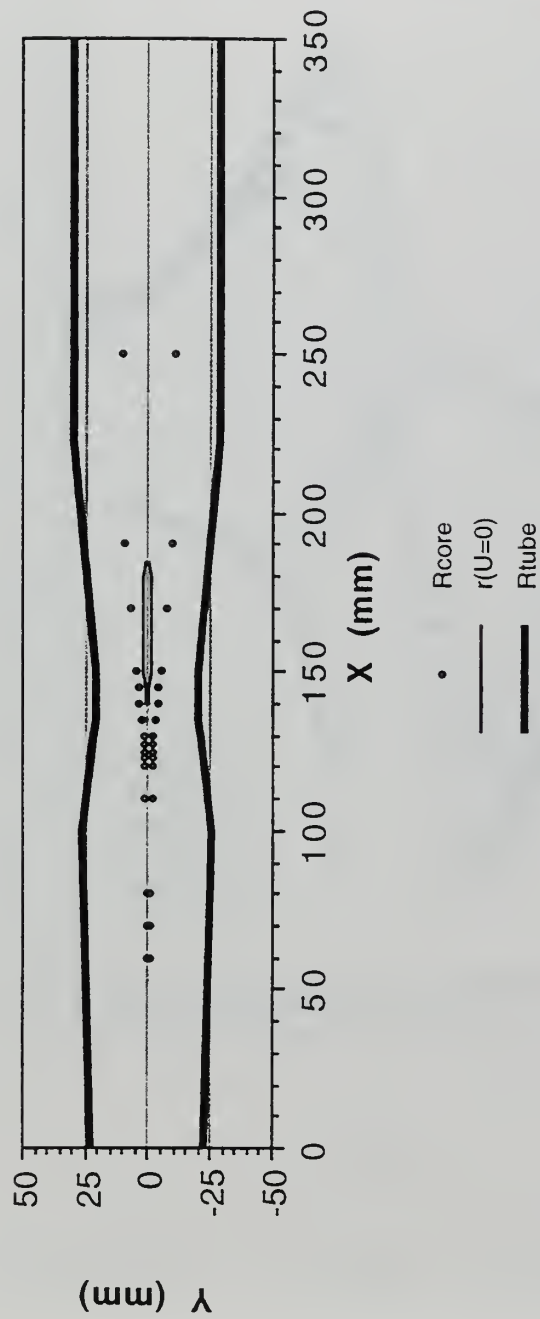


Figure 4-9. Reversed flow region and core radii in the  $Re_D = 230,000/h_6$  flow state.

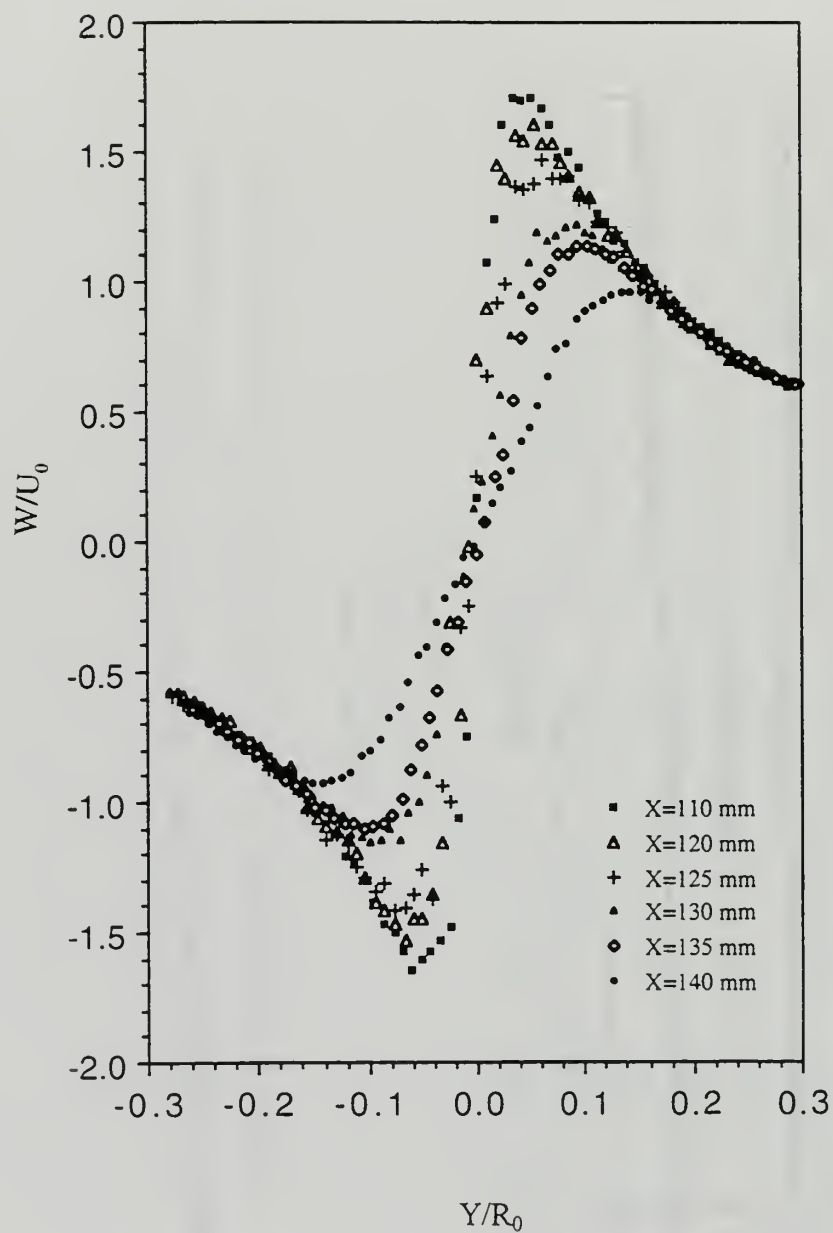


Figure 4-10.  $W/U_0$  profiles at  $X = 110$  mm to  $X = 140$  mm in the  $Re_D = 230,000/h6$  flow state.

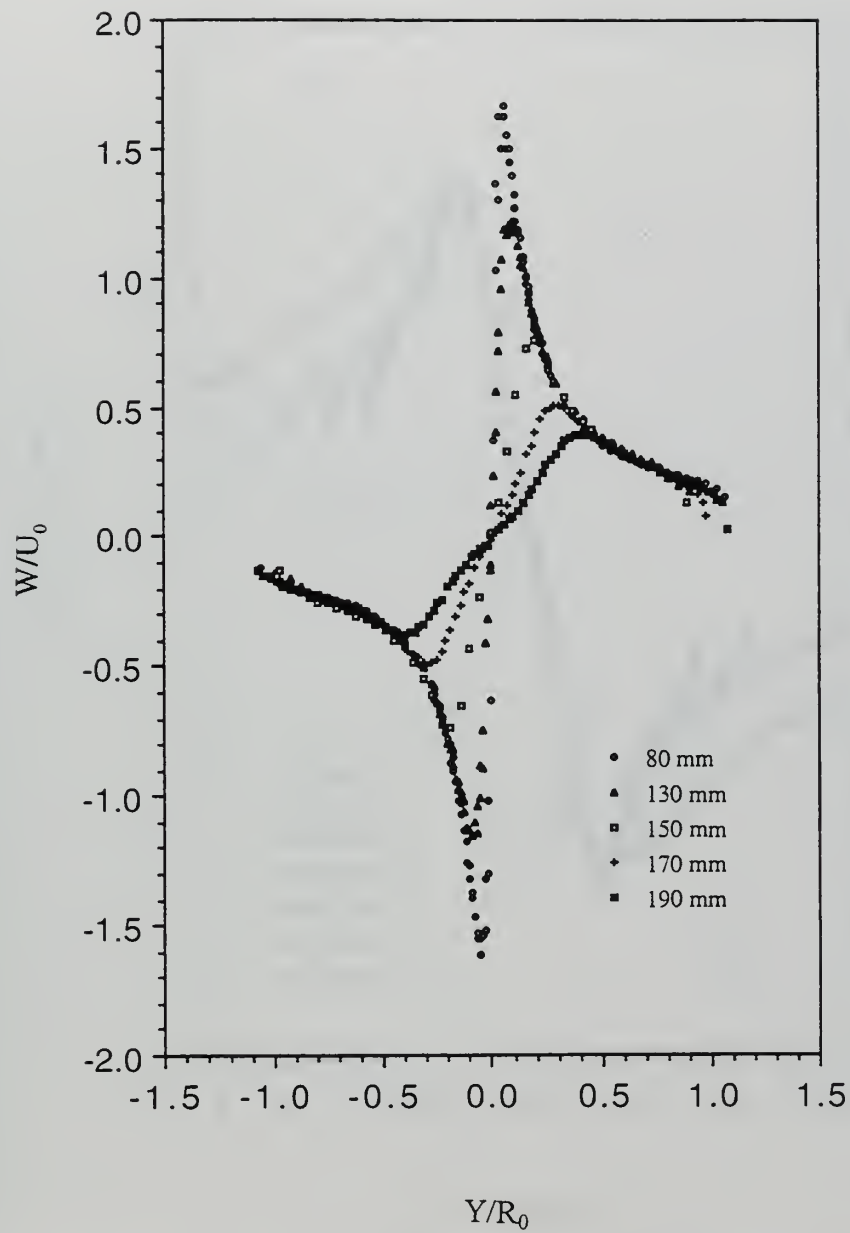


Figure 4-11.  $W/U_0$  profiles at  $X = 80$  mm to  $X = 190$  mm in the  $Re_D = 230,000/h_6$  flow state.



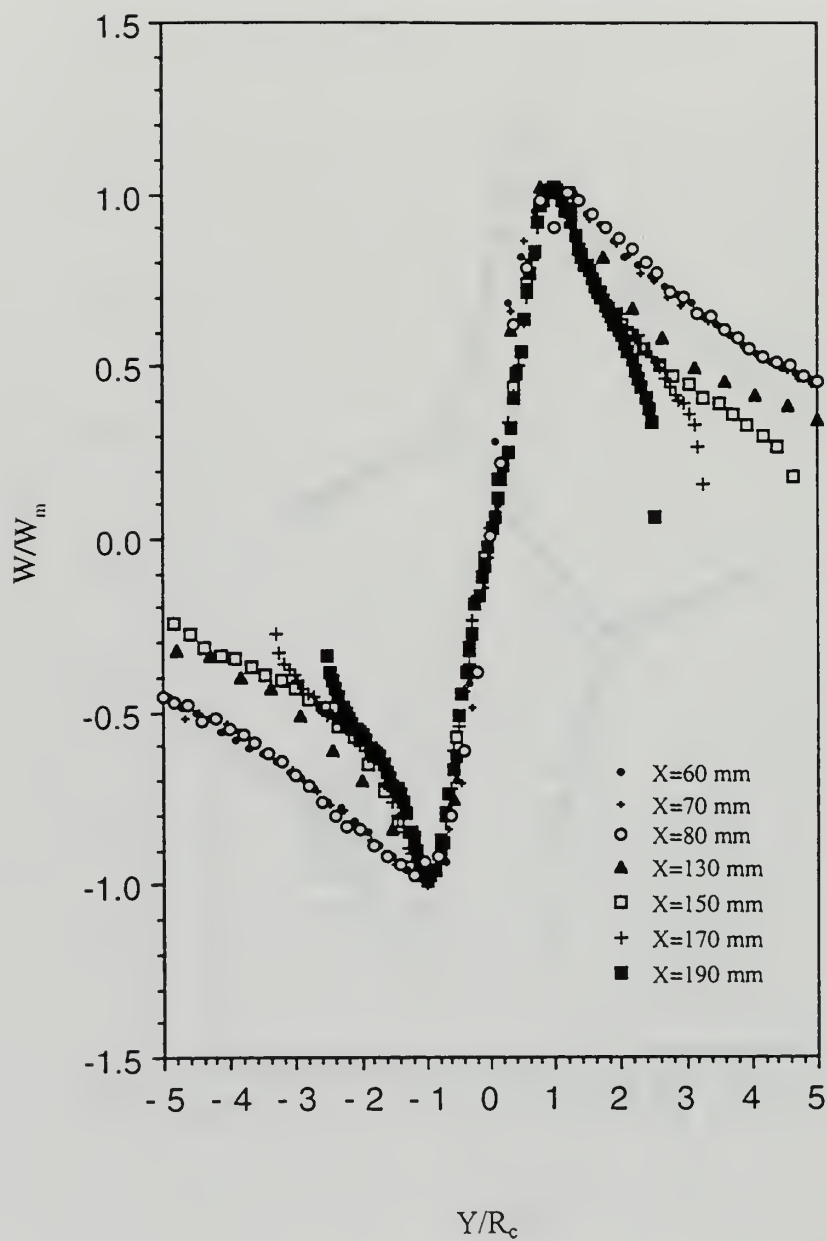


Figure 4-12.  $W/W_m$  vs.  $Y/R_c$  at various sections in the  $Re_D = 230,000/h6$  flow state.

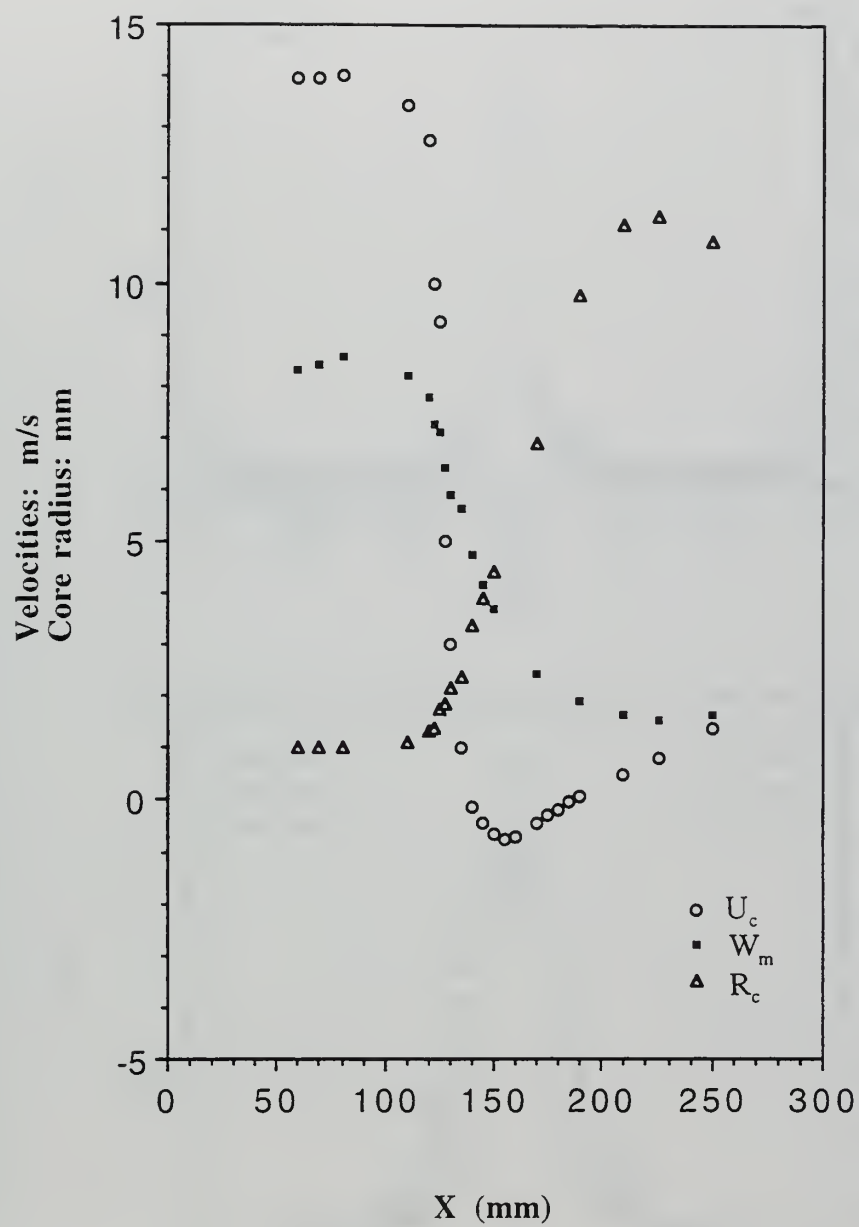


Figure 4-13. Variation of the  $U_c$ ,  $W_m$ , and  $R_c$  with  $X$ .

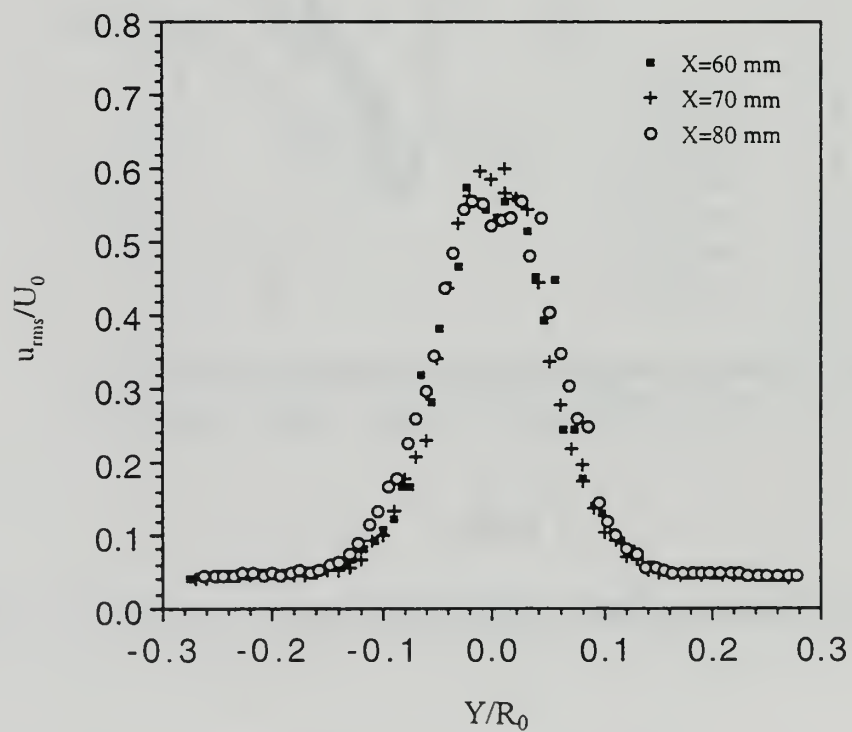
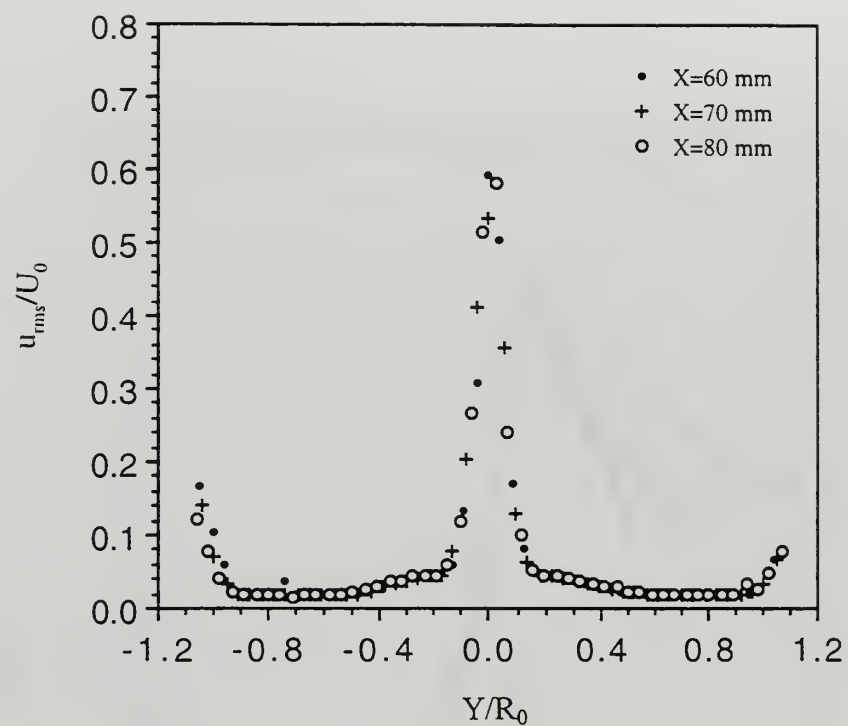


Figure 4-14.  $u_{rms}/U_0$  profiles in the inlet region of the  $Re_D = 230,000/h6$  flow state.

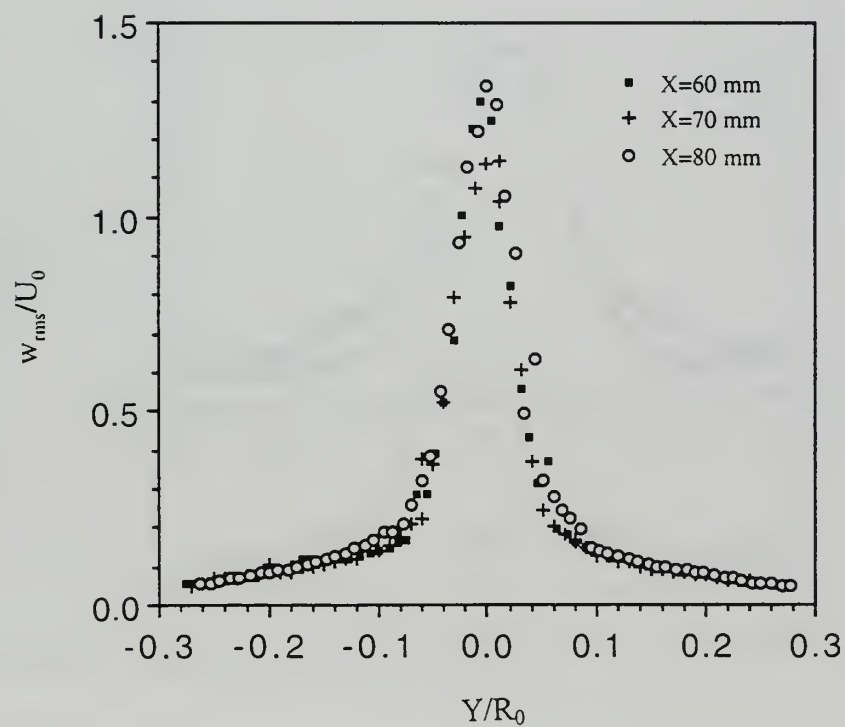
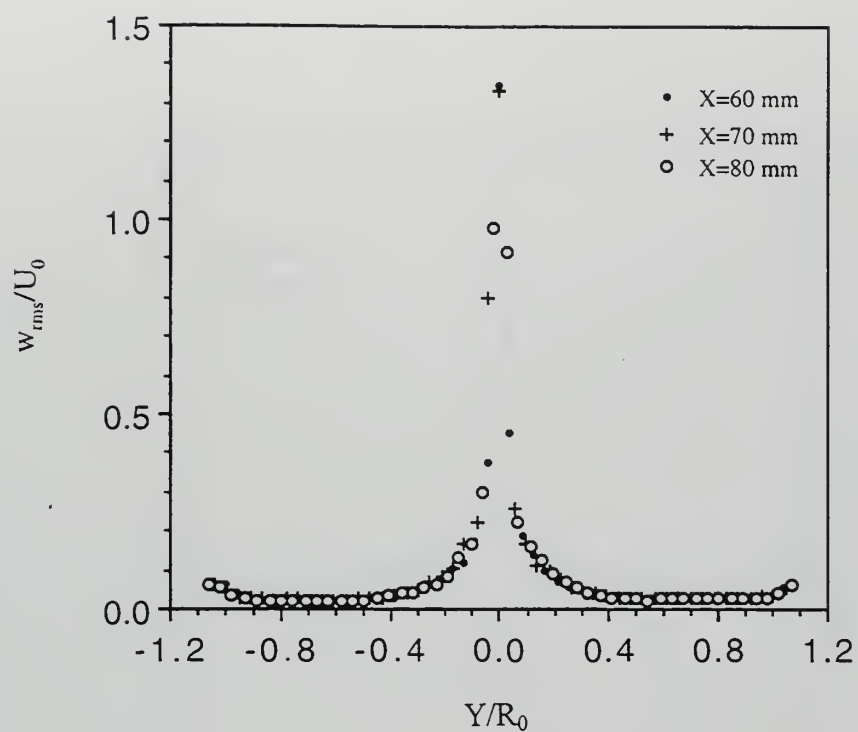


Figure 4-15.  $w_{rms}/U_0$  profiles in the inlet region of the  $Re_D = 230,000/h6$  flow state.



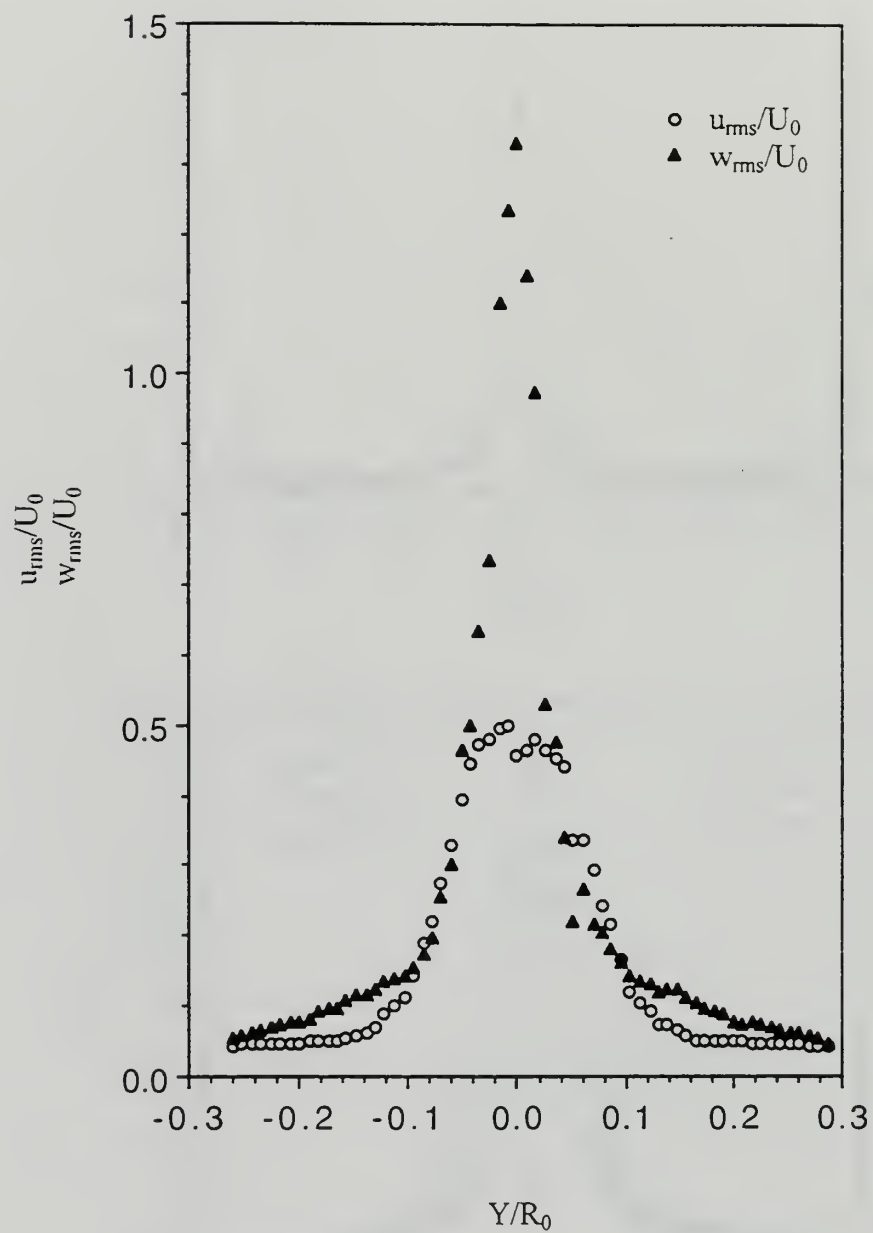


Figure 4-16.  $u_{rms}/U_0$  and  $w_{rms}/U_0$  vs.  $Y/R_0$  at  $X = 110$  mm in the  $Re_D = 230,000/h6$  flow state.

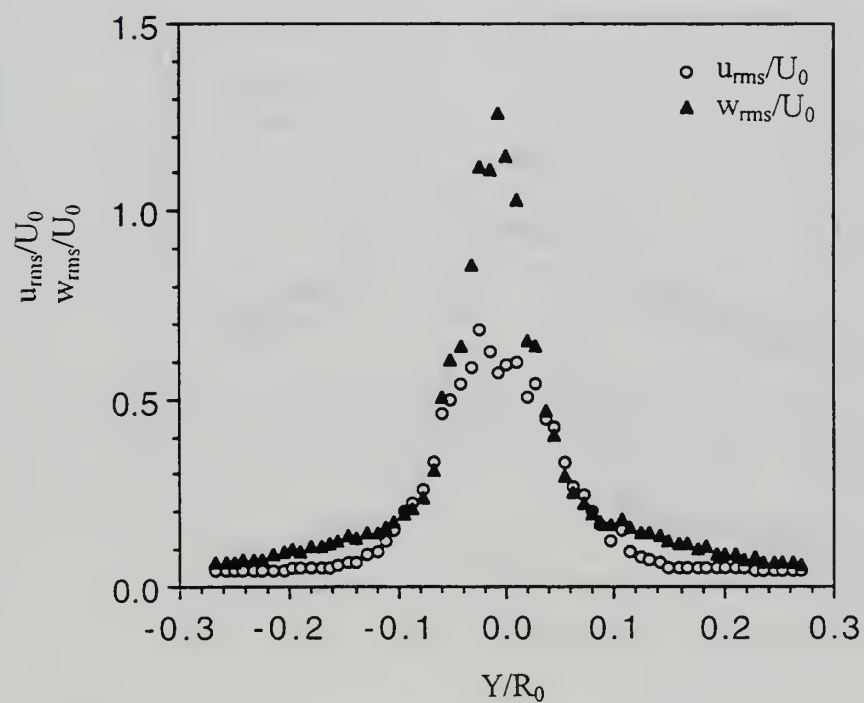
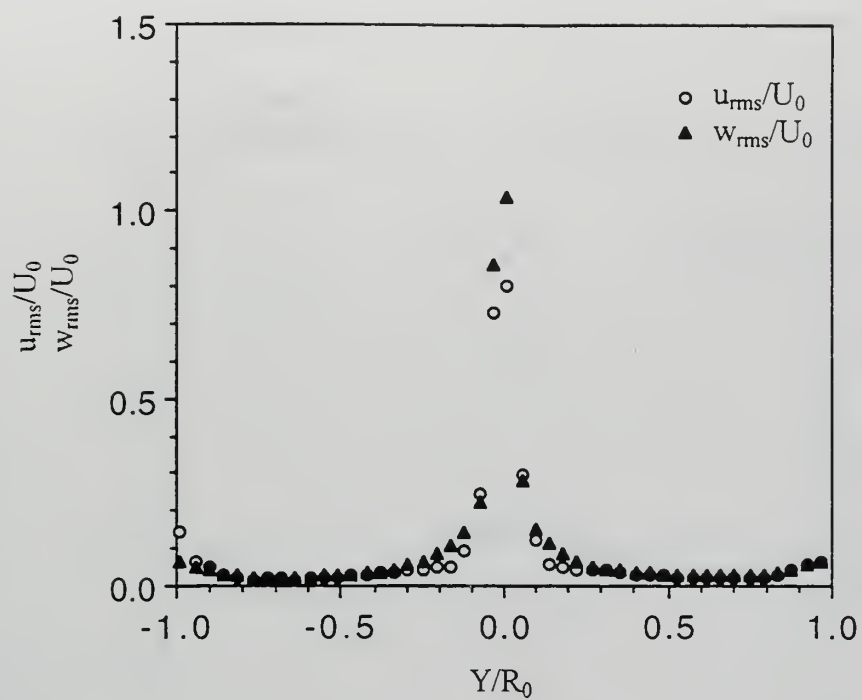


Figure 4-17.  $u_{rms}/U_0$  and  $w_{rms}/U_0$  vs.  $Y/R_0$  at  $X = 120$  mm in the  $Re_D = 230,000/h6$  flow state.

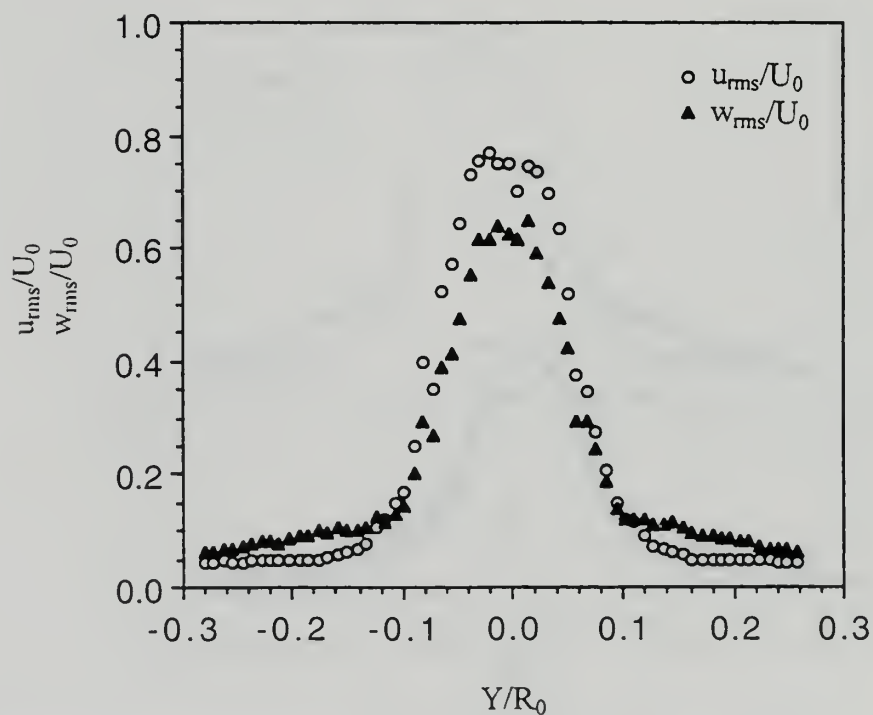
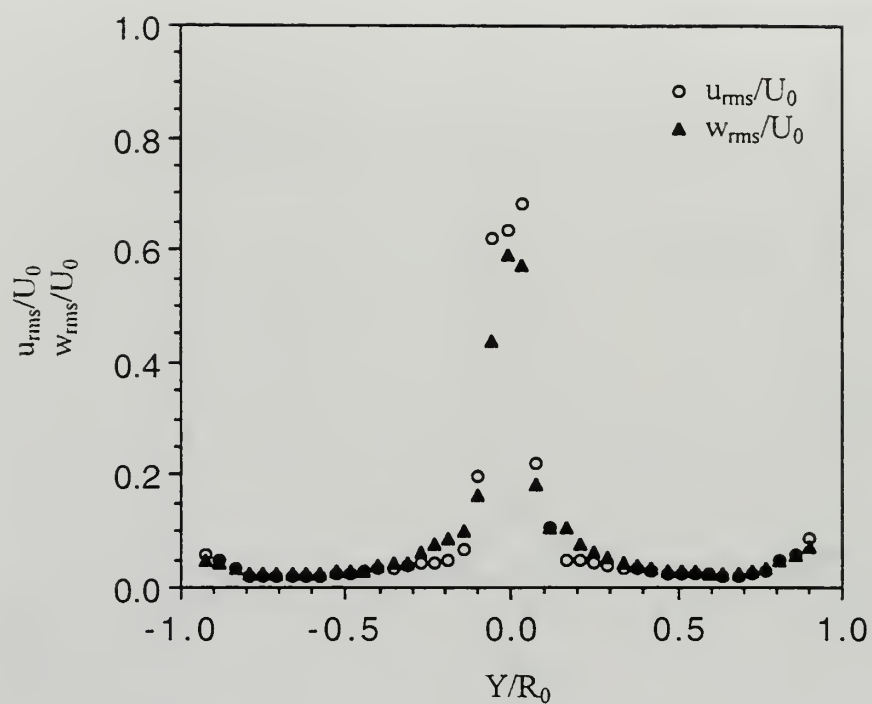


Figure 4-18.  $u_{rms} / U_0$  and  $w_{rms} / U_0$  vs.  $Y/R_0$  at  $X = 130$  mm in the  $Re_D = 230,000/h_6$  flow state.

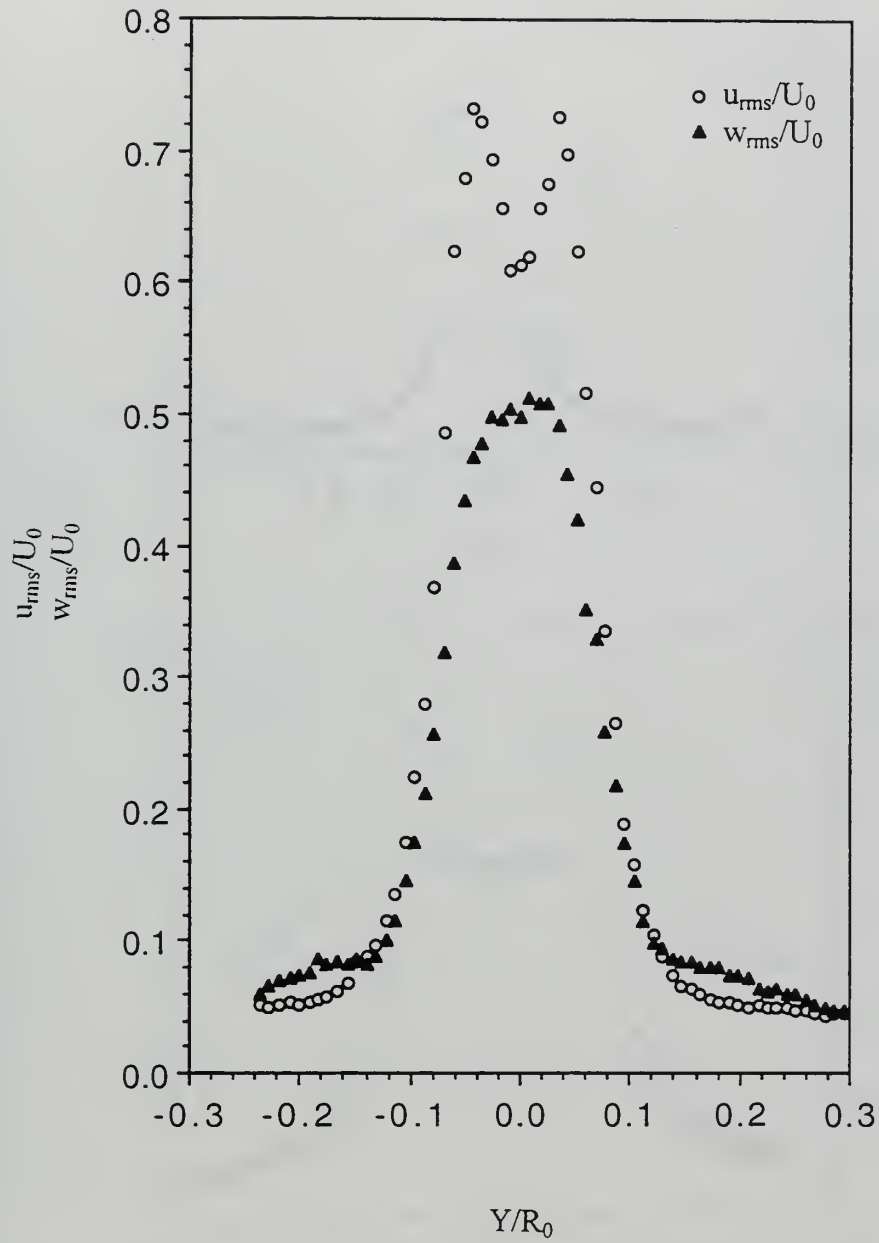


Figure 4-19.  $u_{rms} / U_0$  and  $w_{rms} / U_0$  vs.  $Y/R_0$  at  $X = 135$  mm in the  $Re_D = 230,000/h6$  flow state.



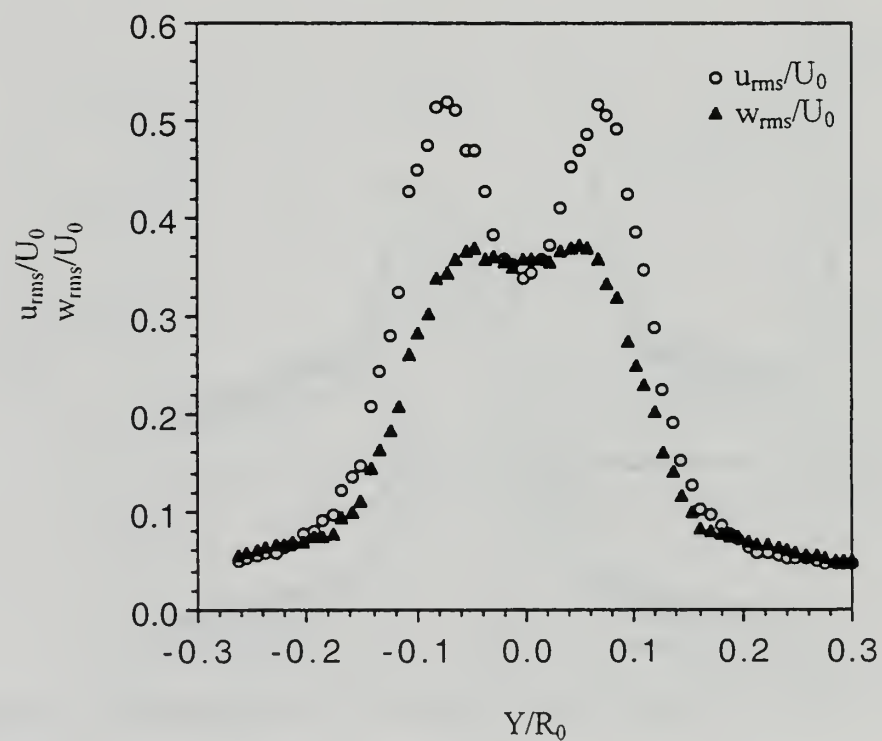
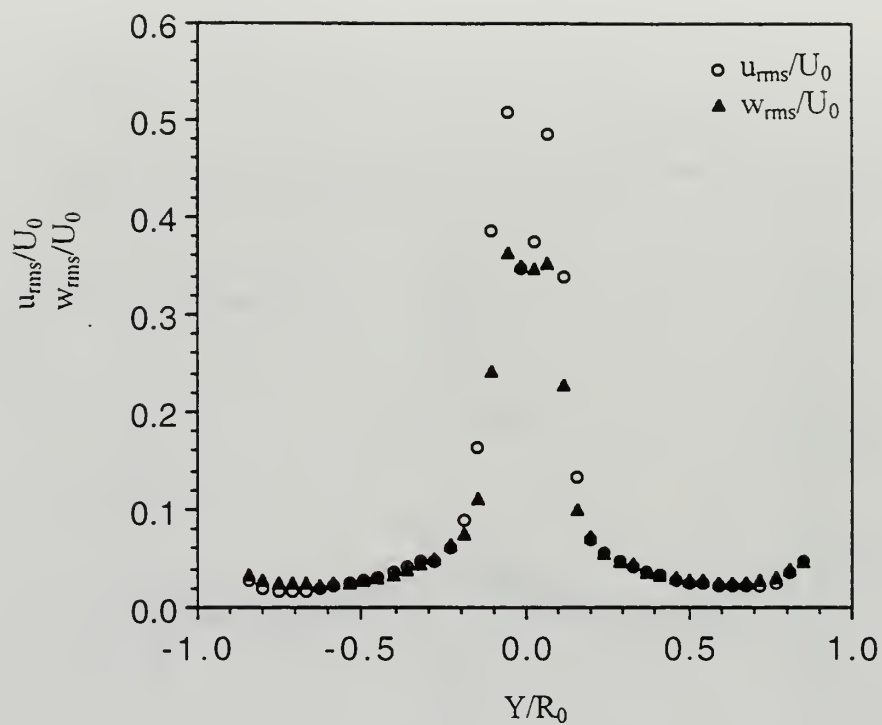


Figure 4-20.  $u_{rms} / U_0$  and  $w_{rms} / U_0$  vs.  $Y/R_0$  at  $X = 140$  mm in the  $Re_D = 230,000/h6$  flow state.

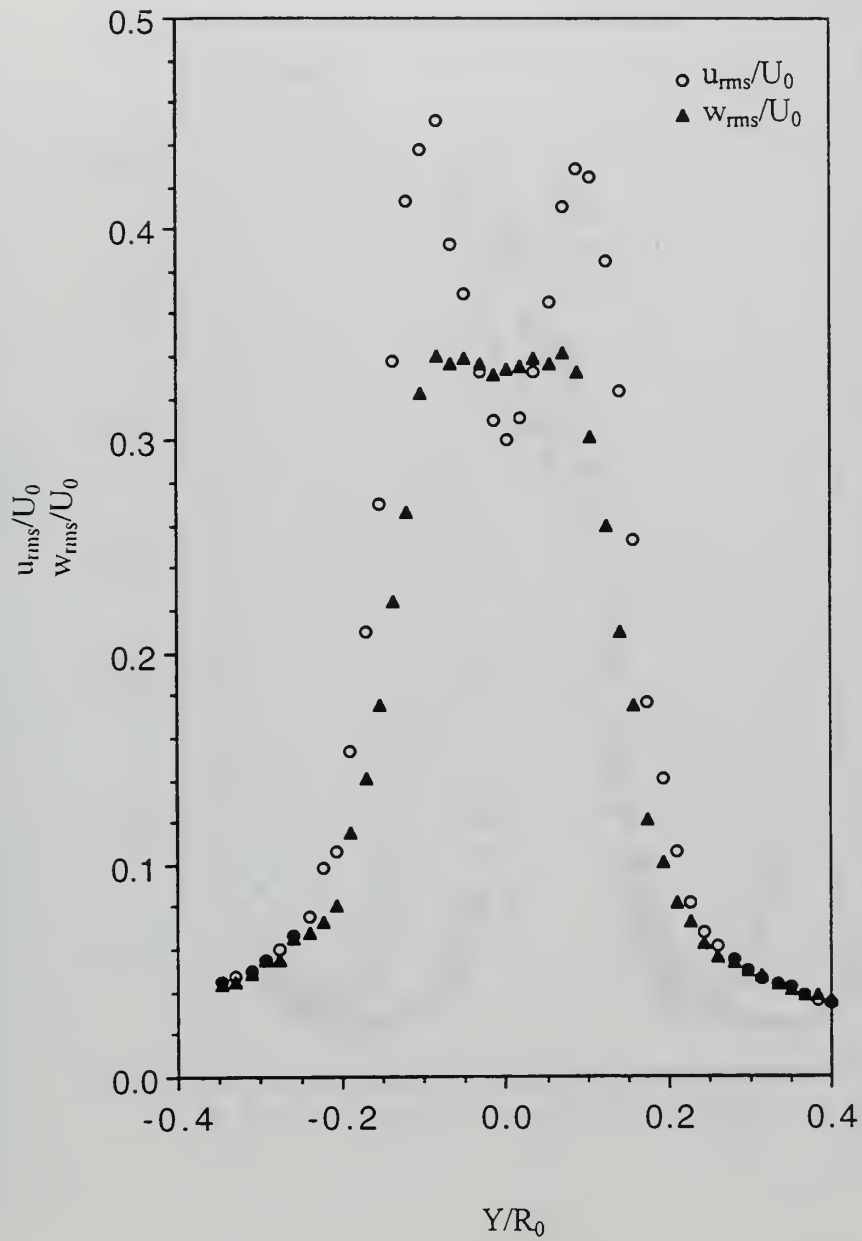


Figure 4-21.  $u_{rms} / U_0$  and  $w_{rms} / U_0$  v vs.  $Y/R_0$  at  $X = 145$  mm in the  $Re_D = 230,000/h6$  flow state.

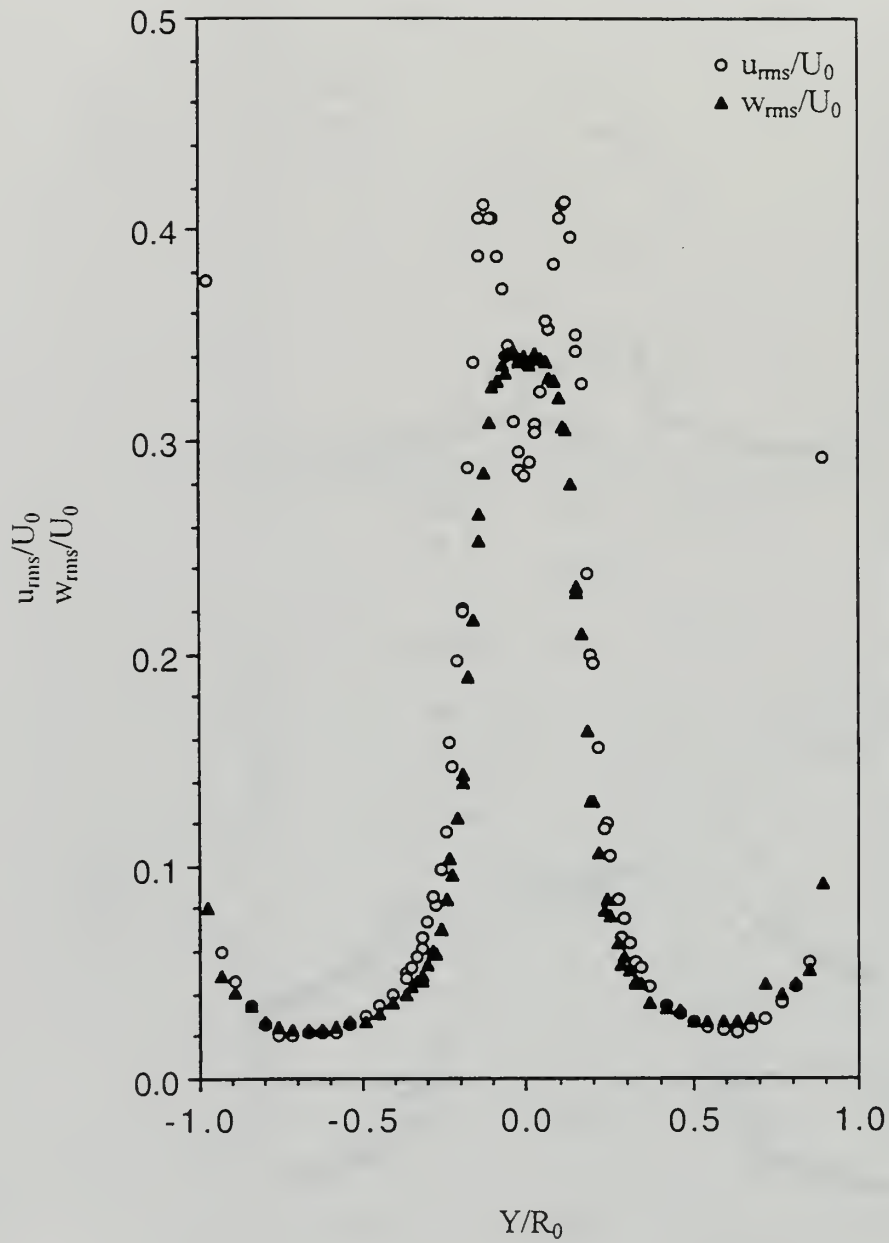


Figure 4-22.  $u_{rms} / U_0$  and  $w_{rms} / U_0$  vs.  $Y/R_0$  at  $X = 150$  mm in the  $Re_D = 230,000/h_6$  flow state.

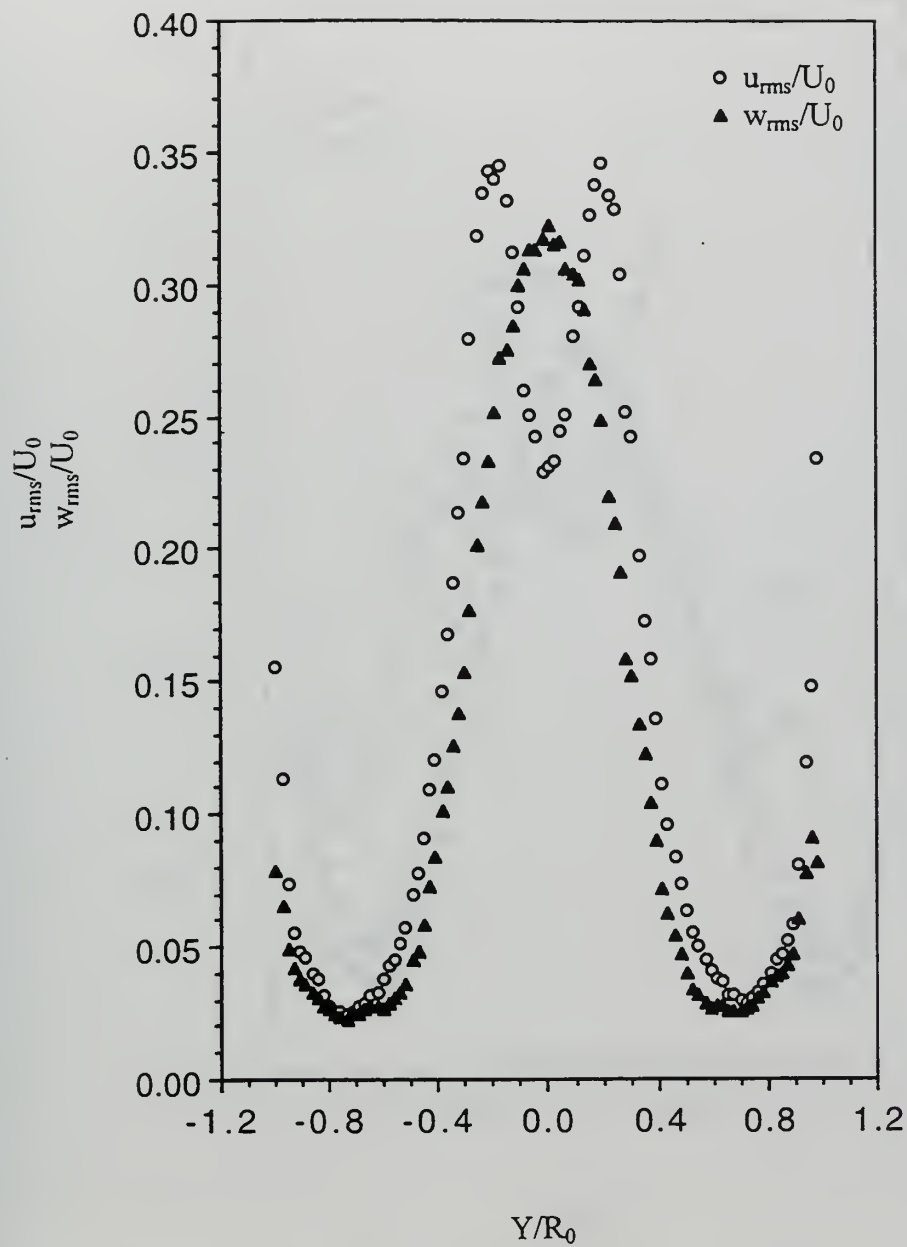


Figure 4-23.  $u_{rms} / U_0$  and  $w_{rms} / U_0$  vs.  $Y/R_0$  at  $X = 170$  mm in the  $Re_D = 230,000/h_6$  flow state.



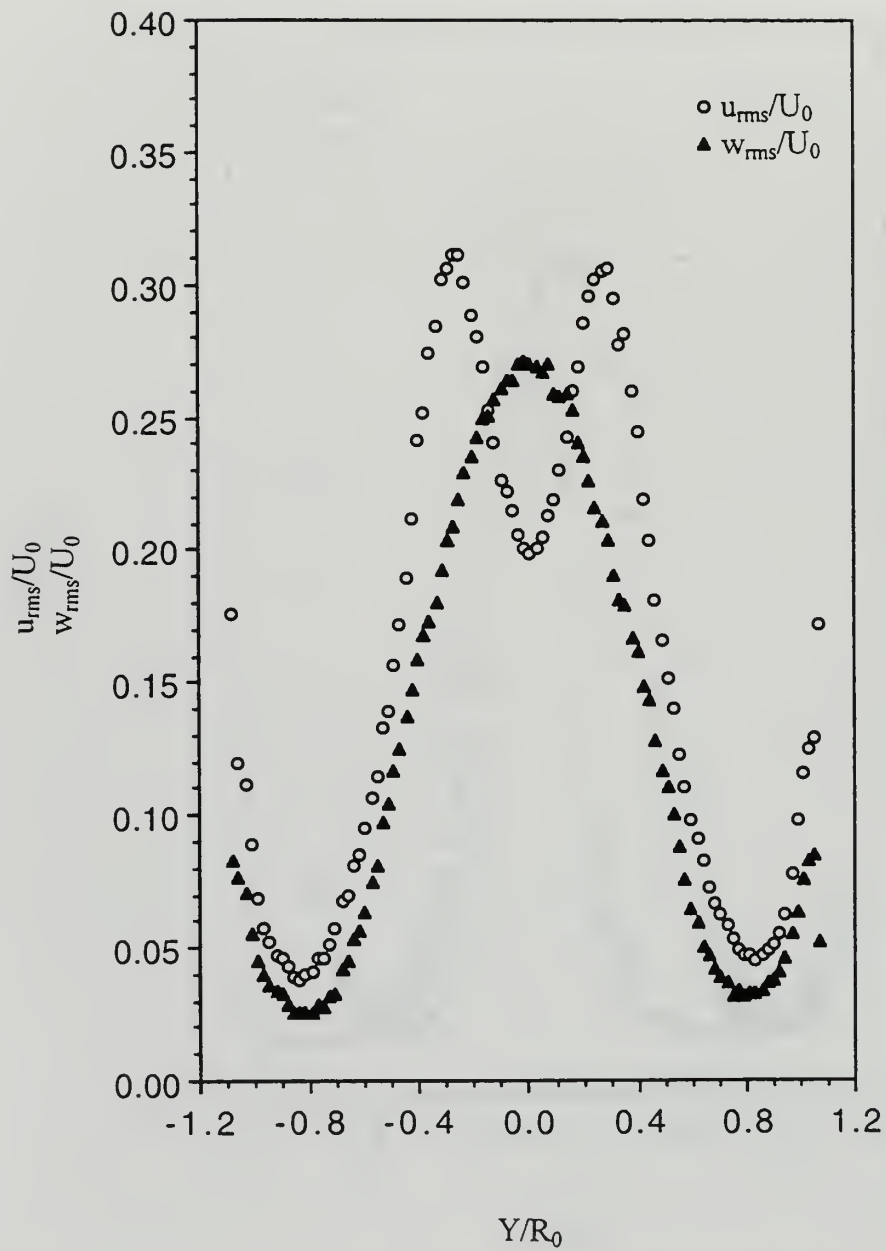


Figure 4-24.  $u_{rms} / U_0$  and  $w_{rms} / U_0$  vs.  $Y/R_0$  at  $X = 190$  mm in the  $Re_D = 230,000/h_6$  flow state.

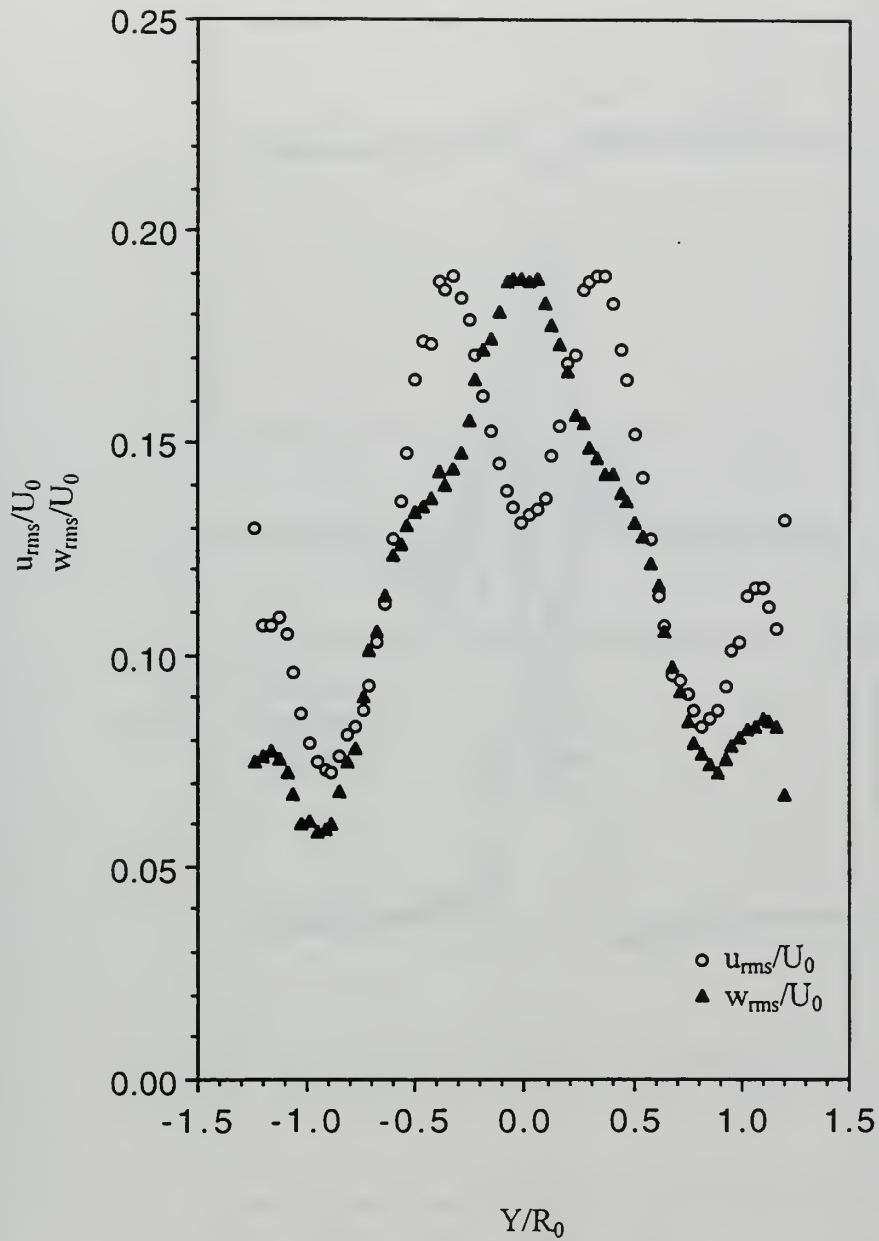


Figure 4-25.  $u_{rms} / U_0$  and  $w_{rms} / U_0$  vs.  $Y/R_0$  at  $X = 250$  mm in the  $Re_D = 230,000/h6$  flow state.

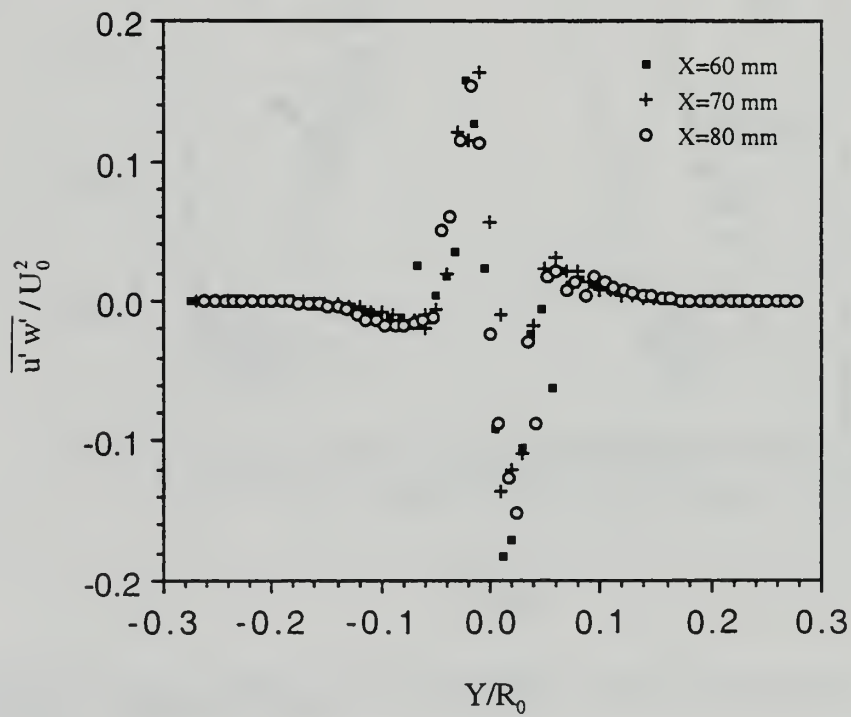
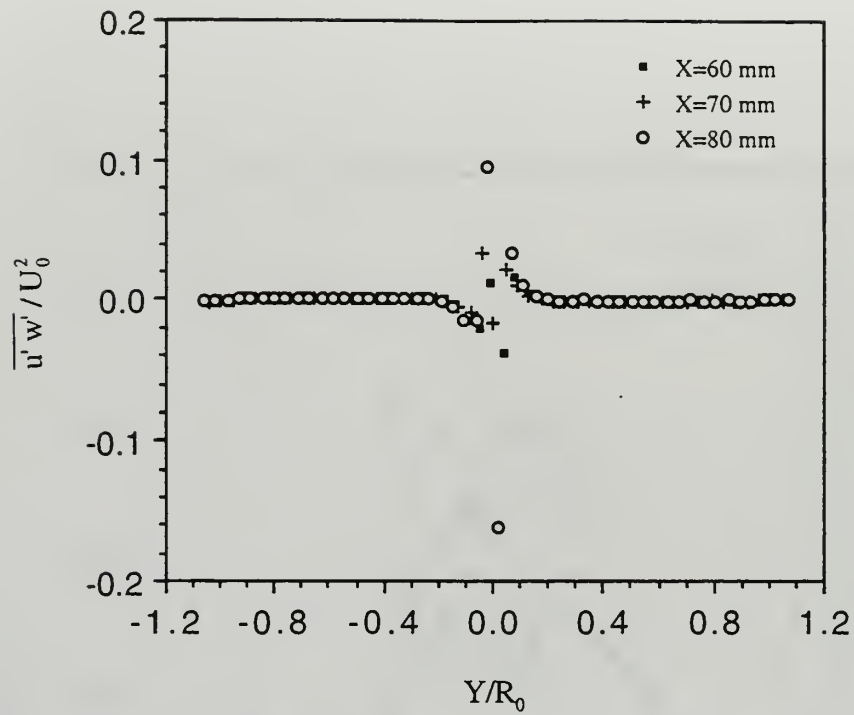


Figure 4-26.  $\overline{u'w'}/U_0^2$  vs.  $Y/R_0$  in the inlet region of the  $Re_D = 230,000/h6$  flow state.

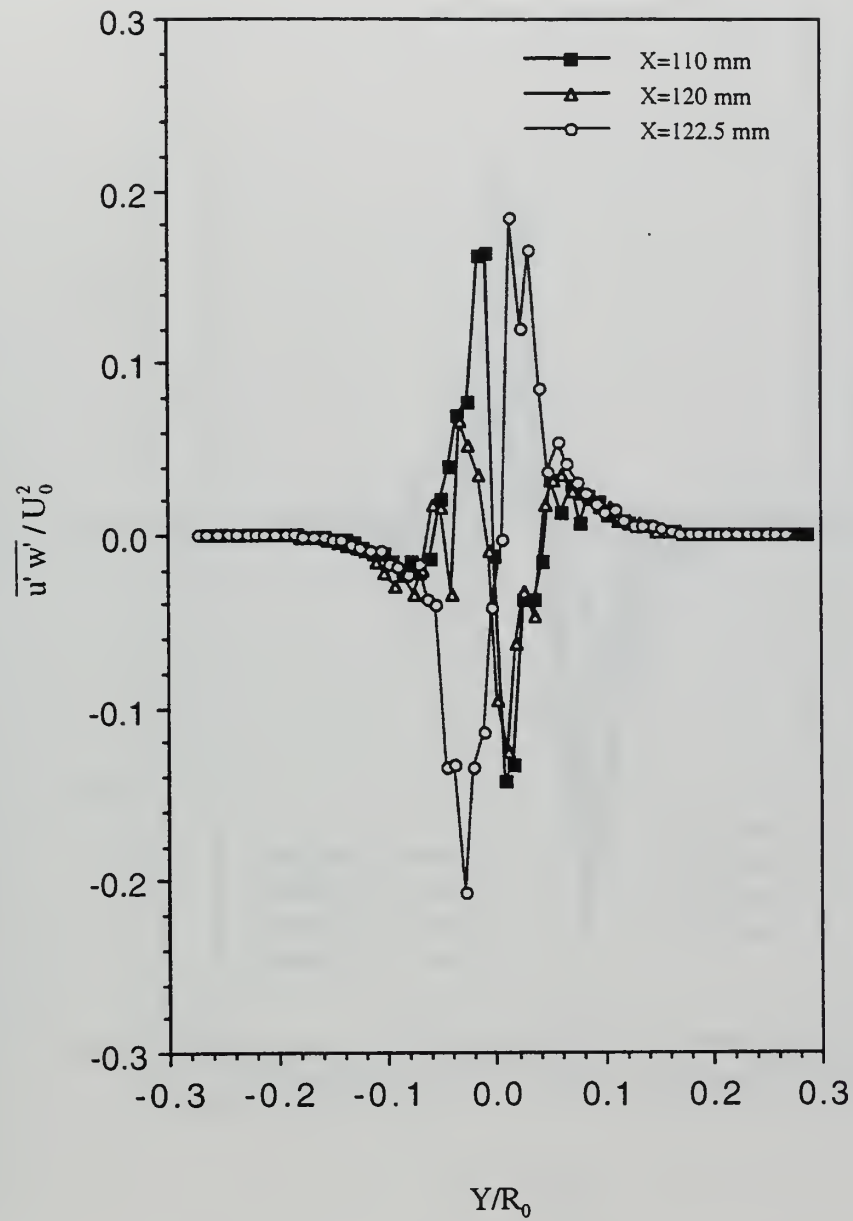


Figure 4-27.  $\overline{u'w'}/U_0^2$  vs.  $Y/R_0$  at  $X = 110$  mm to  $X = 122.5$  mm in the  $Re_D = 230,000/h_6$  flow state.



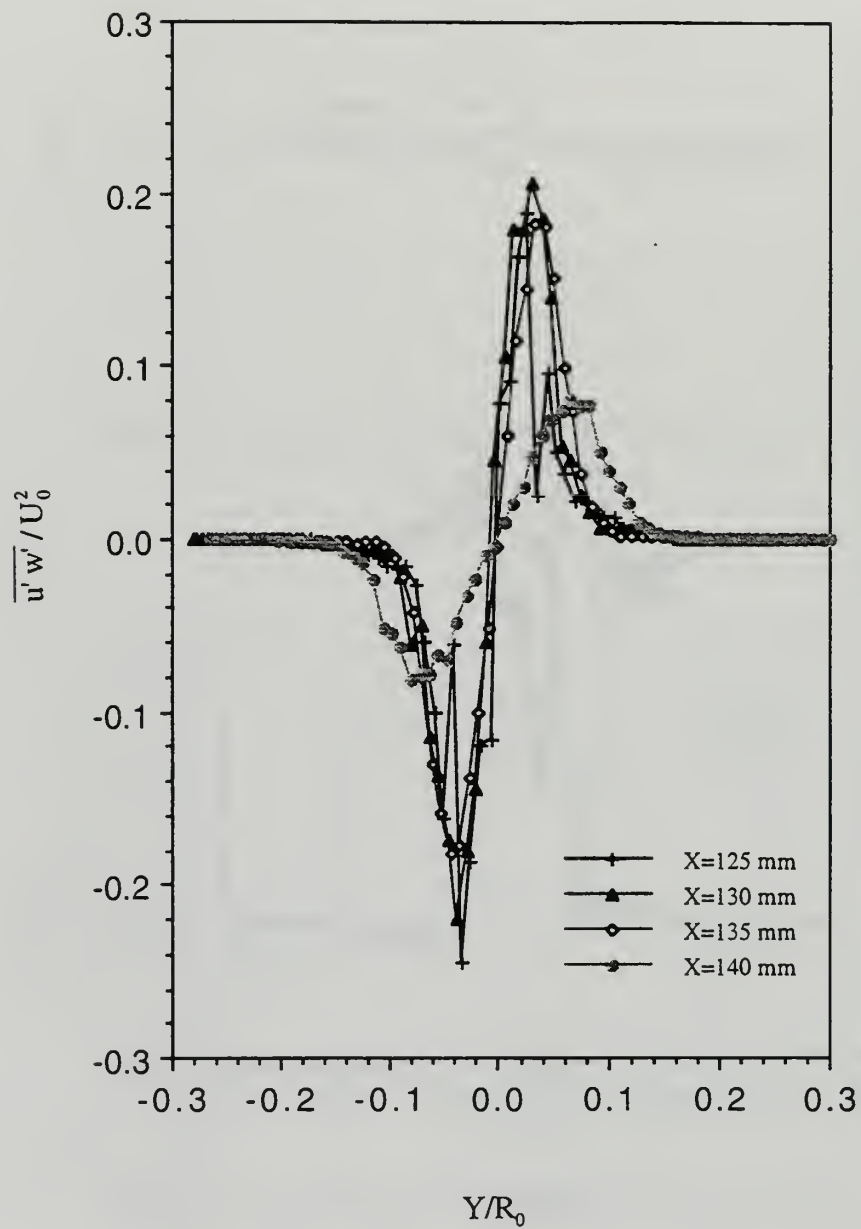


Figure 4-28.  $\overline{u'w'}/U_0^2$  vs.  $Y/R_0$  at  $X = 125$  mm to  $X = 140$  mm in the  $Re_D = 230,000/h6$  flow state.

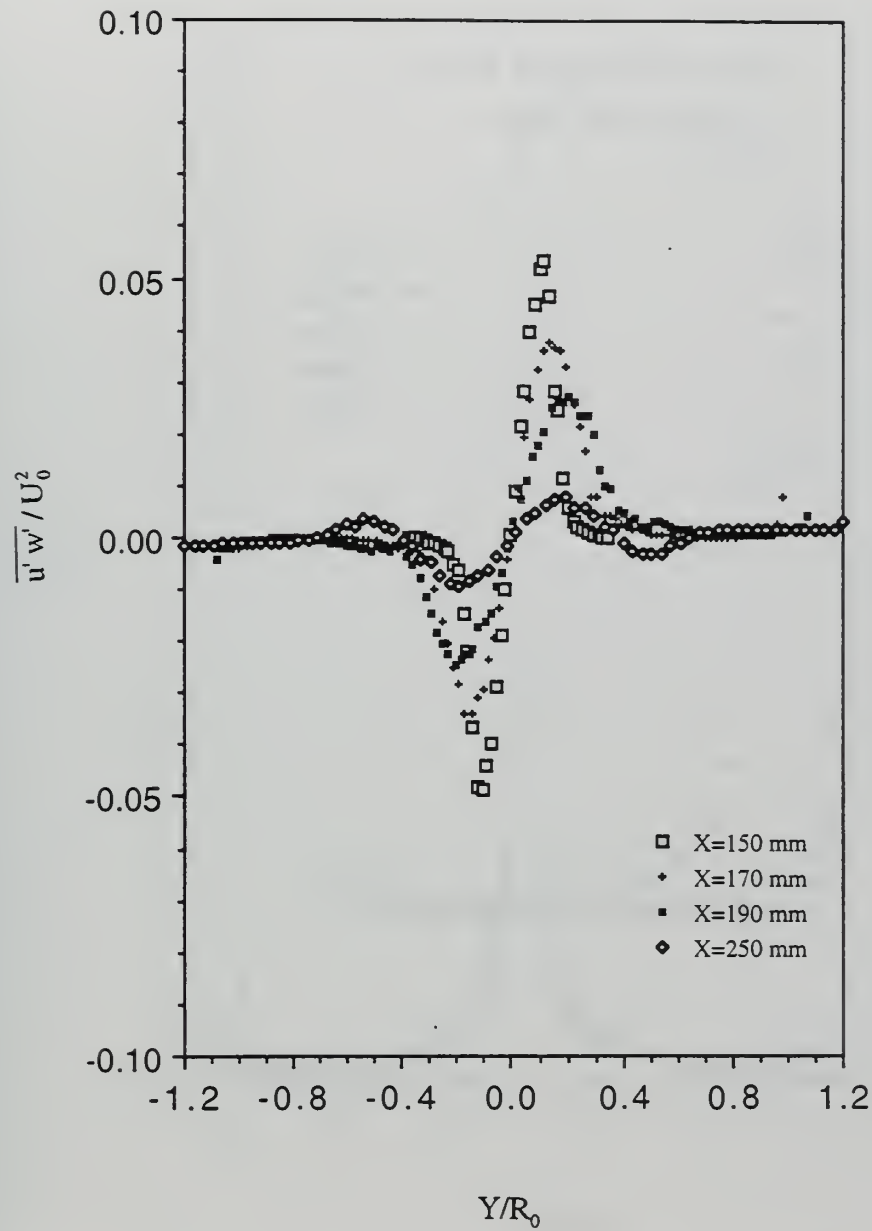


Figure 4-29.  $\overline{u'w'}/U_0^2$  vs.  $Y/R_0$  at  $X = 150$  mm to  $X = 250$  mm in the  $Re_D = 230,000/h6$  flow state.

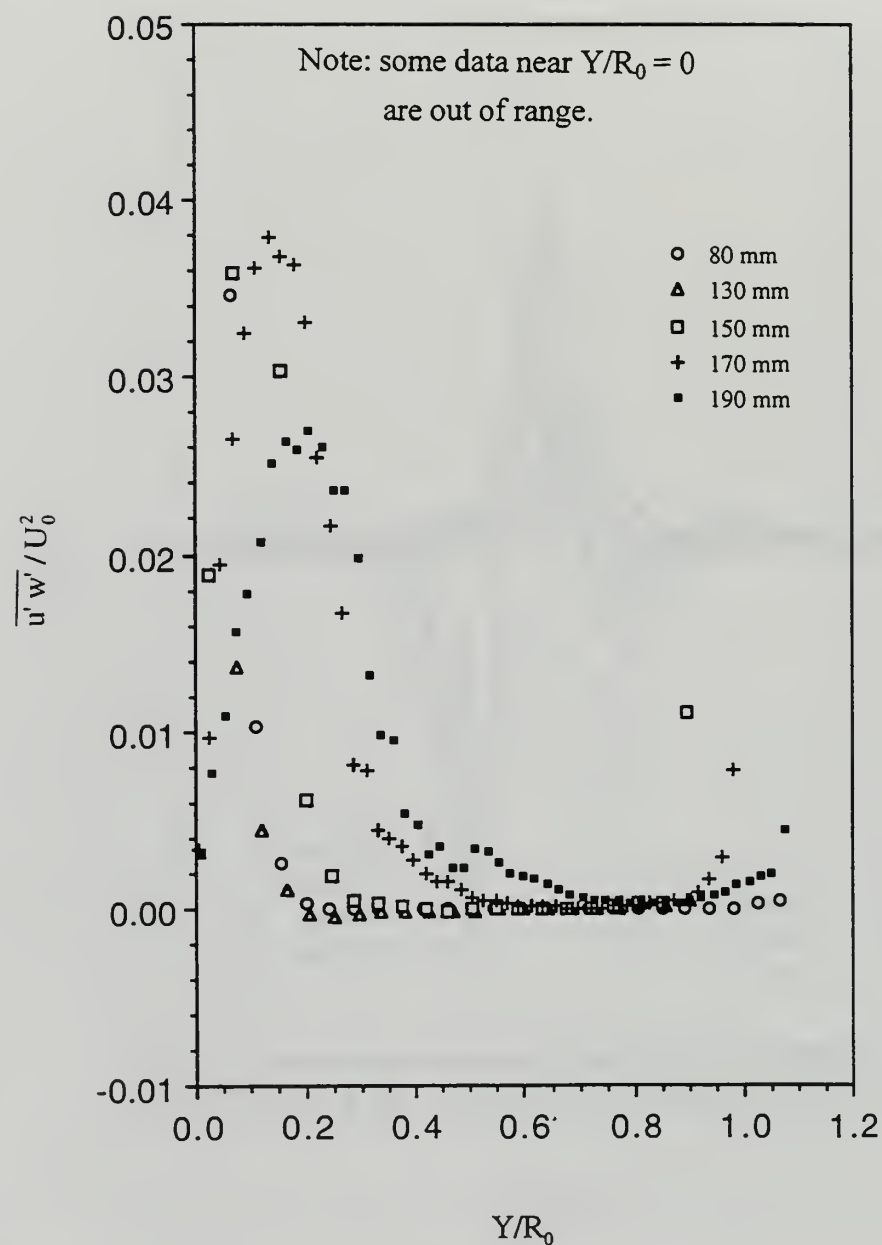


Figure 4-30.  $\overline{u'w'}/U_0^2$  vs.  $Y/R_0$  at  $X = 80$  mm to  $X = 190$  mm in the  $Re_D = 230,000/h6$  flow state.

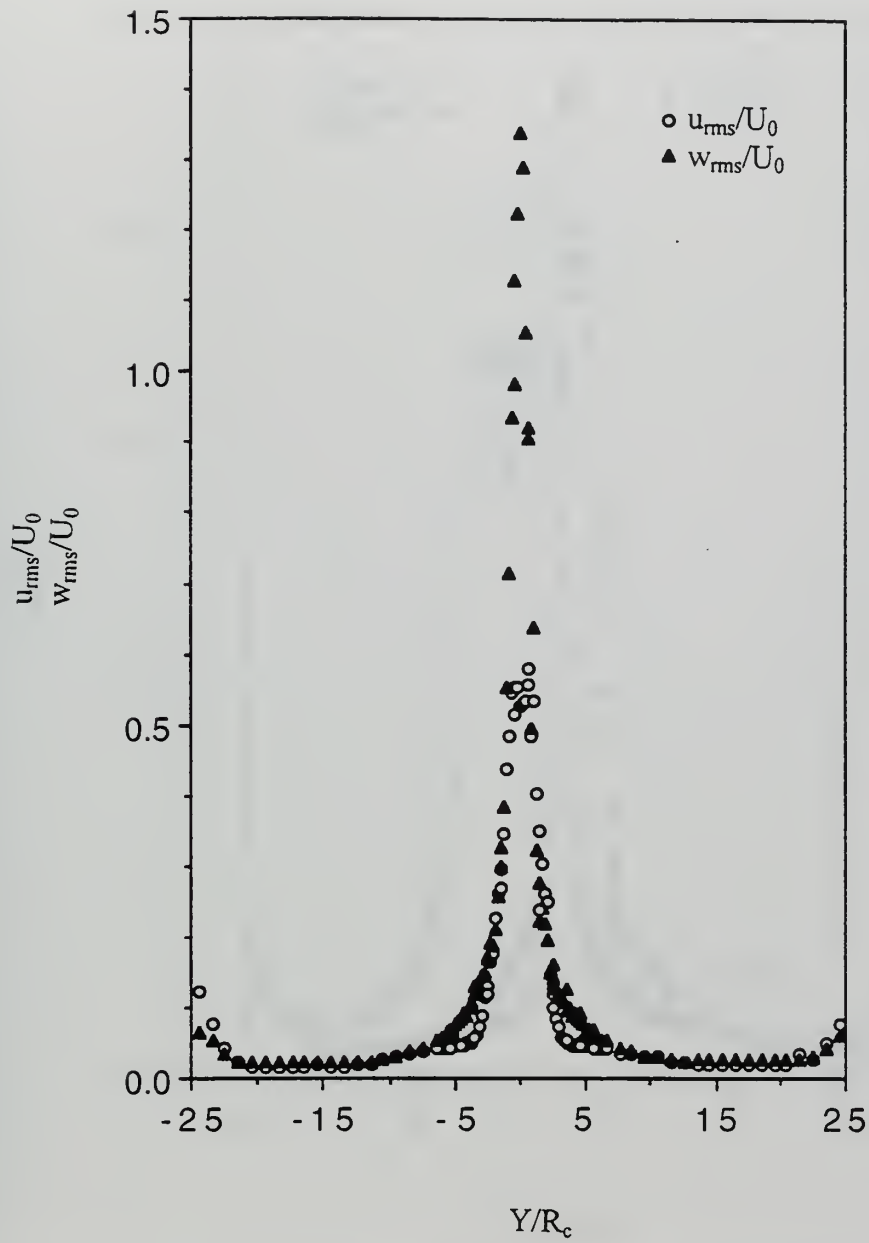


Figure 4-31.  $u_{rms} / U_0$  and  $w_{rms} / U_0$  vs.  $Y/R_c$  at  $X = 80$  mm in the  $Re_D = 230,000/h_6$  flow state.



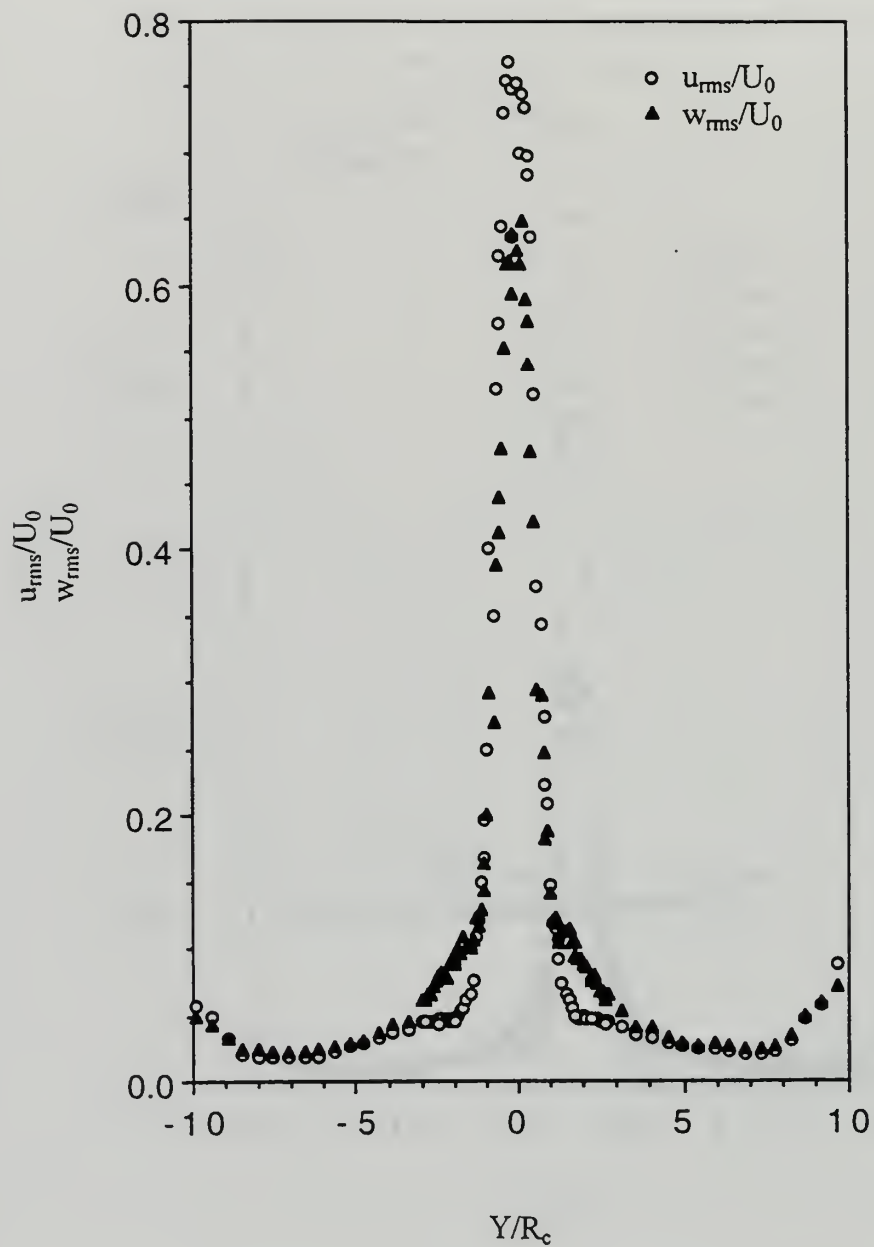


Figure 4-32.  $u_{rms} / U_0$  and  $w_{rms} / U_0$  vs.  $Y/R_c$  at  $X = 130$  mm in the  $Re_D = 230,000/h_6$  flow state.

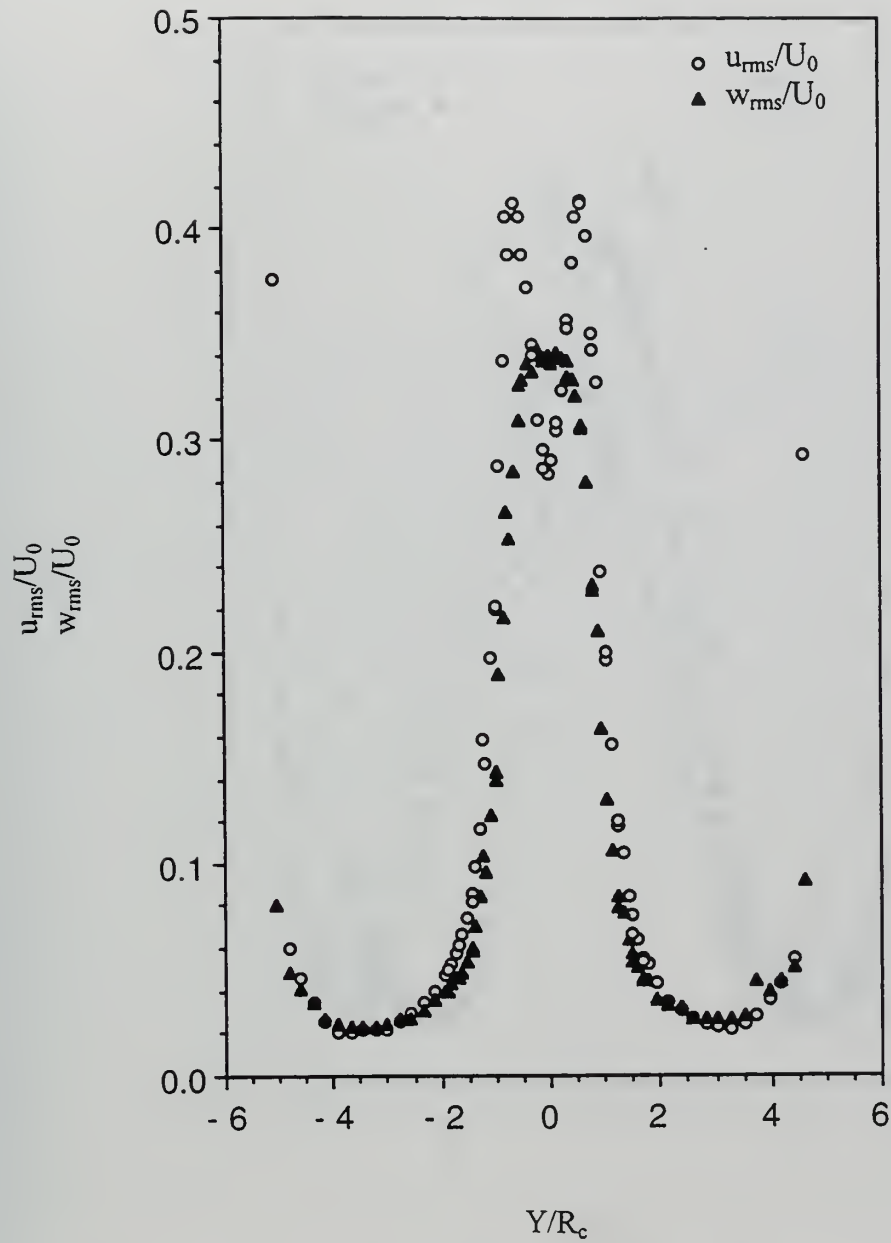


Figure 4-33.  $u_{rms} / U_0$  and  $w_{rms} / U_0$  vs.  $Y/R_c$  at  $X = 150$  mm in the  $Re_D = 230,000/h6$  flow state.

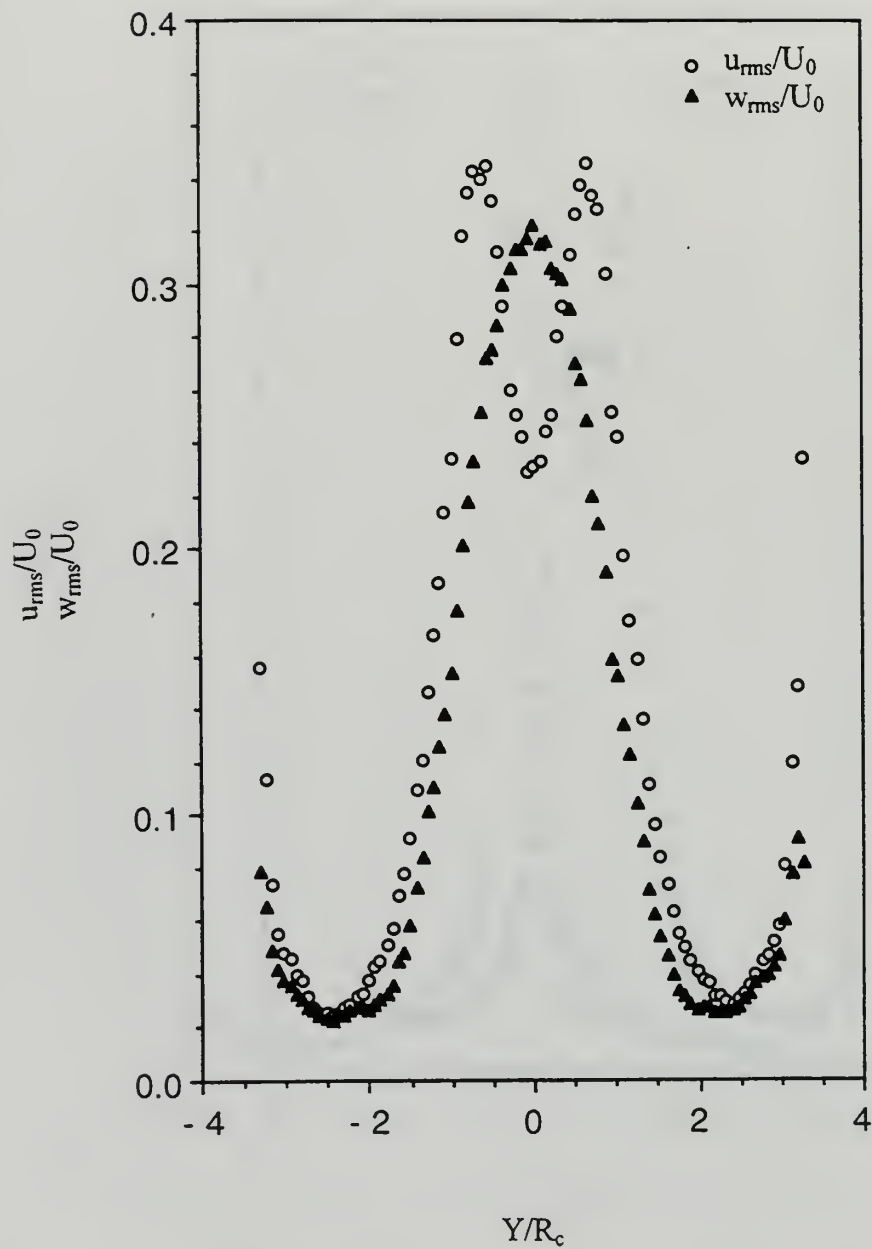


Figure 4-34.  $u_{rms} / U_0$  and  $w_{rms} / U_0$  vs.  $Y/R_c$  at  $X = 170$  mm in the  $Re_D = 230,000/h6$  flow state.

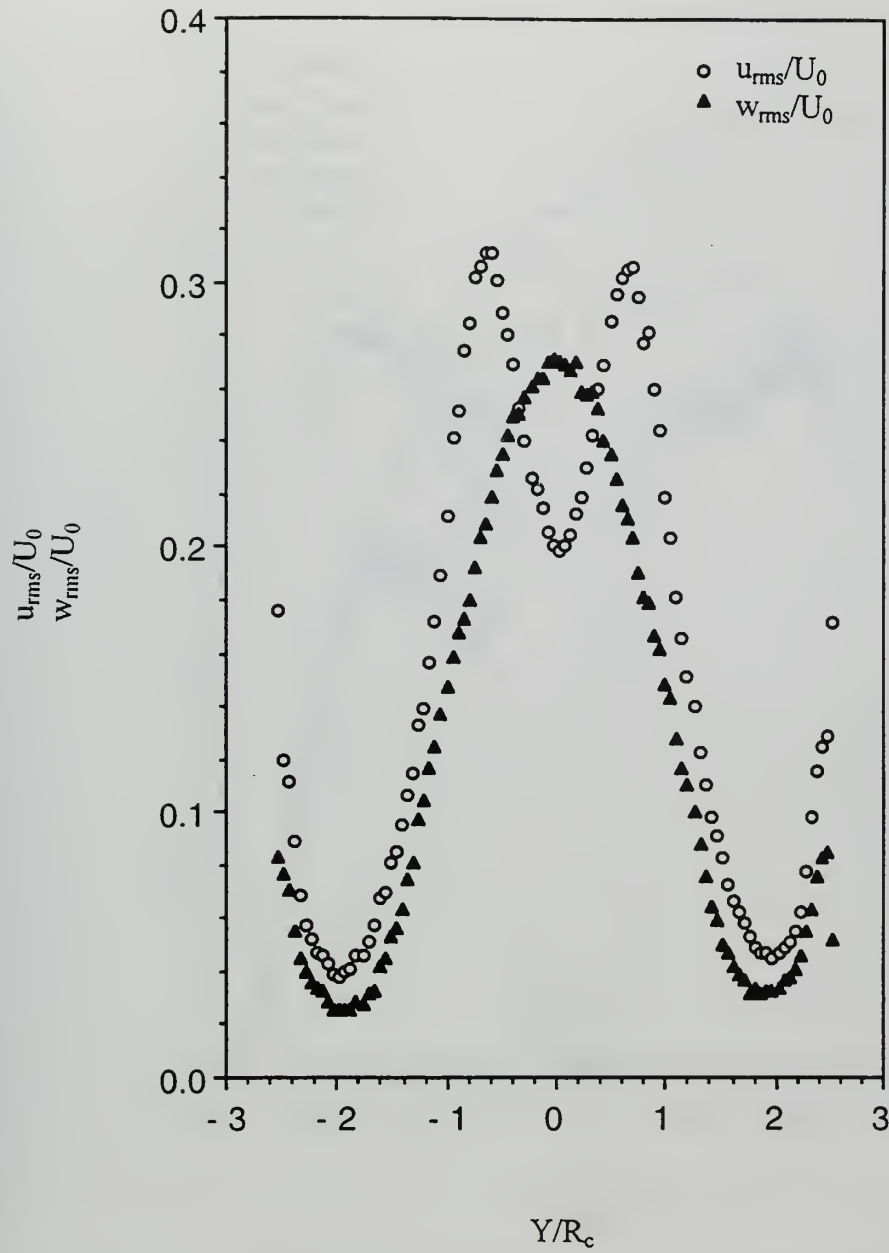


Figure 4-35.  $u_{rms}/U_0$  and  $w_{rms}/U_0$  vs.  $Y/R_c$  at  $X = 190$  mm in the  $Re_D = 230,000/h6$  flow.



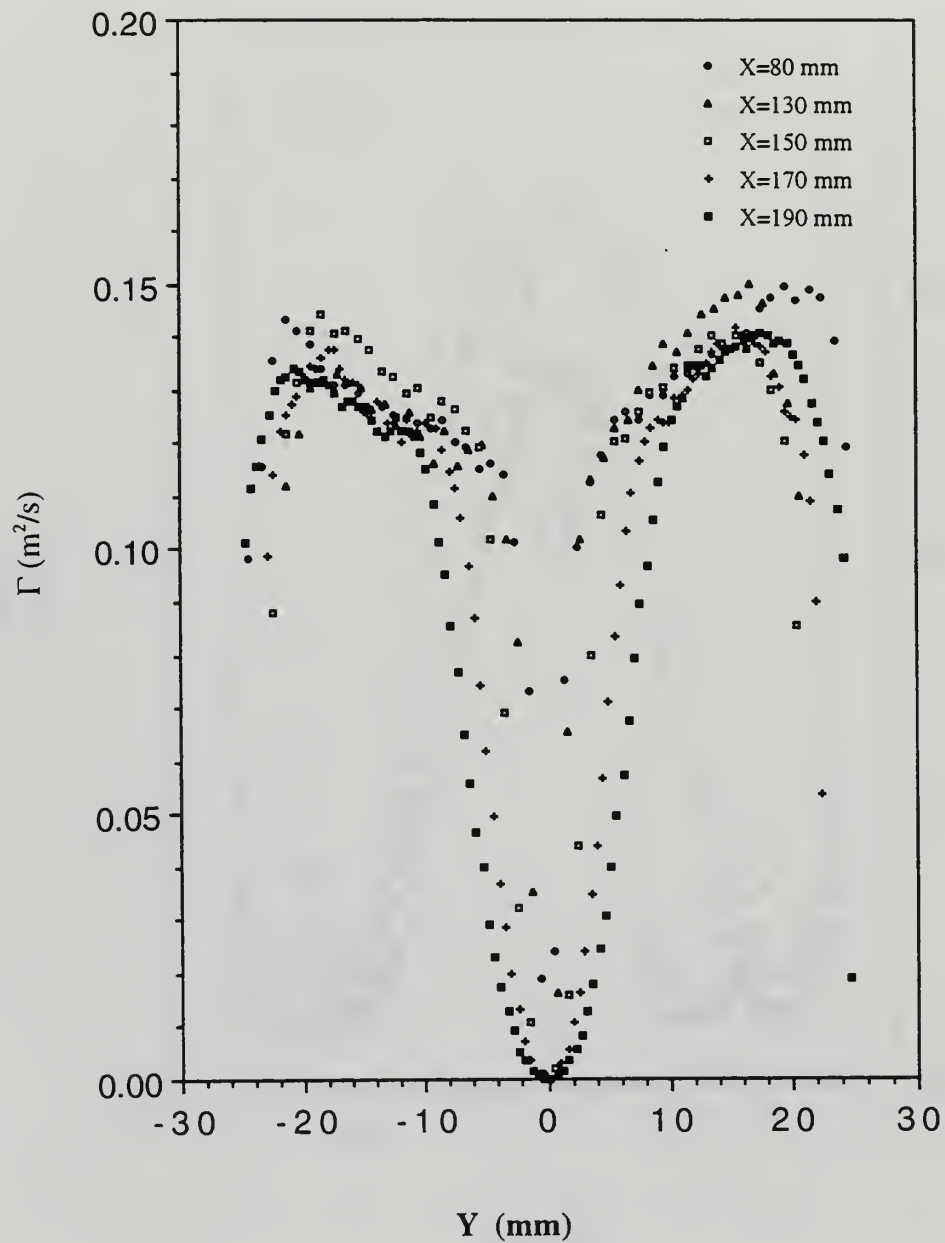


Figure 4-36. Circulation ( $\Gamma$ ) profiles at  $X = 80$  mm to  $X = 190$  mm in the  $Re_D = 230,000/h_6$  flow state.

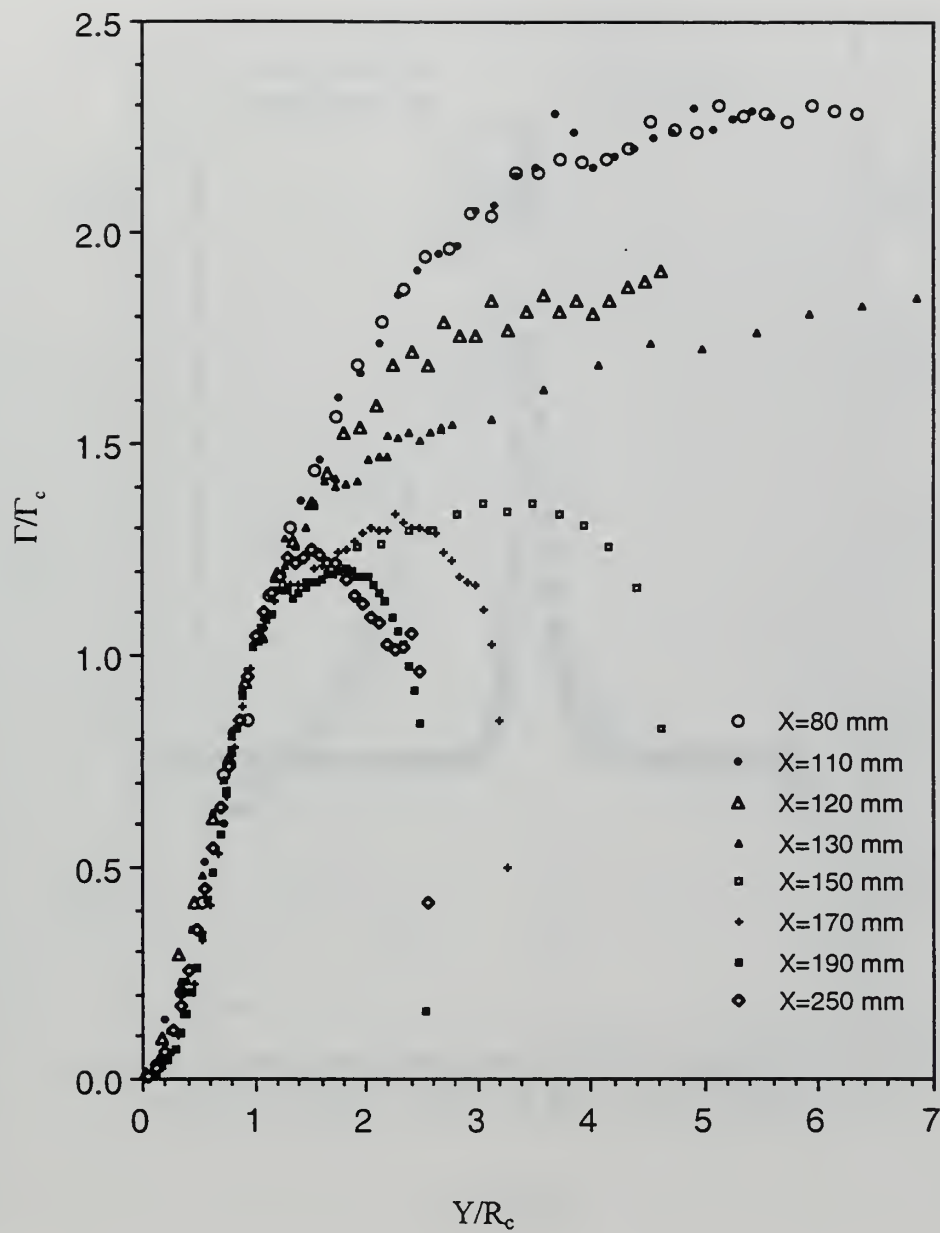


Figure 4-37. Normalized circulation ( $\Gamma/\Gamma_c$ ) at  $X = 80$  mm to  $X = 250$  mm in the  $Re_D = 230,000/h_6$  flow state.

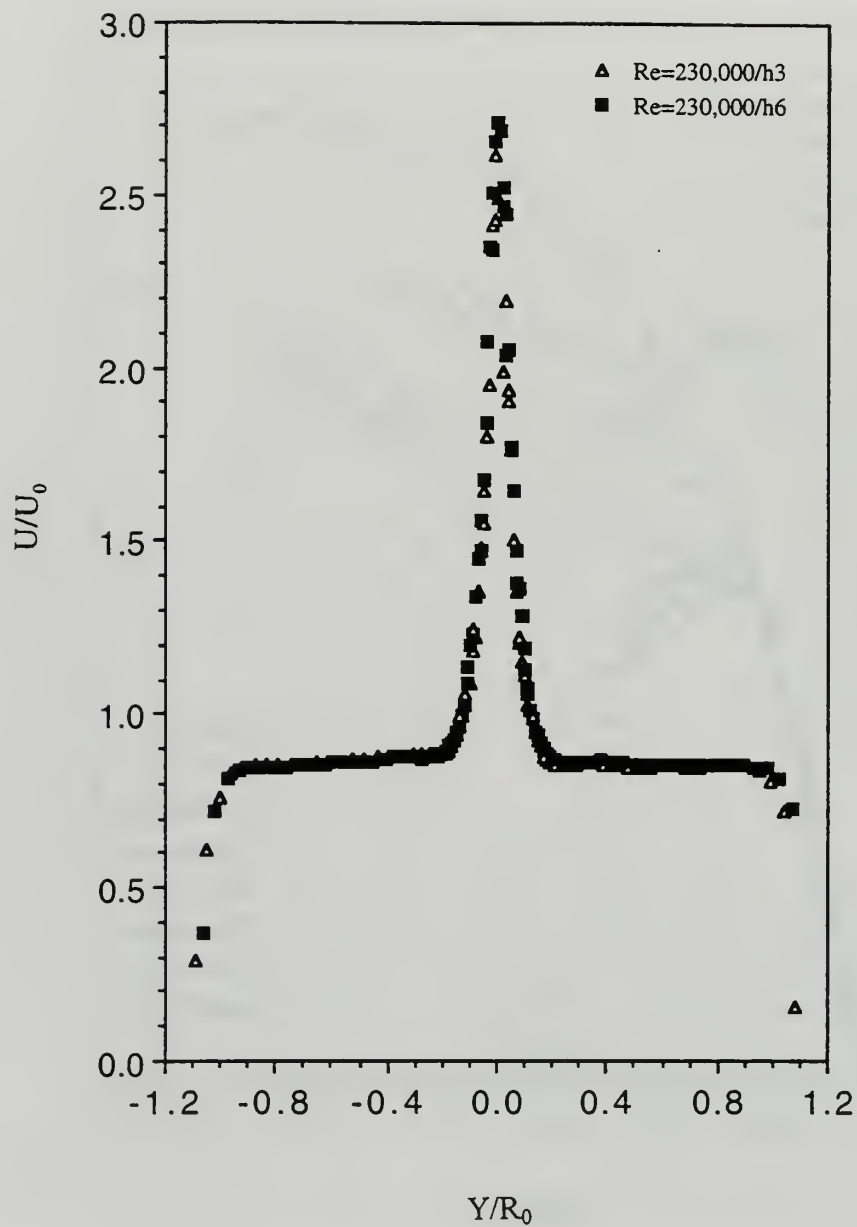


Figure 4-38.  $U/U_0$  profiles at the inlet of the  $Re_D = 230,000$  flow state.

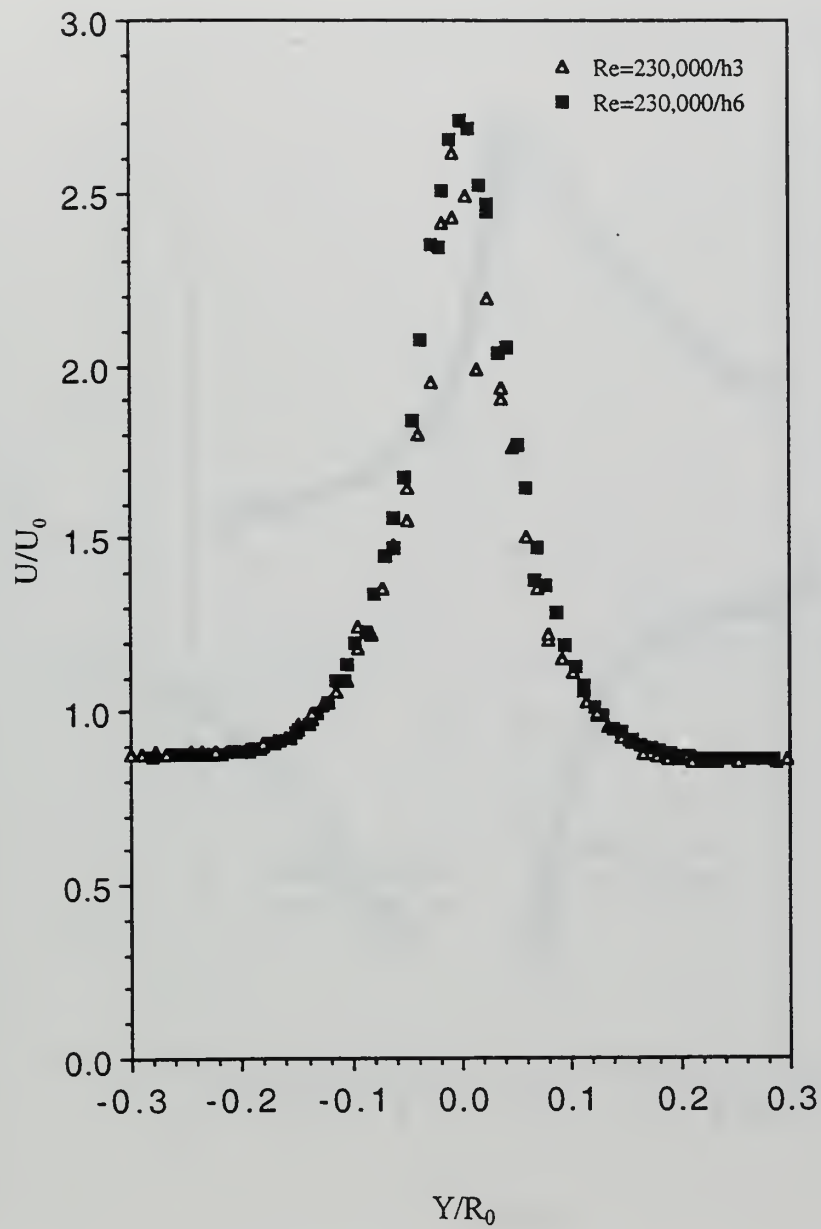


Figure 4-39.  $U/U_0$  profiles at the inlet in the core region of the  $Re_D = 230,000$  flow state.



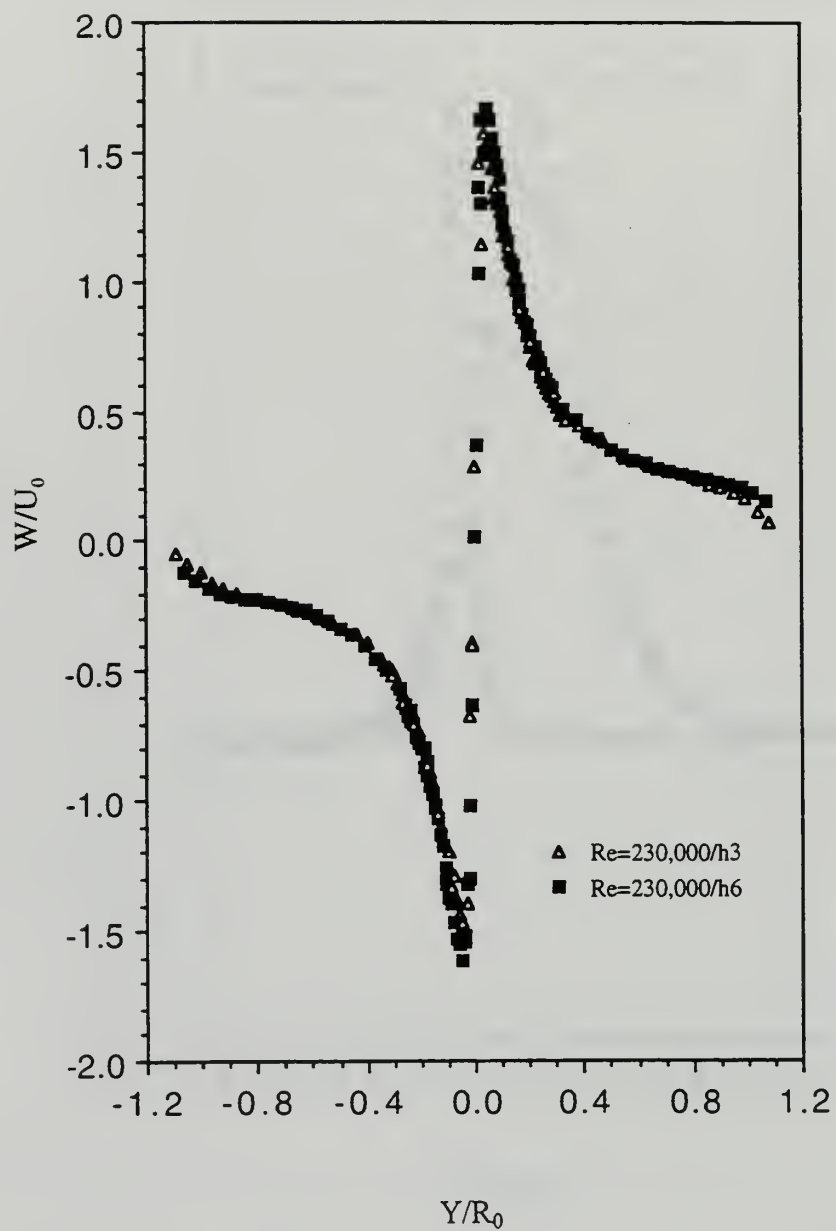


Figure 4-40.  $W/U_0$  profiles at the inlet of the  $Re_D = 230,000$  flow state.

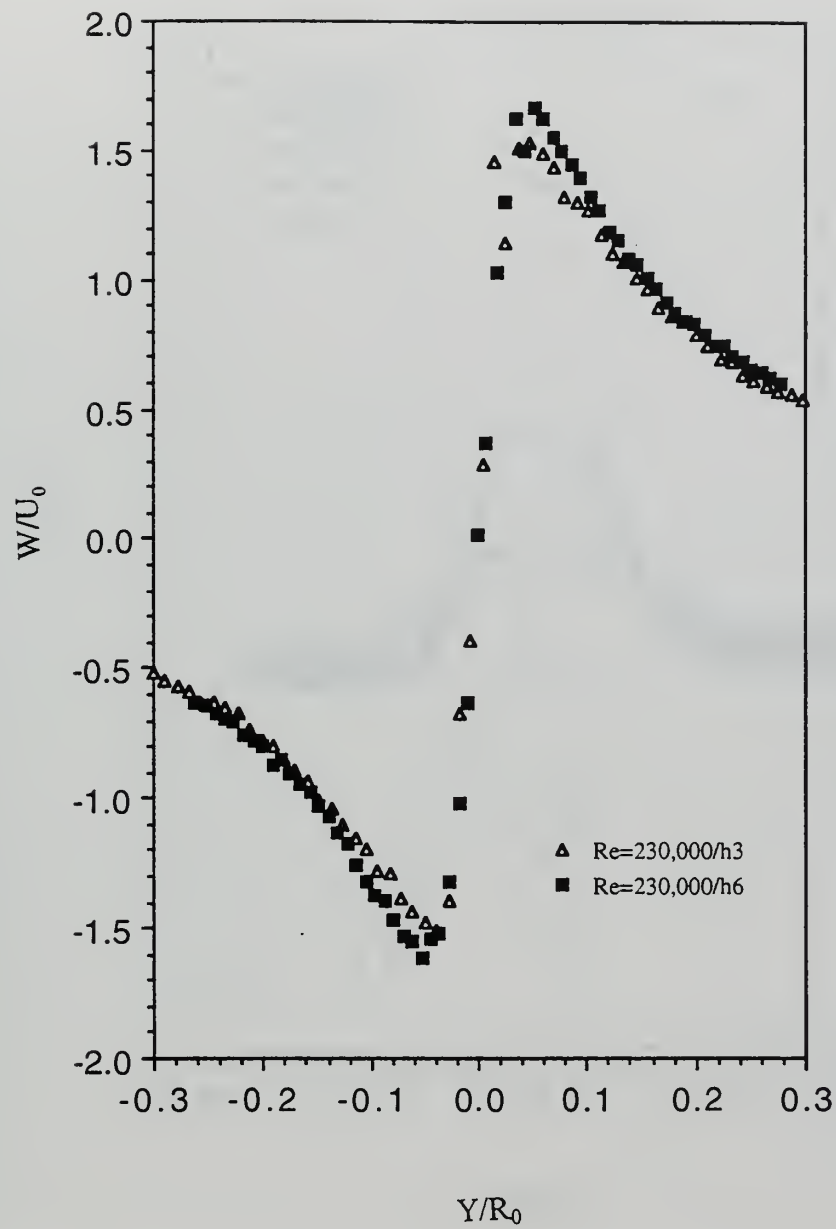


Figure 4-41.  $W/U_0$  profiles at the inlet of the  $Re_D = 230,000$  flow state (core region).

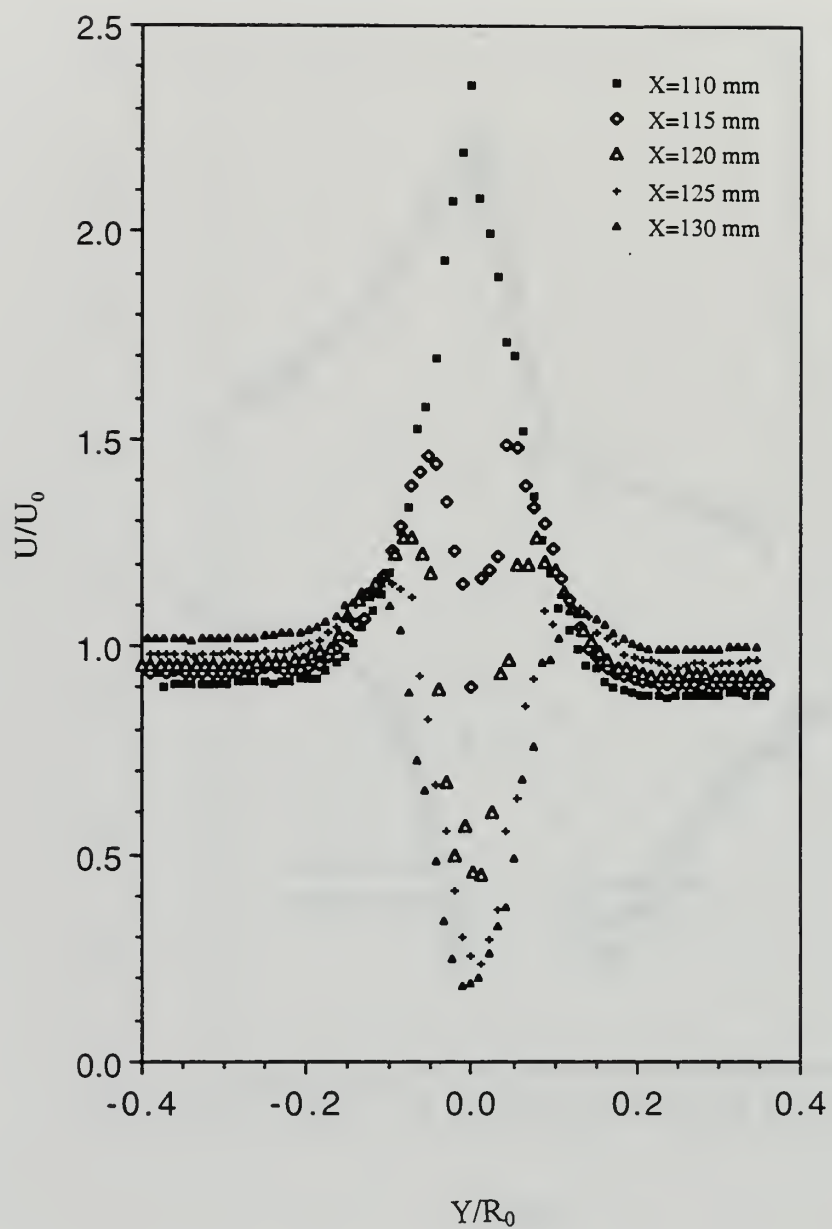


Figure 4-42.  $U/U_0$  profiles in the breakdown region of the  $Re_D = 230,000/h3$  flow state.

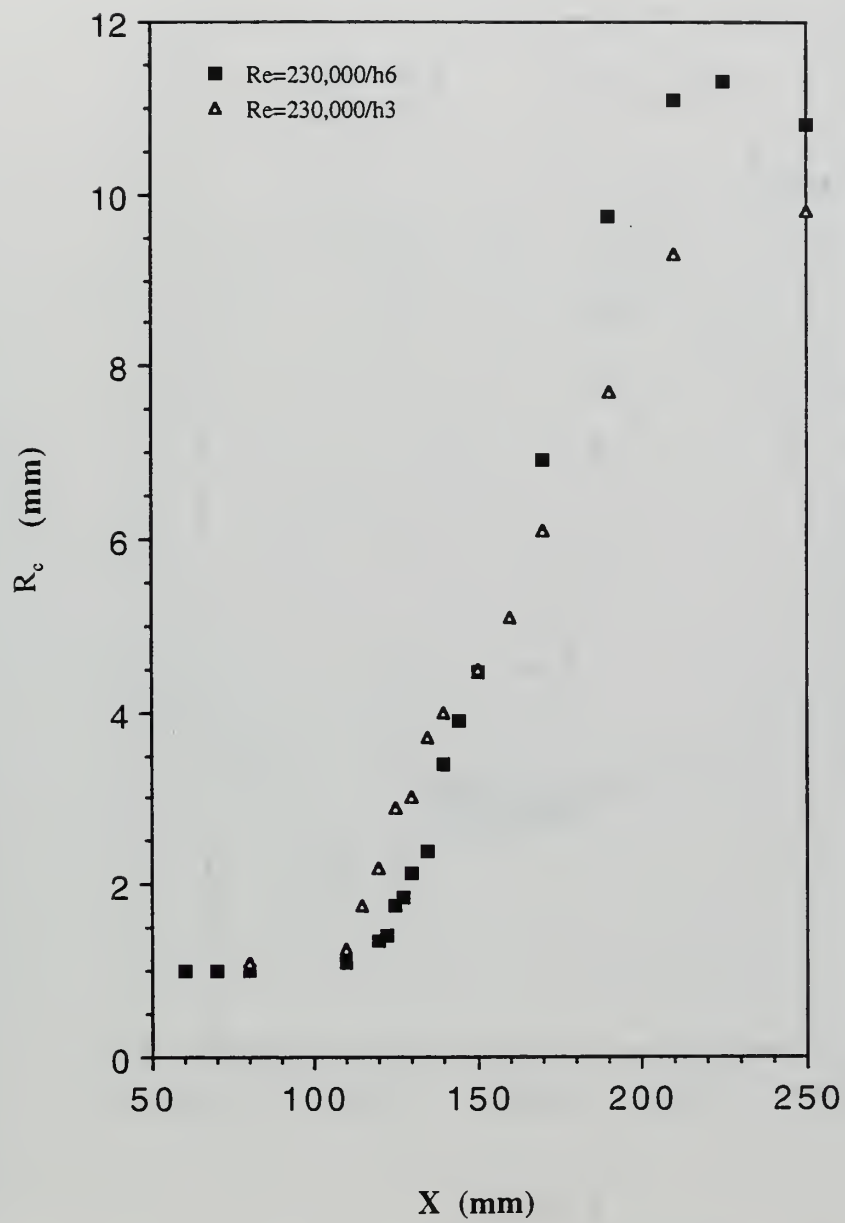


Figure 4-43.  $R_c$  vs.  $X$  in the  $Re_D = 230,000$  flow states.



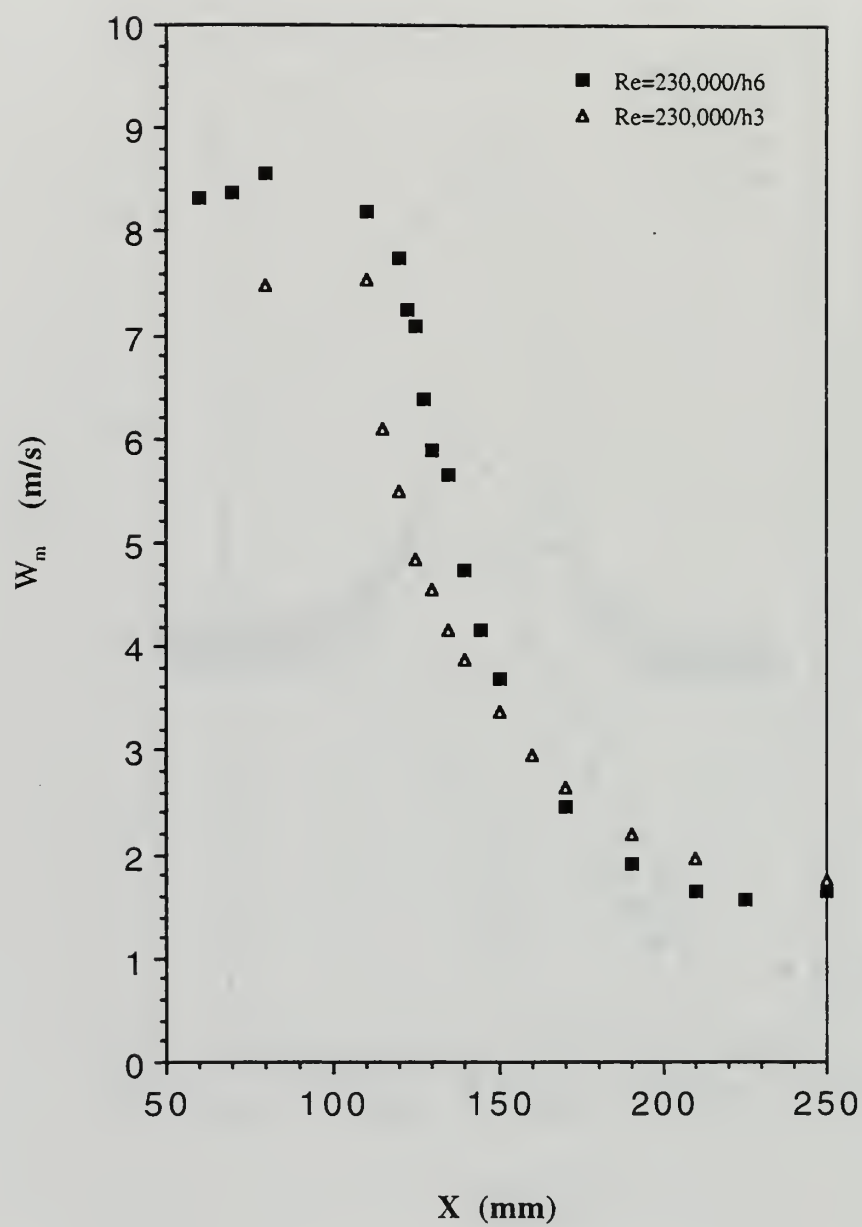


Figure 4-44.  $W_m$  vs.  $X$  in the  $Re_D = 230,000$  flow states.

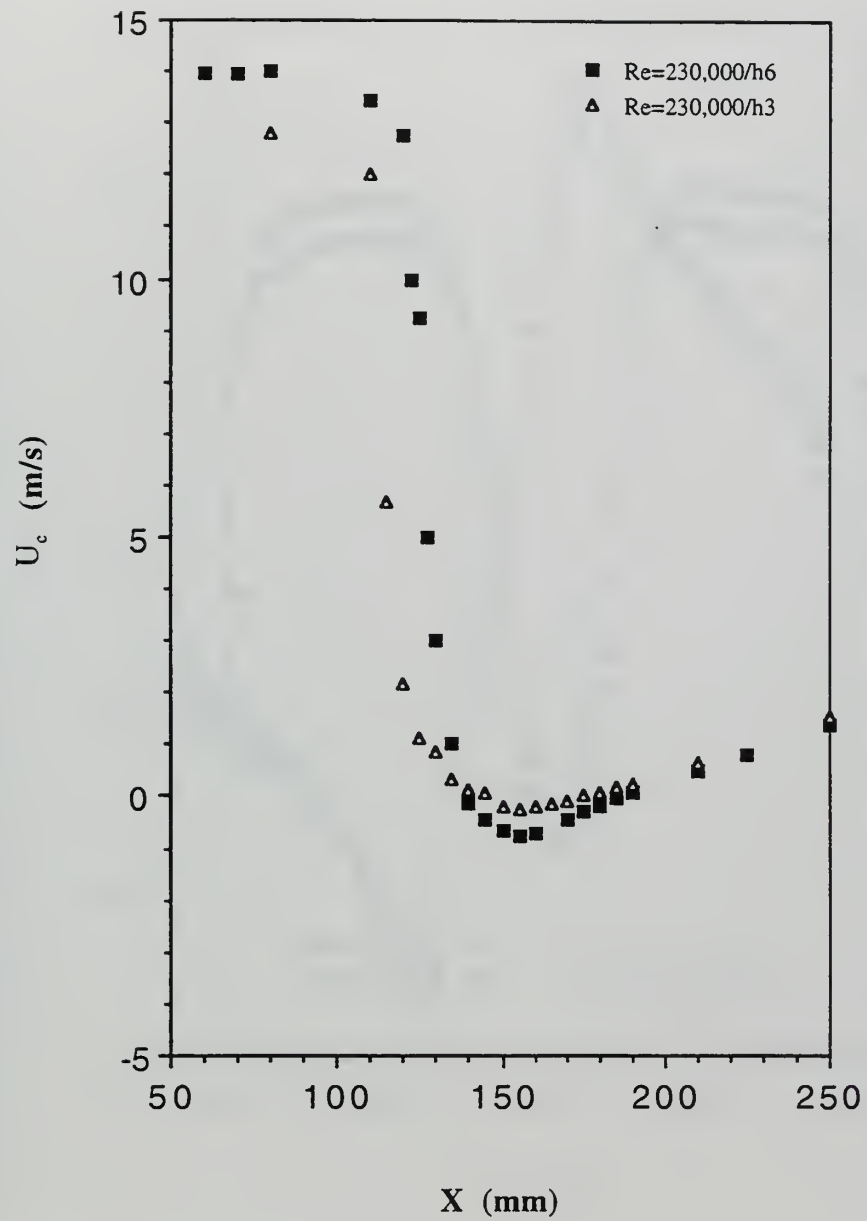


Figure 4-45.  $U_c$  vs.  $X$  in the  $Re_D = 230,000$  flow states.

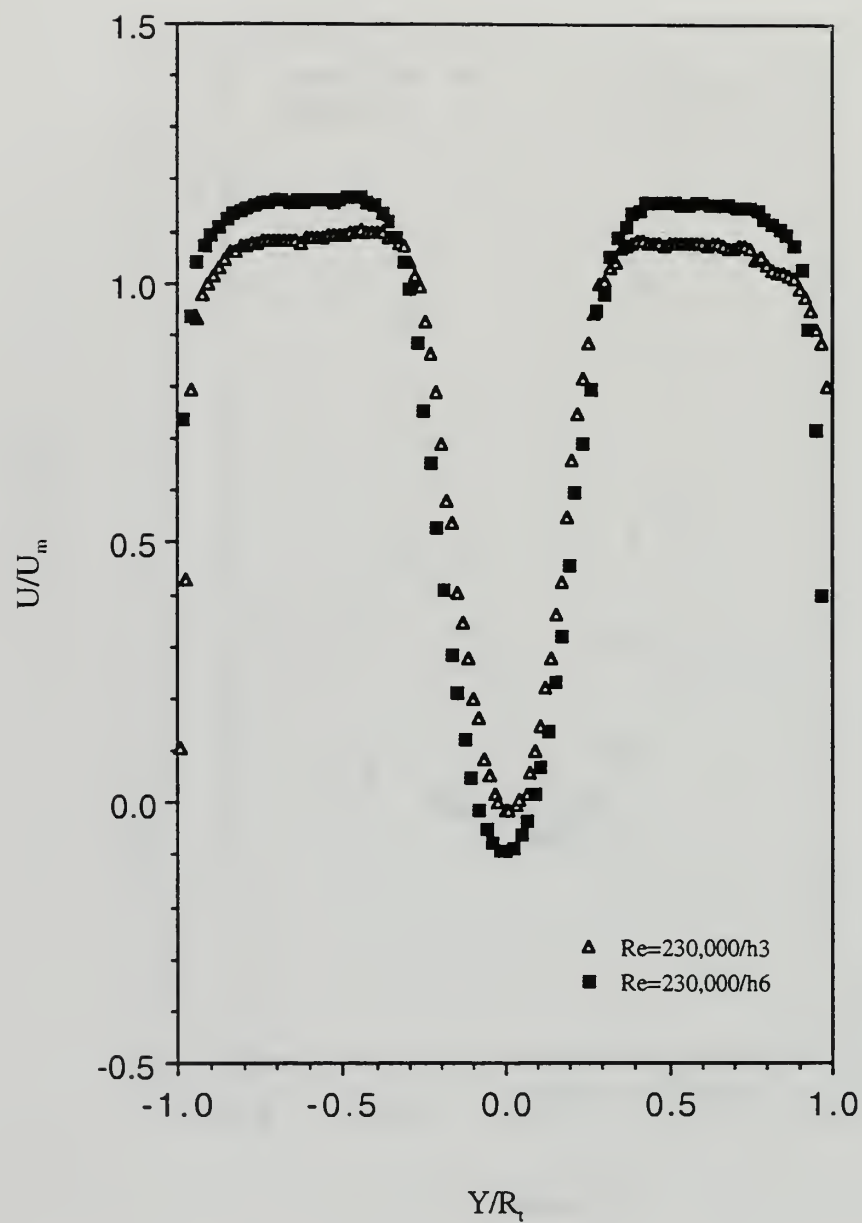


Figure 4-46.  $U/U_m$  vs.  $Y/R_t$  at  $X = 170$  in the  $Re_D = 230,000$  flow states.

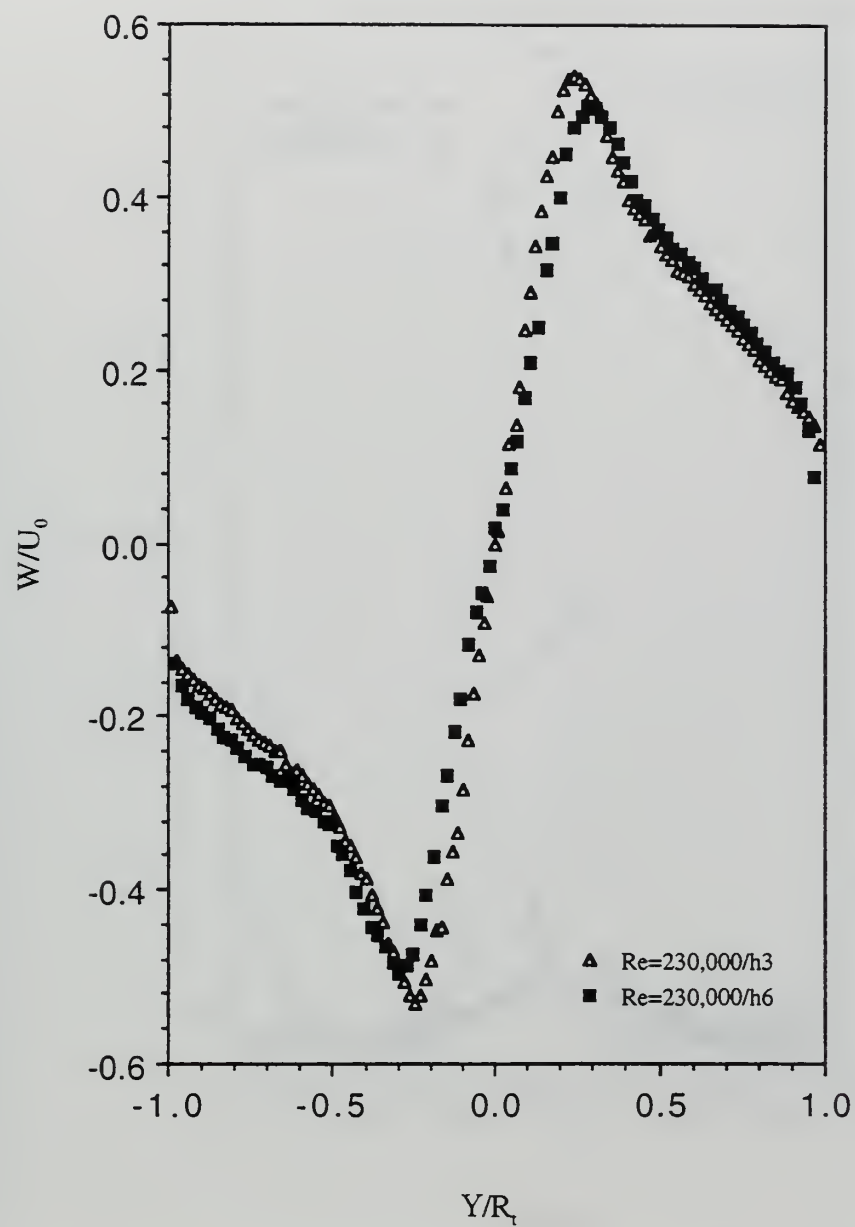


Figure 4-47.  $W/U_0$  vs.  $Y/R_t$  at  $X = 170$  mm in the  $Re_D = 230,000$  flow states.



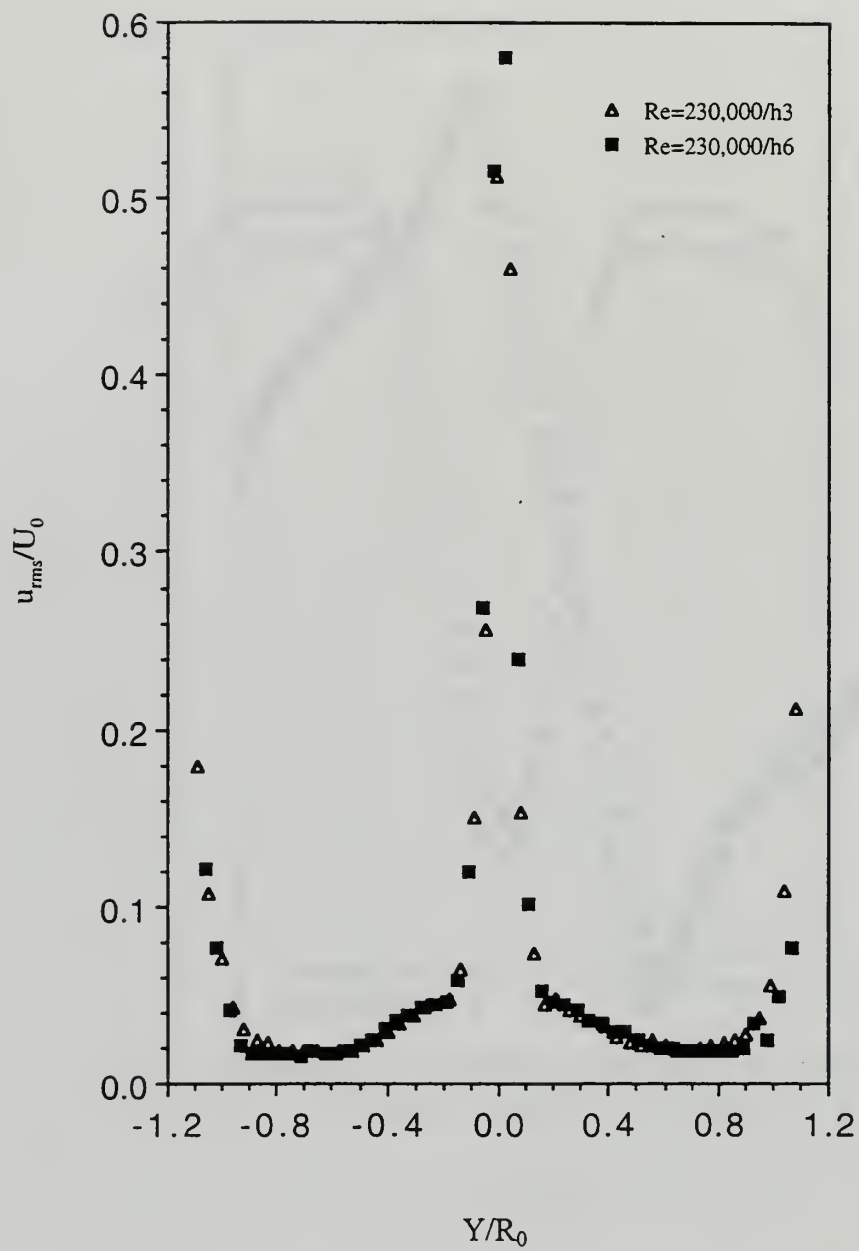


Figure 4-48.  $u_{rms}/U_0$  vs.  $Y/R_0$  at  $X = 80$  mm in the  $Re_D = 230,000$  flow states.

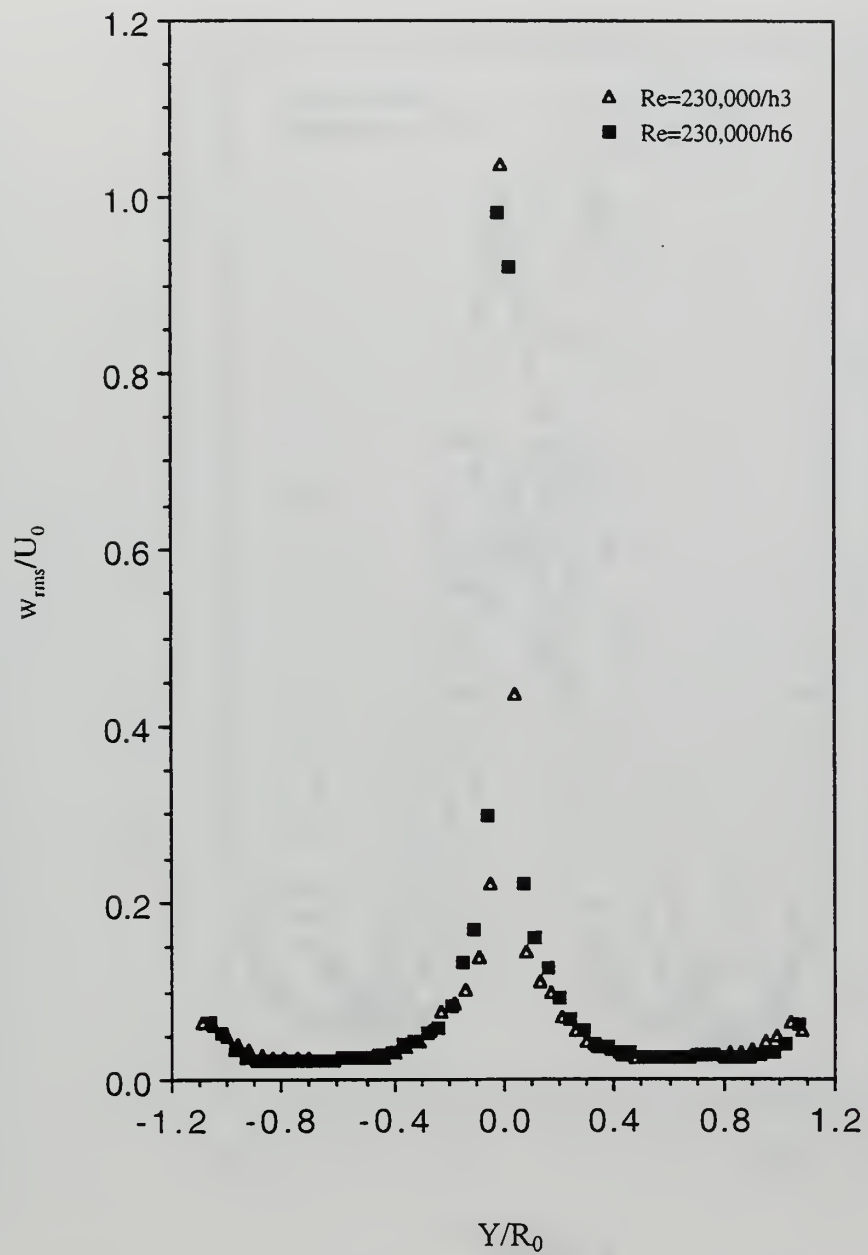


Figure 4-49.  $w_{rms}/U_0$  vs.  $Y/R_0$  at  $X = 80$  mm in the  $Re_D = 230,000$  flow states.

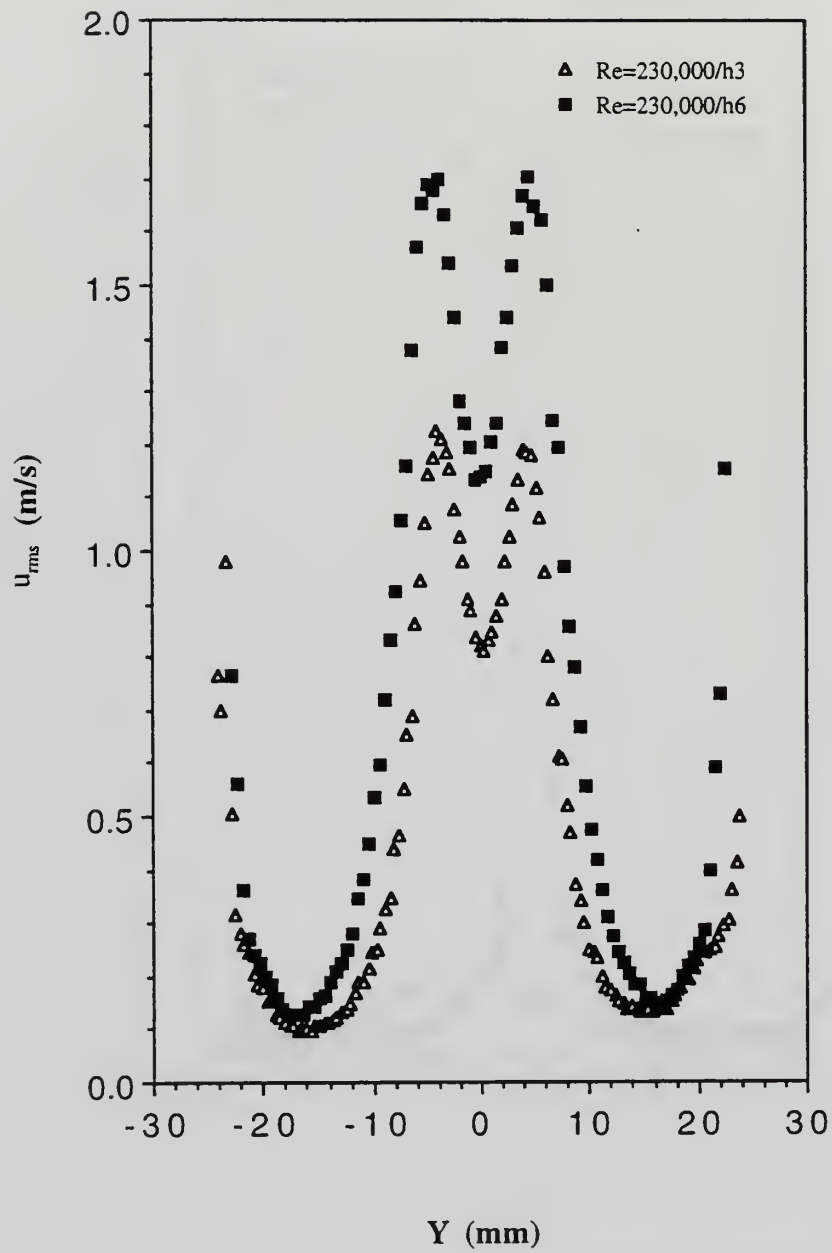


Figure 4-50.  $u_{rms}$  vs.  $Y$  at  $X = 170$  mm in the  $Re_D = 230,000$  flow states.

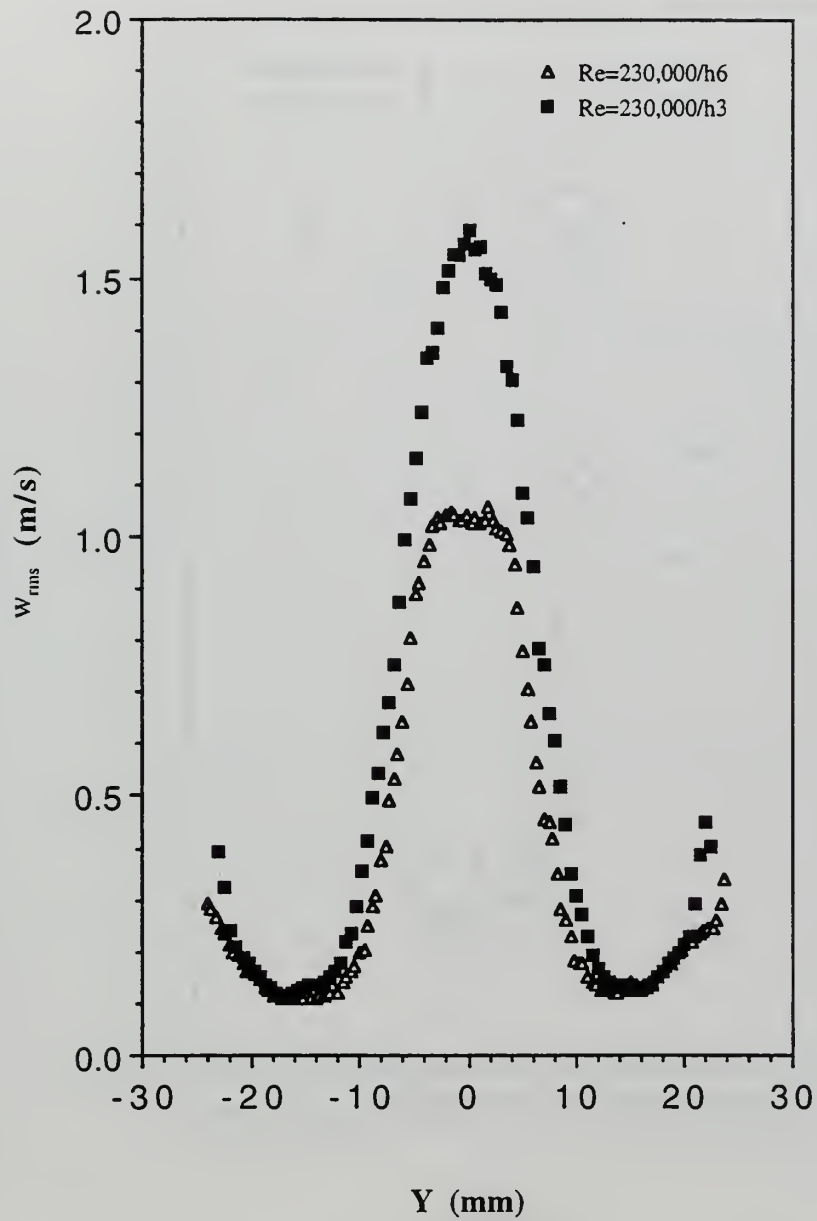


Figure 4-51.  $w_{rms}$  vs.  $Y$  at  $X = 170$  mm in the  $Re_D = 230,000$  flow states.

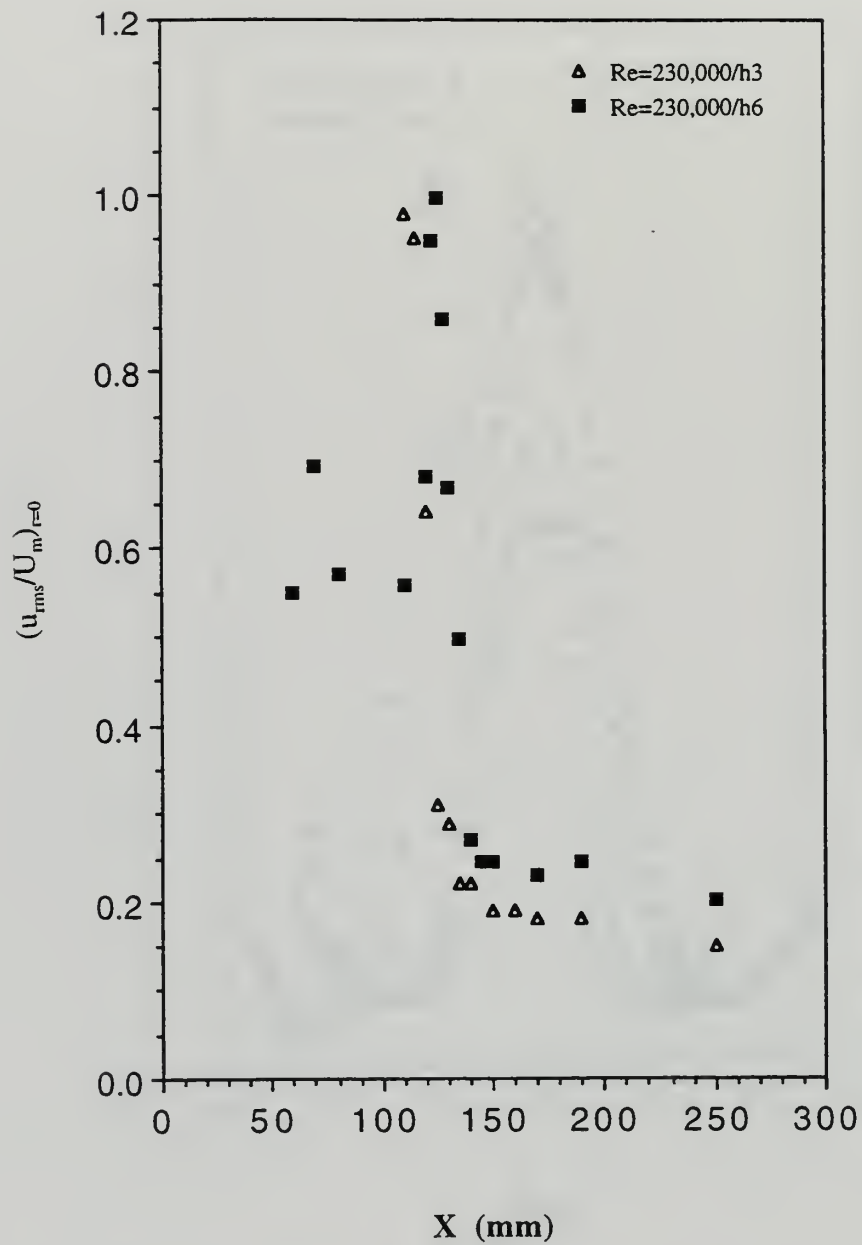


Figure 4-52. Axial variation of  $(u_{rms}/U_m)_{r=0}$  in the  $Re_D = 230,000$  flow states.



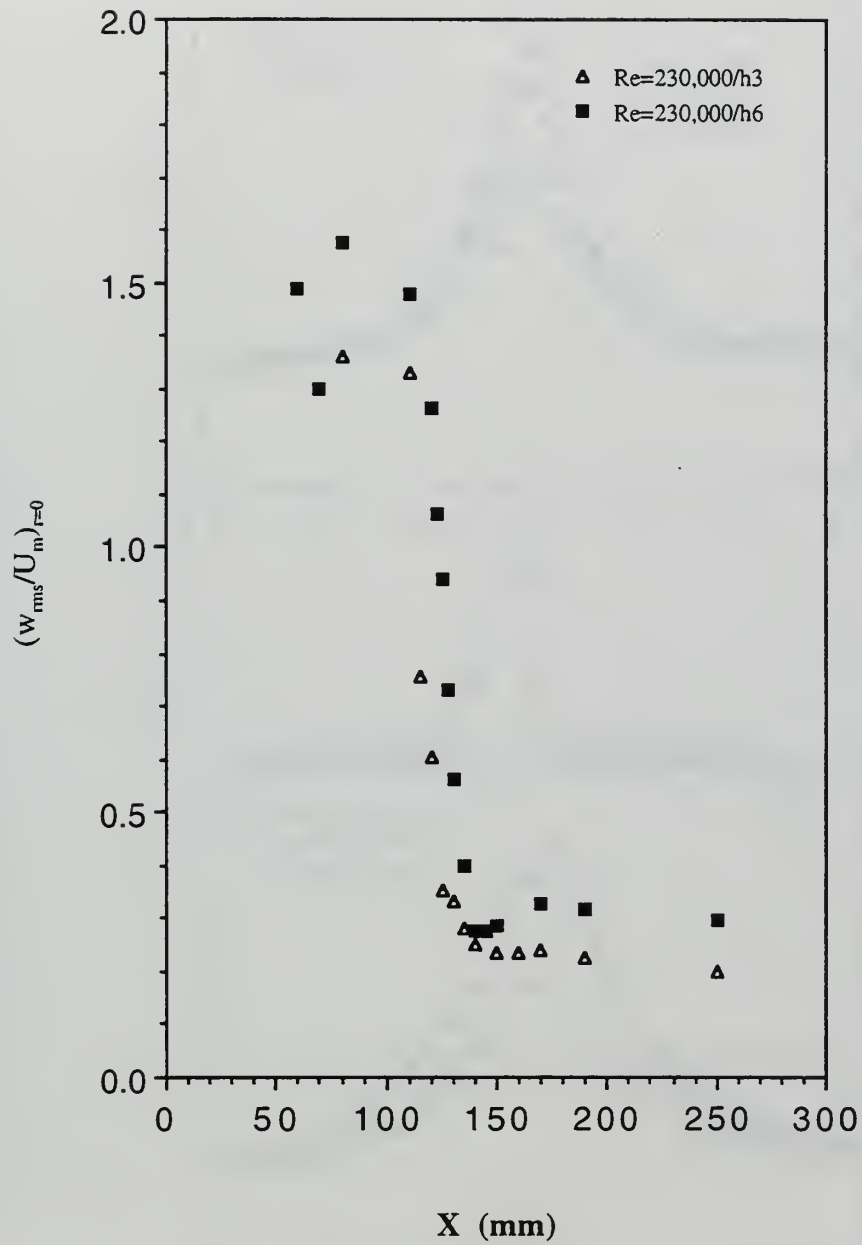


Figure 4-53. Axial variation of  $(w_{rms}/U_m)_{r=0}$  in the  $Re_D = 230,000$  flow states.

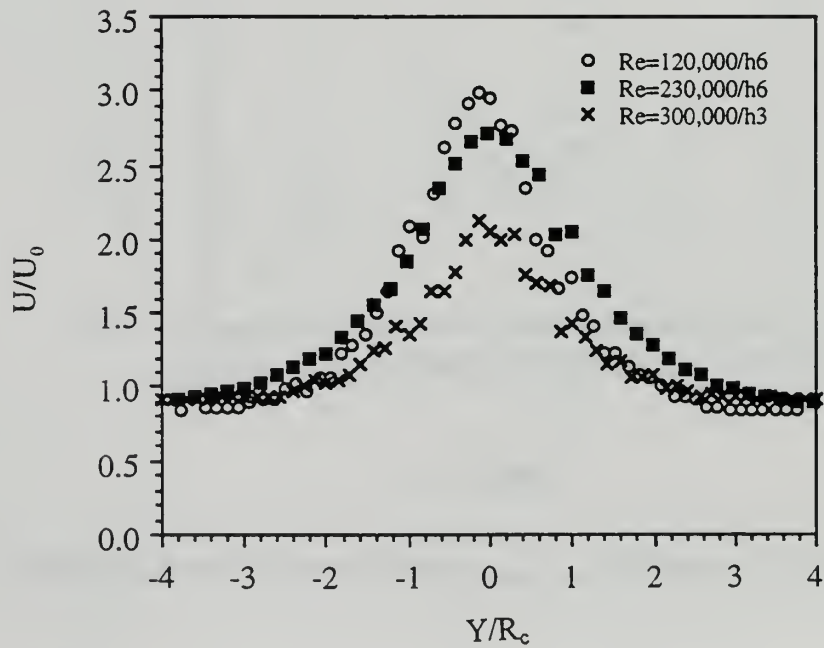
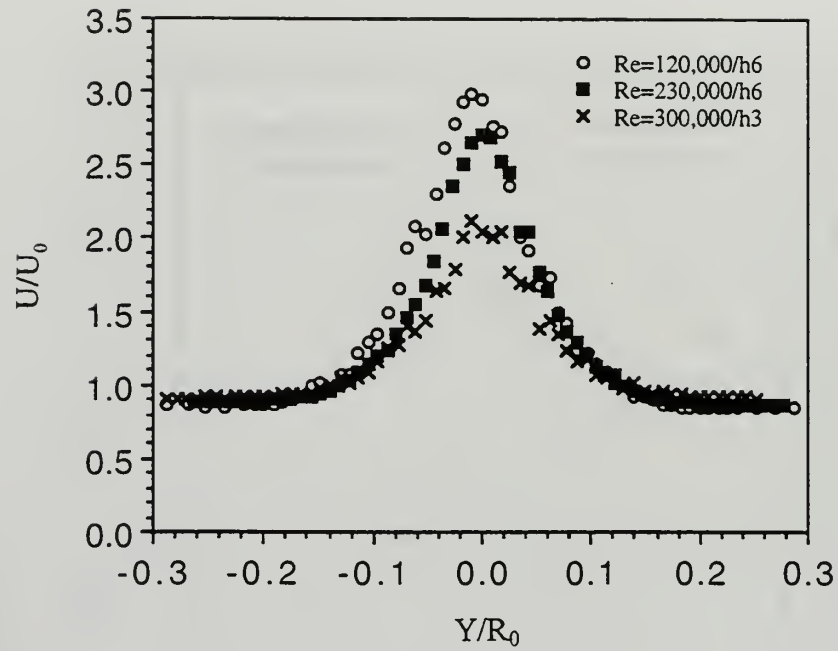


Figure 4-54.  $U/U_0$  profiles in the inlet region of various  $Re_D$ /tube flow states (core region).

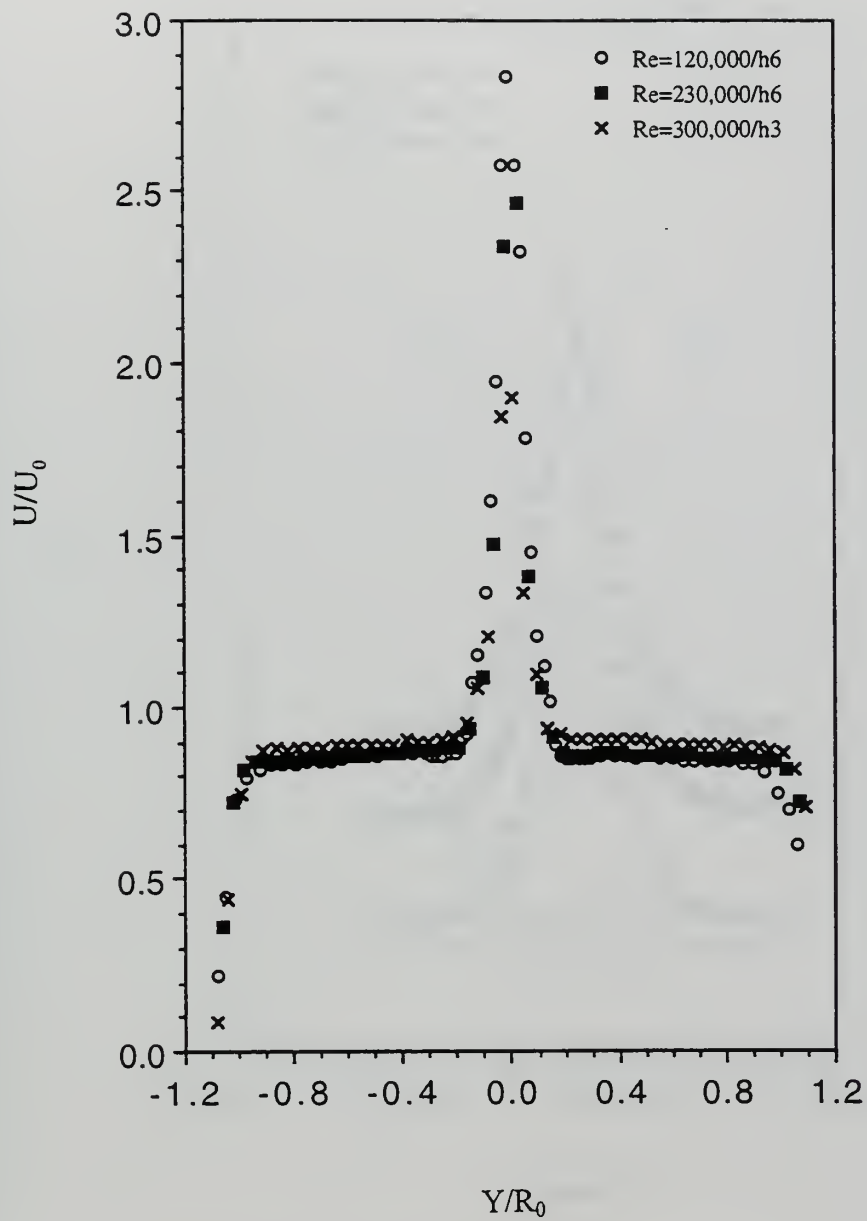


Figure 4-55.  $U/U_0$  profiles in the inlet region of various  $Re_D$ /tube flow states (full tube).

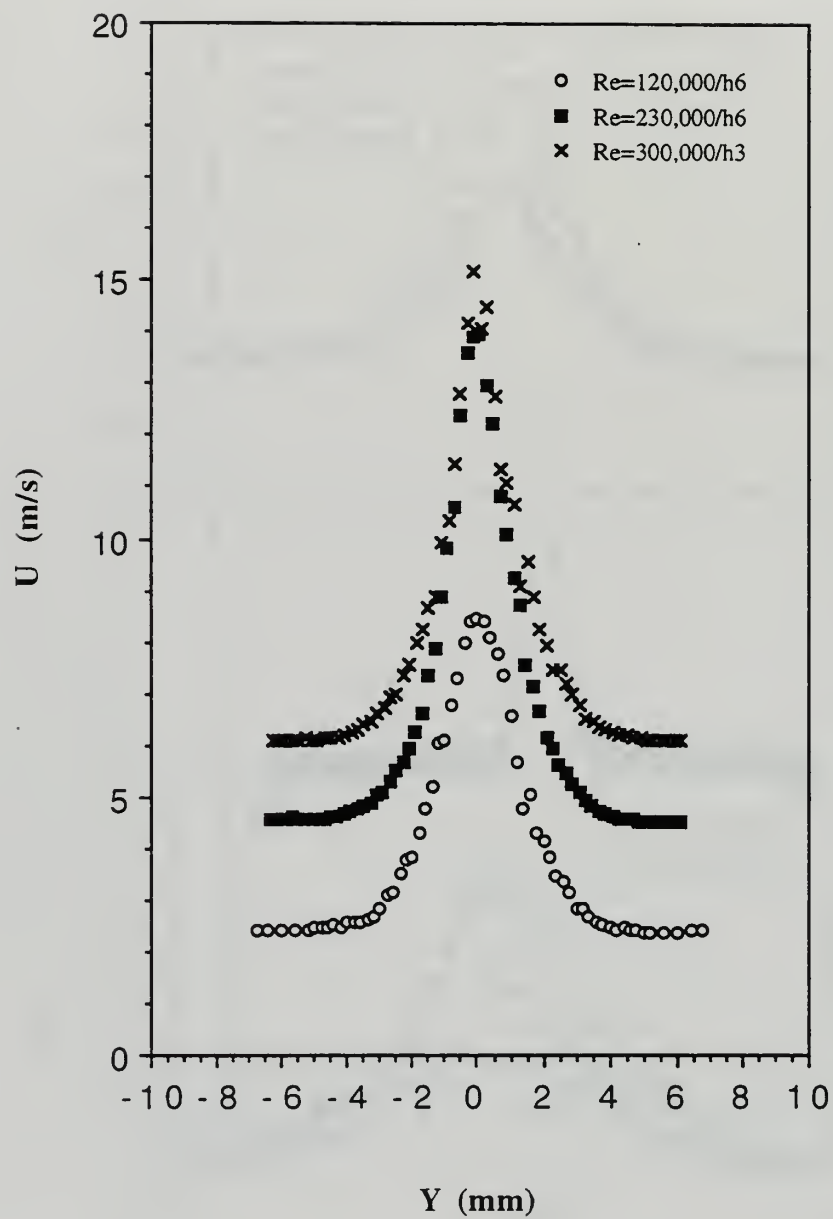


Figure 4-56.  $U$  profiles in the inlet region of various  $Re_D$ /tube flow states.

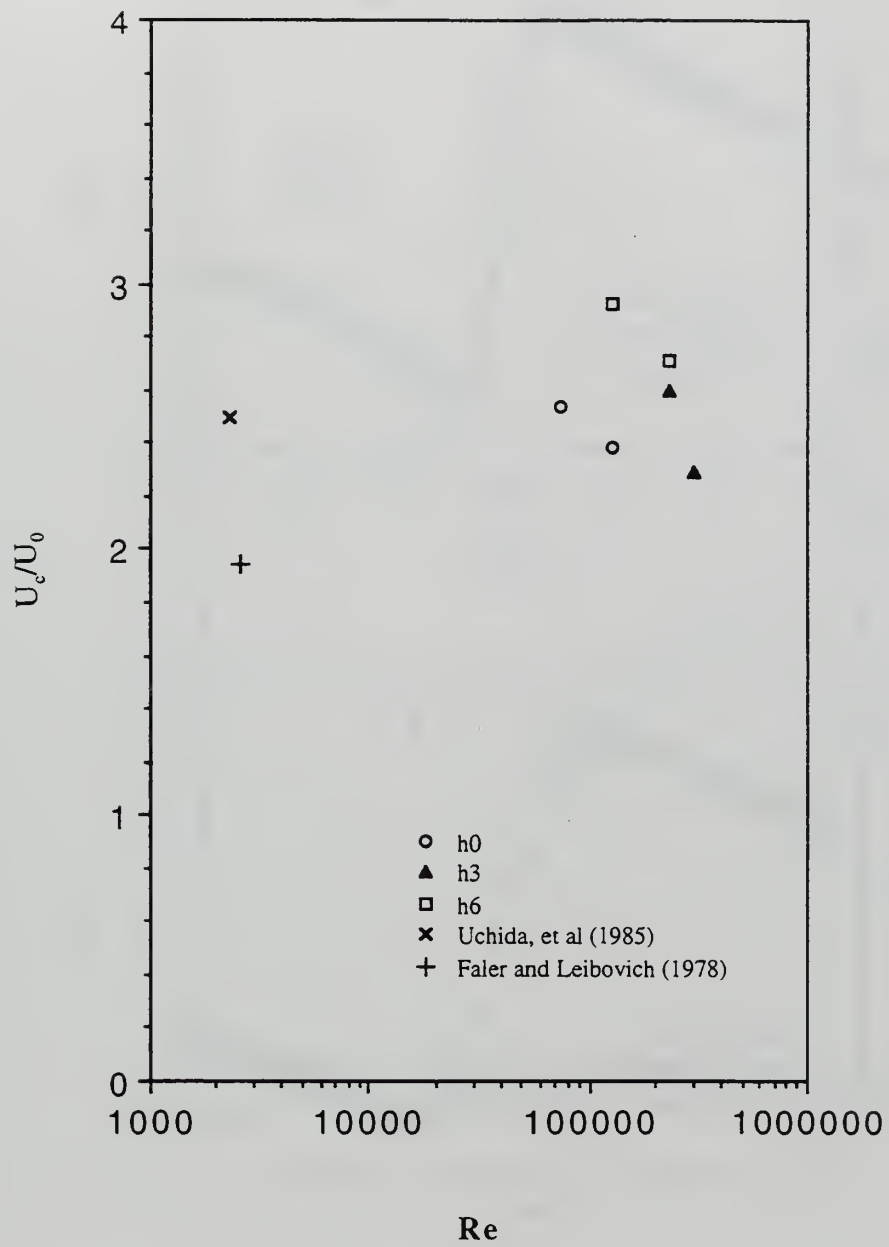


Figure 4-57. Variation of  $U_c/U_0$  with  $Re_D$ .



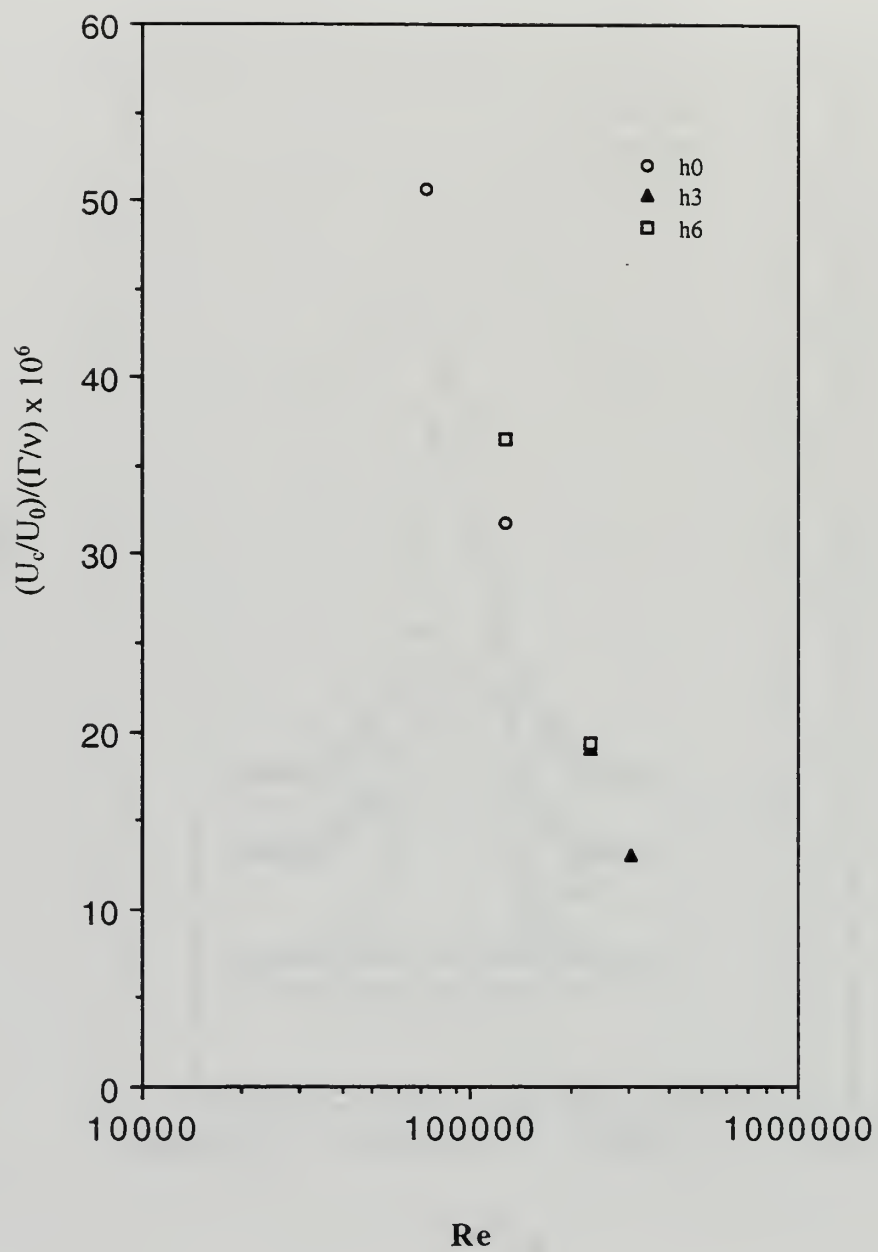


Figure 4-58. Variation of  $(U_c/U_0)/(\Gamma/\nu)$  with  $Re_D$ .

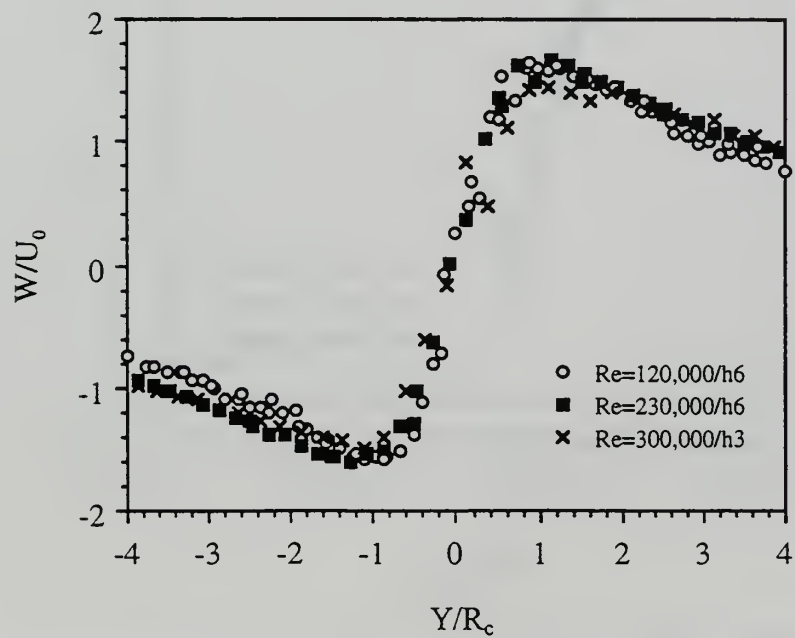
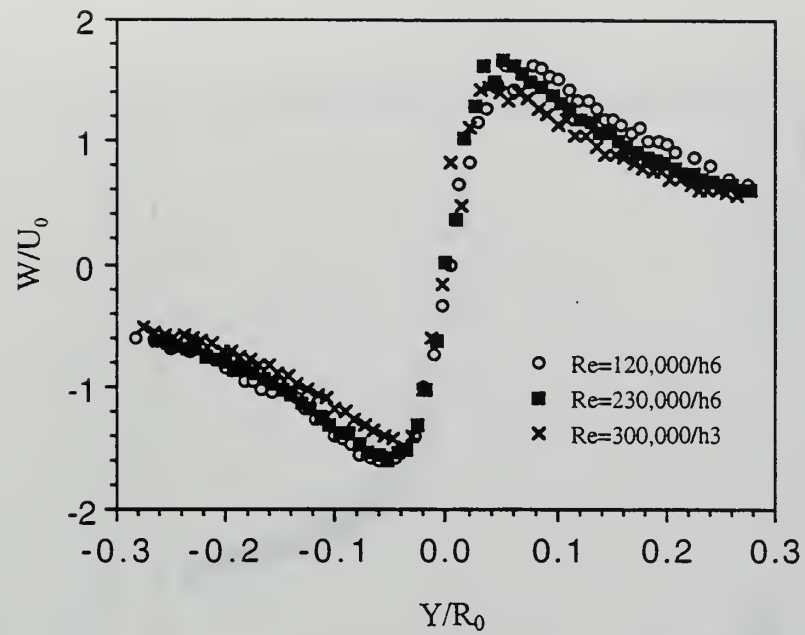


Figure 4-59.  $W/U_0$  profiles in the inlet region of various  $Re_D$ /tube flow states (core region).

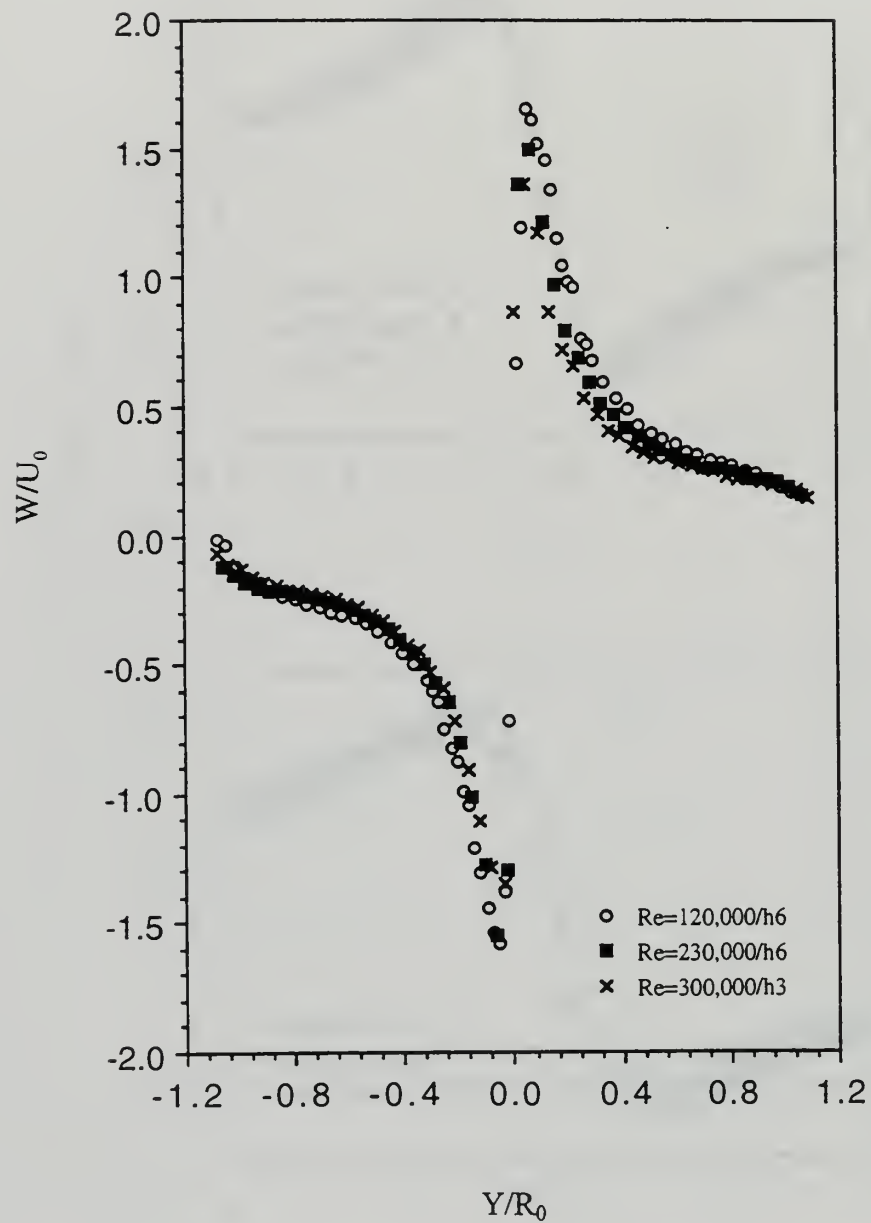


Figure 4-60.  $W/U_0$  profiles in the inlet region of various  $Re_D$ /tube flow states (full tube).

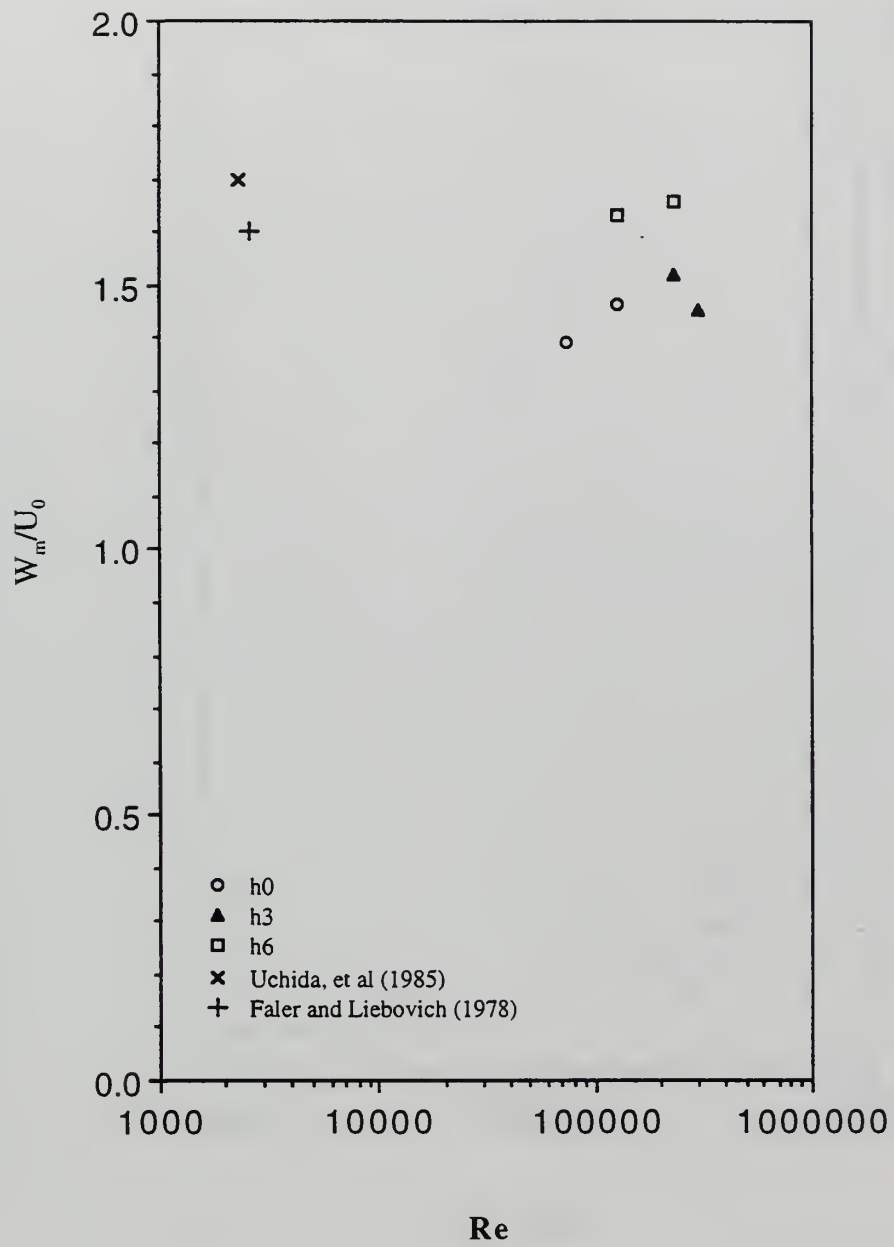


Figure 4-61. Variation of  $W_m/U_0$  with  $Re_D$ .

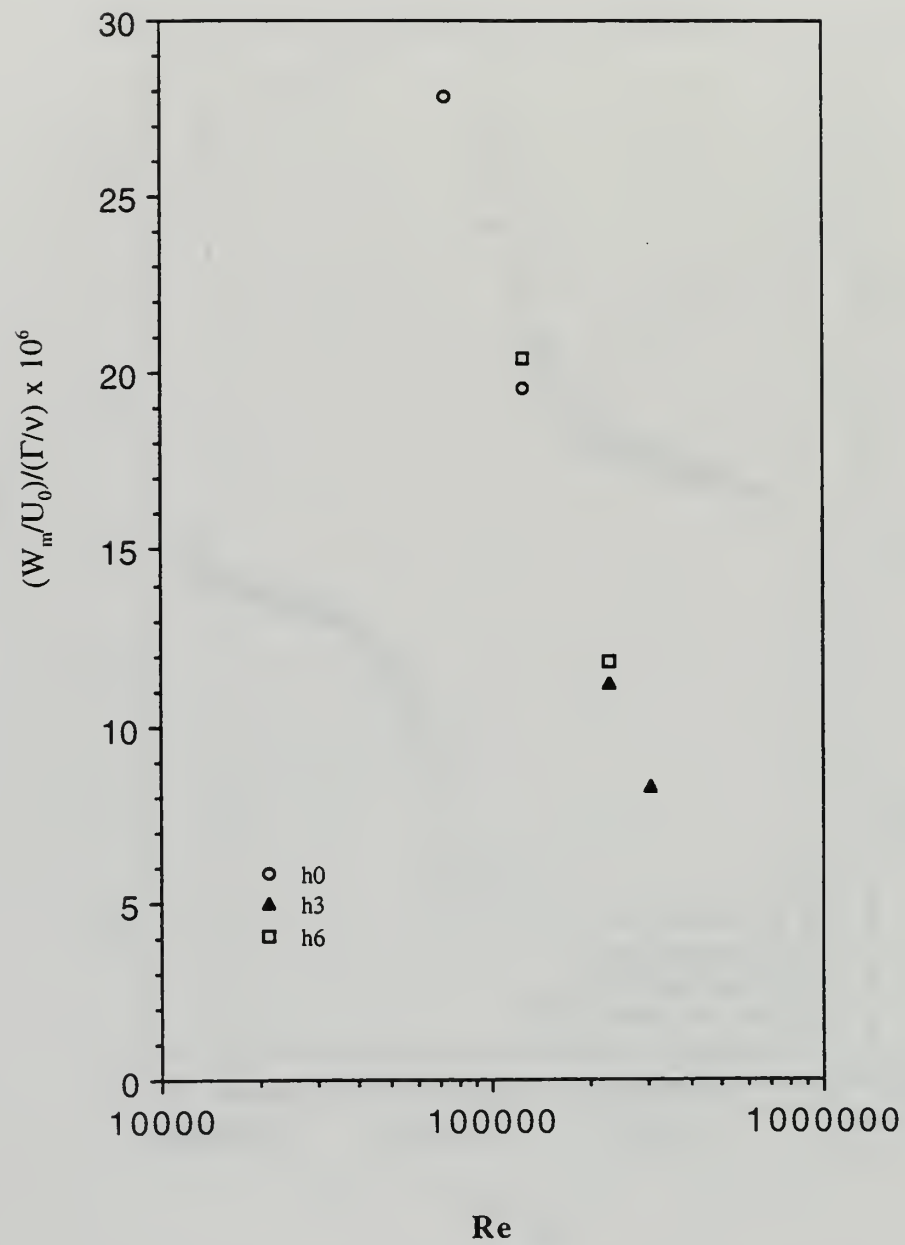


Figure 4-62. Variation of  $(W_m/U_0)/(\Gamma/\nu)$  with  $Re_D$ .



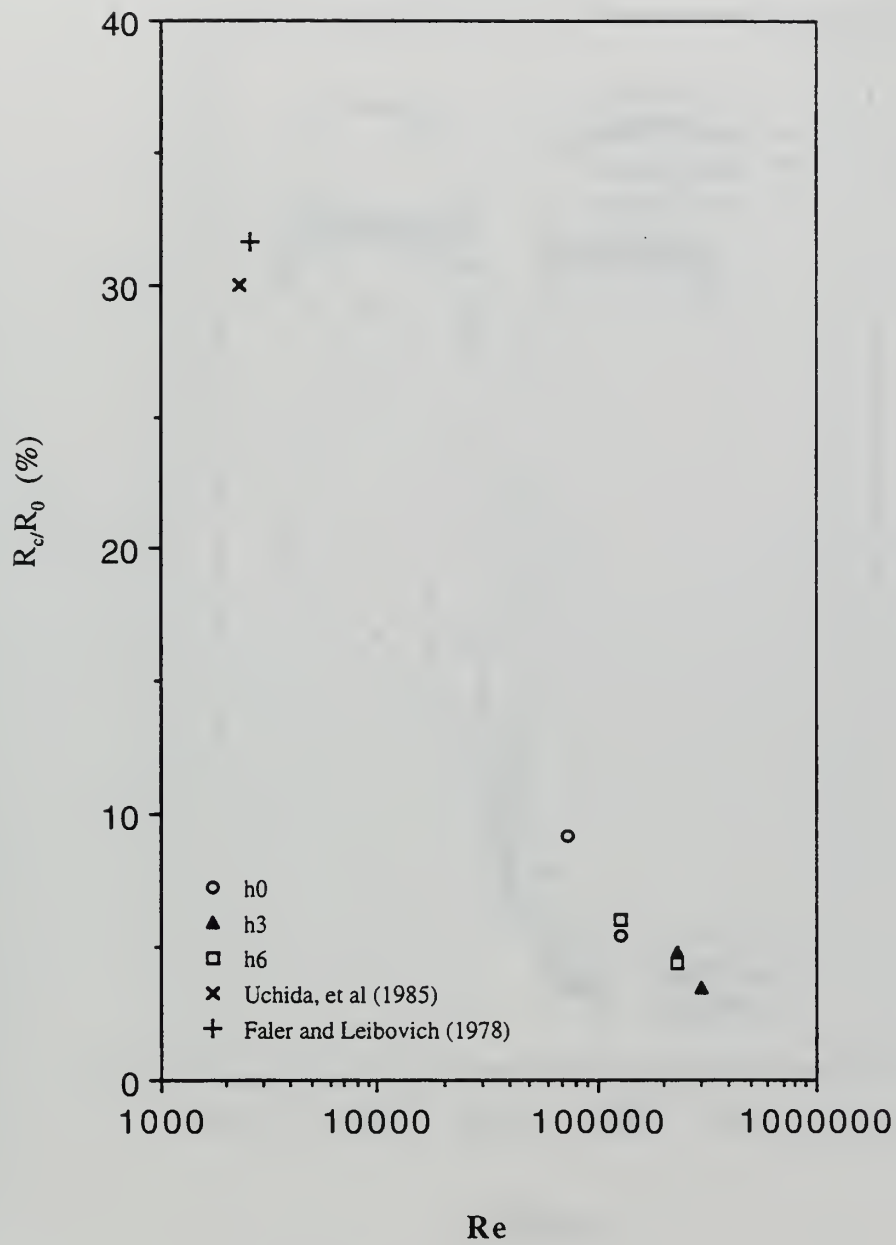


Figure 4-63. Variation of  $R_c/R_0$  with  $Re_D$ .

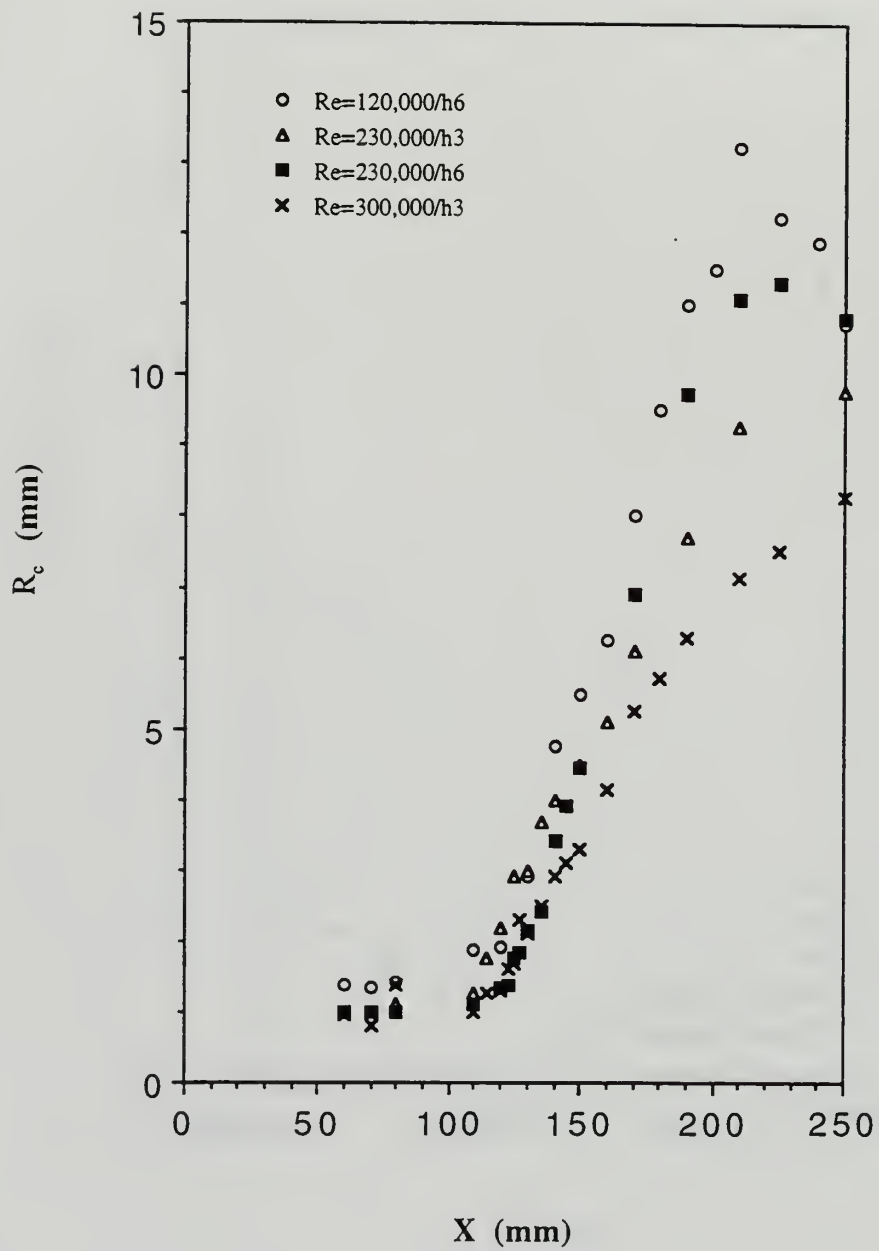


Figure 4-64. Axial Variation of  $R_c$  in various  $Re_D$ /tube flow states.

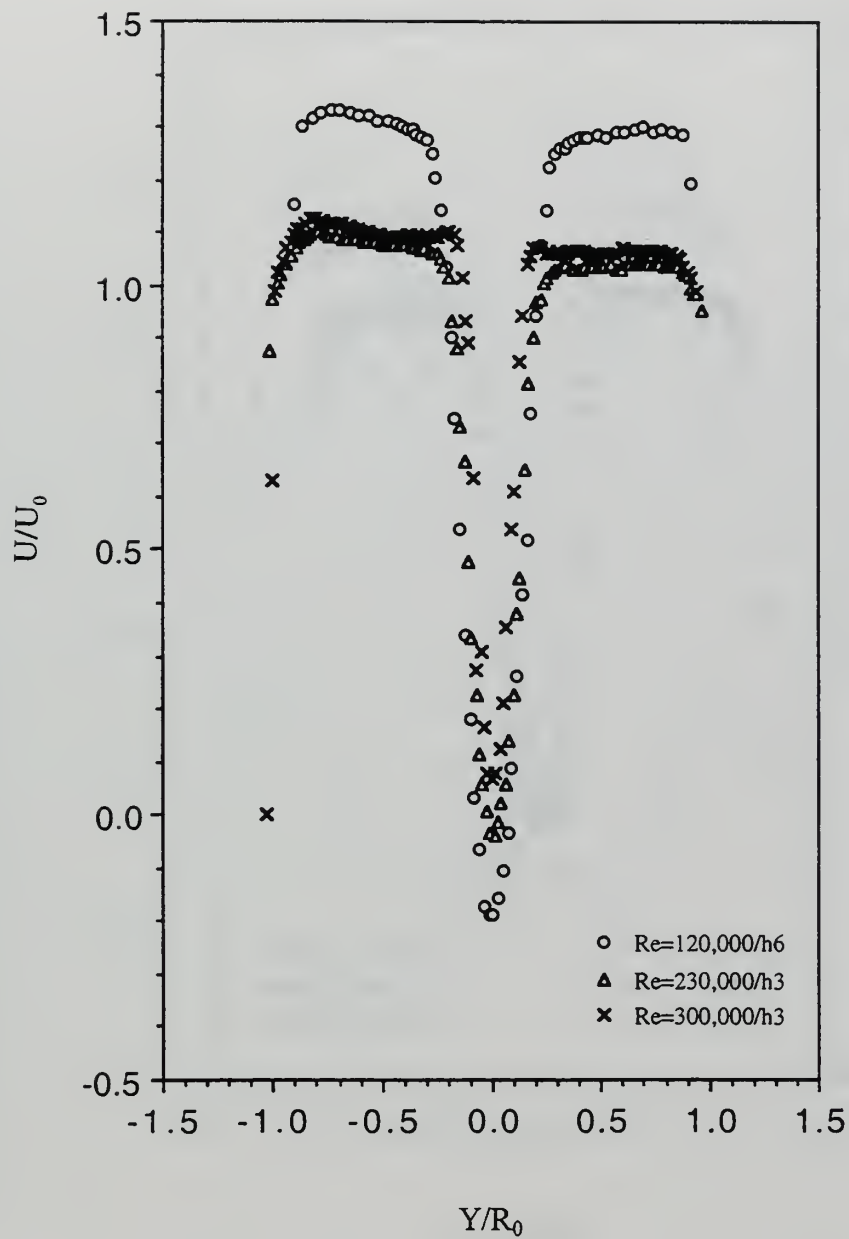


Figure 4-65.  $U/U_0$  vs.  $Y/R_0$  at  $X = 150$  mm in various  $Re_D$ /tube flow states.

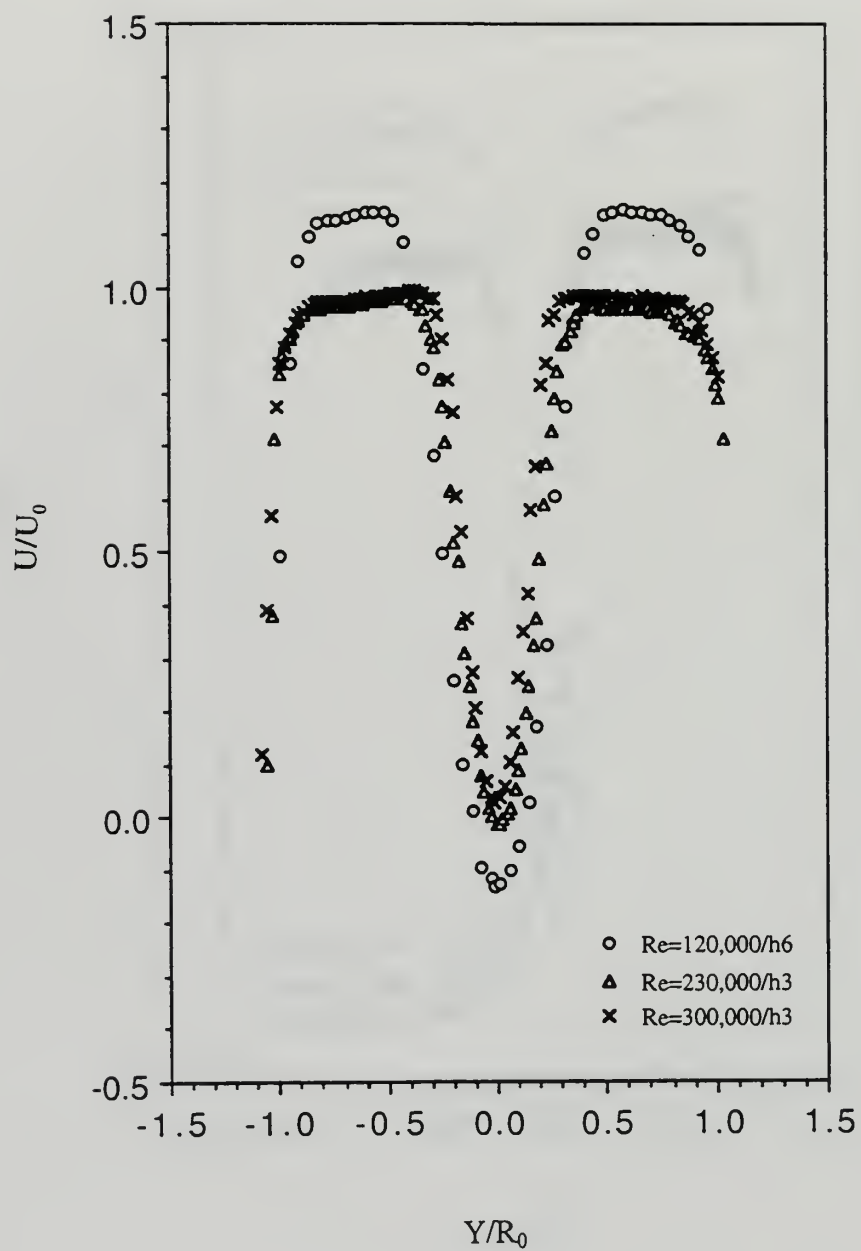


Figure 4-66.  $U/U_0$  vs.  $Y/R_0$  at  $X = 170$  mm in various  $Re_D$ /tube flow states.

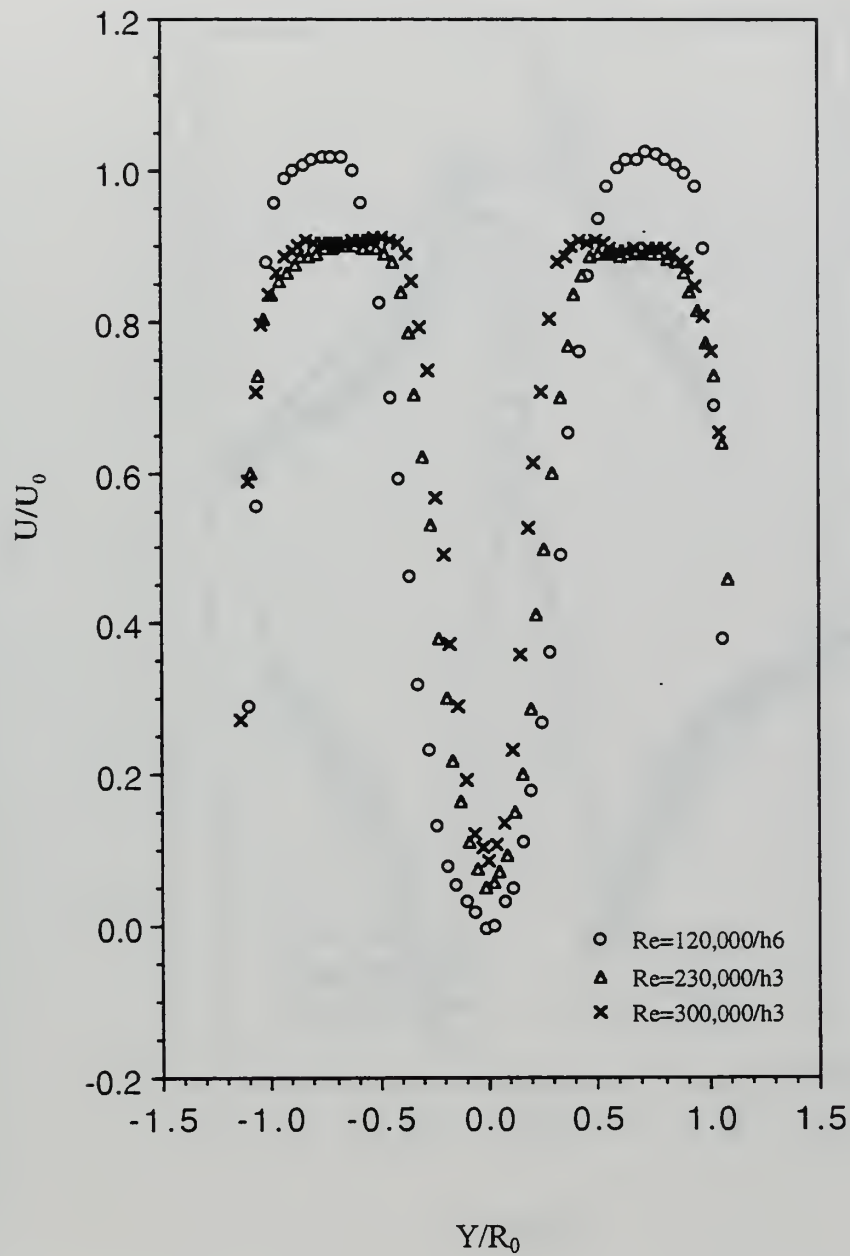


Figure 4-67.  $U/U_0$  vs.  $Y/R_0$  at  $X = 190$  mm in various  $Re_D$ /tube flow states.



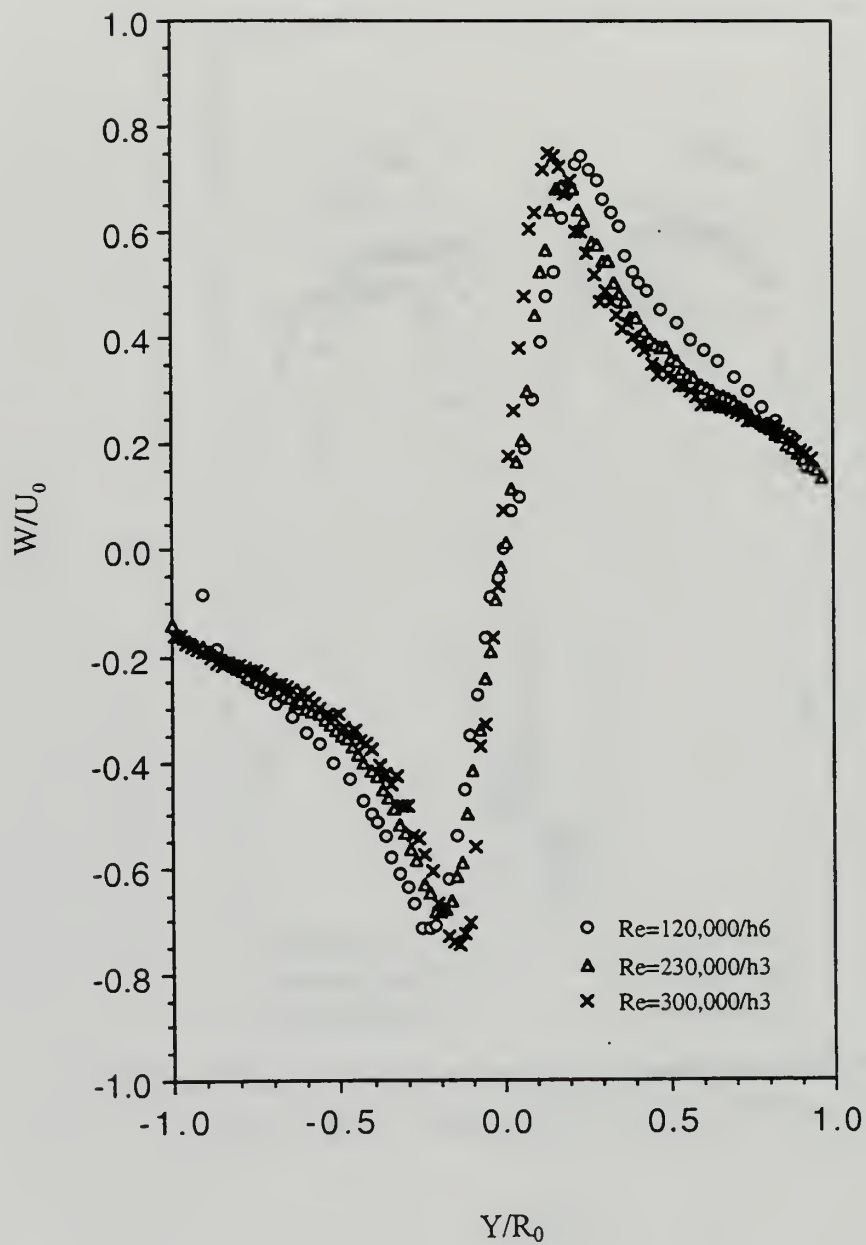


Figure 4-68.  $W/U_0$  vs.  $Y/R_0$  at  $X = 150$  mm in various  $Re_D$ /tube flow states.

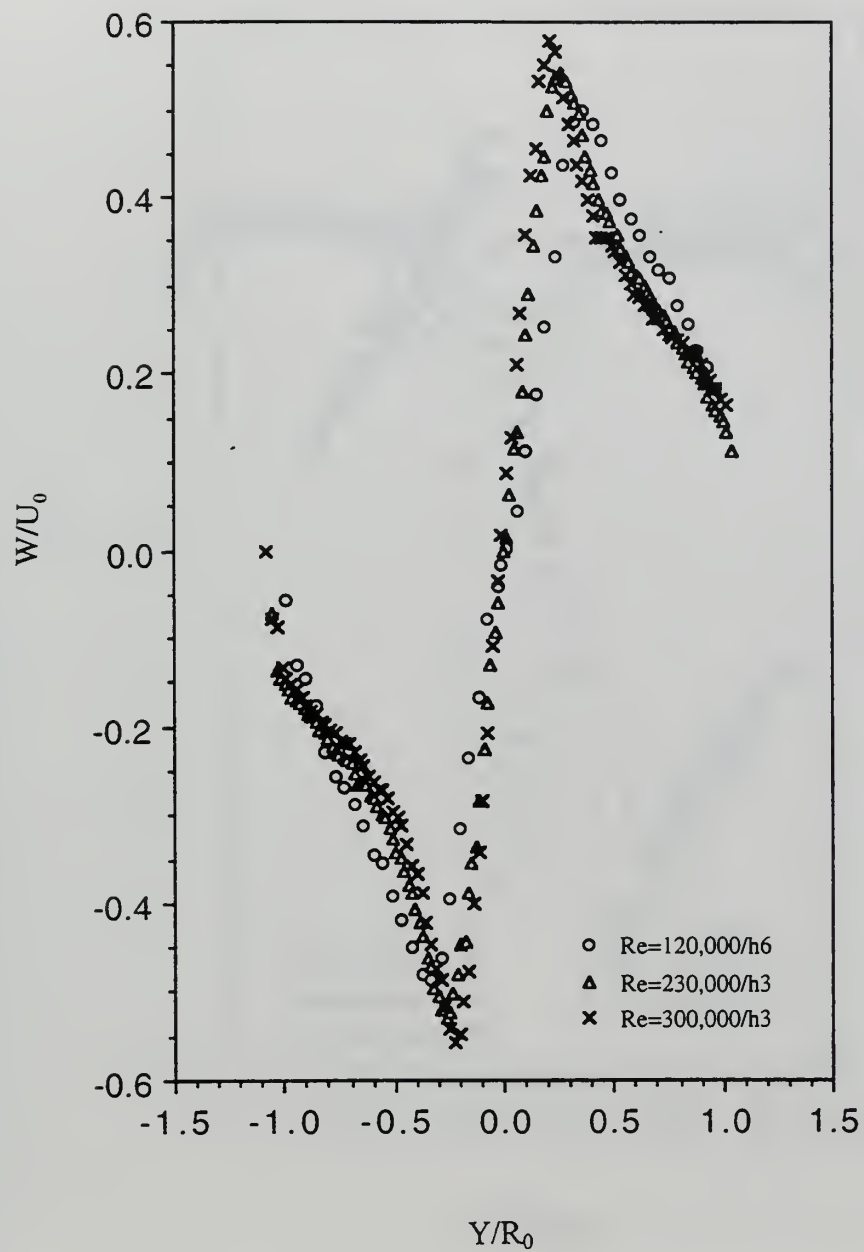


Figure 4-69.  $W/U_0$  vs.  $Y/R_0$  at  $X = 170$  mm in various  $Re_D$ /tube flow states.

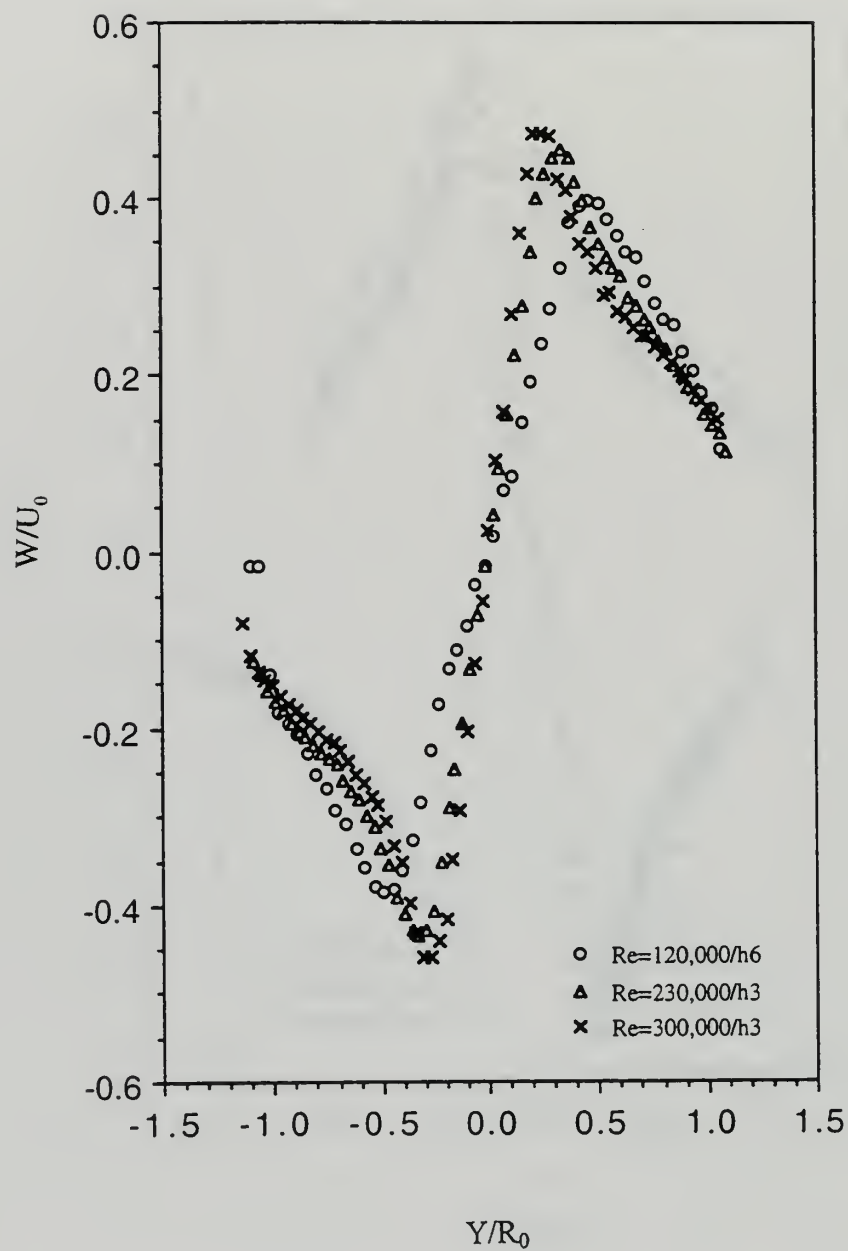


Figure 4-70.  $W/U_0$  vs.  $Y/R_0$  at  $X = 190$  mm in various  $Re_D/tube$  flow states.

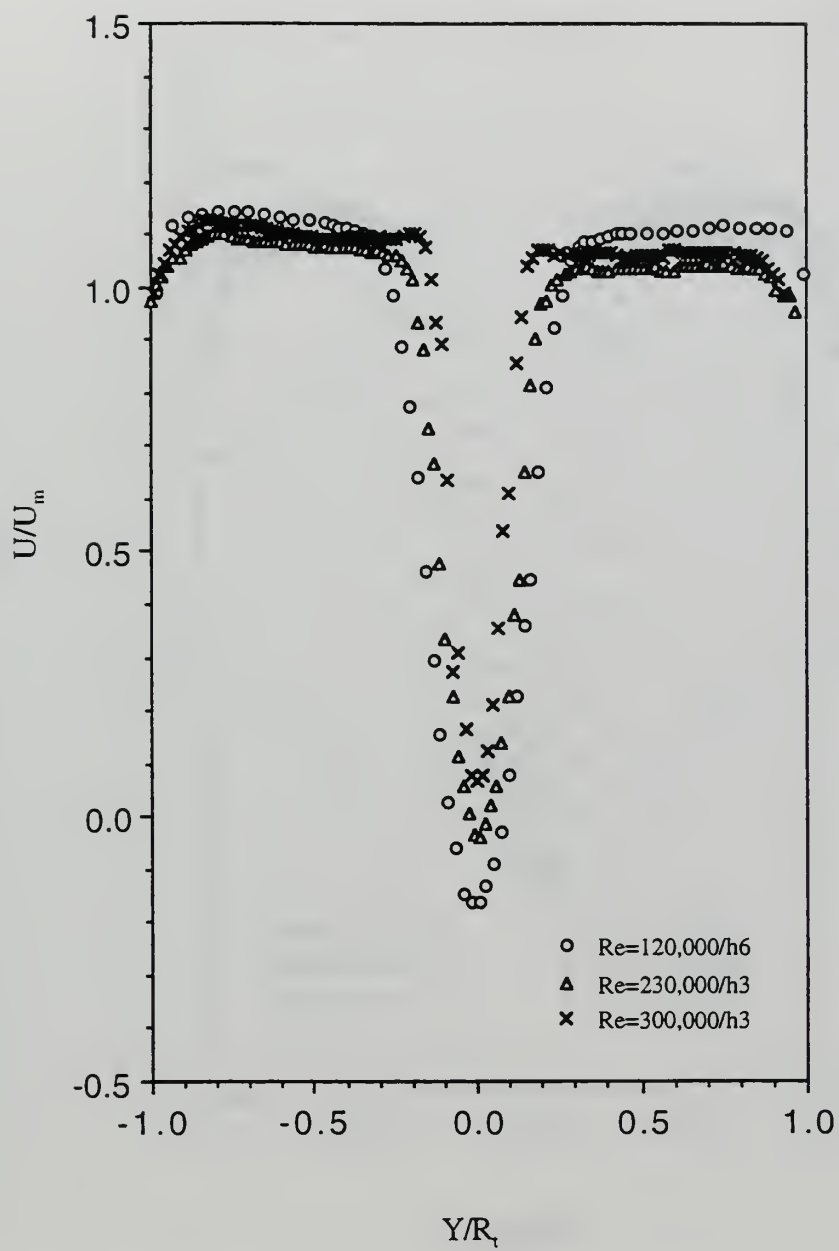


Figure 4-71.  $U/U_m$  vs.  $Y/R_t$  at  $X = 150$  mm in various  $Re_D$ /tube flow states.

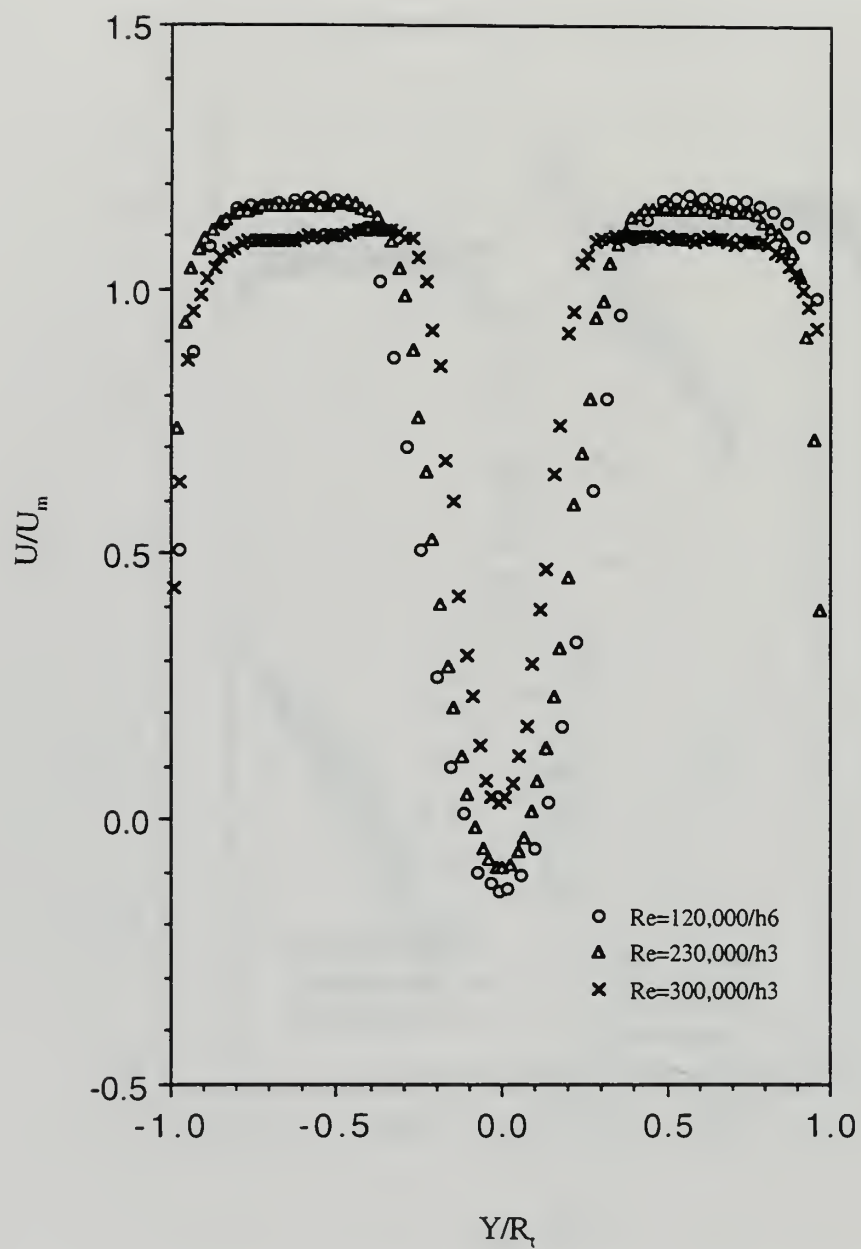


Figure 4-72.  $U/U_m$  vs.  $Y/R_t$  at  $X = 170$  mm in various  $Re_D$ /tube flow states.



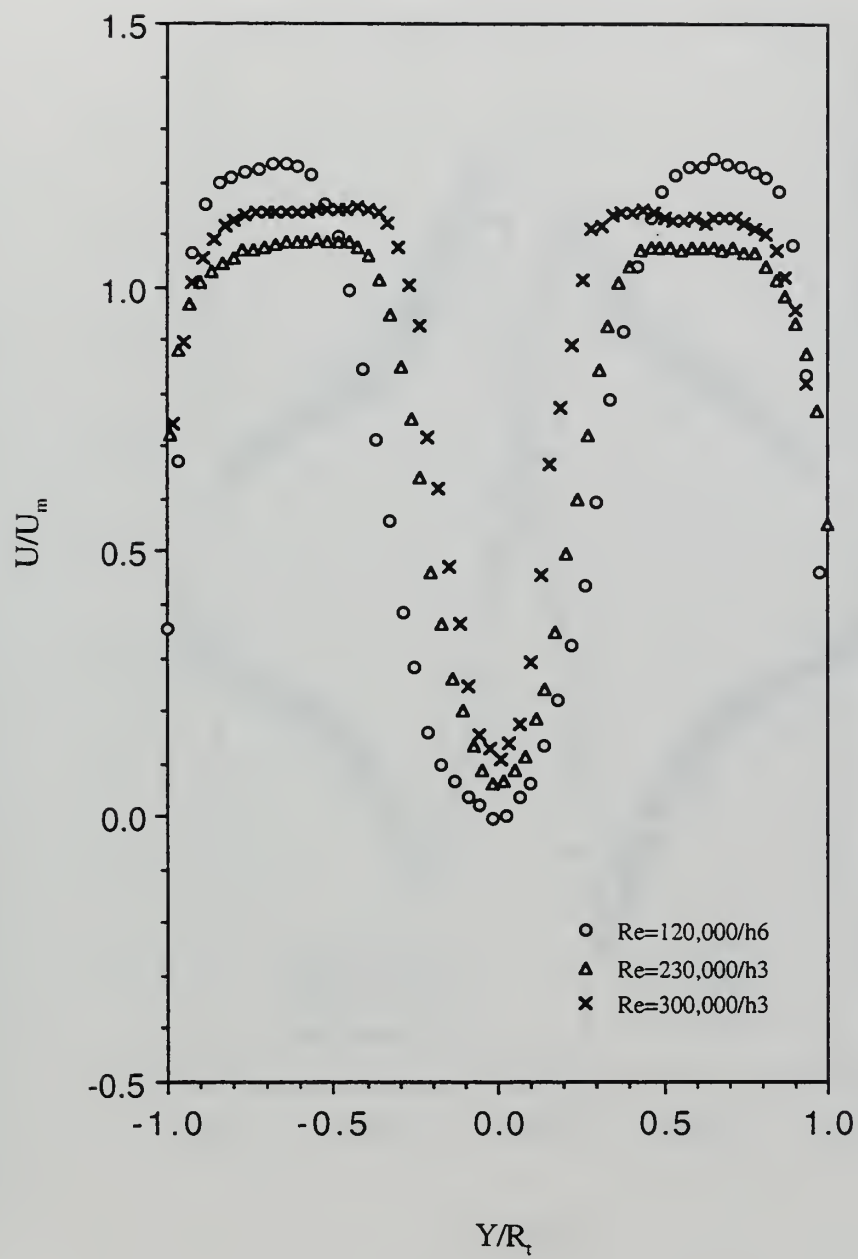


Figure 4-73.  $U/U_m$  vs.  $Y/R_t$  at  $X = 190$  mm in various  $Re_D$ /tube flow states.

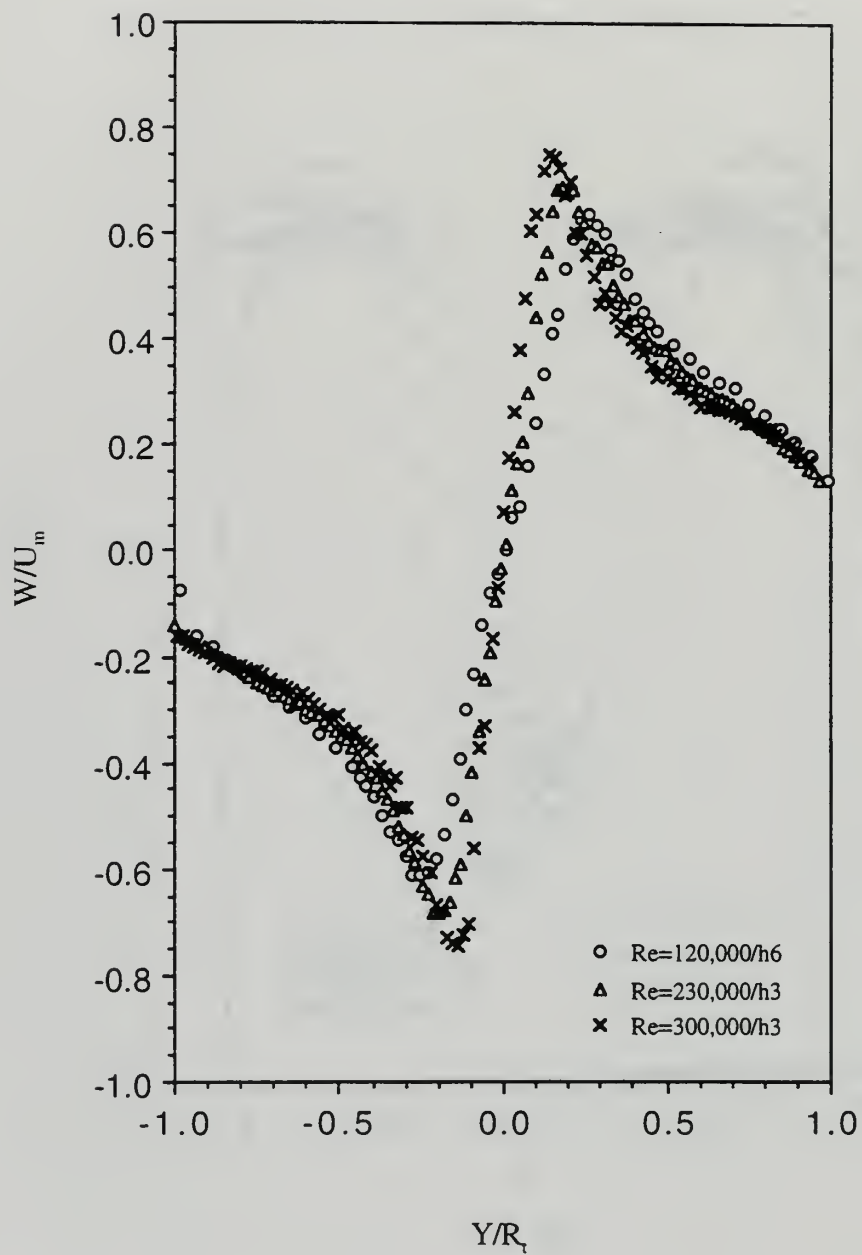


Figure 4-74.  $W/U_m$  vs.  $Y/R_t$  at  $X = 150$  mm in various  $Re_D$ /tube flow states.

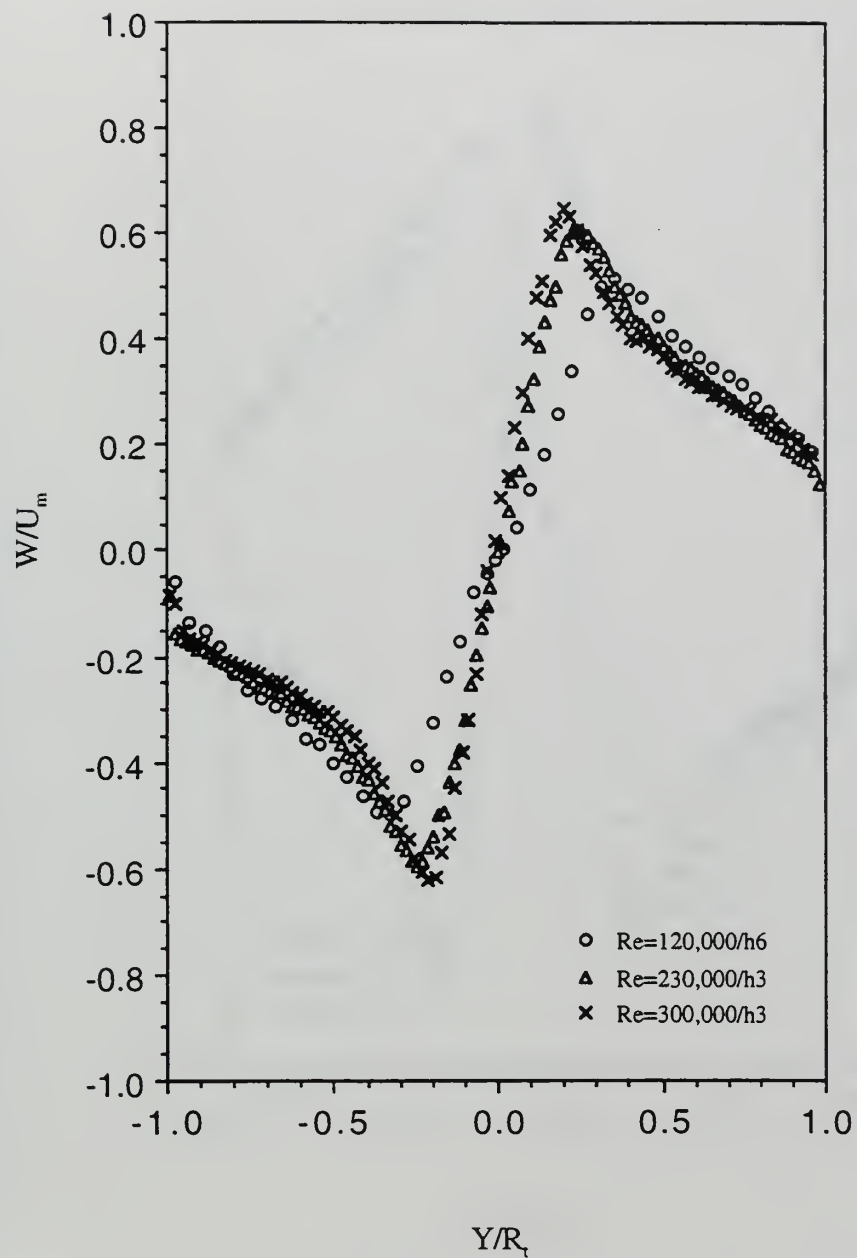


Figure 4-75.  $W/U_m$  vs.  $Y/R_t$  at  $X = 170$  mm in various  $Re_D$ /tube flow states.

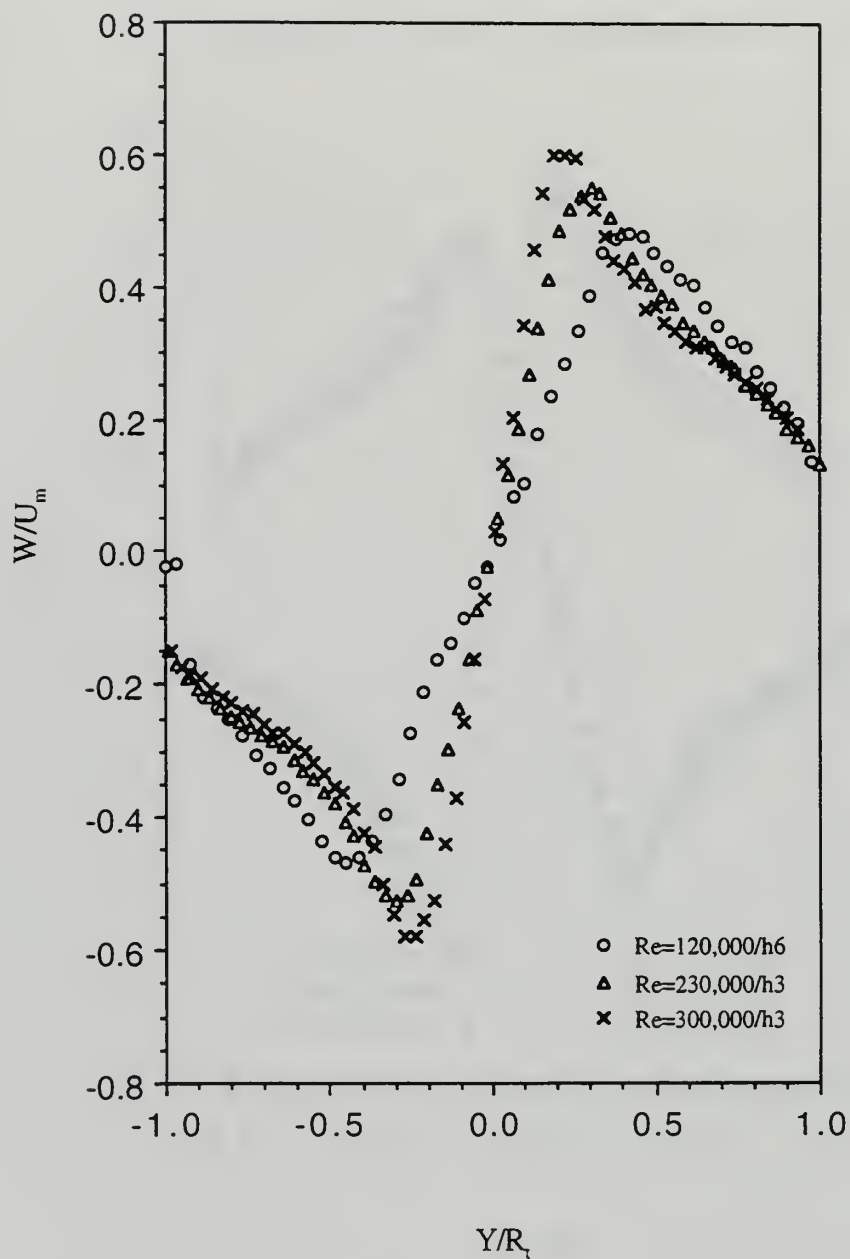


Figure 4-76.  $W/U_m$  vs.  $Y/R_t$  at  $X = 190$  mm in various  $Re_D$ /tube flow states.

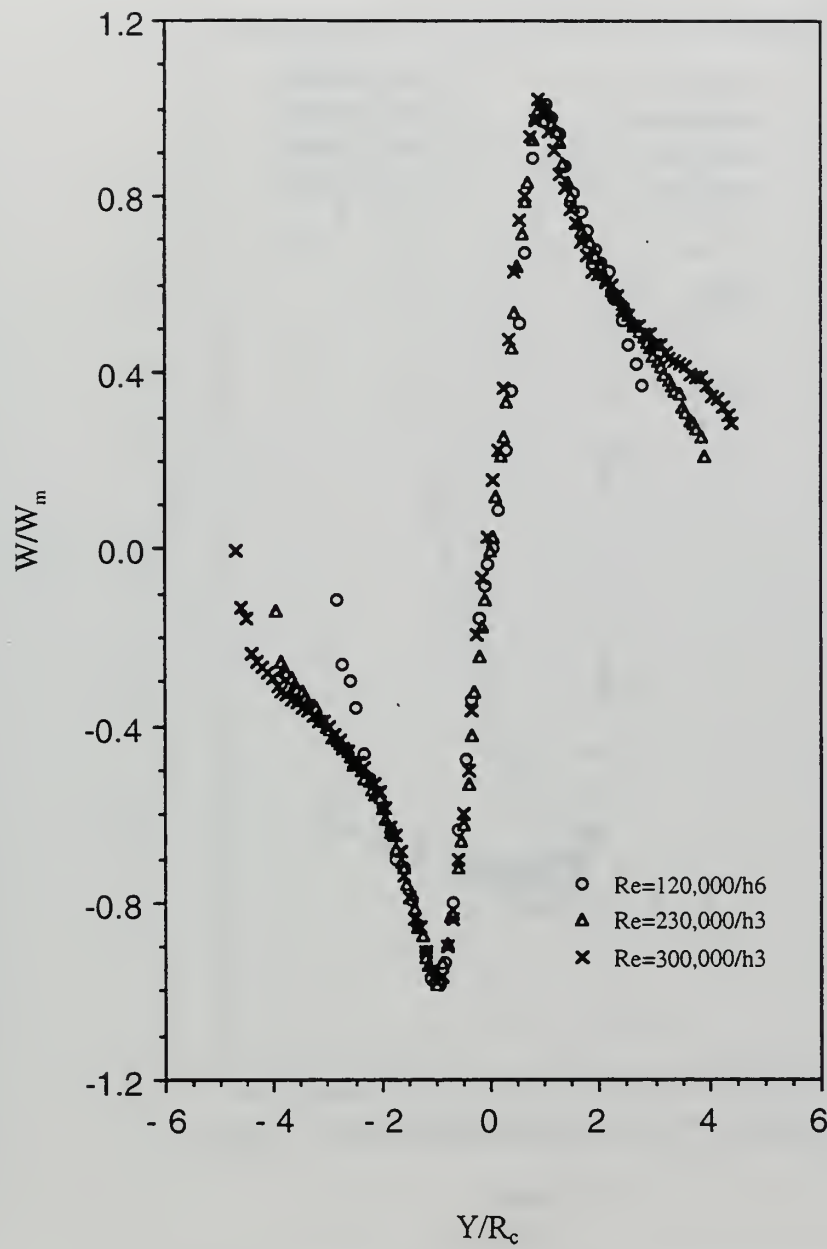


Figure 4-77.  $W/W_m$  vs.  $Y/R_c$  at  $X = 170$  mm in various  $Re_D/tube$  flow states.



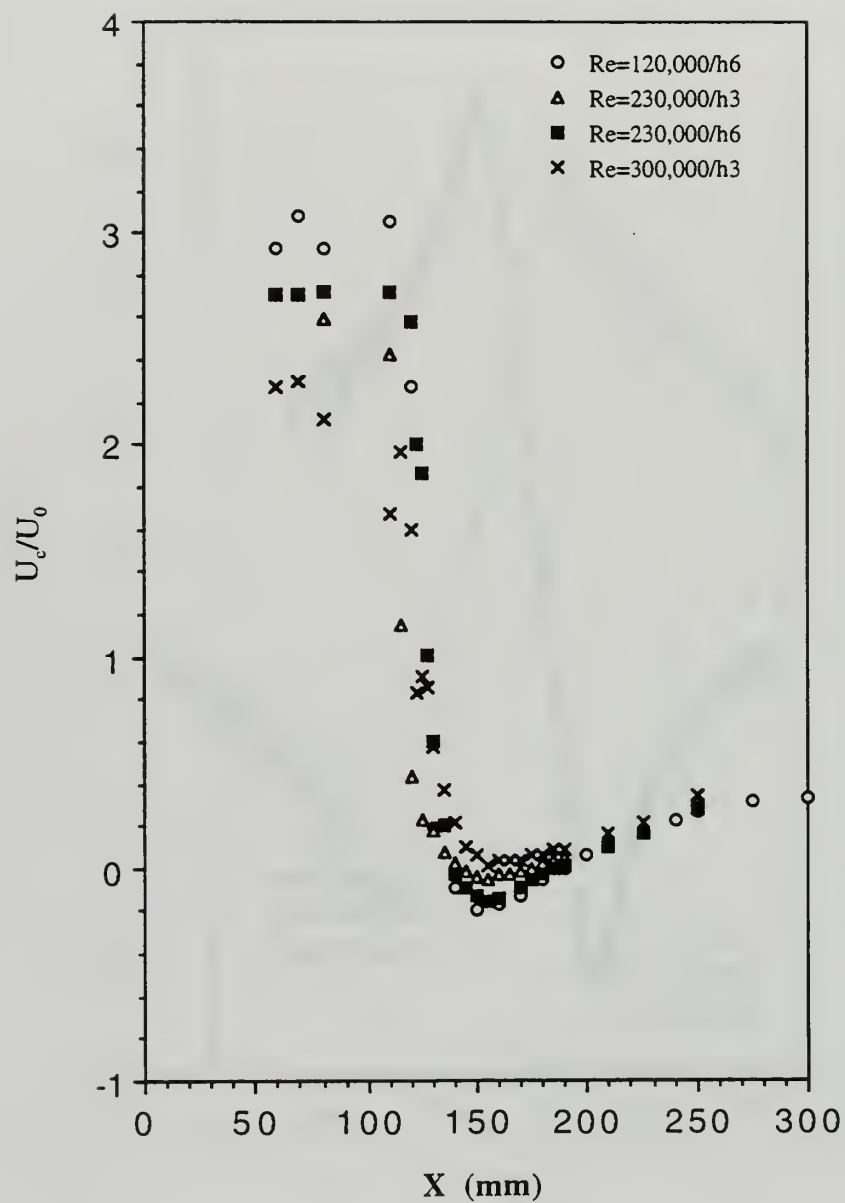


Figure 4-78. Axial variation of  $U_c/U_0$  in various  $Re_D$ /tube flow states.

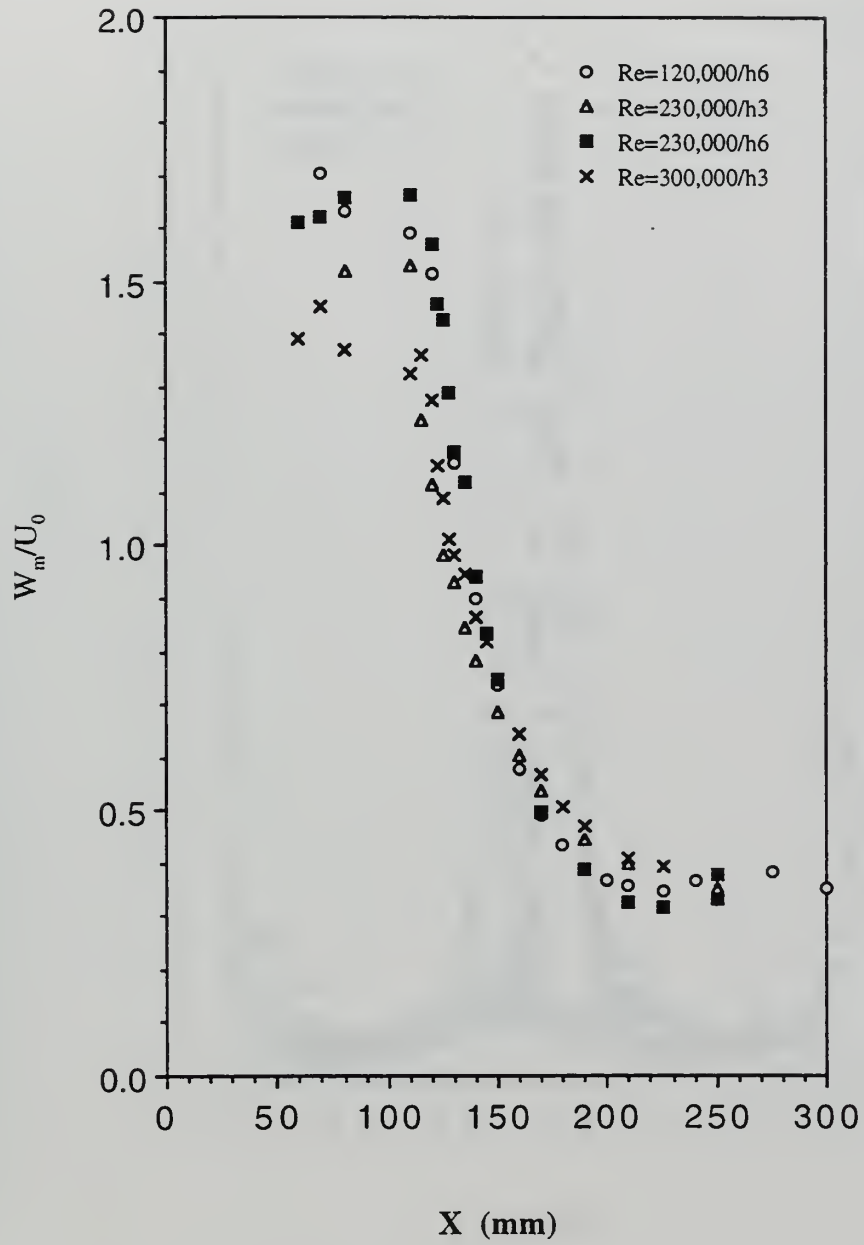


Figure 4-79. Axial variation of  $W_m/U_0$  in various  $Re_p$ /tube flow states.

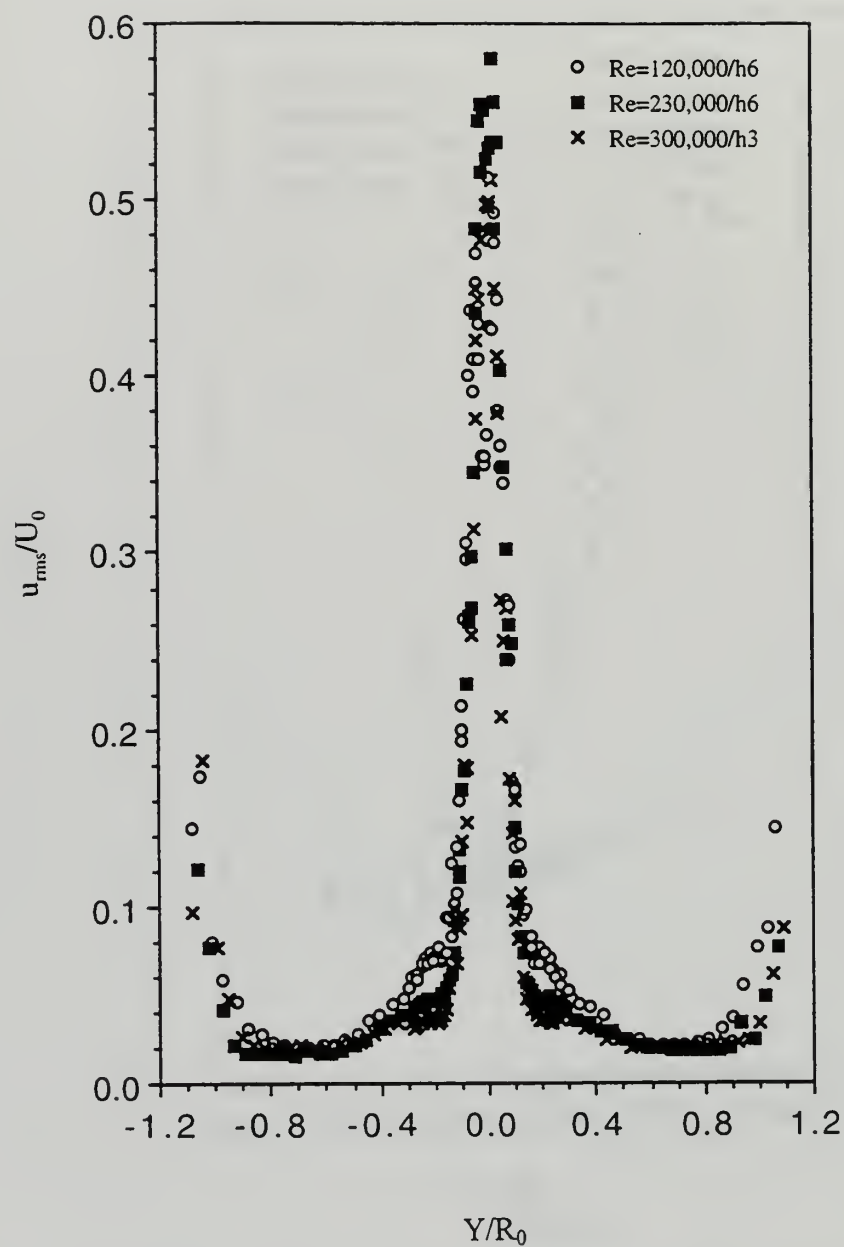


Figure 4-80.  $u_{rms}/U_0$  profiles in the inlet region of various  $Re_D$ /tube flow states.

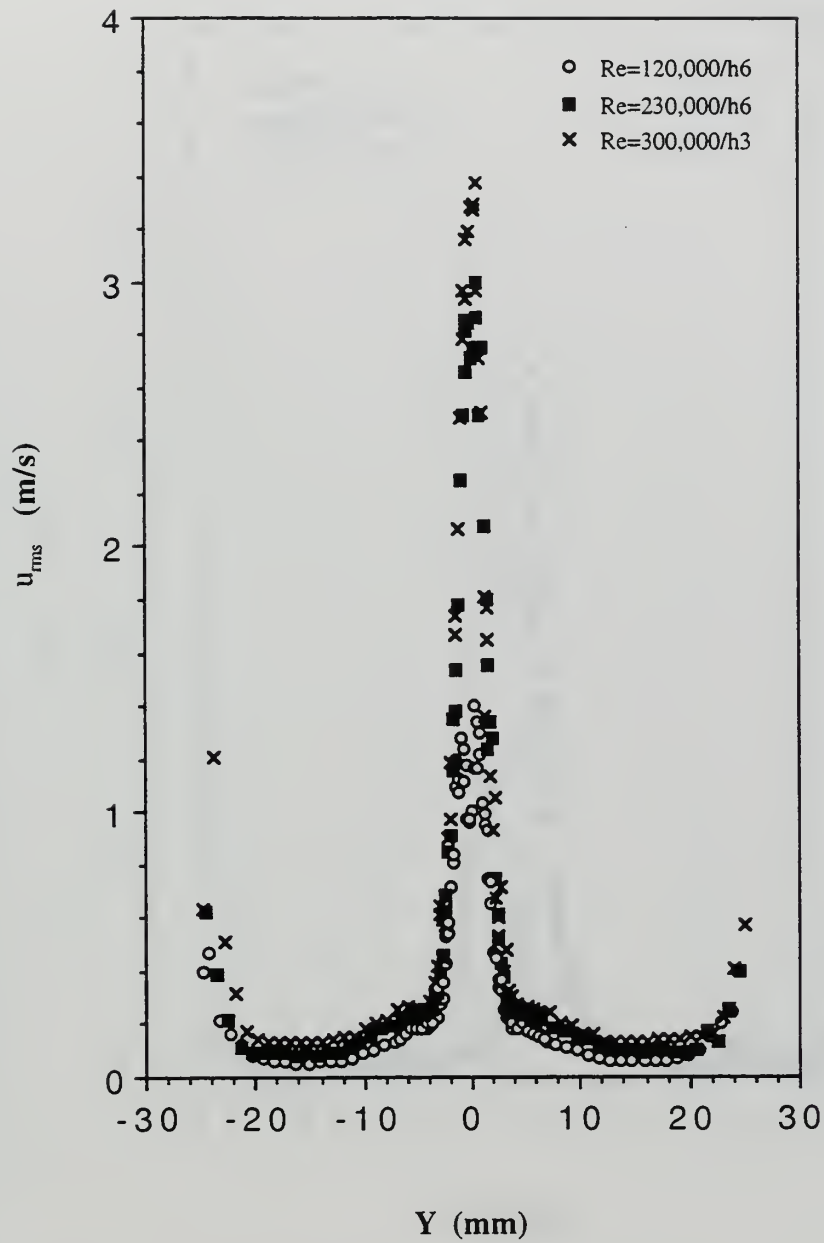


Figure 4-81.  $u_{rms}$  profiles in the inlet region of various  $Re_D/tube$  flow states.

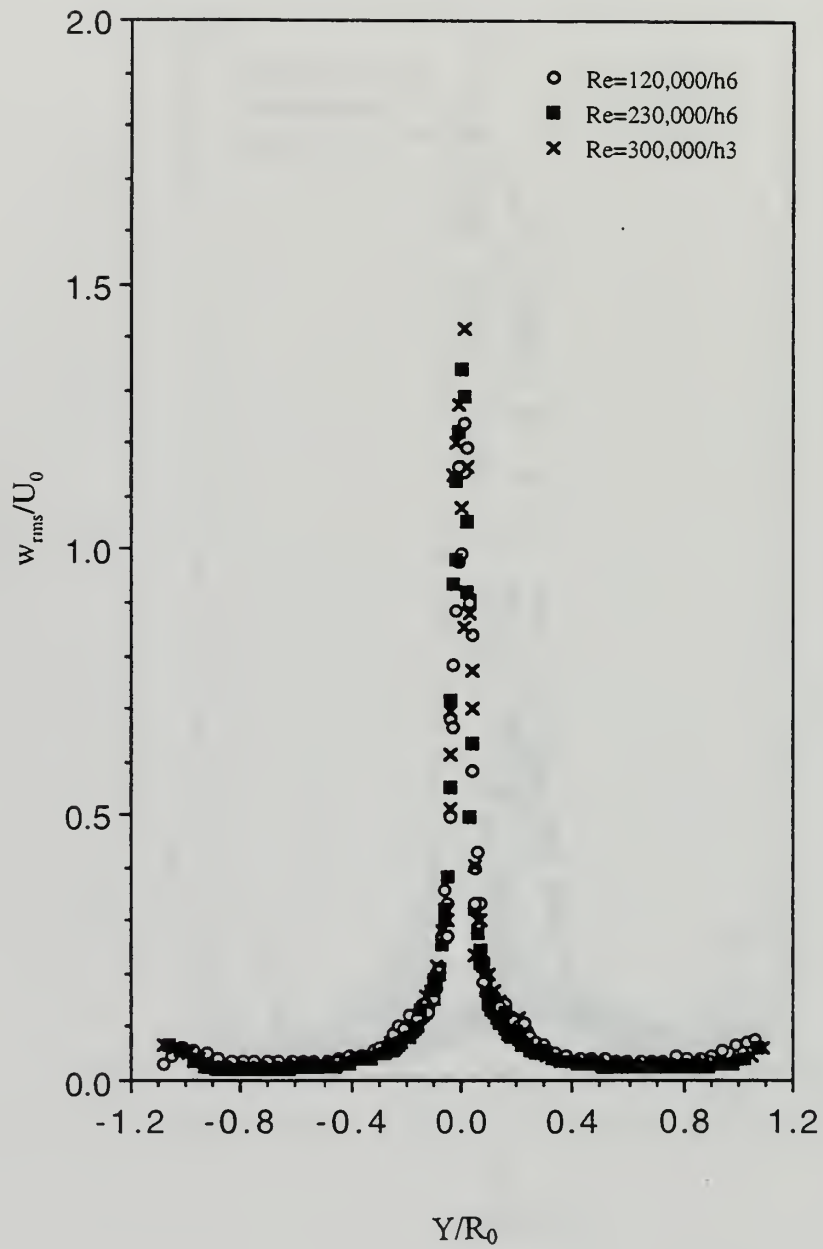


Figure 4-82.  $w_{rms}/U_0$  profiles in the inlet region of various  $Re_D$ /tube flow states.



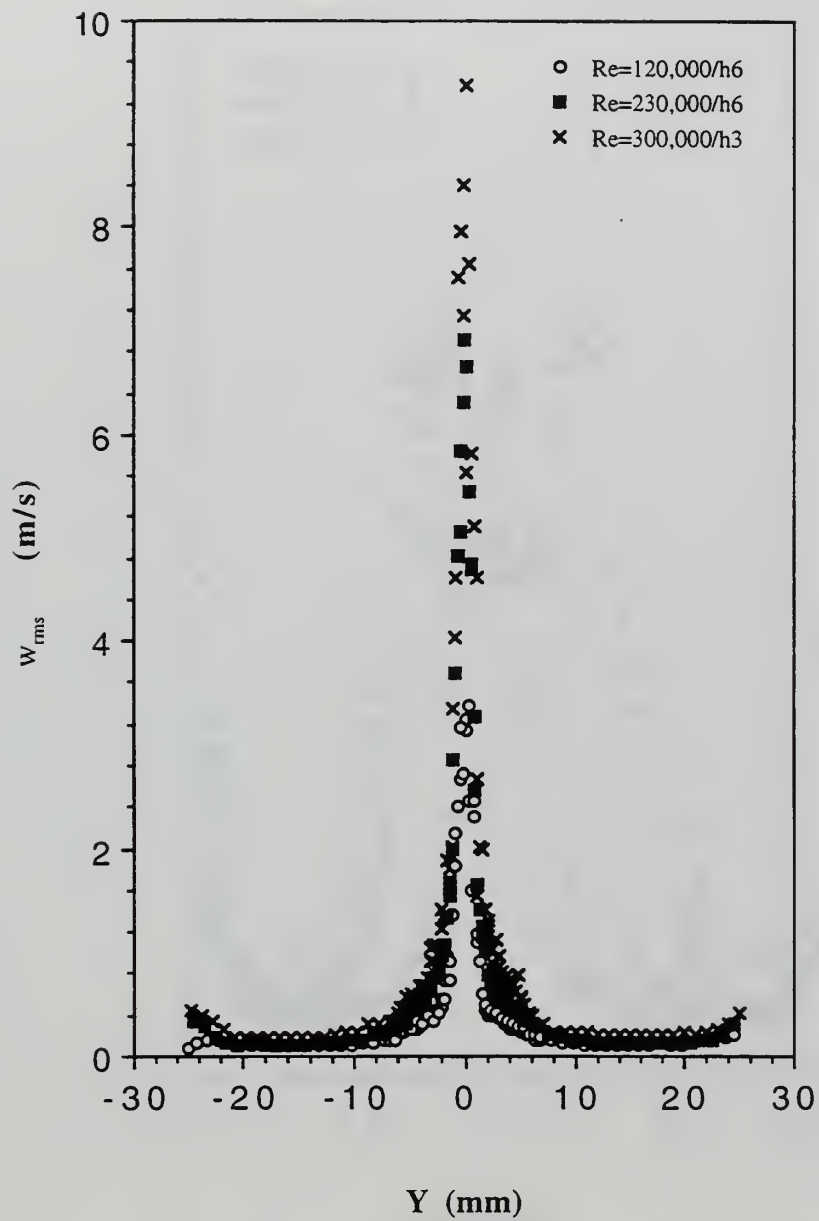


Figure 4-83.  $w_{rms}$  profiles in the inlet region of various  $Re_D/tube$  flow states.

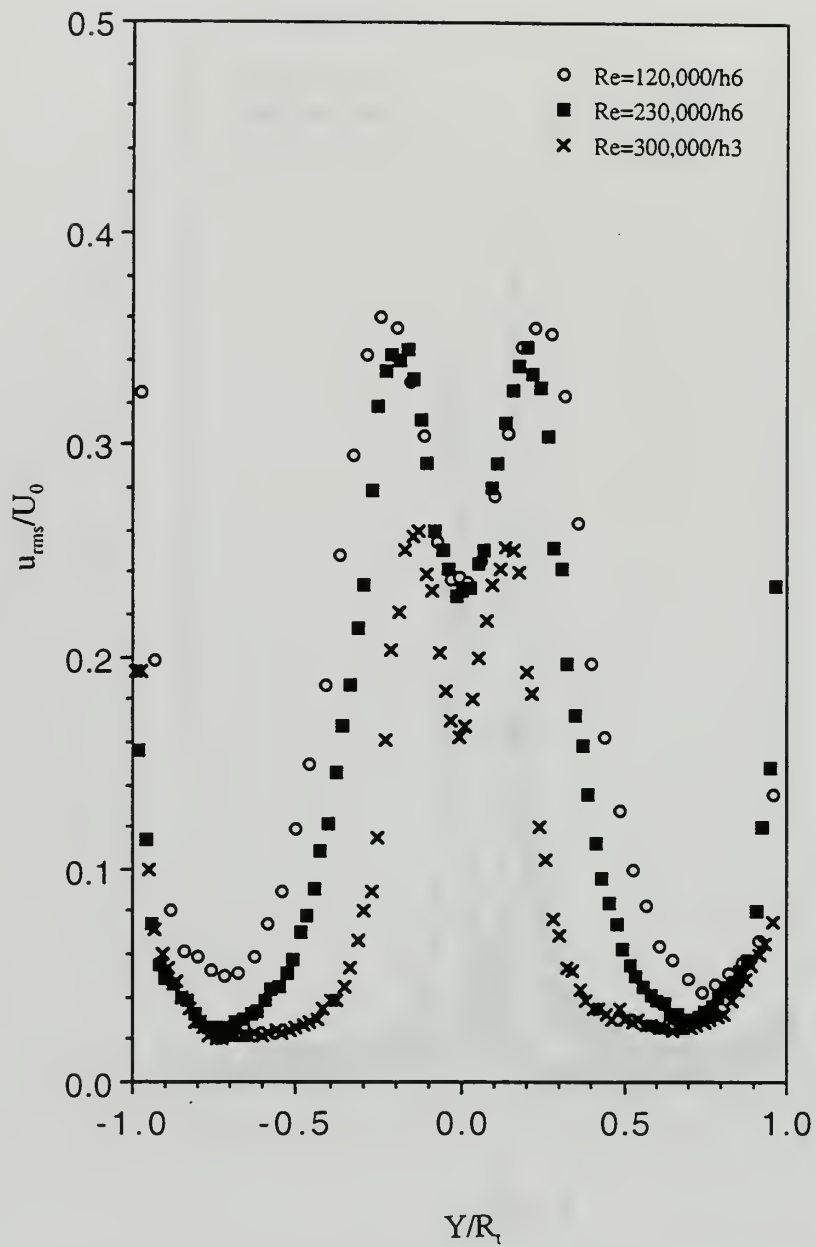


Figure 4-84.  $u_{rms}/U_0$  profiles in the wake region of various  $Re_D$ /tube flow states.

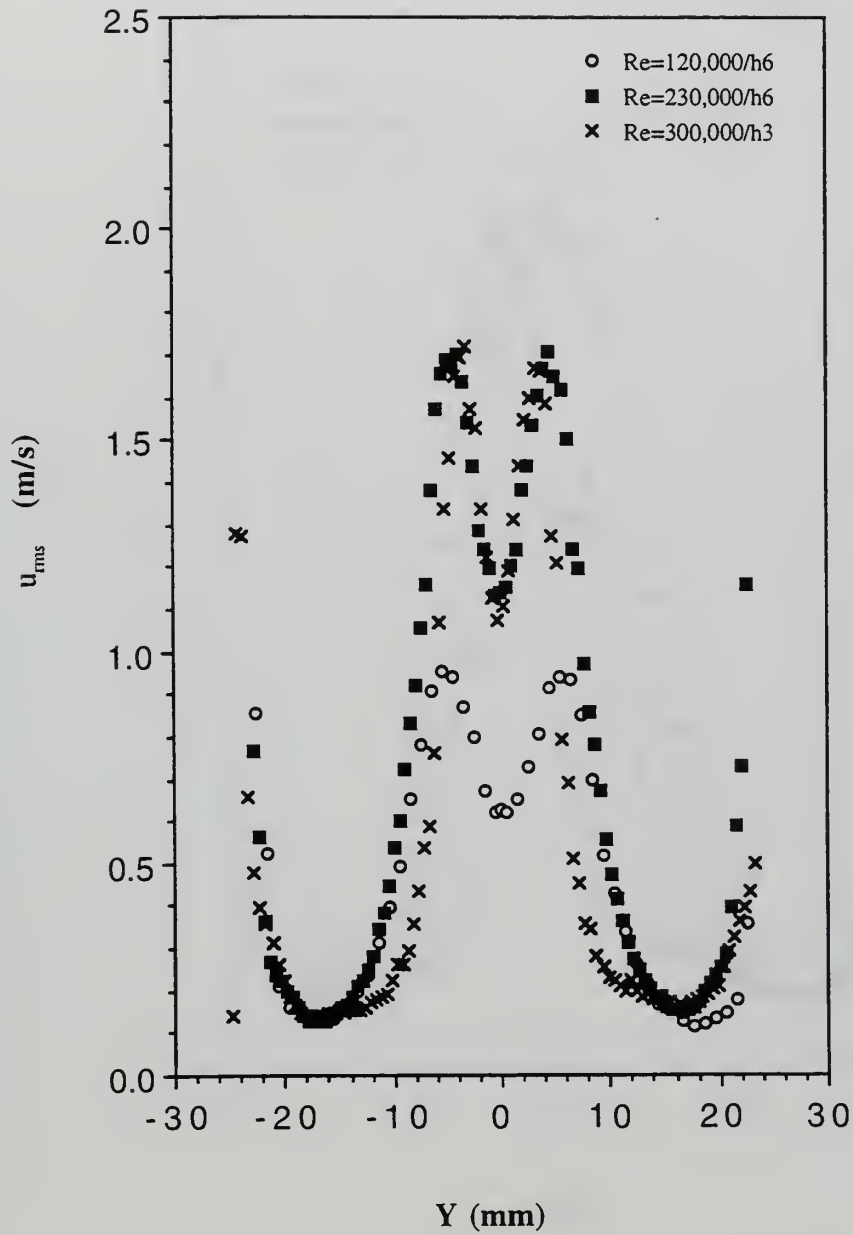


Figure 4-85.  $u_{rms}$  profiles in the wake region of various  $Re_D$ /tube flow states.

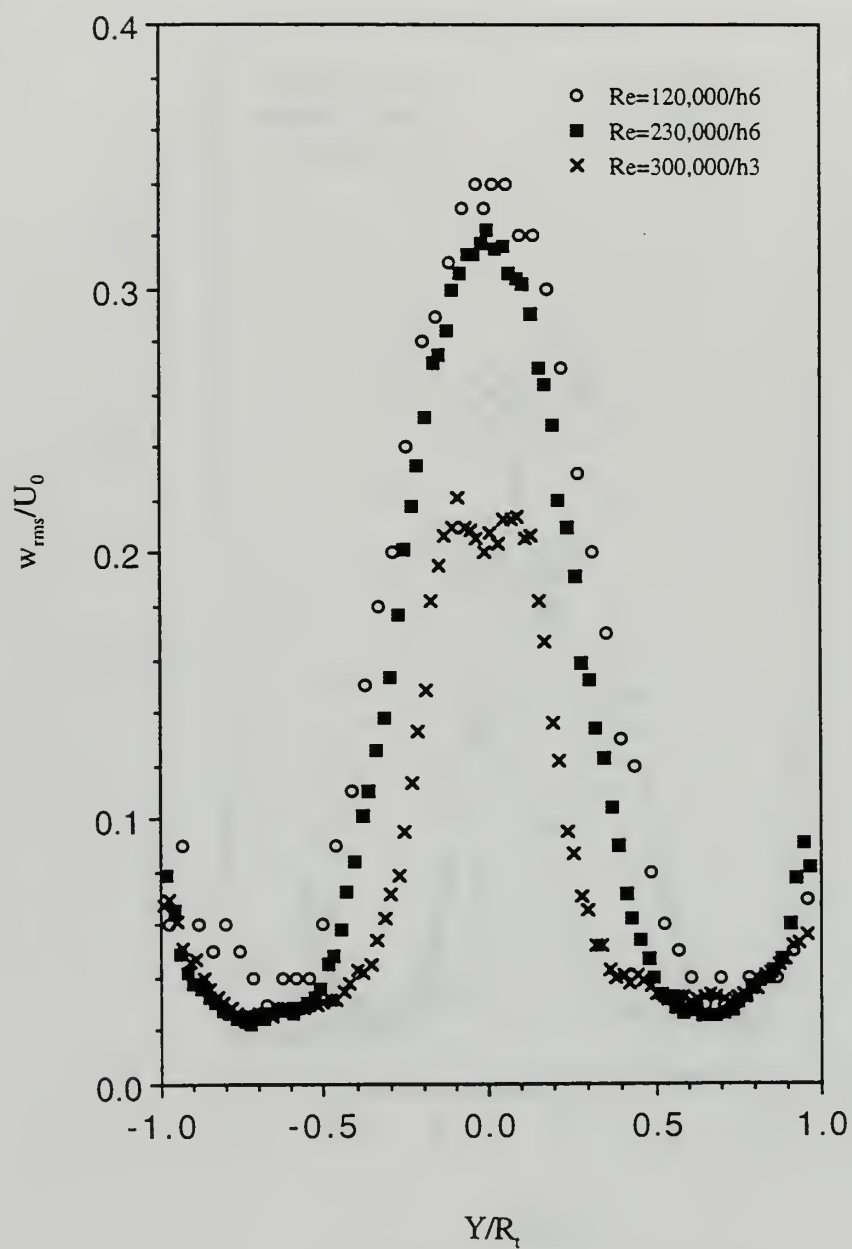


Figure 4-86.  $w_{rms}/U_0$  profiles in the wake region of various  $Re_D$ /tube flow states.

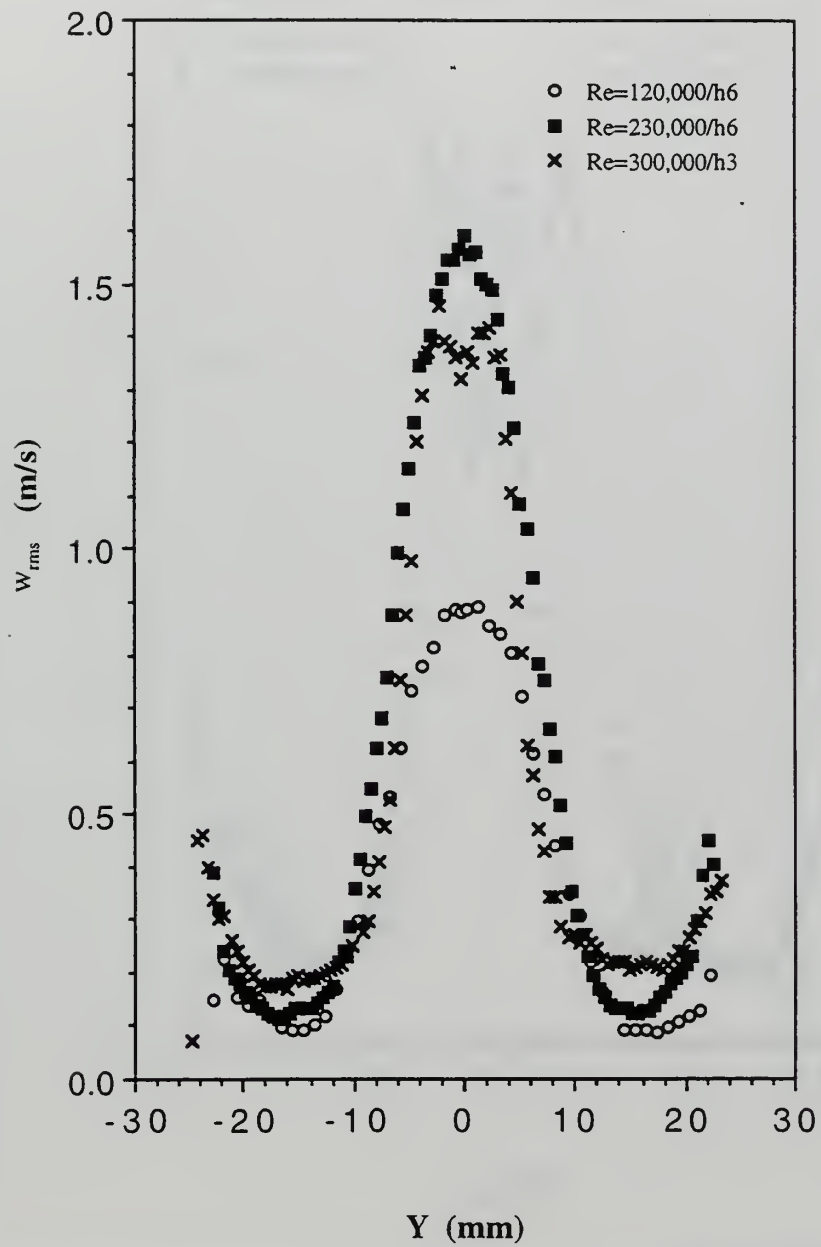


Figure 4-87.  $w_{rms}$  profiles in the wake region of various  $Re_D$ /tube flow states.



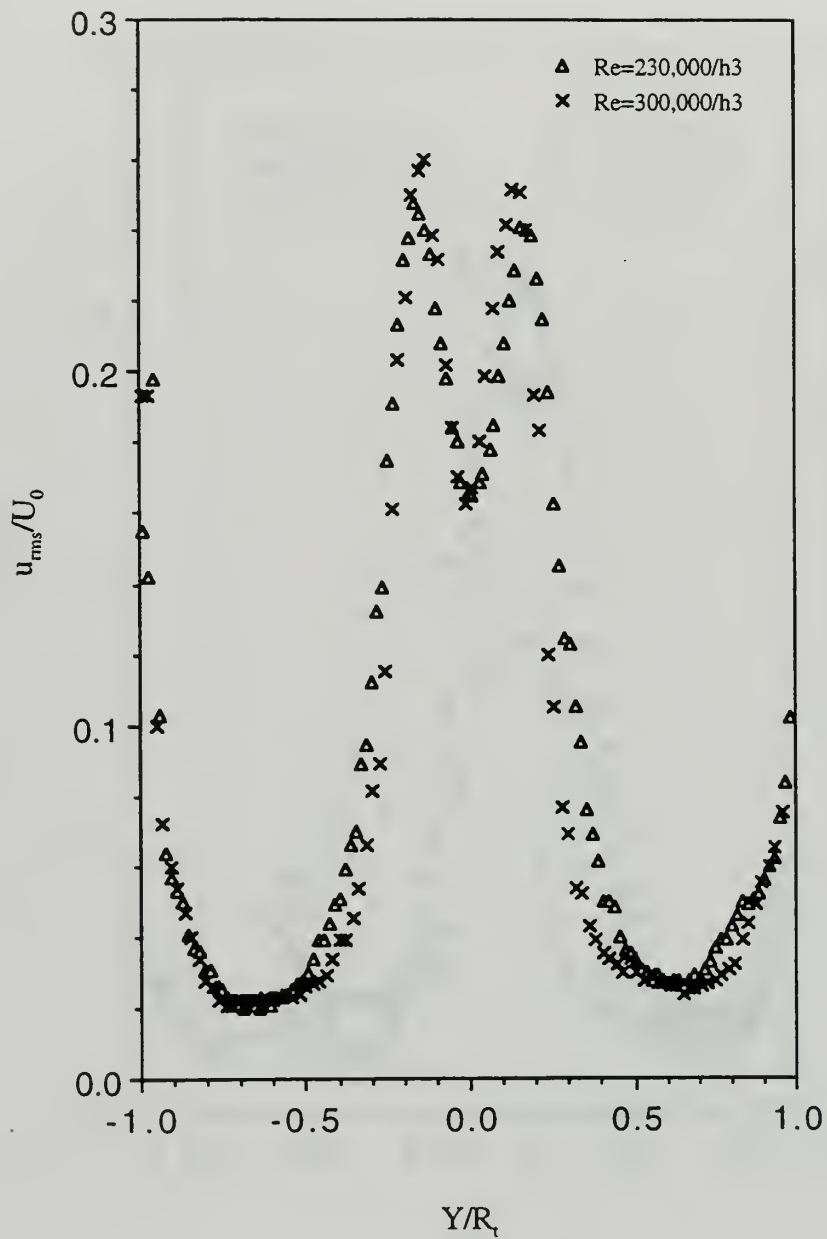


Figure 4-88.  $u_{rms}/U_0$  (vs.  $R_t$ ) profiles in the wake region of two high  $Re_D$  flow states.

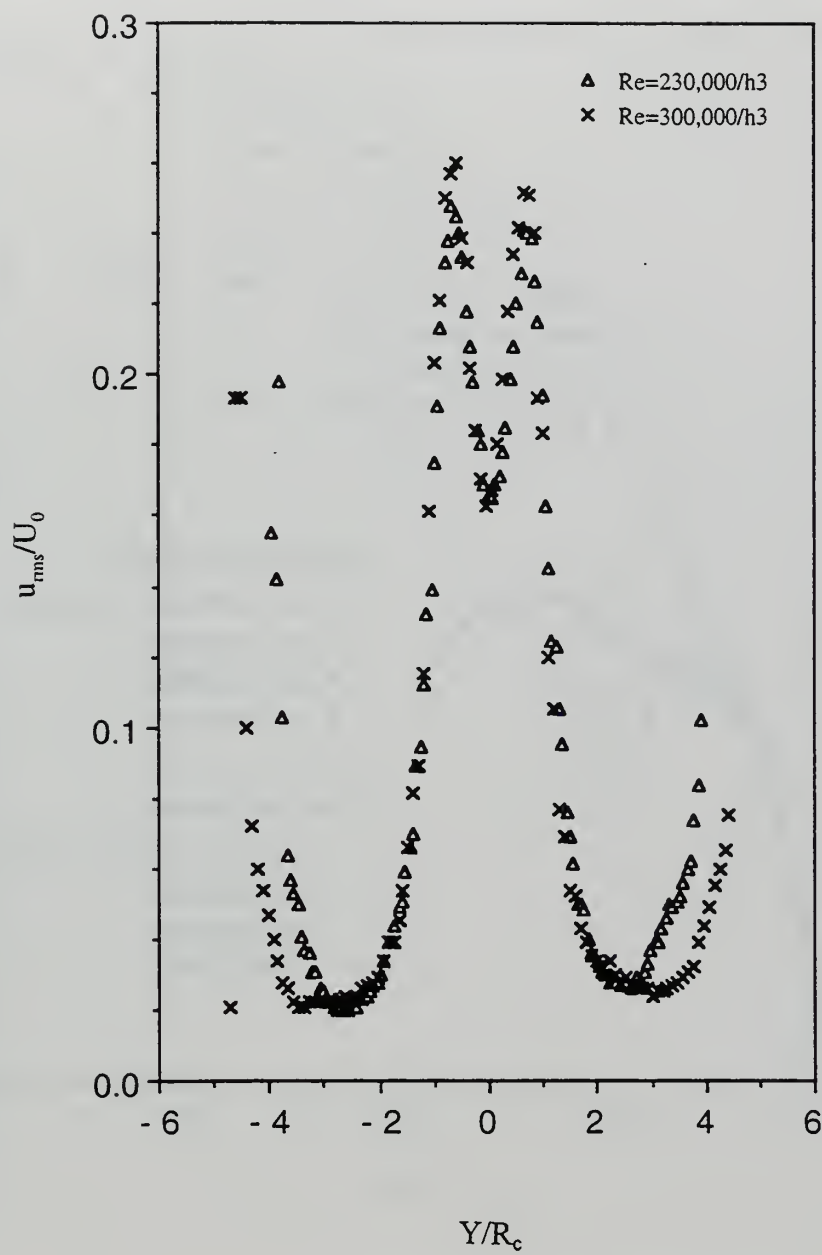


Figure 4-89.  $u_{rms}/U_0$  (vs.  $R_c$ ) profiles in the wake region of two high  $Re_D$  flow states.

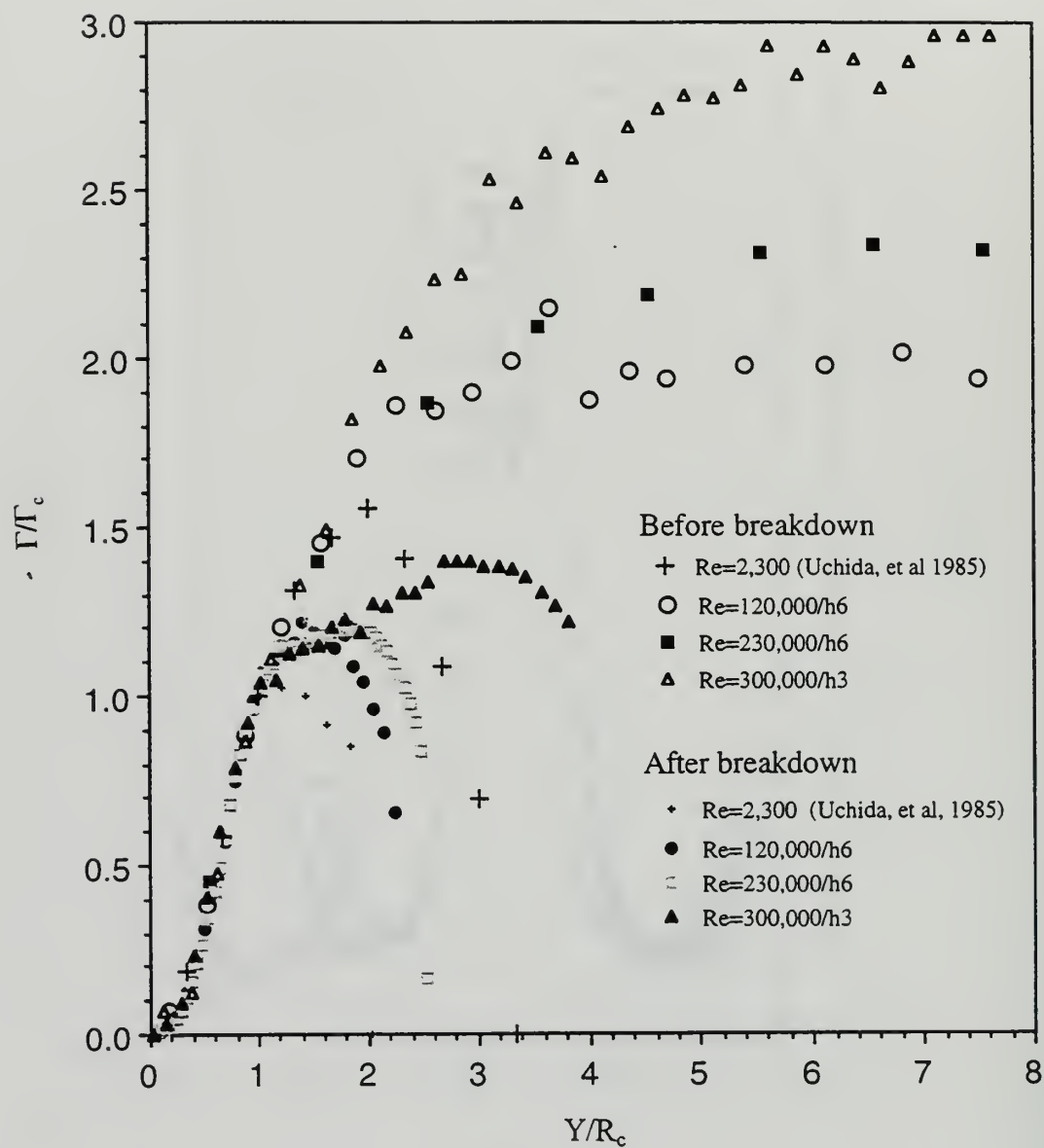


Figure 4-90.  $\Gamma_c/\Gamma$  profiles in various flow states.

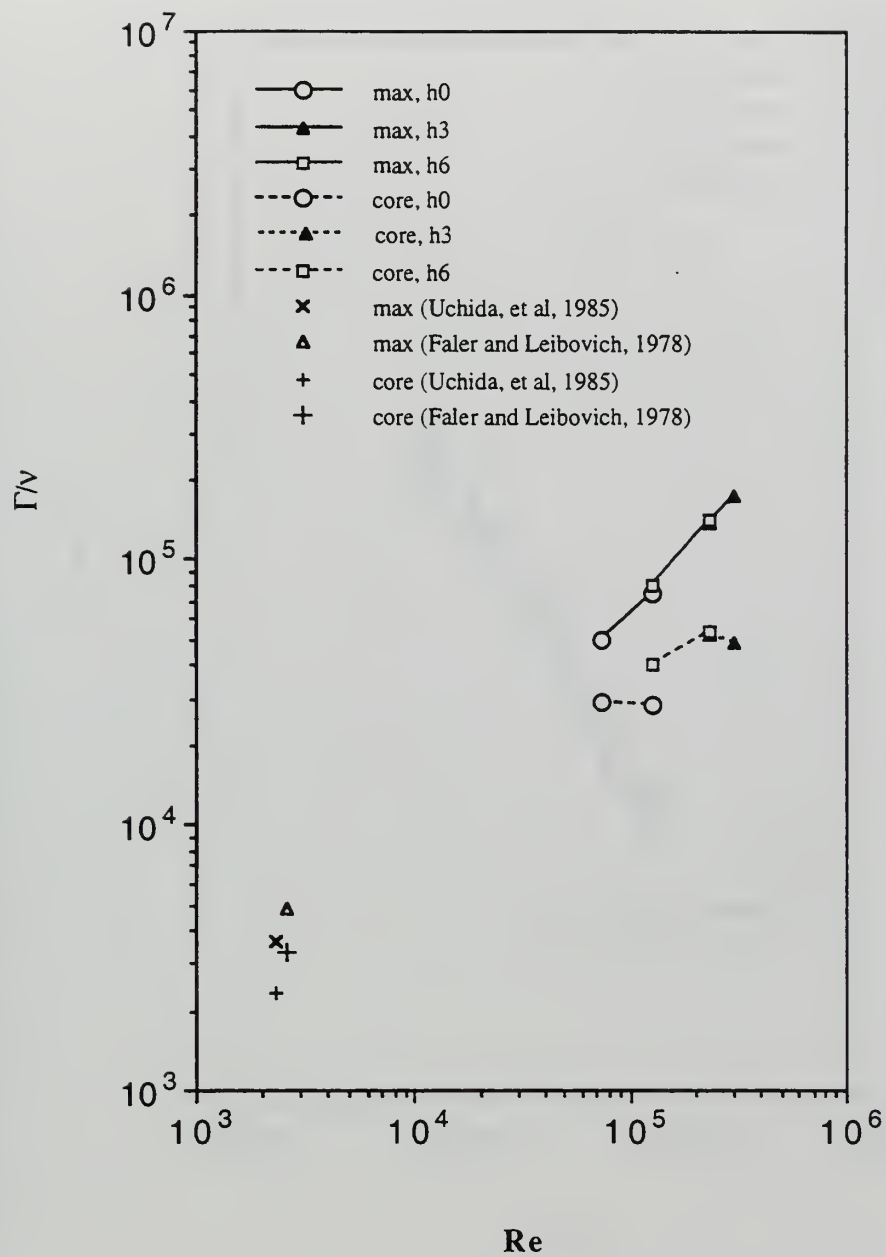


Figure 4-91. Variation of  $\Gamma/v$  and  $\Gamma_c/v$  with  $Re_D$ .

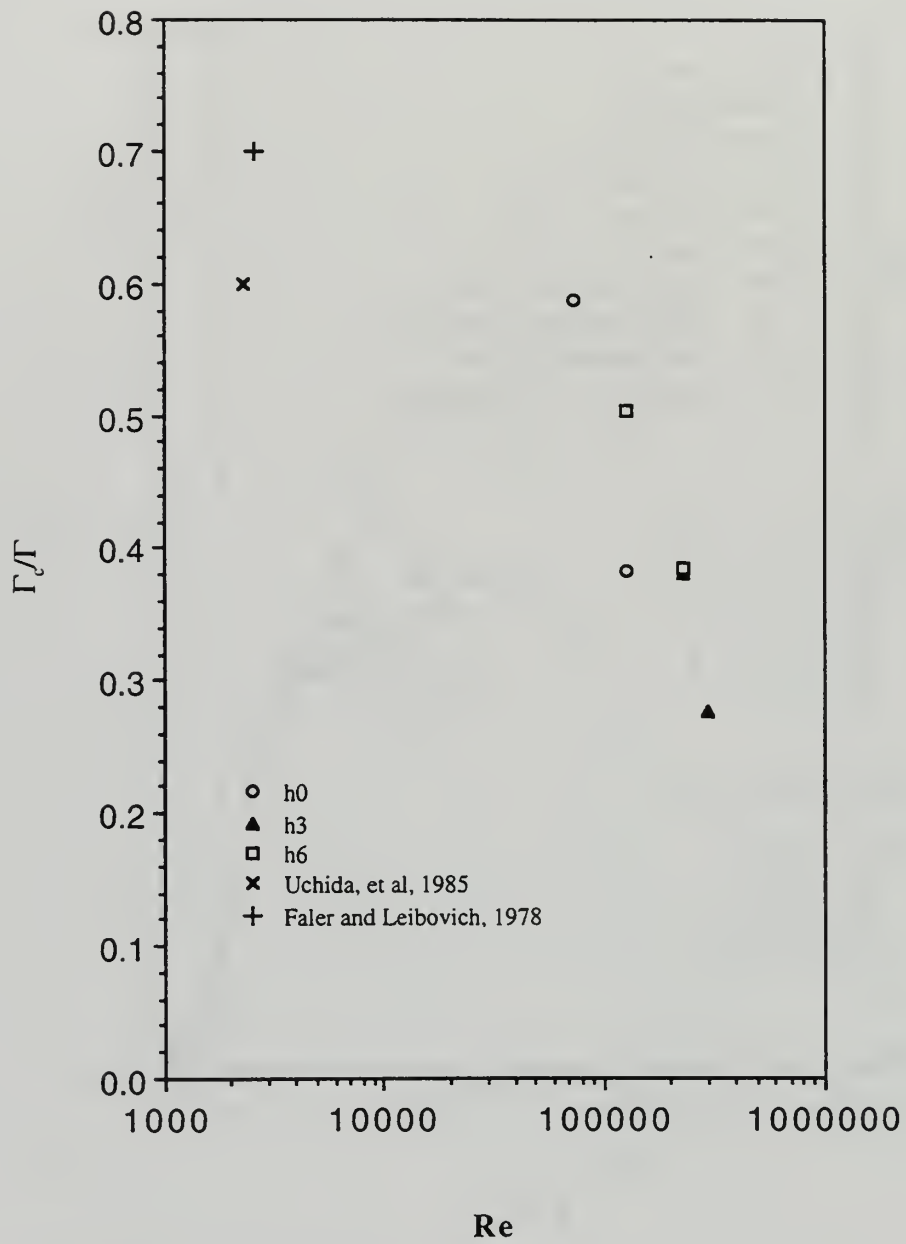


Figure 4-92. Variation of  $\Gamma_c/\Gamma$  with  $Re_D$ .



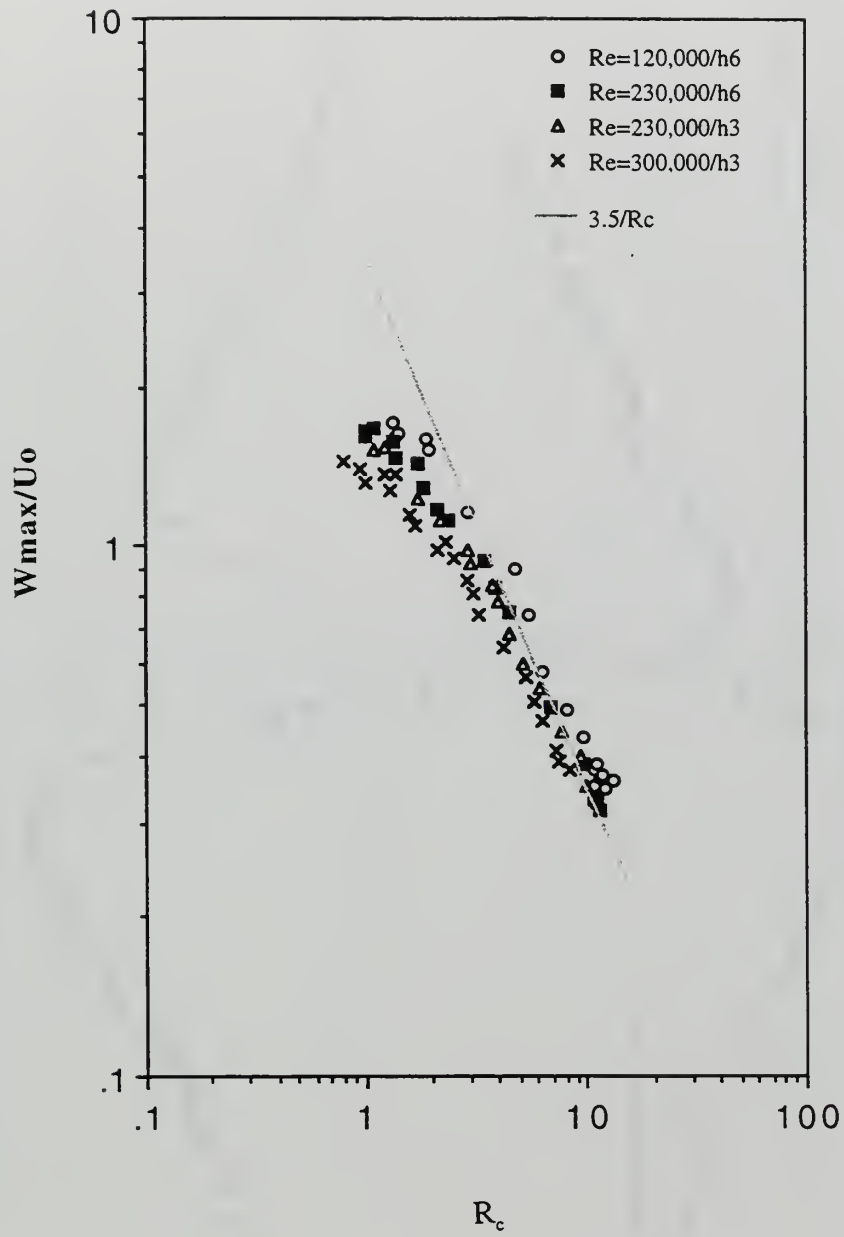


Figure 4-93.  $W_m/U_0$  vs.  $R_c$  for all flow configurations and sections.

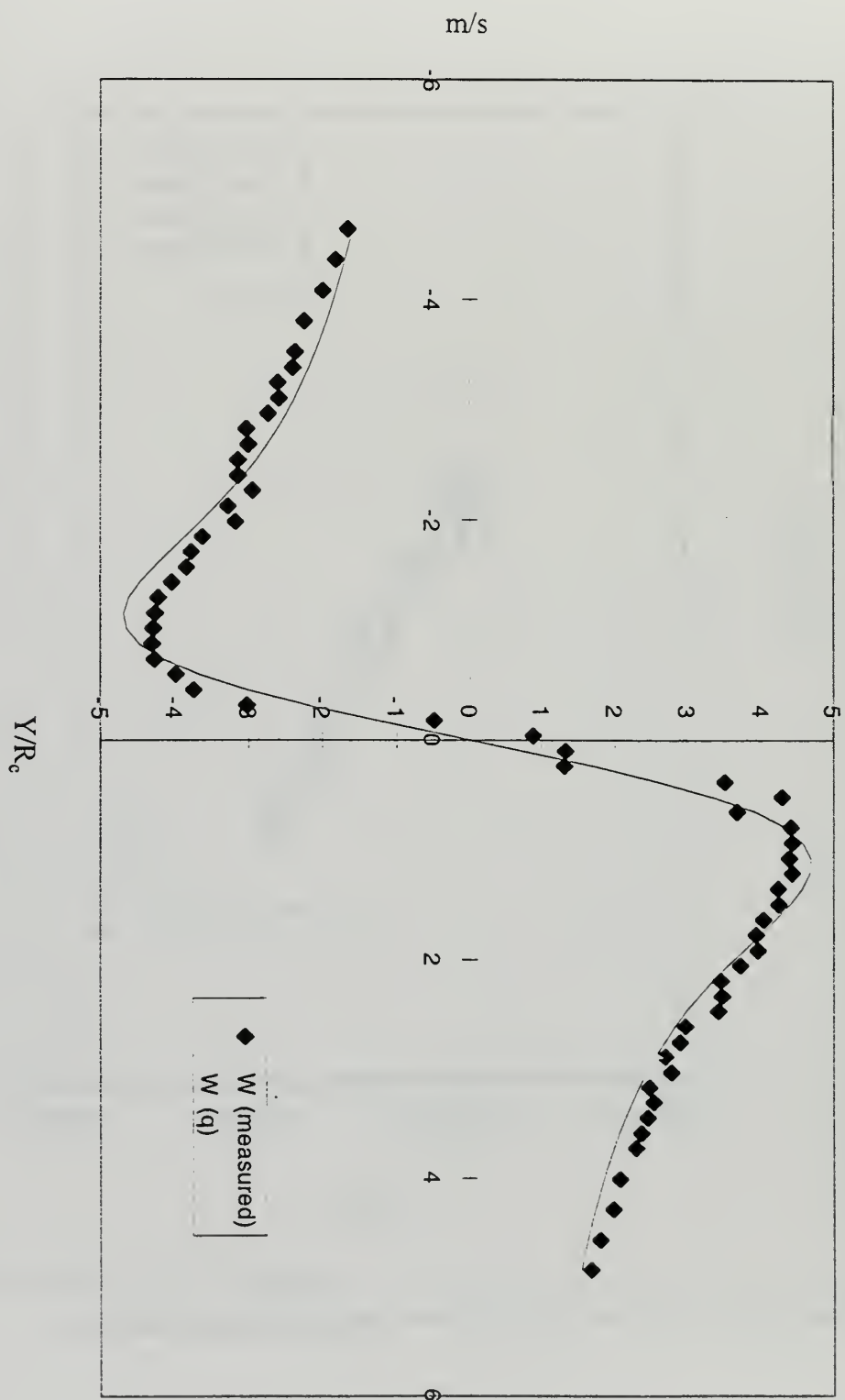


Figure 4-94. Measured and q-vortex inlet tangential velocity profiles of the  $Re_D = 120,000/h_6$  flow state.

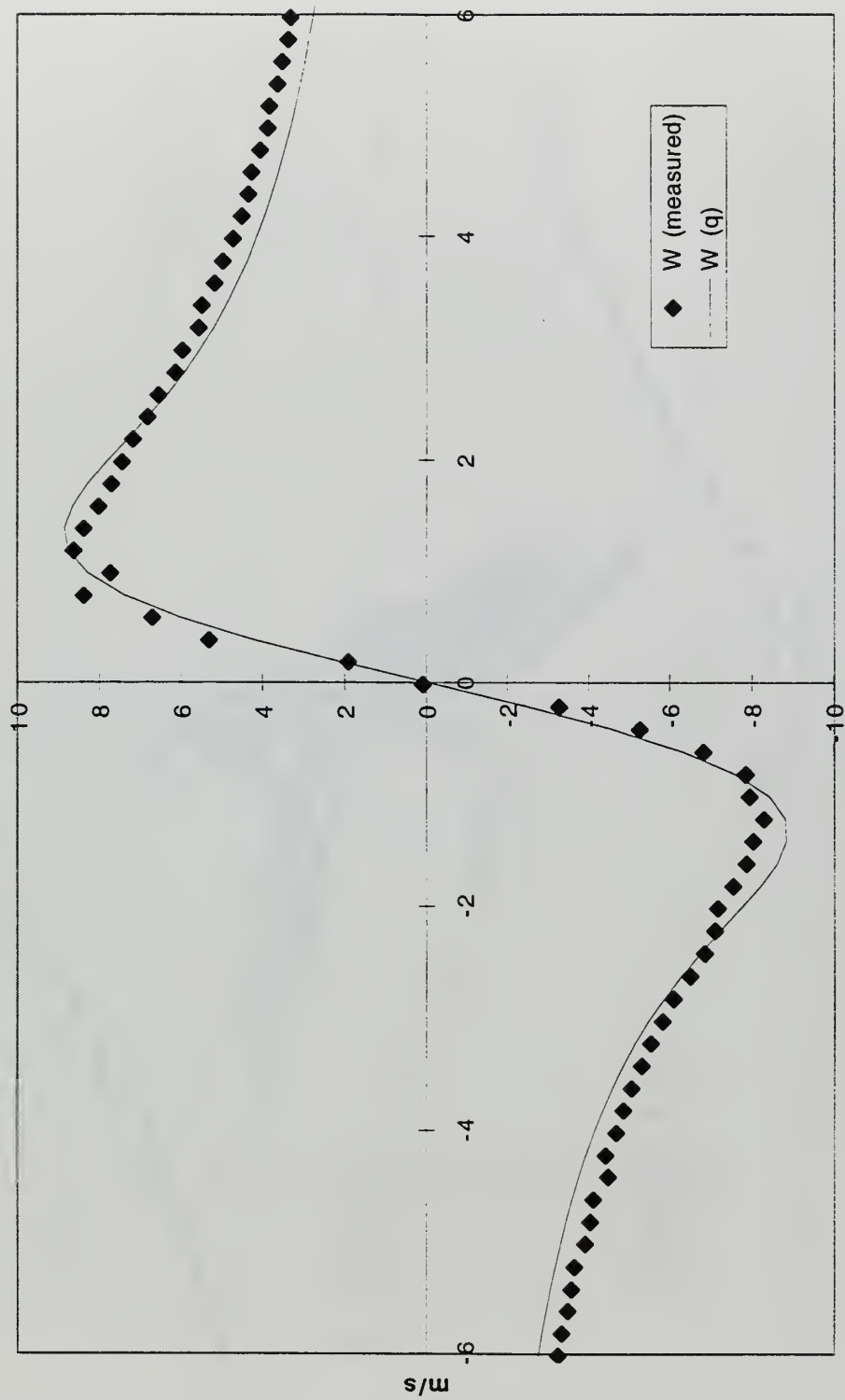


Figure 4-95. Measured and q-vortex inlet tangential velocity profiles of the  $Re_D = 230,000/h_6$  flow state.

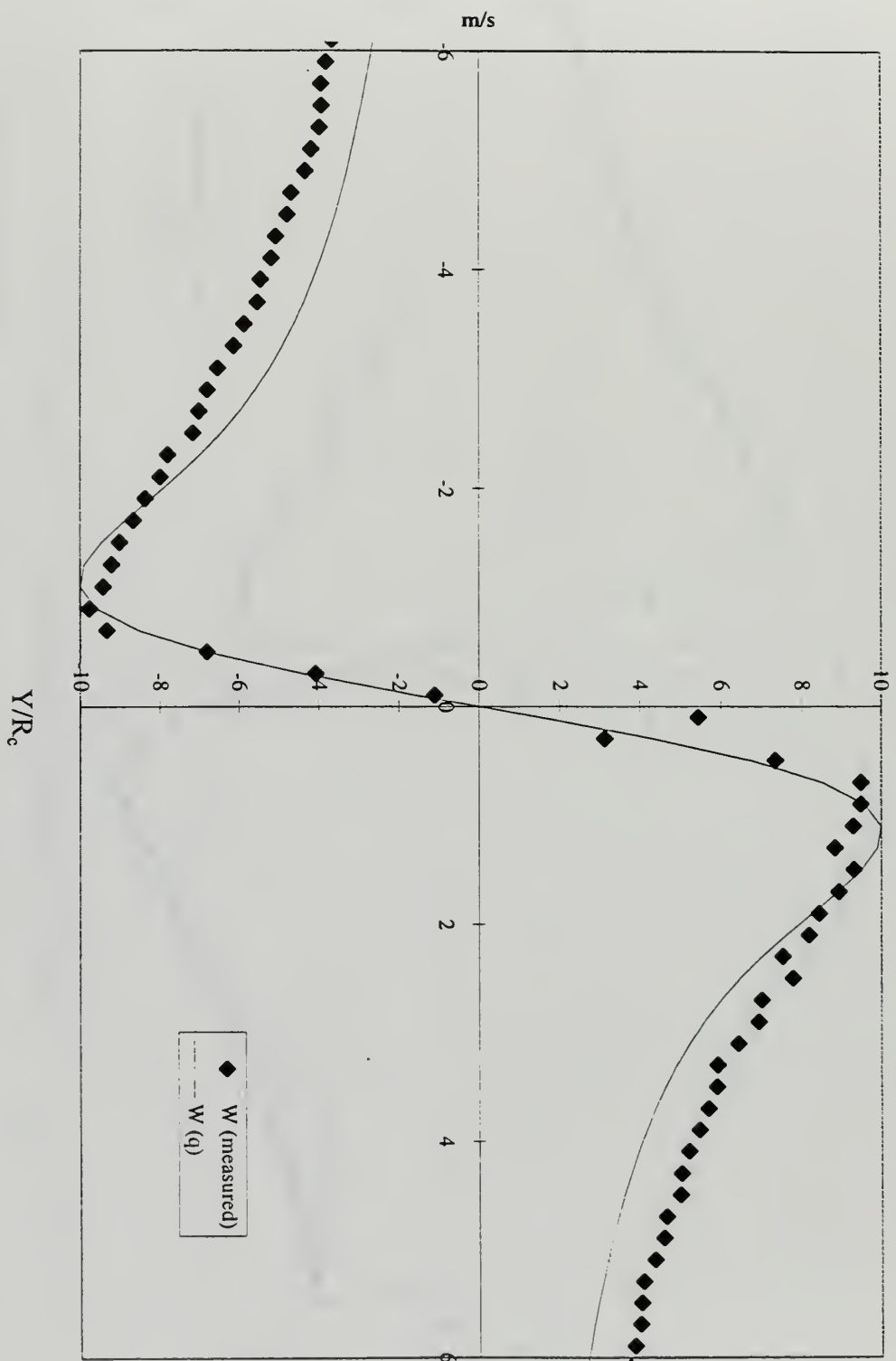


Figure 4-96. Measured and q-vortex inlet tangential velocity profiles of the  $Re_D = 300,000/h^3$  flow state.

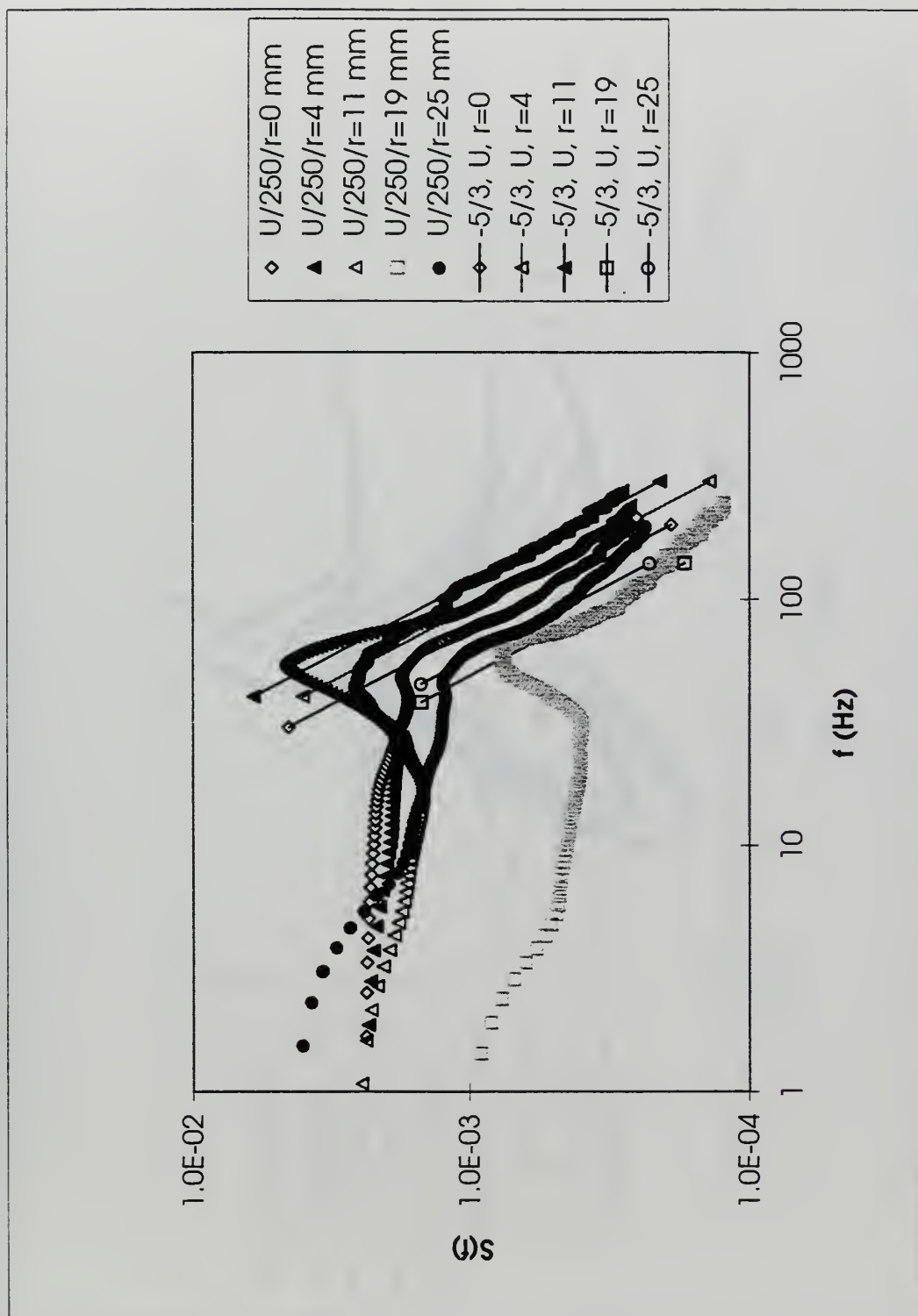


Figure 4-97. Spectra of U at X = 250 mm in the  $Re_D = 230,000/h6$  flow.





Figure 4-98. Spectra of  $W$  at  $X = 250$  mm in the  $Re_D = 230,000/h6$  flow.

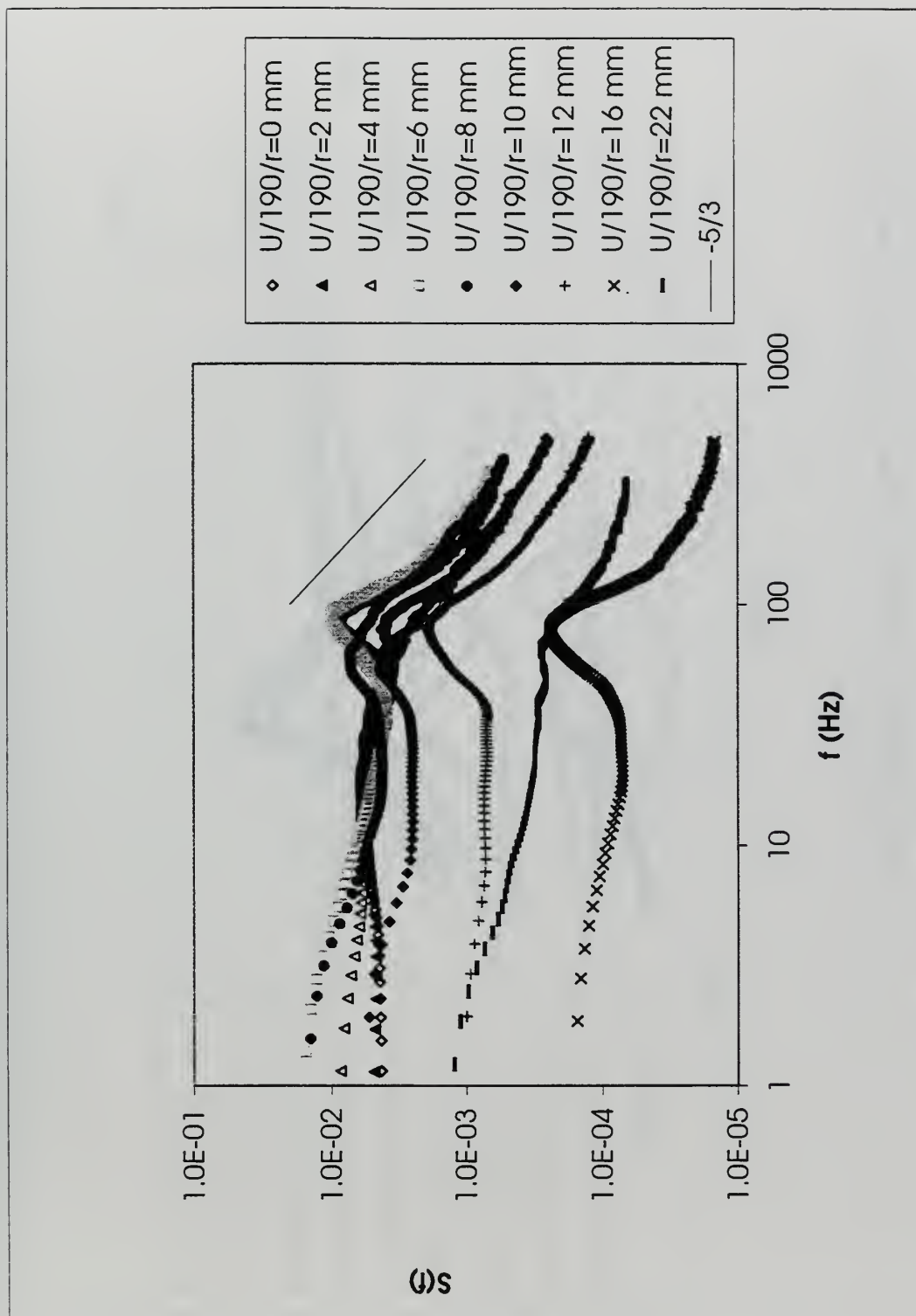


Figure 4-99. Spectra of U at X = 190 mm in the  $Re_D = 230,000/h6$  flow.

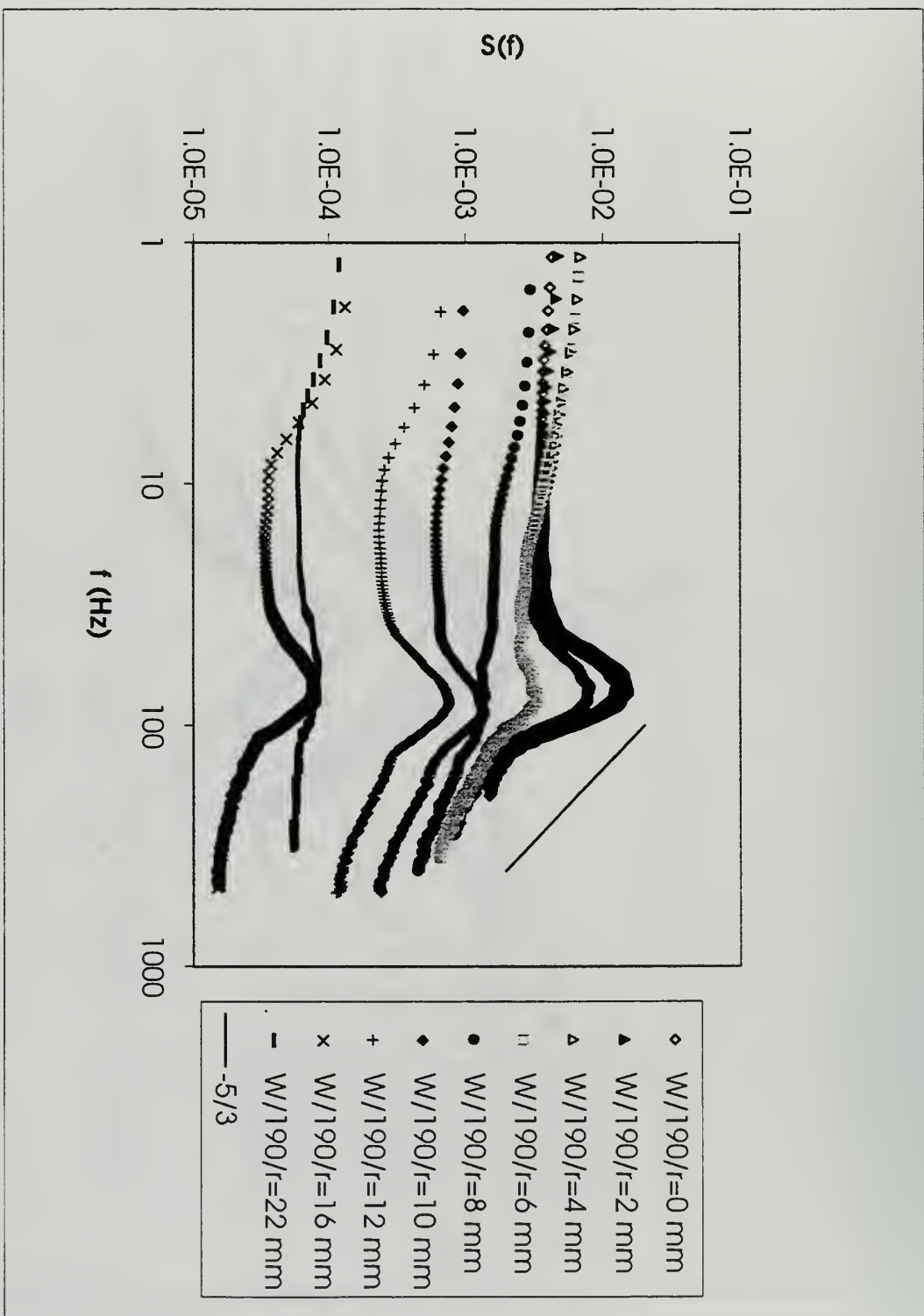


Figure 4-100. Spectra of  $W$  at  $X = 190$  mm in the  $Re_D = 230,000/h_6$  flow.

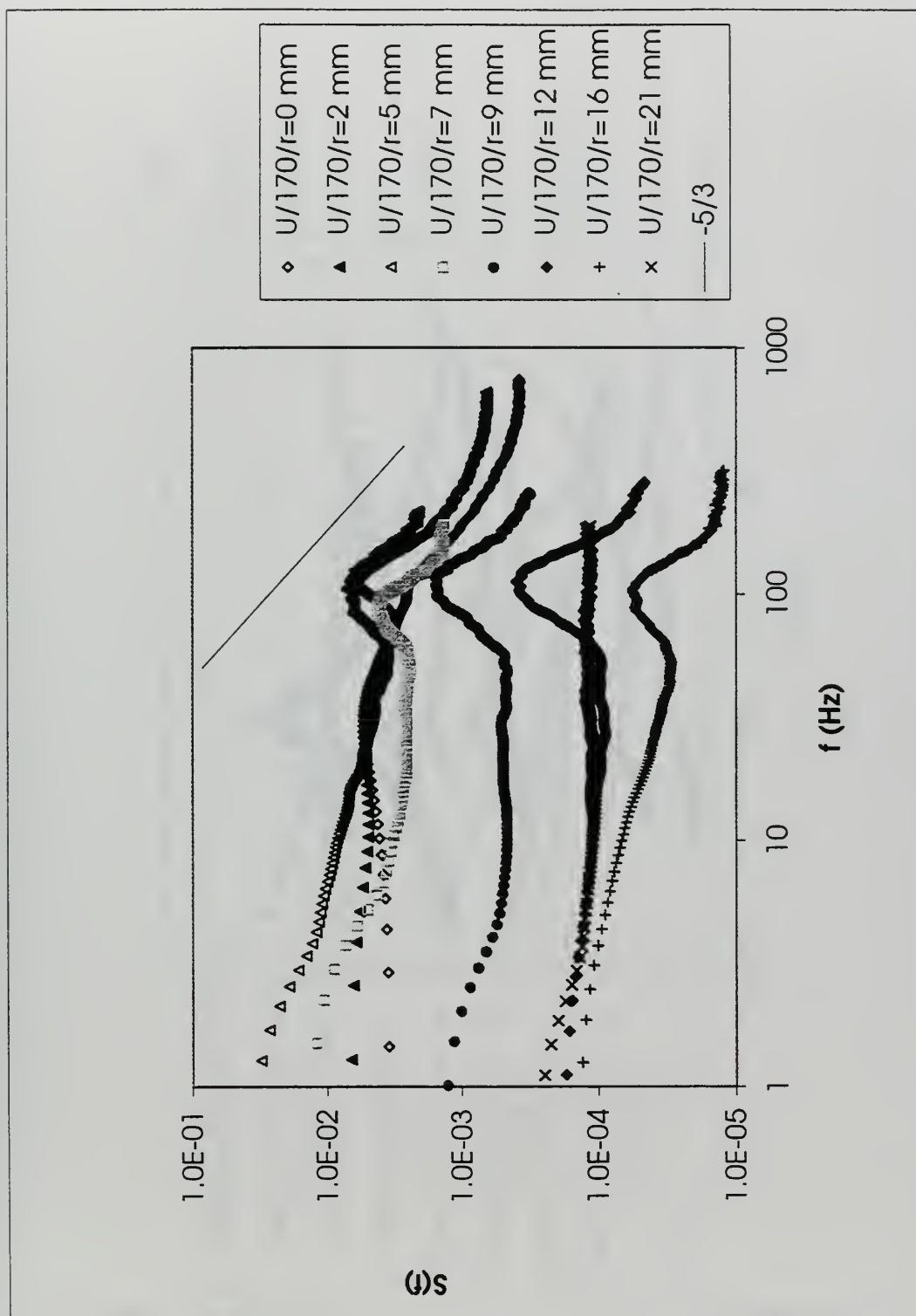


Figure 4-101. Spectra of  $U$  at  $X = 170$  mm in the  $Re_D = 230,000/h6$  flow.

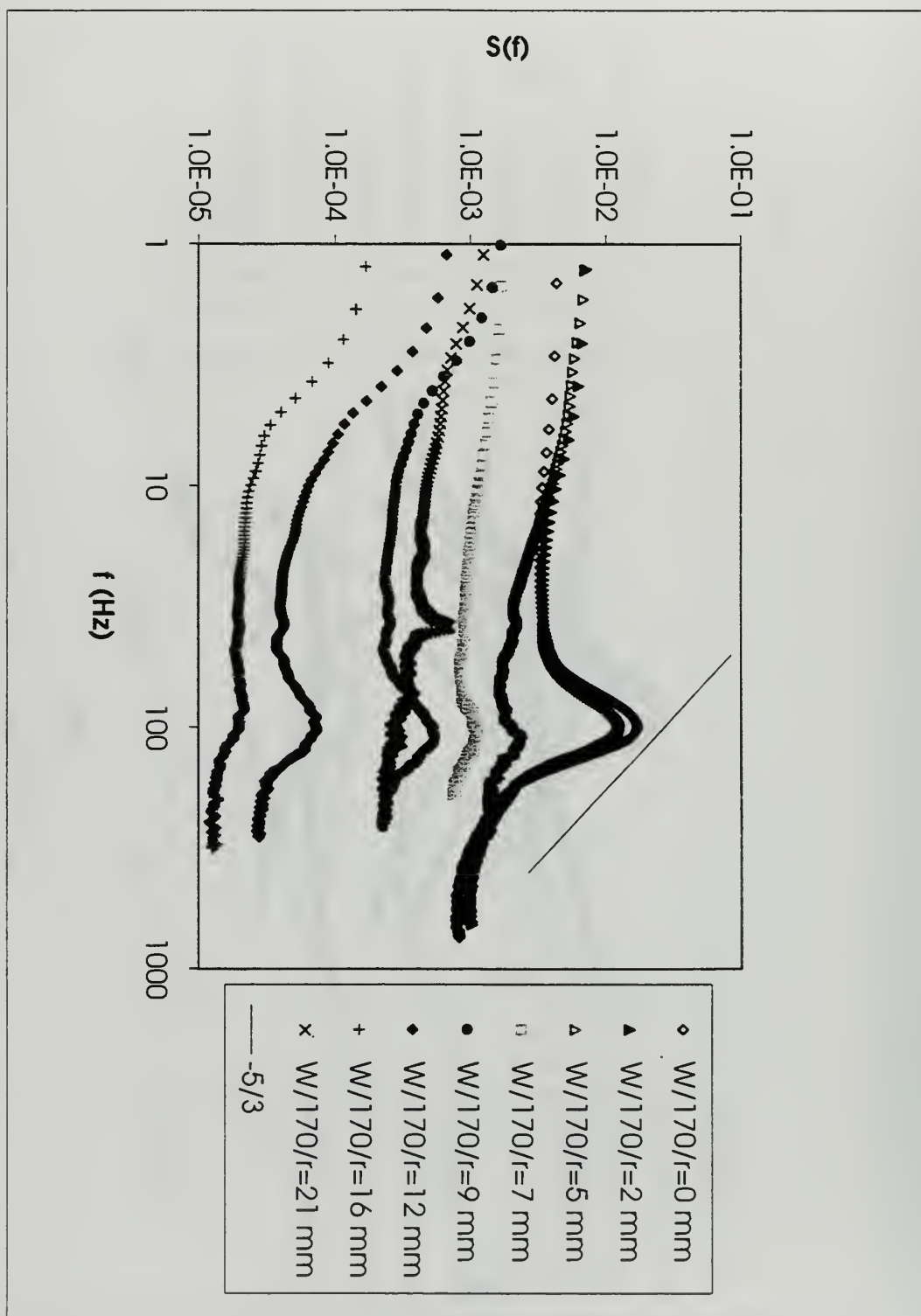


Figure 4-102. Spectra of  $W$  at  $X = 170$  mm in the  $Re_D = 230,000/h_6$  flow.



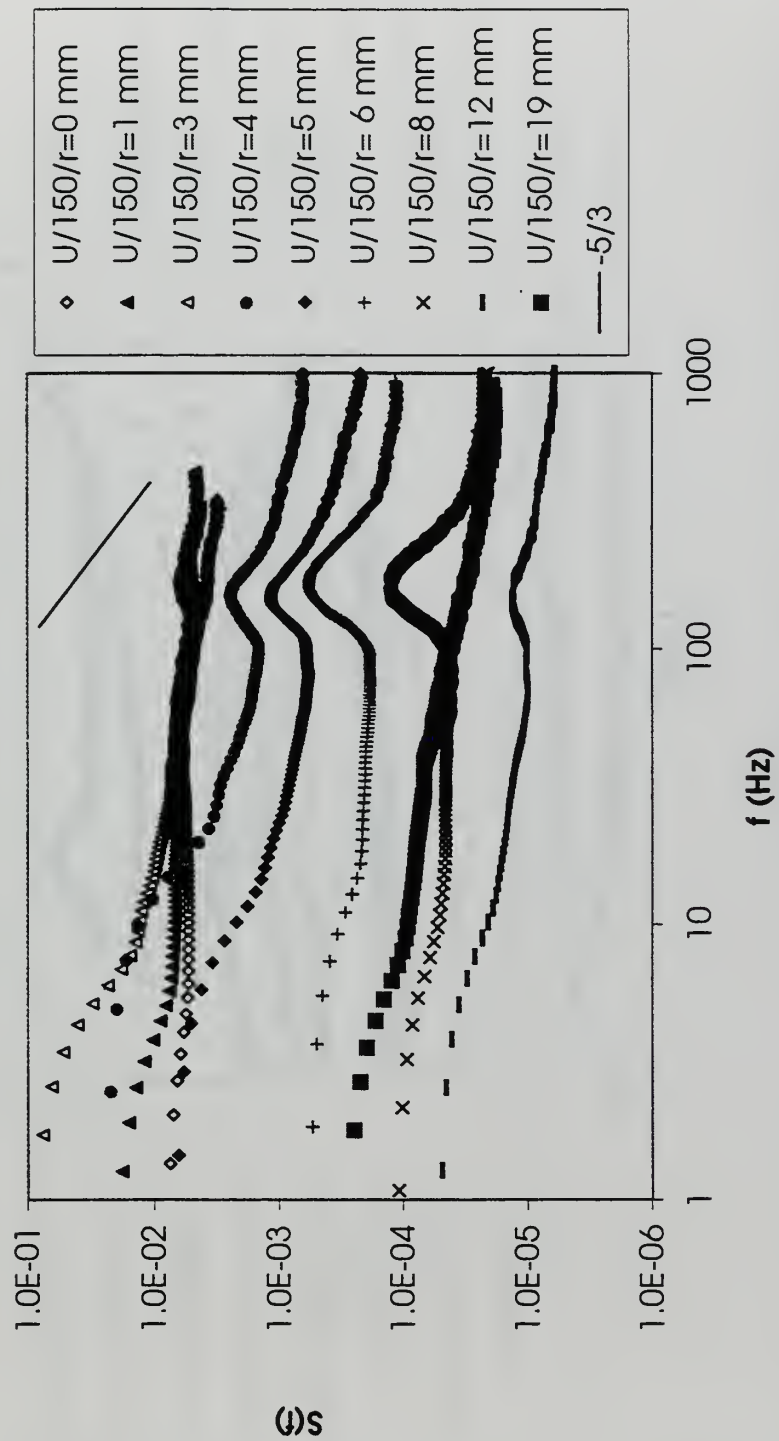


Figure 4-103. Spectra of  $U$  at  $X = 150$  in the  $Re_D = 230,000/h/6$  flow.

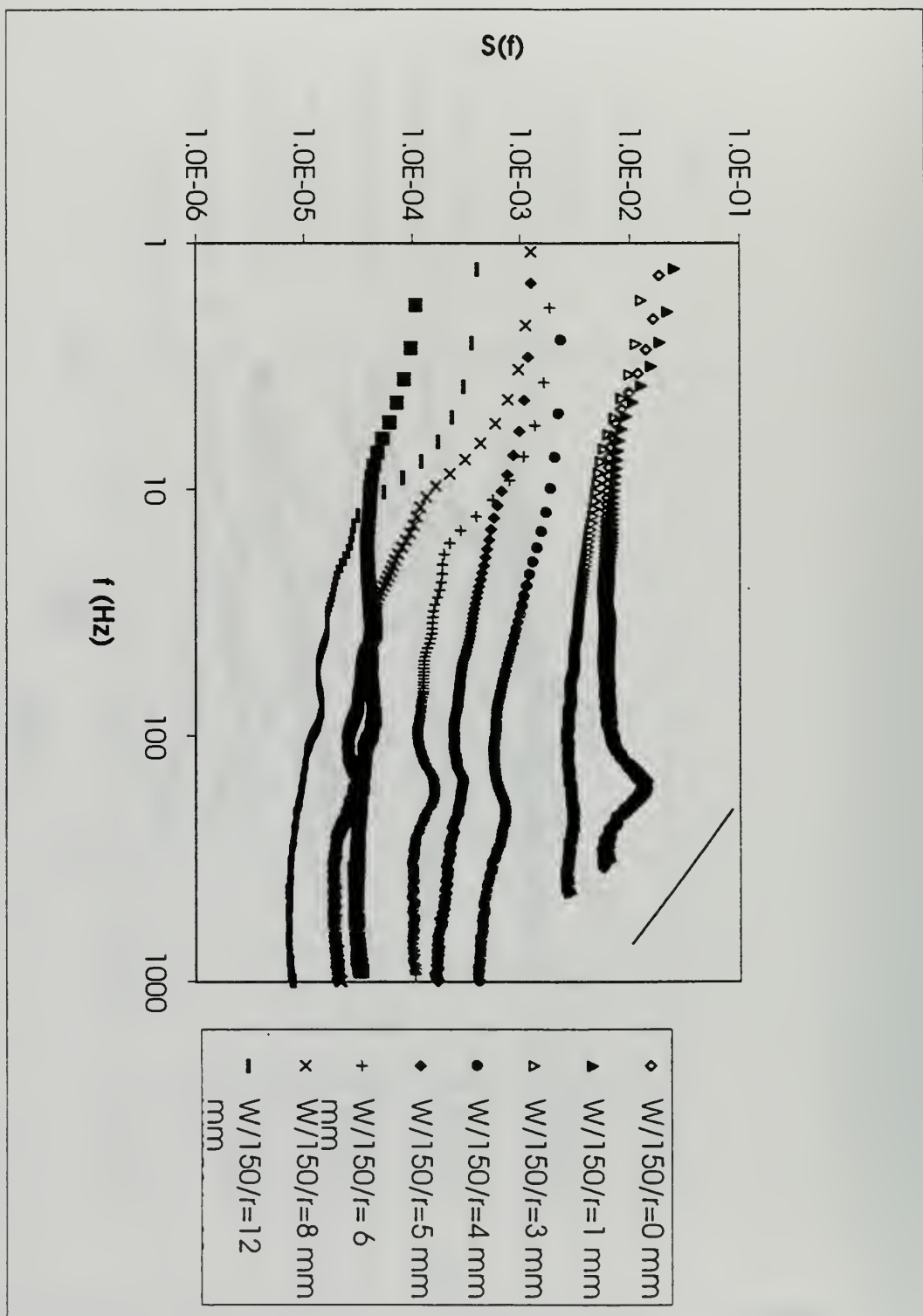


Figure 4-104. Spectra of  $W$  at  $X = 150$  mm in the  $Re_D = 230,000/h_6$  flow.

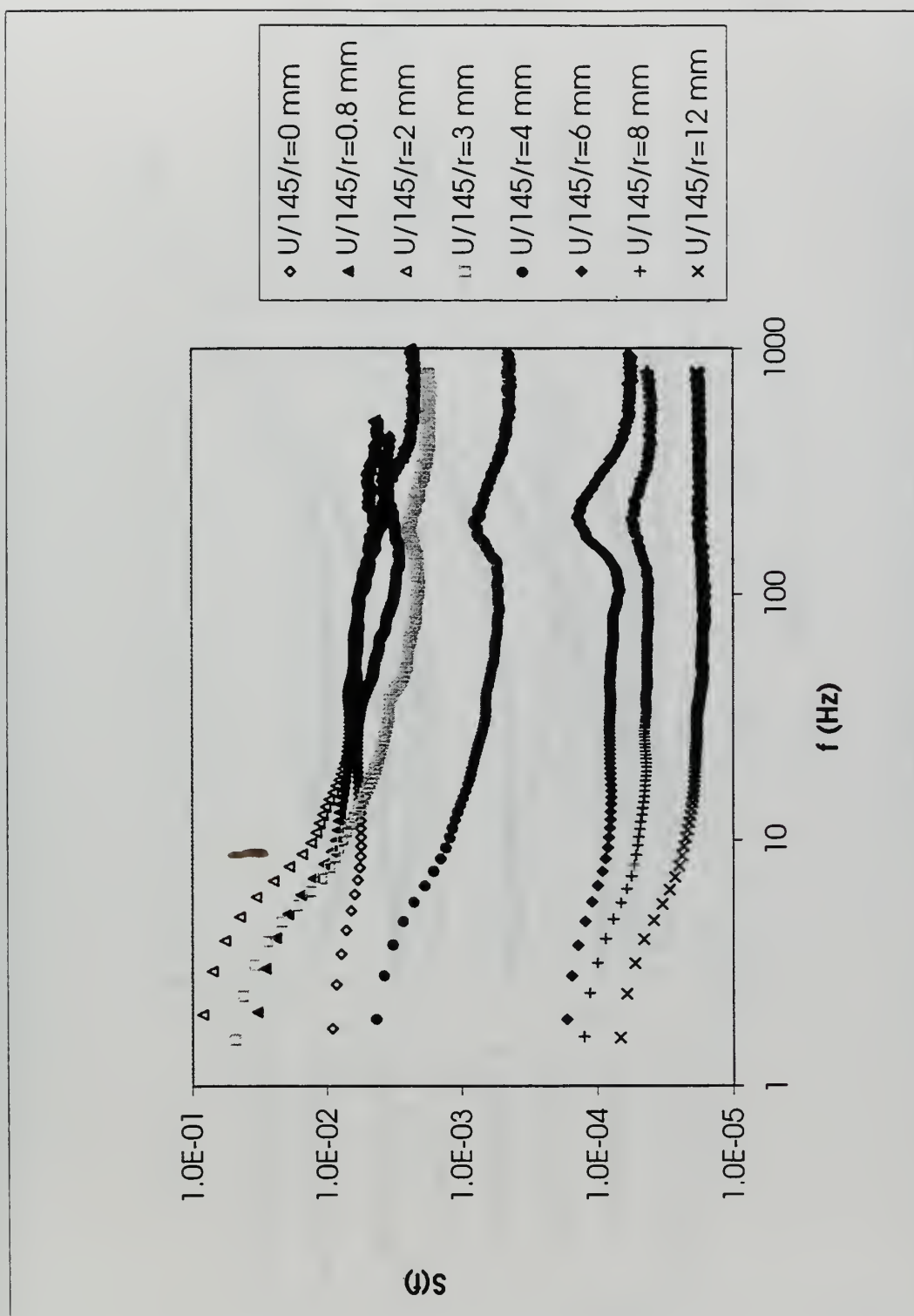


Figure 4-105. Spectra of  $U$  at  $X = 145$  mm in the  $Re_D = 230,000/h_6$  flow.

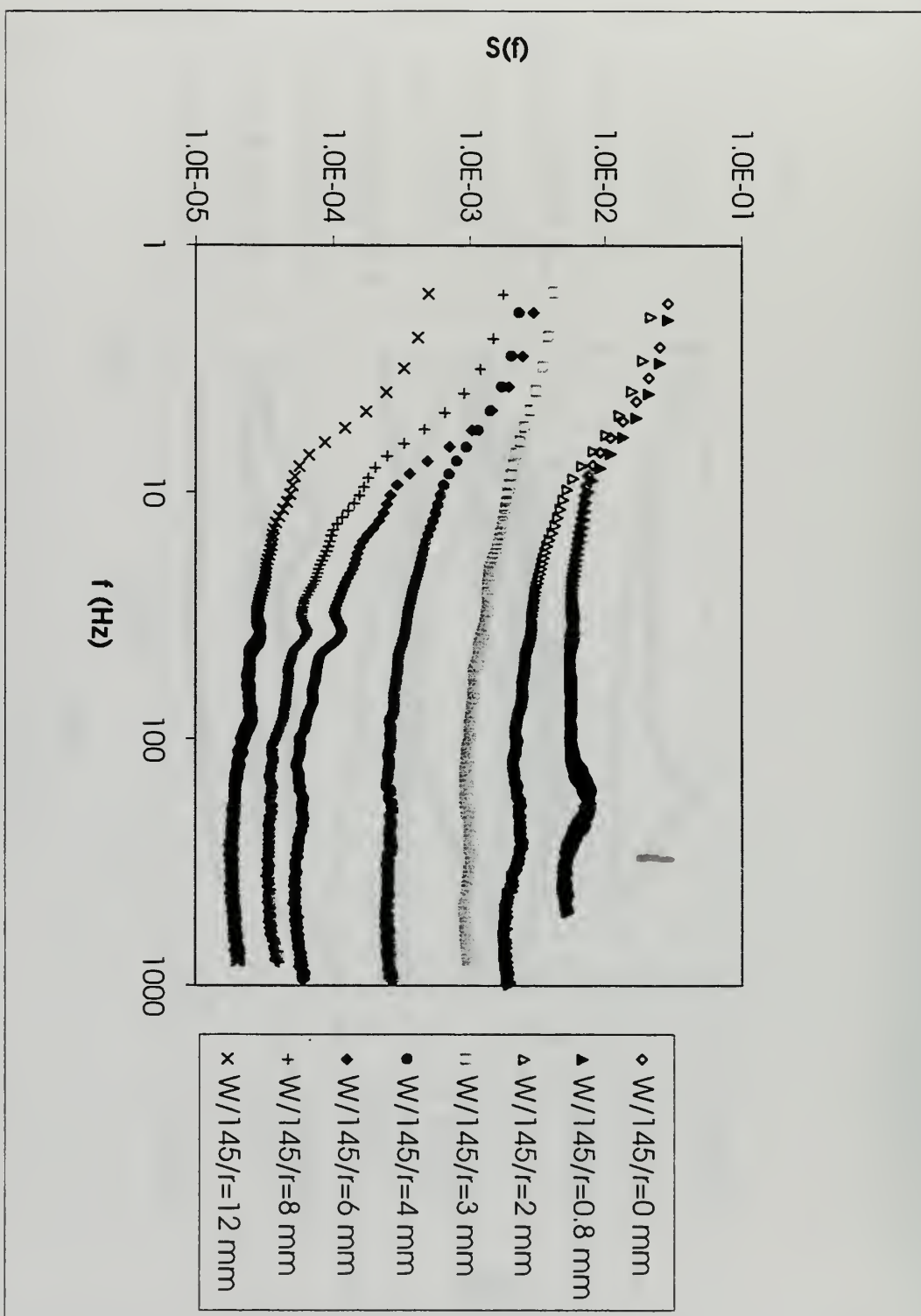


Figure 4-106. Spectra of  $W$  at  $X = 145$  mm in the  $Re_D = 230,000/h6$  flow.

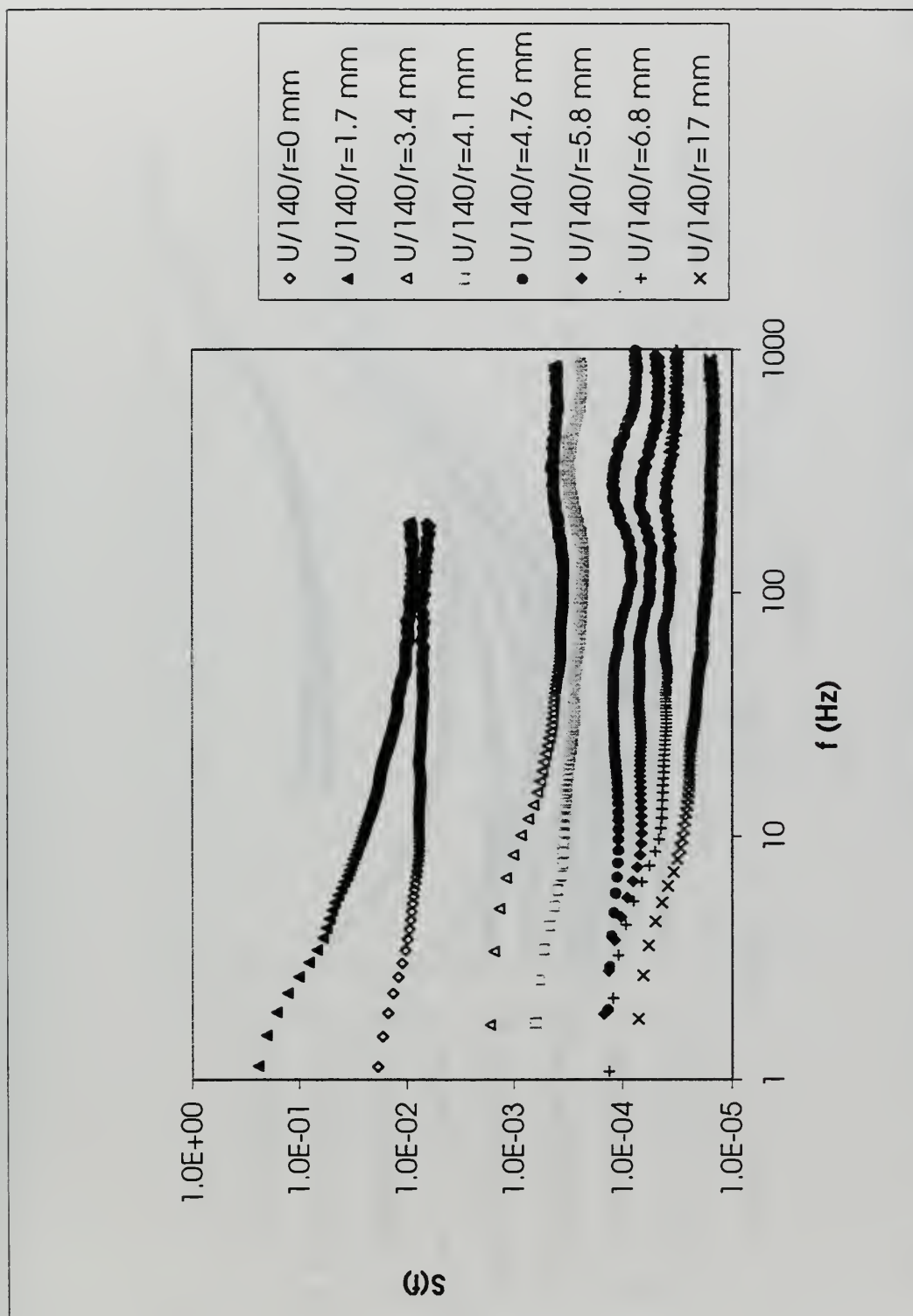


Figure 4-107. Spectra of U at  $X = 140$  mm in the  $Re_D = 230,000/h6$  flow.



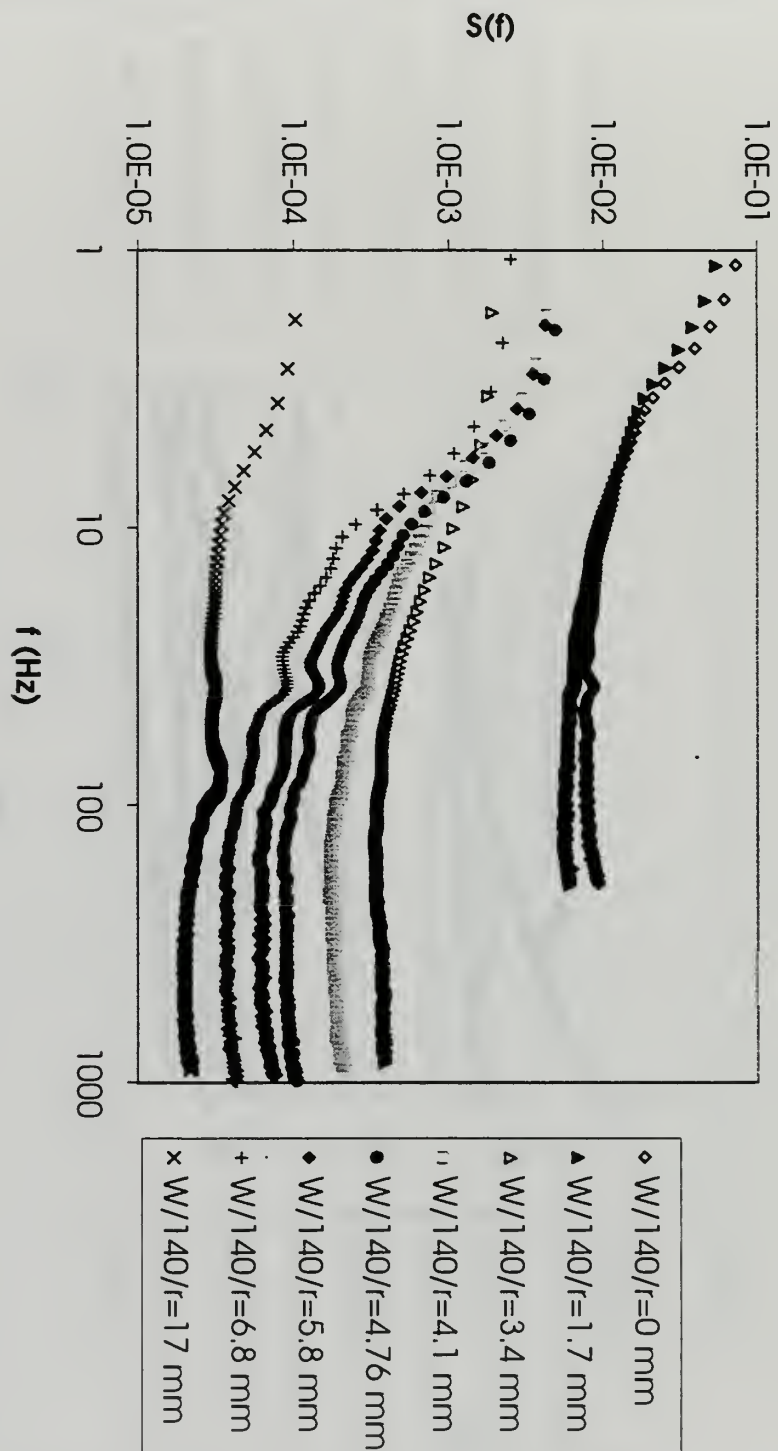


Figure 4-108. Spectra of  $W$  at  $X = 140$  mm in the  $Re_D = 230,000/h6$  flow.

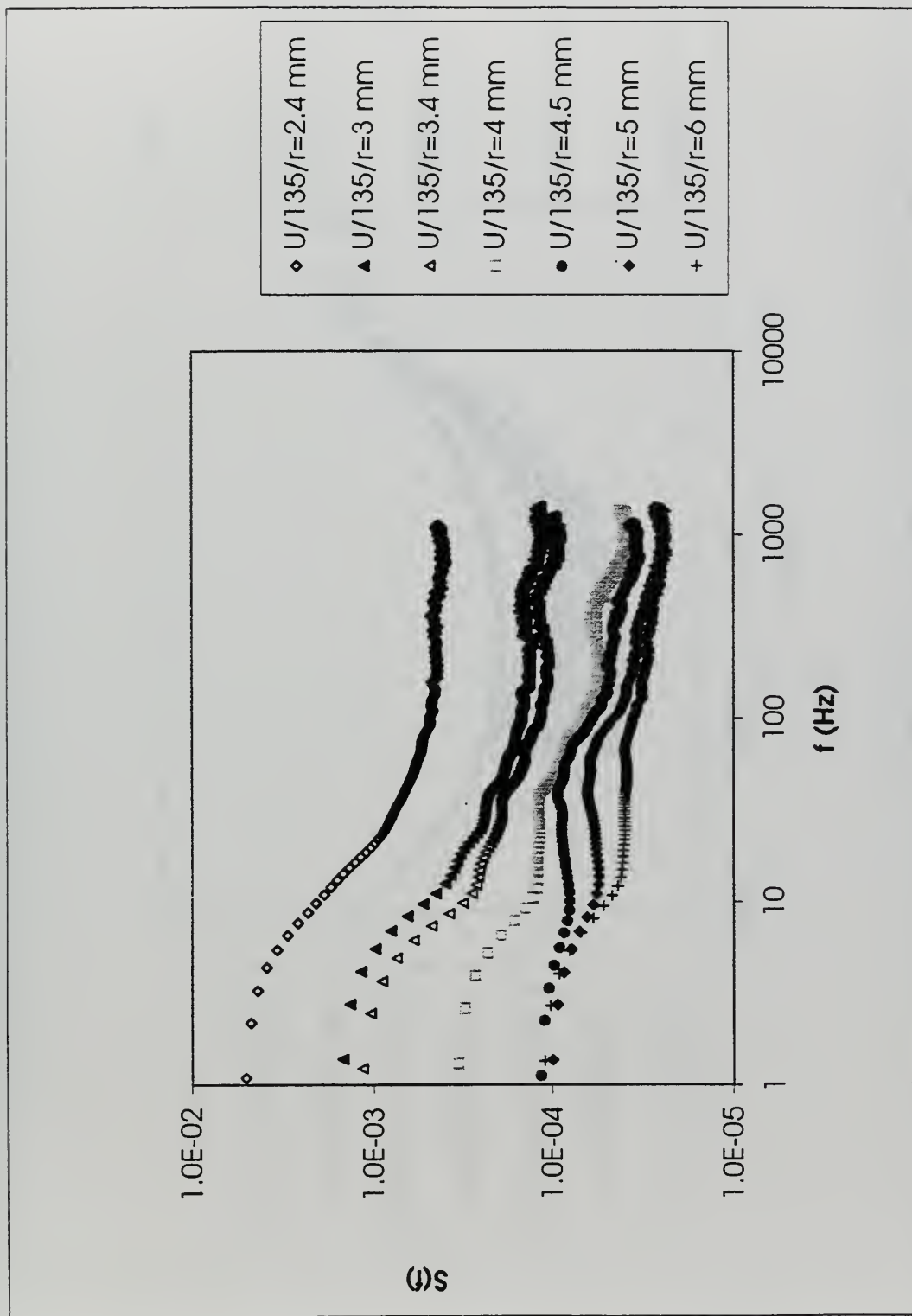


Figure 4-109. Spectra of  $U$  at  $X = 135$  mm in the  $Re_D = 230,000/h_6$  flow.

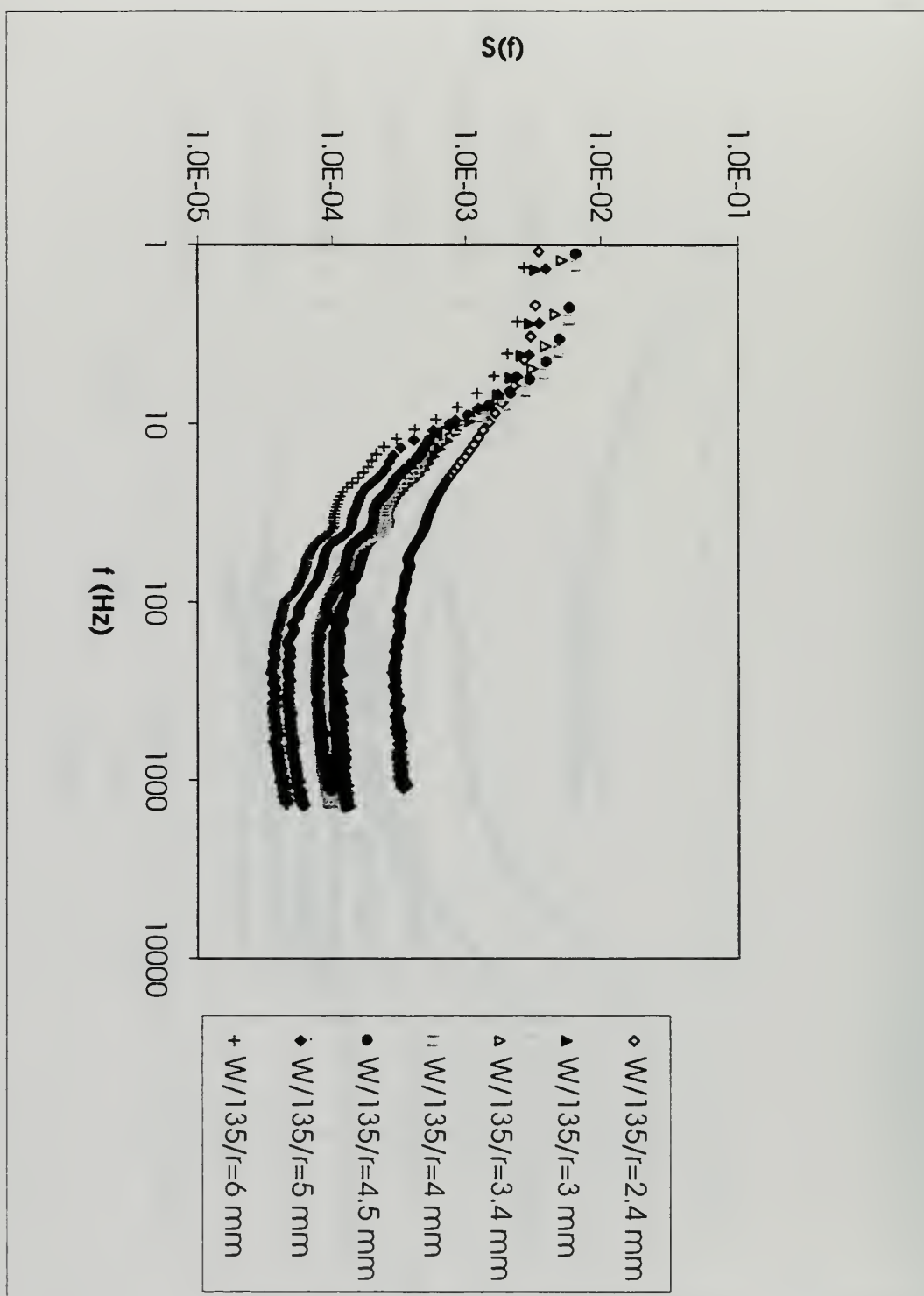


Figure 4-110. Spectra of  $W$  at  $X = 135$  mm in the  $Re_D = 230,000/h6$  flow.

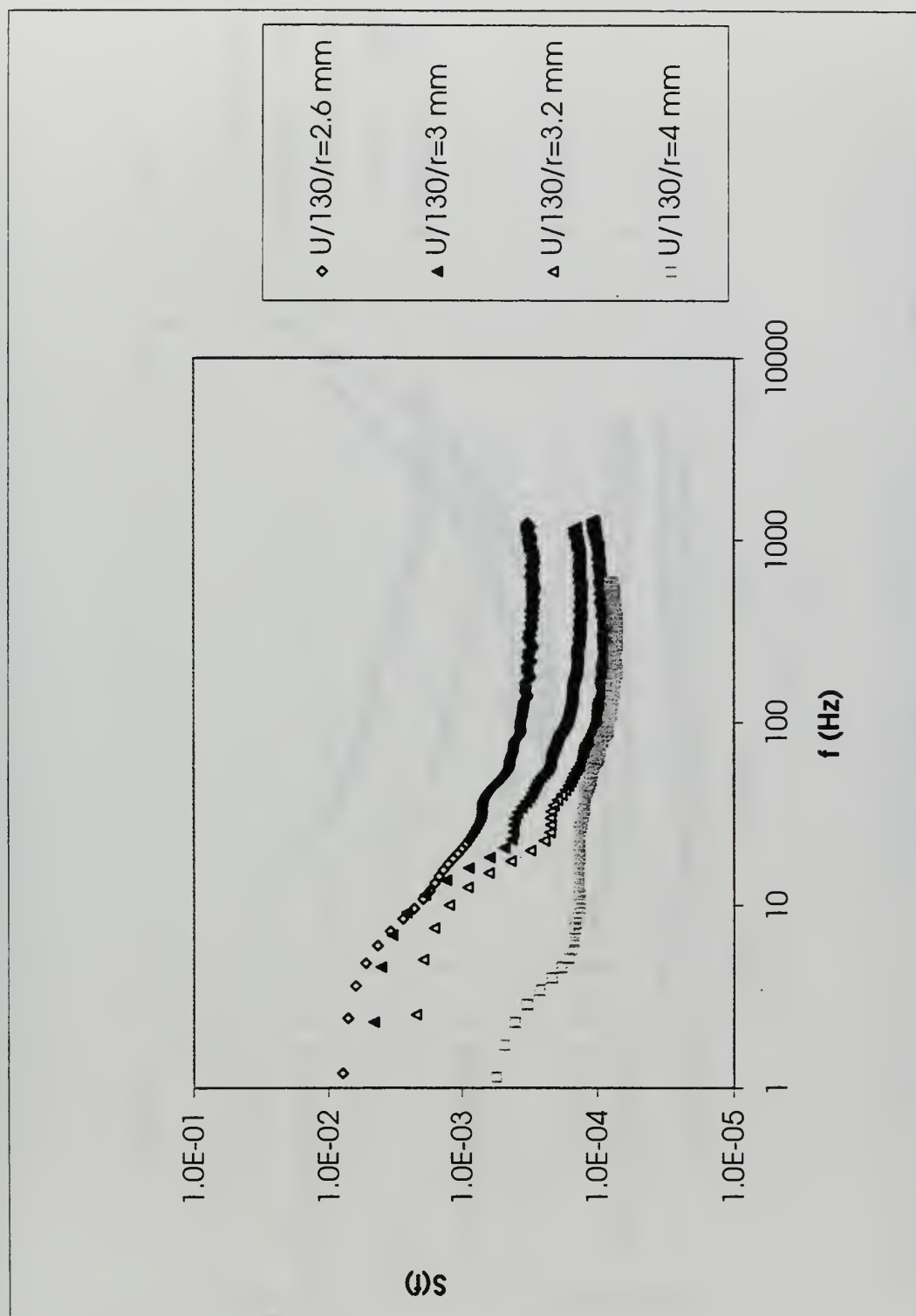


Figure 4-111. Spectra of  $U$  at  $X = 130$  mm in the  $Re_D = 230,000/h6$  flow.

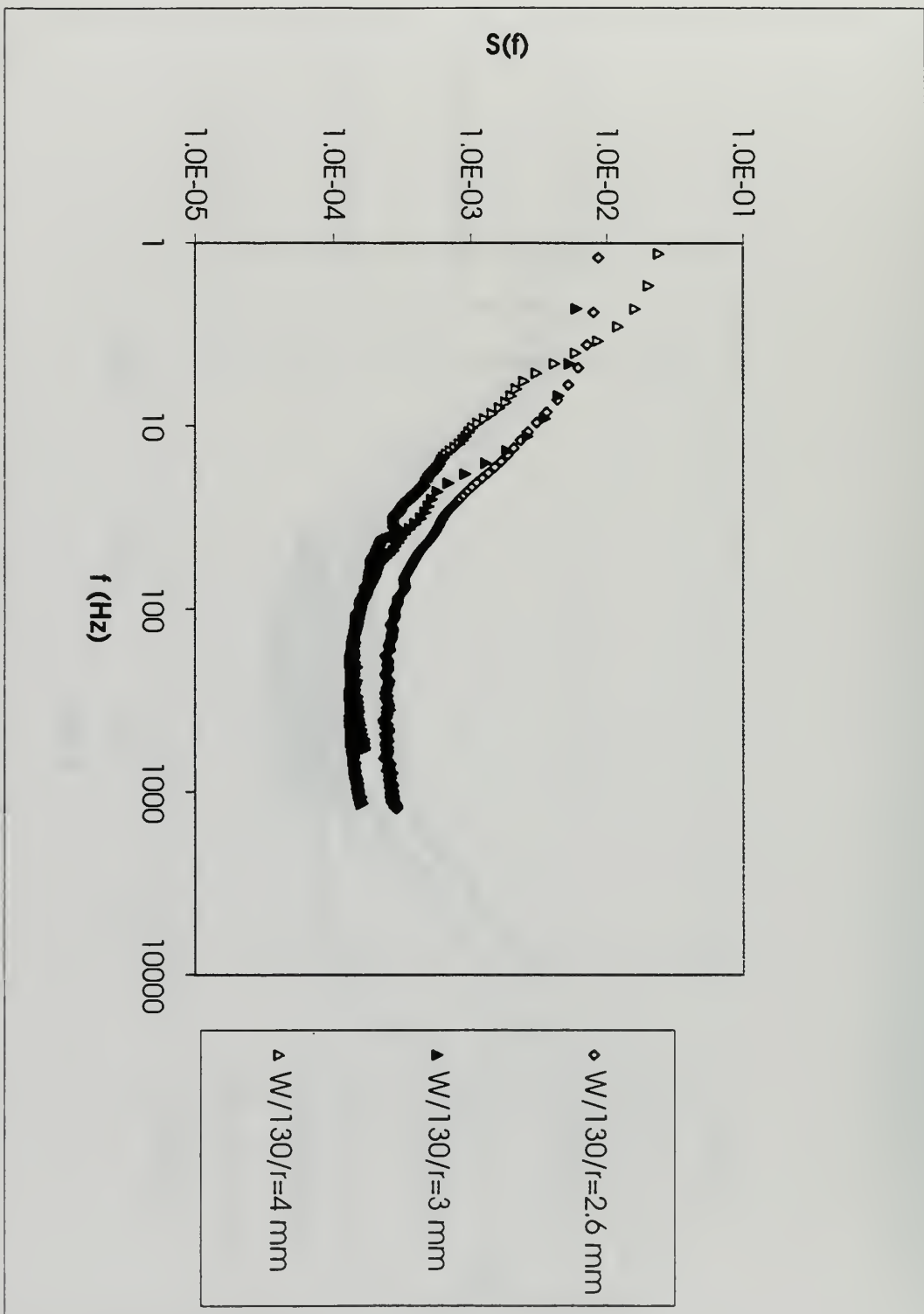


Figure 4-112. Spectra of  $W$  at  $X = 130$  mm in the  $Re_D = 230,000/h6$  flow.



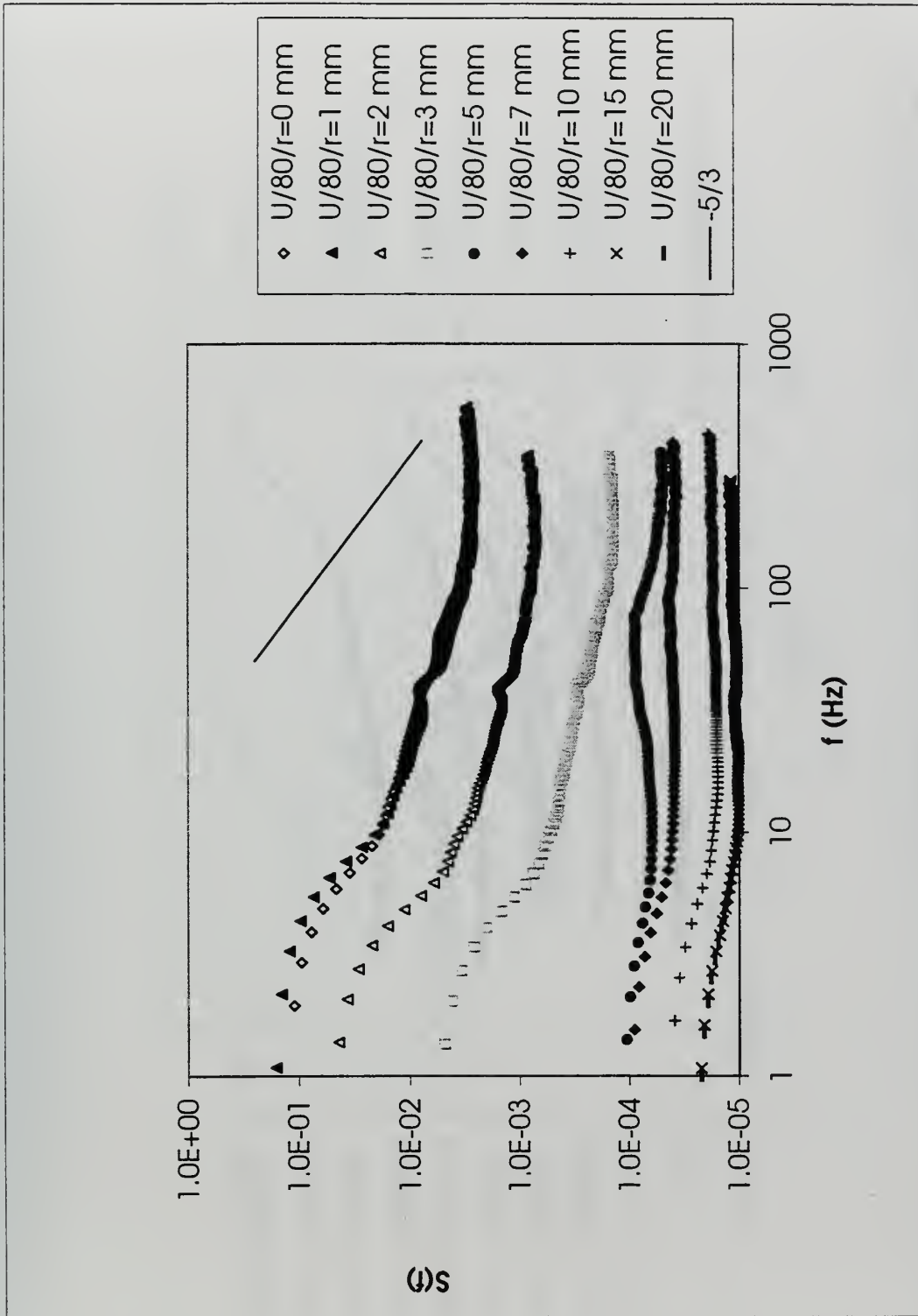


Figure 4-113. Spectra of U at X = 80 mm in the  $Re_D = 230,000/h_6$  flow.

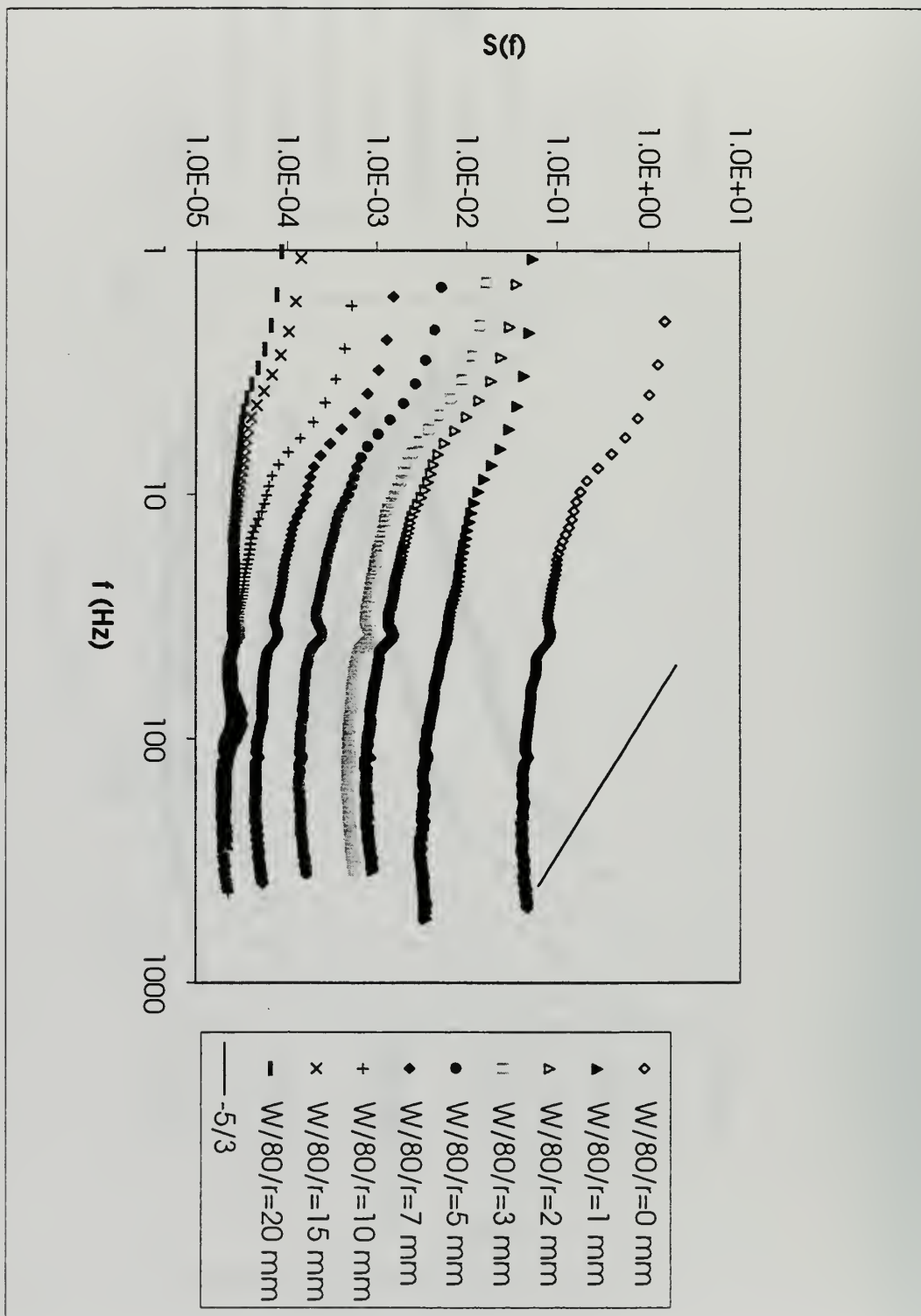


Figure 4-114. Spectra of  $W$  at  $X = 80$  mm in the  $Re_D = 230,000/h_6$  flow.

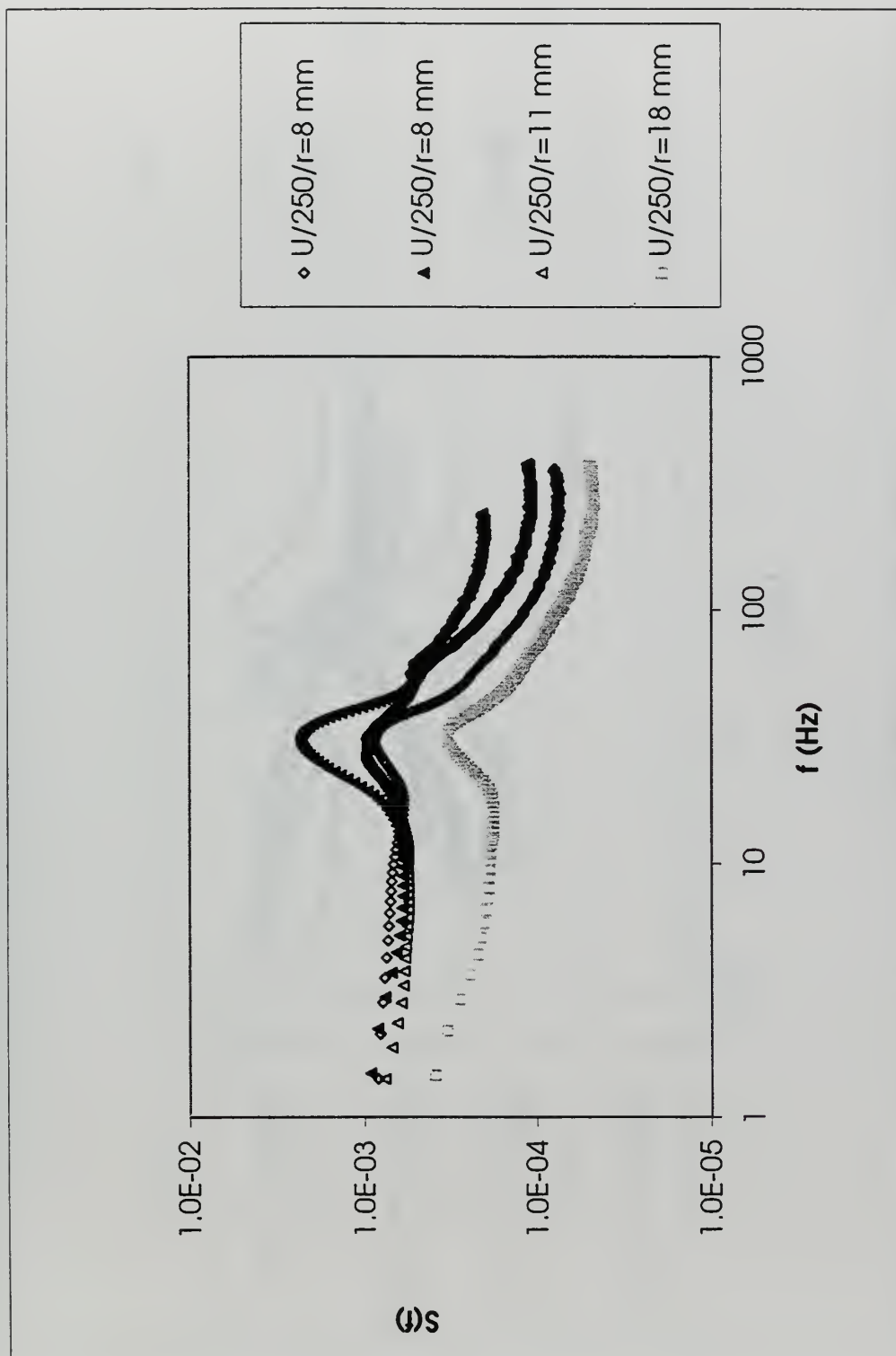


Figure 4-115. Spectra of  $U$  at  $X = 250$  mm in the  $Re_D = 120,000/h\delta$  flow.

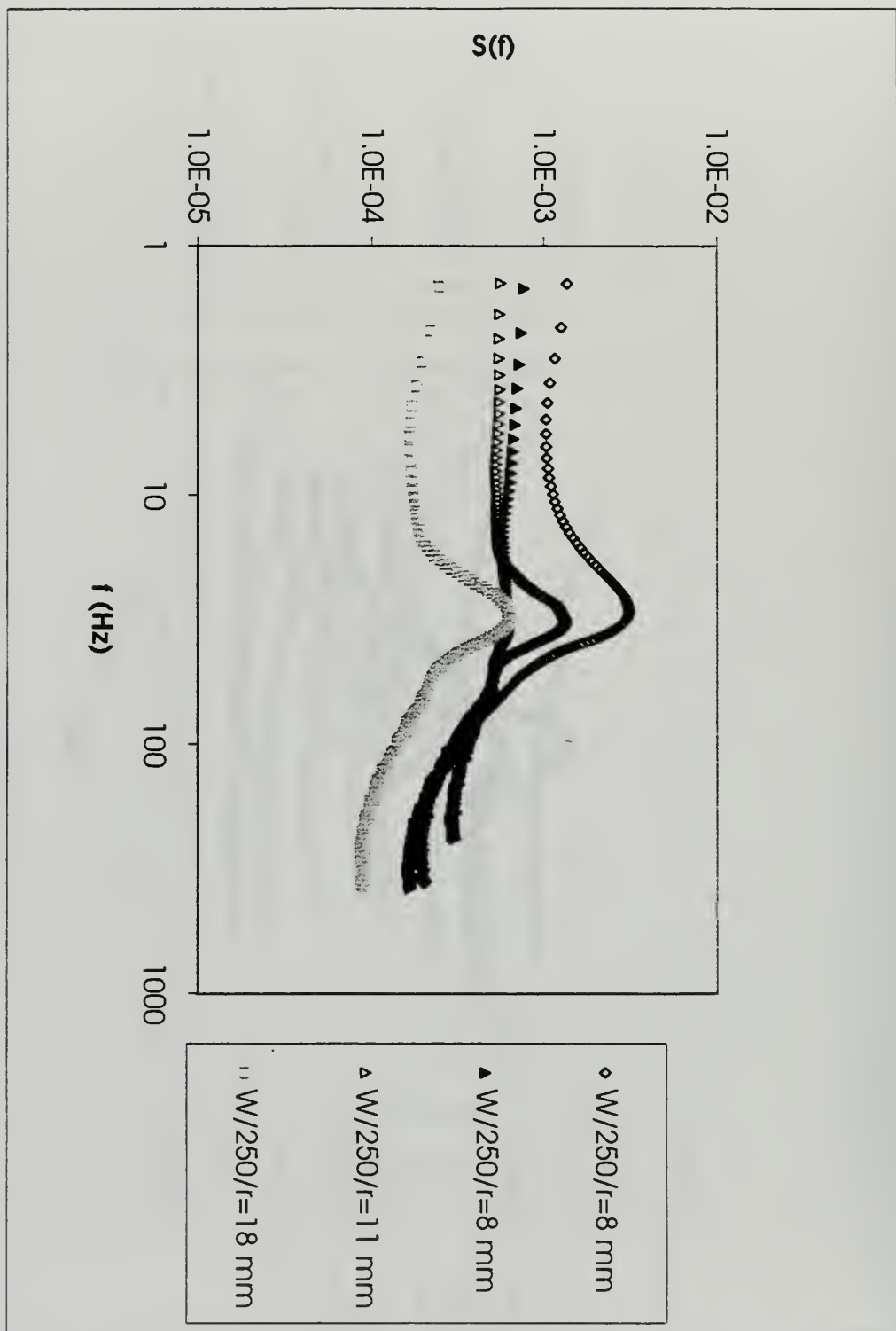


Figure 4-116. Spectra of  $W$  at  $X = 250$  mm in the  $Re_D = 120,000/h6$  flow.

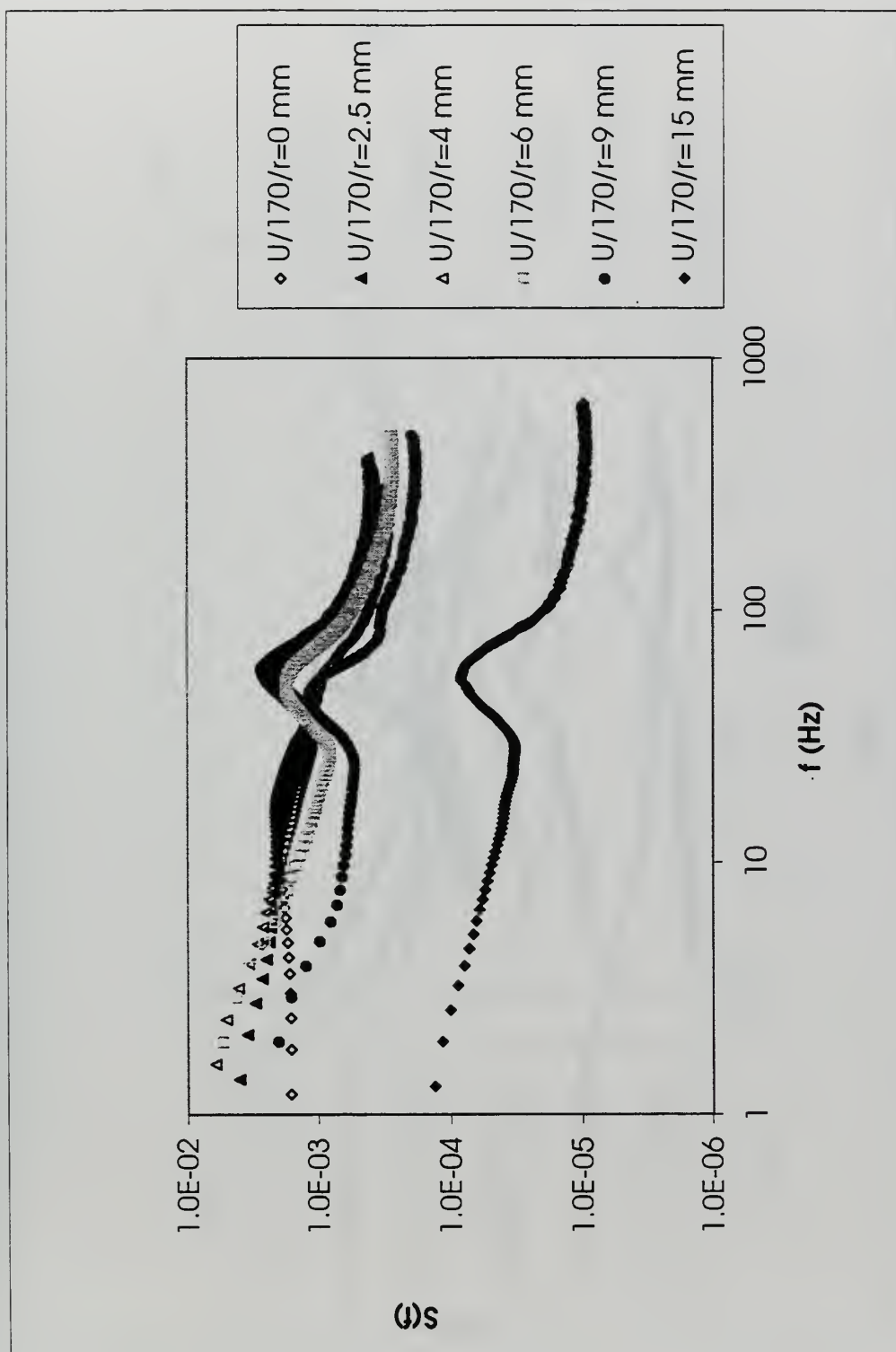


Figure 4-117. Spectra of U at  $X = 170$  mm in the  $Re_D = 120,000/h6$  flow.



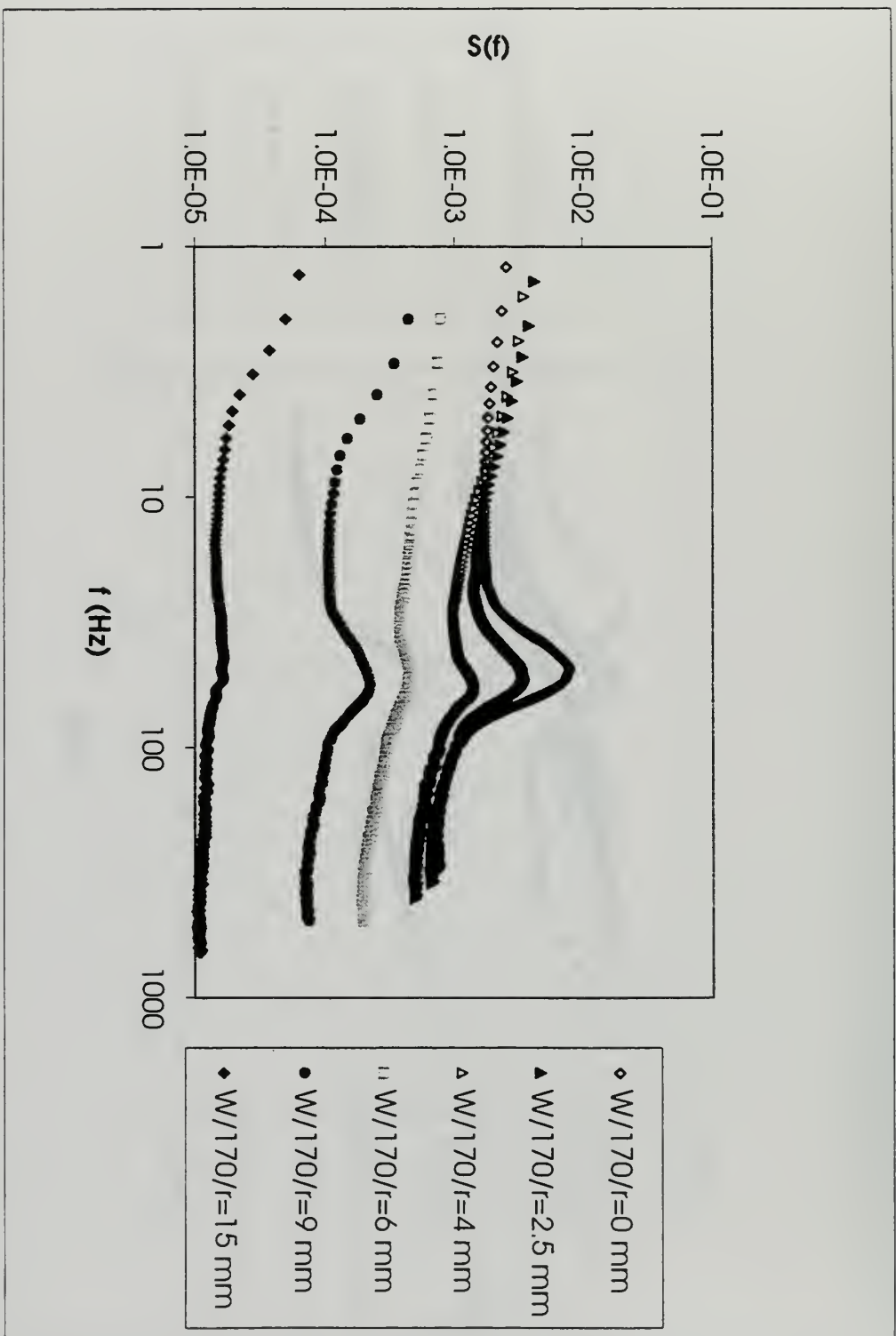


Figure 4-118. Spectra of  $W$  at  $X = 170$  mm in the  $Re_D = 120,000/h_6$  flow.

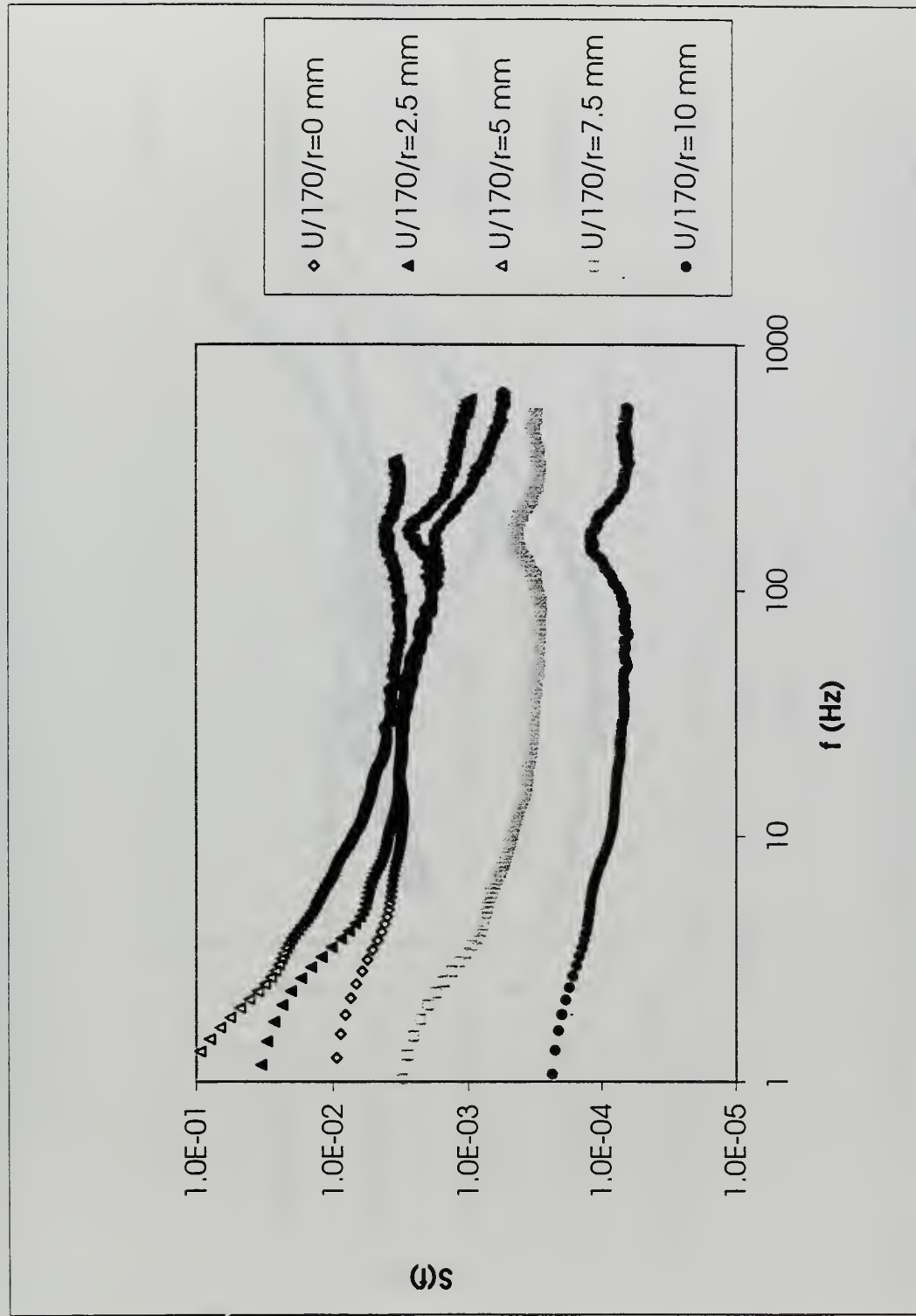


Figure 4-119. Spectra of U at X = 170 mm in the  $Re_D = 300,000/h^3$  flow.

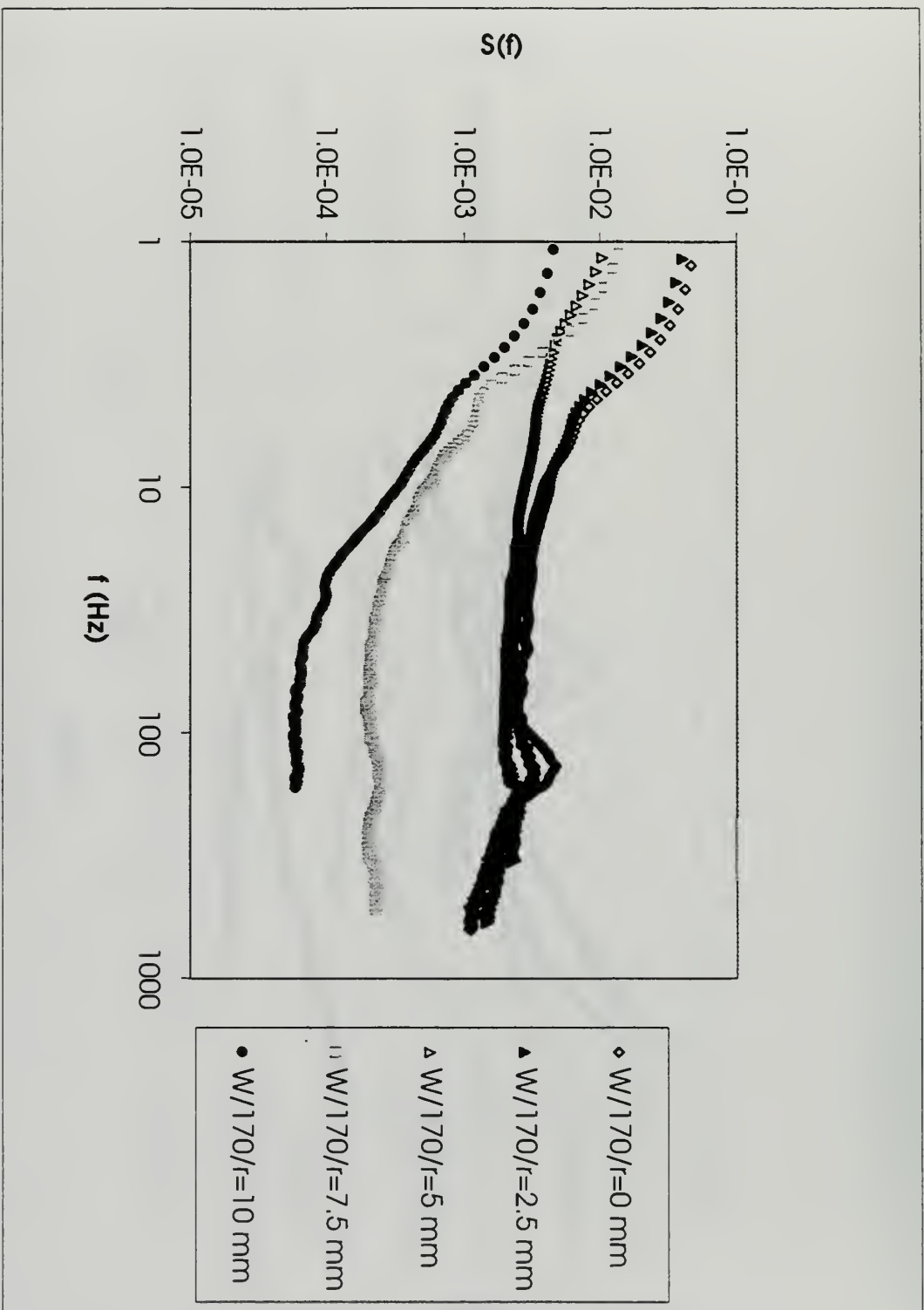


Figure 4-120. Spectra of  $W$  at  $X = 170$  mm in the  $Re_D = 300,000/h^3$  flow.

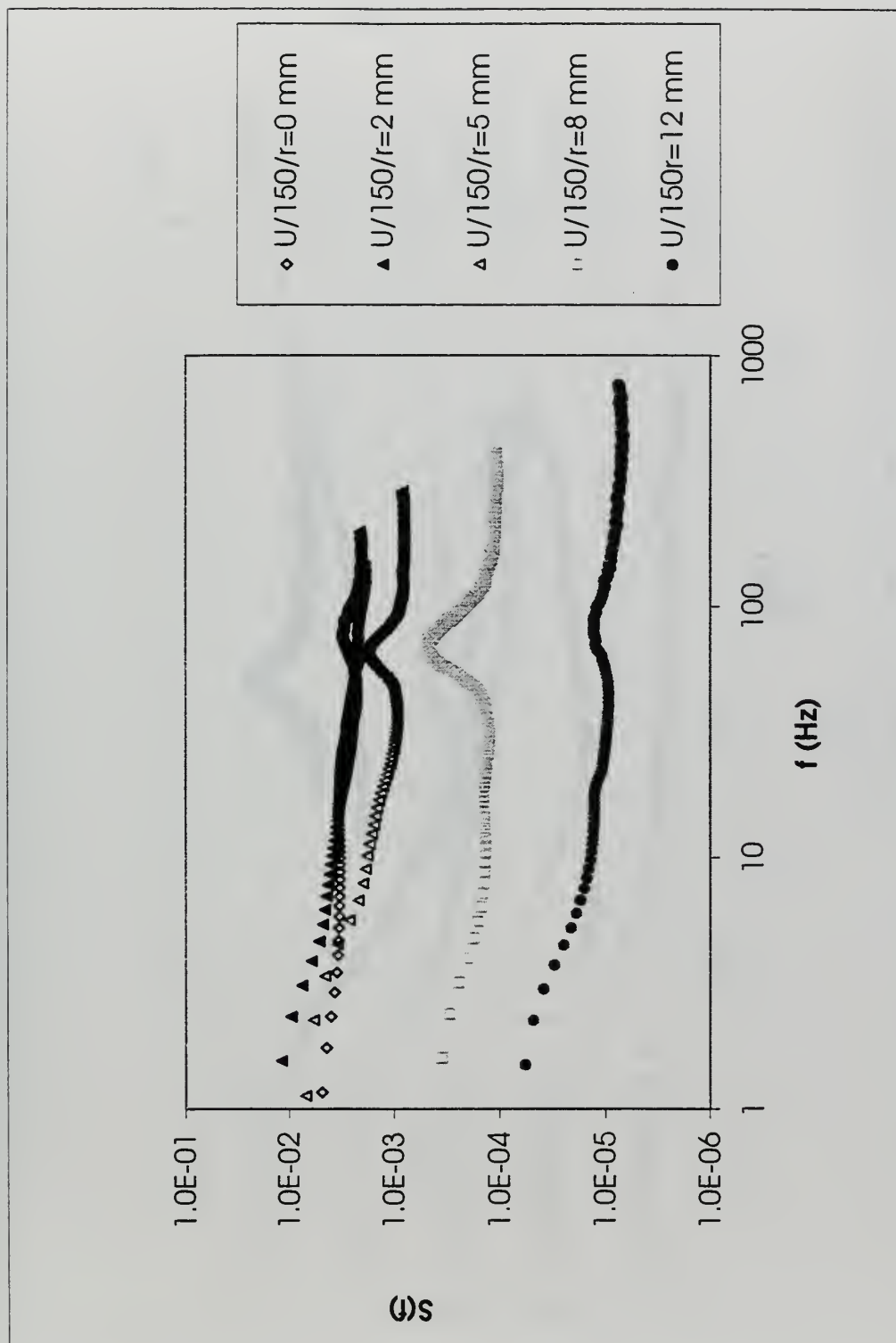


Figure 4-121. Spectra of U at X = 150 mm in the  $Re_D = 120,000/h_6$  flow.

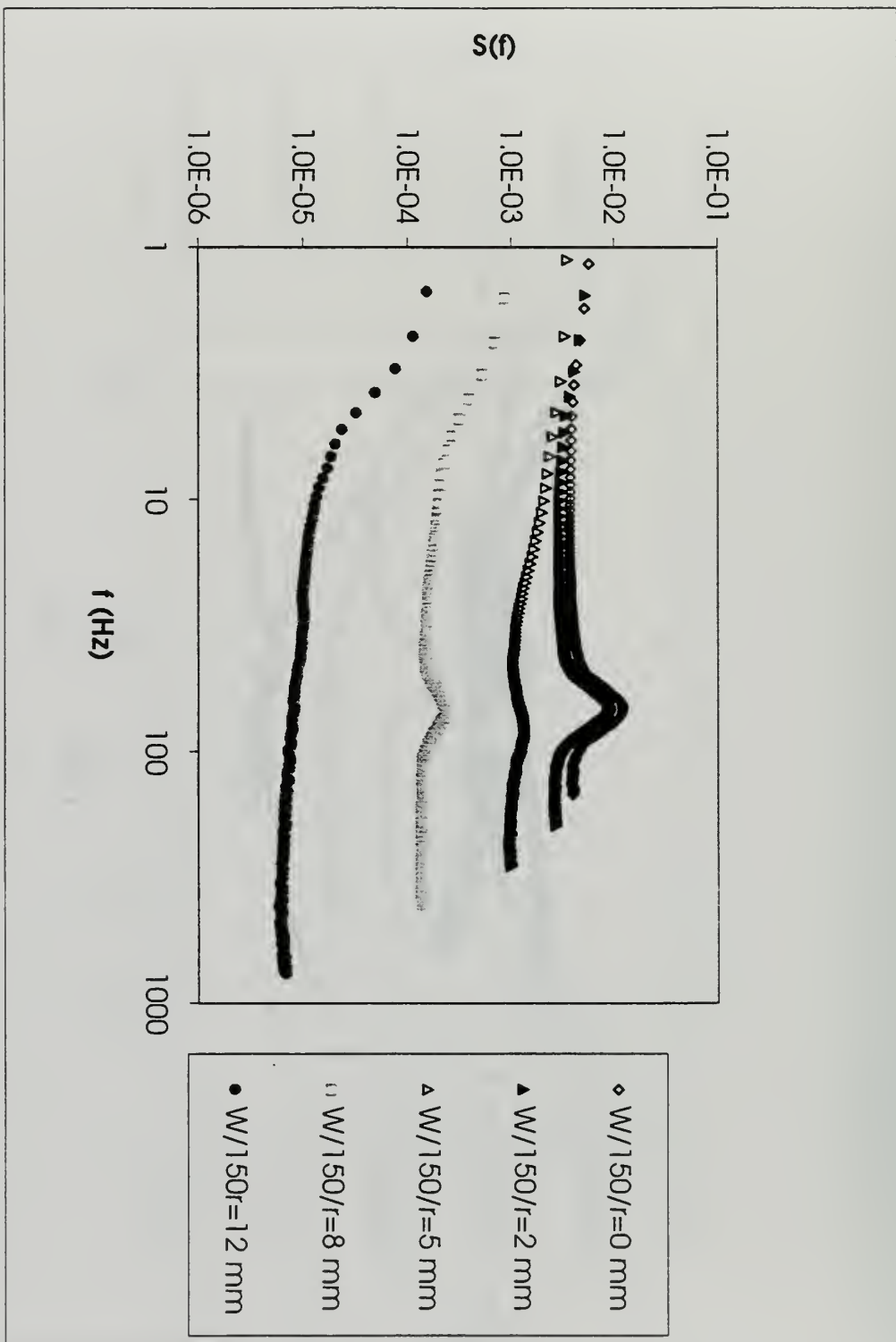


Figure 4-122. Spectra of  $W$  at  $X = 150$  mm in the  $Re_D = 120,000/h_6$  flow.



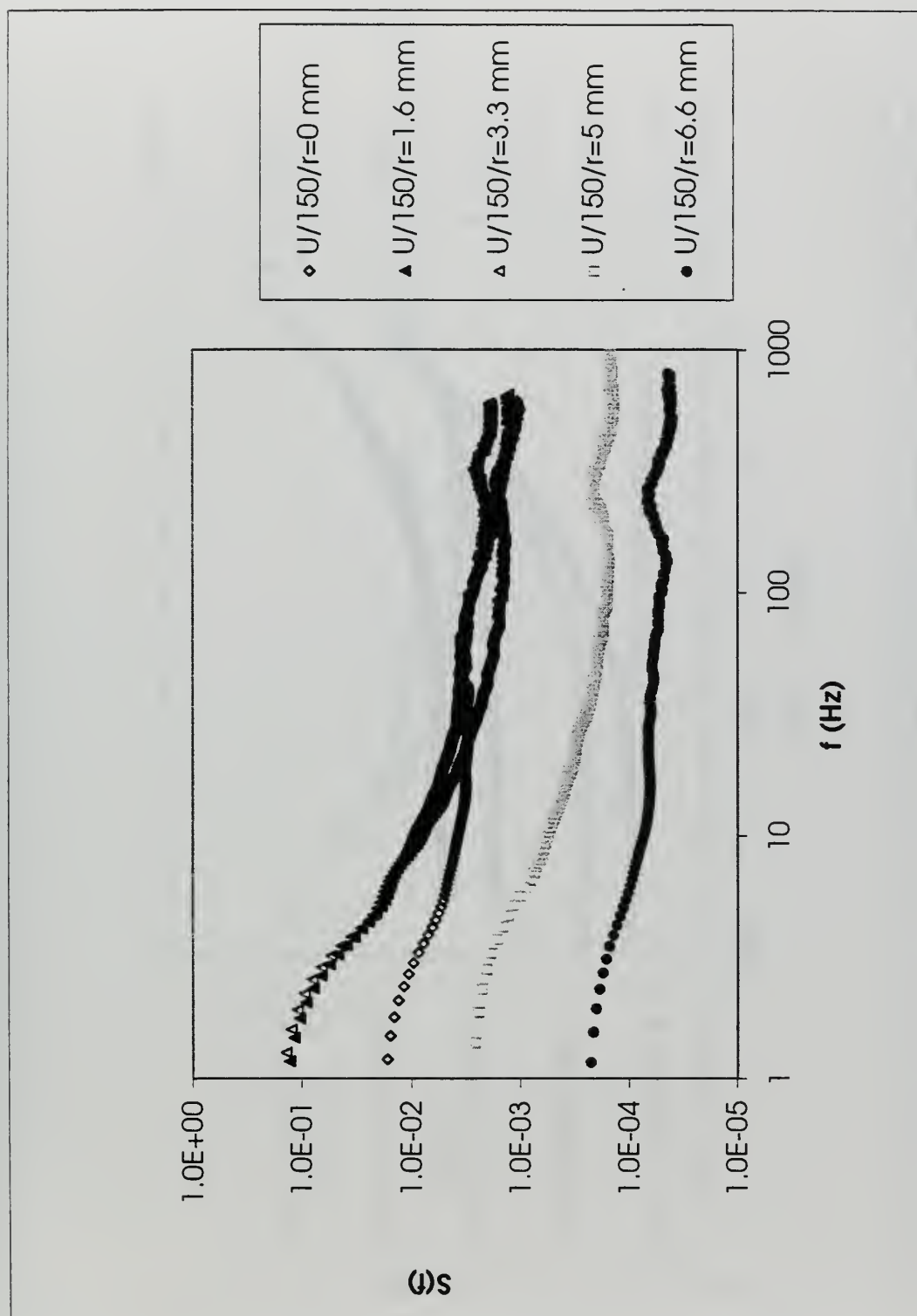


Figure 4-123. Spectra of  $U$  at  $X = 150$  mm in the  $Re_D = 300,000/h^3$  flow.

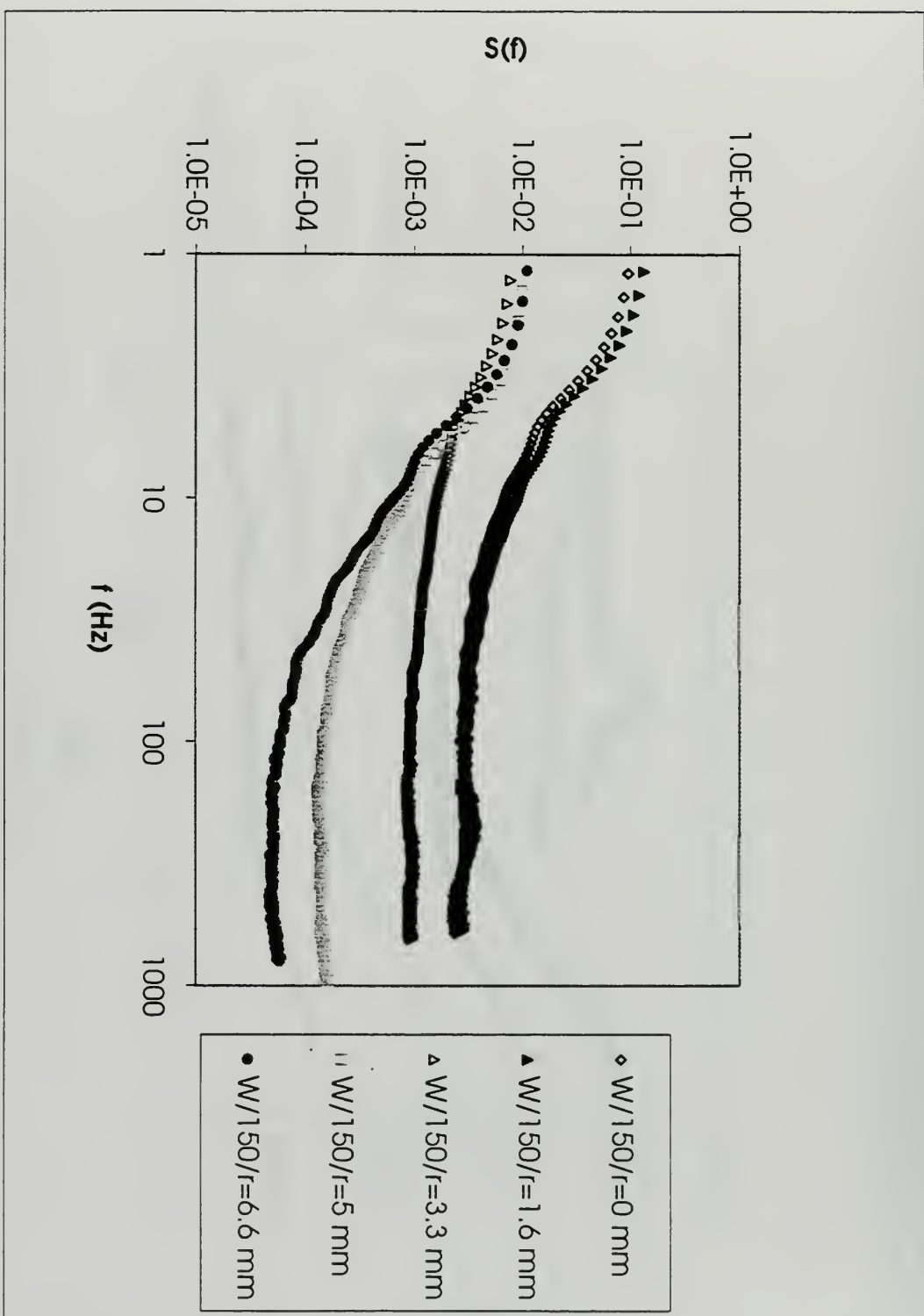


Figure 4-124. Spectra of  $W$  at  $X = 150$  mm in the  $Re_D = 300,000/h^3$  flow.

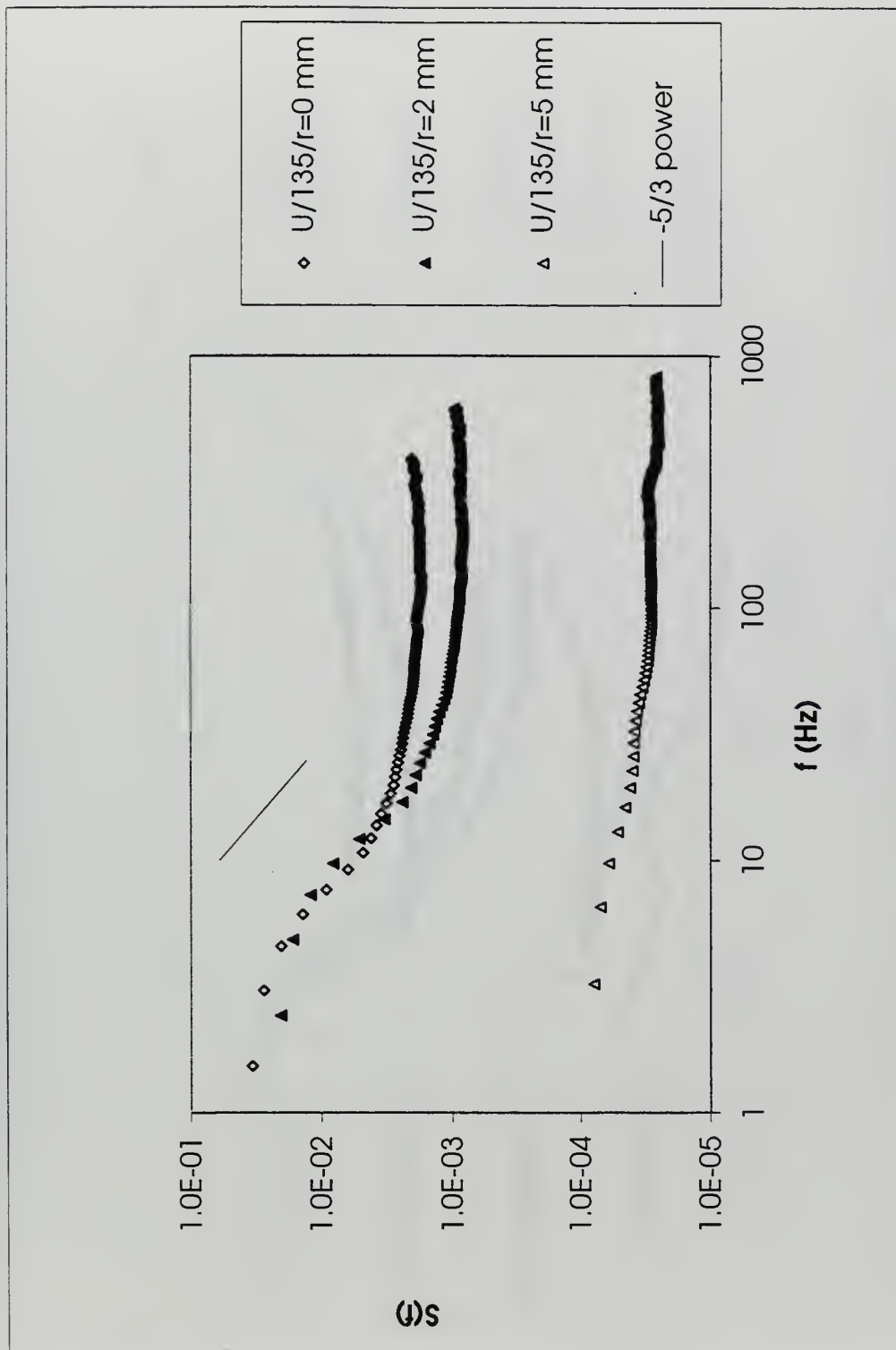


Figure 4-125. Spectra of U at  $X = 135$  mm in the  $Re_D = 120,000/h_6$  flow.

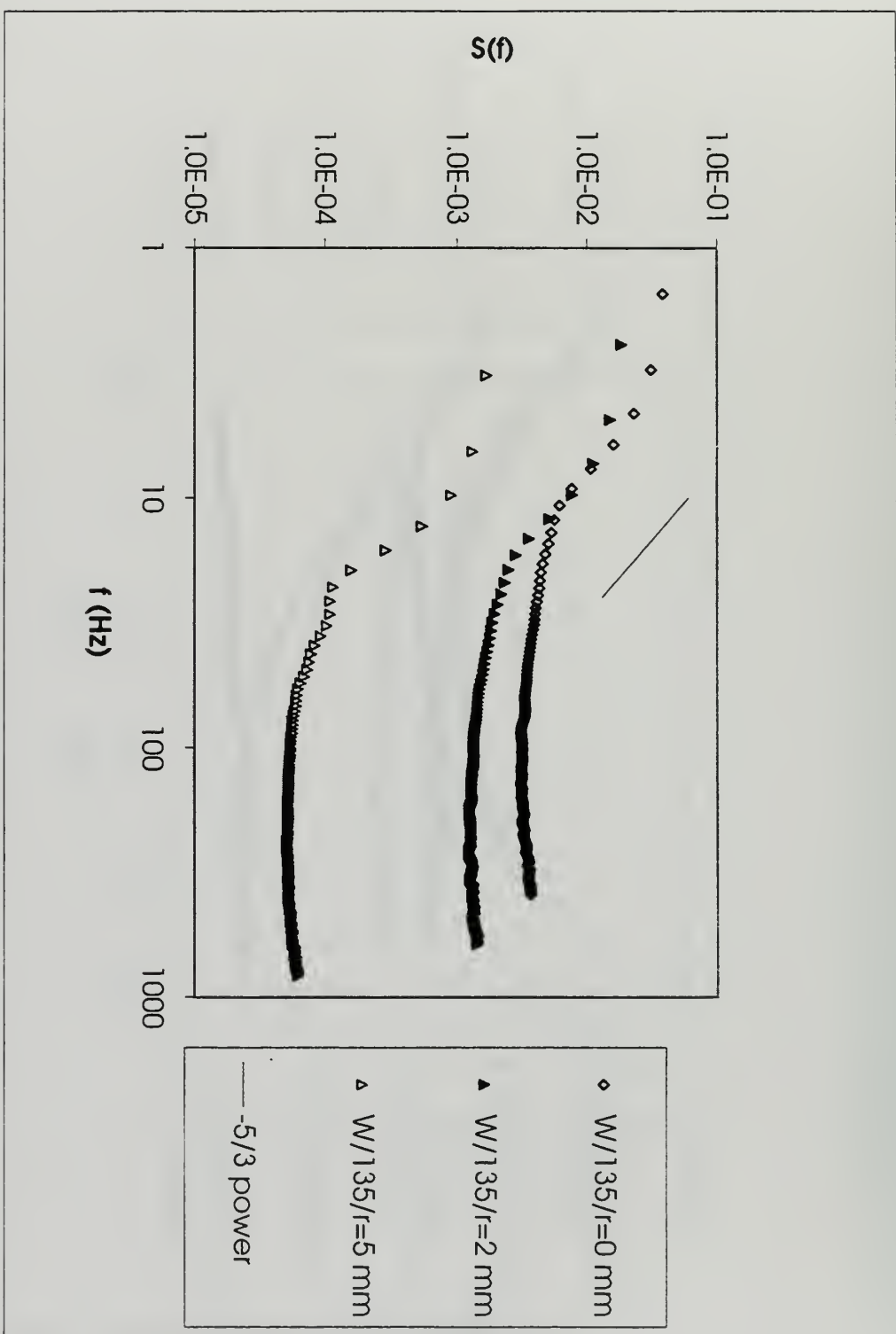


Figure 4-126. Spectra of  $W$  at  $X = 135$  mm in the  $Re_D = 120,000/h_6$  flow.

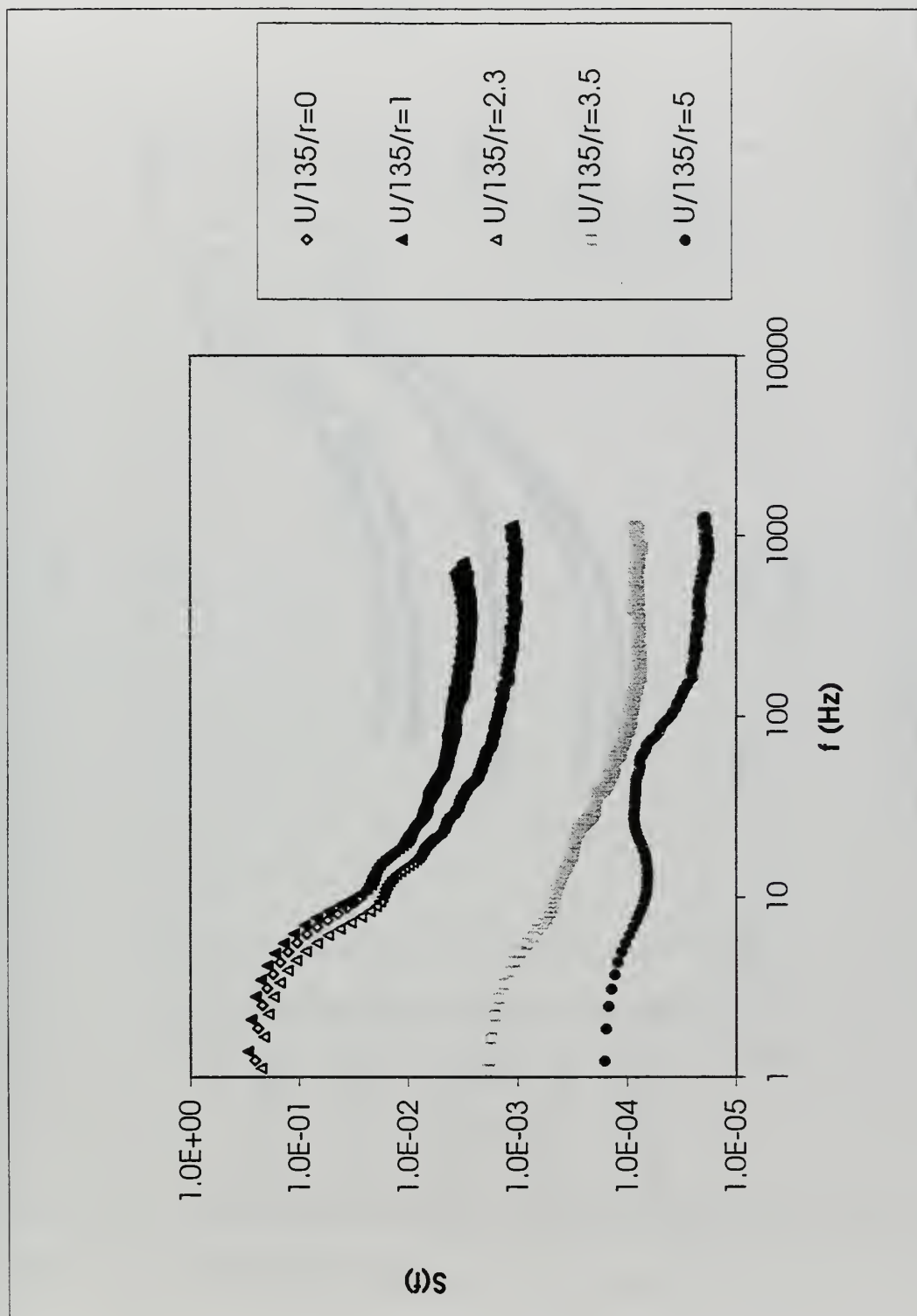
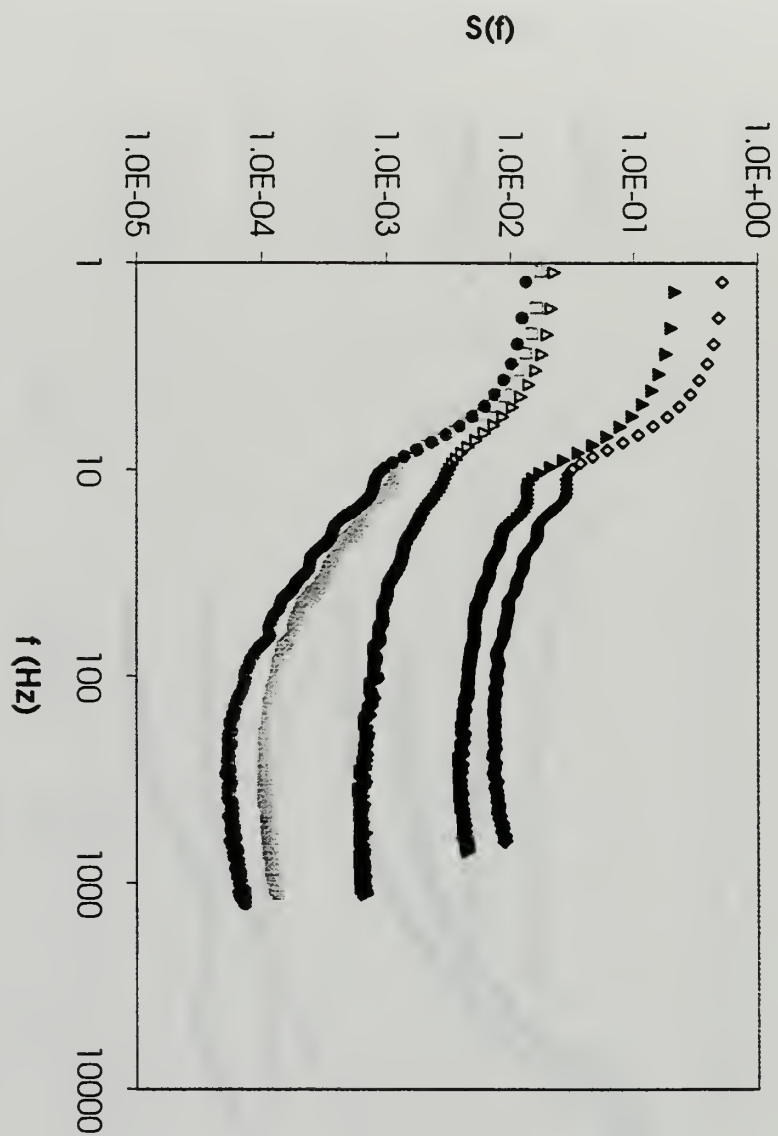


Figure 4-127. Spectra of  $U$  at  $X = 135$  mm in the  $Re_D = 300,000/h^3$  flow.





- ◊  $W/135/r=0$
- ▲  $W/135/r=1$
- △  $W/135/r=2.3$
- $W/135/r=5$

Figure 4-128. Spectra of  $W$  at  $X = 135$  mm in the  $Re_D = 300,000/h^3$  flow.

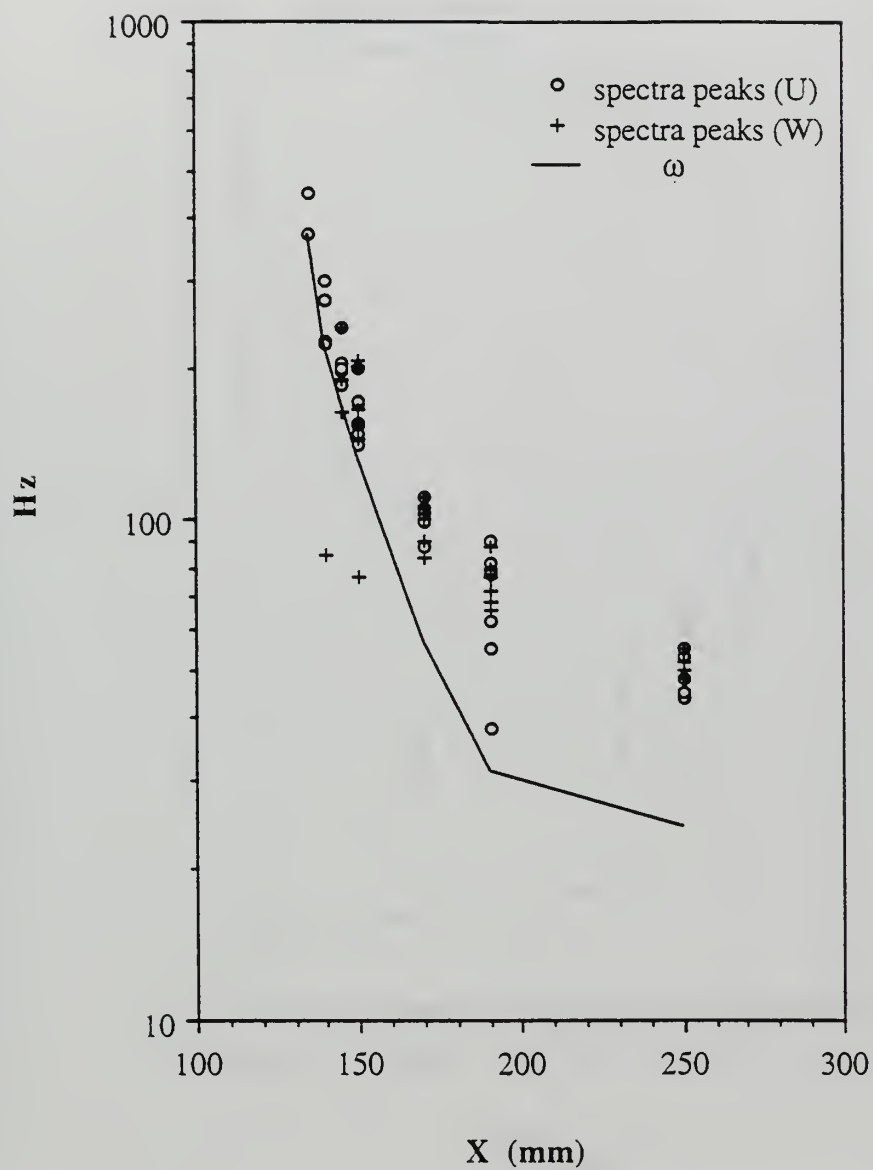


Figure 4-129. Axial variation of frequency of spectral peaks and core rotation rate in the  $Re_D = 230,000/h_6$  flow state.

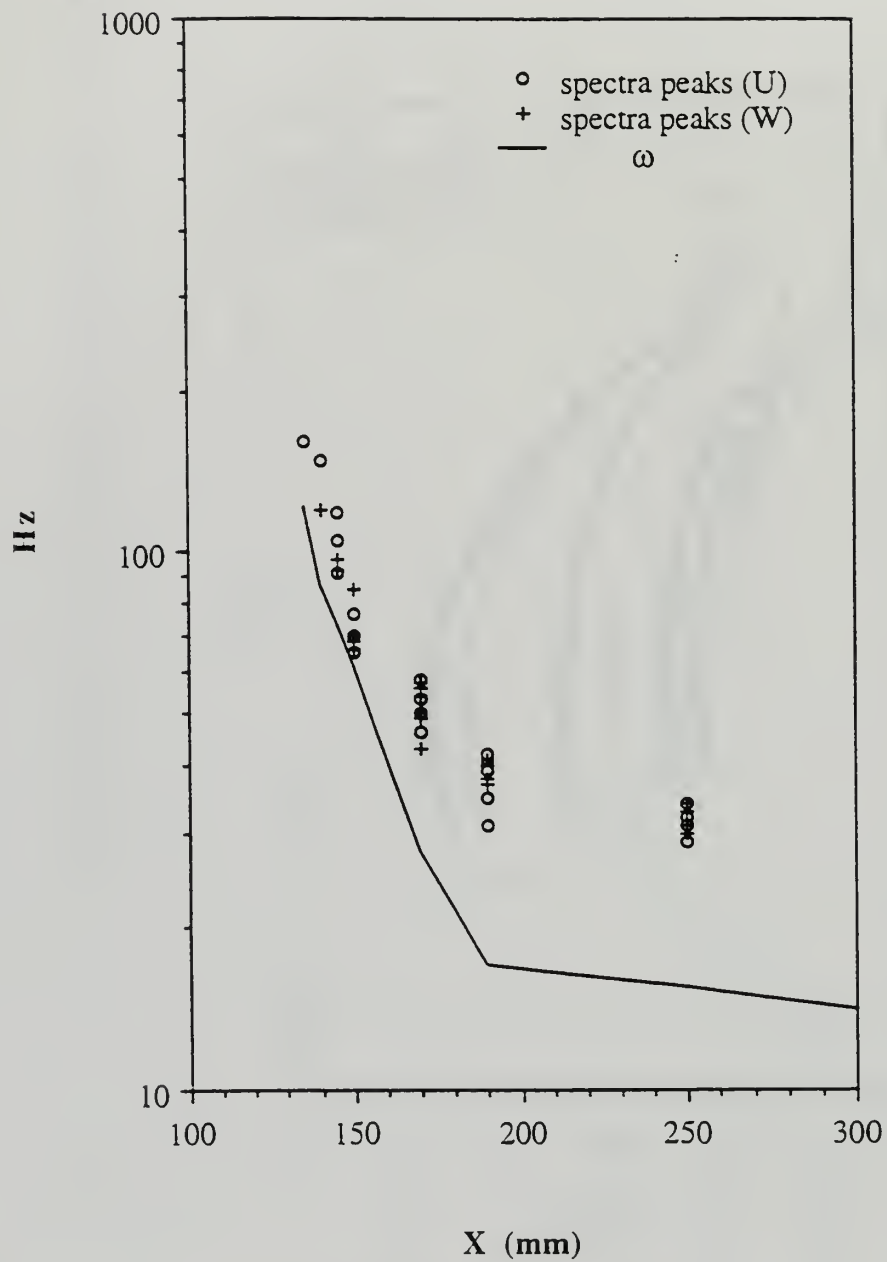


Figure 4-130. Axial variation of frequency of spectral peaks and core rotation rate in the  $Re_D = 120,000/h_6$  flow state.

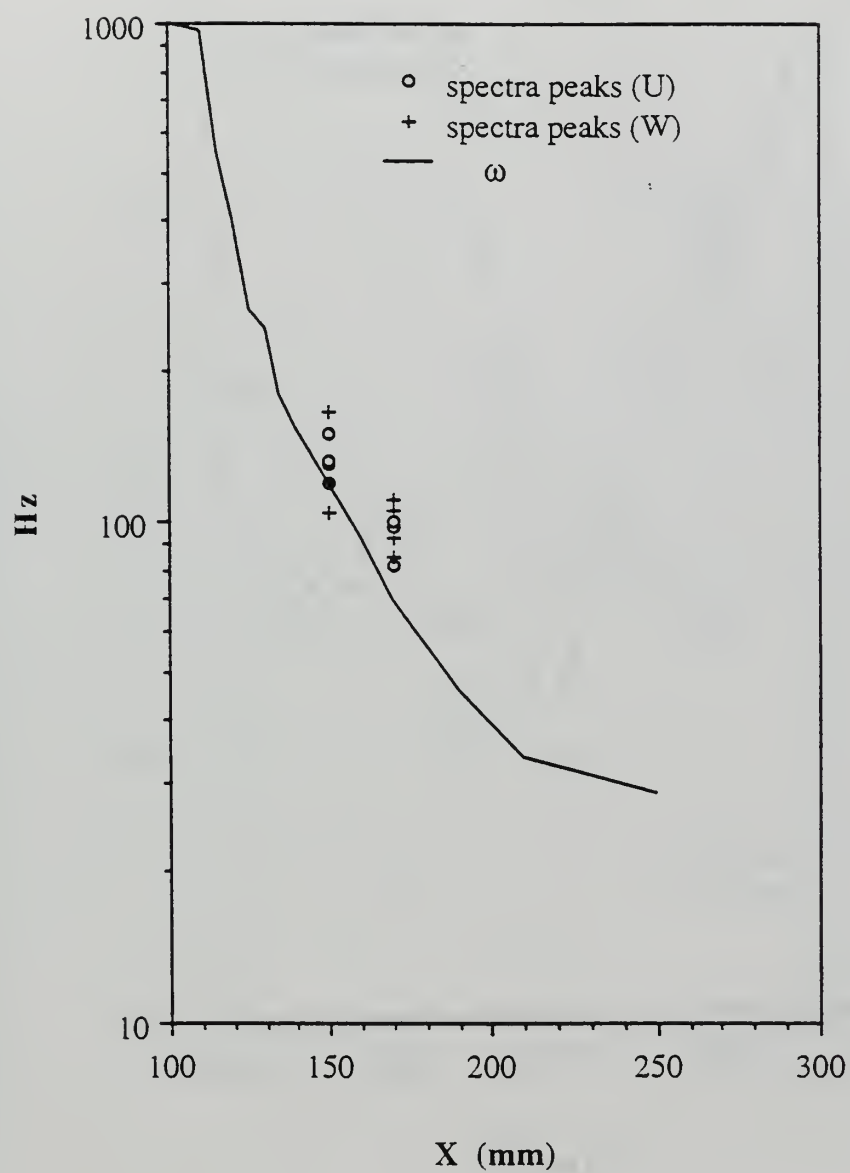


Figure 4-131. Axial variation of frequency of spectral peaks and core rotation rate in the  $Re_D = 230,000/h3$  flow state.

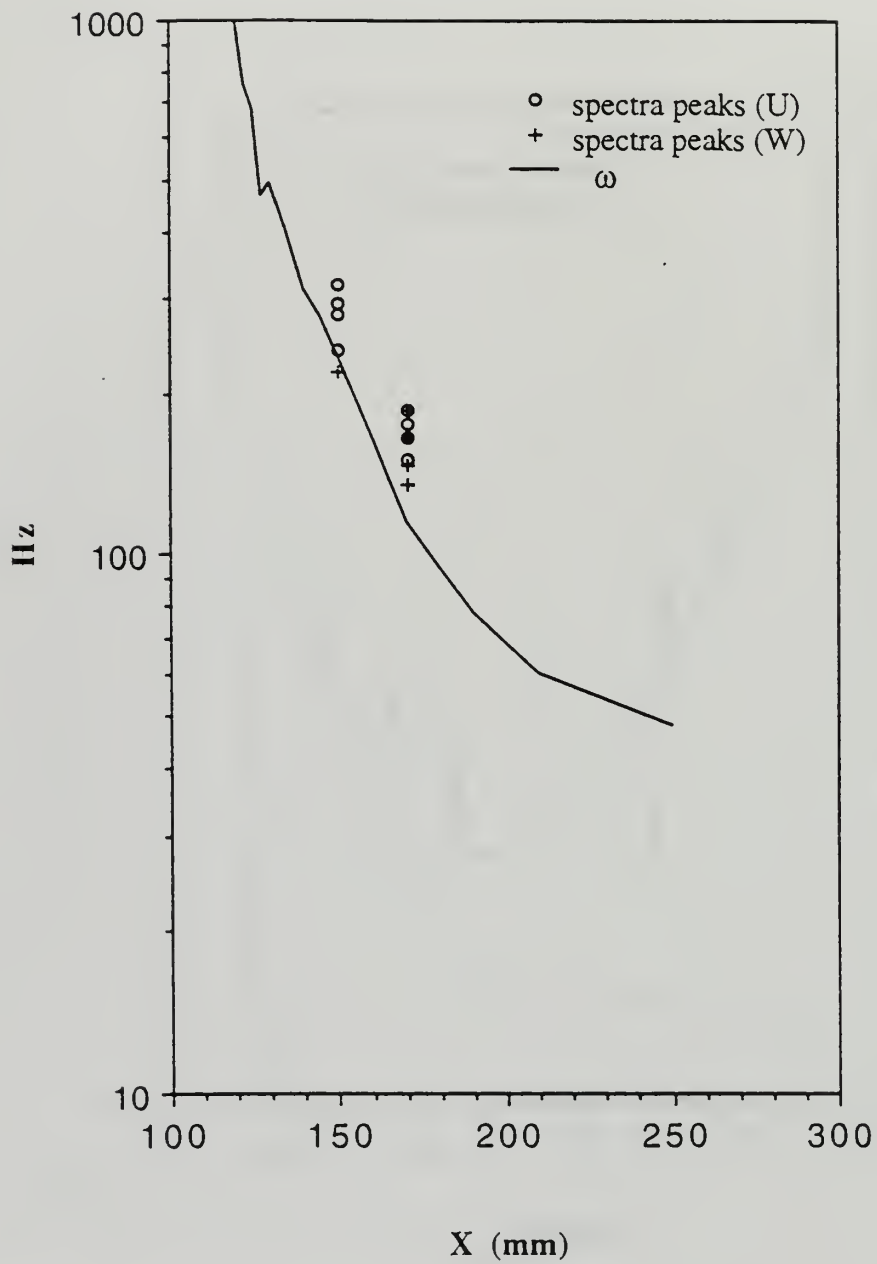


Figure 4-132. Axial variation of frequency of spectral peaks and core rotation rate in the  $Re_D = 300,000/h3$  flow state.



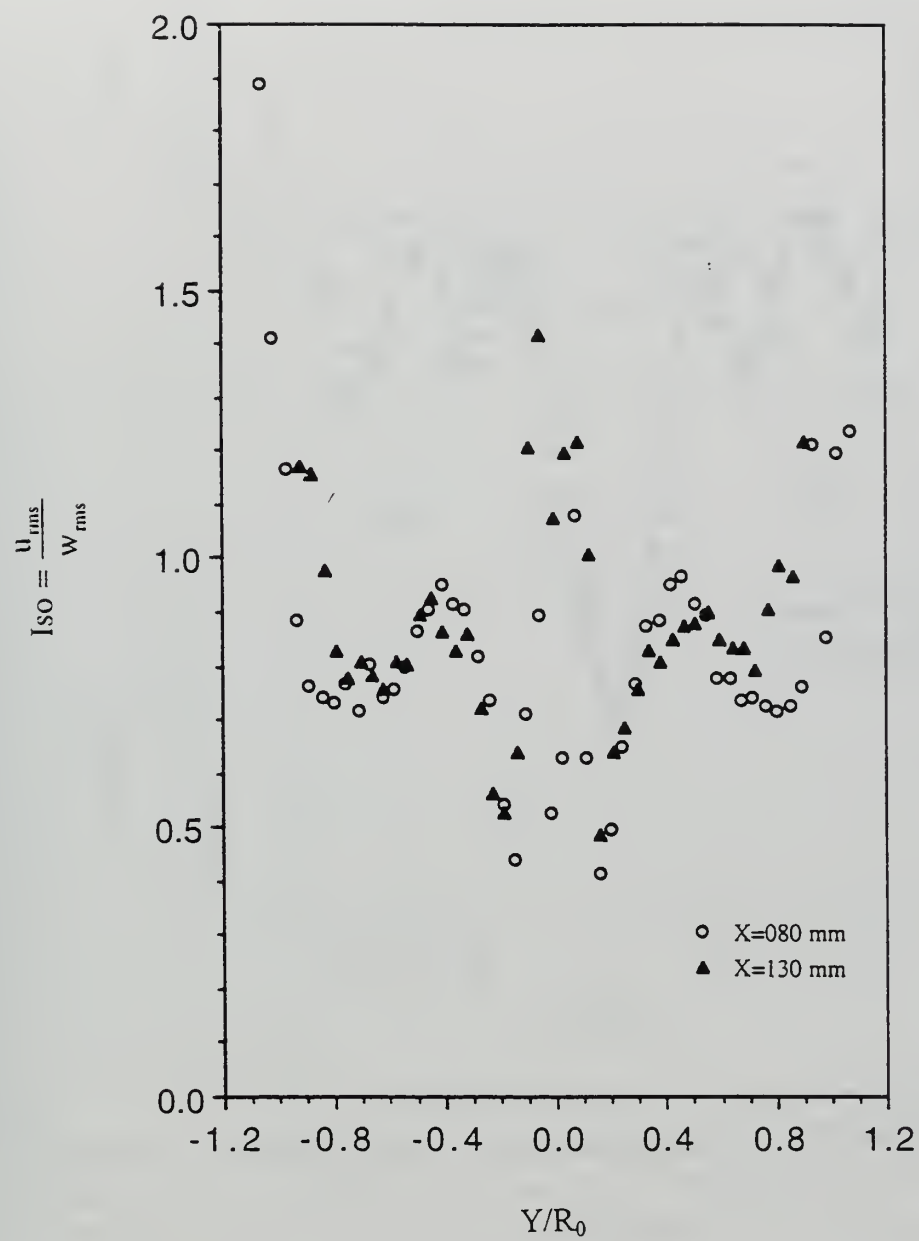


Figure 4-133. Isotropy parameter in the upstream sections of a swirling flow with vortex breakdown.

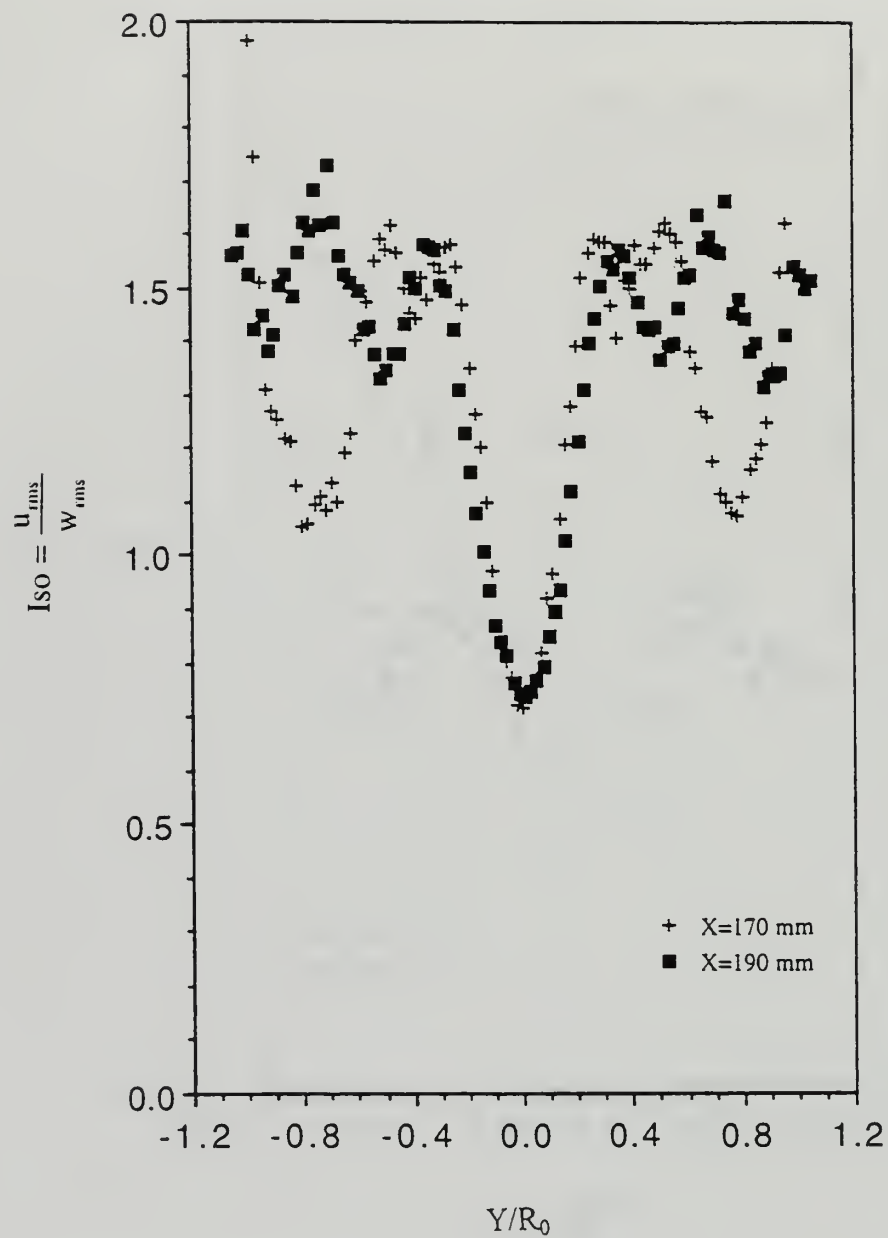
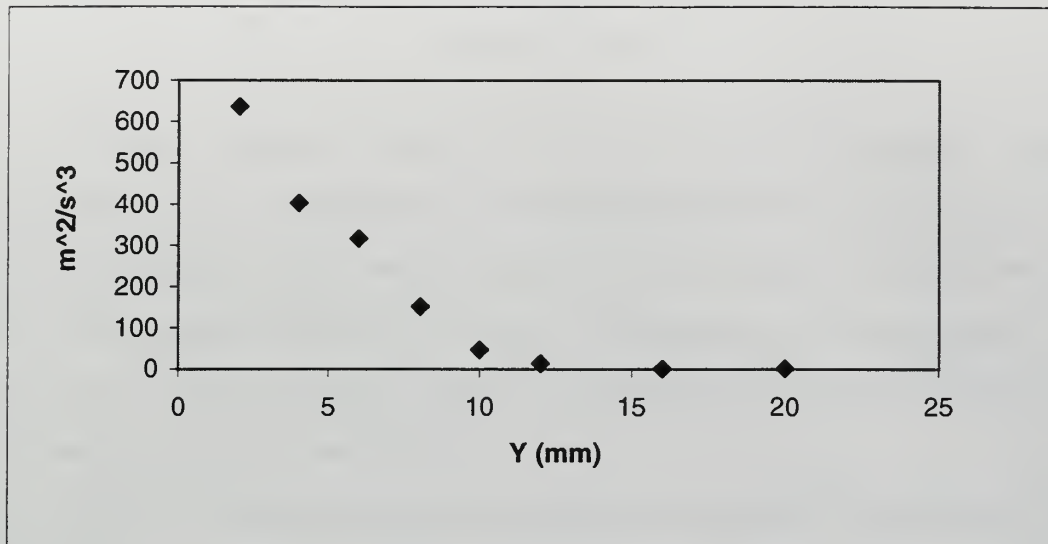
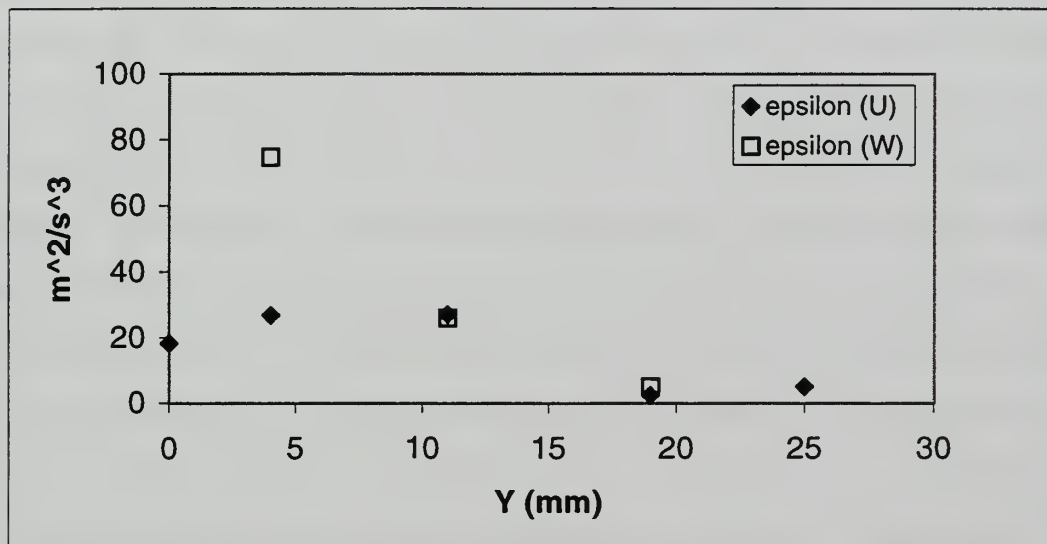


Figure 4-134. Isotropy parameter in the downstream sections of a swirling flow with vortex breakdown.



a.



b.

Figure 4-135. Turbulence kinetic energy dissipation rates in the wake of a vortex breakdown.  $Re_D = 230,000/h_6$  flow state. Vortex breakdown at  $X = 135$  mm. (a.) Dissipation determined from the axial velocity spectra at  $X = 190$  mm. (b.) Dissipation determined from the axial and tangential velocity spectra at  $X = 250$  mm.

THE  
JOURNAL  
OF  
THE  
ROYAL  
ANTHROPOLOGICAL  
INSTITUTE  
OF GREAT  
BRITAIN  
AND IRELAND  
VOLUME  
LXXV  
PART I  
1905  
LONDON  
PUBLISHED BY THE  
INSTITUTE  
11, BEDFORD SQUARE, W.C.1  
1905

## APPENDIX B. MEASUREMENT DETAILS AND EXPERIMENTAL UNCERTAINTY

The most important characteristics of the LDV system were described in the body of the thesis. Here, we will describe a few of the additional details which would be useful to those who might wish to repeat the experiments or to compare the present results with those which might be obtained in the future. Furthermore, it is of importance to know some of these details because they effect the uncertainties and the quality of the data in the assessment of the numerical models.

The LDV probes had a beam separation of 38 mm, and a focal length of 500 mm. The total angle between the heads was  $24^\circ$ . It was fully realized at the onset that the larger the said angle the smaller the measurement volume. However, additional constrictions define not only the included angle but also the overall objectives that are achievable. In the present case, the use of a heavy stainless steel chamber and 12-mm thick Plexiglas windows (140 mm by 457 mm) and, most importantly, the region of the vortex to be subjected to measurements (approximately 250 mm) made it absolutely necessary that the included angle be reduced to  $24^\circ$ . It is this value plus the other optical characteristics of the LDV probes and receiving optics that determined the measurement volume characteristics. The forward scatter receiving optics were mounted such that the off-axis collection angle was approximately  $10^\circ$  below horizontal. It was known from Mie Scattering Theory that a smaller collection angle would have yielded larger data rates, but only at the expense of a larger measurement volume.

The diameter of the said volume was less than 100 mm and the length was approximately 1200 mm. The beams were made to pass through a 100 mm pinhole which fixed the diameter. However, the length was determined, only approximately, through additional calculations for a number of reasons. These are, the differences in the wavelengths of the blue (measuring tangential velocity), green, and violet beams (measuring axial and radial velocities), the variations in their diameter, the intersections of



three separate volumes defining a very complex common volume, and, to make the matters more complex, the calculation of the velocity components from the joint measurements provided by these volumes. Should the estimated measurement volume appear to be about tenfold the diameter and thus relatively large, one needs to be reminded that similar and careful experiments by others (e.g., Rodi and Nezu (1986) and Nejad, et al (1989)) also show that their measurements volumes were just as long and just as comparable to that encountered in the present investigation. Clearly, in the region where the velocity gradients are extremely large (which also happens to be the region of other problems exhibited by nature, such as meandering and darting), the probe volume length will be important. However, outside the core region the measurements should be comparable with any other LDV measurements carried out in swirling flows. The distinction of the present study from all others and the resulting complexity are in the fact that no one has ever carried out LDV measurements in the region of a vortex core with a radius as small as  $\sim 1$  mm and tangential velocities as large as 10 m/s or so. The foregoing has carefully noted the sizes, the volumes and facts as they have been encountered.

One must also add that the variations in the size of the particles (up to about 10  $\mu\text{m}$ ), the size distribution of the particles in the radial as well as axial directions (in the regions of rapid acceleration or deceleration), and the instantaneous position of these particles within the volume dictated in part the overall accuracy of the measurements. Naturally occurring particles in the system were used, and no additional seeding was required. Using the method outlined by Adrian (1996), a conservative estimate of the 3-dB frequency response of these particles (using the density of sand) in water is at least 63 kHz, well above the rotation rate of the fluid.

Another important aspect of the experimental system as far as the measurement accuracies are concerned is the diffraction of the beams through different media: air, Plexiglas, and water. This subject has been discussed in great length since the inception and first use of the LDV concept (see, e.g., Faler, 1976) and it will suffice to note that the

corresponding traversing distances in the air (as provided by the traversing system) to that in the water were properly corrected. In the present experiment, the transverse motion of the measurement volume in water was 1.33 times greater than that in the air. The final position of the measurement volume was known to within about 0.05 mm. This, in combination with the local flow gradient, contributed to the overall uncertainty of the final results.

Experimental uncertainty was estimated in accordance with accepted methods (e.g., Moffat (1982), Kline (1985)). Where possible, manufacturers data or experimentally determined system errors were used. The estimated uncertainties are given in Tables B-1 through B-5.

Quantity	Nomenclature	Uncertainty
$Q$	flow rate	3 %
$D_0, R_0$	inlet tube radius	0.5 %
$U_0$	inlet velocity	3.5 %
$Re_D$	Reynolds number (tube)	6.5 %
$Re_r$	Reynolds number (circulation)	12 %
$\Gamma$	circulation(max)	11 %
$\Gamma_c$	circulation(core edge)	13 %
$\Gamma_c/\Gamma$	fraction of vorticity in core	17 %

Table B-1. Uncertainty of various experimental quantities.

Overall uncertainty (% Uo)		Re=70,000	Re=120,000	Re=120,000	Re=230,000	Re=230,000	Re=230,000	Re=300,000
		tube h0	tube h0	tube h6	tube h6	tube h6	tube h3	tube h3
U		8%	10%	10%	10%	11%	10%	9%
W		5%	7%	7%	7%	9%	8%	9%

U, sources of uncertainty Uncertainty of measurement due to random error:								
		0.8%	0.6%	0.5%	0.6%	0.6%	0.6%	0.6%
	Uncertainty of Result due to measurement system: position error and velocity gradient:	6.4%	6.6%	7.3%	6.7%	6.7%	6.4%	5.7%
		3.8%	7.6%	6.7%	8.6%	7.2%	7.2%	7.2%

W, sources of uncertainty Uncertainty of measurement due to random error								
		1.9%	1.1%	1.5%	1.6%	1.6%	1.4%	1.6%
	Uncertainty of Result due to measurement system: due to traverse position:	2.5%	2.7%	2.9%	2.9%	2.9%	2.7%	2.6%
		3.3%	6.9%	5.7%	8.3%	6.9%	6.9%	8.1%

Table B-2. Estimated experimental uncertainty of velocity measurements in the upstream sections, inside the vortex core.

Overall uncertainty (% U <sub>0</sub> )		Re=70,000	Re=120,000	Re=120,000	Re=230,000	Re=230,000	Re=300,000
U	W	tube h0	tube h0	tube h6	tube h6	tube h3	tube h3
		4%	3%	3%	3%	3%	3%
		4%	3%	2%	3%	3%	3%

U, sources of uncertainty						
Uncertainty of measurement due to random error:	2.8%	1.4%	0.6%	0.7%	0.4%	0.6%
Uncertainty of Result due to measurement system: position error and velocity gradient:	2.5% 0.7%	2.5% 0.4%	2.5% 1.1%	2.5% 1.5%	2.5% 1.2%	2.5% 1.4%

W, sources of uncertainty						
Uncertainty of measurement due to random error	3.2%	1.6%	0.5%	0.5%	0.4%	0.5%
Uncertainty of Result due to measurement system: due to traverse position:	1.8% 0.6%	1.8% 1.1%	1.8% 1.2%	1.8% 2.3%	1.8% 2.0%	1.8% 2.5%

Table B-3. Estimated experimental uncertainty of velocity measurements in the upstream sections, outside the vortex core.



Overall uncertainty (% Uo)		Re=70,000	Re=120,000	Re=120,000	Re=230,000	Re=230,000	Re=300,000
U W	tube h0	3%	3%	3%	3%	3%	3%
	tube h3	3%	3%	3%	3%	2%	3%
U, sources of uncertainty							
Uncertainty of measurement due to random error:		0.8%	0.6%	0.5%	0.6%	0.6%	0.6%
Uncertainty of Result due to due to measurement system:		2.5%	2.5%	2.5%	2.5%	2.5%	2.5%
position error and velocity gradient:		0.7%	0.4%	1.1%	1.5%	1.2%	1.4%
W, sources of uncertainty							
Uncertainty of measurement due to random error		1.9%	1.1%	1.5%	1.6%	1.4%	1.6%
Uncertainty of Result due to measurement system:		1.8%	1.8%	1.8%	1.8%	1.8%	1.8%
due to traverse position:		0.6%	2.3%	0.9%	1.4%	1.0%	1.5%

Table B-4. Estimated experimental uncertainty of velocity measurements in the downstream sections.

Region	Quantity	Uncertainty
Upstream $r \leq 3 R_c$	$u_{rms}/U_0$ $w_{rms}/U_0$ $\overline{u' w'} / U_0^2$	not reliable
Upstream $r \geq 3 R_c$	$u_{rms}/U_0$ $w_{rms}/U_0$ $\overline{u' w'} / U_0^2$	6 % 6 % 9 %
Downstream	$u_{rms}/U_0$ $w_{rms}/U_0$ $\overline{u' w'} / U_0^2$	6 % 6 % 9 %

Table B-5. Uncertainty of turbulence measurements.

## LIST OF REFERENCES

- Abujelala, M. T., and Lilley, D. G. (1984) Limitations and Empirical Extensions of the  $k - \epsilon$  Model as Applied to Turbulent Confined Swirling Flows, *Chem. Eng. Commun.*, Vol. 31, pp. 223-236.
- Abujelala, M. T., and Lilley, D. G. (1985) Confined Trubulent Swirling Recirculating Flow Predictions, NASA-CR-174917.
- Althaus, W., Brücker, C., and Weimer, M. (1995) Breakdown of Slender Vortices, *Fluid Vortices*, Kluwer Academic Publishers, ed. Green, S. I., Chapter IX, pp. 373-426.
- Althaus, W., Krause, E., Hofhaus, J., and Weimer, M. (1995) Bubble- and Spiral- Type Breakdown of Slender Vortices, *Exp. Thermal and Fluid Science*, Vol. 11, pp. 276-284.
- Azad, R. S., and Kassab, S. Z. (1989) New Method of Obtaining Dissipation, *Exp. Fluids*, Vol. 7, pp. 81-87.
- Baker, G. R., Barker, S. J., Bofah, K. K., and Saffman, P. G. (1974) Laser Anenometer Measurements of Trailing Vortices in Water, *J. Fluid Mech.*, Vol. 65, part 2, pp. 325-336.
- Batchelor, G. K. (1964) Axial Flow in Trailing Line Vortices, *J. Fluid Mech.*, Vol. 20, part 4, pp. 645-658.
- Bellamy-Knights, P. G. (1976) A Note on Vortex Breakdown in a Cylindrical Tube, *J. Fluids Eng.*, June, 1974, pp. 322-323.
- Bendat, J. S., and Piersol, A. G. (1986) Random Data Analysis and Measurement Procedures, Wiley and Sons.
- Benjamin, T. B. (1962) Theory of the Vortex Breakdown Phenomenon, *J. Fluid Mech.*, Vol. 14, No. 4, pp. 593-629.
- Benjamin, T. B. (1965) Significance of the Vortex Breakdown Phenomenon, *J. Basic Eng.*, June, 1965, pp. 518-524.
- Bossel, H. H. (1969) Vortex Breakdown Flowfield, *Phys. Fluids*, Vol. 12, No. 3, pp. 498-508.
- Bradshaw, P. (1971) An Introduction to Turbulence and its Measurement, Pergamon Press Ltd., Headington Hill Hall, Oxford.

Bradshaw, P. (1994) Turbulence: The Chief Outstanding Difficulty of our Subject, *Exp. in Fluids*, No. 16, pp. 203-216.

Bradshaw, P. (1996) Understanding and Prediction of Turbulent Flow, *Int. J. Heat and Fluid Flow*, Vol. 18, pp. 45-54.

Browne, L. W. B., Antonia, R. A., and Shah, D. A. (1987) Turbulent Energy Dissipation in a Wake, *J. Fluid Mech.*, Vol. 179, pp. 307-326.

Brücker, C. (1993) Study of Vortex Breakdown by Particle Tracking Velocimetry (PTV) Part 2: Spiral-Type Vortex Breakdown, *Exp. in Fluids*, Vol. 14, pp. 133-139.

Brücker, C. and Althaus, W. (1992) Study of Vortex Breakdown by Particle Tracking Velocimetry (PTV) Part 1: Bubble-Type Vortex Breakdown, *Exp. in Fluids*, Vol. 13, pp. 339-349.

Caughey, S.J., and Palmer, S.G. (1979) Some Aspects of Turbulence Structure Through the Depth of the Convective Boundary Layer, *Quart. J. R. Met. Soc.*, Vol. 185, pp. 811-827.

Chao, Y. C., Leu, J. H., Hung, Y. F., and Lin, C. K. (1991) Downstream Boundary Effects on the Spectral Characteristics of a Swirling Flowfield, *Exp. in Fluids*, No. 10, pp. 341-348.

Chow, J. S., Zilliac, G. G., and Bradshaw, P. (1997) Mean and Turbulence Measurements in the Near Field of a Wingtip Vortex, *AIAA J.*, Vol. 35, No. 10, pp. 1561-1567.

Corsiglia, V.R., Schwind, R.G., and Chigier, N.A. (1973) Rapid Scanning, Three-Dimensional Hot Wire Anemometer Surveys of Wing-tip Vortices, *J. Aircraft*, Vol. 10, No. 12.

Dahm, W. J. A., and Southerland, K. B. (1997) Experimental Assessment of Taylor's Hypothesis and its Applicability to Dissipation Estimates in Turbulent Flows, *Phys. Fluids*, Vol. 9, No. 7, pp. 2101-2107.

Delery, J. M. (1994) Aspects of Vortex Breakdown, *Prog. Aerospace Sci.*, Vol. 30, pp. 1-59.

Deng, Q., and Gursul, I. (1997) Vortex Breakdown over a Delta Wing with Oscillating Leading Edge Flaps, *Experiments in Fluids*, No. 23, pp. 347-352.



- Devenport, W. J., Rife, M. C., Liapis, S. I., and Follin, G. J. (1996) The Structure and Development of a Wing-tip Vortex, *J. Fluid Mech.*, Vol. 312, pp. 67-106.
- Doviak, R. J., and Zrníc, D. S. (1993) *Doppler Radar and Weather Observations*, 2nd Ed., Academic Press, Inc.
- Eisele, K., Zhang, Z., Casey, M. V., Gulich, J., and Schachenmann, A. (1997) Flow Analysis in a Pump Diffuser- Part 1: LDA and PTV Measurements of the Unsteady Flow, *J. Fluids Eng.* Vol. 119, pp. 968-977.
- Elsner, J. W., and Elsner, W. (1996) On the Measurement of Turbulence Energy Dissipation, *Meas. Sci. Technology*, Vol. 7, pp. 1334-1348.
- Escudier, M. (1988) Vortex Breakdown: Observations and Explanations, *Prog. Aerospace Sci.*, Vol. 25, pp. 189-229.
- Faler, J. H. (1976) Some Experiments in Swirling Flows: Detailed Velocity Measurements of a Vortex Breakdown using a Laser Doppler Anemometer, NASA CR-13115.
- Faler, J. H., and Leibovich, S. (1978) An Experimental Map of the Internal Structure of a Vortex Breakdown, *J. Fluid Mech.*, Vol. 86, part 2, pp. 313-335.
- Garg, A. K., and Liebovich, S. (1979) Spectral Characteristics of Vortex Breakdown Flowfields, *Phys. Fluids*, Vol. 22, No. 11, pp. 2053-2064.
- Green, S. I., and Acosta, A. J. (1991) Unsteady Flow in Trailing Vortices, *J. Fluid Mechanics*, Vol. 227, pp. 107-134.
- Gursul, I. (1995) Criteria for Location of Vortex Breakdown over Delta Wings, *Aeronautical Journal*, May, 1995, pp. 194-196.
- Gursul, I. (1996) Effect of Nonaxisymmetric Forcing on a Swirling Jet with Vortex Breakdown, *J. Fluids Eng.*, Vol. 118, pp. 316-321.
- Hall, M. G. (1972) Vortex Breakdown, *Annual Review of Fluid Mechanics*, Vol. 4, pp. 195-218.
- Hanjalic, K. (1994) Advanced Turbulence Closure Models: A View of Current Status and Future Prospects, *Int. J. Heat and Fluid Flow*, Vol. 15, No. 3, pp. 178-203.



- Harvey, J. K. (1962) Some Observations of the Vortex Breakdown Phenomenon, *J. Fluid Mech.*, Vol. 14, part 4, pp. 585-592.
- Hinze, J. O. (1975) Turbulence, Second Edition, McGraw Hill Series in Mechanical Engineering.
- Hogg, S., and Leschziner, M. A. (1989) Computation of Highly Swirling Confined Flow with a Reynolds Stress Turbulence Model, *AIAA J.*, Vol. 27, No. 1, pp. 57-63.
- Howard, L. N., and Gupta, A. S. (1962) On the Hydrodynamic and Hydromagnetic Stability of Swirling Flows, *J. Fluid Mech.*, Vol. 14, pp. 463-476.
- Jones, W. P., and Pascau, A. (1989) Calculation of Confined Swirling Flows with a Second Moment Closure, *J. Fluids Eng.*, Vol. 111, pp. 248-255.
- Kaimal, J. C., Wyngaard, J. C., Izumi, Y., and Cote, R. (1972) Spectral Characteristics of Surface-Layer Turbulence, *Quarterly J. R. Meteorological Soc.*, Vol. 98, pp. 563-589.
- Kihm, K. D., Chigier, N., and Sun, F. (1990) Laser Doppler Velocimetry Investigation of Swirler Flowfields, *J. Propulsion*, Vol. 6, No. 4, pp. 364-374.
- Klebanoff, P.S. (1954) Characteristics of Turbulence in a Boundary Layer with Zero Pressure Gradient, NACA Technical Note 3178.
- Kline, S. J. (1985) The Purposes of Uncertainty Analyses, *J. Fluids Eng.*, Vol. 107, pp. 153-160.
- Lai, Y. G. (1996) Predictive Capabilities of Turbulence Models for a Confined Swirling Flow, *AIAA J.*, Vol. 34, No. 8, pp. 1743-1745.
- Launder, B. E. (1989) Second-Moment Closure and its Use in Modelling Turbulent Industrial Flows, *Int. J. Num. Meth. Fluids*, Vol. 9, pp. 963-985.
- Launder, B. E., and Spalding, D. B. (1974) The Numerical Computation of Turbulent Flows, *Comp. Methods in Appl. Mechanics and Eng.*, Vol. 3, pp. 269-289.
- Lawn, C. J. (1971) The Determination of the Rate of Dissipation in Turbulent Pipe Flow, *J. Fluid Mech.*, Vol. 48, part 3, pp. 447-505.
- Leibovich, S. (1970) Weakly Non-linear Waves in Rotating Fluids, *J. Fluid Mech.*, Vol. 42, part 4, pp. 803-822.

- Leibovich, S. (1978) The Structure of Vortex Breakdown, *Annual Review of Fluid Mechanics*, Vol. 10, pp. 221-246.
- Lessen, M. , Singh, P. J., and Paillet, F. (1974) The Stability of a Trailing Line Vortex. Part 1. Inviscid Theory, *J. Fluid Mech.*, Vol. 64, Part 4, pp. 753-763.
- Lilley, D. G. (1977) Swirl Flows in Combustion: A Review, *AIAA J.*, Vol. 15, No. 8, pp. 1063-1078.
- Ligrani, P. M., and Moffat, R. J. (86) Structure of Transitionally Rough and Fully Rough Turbulent Boundary Layers, *J. Fluid Mech.*, Vol. 162, pp. 69-98.
- Lowson, M. V., and Riley, A. J. (1995) Vortex Breakdown Control by Delta Wing Geometry, *J. Aircraft*, Vol. 32, No. 4, pp. 832-838.
- Ludwig, H. (1962) Zur Erklärung der Instabilität der über angestellten Deltaflügeln auftretenden freien Wirbelkerne, *Z. Flugwiss.*, Vol. 10, No. 6, pp. 242-249.
- Marvin, J. G. (1995) Perspective on Computational Fluid Dynamics Validation, *AIAA J.* Vol. 33, No. 10, pp. 1778-1787.
- Moffat, R. J. (1982) Contributions to the Theory of Single-Sample Uncertainty Analysis, *J. Fluids Eng.*, Vol. 104, pp. 250-260.
- Myose, R. Y., and Blackwelder, R. F. (1995) Control of Streamwise Vortices Using Selective Suction, *AIAA J.*, Vol. 33, No. 6, pp. 1076-1080.
- Nakamura, Y., and Uchida, S. (1987) Several Approaches to the Study of Vortex Breakdown, 2nd International Colloquium on Vortical Flows, BBC Research Center, Switzerland.
- Nezu, I., and Rodi, W. (1986) Open-channel Flow Measurements with a Laser Doppler Anemometer, *J. Hydraulic Eng.*, Vol. 112, No. 5.
- Nejad, A. S., Vanka, S. P., Favaloro, S. C., Samimy, M., and Langenfeld, C. (1989) Application of Laser Velocimetry for Characterization of Confined Swirling Flow, *J. Fluids Eng.*, Vol. 111, pp. 36-45.
- Parmenter, K. , and Rockwell, D. (1990) Transient Response of Leading-Edge Vortices to Localized Suction, *AIAA J.*, Vol. 28, No. 6, pp. 1131-1133.

- Okwuobi, P. A. C., and Azad, R. S. (1973) Turbulence in a Conical Diffuser with Fully Developed Flow at Entry, *J. Fluid Mech.*, Vol. 57, No. 3, pp. 603-622.
- Rodi, W., Ferziger, J. H., Breuer, M., and Pourquie, M. (1997) Status of Large Eddy Simulation: Results of a Workshop, *J. Fluids Eng.*, Vol. 119, pp. 248-262.
- Rusak, Z. (1998). The Interaction of Near-Critical Swirling Flows in a Pipe with Inlet Azimuthal Vorticity Perturbations. *Phys. Fluids*, Vol. 10, No. 7, pp. 1672-1684.
- Rusak, Z., Judd, K. P., and Wang, S. (1997a) The Effect of Small Pipe Divergence on Near Critical Swirling Flows. *Phys. Fluids*, Vol. 9, No. 8, pp. 2273-2285.
- Rusak, Z., Wang, S., and Whiting, C. (1996) Numerical Computations of Axisymmetric Vortex Breakdown in a Pipe, AIAA Paper No. 96-0801.
- Rusak, Z., Wang, S., and Whiting, C. H. (1998). The Evolution of a Perturbed Vortex in a Pipe to Axisymmetric Vortex Breakdown. *J. Fluid Mech.*, Vol. 366, pp. 211-237.
- Rusak, Z., Whiting, C. H., and Wang, S. (1997b) Axisymmetric Breakdown of a Q-Vortex in a Pipe, AIAA Paper No. 97-0441.
- Sarpkaya, T. (1971a) On Stationary and Travelling Vortex Breakdowns, *J. Fluid Mech.*, Vol. 45, part 3, pp. 545-559.
- Sarpkaya, T. (1971b) Vortex Breakdown in Swirling Conical Flows, *AIAA J.*, Vol. 9, No. 9, pp. 1792-1799.
- Sarpkaya, T. (1974) Effect of the Adverse Pressure Gradient on Vortex Breakdown, *AIAA J.*, Vol. 12, No. 5, pp. 602-607.
- Sarpkaya, T. (1995a) Turbulent Vortex Breakdown, *Phys. Fluids*, Vol. 7, No. 10, pp. 2301-2303.
- Sarpkaya, T. (1995b) Vortex Breakdown and Turbulence. AIAA Paper No. 95-0433.
- Sarpkaya, T. (1998) Decay of Wake Vortices of Large Aircraft, AIAA Paper No. 98-0592.
- Schenck, T., Petrovic, D.V., Jovanovic, J., and Durst, F. (1998) Turbulent Dissipation Measurements in a Plane Wake Flow, *Proceedings of FEDSM '98*, ASME Fluids Engineering Division Summer Meeting, June 21-25, Washington, D.C.



- Spall, R. E. (1996) Transition from Spiral- to Bubble- Type Vortex Breakdown, *Phys. Fluids*, Vol. 8, No. 5, pp. 1330-1332.
- Spall, R. E., Gatski, T. B., and Ash, R. L. (1990) The Structure and Dynamics of Bubble-type Vortex Breakdown, *Proc. R. Soc. London A*, Vol. 429, pp. 613-637.
- Spall, R. E., Gatski, T. B., and Grosch, C. E. (1987) A Criterion for Vortex Breakdown, *Phys. Fluids*, Vol. 30, No. 11, pp. 3434-3440.
- Spall, R. E., and Gatski, T. B. (1995) Numerical Calculations of Three-dimensional Turbulent Vortex Breakdown, *Int. Journal for Num. Methods in Fluids*, Vol. 20, pp. 307-318.
- Spall, R. E., and Gatski, T. B. (1991) A Computational Study of the Topology of Vortex Breakdown, *Proc. R. Soc. Lond. A*, Vol. 435, pp. 321-337.
- Squire, H. B. (1960) Analysis of the Vortex Breakdown Phenomenon. Part 1, Imperial College of Science and Technology, Aeronautics Department Report No. 102.
- Stuart, J. T. (1987) A Critical Review of Vortex-Breakdown Theory, *Vortex Control and Breakdown Behaviour*, Second International Colloquium on Vortical Flows, Baden, Switzerland, April 6-7, 1987.
- Suematsu, Y., Ito, T., Niimi, T., and Nakamura, T. (1982) Vortex Breakdown Phenomena in a Circular Pipe, *Bulletin of the JSME*, Vol. 25, No. 199, pp. 38-45.
- Syred, N., and Beer, J. M. (1974) Combustion in Swirling Flows: A Review, *Combustion and Flame*, Vol. 23, pp. 143-201.
- Tennekes, H., and Lumley, J. L. (1972) A First Course in Turbulence, MIT Press, Cambridge, MA.
- Uchida, S., Nakamura, Y., and Ohshawa, M. (1985) Experiments on the Axisymmetric Vortex Breakdown in a Swirling Air Flow, *Trans. Japan Soc. Aero. Space Sci.*, Vol. 27, No. 78, pp. 206-216.
- Virk, H. P. S., and Azad, R. S. (1992) Corroboration of the New Method of Obtaining Dissipation in Wake Flow, *AIAA J.*, Vol. 30, No. 4, pp. 982-987.
- Volkert, J., Tropea, C., Domann, R., and Hubner, W. (1996) Combined Application of Particle Imaging Velocimetry (PIV) and Laser Doppler Anenometry (LDA) to Swirling

Flows under Compression, 8th Int. Symp. on Appl. of Laser Techniques to Fluid Mechanics.

Wang, S., and Rusak, Z. (1996a). On the Stability of an Axisymmetric Rotating Flow in a Pipe. *Phys. Fluids*, Vol. 8, No. 4, pp. 1007-1016.

Wang, S., and Rusak, Z. (1996b). On the Stability of Non-columnar Swirling Flows. *Phys. Fluids*, Vol. 8, No. 4, pp. 1017-1023.

Wang, S., and Rusak, Z. (1997a). The Effect of Slight Viscosity on a Near-critical Swirling Flow in a Pipe. *Phys. Fluids*, Vol. 9, No. 7, pp. 1914-1927.

Wang, S., and Rusak, Z. (1997b). The Dynamics of a Swirling Flow in a Pipe and Transition to Axisymmetric Vortex Breakdown. *J. Fluid Mech.*, Vol. 340, pp. 177-223.

Westphal, R. V., and Mehta, R. D. (1989) Interaction of an Oscillating Vortex with a Turbulent Boundary Layer, *Exp. in Fluids*, Vol. 7, pp. 405-411.

Yadav, A. K., Raman, S., and Sharan, M. (1996) Surface Layer Turbulence Spectra and Dissipation Rates During Low Winds in the Tropics, *Boundary-Layer Meteorology*, Vol. 79, pp. 205-223.

Yang, H., and Gursul, I. (1997) Vortex Breakdown over Unsteady Delta Wings and its Control, *AIAA J.*, Vol. 35, No. 3, pp. 571-574.

Zhang, Z., Eilele, K., and Hirt, F. (1997) The Influence of Phase-Averaging Window size on the Determination of Turbulence Quantities in Unsteady Turbulent Flows, *Exp. in Fluids*, Vol. 22, pp. 265-267.



## INITIAL DISTRIBUTION LIST

	No. Copies
1. Defense Technical Information Center.....2 8725 John J. Kingman Rd., STE 0944 Ft. Belvoir, VA 22060-6218	
2. Dudley Knox Library.....2 Naval Postgraduate School 411 Dyer Rd. Monterey, CA 93943-5101	
3. Department Chairman, Code ME..... 2 Department of Mechanical Engineering Naval Postgraduate School Monterey, CA 93943-5000	
4. Professor T. Sarpkaya, Code ME-SL ..... 5 Department of Mechanical Engineering Naval Postgraduate School Monterey, CA 93943-5000	
5. Curricular Officer, Code 34..... 1 Department of Mechanical Engineering Naval Postgraduate School Monterey, CA 93943-5000	
6. Curricular Officer, Code 33..... 1 Department of Combat Systems Naval Postgraduate School Monterey, CA 93943-5000	
7. LCDR Francis G. Novak..... 2 Division 334 Office of Naval Research 800 N. Quincy St. Arlington, VA 22217-5660	





3

483NP6  
TH

2544

10/99 22527-200

10/99

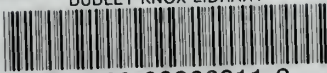








DUDLEY KNOX LIBRARY



3 2768 00366811 2